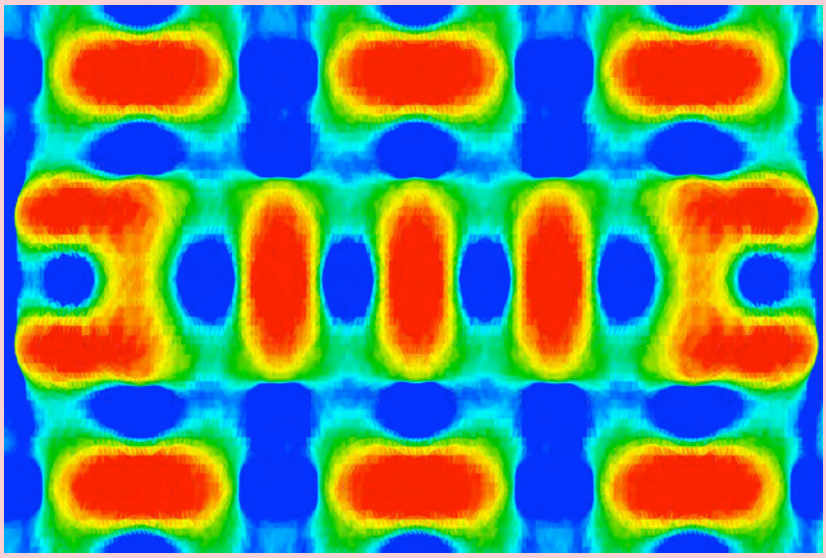
ISSN 2188-5001

MATERIALS DESIGN AND
CHARACTERIZATION LABORATORY

SUPERCOMPUTER CENTER

ACTIVITY REPORT 2024



THE UNIVERSITY OF TOKYO

Materials Design and Characterization Laboratory (MDCL)

The MDCL was established as the third research facility of the Institute for Solid State Physics (ISSP) when the latter was reorganized in May 1996. Its aim is to promote material science with an emphasis on the "DSC cycle", where DSC stands for design, synthesis and characterization, three processes for developing new materials.

The MDCL consists of two sections, Materials Design (MD) section and Materials Synthesis and Characterization (MSC) section. The Supercomputer Center of the ISSP (SCC-ISSP) is placed in the MD section, while in the MSC section there are seven laboratories for joint use; Materials Synthesis Laboratory, Chemical Analysis Laboratory, X-ray Diffraction Laboratory, Electron Microscope Laboratory, Electromagnetic Measurement Laboratory, Spectroscopy Laboratory, and High-Pressure Synthesis Laboratory.

Almost all the facilities of the MDCL are open to scientists in Japan through the User Programs conducted by two steering committees of the MDCL. One is the steering committee of the SCC-ISSP, under which the Supercomputer Project Advisory Committee is placed for reviewing proposals. The other is the steering committee of the MSC facilities. More than half of the members of these committees are from the outside of ISSP.

COVER FIGURE

Color Map of regional chemical potential on a diamond surface.
See Page 16–23, M. FUKUDA, "Surface Structure Analysis and Atomic Force Microscopy Simulation Using DFT".

PREFACE

The Supercomputer Center (SCC) is a part of the Materials Design and Characterization Laboratory (MDCL) of ISSP. Its mission is to serve the whole community of computational condensed-matter physics of Japan providing it with high performance computing environment. In particular, the SCC selectively promotes and supports large-scale computations. For this purpose, the SCC invites proposals for supercomputer-aided research projects and hosts the Steering Committee, as mentioned below, that evaluates the proposals.

The ISSP supercomputer system consists of two subsystems: System B, which was last replaced in Oct. 2020, is intended for larger total computational power and has more nodes with relatively loose connections whereas System C is intended for higher communication speed among nodes. System B (ohtaka) consists of 1680 CPU nodes of AMD EPYC 7702 (64 cores) and 8 FAT nodes of Intel Xeon Platinum 8280 (28 cores) with total theoretical performance of 6.881 PFlops. System C was replaced in June 2022 and the current system (kugui) consists of 128 CPU nodes of AMD EPYC 7763 (64 cores) and 8 ACC nodes of AMD EPYC 7763 (64 cores) NVIDIA A100 40GB for HGX with total theoretical performance of 0.973 PFLOPS.

In addition to the hardware administration, the SCC puts increasing effort on the software support. Since 2015, the SCC has been conducting “Project for advancement of software usability in materials science (PASUMS).”In this project, for enhancing the usability of the ISSP supercomputer system, we conduct several software-advancement activities: developing new application software that runs efficiently on the ISSP supercomputer system, adding new functions to existing codes, help releasing private codes for public use, creating/improving manuals for public codes, etc. Two target programs were selected for fiscal year 2024: (1) ODAT-SE (proposal made by T. Hoshi (National Institute for Fusion Science)), and (2) DCore (proposal made by J. Otsuki (Okayama Univ.)). In addition, since 2021, we have been maintaining the data repository service for secure storage and enhanced usability of results of numerical calculation.

All staff members of university faculties or public research institutes in Japan are invited to propose research projects (called User Program). The proposals are evaluated by the Steering Committee of SCC. Peer-reviewing is done by the Supercomputer Project Advisory Committee. In fiscal year 2024, totally 374 projects were approved including the ones under the framework of Supercomputing Consortium for Computational Materials Science (SCCMS), which specially supports FUGAKU and other major projects in computational materials science.

The research projects are roughly classified into the following three (the number of projects approved):

First-Principles Calculation of Materials Properties (190)
Strongly Correlated Quantum Systems (34)
Cooperative Phenomena in Complex, Macroscopic Systems (141)
SCCMS projects (9)

In all the three categories, most proposals involve both methodology and applications. The results of the projects are reported in 'Activity Report 2024' of the SCC. Every year 3-4 projects are selected for “invited papers” and published at the beginning of the Activity Report. In the Activity Report 2024, the following three invited papers are included:

“Surface Structure Analysis and Atomic Force Microscopy Simulation Using DFT”,
Masahiro FUKUDA (ISSP)

“Magnetic-Field Control of Visons in Kitaev Quantum Spin Liquids under Energy Dissipation”
Chihiro HARADA, Atsushi ONO, and Joji NASU (Tohoku Univ.)

“Development of Open Data Analysis Tool for Science and Engineering (ODAT-SE)”
Takeo HOSHI, Akito NAKANO (National Institute for Fusion Science), Tatsumi AOYAMA, Yuichi MOTOYAMA, and Kazuyoshi YOSHIMI (ISSP)

June 16, 2025

Naoki Kawashima
(Chairman of the steering committee, SCC, ISSP)

CONTENTS

PREFACE

1 OUTLINE **1**

1.1 Supercomputer System 1
1.2 Project Proposals 1
1.3 Committees 3
1.4 Staff 7

2 STATISTICS (SCHOOL YEAR 2024) **7**

2.1 System and User Statistics 7
2.2 Queue and Job Statistics 8
2.3 Project for Advancement of Software Usability in Materials Science 11
2.4 ISSP Data Repository 11

3 RESEARCH REPORTS **15**

3.1 Invited Articles 15
3.2 First-Principles Calculation of Material Properties 40
3.3 Strongly Correlated Quantum Systems 211
3.4 Cooperative Phenomena in Complex Macroscopic Systems 246
3.5 SCCMS Projects 367
3.6 Software Advancement Projects and Workshop Support 377

4 PUBLICATION LIST **383**

ISSP Joint Research Projects 384
SCCMS Projects 437

5 THESES **439**

Doctor Theses 440
Master Theses 443

1 OUTLINE

1.1 Supercomputer System

In School year 2024 (SY 2024), the ISSP supercomputer center provided users with System B - Dell PowerEdge C6525/R940 system named "ohtaka" and System C - HPE Apollo 2000 Gen10 Plus/HPE Apollo 6500 Gen10 Plus system named "kugui". System B is a massively-parallel supercomputer with two types of compute nodes: 8 "Fat" nodes and 1680 "CPU" nodes. "Fat" nodes are each comprised of four Intel Xeon Platinum 8280 CPUs (28 cores/CPU) and 3 TB of memory per node. "CPU" nodes have two AMD EPYC 7702 CPUs (64 cores/CPU) and 256 GB of memory per node. System B achieves about 6.881 PFLOPS in theoretical peak performance with high power efficiency. The subsystem comprised of only CPU nodes ranks 87st in the Nov. 2020 Top 500 List, which is a ranking based on total performance measured by the HPL benchmark. The compute nodes communicate to each other through HDR100 Infiniband and are connected in fat tree topology. SY 2024 was the fifth year of the operation of the current System B. System C is a massively-parallel supercomputer with two types of compute nodes: 128 "CPU" nodes and 8 "ACC" nodes. "CPU" nodes are each comprised of two AMD EPYC 7763 CPUs (64 cores/CPU) and 256 GB of memory. The compute nodes communicate to each other through HDR200 Infiniband and are connected in fat tree topology. "ACC" nodes are each comprised of one AMD EPYC 7763 CPUs (64 cores/CPU), four NVIDIA A100 40GB for HGX GPUs and 256 GB of memory. System C achieves 973 TFLOPS in theoretical peak performance. SY 2024 was the third year of the operation of the current System C. As shown in Fig. 1, users can access both systems via the Internet using SSH public key authentication. For further details, please contact ISSP Supercomputer Center (SCC-ISSP).

[Correspondence: center@issp.u-tokyo.ac.jp]

1.2 Project Proposals

The ISSP supercomputer system provides computation resources for scientists working on condensed matter sciences in Japan. All scientific staff members (including post-docs) at universities or public research institutes in Japan can submit proposals for projects related to research activities on materials and condensed matter sciences. These proposals are peer-reviewed by the Advisory Committee members (see Sec. 1.3), and then the computation resources are allocated based on the review reports. The leader of an approved project can set up user accounts for collaborators. Other types of scientists, including graduate students, may also be added. Proposal submissions, peer-review processes, and user registration are all managed via a web system.

The computation resources are distributed in a unit called "point", determined as a function of available CPU utilization time and consumed disk resources. There

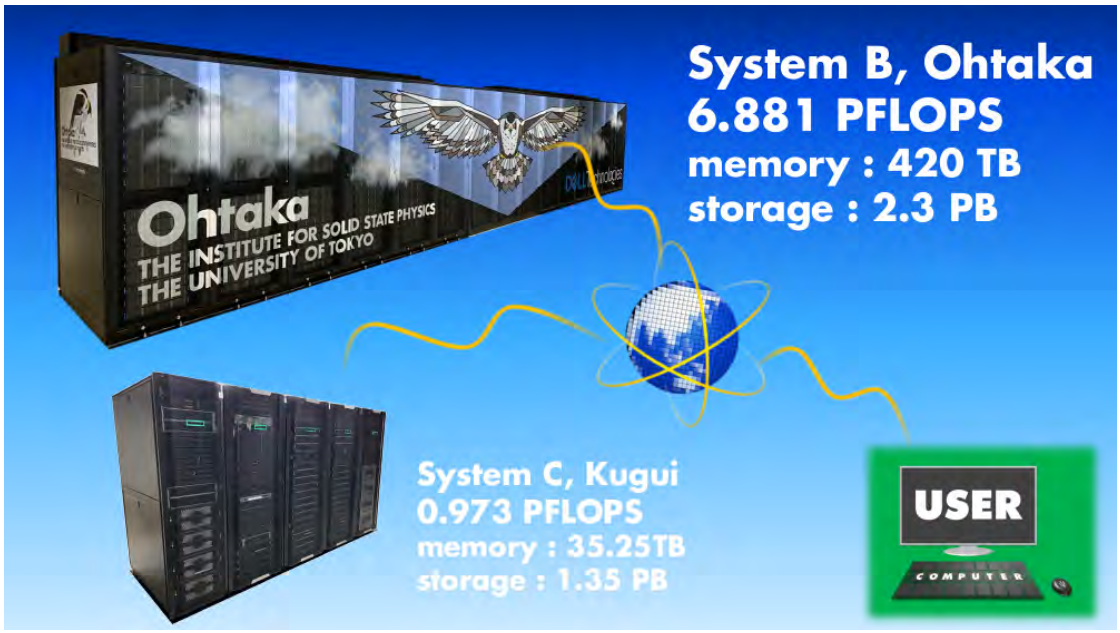


Figure 1: Supercomputer System at the SCC-ISSP

were calls for six classes of research projects in SY 2024. The number of projects and the total number of points that were applied for and approved in this school year are listed in Table 1.

- Class A is for trial use by new users; proposals for Class A projects are accepted throughout the year.
- Proposals for projects in Classes B (small), C (mid-size), E (large-scale), and S (exceptional) can be submitted twice a year. Approved projects in Classes A, B, C, and E continue to the end of the school year.
- In Class D, projects can be proposed on rapidly-developing studies that need to perform urgent and relatively large calculations. An approved project continues for 6 months from its approval.
- Class S is for projects that are considered extremely important for the field of condensed matter physics and requires extremely large-scale computation. The project may be carried out either by one research group or cooperatively by several investigators at different institutions. A project of this class should be applied with at least 10,000 points; there is no maximum. We require group leaders applying for Class S to give a presentation on the proposal to the Steering Committee of the SCC-ISSP. Class S projects are carried out within one year from its approval.
- Project leaders can apply for points so that the points for each system do not exceed the maximum point shown in this table.

Table 1: Classes of research projects in SY 2024. Total points listed in this table are rounded. In Class D, we collect information about the projects ended in each semester.

Class	Maximum Points		Application	# of Proj.	Total points			
					Applied		Approved	
	Sys–B	Sys–C			Sys–B	Sys–C	Sys–B	Sys–C
A	100	50	any time	28	2.8k	1.4k	2.8k	1.4k
B	650	100	twice a year	116	68.7k	7.7k	45.0k	6.2k
C	6.5k	500	twice a year	189	968.4k	57.7k	524.2k	41.5k
D	10k	500	any time	10	50.5k	3.3k	38.6k	2.4k
E	20k	1.5k	twice a year	22	401.0k	28.1k	209.0k	19.2k
S	–	–	twice a year	0	0	0	0	0
SCCMS				9	21.0k	1.7k	21.0k	1.7k
Total				374	1512.4k	99.9k	840.6k	72.4k

In addition, from SY 2016, ISSP Supercomputer has been providing 20% of its computational resources for Supercomputing Consortium for Computational Materials Science (SCCMS), which aims at advancing parallel computations in condensed matter, molecular, and materials sciences on the 10-PFlops K Computer and the exascale post-K project. From SY 2020, up to 10% of the computational resources have been provided for SCCMS. Computational resources have also been allotted to Computational Materials Design (CMD) workshops, as well as CCMS hands-on workshops.

1.3 Committees

In order to fairly manage the projects and to smoothly determine the system operation policies, the Materials Design and Characterization Laboratory (MDCL) of the ISSP has organized the Steering Committee of the MDCL and the Steering Committee of the SCC-ISSP, under which the Supercomputer Project Advisory Committee (SPAC) is formed to review proposals. The members of the committees in SY 2024 were as follows:

Steering Committee of the MDCL

OKAMOTO, Yoshihiko	ISSP (Chair person)
KAWASHIMA, Naoki	ISSP
YAMAURA, Jun-ichi	ISSP
OZAKI, Taisuke	ISSP
NOGUCHI, Hiroshi	ISSP
KITAGAWA, Kentaro	ISSP
SUGINO, Osamu	ISSP
KUBO, Momoji	Tohoku Univ.

HUKUSHIMA, Koji	Univ. of Tokyo
OHGUSHI, Kenya	Tohoku Univ.
NUNOURA, Teppei	Univ. of Tokyo
OTSUKI, Junya	Okayama Univ.
OBA, Fumiyasu	Science Tokyo
KUDO, Kazutaka	Osaka Univ.
MATSUDA, Tatsuma	Tokyo Metropolitan Univ.

Steering Committee of the SCC-ISSP

KAWASHIMA, Naoki	ISSP (Chair person)
NOGUCHI, Hiroshi	ISSP
OZAKI, Taisuke	ISSP
SUGINO, Osamu	ISSP
TSUNETSUGU, Hirokazu	ISSP
KATO, Takeo	ISSP
NAKAJIMA, Taro	ISSP
FUKUDA, Masahiro	ISSP
IDO, Kota	ISSP
NAKANO, Hiroyoshi	ISSP
TAKAHASHI, Jun	ISSP
NAKAJIMA, Kengo	Univ. of Tokyo
OTSUKI, Junya	Okayama Univ.
YAMAJI, Youhei	NIMS
KASAMATSU, Shusuke	Yamagata Univ.
HUKUSHIMA, Koji	Univ. of Tokyo
KITAO, Akio	Science Tokyo
HAMADA, Ikutaro	Osaka Univ.
TODO, Synge	Univ. of Tokyo
KUBO, Momoji	Tohoku Univ.
OBA, Fumiyasu	Science Tokyo
WATANABE, Hiroshi	Keio Univ.
YOSHIMI, Kazuyoshi	ISSP
YATA, Hiroyuki	ISSP
FUKUDA, Takaki	ISSP
MOTOYAMA, Yuichi	ISSP

Supercomputer Project Advisory Committee

KAWASHIMA, Naoki	ISSP (Chair person)
OZAKI, Taisuke	ISSP
NOGUCHI, Hiroshi	ISSP
SUGINO, Osamu	ISSP
TSUNETSUGU, Hirokazu	ISSP
NAKAJIMA, Taro	ISSP

KATO, Takeo	ISSP
FUKUDA, Masahiro	ISSP
IDO, Kota	ISSP
NAKANO, Hiroyoshi	ISSP
TAKAHASHI, Jun	ISSP
NAKAJIMA, Kengo	Univ. of Tokyo
TODO, Synge	Univ. of Tokyo
KUBO, Momoji	Tohoku Univ.
OBA, Fumiyasu	Science Tokyo
WATANABE, Hiroshi	Keio Univ.
HUKUSHIMA, Koji	Univ. of Tokyo
OTSUKI, Junya	Okayama Univ.
KITAO, Akio	Science Tokyo
HAMADA, Ikutaro	Osaka Univ.
KASAMATSU, Shusuke	Yamagata Univ.
YAMAJI, Youhei	NIMS
SHIBATA, Naokazu	Tohoku Univ.
AKAGI, Kazuto	Tohoku Univ.
YANASE, Yoichi	Kyoto Univ.
HATSUGAI, Yasuhiro	Univ. of Tsukuba
OKADA, Susumu	Univ. of Tsukuba
KOBAYASHI, Nobuhiko	Univ. of Tsukuba
HOTTA, Takashi	Tokyo Metropolitan Univ.
MATSUKAWA, Hiroshi	Aoyama Gakuin Univ.
YAMAUCHI, Jun	Keio Univ.
HAGITA, Katsumi	National Defense Academy
KONTANI, Hiroshi	Nagoya Univ.
YUKAWA, Satoshi	Osaka Univ.
SUGA, Seiichiro	Univ. of Hyogo
YASUDA, Chitoshi	Univ. of the Ryukyus
KIM, Kang	Osaka Univ.
MORIKAWA, Yoshitada	Osaka Univ.
KOGA, Akihisa	Science Tokyo
SHIMOJO, Fuyuki	Kumamoto Univ.
TAKETSUGU, Tetsuya	Hokkaido Univ.
TSURUTA, Kenji	Okayama Univ.
HAMAGUCHI, Satoshi	Osaka Univ.
NISHIDATE, Kazume	Iwate Univ.
KAGESHIMA, Hiroyuki	Shimane Univ.
ISHII, Fumiyuki	Kanazawa Univ.
TATETSU, Yasutomi	Meio Univ.
YANAGISAWA, Susumu	Univ. of the Ryukyus
SHUDO, Ken-ichi	Yokohama Natl. Univ.
OHMURA, Satoshi	Hiroshima Inst. Tech.
NOGUCHI, Yoshifumi	Shizuoka Univ.

NAKAMURA, Kazuma	Kyushu Inst. Tech.
GOHDA, Yoshihiro	Science Tokyo
RAEBIGER, Hannes	Yokohama Natl. Univ.
KAWARABAYASHI, Tohru	Toho Univ.
KATO, Yusuke	Univ. of Tokyo
NASU, Joji	Tohoku Univ.
HOTTA, Chisa	Univ. of Tokyo
ISOBE, Masaharu	Nagoya Inst. Tech.
TANAKA, Shu	Keio Univ.
HIGUCHI, Yuji	Kyushu Univ.
KAWAMURA, Mitsuaki	Univ. of Tokyo
MOTOME, Yukitoshi	Univ. of Tokyo
ONO, Tomoya	Kobe Univ.
KOBAYASHI, Kazuaki	NIMS
TATEYAMA, Yoshitaka	NIMS
TAMURA, Ryo	NIMS
TADA, Tomofumi	Kyushu Univ.
HATANO, Naomichi	Univ. of Tokyo
YOSHINO, Hajime	Osaka Univ.
OKUMURA, Hisashi	NINS-ExCELLS
HOSHI, Takeo	NIFS-PQP
TSUNEYUKI, Shinji	Univ. of Tokyo
SUZUKI, Takafumi	Univ. of Hyogo
YOSHIMOTO, Yoshihide	Univ. of Tokyo
TOHYAMA, Takami	Tokyo Univ. of Sci.
ARITA, Ryotaro	Univ. of Tokyo
OGATA, Masao	Univ. of Tokyo
WATANABE, Satoshi	Univ. of Tokyo
YABANA, Kazuhiro	Univ. of Tsukuba
FURUKAWA, Nobuo	Aoyama Gakuin Univ.
KUROKI, Kazuhiko	Osaka Univ.
TANAKA, Yukio	Nagoya Univ.
KUSAKABE, Koichi	Univ. of Hyogo
SAKAI, Toru	Univ. of Hyogo
ISHIBASHI, Shoji	AIST
OTANI, Minoru	Univ. of Tsukuba
TOMITA, Yusuke	Shibaura Inst. Tech.
SHIRAISHI, Kenji	Nagoya Univ.
OGUCHI, Tamio	Osaka Univ.
KAWAKATSU, Toshihiro	Tohoku Univ.
OTSUKI, Tomi	Sophia Univ.
ODA, Tatsuki	Kanazawa Univ.
ARAI, Noriyoshi	Keio Univ.
UNEYAMA, Takashi	Nagoya Univ.
MORITA, Satoshi	Keio Univ.

FUKUSHIMA, Tetsuya	AIST
HAYAMI, Satoru	Hokkaido Univ.
NOMURA, Yusuke	Tohoku Univ.
TSUJI, Yuta	Kyushu Univ.
NOZAWA, Kazuki	Kagoshima Univ.
TEN-NO, Seiichiro	Kobe Univ.
SEINO, Kaori	Kyushu Inst. Tech.
OHNISHI, Masato	Univ. of Tokyo
SHINODA, Wataru	Oakayama Univ.

1.4 Staff

The following staff members of the SCC-ISSP usually administrate the ISSP Supercomputer.

KAWASHIMA, Naoki	Professor (Chair person)
NOGUCHI, Hiroshi	Associate Professor
OZAKI, Taisuke	Professor
SUGINO, Osamu	Professor
IDO, Kota	Research Associate
FUKUDA, Masahiro	Research Associate
NAKANO, Hiroyoshi	Research Associate
TAKAHASHI, Jun	Research Associate
YOSHIMI, Kazuyoshi	Project Researcher
AOYAMA, Tatsumi	Project Researcher
MOTOYAMA, Yuichi	Technical Specialist
YATA, Hiroyuki	Technical Specialist
FUKUDA, Takaki	Technical Specialist
ARAKI, Shigeyuki	Project Academic Specialist

2 STATISTICS (SCHOOL YEAR 2024)

2.1 System and User Statistics

In the following, we present statistics for operation time taken in the period from April 1st 2024 to March 31th 2025 (SY 2024). In Table 2, we show general statistics of the supercomputer system in SY 2024. The total numbers of compute nodes in System B "ohtaka" and System C "kugui" are 1688 and 136, respectively. Consumed disk points amount to about a few percent of the total consumed points in both System B and System C.

In Fig. 2, availabilities, utilization rates, and consumed points in Systems B and C are plotted for each month. Throughout the school year, the availability and the utilization rates were very high: the availability and the utilization rates

Table 2: Overall statistics of SY 2024

	System B ohtaka	System C kugui
total service time ($\times 10^3$ node·hours)	14377	1164
number of executed jobs	487879	149725
total consumed points ($\times 10^3$ point)	491	28
CPU points ($\times 10^3$ point)	466	27
disk points ($\times 10^3$ point)	25	1
total exec. time ($\times 10^3$ node·hours)	13232	1016
availability	97.76%	97.71%
utilization rate	91.47%	87.20%

exceed about 90% and 80% throughout most of the year, respectively. Note that the decline of the availabilities on Sep. is due to a planned power outage at ISSP.

The user statistics are shown in Fig. 3. The horizontal axis shows the rank of the user/group arranged in the descending order of the execution time (hour×nodes). The execution time of the user/group of the first rank is the longest. The vertical axis shows the sum of the execution time up to the rank. From the saturation points of the graphs, the numbers of "active" users of Systems B and C are around 500 and 100, respectively. The maximum ranks in the graphs correspond to the number of the users/groups that submitted at least one job.

2.2 Queue and Job Statistics

Queue structures of Systems B and C in SY 2024 are shown in Tables 3 and 4, respectively. In System B "ohtaka", users can choose from two types of compute nodes; jobs submitted to queues with "cpu" and "fat" at the end of their queue names are submitted to CPU and Fat nodes, respectively. In System C, there are two types of compute nodes: CPU and ACC nodes. Jobs submitted to queues with "cpu" and "acc" at the end of their queue names are submitted to CPU and ACC nodes, respectively, If users submit a job to queues with "accs" at the end of their queue names, the job runs in the ACC node shared by other jobs of "accs" queues. See Sec. 1.1 for a description of each type of compute node. The user then has to choose the queue according to the number of nodes to use and the duration of their calculation jobs. Queue names starting with "F" are for jobs taking 24 hours or less, while those starting with "L" can run much longer up to 120 hours. More nodes are allotted to "F" queues in order to maximize the turnaround time of user jobs. The queue names starting with "i" are used for interactive debugging of user programs and the elapsed time limit is 30 minutes. The number following "F", "L", or "i" correspond to the number of nodes that can be used by one user job. Although we do not mention here in detail, to promote utilization of the massively parallel supercomputer, background queues (queue name starting with "B") for

Table 3: Queue structures of System B in SY 2024

System B, ohtaka

queue name	Elapsed time limit (hr)	# of nodes /job	# of nodes /queue	Memory limit (GB)	job points /(node·day)
F1cpu	24	1	600	230/node	1
L1cpu	120	1	300	230/node	1
F4cpu	24	2–4	216	230/node	1
L4cpu	120	2–4	108	230/node	1
F16cpu	24	5–16	288	230/node	1
L16cpu	120	5–16	144	230/node	1
F36cpu	24	17–36	72	230/node	1
L36cpu	120	17–36	36	230/node	1
F72cpu	24	72	576	230/node	1
L72cpu	120	72	288	230/node	1
F144cpu	24	144	432	230/node	1
L144cpu	120	144	144	230/node	1
i8cpu	0.5	1–8	72	230/node	1
F2fat	24	1–2	7	2900/node	4
L2fat	120	1–2	3	2900/node	4
i1fat	0.5	1	1	2900/node	4

Systems B and C which charge no points for the jobs have also been open.

To prevent overuse of the storage, points are charged also for usage of disk quota in the systems, as shown in Table 5. Disk points are revised often for optimal usage of the resources by examining usage tendencies. Due to the increase in the number of user accounts, the long-term data storage space, `/home`, in System B has been used more than expected. Therefore, to limit its use, from August, the default disk quota of `/home` space in System B has been reduced from 600 GB to 300 GB. To compensate for the decrease in the disk quota, we started to operate a new disk space, `/home2`, in System B from October. This space has a disk quota of 300 GB for each user, but the capacity cannot be expanded as the other disk spaces. The data in `/home2` space are not deleted automatically as in `/home` space.

The number of jobs, average waiting time, and total execution time in each queue are shown in Tables 6 and 7. In Systems B and C, a large portion of jobs have been executed in "F" queues. The largest amount of the execution time has been consumed in "F72cpu" and "F1cpu" queues for Systems B and C, respectively. However, substantial number of jobs were run in every queue, suggesting that a wide variety of user needs are met by this queuing scheme. In most of these queues, the queue settings meet the user's tendencies in that the waiting times are on the order of the elapsed-time limit.

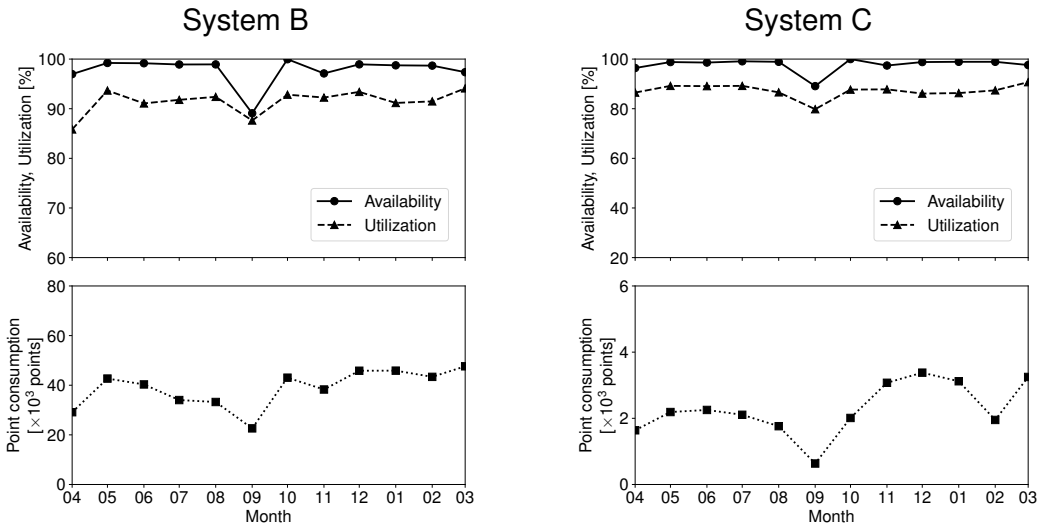


Figure 2: Availabilities, utilization rates and point consumptions of each month during SY 2024.

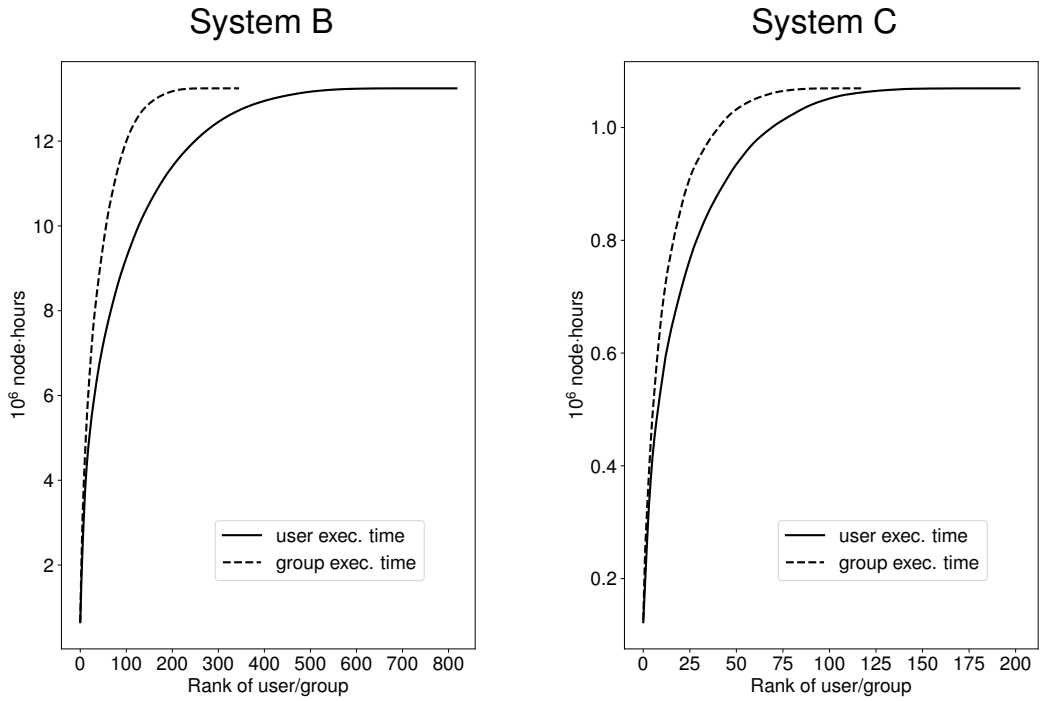


Figure 3: User statistics. The horizontal axis shows the rank of the user/group arranged in the descending order of the execution time (hour×nodes). The vertical axis shows the sum of the execution time up to the rank.

Table 4: Queue structures of System C in SY 2024

System C, kugui

queue name	Elapsed time limit (hr)	# of nodes /job	# of nodes /queue	Memory limit (GB)	job points /(node·day)
i2cpu	0.5	1–2	8	240/node	1
F1cpu	24	1	120	240/node	1
L1cpu	120	1	60	240/node	1
F4cpu	24	2–4	32	240/node	1
L4cpu	120	2–4	16	240/node	1
F16cpu	24	5–16	64	240/node	1
L16cpu	120	5–16	32	240/node	1
F1accs	24	1	3	$60\times N_{\mathrm{GPU}}$	1
L1accs	120	1	1	$60\times N_{\mathrm{GPU}}$	1
i1accs	0.5	1	1	$60\times N_{\mathrm{GPU}}$	1
F2acc	24	1–2	4	240/node	1
L2acc	120	1–2	2	240/node	1

* N_{GPU} in ACC queues denotes the number of occupied GPUs.

2.3 Project for Advancement of Software Usability in Materials Science

From School Year 2015, the supercomputer center (SCC) has started "Project for advancement of software usability in materials science". In this project, for enhancing the usability of the supercomputer system in ISSP, we perform some software-advancement activity such as implementing a new function to an existing code, releasing a private code on Web, writing manuals. Target programs are publicly offered in December and selected in the review by the Steering Committee of SCC. The projects are carried out by the software development team composed of three members in ISSP. In SY 2024, two projects were selected as listed in Table 8.

2.4 ISSP Data Repository

From School Year 2021, the supercomputer center (SCC) has started to operate ISSP Data Repository (ISSP-DR) for accumulating and utilizing research data in materials science. GitLab is used as the data management system, and a portal site is provided as a data registration and search system for the registered data. By using ISSP-DR, it is possible to store and publish research data used in pa-

Table 5: Disk points of Systems B and C

		point/day
System B ohtaka	`/home` (Apr.-Aug.)	$0.001 \times \theta(q - 600)$
	`/home` (Aug.-Mar.)	$0.001 \times \theta(q - 300)$
	`/work`	$0.0001 \times \theta(q - 6000)$
System C kugui	`/home`	$0.001 \times \theta(q - 150)$
	`/work`	$0.0001 \times \theta(q - 1500)$

* q is denoted in unit of GB.
* $\theta(x)$ is equal to the Heaviside step function $H(x)$ multiplied by x, i.e., $xH(x)$.

pers and datasets useful in the field of condensed matter science. Users of ISSP Supercomputer are welcome to apply for and use ISSP-DR.

Table 6: Number of jobs, average waiting time, total execution time, and average number of used nodes per job in each queue of System B.

System B, ohtaka

queue	# of Jobs	Waiting Time (hour)	Exec. Time ($\times 10^3$ node·hour)	# of nodes
F1cpu	76858	28.64	170.53	1.00
L1cpu	5036	41.31	94.34	1.00
F4cpu	150704	19.09	1298.27	2.53
L4cpu	5273	111.99	500.81	3.41
F16cpu	28042	31.12	1761.36	9.72
L16cpu	1699	83.33	528.83	10.44
F36cpu	1355	31.18	327.82	28.24
L36cpu	197	109.18	134.02	23.22
F72cpu	7843	52.14	3258.75	72.00
L72cpu	200	62.22	403.55	72.00
F144cpu	3169	26.37	1839.38	144.00
L144cpu	117	75.91	629.03	144.00
i8cpu	184887	0.12	150.22	4.78
F2fat	5390	61.47	29.75	1.15
L2fat	382	21.65	14.40	1.15
i1fat	2079	0.06	0.34	1.00

Table 7: Number of jobs, average waiting time, total execution time, and average number of used nodes per job in each queue of System C.

System C, kugui

queue	# of Jobs	Waiting Time (hour)	Exec. Time ($\times 10^3$ node·hour)	# of nodes
i2cpu	20797	2.75	4.23	1.56
F1cpu	34242	5.26	149.29	1.00
L1cpu	2919	15.58	95.08	1.00
F4cpu	6032	10.64	106.23	2.93
L4cpu	203	27.31	32.48	3.23
F16cpu	2446	18.58	136.02	9.57
L16cpu	156	17.46	47.59	10.85
i1accs	23756	0.51	3.13	1.00
F1accs	8340	24.86	54.53	1.00
L1accs	382	35.80	9.76	1.00
F2acc	4514	19.58	18.79	1.04
L2acc	113	14.76	3.34	1.08

Table 8: List of Project for advancement of software usability in materials science for SY 2024.

Project Proposer	Project Name
Takeo Hoshi National Institute for Fusion Science	Generalization of data-analysis framework for advanced measurements
Junya Otsuki Okayama University	Adding dynamical susceptibility calculation to dynamical mean-field software DCore

3 RESEARCH REPORTS

3.1 Invited Articles

Surface Structure Analysis and Atomic Force Microscopy Simulation Using DFT 16

Masahiro FUKUDA

Magnetic-Field Control of Visons in Kitaev Quantum Spin Liquids under Energy Dissipation 24

Chihiro HARADA, Atsushi ONO, and Joji NASU

Development of Open Data Analysis Tool for Science and Engineering (ODAT-SE) 32

Takeo HOSHI, Akito NAKANO, Tatsumi AOYAMA, Yuichi MOTOYAMA, and Kazuyoshi YOSHIMI

Surface Structure Analysis and Atomic Force Microscopy Simulation Using DFT

Masahiro FUKUDA
Institute for Solid State Physics, University of Tokyo
Kashiwa-no-ha, Kashiwa, Chiba 277-8581

Abstract

We review recent studies on the structure analysis of silicene on Ag(111) and diamond (001) surfaces using atomic force microscopy (AFM), its simulations based on density functional theory (DFT), and regional chemical potential (RCP) analysis. These studies are expected to contribute to atomic-scale material design and to the understanding of surface structures and their formation processes.

1 Introduction

In recent years, advances in experimental techniques such as Scanning Tunneling Microscopy (STM) and AFM have expanded the scope of condensed matter physics from bulk properties of solids to surface properties of materials. At material surfaces, phenomena such as crystal growth and surface reactions occur that cannot be explained solely by bulk properties, making this a highly attractive field of research. On the other hand, in the field of theoretical calculations, advancements such as band structure analysis using the unfolding method [1] and the development of computational methods for calculating absolute core-level binding energies in solids [2] have made it possible to directly compare experimental results with electronic structure calculations based on DFT. As a result, DFT calculations are playing an increasingly important role in understanding surface states of solids.

Furthermore, large-scale electronic structure calculations now allow for the direct evaluation of electron transmission probabilities and interatomic forces between a probe and a material surface, enabling detailed comparisons with STM and AFM measurements. In other words, improvements in computational performance, the development of computational methods, and the advancement of massively parallel first-principles calculation codes have created an environment where large-scale first-principles calculations on realistic systems are feasible, paving the way for close collaboration between theory and experiment.

In this report, we present our recent studies on the identification of surface structures and the evaluation of interactions with AFM tips [3–5], conducted through a combination of AFM experiments and DFT calculations by OpenMX [6]. Particular emphasis is placed on the computational aspects, with a detailed discussion of the DFT calculation process for material surfaces and force calculations for AFM simulation. Furthermore, we report the proposal of a novel analysis and visualization method based on the RCP, which enables the prediction of chemical bonding forces between material surfaces and AFM tip [7].

2 DFT calculations for material surfaces

In this section, we describe how to construct surface structures by DFT calculations, using recent our study of 4×4 silicene on an

Ag(111) surface [3] as a representative example. The computational details are described in Appendix A.

First, we performed geometry optimization and cell optimization of the bulk Ag structure using its primitive cell. The obtained primitive cell was symmetrized using spglib [8], because slight distortions in the primitive cell can affect the behavior of band degeneracy points when applying band structure calculations such as the unfolding method for surface structures.

Next, we constructed a layered slab structure with a (111) surface orientation based on the optimized primitive cell. The thickness of the atomic layers was set to approximately 5–7 layers. In systems where a two-dimensional material such as silicene is adsorbed on the substrate surface, particular care must be taken, since the structure of the 2D material can be significantly influenced by the slab thickness.

In some cases, even increasing the slab thickness may not be sufficient to prevent the electronic states from the dangling bonds on the bottom side of the substrate from affecting the surface electronic structure. In such cases, surface passivation, such as hydrogen termination, may be required.

Subsequently, we performed geometry optimization for the primitive cell of Ag(111) surface, with the bottom two atomic layers fixed. A vacuum layer of about 20 Å was inserted along the surface normal direction to eliminate periodic interactions in that direction. In OpenMX, the number of grids which is determined by the cell size and the energy cutoff is used both for numerical integrations and for solving the Poisson equation. Therefore, careful attention must be paid to these parameters.

Finally, we constructed a supercell of the Ag(111) surface and placed a silicene structure on top, followed by geometry optimization.

3 Identification of the structures of silicene on Ag(111) surface

It is difficult to theoretically predict how silicene buckles and forms a commensurate structure with the Ag(111) surface, due to the vast number of possible initial configurations. Therefore, experimental insight into the structure model is essential for guiding theoretical calculations. In Ref. [3], the AFM topography image shown in a pink lattice of Fig. 1 (a) suggested that 4×4 α-phase silicene (Fig. 2 (a)) is observed on the Ag(111) surface.

In addition, a structure with a Si adatom on silicene was also observed as shown in a black lattice of Fig. 1 (a) and (b), and it was suggested that this corresponds to the 4×4 β-T4′-phase (Fig. 2 (d)). However, in the AFM experiment, the atomic structure of the underlying silicene cannot be clearly identified due to the influence of the Si adatom located at the top. To determine the stable silicene structure with a Si adatom, DFT calculations were performed under various computational conditions as shown in Table 1 using the 4×4 α-phase and 4×4 β-phase as initial guesses. Based on the DFT results with a $3 \times 3 \times 1$ k-point mesh, an energy cutoff of 300 Ry, and a 7-layer Ag slab model, it was revealed that the α-phase silicene transitions to the β-T4′-phase as a result of the addition of a Si adatom. In this study, we have paved the way for material design by inducing a phase transition in silicene through the manipulation of silicon adatoms using an AFM probe.

4 Force curve and topography of AFM

Since AFM estimates the positions and heights of atoms based on the magnitude of interatomic forces, it does not necessarily determine the exact nuclear positions of the most stable structure. Therefore, in some cases, it can be

Table 1: Relative energy convergence for the number of Ag layers by GGA with a $3 \times 3 \times 1$ ($1 \times 1 \times 1$) mesh of k points and the cut off energy $E_{cut} = 300$(Ry) (220(Ry)). The values in red represent more stable phase. Adapted from Ref. [3], Copyright (2023), with permission from Elsevier.

Accuracy	Phase	Adatom	Relative energy (eV)				
			3 layers	5 layers	6 layers	7 layers	8 layers
k-point: $1 \times 1 \times 1$,	α	no	0.0000	0.2147	0.2398	—	—
$E_{cut} = 220$(Ry)	β	no	0.0953	0.0000	0.0000	—	—
	α	no	0.0000	0.0179	0.0000	0.0000	0.0000
k-point: $3 \times 3 \times 1$,	β	no	0.0997	0.0000	0.0087	0.0645	0.0490
$E_{cut} = 300$(Ry)	α	T4'	0.0036	0.0061	0.4489	0.4398	0.4025
	β	T4'	0.0000	0.0000	0.0000	0.0000	0.0000

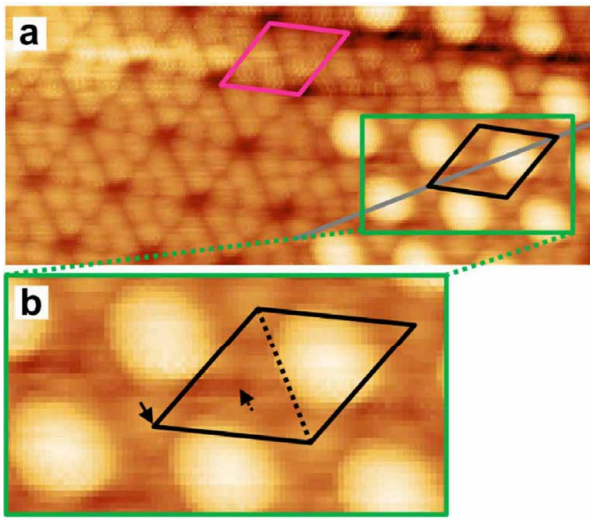


Figure 1: AFM topographic images of 4×4 silicene on Ag(111) surface. The lattice in pink (black) represents primitive cell of α-phase (β-T4′-phase). Adapted from Ref. [3], Copyright (2023), with permission from Elsevier.

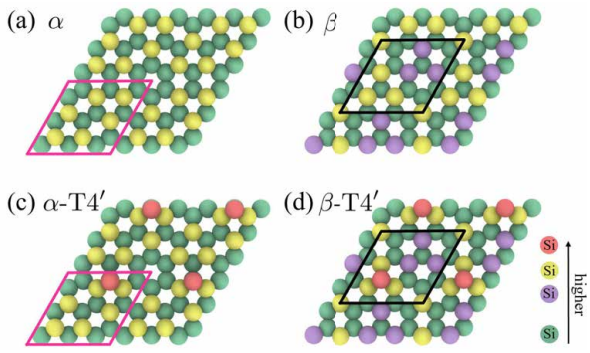


Figure 2: (a) α-phase, (b) β-phase, (c) α-T4′-phase, and (d) β-T4′-phase of 4×4 silicene on Ag(111) surface. Adapted from Ref. [3], Copyright (2023), with permission from Elsevier.

crucial to compute the interatomic forces between the AFM tip model and the surface using DFT calculations for comparison with experimental results.

As models for non-contact or near-contact AFM tips, structures formed on Si(111) (Fig. 3(a)) and Si(001) surfaces (Fig. 3(b)) are commonly used [9–11]. These tips have a dangling bond protruding from the apex atom, which can generate a strong attractive force due to chemical bonding when the surface atoms are chemically active. This strong interaction enables high-resolution AFM topographic imaging.

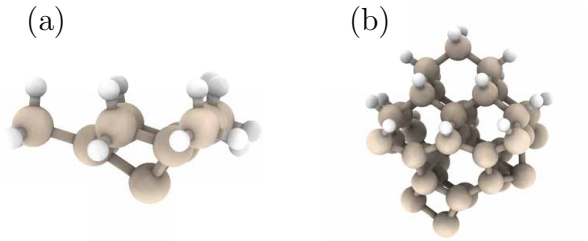


Figure 3: Models of Si tip formed on (a) Si(111) surface and (b) Si(001) surface. The spheres in white represent hydrogen terminations. The other spheres represent Si atoms.

It is known that the tip formed on Si(111) surface tends to exhibit stronger chemical bonding interactions with the material surface. While both models often reproduce experimentally observed interatomic forces well, they should be used carefully. This is because in cases with highly corrugated surface structures, atoms other than the apex atom may in-

Total force acting on nuclei

$$F = \sum_{k=1}^{N_{\mathrm{atom}}} \frac{\partial E_{tot}}{\partial \tau_k} \qquad \tau_k : \text{coordinates for nuclei}$$

$$= \sum_{k=1}^{N_{\mathrm{tip}}} \frac{\partial E_{tot}}{\partial \tau_k^t} + \sum_{k=1}^{N_{\mathrm{sample}}} \frac{\partial E_{tot}}{\partial \tau_k^s}$$

Force between the tip and the surface

$$F_{ts} = \sum_{k=1}^{N_{\mathrm{tip}}} \frac{\partial E_{tot}}{\partial \tau_k^t}$$

$$\Delta E_{tot}(z) \approx \sum_{k=1}^{N_{\mathrm{tip}}} \frac{\partial E_{tot}(z)}{\partial \tau_k^t} \Delta z$$

$$\therefore F_{ts}(z) = \frac{dE_{tot}(z)}{dz} \approx \sum_{k=1}^{N_{\mathrm{tip}}} \frac{\partial E_{tot}(z)}{\partial \tau_k^t}$$

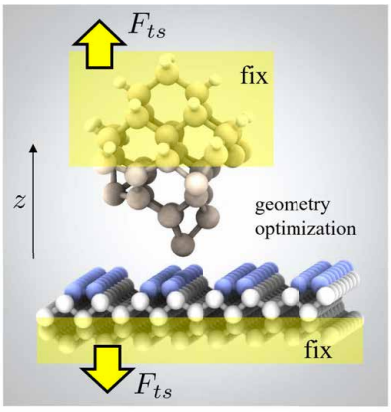


Figure 4: DFT force calculation method for AFM.

teract with the surface. In experiments, chemically inactive tips are also sometimes employed by attaching a CO molecule to the apex of the AFM tip.

The force calculation method based on DFT is summarized in Fig. 4. The structure was optimized while fixing the uppermost atoms of the tip and the bottom atoms of the substrate. The interatomic force acting on the tip was calculated as the sum of the Hellmann–Feynman forces acting on the atoms composing the tip.

In our study of the atomic observation on diamond (001) dimer surfaces with/without hydrogen termination [4], we experimentally demonstrated that strong chemical bonding between C–C dimers on the surface and the AFM tip leads to high-resolution AFM topographic imaging as shown in Fig. 5. In addition, it was found that the distance between the local minima in the force, which arises from the interaction with the AFM tip rather than the original interatomic distance, agrees well between the experimental observations and the DFT calculations using an AFM tip model (Fig. 3 (a)). This revealed that partial breaking of the dimer bonds occurs during the interaction as shown in Fig. 5.

Another example of a force curve obtained from DFT calculations was presented in Ref. [5], where a five-carbon-dimer ribbon on a clean diamond (001) surface was investigated, as shown in Fig. 6. According to the constant-force AFM results shown in Figs. 6 (a) and (c), the tip height becomes lower over the atoms of the dimers at both ends of the dimer ribbon, giving the impression that the edge dimers are located at a lower height. However, geometry optimization using DFT showed no significant difference in atomic height. To investigate this, we calculated force curves during constant-height lateral movement across the same path as the experiment and found that the force acting on the edge dimer atoms was indeed weaker. What, then, causes the weaker force observed on the edge dimer atoms? This will be clarified in the following section based on an analysis using the RCP. Although we do not discuss it in detail here, in our study of Ref. [5], formation energies were calculated by DFT for various dimer ribbons on the clean diamond (001) surface. The results indicate that ribbons composed of an odd number of dimers are more stable, which was confirmed by high-resolution AFM observations. This may provide a guideline for future structural predictions and insights into growth mechanisms of diamond surfaces.

5 Visualization of chemical active region

As discussed above, the atomic positions obtained from geometry optimization by DFT are not sufficient to fully interpret AFM im-

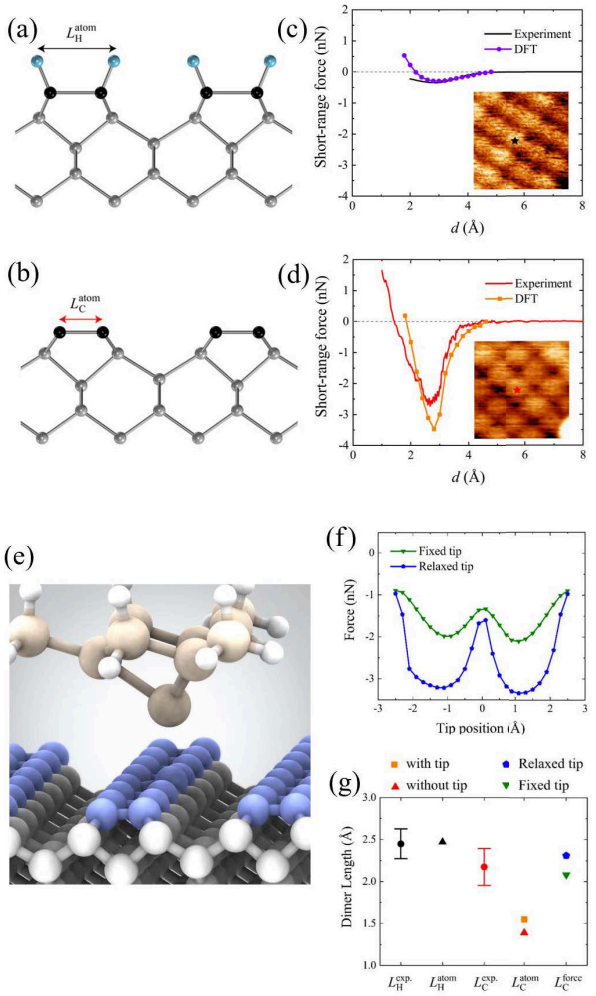


Figure 5: Side views of (a) a model of hydrogenated diamond (001) and (b) a model of clean diamond (001). Force curves for (c) hydrogenated diamond (001) and (d) clean diamond (001) with the tip during vertical movement. (e) One of the models for DFT force curve calculations. The sphere in blue represent the C-C dimer formed on the diamond (001) surface. (f) Force acting on the tip during lateral movement across the C–C dimer bond, with and without atomic relaxation of the tip. (g) Dimer length obtained by AFM experiment and DFT calculations. Distance between the local minima in force (L_C^{force}) for a fixed/relaxed tip was estimated from Fig.(f). Adapted from Ref. [4], Copyright (2025), American Chemical Society.

ages. This is because chemically active regions, such as dangling bonds and double bonds on the material surface, can strongly interact with the dangling bond of the Si tip in the AFM, resulting in behavior that differs significantly from other regions. Recent our theoretical study revealed that a local RCP analysis method based on an energy window scheme [7] enables us to quantitatively estimate the selectivity of atomic and molecular adsorption on surfaces, as well as the strength of chemical bonding forces between a probe tip and a surface in AFM measurements.

The local RCP is defined as

$$\mu_R^\tau(\vec{r}) \equiv \frac{\Delta\varepsilon_\tau(\vec{r})}{\Delta n(\vec{r})} \approx \frac{\varepsilon_{\tau,\mathrm{ew}}(\vec{r})}{n_{\mathrm{ew}}(\vec{r})}, \tag{1}$$

where $\Delta\varepsilon_\tau(\vec{r})$ and $\Delta n(\vec{r})$ are variations of regional energy density and electron number density, respectively, under a given perturbative electron excitation. We call the last approximation an "energy window scheme", where the physical quantities are calculated in an energy range of $\mu_{\mathrm{low}} < \mu < \mu_{\mathrm{up}}$ using the Fermi function with broadening factors $\tilde{T}_{\mathrm{low}}$ and $\tilde{T}_{\mathrm{up}}$ as follows.

$$n_{\mathrm{ew}}(\vec{r}) = \int_{-\infty}^{\infty} dE n(\vec{r},E)\left[f_{\mathrm{up}}(E) - f_{\mathrm{low}}(E)\right], \tag{2}$$

$$\varepsilon_{\tau,\mathrm{ew}}(\vec{r}) = \int_{-\infty}^{\infty} dE \varepsilon_\tau(\vec{r},E)\left[f_{\mathrm{up}}(E) - f_{\mathrm{low}}(E)\right], \tag{3}$$

where the Fermi function is defined as $f_\lambda(E) \equiv f(E,\mu_\lambda,\tilde{T}_\lambda) \equiv 1/(1+e^{(E-\mu_\lambda)/\tilde{T}_\lambda})$. The energy-dependent electron number density $n(\vec{r},E)$ and regional energy density $\varepsilon_\tau(\vec{r},E)$ are given in Appendix in Ref. [7]. The local RCP, in contrast to the conventional chemical potential, is spatially dependent, and the value of the local RCP on the material surface $\mu_R^\tau(\vec{r}_{\mathrm{surf}})$ indicates the chemical activity originating from the electron-donating ability at each point.

We have developed a highly parallelized local physical quantity calcula-

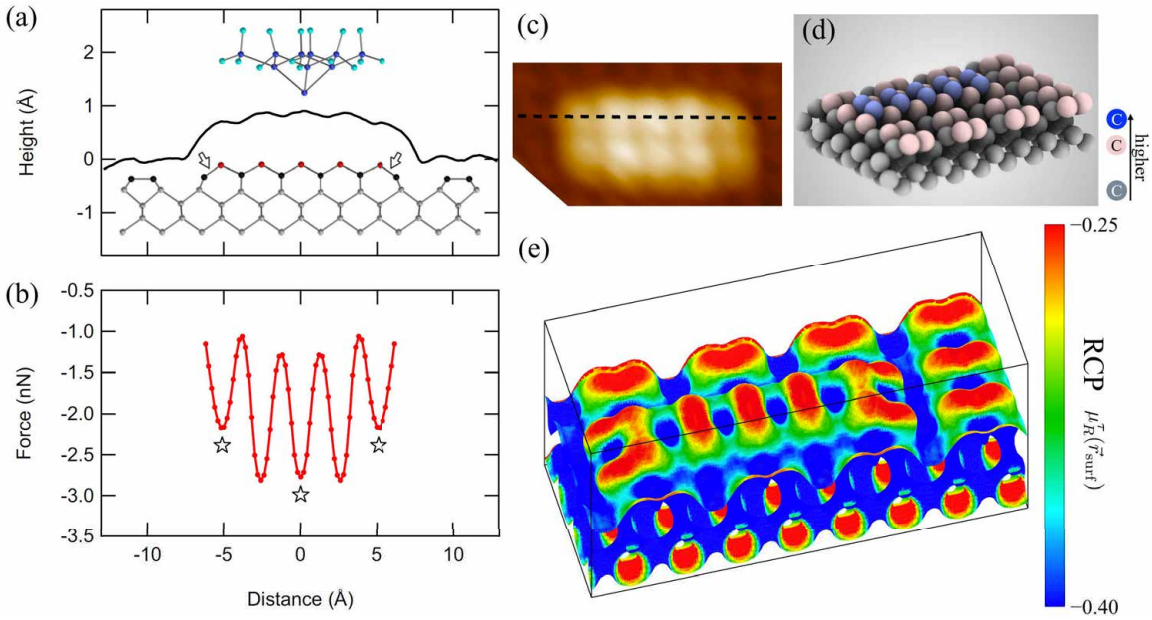


Figure 6: (a) Line profile of a five carbon dimers ribbon on the black dotted line of the AFM topographic image shown in (c), and (b) corresponding force acting on the tip during a constant height scan 3Å above the carbon atoms of the dimer ribbon before relaxation along one side of the ribbon, indicated by the black dotted line in (c). (d) Structure model of the five carbon dimers ribbon on the clean diamond (001) surface. (e) Regional chemical potential $\mu_R^\tau(\vec{r}_{\rm surf})$ in the energy range between -2 eV and 0 eV plotted on the material surface defined by zero kinetic energy density. Adapted from Ref. [5], licensed under CC BY 4.0, and Ref. [7].

tion code, FLPQ [12], which supports MPI/OpenMP hybrid parallel calculations, and FLPQViewer [13] to visualize the local RCP. In Fig. 6 (e), the distribution of the local RCP on the surface, which is defined by the zero kinetic energy density, for five carbon dimers ribbon on the diamond (001) surface is visualized. The red region shown in Fig. 6 (e) corresponds to the high local RCP originating from the C-C double bonds, which are highly chemically active regions. The Fig. 6 (e) revealed that the dimers previously thought to be located at both ends actually form double bonds with the underlying carbon atoms, indicating that their electronic states are essentially different from those of the central dimers. This RCP analysis has paved the way for understanding the chemically active regions on the material surface at the atomic scale.

6 Summary

In this report, we have reviewed our recent studies [3–5, 7] on surface structure analysis and AFM simulation using DFT, focusing on computational aspects. The combined approach of numerical simulations and experimental investigations is expected to shed light on unexplored atomic-scale surface structures and their formation processes.

7 Acknowledgement

I would like to thank Taisuke Ozaki, Yoshiaki Sugimoto, Masato Senami, Yuuki Yasui, Yuuki Adachi, Runnan Zhang, Masahiko Ogura, Toshiharu Makino, and Daisuke Takeuchi for their valuable support and collaboration on various aspects of these research. The computation in these work has been done using the facilities of the Supercomputer Center, the Institute for Solid State Physics, the University

of Tokyo (ISSPkyodo-SC-2023-Ba-0073, 2024-Ba-0053).

A Computational details

The DFT calculations within a generalized gradient approximation (GGA) [14, 15] were performed for the geometry relaxations and variable cell optimizations using the OpenMX code [6] based on norm-conserving pseudopotentials generated with multireference energies [16] and optimized pseudoatomic basis functions [17]. The standard basis set we used are listed in OpenMX website [18]. The qualities of the basis functions and fully relativistic pseudopotentials were carefully benchmarked by the delta gauge method [19] to ensure the accuracy of our calculations. An electronic temperature of 300 K is used to count the number of electrons by the Fermi-Dirac function. The regular mesh of 240 Ry in real space was basically used for the numerical integration and for the solution of the Poisson equation [20]. For bulk systems, cell vectors and internal coordinates are simultaneously optimized without any constraint by using a combination scheme of the rational function (RF) method [21] and the direct inversion iterative sub-space (DIIS) method [22] with a BFGS update [23–26] for the approximate Hessian. For material surfaces (slab models), only internal coordinates are optimized under fixed lattice and a few fixed bottom layers. The force on each atom was relaxed to be less than 0.0003 Hartree/Bohr.

Calculations of the local RCPs and the kinetic energy density were performed by FLPQ module [12] in QEDalpha package [27]. FLPQViewer [13] and Speck [28] were used for visualization of the atomic structures, RCPs, and other properties. Similar functions are available in 3D Viewers such as OpenMX Viewer [29] and Fermisurfer [30]. The atomic unit is used for $\mu_R^\tau(\vec{r})$ (i.e. 1 Hartree/Bohr^3 = 183.631 eV/Å^3).

Computational data are available at the ISSP data repository [31–33].

References

[1] C.-C. Lee, Y. Yamada-Takamura, and T. Ozaki, J. Phys. Condens. Matter **25**, 345501 (2013).

[2] T. Ozaki and C.-C. Lee, Phys. Rev. Lett. **118**, 026401 (2017).

[3] Y. Adachi, R. Zhang, X. Wang, M. Fukuda, T. Ozaki, and Y. Sugimoto, Applied Surface Science **630**, 157336 (2023).

[4] R. Zhang, Y. Yasui, M. Fukuda, T. Ozaki, M. Ogura, T. Makino, D. Takeuchi, and Y. Sugimoto, Nano Letters **25**, 1101 (2025).

[5] R. Zhang, Y. Yasui, M. Fukuda, M. Ogura, T. Makino, D. Takeuchi, T. Ozaki, and Y. Sugimoto, Phys. Rev. Res. **7**, 023036 (2025).

[6] T. Ozaki et al., OpenMX *package*, `http://www.openmx-square.org/`.

[7] M. Fukuda, M. Senami, Y. Sugimoto, and T. Ozaki, arXiv preprint arXiv:2505.04053 (2025).

[8] A. Togo and I. Tanaka, arXiv preprint arXiv:1808.01590 (2018).

[9] P. Pou, S. A. Ghasemi, P. Jelínek, T. Lenosky, S. Goedecker, and R. Pérez, Nanotechnology **20**, 264015 (2009).

[10] S. Jarvis, A. Sweetman, J. Bamidele, L. Kantorovich, and P. Moriarty, Phys. Rev. B **85**, 235305 (2012).

[11] Y. Sugimoto, A. Yurtsever, M. Abe, S. Morita, M. Ondráček, P. Pou, R. Pérez, and P. Jelínek, ACS Nano **7**, PMID: 23906095, 7370 (2013).

[12] M. Fukuda, FLPQ *package*, `https://github.com/mfukudaQED/FLPQ`.

[13] M. Fukuda, FLPQViewer, `https://github.com/mfukudaQED/FLPQViewer`.

[14] W. Kohn and L. J. Sham, Phys. Rev. **140**, A1133 (1965).

[15] J. P. Perdew, K. Burke, and M. Ernzerhof, Phys. Rev. Lett. **77**, 3865 (1996).

[16] I. Morrison, D. M. Bylander, and L. Kleinman, Phys. Rev. B **47**, 6728 (1993).

[17] T. Ozaki, Phys. Rev. B **67**, 155108 (2003).

[18] T. Ozaki, *Standard basis sets of openmx*, Available at `https://www.openmx-square.org/openmx_man3.9/node27.html`.

[19] K. Lejaeghere, G. Bihlmayer, T. Björkman, P. Blaha, S. Blügel, V. Blum, D. Caliste, I. E. Castelli, S. J. Clark, A. Dal Corso, S. de Gironcoli, T. Deutsch, J. K. Dewhurst, I. Di Marco, C. Draxl, M. Dułak, O. Eriksson, J. A. Flores-Livas, K. F. Garrity, L. Genovese, P. Giannozzi, M. Giantomassi, S. Goedecker, X. Gonze, O. Grånäs, E. K. U. Gross, A. Gulans, F. Gygi, D. R. Hamann, P. J. Hasnip, N. A. W. Holzwarth, D. Iuşan, D. B. Jochym, F. Jollet, D. Jones, G. Kresse, K. Koepernik, E. Küçükbenli, Y. O. Kvashnin, I. L. M. Locht, S. Lubeck, M. Marsman, N. Marzari, U. Nitzsche, L. Nordström, T. Ozaki, L. Paulatto, C. J. Pickard, W. Poelmans, M. I. J. Probert, K. Refson, M. Richter, G.-M. Rignanese, S. Saha, M. Scheffler, M. Schlipf, K. Schwarz, S. Sharma, F. Tavazza, P. Thunström, A. Tkatchenko, M. Torrent, D. Vanderbilt, M. J. van Setten, V. Van Speybroeck, J. M. Wills, J. R. Yates, G.-X. Zhang, and S. Cottenier, Science **351**, aad3000 (2016).

[20] T. Ozaki and H. Kino, Phys. Rev. B **72**, 045121 (2005).

[21] A. Banerjee, N. Adams, J. Simons, and R. Shepard, The Journal of Physical Chemistry **89**, 52 (1985).

[22] P. Csaszar and P. Pulay, Journal of Molecular Structure **114**, 31 (1984).

[23] C. G. BROYDEN, IMA Journal of Applied Mathematics **6**, 76 (1970).

[24] R. Fletcher, The Computer Journal **13**, 317 (1970).

[25] D. Goldfarb, Mathematics of Computation **24**, 23 (1970).

[26] D. F. Shanno, Mathematics of Computation **24**, 647 (1970).

[27] M. Senami, K. Ichikawa, A. Tachibana, M. Fukuda, and K. Soga, QEDalpha *package*, `https://github.com/mfukudaQED/QEDalpha`.

[28] R. Terrell, Speck, `https://github.com/wwwtyro/speck`.

[29] Y.-T. Lee and T. Ozaki, Journal of Molecular Graphics and Modelling **89**, 192 (2019).

[30] M. Kawamura, Computer Physics Communications **239**, 197 (2019).

[31] M. Fukuda, *Computational data for applied surface science, 157336 (2023).* `https://isspns-gitlab.issp.u-tokyo.ac.jp/masahiro.fukuda/T4_silicene_Si_adatom_on_Ag111`, 2023.

[32] M. Fukuda, *Computational data for nano letters* **25***, 1101 (2025).* `https://isspns-gitlab.issp.u-tokyo.ac.jp/masahiro.fukuda/C001_dimer_chain_AFM`, 2025.

[33] M. Fukuda, *Computational data for phys. rev. research* **7***, 023036 (2025).* `https://isspns-gitlab.issp.u-tokyo.ac.jp/masahiro.fukuda/C001_dimer_ribbon_AFM`, 2025.

Magnetic-field control of visons in Kitaev quantum spin liquids under energy dissipation

Chihiro HARADA, Atsushi ONO, and Joji NASU
Department of Physics, Tohoku University
Sendai 980-8578

1 Introduction

Insulating magnets that remain disordered even at zero temperature due to strong quantum fluctuations are known as quantum spin liquids (QSLs). They have been the subject of extensive research since the pioneering proposal by P. W. Anderson [1]. In particular, the Kitaev model has garnered significant attention in recent years, as it provides an exactly solvable QSL ground state and offers promising applications in topological quantum computing [2].

The Kitaev model is an $S = 1/2$ quantum spin system with bond-dependent Ising-type interactions on a two-dimensional honeycomb lattice [3, 4]. Elementary excitations in this model are characterized by the fractionalization of spin degrees of freedom into two types of quasiparticles: itinerant Majorana fermions and localized excitations known as visons. When a weak magnetic field is applied, an energy gap opens in the Majorana fermion spectrum, stabilizing a chiral spin liquid. In this phase, each vison hosts a zero-energy state of a Majorana fermion, referred to as a Majorana zero mode. The composite particle formed by a vison and its associated Majorana zero mode behaves as a non-Abelian anyon, obeying exotic exchange statistics distinct from those of bosons or fermions and serving as a fundamental building block for topological quantum computation.

To utilize such non-Abelian anyons for quantum computation, it is essential not only to observe them but also to enable their creation, manipulation, and annihilation in a well-controlled manner. While theoretical studies have proposed methods to detect the spatial positions of these anyons [5, 6], less is known for their real-time dynamics. Since the Kitaev model is a quantum spin model, the control of non-Abelian anyons might be achieved by applying external magnetic fields.

In this report, we explore the possibility of vison control by numerically simulating the time evolution of excited states in QSLs. In our previous studies, we introduced time-dependent local magnetic fields to achieve vison control and performed numerical simulations of the corresponding dynamics [7]. We also demonstrated the importance of including energy relaxation processes to stabilize such control, where energy dissipation can suppress the smearing of the vison wave function accompanied by a Majorana zero mode, thereby enabling stable manipulation of non-Abelian anyons [8]. In addition to reviewing these findings, we present a detailed analysis of the time evolution of the total energy and demonstrate that two distinct time scales emerge, attributed to spin fractionalization into two quasiparticles during the energy relaxation process.

2 Model

The Kitaev model, proposed by A. Kitaev [2], is a quantum spin model with $S = 1/2$ spins

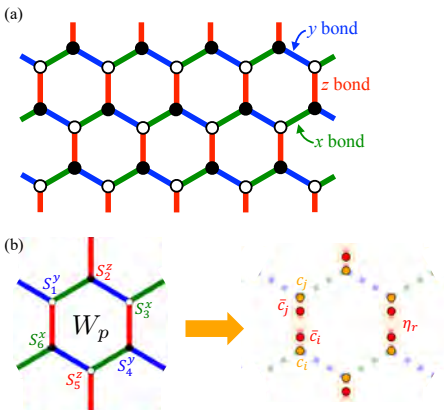


Figure 1: (a) Schematic illustration of the lattice structure on which the Kitaev model is defined. Green, blue, and red lines represent the x, y, and z bonds, respectively. Filled and open circles are sites belonging to the A and B sublattices, respectively. (b) Schematic picture of the $\mathbb{Z}_2$ flux operator W_p defined on the hexagonal plaquette p and its Jordan-Wigner transformation representation, where Majorana fermions c_j and $\bar{c}_j$, which are represented by orange an red circles, respectively, are introduced at each site. The $\mathbb{Z}_2$ variable η_r is defined on each z bond r.

defined on a honeycomb lattice, as shown in Fig. 1(a), and its Hamiltonian is given by

$$\mathcal{H}_K = -J\sum_{\langle ij\rangle_x} S_i^x S_j^x - J\sum_{\langle ij\rangle_y} S_i^y S_j^y - J\sum_{\langle ij\rangle_z} S_i^z S_j^z, \tag{1}$$

where J is the coupling constant for the three types of bonds, and $\langle ij\rangle_\gamma$ denotes the nearest-neighbor sites connected by the bond $\gamma = x, y, z$ [see Fig. 1(a)]. Note that the honeycomb lattice can be decomposed into two sublattices, A and B, as shown in Fig. 1(b).

To solve this model, we apply the Jordan-Wigner transformation, which maps the spin operators to Majorana fermions c_j and $\bar{c}_j$, as follows: $S_j^x = \frac{1}{2}c_j\tau_j$, $S_j^y = -\frac{1}{2}\bar{c}_j\tau_j$, and $S_j^z = \frac{i}{2}c_j\bar{c}_j$ for j belonging to the A sublattice, and $S_j^x = \frac{1}{2}\bar{c}_j\tau_j$, $S_j^y = -\frac{1}{2}c_j\tau_j$, and $S_j^z = \frac{i}{2}\bar{c}_jc_j$ for j belonging to the B sublattice, where $\tau_j = \prod_{j'<j}(-2S_{j'}^z)$ [9–14]. This transformation is schematically illustrated in Fig. 1(c). Using this transformation, the Hamiltonian can be expressed in terms of Majorana fermions as follows:

$$\mathcal{H}_K = -\frac{iJ_x}{4}\sum_{\langle ij\rangle_x} c_ic_j - \frac{iJ_y}{4}\sum_{\langle ij\rangle_y} c_ic_j - \frac{iJ_z}{4}\sum_{\langle ij\rangle_z} \eta_r c_ic_j, \tag{2}$$

where r is the label of the z-bond, and $\eta_r = i\bar{c}_i\bar{c}_j$ is a $\mathbb{Z}_2$ variable taking values of ±1, defined on each z-bond.

In this model, there is a conserved $\mathbb{Z}_2$ quantity called flux W_p on each hexagonal plaquette p, defined by the product of the spin operators as

$$W_p = 2^6\prod_{j\in p} S_j^\gamma, \tag{3}$$

where the component γ is determined as shown in Fig. 1(b). Moreover, this quantity can be expressed as $W_p = \prod_{r\in p}\eta_r$, indicating that the flux is written solely in terms of $\{\bar{c}_j\}$ and is independent of the Majorana fermions $\{c_j\}$. Since $[\mathcal{H}_K, W_p] = [\mathcal{H}_K, \eta_r] = 0$, the eigenstates of the Hamiltonian can be classified by the eigenvalues of W_p, which take values ±1, or equivalently by those of η_r. The ground state of the Hamiltonian belongs to the sector with $W_p = 1$ for all p, which is called the flux-free sector [2, 15]. Flux sectors with $W_p = -1$ correspond to excited states of the system, and each flux with $W_p = -1$ is regarded as a local excitation. This excitation is called a vison.

Here, we apply a uniform magnetic field to $\mathcal{H}_K$. Unfortunately, magnetic fields violate the exact solvability of the model since they do not commute with the flux operator W_p. To avoid this difficulty, Kitaev introduced a weak magnetic field term $\mathcal{H}_\kappa$ using third-order perturbation theory [2]:

$$\mathcal{H}_\kappa = -\kappa\sum_{\langle\langle jj'j''\rangle\rangle_{\gamma\gamma'\gamma''}} S_j^\gamma S_{j'}^{\gamma'} S_{j''}^{\gamma''}, \tag{4}$$

where $\langle\langle jj'j''\rangle\rangle_{\gamma\gamma'\gamma''}$ denotes three neighboring sites connected by γ and γ'' bonds, and γ' is chosen to be distinct from both γ and γ''. In the Majorana representation, $\mathcal{H}_\kappa$ corresponds to next-nearest-neighbor hopping terms of $\{c_j\}$. This leads to nonzero Chern numbers for the itinerant Majorana fermions $\{c_j\}$, resulting in the emergence of chiral Majorana edge states and the quantization of the thermal Hall conductance in the zero-flux sector [2]. Additionally, when visons are excited, each vison is accompanied by a Majorana zero mode, which is a zero-energy state of Majorana fermions. We attempt to manipulate visons with Majorana zero modes by applying a local magnetic field to the system in addition to the uniform field $\mathcal{H}_\kappa$. To this end, we introduce a time-dependent local field term $\mathcal{H}_h$ to the Hamiltonian as follows:

$$\mathcal{H} = \mathcal{H}_K + \mathcal{H}_\kappa + \mathcal{H}_h, \tag{5}$$

where $\mathcal{H}_h$ is given by

$$\mathcal{H}_h = -\sum_j h_j(t) S_j^z. \tag{6}$$

3 Time-dependent mean-field theory

In the presence of the magnetic field $\mathcal{H}_h$, the Hamiltonian $\mathcal{H}$ does not commute with the flux operator W_p, and visons can propagate throughout the system. This situation also indicates that the Majorana fermions $\{\bar{c}_j\}$ are no longer localized, and we must treat terms like $c_i c_j \eta_r$ as interactions between c- and $\bar{c}$-Majorana fermions, as seen, for example, in the last term of Eq. (2). To account for the interaction effects, we employ a time-dependent mean-field theory. In this framework, the term $i\bar{c}_i\bar{c}_j i c_i c_j$ is decoupled as $\langle i\bar{c}_i\bar{c}_j\rangle i c_i c_j + i\bar{c}_i\bar{c}_j\langle i c_i c_j\rangle - \langle i c_i\bar{c}_j\rangle i c_j\bar{c}_j - i c_i\bar{c}_j\langle i c_j\bar{c}_j\rangle + \langle i c_i\bar{c}_j\rangle i c_j\bar{c}_i + i c_i\bar{c}_j\langle i c_j\bar{c}_i\rangle + \text{const.}$ Using this decoupling, we can express the Hamiltonian in a quadratic form of Majorana fermions as

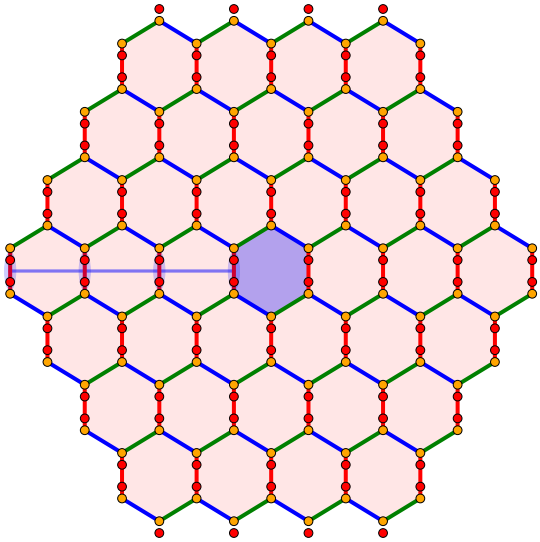


Figure 2: Schematic illustration of the vison excited on the plaquette at the center of the cluster. This vison configuration is realized by setting $\eta_r = -1$ for the z bonds intersecting with the blue line.

$$\mathcal{H}_{\rm MF} = \frac{i}{4}\sum_{ll'} \gamma_l \mathcal{A}_{ll'} \gamma_{l'} + C, \tag{7}$$

where $\{\gamma_l\} = \{c_1, c_2, \cdots, c_N, \bar{c}_1, \cdots, \bar{c}_N\}$, N is the number of sites in the system, $\mathcal{A}$ is a $2N \times 2N$ skew symmetric matrix, and C is a constant term independent of $\{\gamma_l\}$.

To diagonalize the Hamiltonian, we adopt the Schur decomposition method for the skew-symmetric matrix $\mathcal{A}$. In this decomposition, the matrix $\mathcal{A}$ is transformed into a block diagonal form by a real orthogonal matrix Q as follows:

$$Q^T \mathcal{A} Q = \begin{pmatrix} \begin{smallmatrix} 0 & \varepsilon_1 \\ -\varepsilon_1 & 0 \end{smallmatrix} & & & & \\ & \begin{smallmatrix} 0 & \varepsilon_2 \\ -\varepsilon_2 & 0 \end{smallmatrix} & & & \\ & & \ddots & & \\ & & & \ddots & \\ & & & & \begin{smallmatrix} 0 & \varepsilon_N \\ -\varepsilon_N & 0 \end{smallmatrix} \end{pmatrix}. \tag{8}$$

In each block, the matrix $Q^T\mathcal{A}Q$ can be diagonalized, and each eigenvalue ε_λ is paired with its negative counterpart, $-\varepsilon_\lambda$.

In the present calculations, we consider the hexagon cluster shown in Fig. 2. We assume that $h_j(t) = 0$ at the initial time $t = 0$, and introduce a vison excitation in the initial state of the system. To realize this configuration, we set $\eta_r = -1$ for the z bonds intersecting with the blue line shown in Fig. 2.

We calculate the time evolution based on the mean-field Hamiltonian $\mathcal{H}_{\mathrm{MF}}$. The wave function $|\Psi(t)\rangle$ obeys the Schrödinger equation, expressed as

$$i\frac{\partial}{\partial t}|\Psi(t)\rangle = \mathcal{H}_{\mathrm{MF}}(t)\,|\Psi(t)\rangle\,. \tag{9}$$

Here, we introduce the density matrix $\rho_{ll'}(t)$, defined as

$$\rho_{ll'}(t) = \frac{1}{2}\,\langle\Psi(t)|\,\gamma_{l'}\gamma_l\,|\Psi(t)\rangle\,. \tag{10}$$

From Eq. (9), we derive the following von Neumann equation:

$$\frac{\partial\rho}{\partial t} = [\mathcal{A},\rho]. \tag{11}$$

We evaluate the time evolution of the mean fields $\langle\Psi(t)|\,\gamma_{l'}\gamma_l\,|\Psi(t)\rangle$ using this equation. Note that, since $\mathcal{A}$ is a sparse matrix, the commutator $[\mathcal{A},\rho]$ can be computed efficiently even when the system size becomes large [16–18]. In this study, we employ the fourth-order Runge-Kutta method with a time step of $\Delta t/J^{-1} = 0.01$ for the time evolution.

4 Relaxation time approximation

To achieve long-range and long-time control of non-Abelian anyons in realistic setups, it is essential to suppress both the excitation of Majorana fermions and the spreading of the vison wave function. This can be achieved by allowing the energy injected by applied magnetic fields to dissipate from the system [8]. In this work, we incorporate the effect of energy dissipation into the system by considering coupling to an external environment, which is inevitably present in any real system. Specifically, we modify the original equation given in Eq. (11) into the following form:

$$\frac{\partial\rho}{\partial t} - [\mathcal{A},\rho] = I[\rho] \tag{12}$$

Here, the newly introduced term $I[\rho]$ represents a quantum-mechanical scattering term. We assume that the system is coupled to a thermal bath at sufficiently low temperature, and that this term drives the system toward lower energy by dissipating excess energy into the environment.

Regarding the timescale of relaxation, we assume that the relaxation to the instantaneous ground state of $\mathcal{H}_{\mathrm{MF}}$, determined by the mean fields at time t, occurs much faster than the relaxation to the true ground state of the entire system, which does not contain any visons. Within this timescale, it is sufficient to consider only the former relaxation process. Under this assumption, we adopt a relaxation-time approximation for the scattering term $I[\rho]$ in Eq. (12), where the system instantaneously relaxes toward $\rho_{\mathrm{g}}(t)$, the density matrix of the ground state of the instantaneous Hamiltonian $\mathcal{H}_{\mathrm{MF}}(t)$ at time t. In the relaxation-time approximation, the scattering term is expressed as

$$\frac{\partial\rho}{\partial t} - [\mathcal{A},\rho] = -\frac{\rho(t)-\rho_{\mathrm{g}}(t)}{\tau}, \tag{13}$$

where τ is the relaxation time.

5 Results

In this section, we present the results of the time evolution from the initial state containing a vison in the system. Numerical calculations are performed in a hexagonal cluster with $N = 726$.

5.1 Effect of relaxation time

First, we discuss the effect of the relaxation time τ on the time evolution of the system. We prepare the initial state with a vison at the

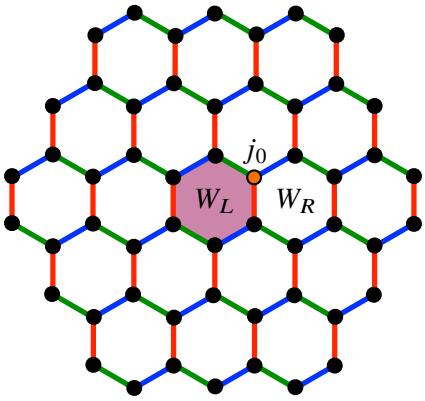


Figure 3: Schematic illustration of the initial state with a vison at the plaquette L with $W_L = -1$. The site j_0 at which the local magnetic field is applied is also presented. By applying the local field, the vison is expected to move to the right neighboring plaquette R.

center of the cluster and apply a local magnetic field at the upper right site j_0 of the plaquette with $W_p = -1$, as presented in Fig. 3. By applying the local magnetic field, the vison is expected to move to the right neighboring plaquette $p' = R$. We also refer to the plaquette p where the vison is initially located as $p = L$. The time dependent local magnetic field at site j_0 is chosen as $h_{j_0}(t) = A\theta(t)\theta(t_{\max} - t)$, where $\theta(t)$ is the Heaviside step function and $t_{\max}$ is the time when the magnetic field is turned off. In this situation, $\langle W_L \rangle + \langle W_R \rangle = 0$ is satisfied, and the local field is turned off when $\langle W_L \rangle = \langle W_R \rangle = 0$. Note that the flux operators W_L and W_R are conserved quantities when $h_{j_0} = 0$, and their expectation values are time-dependent only when $A \neq 0$. Based on the previous study [19], we set the relaxation time τ to be in the range of $10 \lesssim \tau/J^{-1} \lesssim 50$. We also introduce $D_p = (1 - \langle W_p \rangle)/2$, which corresponds to the vison density at plaquette p.

Figure 4(a) shows the time evolution of the vison density with $\kappa/J = 0.1$ and $\tau/J^{-1} = 20$, 30, 50, and ∞ in the presence of a time-dependent local magnetic field with $A/J = 0.08$. In the case of $\tau = \infty$, which corresponds to the situation without relaxation, the vison density does not change after $t_{\max}$. This result suggests that the vison is delocalized over both

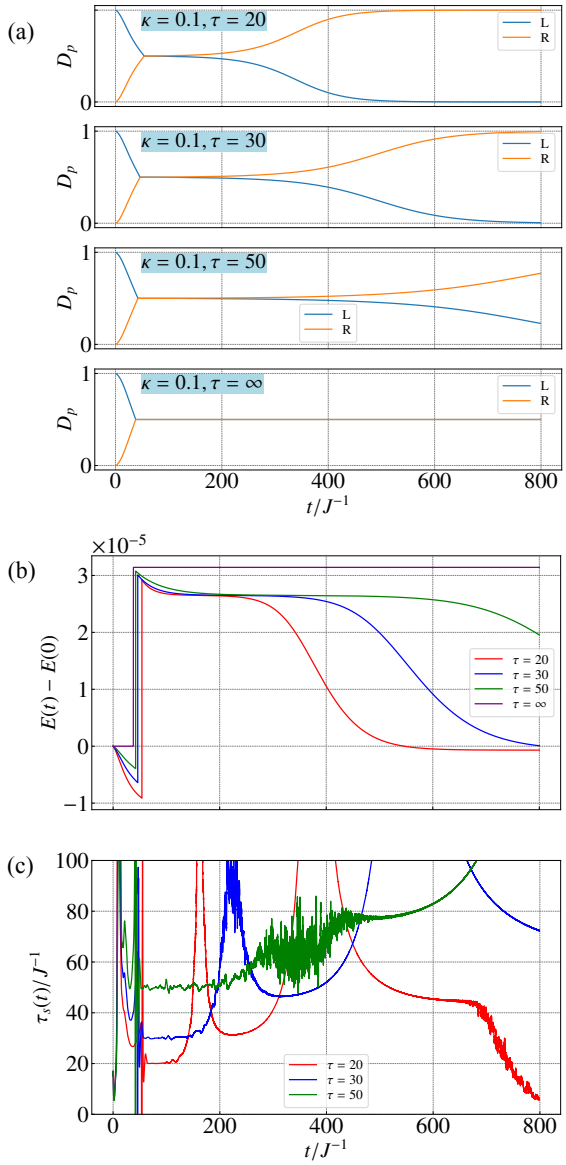


Figure 4: Time evolution of (a) the vison density at the plaquette L and R (see Fig. 3), (b) the total energy $E(t)$, and the relaxation time $\tau_s(t)$, by applying a local magnetic field with $A/J = 0.08$ at the site j_0 in the system with $N = 726$ and $\kappa/J = 0.10$ in the presence of energy dissipation with the several relaxation times.

the L and R plaquettes when relaxation is not taken into account. On the other hand, for finite values of τ, the vison density D_p tends to become localized at the right plaquette R after the magnetic field is turned off. The relaxation proceeds more rapidly for smaller values of τ. Note that the vison density D_p at plaquette R approaches 1 in the presence of relaxation. Based on these results, one can interpret that, in the presence of energy relaxation, spatially extended visons are energetically unstable, which is consistent with a previous study [20], and that an excited vison gradually shrinks into one of the plaquettes as the system relaxes.

To investigate the time evolution of the system in more detail, we also analyze the total energy $E(t)$, which is defined as $E(t) = \langle\Psi(t)|\,\mathcal{H}\,|\Psi(t)\rangle\,/N$. Figure 4(b) shows $E(t) - E(0)$ as a function of t for $\tau = 20$, 30, 50, and ∞. In the case without relaxation ($\tau = \infty$), the total energy is conserved when the magnetic field remains unchanged. In the presence of relaxation, the total energy decreases before the local magnetic field is turned off. The energy reduction is more pronounced for smaller τ. At $t = t_{\max}$, the total energy abruptly increases due to the loss of energy gain from the Zeeman term $\mathcal{H}_h$, similarly to the case without relaxation. In the presence of relaxation, the total energy gradually decreases after the abrupt increase. We find that the energy relaxation proceeds in two distinct stages.

Immediately after the magnetic field is turned off, energy relaxation begins. During this period, as shown in Fig. 4(a), the vison densities D_p for $p = L, R$ remain nearly constant, suggesting that energy dissipation originates primarily from the itinerant Majorana fermion systems. Subsequently, a further decrease in the total energy is observed. According to Fig. 4(a), this energy reduction is accompanied by the localization of the vison at position R. At this stage, the energy approaches its initial value.

To quantitatively discuss the relaxation process, we introduce the relaxation time $\tau_s(t)$ estimated from $E(t)$, which is defined as

$$\frac{1}{\tau_s(t)} = \left|\frac{d}{dt}\ln\left(\frac{dE(t)}{dt}\right)\right| = \left|\frac{1}{dE(t)/dt}\frac{d^2E}{dt^2}\right|. \tag{14}$$

Figure 4(c) shows the time evolution of $\tau_s(t)$ for $\tau = 20$, 30, and 50. In the initial stage of the energy relaxation, $\tau_s(t)$ remains almost constant and is approximately equal to τ, suggesting that the energy relaxation of the itinerant Majorana fermion system is governed by the relaxation time τ. In the subsequent stage of the energy relaxation, $\tau_s(t)$ exceeds τ, indicating that the energy relaxation of the vison system proceeds more slowly than the relaxation time τ. Therefore, we conclude that the energy relaxation of Majorana fermions is clearly distinct from that of visons, and that the relaxation process can be divided into two stages, corresponding to different quasiparticles.

5.2 Comparison with the energy-conserving system

In the previous section, we showed that energy relaxation can localize the vison by applying an atomic-scale local magnetic field. To demonstrate vison manipulation in more realistic situations, we consider the case in which a local magnetic field is applied over wider regions. We perform numerical simulations in a system with $N = 726$ and $\kappa/J = 0.05$, and prepare the initial state with a vison, as shown in Figs. 5(a) and 5(b). The time evolution of the system is computed in the presence of a time-dependent local magnetic field applied to the sites indicated by yellow circles in these figures. The time dependence of the local magnetic field is modeled as a Gaussian function, which is shown on the right side of Fig. 5. In this figure, we present the time evolution of the system in the absence of relaxation (left side) and in the presence of relaxation (right side).

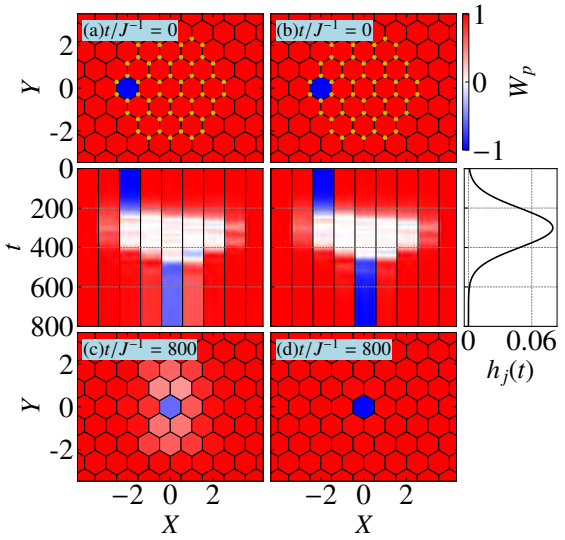


Figure 5: Comparison of the time evolution of vison driving by applying a time-dependent magnetic field in the system including $N = 726$ with $\kappa/J = 0.05$ in the absence and presence of energy dissipation. The time-dependent local field is applied to the sites indicated by yellow circles in (a) and (b). The time dependence of the local magnetic field $h_j(t)$ is shown on the right side. (a),(c) Initial and finnal states of the vison distribution without energy dissipation, and (b),(d) those with energy dissipation ($\tau = 50$).

Figures 5(a) and 5(c) show vison distributions of the initial and final states in the absence of relaxation. The figures between them show the time evolution of $\langle W_p \rangle$ for the plaquettes p that are crossed by the line $Y = 0$. When the amplitude of the local magnetic field reaches its maximum value, the vison is extended over the region where the local magnetic field is applied. After the local field approaches zero, the vison moves to the right side and becomes localized. As presented in Fig. 5(c), the vison is not well localized and its distribution is slightly extended. This is due to the energy injection by the local magnetic field, which is not compensated by energy relaxation.

On the other hand, in the case with relaxation, the vison is displaced by the application of the time-dependent local field and becomes well localized in the final state, as shown in Fig. 5(d), which is in stark contrast to the case without relaxation. This localized behavior is due to energy dissipation by the relaxation term, suggesting that energy relaxation is essential for the manipulation of visons.

6 Conclusion

In summary, we have investigated the time evolution of vison excitations driven by a time-dependent local magnetic field in the Kitaev model with energy dissipation. We performed numerical simulations of the time evolution for an excited vison using time-dependent mean-field theory and the relaxation time approximation. Our results show that the energy relaxation process can be divided into two distinct stages, corresponding to the relaxation of Majorana fermions and visons, respectively. Furthermore, we demonstrated that energy relaxation is essential for vison manipulation, and that visons can be localized by applying a time-dependent local magnetic field when energy dissipation is taken into account.

Acknowledgments

This work was supported by Grant-in-Aid for Scientific Research from JSPS, KAKENHI Grant Nos. JP19K03742, JP20H00122, JP20K14394, JP22H01175, JP23H01129, JP23H04859, JP23H04865, JP23K13052, JP23K25805, and No. JP24K00563. It is also supported by JST PRESTO Grant No. JPMJPR19L5. Parts of the numerical calculations were performed in the supercomputing systems in ISSP, the University of Tokyo.

References

[1] P. W. Anderson, "Resonating valence bonds: a new kind of insulator?", Mater. Res. Bull. **8**, 153 (1973).

[2] A. Kitaev, "Anyons in an exactly solved model and beyond", Ann. Phys. (N. Y.) **321**, 2 (2006).

[3] Y. Motome and J. Nasu, "Hunting Majorana Fermions in Kitaev Magnets", J. Phys. Soc. Jpn. **89**, 012002 (2020).

[4] J. Nasu, "Majorana quasiparticles emergent in Kitaev spin liquid", Prog. Theor. Exp. Phys. **2023**, ptad115 (2023).

[5] M. Udagawa, S. Takayoshi, and T. Oka, "Scanning Tunneling Microscopy as a Single Majorana Detector of Kitaev's Chiral Spin Liquid", Phys. Rev. Lett. **126**, 127201 (2021).

[6] M. O. Takahashi, M. G. Yamada, M. Udagawa, T. Mizushima, and S. Fujimoto, "Nonlocal Spin Correlation as a Signature of Ising Anyons Trapped in Vacancies of the Kitaev Spin Liquid", Phys. Rev. Lett. **131**, 236701 (2023).

[7] C. Harada, A. Ono, and J. Nasu, "Field-driven spatiotemporal manipulation of Majorana zero modes in a Kitaev spin liquid", Phys. Rev. B **108**, L241118 (2023).

[8] C. Harada, A. Ono, and J. Nasu, "Real-time control of non-abelian anyons in kitaev spin liquid under energy dissipation", Phys. Rev. B **110**, 214426 (2024).

[9] H.-D. Chen and J. Hu, "Exact mapping between classical and topological orders in two-dimensional spin systems", Phys. Rev. B **76**, 193101 (2007).

[10] X.-Y. Feng, G.-M. Zhang, and T. Xiang, "Topological Characterization of Quantum Phase Transitions in a Spin-1/2 Model", Phys. Rev. Lett. **98**, 087204 (2007).

[11] H.-D. Chen and Z. Nussinov, "Exact results of the Kitaev model on a hexagonal lattice: spin states, string and brane correlators, and anyonic excitations", J. Phys. A **41**, 075001 (2008).

[12] J. Nasu, M. Udagawa, and Y. Motome, "Vaporization of Kitaev Spin Liquids", Phys. Rev. Lett. **113**, 197205 (2014).

[13] J. Nasu, M. Udagawa, and Y. Motome, "Thermal fractionalization of quantum spins in a Kitaev model: Temperature-linear specific heat and coherent transport of Majorana fermions", Phys. Rev. B **92**, 115122 (2015).

[14] T. Minakawa, Y. Murakami, A. Koga, and J. Nasu, "Majorana-Mediated Spin Transport in Kitaev Quantum Spin Liquids", Phys. Rev. Lett. **125**, 047204 (2020).

[15] E. H. Lieb, "Flux phase of the half-filled band", Phys. Rev. Lett. **73**, 2158 (1994).

[16] N. Tsuji and H. Aoki, "Theory of Anderson pseudospin resonance with Higgs mode in superconductors", Phys. Rev. B **92**, 064508 (2015).

[17] Y. Murakami, D. Golež, T. Kaneko, A. Koga, A. J. Millis, and P. Werner, "Collective modes in excitonic insulators: Effects of electron-phonon coupling and signatures in the optical response", Phys. Rev. B **101**, 195118 (2020).

[18] J. Nasu, Y. Murakami, and A. Koga, "Scattering phenomena for spin transport in a Kitaev spin liquid", Phys. Rev. B **106**, 024411 (2022).

[19] M. Kanega, T. N. Ikeda, and M. Sato, "Linear and nonlinear optical responses in Kitaev spin liquids", Phys. Rev. Res. **3**, L032024 (2021).

[20] V. Lahtinen, "Interacting non-Abelian anyons as Majorana fermions in the honeycomb lattice model", New J. Phys. **13**, 075009 (2011).

Development of Open Data Analysis Tool for Science and Engineering (ODAT-SE)

Takeo Hoshi[1,2], Akito Nakano[1,2], Tatsumi Aoyama [3],
Yuichi Motoyama[3] and Kazuyoshi Yoshimi[3]

[1] *National Institute for Fusion Science,*
322-6 Oroshi-cho, Toki city, Gifu Prefecture, 509-5292, Japan.
[2] *The Graduate University for Advanced Studies, SOKENDAI,*
322-6 Oroshi-cho, Toki city, Gifu Prefecture, 509-5292, Japan.
[3] *The Institute for Solid State Physics, The University of Tokyo, Chiba 277-8581, Japan.*

We developed an open-source software Open Data Analysis Tool for Science and Engineering (ODAT-SE), by the PASUMS project in FY2024 as a major upgrade of 2DMAT (https://www.pasums.issp.u-tokyo.ac.jp/2dmat/). ODAT-SE (2DMAT) was developed for the data analysis of advanced experimental measurements and offers five analysis methods: (i) grid search, (ii) Nelder-Mead optimization, (iii) Bayesian optimization, (iv) replica exchange Monte Carlo method, and (v) population-annealing Monte Carlo method. The parallel computation with ODAT-SE was carried out on the ISSP supercomputers and other supercomputers such as Fugaku. The present report reviews ODAT-SE and a recent application study to determine the surface structure of the 3×3-Si phase on the Al (111) surface by positron diffraction and core-level photoemission spectroscopy.

1. Introduction

One of the fundamental topics in computational science is data analysis in experimental measurements. An open-source data-analysis framework 2DMAT [1] and related tools have been developed for the data analysis in experimental measurements of TWO-Dimensional MATerial structures by the PASUMS project of ISSP at FY2020 and FY2021 and other projects [1-8]. Two-dimensional materials have been a central issue in materials science because of the emergence of physical or chemical phenomena specific to their dimensionality, with promising applications in nanotechnology [9]. 2DMAT is a unified platform for the analysis of different experimental measurement techniques, total-reflection high-energy positron diffraction (TRHEPD) [10], surface X-ray diffraction (SXRD) [11], and low-energy electron

diffraction (LEED) [12] experiments.

Under the PASUMS project in FY2024, the software underwent a redesign, emerging with a new name, ODAT-SE (Open Data Analysis Tool for Science and Engineering) [13], and can be used as an interdisciplinary data-analysis framework beyond solid-state physics.

The present report contains an overview of ODAT-SE for the methodological background, the new features introduced at FY2024, a recent application study, a summary, and a future outlook.

2. Methodological background

The methodological background of the data analysis is an inverse problem [5], in which an observed quantity Y is modeled as a function of a target quantity X ($Y_{\mathrm{cal}} \equiv Y_{\mathrm{cal}}(X)$). Here, Y and X are assumed to be high-dimensional vectors ($X \equiv (X_1, X_2, \dots, X_n), Y \equiv (Y_1, Y_2, \dots, Y_m)$). The function $Y_{\mathrm{cal}}(X)$ is called a direct problem solver and should be prepared for each measurement technique. A typical analysis procedure is an optimization procedure of the residual difference function $F(X;Y) \equiv |Y - Y_{\mathrm{cal}}(X)|^2$ and the optimal solution is written as $X^* \equiv \mathrm{argmin}_X F(X;Y)$, as shown schematically in Fig. 1 (a). In the data analysis in experimental measurements, however, the quantities X and Y always contain uncertainty, and one should often consider the uncertainty quantitatively by Bayesian inference, in which the probability distribution $P(Y|X)$, called likelihood function, is modeled, and the posterior probability distribution $P(X|Y)$ is obtained as a high-dimensional histogram using Monte Carlo methods, as shown in Fig. 1 (b).

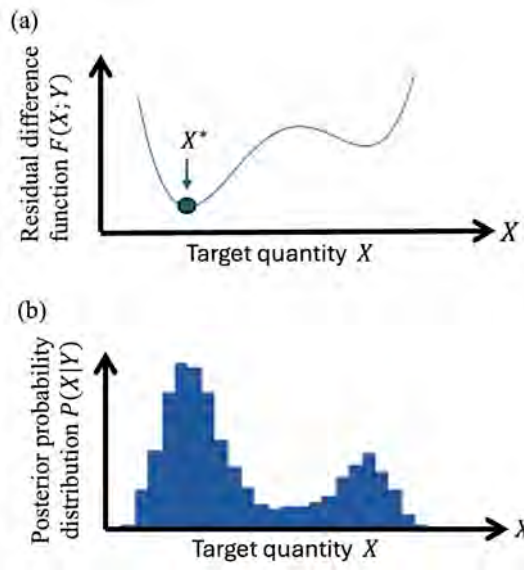


Fig. 1 Schematic diagrams of (a) residual difference function $F(X;Y)$ in optimization procedure and (b) posterior probability distribution $P(X|Y)$ in Bayesian inference

ODAT-SE offers the following five analysis methods: (i) Grid search method: The grid-search method is an algorithm for searching for the minimum value of $F(X;Y)$ by computing $F(X;Y)$ for all candidate points in the parameter space, X prepared in advance. In ODAT-SE, the set of candidate points is equally divided and automatically assigned to each process for trivial parallel computation. (ii) The Nelder-Mead optimization method [5,14]: The method, also known as the

downhill simplex method, is a gradient-free optimization method in which the gradient $\nabla_X F$ is not required. The method is reduced to an iterative local update, and a proper initial guess is needed to avoid local minimum trapping. (iii) Bayesian optimization method: The method gives a black-box optimization, and ODAT-SE uses a Bayesian optimization library, PHYSBO [15,16]. See references [15,16] for details. (iv) Replica exchange Monte Carlo (REMC) method [17] and (v) population-annealing Monte Carlo (PAMC) method [18]: The two methods, commonly parallelized Monte Carlo methods and gives the posterior probability distribution $P(X|Y)$, as in Fig. 1(b), through Bayes' Theorem $P(X|Y) = P(Y|X)P(X)/P(Y)$. The PAMC method is suitable for massively parallel computation with 10^4 MPI processes or more [5].

In ODAT-SE, the four methods, except the Nelder-Mead method, are implemented by parallel computation, which is efficient not only for personal computers but also for supercomputers. So far, the numerical computations have been carried out not only on the supercomputers at ISSP but also on the Wisteria-Odyssey supercomputer at the Information Technology Center, University of Tokyo under the Interdisciplinary Computational Science Program in the Center for Computational Sciences, University of Tsukuba, and the Fugaku supercomputer under the HPCI projects (hp210228, hp210267, hp220248, hp230304, hp240304).

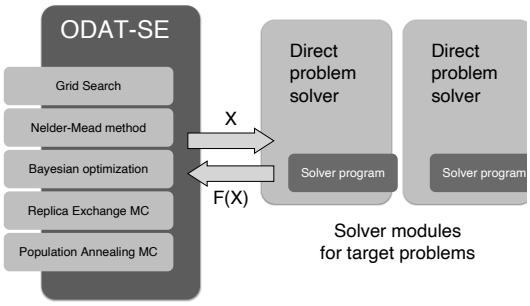


Fig. 2 Schematic diagram of the code structure of ODAT-SE

3. New features of ODAT-SE

This section explains the new features of ODAT-SE. The code structure of ODAT-SE was drawn schematically in Fig. 2. The original architecture in 2DMAT was tightly coupled with specific experimental techniques, limiting its flexibility and reusability across other scientific fields. In ODAT-SE, the architecture explicitly separates "direct problems" (i.e., the physical or statistical models representing the system under investigation) from the optimization or search algorithms. This modular approach enables researchers to apply ODAT-SE not only to 2D material analysis but also to diverse fields; users can easily add their own direct problem solvers or search algorithms tailored to their research needs.

To ensure continuity from 2DMAT, the direct problem solvers originally developed for 2DMAT have been preserved and organized in a dedicated 2DMAT GitHub

repository [19]. These models can still be used within the ODAT-SE framework with minimal modification—users simply need to install them as add-on components. Furthermore, a wide range of sample programs and usage examples has been located at the ODAT-SE Gallery [20], maintained by the ISSP Data Repository. This gallery provides ready-to-use scripts and templates, making it easier for users to adopt ODAT-SE for their specific scientific problems.

One of the significant changes in the transition from 2DMAT to ODAT-SE was the license shift from GPL v.3 to MPL v.2.0 [21]. While the GPL ensured strong copyleft—requiring any derived work to be released under the same license—it also posed barriers to integration with other software or for commercial use. In contrast, the MPL adopts a "file-level copyleft" model, allowing proprietary use and redistribution as long as modifications to MPL-licensed files are disclosed. This change has made ODAT-SE more attractive and accessible to both academic and industrial users, facilitating broader adoption and smoother integration into diverse software ecosystems.

4. A recent application study for the determination of the surface structure of the 3×3-Si phase on the Al (111) surface

This section is devoted to a review of a recent application study for the determination of the surface structure of the 3×3-Si phase on the Al (111) surface by the multiple usages of TRHEPD and core-level photoemission spectroscopy [22]. TRHEPD [10] is a novel experimental probe for two-dimensional materials and has been actively developed in the last decade at large-scale experimental facilities at the Slow Positron Facility (SPF), Institute of Materials Structure Science (IMSS), High-Energy Accelerator Research Organization (KEK) [23]. Fig. 3 shows a schematic diagram of the TRHEPD method. In this method, the observed data Y comes from the diffraction pattern seen on the screen, and the target quantity X is the position of surface and subsurface atoms at a depth of less than one nanometer.

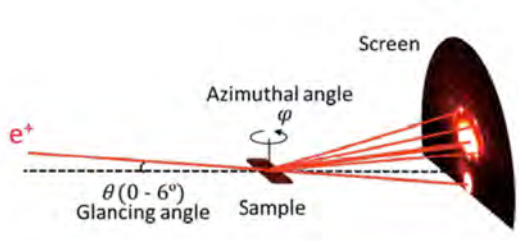


Fig. 3 Schematic diagram of the TRHEPD experiment [23]

ODAT-SE (2DMAT) was used for the data analysis of the TRHEPD experiment under the one-beam condition, in which the specular (00) spot intensities were dominated by the surface-normal component, z-component, of atomic positions. Fig. 4 shows the flat silicene structure model, a candidate of the structure.

In the model, the 3×3 surface unit cell contains eight Si atoms of the surface layer, labeled by '1', '2', …, '8' in Fig. 4, and nine Al atoms of the first sub-surface layer. The residual difference $F(X;Y)$ is given by the difference between the observed and calculated diffraction data. The PAMC analysis was carried out with the seventeen independent parameters of the z coordinates of all the eight atoms (z_1, z_2,.., z_8) of the surface Si layer and all the nine atoms of the first Al layer. As a result, the optimal structure was obtained as the flat structure for both the surface Si layer and the first subsurface Al layer, as shown in Fig. 4. See the original paper [12] for details.

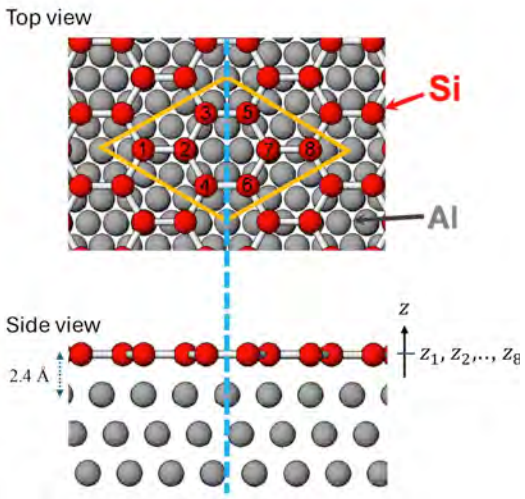


Fig. 4 Top and side views of the schematic diagram of the flat silicene structure model for the 3×3-Si phase on the Al (111) surface. A 3×3 unit cell is depicted. [22]

The analysis indicates the importance of a global search, such as PAMC, because the residual difference function $F(X;Y)$ has many local minima. The existence of local minima is demonstrated in Fig. 5, in which the grid search is carried out only with the surface Si atoms under the constraint of $z_1 = z_2 = z_3 = z_4 = z_5 = z_6 = z_8$ and the residual difference function F is drawn as a contour plot as the function of the common value of $z_1, z_2, z_3, z_4, z_5, z_6, z_8$ and the value z_7. One can find that the global minimum is located at $z_1 = z_2 = z_3 = z_4 = z_5 = z_6 = z_7 = z_8 =$ 2.4 Å, which corresponds to the flat surface structure of Fig. 4. One can also find that a local minim is located at $z_1 = z_2 = z_3 = z_4 = z_5 = z_6 = z_8 = 2.4$ Å and $z_7 = 3.6$ Å, which corresponds to a bucked surface structure. If one uses an iterative local-update algorithm, like the Nelder-Mead algorithm, the optimization algorithm may fail to find the global minimum because of the trapping on local minima.

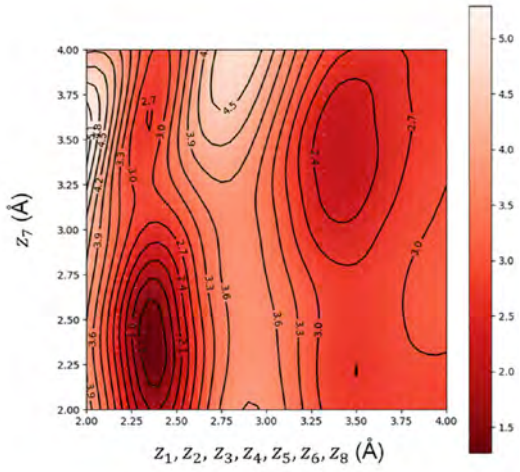


Fig. 5 Contour plot of the residual difference function in TRHEPD for the 3×3-Si phase on the Al (111) surface [22]

Here, we discuss the crucial role of the multiple usage of TRHEPD and core-level photoemission spectroscopy. In the surface analysis by TRHEPD, it should be noted that Al and Si are located next to each other in the periodic table and, thus, have similar scattering potentials for a positron beam. The observed TRHEPD data at the Si surface layer appeared nearly identical without or with Al substitution. This indicated that the surface structure model created uncertainty regarding embedded Al atoms. Si core-level photoemission spectroscopy was also carried out to overcome the above uncertainty because the Si atoms could be bonded with neighboring Si and/or Al atoms. This creates different chemical environments for these Si sites that should result in corresponding chemical shifts in Si core-level photoemission spectra.

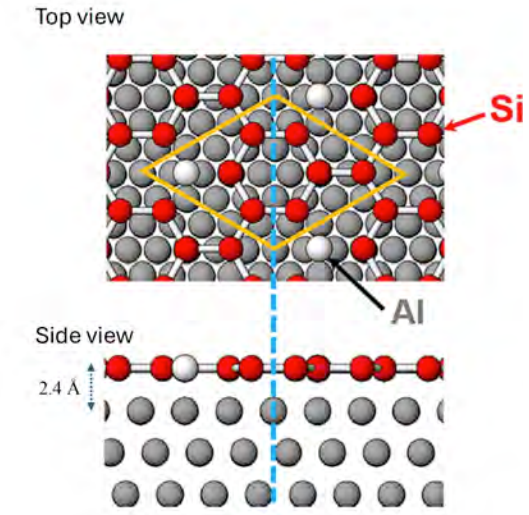


Fig. 6 Top and side views of the schematic diagram of the Al-embedded silicene model structure determined by the multiple usage of TRHEPD and core-level photoemission spectroscopy experiments. [22]

The analysis with TRHEPD and core-level photoemission spectroscopy is concluded in the Al-embedded silicene model structure in Fig.6, in which the eight sites in the 3 × 3 unit cell of the surface layer were occupied by one Al atom and seven Si atoms.

5. Summary and Future Outlook

An open-source data-analysis framework, Open-Data Analysis Tool for Science and Engineering (ODAT-SE), was developed as a major upgrade of 2DMAT. The framework offers various algorithms, mainly for the optimization and Bayesian inference as a global search. ODAT-SE has been redesigned to provide better flexibility and reusability across other scientific fields. A recent application study is reviewed for the determination of surface structure by TRHEPD and core-level photoemission spectroscopy. The analysis indicates the importance of global search and the multiple usage of TRHEPD and core-level photoemission spectroscopy.

A future outlook is the interdisciplinary use of ODAT-SE beyond solid-state physics. Very recently, the present authors launched a new project, the Moonshot R&D Program [24], in the field of fusion science, and ODAT-SE will be used in the project.

References

[1] https://www.pasums.issp.u-tokyo.ac.jp/2dmat/

[2] Kazuyuki Tanaka, Takeo Hoshi, Izumi Mochizuki, Takashi Hanada, Ayahiko Ichimiya, Toshio Hyodo, Development of data-analysis software for total-reflection high-energy positron diffraction (TRHEPD), Acta Physica Polonica A, 137, 188 (2020).

[3] Takeo Hoshi, Daishiro Sakata, Shotaro Oie, Izumi Mochizuki, Satoru Tanaka, Toshio Hyodo, Koji Hukushima, Data-driven sensitivity analysis in surface structure determination using total-reflection high-energy positron diffraction (TRHEPD), Computer Physics Communications 271, 108186/1-7 (2022).

[4] Takashi Hanada, Yuichi Motoyama, Kazuyoshi Yoshimi, Takeo Hoshi, sim-trhepd-rheed – Open-source simulator of total-reflection high-energy positron diffraction (TRHEPD) and reflection high-energy electron diffraction (RHEED), Computer Physics Communications 277, 108371/1-10 (2022).

[5] Yuichi Motoyama, Kazuyoshi Yoshimi, Izumi Mochizuki, Harumichi Iwamoto, Hayato Ichinose, Takeo Hoshi, Data-analysis software framework 2DMAT and its application to experimental measurements for two-dimensional material structures, Computer Physics Communications 280, 108465/1-11 (2022).

[6] Hisashi Kohashi, Harumichi Iwamoto, Takeshi Fukaya, Yusaku Yamamoto, Takeo Hoshi, Performance prediction of massively parallel computation by Bayesian inference, JSIAM Letters 14, 13-16 (2022).

[7] Kazuyuki Tanaka, Izumi Mochizuki, Takashi Hanada, Ayahiko Ichimiya, Toshio Hyodo, Takeo Hoshi, Two-stage data-analysis method for total-reflection high-energy positron diffraction (TRHEPD), JJAP Conf. Series 9, 011301/1-9 (2023).

[8] Shuhei Kudo, Yusaku Yamamoto, Takeo Hoshi, A fast and efficient computation method for reflective diffraction simulations, Computer Physics Communications 296, 109029/1-9 (2024).

[9] Monatomic Two-Dimensional Layers: Modern Experimental Approaches for Structure, Properties, and Industrial Use, edited by Iwao Matsuda, Elsevier (2018).

[10] Yuki Fukaya, Atsuo Kawasuso, Ayahiko Ichimiya, and Toshio Hyodo, Topical Review: Total-reflection high-energy positron, diffraction (TRHEPD) for structure determination of the topmost and immediate sub-surface atomic layers, Journal of Physics D: Applied Physics 52, 013002/1-19 (2019)

[11] R. Feidenhans'l, Surface structure determination by X-ray diffraction, Surface Science Reports 10, 105-188 (1989).

[12] M. A. V. Hove, W. Moritz, H. Over, P. Rous, A. Wander, A. Barbieri, N. Materser, U. Starke, G.A. Somorjai, Automated determination of complex surface structures by LEED, Surface Science Reports 19, 191-229 (1993).

[13] https://github.com/issp-center-dev/ODAT-SE
[14] J. A. Nelder and R. Mead, A Simplex Method for Function Minimization, The Computer Journal 7, 308–313 (1965).
[15] https://www.pasums.issp.u-tokyo.ac.jp/physbo/
[16] Yuichi Motoyama, Ryo Tamura, Kazuyoshi Yoshimi, Kei Terayamam, Tsuyoshi Ueno, Koji Tsuda, Bayesian optimization package: PHYSBO, Computer Physics Communications 278, 108405/1-8 (2022).
[17] Koji Hukushima and Koji Nemoto, Exchange Monte Carlo Method and Application to Spin Glass Simulations, Journal of the Physical Society of Japan 65 1604-1608 (1996).
[18] Koji Hukushima, Yukito Iba, Population annealing and its application to a spin glass, AIP Conference Proceedings 690, 200-206 (2003),
[19] https://github.com/2DMAT
[20] https://isspns-gitlab.issp.u-tokyo.ac.jp/takeohoshi/odat-se-gallery
[21] https://www.mozilla.org/en-US/MPL/2.0/
[22] Yusuke Sato, Yuki Fukaya, Akito Nakano, Takeo Hoshi, Chi-Cheng Lee, Kazuyoshi Yoshimi, Taisuke Ozaki, Takeru Nakashima, Yasunobu Ando, Hiroaki Aoyama, Tadashi Abukawa, Yuki Tsujikawa, Masafumi Horio, Masahito Niibe, Fumio Komori, Iwao Matsuda, Surface structure of the 3×3-Si phase on Al(111), studied by the multiple usages of positron diffraction and core-level photoemission spectroscopy, Physical Review Materials 9, 014002/1-11 (2025).
[23] https://www2.kek.jp/imss/spf/eng/
[24] https://ms10ds.nifs.ac.jp/

3.2 First-Principles Calculation of Material Properties

Theoretical Study on Dynamical Processes at Surfaces and Interfaces using Density Functional Theory and Machine Learning Methods

Yoshitada MORIKAWA
Department of Precision Engineering, Graduate School of Engineering, Osaka University
2-1 Yamadaoka, Suita, Osaka 565-0871

In this fiscal year, we investigated several systems which are important in both fundamental science and applications. Thermal stability of heterogeneous catalysts, along with high activity and selectivity, plays a central role in the catalyst design for industrial applications,1 − 4 e.g., three-way catalyst (TWC) converters to purify emission of exhaust gases or fuel cells. However, the thermal instability originated from the agglomeration (sintering) of metal nanoparticles (NPs) over time under operating condition is the major concern, especially for the catalyst with metal NPs in small sizes. Self-regenerable metal NPs on the oxide surface show great potential to overcome this problem. Metal oxide NPs are highly anchored on the oxide support under oxidative conditions with strong metal − support interaction (MSI) leading to the sintering resistance, while they are subsequently reduced back to active metallic NPs under reductive conditions. This approach is often employed to prepare the ultrastable TWCs in which the platinum-group metal (PGM) NPs are exposed to the high-temperature reduction − oxidation (redox) fluctuations of exhaust gas. PGM-O − M bonds (M is the metal of the support surface) formed in oxidative atmospheres can suppress sintering effectively. We investigated a machine-learning enhanced density functional theory study of Pd_xO_y nanoparticles supported on a $Sr_3Ti_2O_7$ (001) surface and demonstrate that supported oxidized Pd particles fulfill the conditions for the self-regenerative catalysts [1].

We also elucidated the surface facet dependence on the oxygen adsorption and oxidized surface morphology of the diamond (111) and (100) surfaces to give insights that will improve the polishing, etching, and fabrication of diamond devices [2]. Furthermore, We perform machine learning molecular dynamics simulations to gain an atomic-level understanding of the dependence of the graphitization and thermal degradation behavior of diamond to the (111) and (100) surface facets.[3] The interatomic potential is constructed using graph neural network model, trained using energies and forces from spin-polarized van der Waals-corrected density functional theory calculations. Our results show that the C(111) surface is more susceptible to thermal degradation, which occurs from 2850 K through synchronized bilayer exfoliation mechanism. In comparison, the C(100) surface thermally degrade from a higher temperature of 3680 K through the formation of sp1 carbon chains and amorphous sp2-sp3 carbon network. Due to the dangling bonds at the step edges, the stepped surfaces are more susceptible to thermal degradation compared to the corresponding flat surfaces, with the stepped C(111) and C(100) surfaces thermally degrading from 1810 K to 3070 K, respectively. We propose potential applications of this study in diamond tool wear suppression, diamond polishing, and pro-

duction of graphene directly from the diamond surface.

We also conducted collaboration with experimental groups. Using $ab-initio$ calculations of the XPS chemical shift, we identified chemical species on plasma-treated polytetrafluoroethylene (PTFE) surfaces.[4]

We also conducted theoretical calculations on the energies of oxygen reduction and hydrogen insertion reactions with oxygen-deficient perovskite oxides and we demonstrated that the oxygen vacancy ordering in $Sr(Fe_{1-x}Co_x)O_y$ (SFCO) epitaxial films can be stabilized by increasing the Co content ($x \geq 0.3$) and revealed that it plays a key role in promoting proton accommodation into the SFCO lattice. Our results provide guidelines for controlling material properties through the insertion and extraction of hydrogen and for designing and exploring hydrogen-insertion materials.[5]

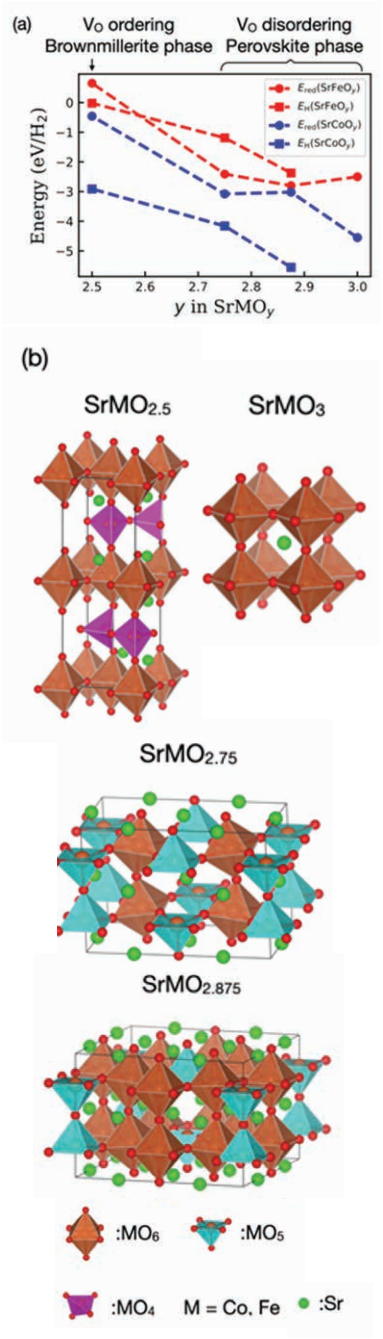


Figure 1: Theoretical investigation of oxygen reduction and protonation of $SrFeO_y$ and $SrCoO_y$. (a) Oxygen reduction energy (E_{red}) and hydrogen insertion energy (E_H) of $SrMO_y$ (M = Fe and Co) as a function of oxygen stoichiometry(y). (b-e) Crystal structures of $SrMO_y$.

References

[1] T. N. Pham, B. A. Choi Tan, Y. Hamamoto, K. Inagaki, I. Hamada, and Y. Morikawa, ACS Catal. **14**, 1443-1458 (2024).

[2] J. I. G. Enriquez, T. Yamasaki, M. Michiuchi, K. Inagaki, M. Geshi, I. Hamada, Y. Morikawa, J. Phys. Chem. C **128**, 6294-6308 (2024).

[3] J. I. G. Enriquez, H. H. Halim, T. Yamasaki, M. Michiuchi, K. Inagaki, M. Geshi, I. Hamada, Y. Morikawa, Carbon **226**, 119223 (2024).

[4] M. Nishino, K. Inagaki, Y. Morikawa, K. Yamamura, and Y. Ohkubo, Appl. Surf. Sci. **655**, 159369 (2024).

[5] Y. Isoda, T. N. Pham, R. Aso, S. Nakamizo, T. Majima, S. Hosokawa, K. Nitta, Y. Morikawa, Y. Shimakawa, and D. Kan, Nature Commun. **16**, 56 (2025).

FTQC Algorithm Implementation for Quantum Chemistry: A Hybrid approach with Quantum- and Super-computer

Yu-ichiro Matsushita

Department of Physics,

The University of Tokyo, Hongo, Tokyo 113-8626

In recent years, quantum computers have been attracting attention in the field of material calculations due to their ability to solve problems that are difficult for conventional supercomputers. In this work, we used the hybrid computing approach combining the supercomputer "ohtaka" at The University of Tokyo and Quantinuum's quantum computer to perform quantum chemistry calculations. A particularly noteworthy achievement was the successful execution of FTQC (Fault-Tolerant Quantum Computing) algorithms for ground state calculation on a real quantum computer using quantum error detection codes, marking the world's first attempt. The calculation target of this study is composite defects in aluminum nitride (AlN) to reveal the great potential as a promising quantum bit material. The successful implementation of FTQC algorithms in this study demonstrated their efficacy in generating highly accurate material property values through quantum chemistry calculations.

For this study, the calculation model involved around 300 atoms, and initial calculations were performed using Density Functional Theory (DFT) on the "ohtaka" supercomputer at The University of Tokyo. A downfolding method was employed to reduce the problem size without sacrificing precision, focusing on the most challenging regions of the system that required high-accuracy calculations. Subsequently, Quantinuum's trapped-ion quantum computer "H1-1" was used to execute FTQC algorithms on the refined model, and quantum error detection codes (Iceberg codes) were applied to mitigate the effects of quantum noise, leading to highly accurate results.

The outcome of this study demonstrated that FTQC algorithms function with high accuracy, successfully determining both the ground and excited states of composite defects, which are promising as quantum bit materials. The FTQC algorithm used in the calculations was the probabilistic imaginary time evolution (PITE) method, which was developed by our group. The PITE method has been mathematically proven to accelerate quantum chemistry calculations, and its successful implementation in this research confirms its potential.

Moreover, the study revealed that composite defects in AlN possess highly unique quantum properties, including spin triplet and spin singlet states, which are particularly valuable for quantum bit applications. This discovery expands the diversity of quantum bit materials. The calculations showed that, compared to an ideal FTQC machine, the current quantum computer hardware can achieve 98% of the ideal FTQC machine's precision. (See Fig.1)

As quantum computers continue to improve, the practical application of FTQC algorithms is expected to accelerate the development of quantum chemistry calculations and materials informatics. The results of this research were released in a press release and idely disseminated.

References

[1] H. Nishi, *et. al.*, Phys. Rev. Applied **23**, 034016 (2025).

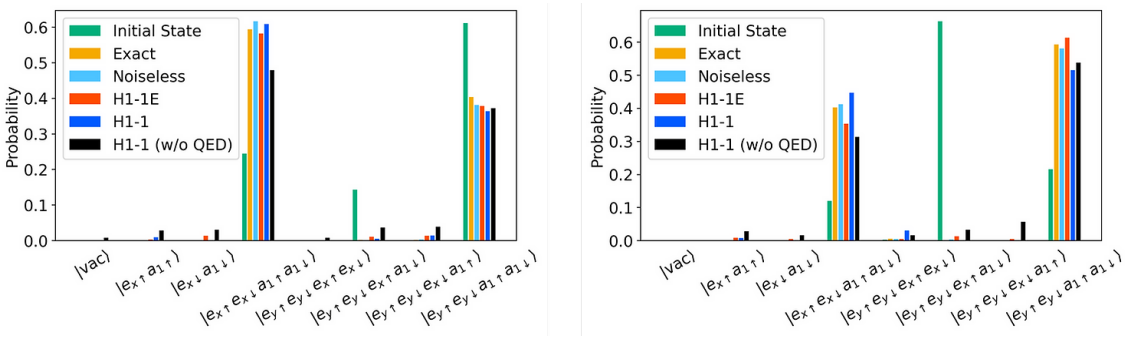


Fig. 1, Execution results on a real quantum computer. The results for the ground state (left figure) and the excited state (right figure). In each figure, the initial state is shown in green, the exact imaginary time evolution method in yellow, the ideal quantum computer without noise in light blue, the simulation results with the noise model in red, the results from the real quantum computer using quantum error detection codes in blue, and the results from the real quantum computer without using quantum error detection codes in black.

Analyses on local properties at complex structures via ab-initio-based methods/ Analyses on correlation between material properties and atomic structures in complex structures via ab-initio-based methods

Satoshi WATANABE
Department of Materials Engineering, the University of Tokyo
7-3-1 Hongo, Bunkyo-ku, Tokyo, 113-8656

1 Introduction

Understanding local properties in complex structures—such as amorphous phases, surfaces, interfaces, and defects—is crucial for advancing new information devices and energy systems. To this end, we have conducted simulations based on ab initio methods, particularly density functional theory (DFT) and machine learning potentials (MLPs).

As research has progressed, the correlation between atomic structures and local properties has become increasingly important. Recently, we have focused our studies on elucidating these correlations. Below, we introduce two of our results from fiscal year 2024.

2 Construction of machine learning potentials for alloy cluster catalysts

High entropy alloys (HEAs), containing five or more elements, have attracted significant attention as potential candidates for various applications. However, identifying optimal HEAs through DFT calculations is computationally expensive due to the vast compositional space. To address this, we constructed machine learning potentials (MLPs) for efficient catalyst discovery [1].

Our target was catalysts for the CO_2 reduction reaction (CO_2RR), where activity and selectivity are closely linked to the adsorption energies of CO molecules and H atoms. We trained MLPs to predict these energies, using DFT data on optimized structures, total energies, and adsorption energies for nine promising elements (Ag, Au, Co, Cu, Ni, Ir, Pd, Pt, Rh). Training data were sourced from both in-house calculations and publicly available data [2, 3, 4].

Unlike previous studies that focused on flat slab models, we constructed MLPs applicable to cluster models, as non-flat surfaces often exhibit superior catalytic activity. Our MLPs achieved mean absolute errors typically below 60 meV for adsorption energies and total energies (per atom), even for clusters of varying size and shape and up to five elements.

Using these MLPs, we identified HEA compositions with the H and CO adsorption energies within desirable ranges for catalysis. This work provides a strong foundation for high-throughput screening of alloy compositions and cluster geometries, addressing current limitations in DFT calculations for HEA clusters.

3 Thermal conductivities of AlN crystals with vacancies

Aluminum nitride (AlN) is widely used in electronic devices, where heat dissipation critically affects performance. Since fabrication processes inevitably introduce defects, it is important to understand how these defects—and their charge states—impact thermal conductivity. While DFT offers high predictive accuracy, it is computationally intensive. Conventional MLPs cannot handle multiple defect charge states, so we previously developed a scheme [5] based on high-dimensional neural network potentials (NNP) [6] to address this.

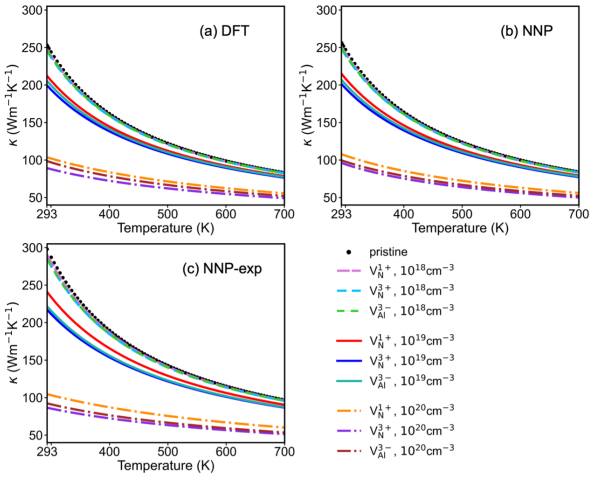


Figure 1: Comparisons of thermal conductivities between pristine AlN and defect-laden AlN predicted using the optimal lattice constants by (a) DFT, (b) NNP and using the experimental lattice constants by (c) NNP. Reprinted from Ref. [7].

In this study [7], we applied this scheme to investigate the effects of nitrogen vacancies in +1 and +3 charge states (V_N^{1+} and V_N^{3+}) and aluminum vacancies in −3 charge state (V_{Al}^{3-}) on the lattice dynamics of AlN. The 2nd and 3rd-order interatomic force constants were calculated using the finite displacement method via the PHONOPY [8] and thirdorder.py [9] codes, respectively. The thermal conductivities were calculated using the AlmaBTE package [10]. The constructed NNP exhibited excellent accuracy, with root mean square errors of 3.55 meV/atom (training) and 3.48 meV/atom (testing) for total energies, and about 69 meV/Å for atomic forces. Phonon bands, phonon scattering rates, and thermal conductivity (κ) predicted by the NNP were in good agreement with DFT results. The results on κ are shown in Fig. 1. We found that V_N^{3+} most significantly reduces κ, followed by V_{Al}^{3-} and then V_N^{1+}. Our findings contradict earlier speculations based solely on mass differences and highlight the critical role of structural distortions in phonon scattering.

References

[1] K. Miyamoto, K. Shimizu, A. K. A. Lu, and S. Watanabe: e-J. Surf. Sci. Nanotechnol., in press.

[2] J. K. Pedersen, T. A. A. Batchelor, and A. Bagger: ACS Catal.**10** (2020) 2169.

[3] K. Tran and Z. W. Ulissi: Nat. Catal. **1** (2018) 696.

[4] M. Scheidgen, et al.: J. Open Source Softw. **8** (2023) 5388.

[5] K. Shimizu, et al.: Phys. Rev. B **106** (2022) 054108.

[6] J. Behler and M. Parrinello: Phys. Rev. Lett. **98** (2007) 146401.

[7] Y. Dou, et al.: Phys. Rev. Mater. **9** (2025) 034601.

[8] A. Togo and I. Tanaka: Scr. Mater. **108** (2015) 1.

[9] A. Togo, L. Chaput, and I. Tanaka: Phys. Rev. B **91** (2015) 094306.

[10] J. Carrete, et al.: Comput. Phys. Commun. **220** (2017) 351.

Development of a first-principles computational method for functional materials

Fumiyuki ISHII, Naoya YAMAGUCHI, Rifky SYARIATI,
Hana Pratiwi KADARISMAN, Shohei MIURA,
Yaotang ZHANG, Yedija Yusua Sibuea TEWENG, Jin INOUE, Sota, YAMATE
Khusnul YAKIN, Wardah AMALIA, Shigetomo YANASE,
Syifa Fauzia Hariyanti PUTURI, Ahmad GHIFFARI, Salsabila Amanda PUTRI
Nanomaterials Research Institute, Kanazawa University
Kanazawa, 920-1192, Japan

1. *High-throughput computational screening of 2D thermoelectric materials*[1]
The pursuit of efficient thermoelectric energy conversion has gained momentum as a solution for waste heat recovery and environmental sustainability. Despite existing repositories documenting electronic characteristics of two-dimensional materials and conventional thermoelectric compounds, a significant knowledge gap persists regarding transverse transport phenomena, specifically anomalous Hall and Nernst conductivities in magnetic 2D systems. To bridge this deficiency, we employed computational high-throughput screening via first-principles density functional theory coupled with Boltzmann transport formalism. Among the investigated systems, transition metal trihalide monolayers emerged as exemplary candidates, with comprehensive analysis of 240 structural variants revealing that $PdBr_3$ and $PtBr_3$ ferromagnetic films demonstrate quantized anomalous Hall transport in both pristine and charge-doped configurations. Spin-orbit interactions induce modest energy gaps (approximately 35 meV and 12 meV for $PdBr_3$ and $PtBr_3$ respectively), establishing these systems as topological Chern insulators characterized by non-trivial Berry curvature distributions and contrasting Chern indices across the chemical potential range.

Our computational analysis uncovered remarkable anomalous Nernst responses in these layered compounds, with $PdBr_3$ exhibiting peak coefficients of -54.1 $\mu V/K$ while $PtBr_3$ demonstrates values reaching -23.3 $\mu V/K$ under ambient conditions with appropriate hole carrier concentrations. The exceptional magnitude of these coefficients stems from the interplay between thermally-driven charge currents and topologically-protected Hall responses, facilitated by the distinctive band topology in proximity to the chemical potential. The tunability of coefficient polarity through electronic doping, together with the enhancement provided by van Hove critical points, positions these materials as attractive platforms for advanced energy conversion technologies, especially in internet-of-things applications demanding versatile thermal energy scavenging capabilities.

2. *Anomalous Nernst effect in $CrGeTe_3$*[2]
We have performed first-principles calculations to investigate the anomalous Nernst effect in ferromagnetic $CrGeTe_3$ thin films and understand the origin of large anomalous transverse thermoelectric effects in two-dimensional ferromagnetic materials. We focused on how Berry curvature contributes to anomalous Hall conductivity, particularly examining the role of nodal lines—degenerate points in the band

structure that become small band gaps when spin-orbit coupling is introduced. In monolayer $CrGeTe_3$, we discovered a circular nodal line in the conduction band energy range of 0.43–0.58 eV, which oscillates with six minima and maxima around the Γ point in k-space.

When we included spin-orbit coupling in the calculations, the nodal line created small band gaps that generated large Berry curvatures, resulting in significant anomalous transverse thermoelectric conductivity α_{xy}. We found peaks in both anomalous Hall conductivity σ_{xy} and anomalous transverse thermoelectric conductivity α_{xy} around $\mu = 0.32$ eV, with magnitudes reaching approximately 10 $(\mu\mathrm{V/K})(e^2/h)$. These findings suggest that ferromagnetic $CrGeTe_3$ thin films exhibit promising anomalous Nernst effects originating from the nodal line structure, making them potential candidates for thermoelectric applications that leverage transverse temperature gradients.

3. *Layer-Resolved Anomalous Hall Effect in Thin Films and Heterointerfaces: First-Principles Study*[3]

This research presents a comprehensive first-principles computational study of the anomalous Hall effect (AHE) with layer-by-layer decomposition in various thin film and heterointerface systems. The research team from Kanazawa University developed an advanced computational methodology that combines local Berry phase approaches [4] with hybrid Wannier functions to analyze the contribution of individual layers to the anomalous Hall conductivity in metallic systems. By calculating Berry phases (Berry curvature) on two-dimensional Brillouin zone meshes and constructing hybrid Wannier functions on the same mesh, the researchers successfully achieved layer-resolved decomposition of the anomalous Hall effect in complex material systems. The computational investigations encompassed single metallic systems including Fe thin films, Cr thin films, and $SrRuO_3$ thin films, as well as ferromagnetic/nonmagnetic heterostructures such as Fe/W and $SrRuO_3/SrIrO_3$. The results revealed characteristic features of layer-resolved anomalous Hall conductivity, demonstrating enhanced conductivity near interfaces and significant contributions from specific layers, which correspond well with important experimental observations in metallic systems. Additionally, the study provided insights into the spatial distribution of the anomalous Hall effect in antiferromagnetic materials, offering new perspectives on topological properties and improving understanding of transport phenomena in complex systems through examination of individual layer contributions.

References

[1] R. Syariati, S.A. Wella, E. Suprayoga, M.S. Muntini, and F. Ishii, J. Phys.: Condens. Matter **37** 025602 (2025).

[2] K. Shibata, E. Suprayoga, R. Syariati, and F. Ishii, *in preparation*.

[3] F. Ishii, H. Kadarisman, Y. Morishima, and N. Yamaguchi, *in preparation*.

[4] H. Sawahata, N. Yamaguchi, S. Minami, and F. Ishii, Phys. Rev. B **107** 024404(2023).

Development of first-principles calculation code RSPACE and design of highly functional interface

Tomoya ONO
Graduate School of Engineering, Kobe University
Rokkodai-cho, Nada, Kobe 657-8501

Silicon carbide (SiC) is a wide-bandgap semiconductor that has attracted considerable attention as a promising material for next-generation power electronics devices, including the **metal-oxide-semiconductor field-effect transistor (MOSFET)**. However, the high channel resistance at the thermally oxidized SiC/SiO_2 interface degrades the performance of SiC MOSFETs, which occurs by the reduction of field-effect mobility, compared to that in the bulk material. Post-oxidation annealing processes using nitrogen-based gases substantially improve this mobility degradation at the interface. In our studies, we utilized the first-principle electronic structure calculations and investigated mobility degradation mechanisms that originate from sources distinct from conventional trap states. Previously, we reported that the conduction band edge (CBE) states exhibit discontinuities in the inversion layer at atomic step edges, which are induced by the Coulomb interaction of oxygen atoms in the SiO_2 layer [1]. In the present study, we extended our analysis to the effect under a more realistic low nitrogen concentration, approximately one-third of which was used in our previous calculations and comparable to the values reported in recent experiments.

In this study, the computations were performed using the **RSPACE code**, which employs a real-space finite-difference approach for density functional theory (DFT) calculations [2]. We considered various slab supercell models of 4H-SiC(0001)/SiO_2 interfaces; Fig. 1 illustrates an example of the atomic-scale structure. The model consists of a SiO_2 region (thickness: 8.2 Å) and a 4H-SiC substrate comprising seven SiC bilayers (thickness: 17.5 Å), where quasi-cubic (k) and hexagonal (h) sites are alternately stacked along the [0001] direction. Furthermore, the computational models are categorized based on both the SiC-side interface (*i.e.* whether the topmost Si layer corresponds to a k site or an h site) and the SiO_2-side structure (*i.e.* whether the interface layer faces a one-fold or three-fold Si-O structure); then, the models are referred to as k1, k3, h1, and h3 interfaces, respectively. For the nitrided region, similar to our previous work [1], we incorporated nitrogen atom defects with a density of 1.22×10^{15} atoms/cm^2.

In this work, we investigated the accumulation of the charge density of the CBE states by using the partial charge (PC) densities defined below:

$$\rho_{\mathrm{PC}} = \sum_{i,k} \left| \int \Psi^*_{i,k}(\boldsymbol{r}) \phi_k(\boldsymbol{r}) d\boldsymbol{r} \right|^2 \times \theta(\epsilon_{i,k} - \epsilon_F)\theta(\epsilon_{max} - \epsilon_{i,k})\Delta_k, \quad (1)$$

where ϵ_F is the Fermi level, θ is the Heaviside function, and $\phi_k(x, y, z)$ is the wavefunction of the CBE states obtained by the thin film models. $\epsilon_{\max}(=\epsilon_F+1.65$ eV), which is the maximum energy of the energy window, is chosen so that the energy window contains the CBE states inside the SiC substrate. The calculated PC before and after annealings are plot-

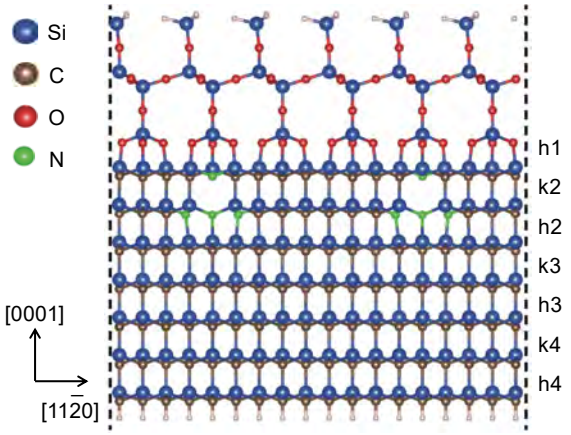


Figure 1: Slab supercell structure of the 4H-SiC/SiO_2 interface after NO annealing. An example is the h3-type model, characterized by a hexagonal (h) site at the SiC interface and a three-fold structure of Si–O bonds.

ted in Fig. 2. The PC values after partial nitridation are insensitive to the change of the nitrided regions. They are lower than those before NO annealing, owing to the screening of the Coulomb interaction from the oxygen atoms by the nitrided layer. However, the partial charge at the interface after partial nitridation remains larger than that after full nitridation, indicating that the effect of NO annealing may be limited.

In addition, we have calculated the carrier scattering property at the interface. The transmission spectrum for the h-type interfaces is shown in Fig. 3.

References

[1] M. Uemoto, N. Funaki, K. Yokota, T. Hosoi, and T. Ono, Appl. Phys. Express **17**, 011009 (2024).

[2] K. Hirose, T. Ono, Y. Fujimoto, and S. Tsukamoto, *First-Principles Calculations in Real-Space Formalism, Electronic Configurations and Transport Properties of Nanostructures* (Imperial College, London, 2005).

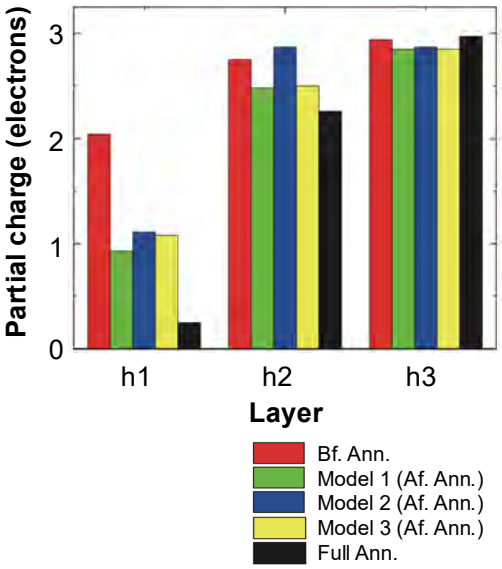


Figure 2: Partial charge densities [Eq. (1)] of the CBE states for various interface structures. Before annealing ("bf. ann.") refers to the pristine h3-type interface model. Model 1 represents the annealed ("af. ann.") structure illustrated in Fig. 1. Model 2 and Model 3 correspond to similar h-type interfaces incorporating nitrogen atoms at different sites. "Full Ann." denotes the model in which all considerable sites are nitrided, as studied in our previous work [1].

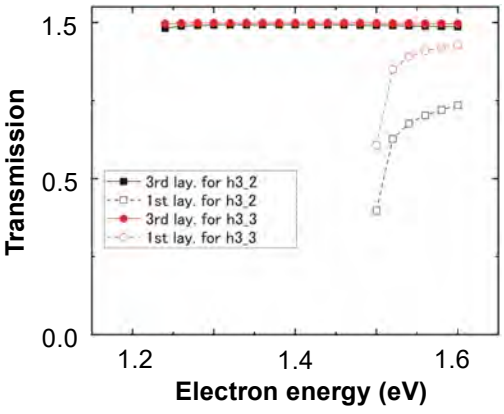


Figure 3: Transmission of h-type interfaces at 1st layer and 3rd layer channels.

Density functional theory study of adsorption and reaction of molecules on solid surfaces and interfaces

Ikutaro Hamada

Department of Precision Engineering, Graduate School of Engineering,

The University of Osaka (aka Osaka Universit)y, 2-1 Yamadaoka, Suita, Osaka 565-0871

Understanding the microscopic details of adsorption and reaction of molecules on surfaces of solid and low-dimensional materials is of critical importance as they play key roles in fundamental chemical processes, such as wetting, as well as technologically relevant ones, such as heterogenous catalytic reactions. We performed density-functional theory (DFT) simulations on organic molecules on a semiconductor surface [1,2], graphene adsorption on a metal surface, bilayers composed of the hydrogen boride (HB) sheets [3], water adsorption on the edges of the HB sheet [4], chemical reactions of various molecules on the HB sheet surface, using different DFT codes including STATE [5] and Quantum-ESPRESSO [6]. Below, I describe the key findings obtained mainly using the system B of the supercomputer facility at ISSP.

We investigated the organic molecules such as C_{60} and PTCDA on the Si(111)(7×7) surface and succeeded in determining their adsorption states, including adsorption sites, corresponding adsorption energies, and vibrational modes. We also investigated graphene on the Rh(111) surface and succeeded in reproducing the Moiré pattern of graphene observed in the experiment. Furthermore, we succeeded in characterizing the adsorption states of single atoms the on graphene/Rh(111) system. For the HB sheets, we clarified the vibrational properties of the HB sheet and bilayers composed of HB sheets and DB sheets using the recently developed computationally efficient package [7] and contributed to the characterization of the experimental vibrational spectroscopy. Furthermore, we investigated the adsorption and reaction of a water molecule at the surface and edge of the HB sheet and found that water dissociation is more facile near the edge region, not on the surface, and suggest that hydrolysis reaction observed in the experiment take place near the edge of the HB sheet. Finally, the carbon dioxide conversion to methane and ethane [8] on the HB sheet is currently under intense investigation and will be published in the near future.

References

[1] Y. Park, I. Hamada, A. Hammud, E. W. Meijer, M. Wolf, T. Kumagai, and A. Shiotari, Nat. Commun. **15**, 6709 (2024).

[2] B. Cirera, S. Liu, Y. Park, I. Hamada, M.

Wolf, A. Shiotari, and T. Kumagai, Phys. Chem. Chem. Phys. **26**, 21325-21331 (2024).

[3] S.-I. Ito, K. I. M. Rojas, Y. Yasuda, N. Noguchi, K. Fukuda, M. Hikichi, Z. Kang, M. Yuan, R. Tsuji, O. Oki, S. Roy, Y. Hikita, I. Matsuda, M. Miyauchi, I. Hamada, and T. Kondo, J. Phys. Chem. Lett. **15**, 10965-10976 (2024).

[4] K. I. M. Rojas, Y. Morikawa, and I. Hamada, Phys. Rev. Materials **8**, 114004 (2024).

[5] STATE documentation, https://state-doc.readthedocs.io/

[6] P. Giannozzi et al., J. Phys. Condens. Matter 21, 395502 (2009).

[7] K. I. M. Rojas, Y. Morikawa, and I. Hamada, J. Open Source Softw. **10**, 7855 (2025).

[8] T. Goto, S.-I. Ito, S. L. Shinde, I. Matsuda, and I. Hamada, H. Hosono, and T. Kondo, Commun. Chem. **5**, 118 (2022).

Development of Anharmonic Phonon Property Database Using First-Principles Calculations

Masato OHNISHI

The Institute of Statistical Mathematics,

Research Organization of Information and Systems, Tachikawa, Tokyo 190-0014, Japan

In recent years, data-driven materials development has been rapidly advancing. For inorganic materials in particular, in addition to conventional databases such as the Materials Project, large and newly released databases like DeepMind GNoME (2023) [1], META OMat24 (2024) [2], and Microsoft MatterK (2025) [3] have also become available. However, these databases often lack thermal property data or cover only a limited materials space. Moreover, thermal properties can vary significantly depending on factors such as impurities and carrier concentration, highlighting the need for thermal property databases constructed through theoretical calculations under well-defined conditions.

In this study, we developed automation software for calculating anharmonic phonon properties, named auto-kappa (Fig. 1), which enables the computation of mode-dependent phonon lifetimes, temperature-dependent thermal conductivities, and spectral thermal conductivities. Using this software, we constructed the anharmonic phonon property database through high-throughput first-principles calculations. As a result, we obtained

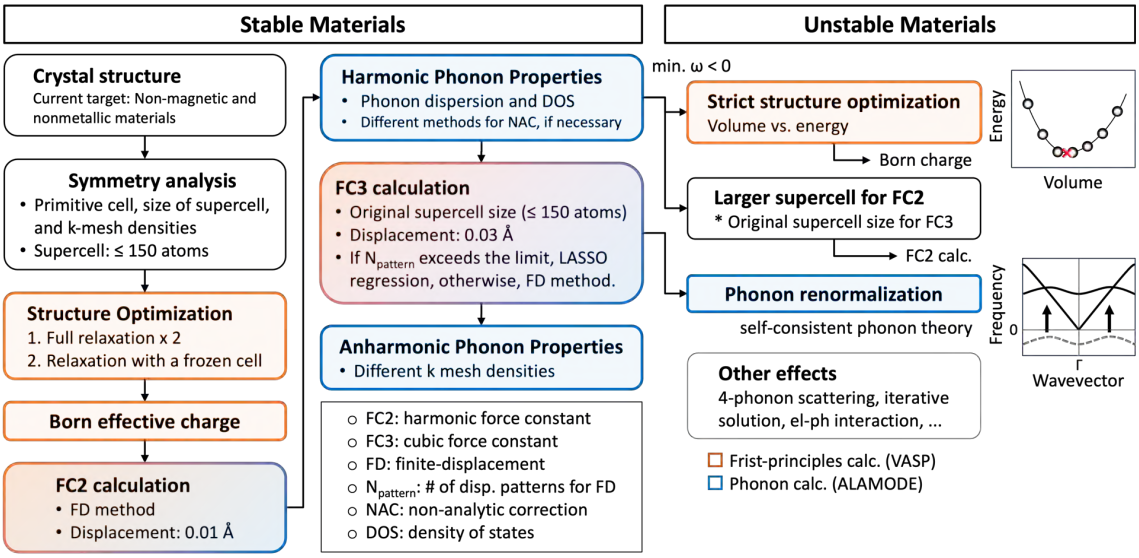


Fig. 1. Automated workflow for anharmonic phonon properties.

anharmonic phonon properties for over 6,000 inorganic materials. Leveraging this dataset, we demonstrated deep-learning scaling laws and screened for materials with high and low thermal conductivity from the GNoME database, which contains over 230,000 novel compounds. This work has been recently submitted to npj Computational Materials and arXiv. The developed software and database will be made publicly available upon the publication of the paper. The database is expected to be utilized in materials development across a diverse range of fields, including not only thermal properties but also mechanical, electronic, electrical, magnetic, and optical properties.

References

[1] Merchant, A. et al. Scaling deep learning for materials discovery. Nature 624, 80–85 (2023).

[2] Barroso-Luque, L. et al. Open Materials 2024 (OMat24) Inorganic Materials Dataset and Models. arXiv (2024) doi:10.48550/arxiv.2410.12771.

[3] Li, J. et al. Probing the Limit of Heat Transfer in Inorganic Crystals with Deep Learning. arXiv (2025) doi:10.48550/arxiv.2503.11568.

Analysis of thermal transport in disordered systems

Junichiro SHIOMI

Department of Mechanical Engineering,

The University of Tokyo, Hongo 7-3-1, Bunkyo-ku, Tokyo 113-8656, Japan

We investigated thermal transport behaviour in various complex systems. This year, we focused on the heat transport property of $FeCl_3$-graphite intercalation compounds and thermal transport suppression due to impurity addition in bulk disordered systems like amorphous silicon.

1. $FeCl_3$-graphite intercalation compounds

This study extends previous research on graphite and its intercalation with $FeCl_3$ to further elucidate the thermal conductivity behavior across different intercalation stages. In this context, "Stage-n" denotes the number of graphene layers between adjacent intercalant layers. Using non-equilibrium molecular dynamics (NEMD) simulations, we previously observed a non-monotonic trend in thermal conductivity, characterized by an initial decrease followed by an increase. Our findings suggest a transition from a coherent transport regime at lower stages to an incoherent regime at higher stages. Notably, Stage-3 exhibits an unexpected increase in thermal conductivity compared to Stage-2, before subsequently decreasing. To investigate the underlying mechanisms, we performed Spectral Energy Density (SED) analysis to extract phonon dispersion relations as a function of frequency and wavevector. This enabled the calculation of key thermal properties, including phonon mean free path and coherence length. The observed reduction in mean free paths and an increase in coherence lengths (Fig. 1a, b) relative to pristine graphite provide insight into the suppression of thermal conductivity in $FeCl_3$-intercalated graphite.

2. Impurity addition in bulk a-Si

In this study, NEMD simulations were performed on amorphous silicon (a-Si) to investigate the impact of impurities on thermal transport. In amorphous materials, thermal conduction is governed by both propagating modes (propagons) and non-propagating modes (diffusons), making it challenging to characterize the effect of impurities on vibrational modes [1,2]. Impurities were introduced by randomly substituting Si atoms with heavier Si isotopes at varying atomic concentrations (at%). The calculated thermal conductivity values (Fig. 2a) reveal a reduction of 10–20% at 10 at% impurity concentration, aligning with experimental observations. Density of states calculations confirmed that this reduction is not due to a decrease in the

speed of sound caused by mass effects. Interestingly, the Allen-Feldman theory [2], which predicts similar thermal conductivity for pure and impure amorphous systems, fails to capture this suppression. Further analysis using normal mode decomposition (NMD) method (Fig. 2b) suggests that impurity scattering does not significantly suppress relaxation times. However, participation ratio (PPR) calculations based on eigenmodes (Fig. 2c) indicate increased mode localization with impurity addition, which likely contributes to the observed thermal conductivity suppression

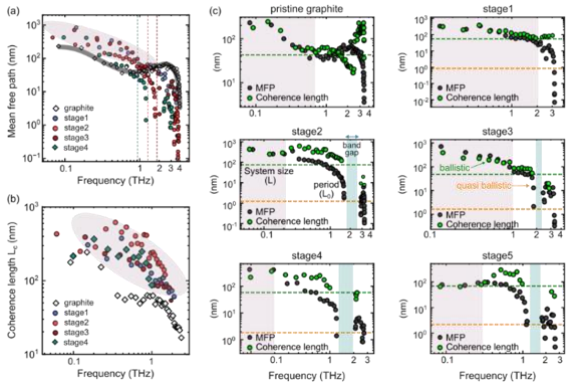


Fig. 1. Comparison of a) mean free path and b) coherence length with respect to frequency between stages 1-4 and pristine graphite. c) Expanded plots for direct comparison of mean free path and coherence length for each stage and pristine graphite

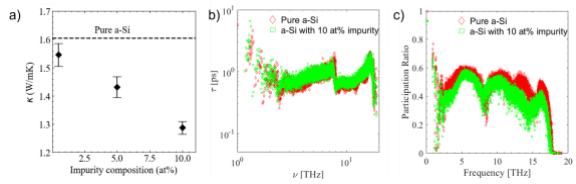


Fig. 2 a) Thermal conductivity variation with respect to the composition of heavy Si, b) Relaxation time as a function of frequency and c) Participation ratio as a function of frequency for pure a-Si and a-Si with 10 at% of heavy Si. The above results were obtained for heavy Si with mass twice that of pure Si.

References

[1] J.M. Larkin et al., Phy. Review B., 89, 144303 (2014)

[2] P. B. Allen et al., Philosophical Magazine, 79, 11-12 (1999)

Reduction of Rare Metals in Fuel Cell and Formic Acid Decomposition Catalysts

Norihito Sakaguchi

Center for Advanced Research of Energy and Materials, Faculty of Engineering, Hokkaido University, Sapporo, Hokkaido 060-8628

We investigated the effects of adsorbates on the adsorption energy and diffusion barrier of single Pt atoms and Pt dimers supported on the light-element doped graphene using first-principles calculations based on density functional theory (DFT). We also investigated the catalytic selectivities of the single Pt atoms supported on the light-element doped graphene in formic acid decomposition reactions. We have also studied the adsorption states of a CO monolayer on Ag(111) surfaces.

First, we investigated the adsorption energy and diffusion barrier of single Pt atoms and Pt dimers supported on the light-element doped graphene. We performed the total energy and electronic structure calculations using the Vienna Ab initio Simulation Package (VASP). We installed a parallelized VASP with Intel® MPI Library and Intel® Math Kernel Library. We showed that the adsorption energy and diffusion barrier of single Pt atoms and Pt dimers drastically change by the adsorption of atoms and molecules.[1] In some cases, the diffusion barrier of the single Pt atoms and Pt dimers becomes less than 0.1 eV. However, the effects of adsorbates were complex, and a systematic understanding of their effects was not available.

We investigated the catalytic selectivities of the single Pt atoms supported on the light-element doped graphene in formic acid decomposition reactions. We considered four reaction pathways: two for hydrogen production and two for water production. We found that the light-element dopants in graphene can significantly change the catalytic selectivities.

We investigated the adsorption states of a CO monolayer on Ag(111) surfaces.[2] The obtained adsorption energy and adsorption structure show good agreement with experimental results. We also revealed that structural fluctuation can occur very easily with small activation barriers. This result explains the experimentally observed structural fluctuation in low-temperature conditions.

References

[1] Y. Kunisada, N. Sakaguchi, Catalysts and Catalysis 66 (2024) 259.

[2] M. Kimura, Y. Kunisada, Y. Sugimoto, Adv. Mater. Interfaces in press

Development of First-Principles GWΓ Method

Yoshifumi NOGUCHI

Department of Applied Chemistry and Biochemical Engineering, Graduate School of Engineering, Shizuoka University, Johoku 3-5-1, Hamamatsu, Shizuoka 432-8561, Japan

Considering first-order three-point vertex function ($\Gamma = 1 + iGGW$), we have developed a first-principles GWΓ method, which intrinsically goes beyond a conventional GW approximation [1], with the three-point vertex function approximated as unity ($\Gamma = 1$). To demonstrate the computational accuracy of the GWΓ method and contributions of newly added higher-order terms (or first-order three-point vertex functions) to the GW one-electron self-energy operator, we simulated the B1*s*, C1*s*, N1*s*, O1*s*, and F1*s* core-electron binding energies (BEs) of 19 small molecules, and directly compared them with the available experimental data without any artificial shifts. Table I lists mean absolute errors (MAEs) of the LDA Kohn-Sham orbital energies, and GW and GWΓ quasiparticle energies. It is well-known that LDA results significantly underestimate experimental BEs by approximately 20-34 eV. Herein, this underestimation was improved by simply replacing the LDA exchange-correlation potential with the GW one-electron self-energy operator; however, an error of several eV would remain. The shortcomings of GW method for the BEs were similar to those previously reported [2]. Additionally, the errors of GW method were reduced by the GWΓ method to 1.09-1.78 eV for B1*s*, C1*s*, N1*s*, O1*s*, and F1*s* BEs [3]. Because the present GW and GWΓ methods were executed with a one-shot (not self-consistent) version, the use of LDA one-electron wave functions was not sufficiently localized to describe the core-electron, thus potentially leading to errors in the GWΓ methods.

Table I. MAE of LDA, GW, and GWΓ (in eV)

	LDA	GW	GWΓ
B1*s*	20.21	3.71	1.09
C1*s*	25.19	5.14	1.35
N1*s*	28.35	6.94	1.60
O1*s*	31.97	7.80	1.78
F1*s*	34.33	5.78	0.45

References

[1] M. S. Hybertsen and S. G. Louie, Phys. Rev. Lett. **55**, 1418 (1985).

[2] M. J. van Setten, R. Costa, F. Viñes, and F. Illas, J. Chem. Theory Comput. **14**, 877 (2018).

[3] K. Yoneyama, Y. Noguchi, and K. Ohno, J. Chem. Phys. **161**, 154102 (2024).

Electrochemical reaction analysis using density functional calculation + implicit solvation model 6

Jun HARUYAMA

Pioneering Research Institute, RIKEN, 2-1 Hirosawa, Wako, Saitama 351-0198

Hydrogen energy conversion technologies such as fuel cells and water electrolysis devices are essential for realizing sustainable society. The investigation of fast hydrogen transport materials has attracted concerns. Recently, Ba–Li oxyhydride, $Ba_{1.75}LiH_{2.7}O_{0.9}$ (BLHO), shows the ionic conductivity of 10^{-5}–10^{-7} S/cm with activation energy of c.a. 103 kJ/mol at low temperatures ($T \leq 300$ °C, T is temperature) and 10^{-2} S/cm at high temperatures (300 °C < T), which conducting career has been certified as hydride ion (negative charge hydrogen, H^-). [1] In this study, we investigate H^- diffusion mechanism by first-principles molecular dynamics (FPMD) simulations.

To reproduce the occupancy ratios, the crystal structures of BLHO at low- (β) and high-temperature (δ) phases were modeled as 2×4×1 and 4×4×1 supercells as shown in Figs. 1 (a) and (b), respectively. We performed FPMD simulations with Perdew–Burke–Ernzerhof (PBE) exchange-correlation functional [2] by Vienna Ab initio Simulation Package (VASP) [3] in thermal equilibrium conditions (T = 500, 700, 900, and 1100 K) for several hundred ps. Then, the self-diffusion coefficient D, Lindemann indices (the indicators of liquid-solid transition), [4] and van Hove time correlation functions [5] of H were calculated from FPMD trajectories.

From the mean square displacements (MSD) of H atoms, we obtained *ab* plane and *c*-axis decomposed D values. The former values are plotted in Fig. 1 (c). The diffusion process in *ab* plane corresponds to the H^- hopping between anion equatorial sites. The estimated values of D are consistent with that obtained by the quasi-elastic neutron scattering (QENS) analysis (3–4×10^{-7} cm^2/s). [1] However, the activation energies E_a estimated from D values are 0.52–0.55 eV for both phases, which values are different from the estimated values from experimental ionic conductivity, E_a =1.0 eV (300 °C < T), but consistent with the analyses of elastic and inelastic neutron scattering intensities, E_a =0.6 eV (300 °C < T). [1] From the comparison, it is indicated that the rate-determining process of conductivity is not the *ab*-plane diffusion, but rather to the c-axis diffusion, ion movement at crystallite interfaces, or collective motions that cannot be accounted for our short time scale simulations.

Moreover, the Lindemann indices were calculated for Ba, Li, O, and H atoms as

shown in Fig. 1 (d). We found that the Lindemann index of H exceeds the threshold for a solid-liquid transition (= 0.1) at high temperatures above 700 K, which suggests the sublattice melting of anion equatorial sites and the superionic conduction of H^- in BLHO. We will discuss c-axis dynamics, collective motion, and diffusion mechanism of H^- from the time correlation function in future studies.

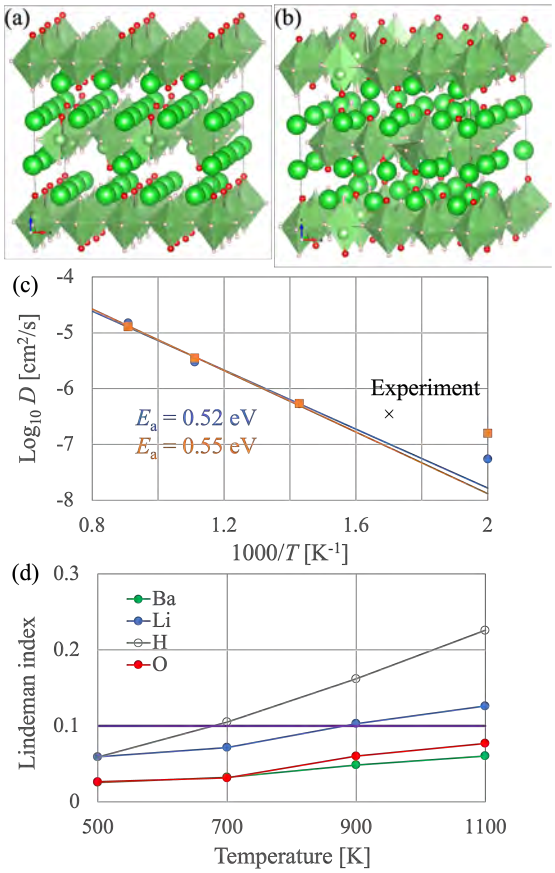


Figure 1: (a) β- and (b) δ-phase BLHO models. The VESTA package [6] was used to visualize the structures. (c) Diffusion coefficients D as a function of inverse temperature. The blue and orange squares represent β- and δ-phase values, respectively. The black cross mark represents D obtained by QENS analysis. [1] The blue and orange lines represent linear relation corresponds to the activation energies of 0.52 and 0.55 eV, respectively. (d) Lindeman indices as a function of temperature. The green, blue, gray, and red circles represent the Lindeman indices of Ba, Li, H, and O atoms, respectively. The black line is the criterion of liquid-solid transition.

References

[1] F. Takeiri, A. Watanabe, K. Okamoto, D. Bresser, S. Lyonnard, B. Frick, A. Ali, Y. Imai, M. Nishikawa, M. Yonemura, T. Saito, K. Ikeda, T. Otomo, T. Kamiyama, R. Kanno, and G. Kobayashi, *Nat. Mater.* **21**, 325 (2022).

[2] J.P. Perdew, K. Burke, and M. Ernzerhof, *Phys. Rev. Lett*. **77**, 3865 (1996).

[3] G. Kresse and J. Hafner, *Phys. Rev. B* **47**, 558 (1993); G. Kresse and J. Furthmüller, *Phys. Rev. B* **54**, 11169 (1996); G. Kresse and J. Furthmüller, *Comput. Mat. Sci.* **6** , 15 (1996).

[4] X. He, Y. Zhu, and Y. Mo, *Nat. Comm.* **8**, 15893 (2017).

[5] Y. Zhou, M. Karplus, K. D. Ball, and R. Stephen Berry, *J. Chem. Phys.* **116**, 2323 (2002).

[6] K. Momma and F. Izumi, *J. Appl. Crystallogr.* **44**, 1272 (2011).

Theoretical Studies on New Types of Electron Trap Defects Originated from Localized Floating States in a-SiN towards Flash Memories Application

Kenji SHIRAISHI

Institute for Materials and Systems for Sustainability,

Nagoya University, Furo-cho, Chikusa-ku, Nagoya, Aichi 464-8601

Catching and emitting electronic charges in a localized region of a material corresponds to writing and reading information data in memory devices. This could in principle be done by ordinary gap states. Yet, such states are generally prone to act as permanent traps for charge carriers mainly because of structural reconstructions occurring upon carrier trapping and/or emitting: This makes the capture and release events uncontrollable and even resulting in a degradation of the sought memory function. The localized floating states (LFS) identified, analyzed and characterized in this work is free from such structural reconstruction, not giving rise to any bonding or antibonding state but becoming reversible charge hosting and releasing centers. In our specific work on non-stoichiometric SiN systems, these LFSs exist in cavities free from structural or electronic defects. They arise just because of the networking of amorphous SiN when the amount of Si exceeds the reference one of Si_3N_4, resulting in empty spaces surrounded by an excess of four-fold coordinated Si atoms. Their active role in accepting up to two electrons has been rationalized in terms of well assessed bond descriptors, allowing for a quantitative interpretation of the peculiarity of LFS. Moreover, the preferred occupation of LFSs with respect to regular antibonding states populating the LUMO band by additional electrons can be explained in terms of local electrostatic potential, resulting more attractive of at least a factor of two in comparison with other unoccupied states, with these empty cavities acting as a sort of virtual cation able to attract the supplied electrons. Moreover, we show that the relative amount of Si and N is a way to control the arising of these states and to minimize the presence of other defects such as DBs, generally responsible for degradation, with direct practical consequences for the realization of devices. This stoichiometry tuning enhances device performance function of flash memory devices and guidelines for their design [1].

References

[1] T. Nagahashi, H. Karasawa, R. Horiike, A. Oshiyama and K. Shiraishi, IEEE Electron Devices Technology and Manufacturing (EDTM) 2025 – in press.

Clarification of Hole Trap at GaN/SiO_2 Interfaces and Fabrication of GaN-MOSFET

Kenji SHIRAISHI

Institute for Materials and Systems for Sustainability,

Nagoya University, Furo-cho, Chikusa-ku, Nagoya, Aichi 464-8601

Experiments in the past suggest that hole traps at GaN/SiO_2 interfaces are reduced with heavily Mg-doped GaN epitaxial layers [1,2], but its physical origin is unclear. In this study, we investigate by first-principles calculations the interaction between substitutional Mg atoms at Ga sites (MgGa) and O vacancy (V_O) in a nanometer-scale Ga-oxide (GaO_x) interfacial layer which is inevitably formed at GaN/SiO_2 interface, and clarify the physical reason why Mg passivates hole traps. Our calculations show that MgGa and V_O become stable by forming 2MgGa-V_O complex in GaO_x. In addition, while V_O form deep hole traps in the band gap of GaN, Mg attachment to V_O makes the hole-trap level shift upward substantially (Fig. 2) and thus 2MgGa-V_O induces no hole traps [3]. These results indicate that hole traps originated from V_O are passivated by the formation of a complex of MgGa atoms and V_O.

References

[1] H. Mizobata, Y. Wada, M. Nozaki, T. Hosoi, T. Shimura, and H. Watanabe, Appl. Phys. Express **13**, 081001 (2020).

[2] K. Tomigahara, M. Hara and H. Watanabe, Appl. Phys. Express **17**, 081002 (2024).

[3] S. Hattori, A. Oshiyama, K. Shiraishi, Applied Physics Letters **125**, 161601 (2024).

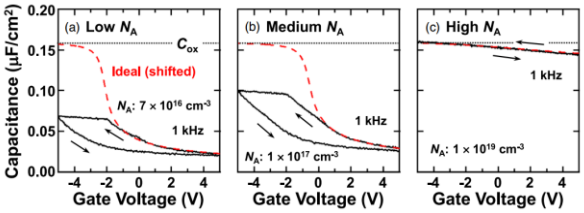


Fig.1: Experimental results of hole trap reduction by Mg incorporation. Hole trap reduction can be seen in case of heavily Mg incorporation. [Ref.1]

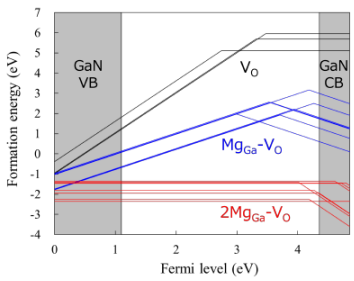


Fig.2: Formation energy diagram of Mg-V_O systems.

Clarification of Microscopic Mechanisms of Semiconductor Epitaxial Growth and Device-Interface Formation by Large-Scale Quantum-Theory-Based Computations[#]

Atsushi Oshiyama*

Institute of Materials and Systems for Sustainability, Nagoya University

Furo-cho, Chikusa-ku, Nagoya 464-8601

In the fiscal year of 2024, on the basis of the total-energy electronic-structure calculations and molecular dynamics simulations within the density-functional theory (DFT), we have studied the epitaxial growth of wide-gap semiconductors, atomic and electronic structures of semiconductor-insulator interfaces, and mechanisms of atomic diffusion in semiconductors. The main computational tools are our RSDFT (Real Space DFT) code and CPMD (Car-Parrinello Molecular Dynamics) code as well as VASP code. Specifically, we have clarified 1) that oxygen vacancy which is the major origin of hole traps at GaN/SiO_2 interfaces is passivated by doping either Mg[1] or B[2] impurities, contributing to better performance of MOS devices, 2) that implanted Mg atoms migrate in GaN via the carrier recombination processes, hereby sit at the Ga site and work as acceptors [3], 3) that in amorphous SiN which is a core part of the 3D NAND flash memory, peculiar electron states called localized floating states are nurtured in its internal space and work as charge centers, thereby making the amorphous the robust memory unit [4]. I will explain the issue 3) below.

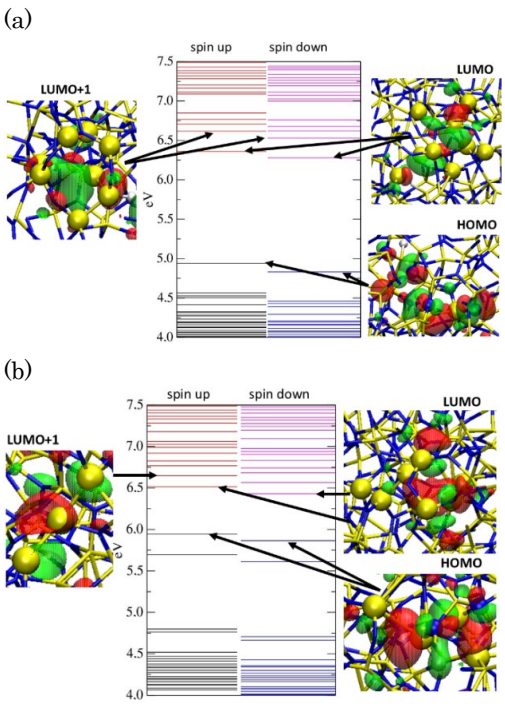


Figure: Panels (a) and (b) show the Kohn-Sham electronic levels and the related orbitals of the three hydrogenated systems r=1.22, 1.125 and 1.10, respectively. The atom color code is blue for N and yellow for Si with most relevant atoms highlighted as balls. The energy levels are colored in black (occupied states) and red (empty states) for α spin-up states and blue (occupied states) and magenta (empty states) for β spin-down states. The orbitals are shown at isosurface values of $\pm 5\times10^{-2}$ $1/Å^{3/2}$ corresponding to 30% of the full amplitude; red and green colors refer to positive and negative amplitudes, respectively.

Amorphous silicon nitride (a-Si_xN_y) is a premier element for a wealth of applications. In particular, it has replaced Si floating gates in flash-memory technology and now become indispensable materials which sustain our data-driven society. Device performance is tuned by changing its stoichiometry with respect to the standard x=3, y=4 (Si_3N_4) composition. Si rich (N poor) materials are usually used in the industry. Also hydrogen atoms are incorporated to guarantee the device operation. The mechanism of the memory function, i.e., which electron states are responsible for the read/write operation, is totally unknown, however.

Following the experimental information about the stoichiometry, we have prepared 3 amorphous samples with r = 1.22, 1.125 and 1.10 where r = [amount of N] / [amount of Si]: In our supercell model these correspond to (153Si+187N), (160Si+180N) and (162Si+178N), respectively. Hydrogen atoms (1 to 3, corresponding to the experimental situation) are added to mimic the hydrogenated systems. The amorphous samples were made by the melt-quench technique: At T=2500K each 3 system is well equilibrated for at least 50 ps and becomes liquid; then the systems were cooled down to 300K with the cooling rate of 9.56 K/ps, and kept at 300K for 150 ps; finally the systems are annealed to 0K and reach the optimized geometries.

In the obtained amorphous samples without hydrogenation, several point defects such as 3-fold coordinated Si (dangling bond), 5 fold coordinated Si as well as 2-fold N appear. The four-fold coordinated Si shows a very interesting feature: The geometries of SiN_4, Si-Si-N_3 and Si-SiN_2)-Si induce an interesting electron states near the conduction band minimum and even in the gap; the states are distributed in the backyard of the 4-folded coordinated Si, floating in the interstitial region of the material (*floating states*). Upon hydrogenation, the under- and over-coordinated point defects are passivated, but these floating states survive and generate gap states. The calculated Kohn-Sham orbitals in hydrogenated amorphous are shown in Figure. An important thing which we have found is that such gap state captures and emits an electron without any bond reconstruction, indicating the reversible capture and emission, in other words, the durable read and write process. We argue this floating state guarantees the function of current flash memories.

(The group id for this work is k0042)

in collaboration with Kenji Shiraishi, Mauro Boero and other young students.

*Present address: CIES, Tohoku University

Related publications

[1] S. Hattori, A. Oshiyama, and K. Shiraishi, Appl. Phys. Lett. **125**, 161601 (2024).
[2] Y. Zhao, A. Oshiyama and K. Shiraishi, Appl. Phys. Exp. submitted (2025).
[3] Y. Zhao, K. Shiraishi, T. Narita, and A. Oshiyama, Phys. Rev. B **110**, L081201 (2024).
[4] M. Boero, K. Shiraishi, T. Nagahashi, F. Nanataki, and A. Oshiyama, Phys. Rev. Mat., submitted (2025)

Analyses on electronic structure and magnetic anisotropy in high-performance spintronics magnetic materials and parallelization development/application in quasi-particle self-consistent *GW*

Tatsuki ODA[1,2], Rinku MAJUMDER[2], Jakub LUTSINEC[2], Akatov ARTUR[2], Takumi KATSUTA[2], Haruya Niwa[2], Hikaru Yamaguchi[2], Masao OBATA[1,2]

[1]*Institute of Science and Engineering, Kanazawa University, Kanazawa, Ishikawa 920-1192*

[2]*Graduate School of Natural Science and Technology, Kanazawa University, Kanazawa, Ishikawa, 920-1192*

We have studied electronic structure in several systems of non-magnetic or magnetic material by means of the density functional theory (DFT) or the quasi-particles self-consistent *GW* (QSGW) [1]. Concerned with the latter calculation, we have successfully optimized the time-consuming parts in the code for reducing the computational time. We have also developed the evaluation scheme in the calculation of magnetic anisotropy energy (MAE) in the density functional theory (DFT) code.

(A) MAE in the alloy containing heavy elements

Promising candidates for recording media, such as FePt alloys, have large magnetic anisotropy energy. This calculation aims to analyze the origin of MAE in a multilayer system of Pt/Fe/Pt. For this aim, in addition to a procedure of direct total energy calculation, the analysis for seeking the origins of anisotropy has been required. We have developed a new approach of force theorem method.

(B) Halide perovskites by QSGW

Halide perovskites are attracting attention because their bandgap and optical properties can be adjusted by varying the halogen composition. The present case is an application to $CH_3NH_3PbI_3$ and analyze its optical properties. Additionally, we investigated the effects of spin-orbit interaction (SOI) and structural changes on both the electronic states and several optical spectra using the exchange-correlation potential obtained from the QSGW calculations.

(C) Transparent superconductor by QSGW

Transition-metal-oxide $LiTi_2O_4$ is one of transparent superconductor and it is only superconductor in spinel oxides. Until now, the approach from the density functional theory (DFT) has revealed its electronic structures and provided frameworks to its superconductivity. The present calculation investigated its electronic states using the QSGW. The resulting one-particle electronic structure is nicely consistent with the transparency

for visible light observed in the optical measurement. We investigate the spectra of electron energy loss spectroscopy as well as the optical spectra obtained from the dielectric polarization function. As a result, the former indicates a strong quasi-plasmon peak in the low frequency range [2].

(D) Fe_3X (X=Pd, Pt) by QSGW

We investigated electronic structures and generalized susceptibilities in cubic Fe_3X (X=Pd, Pt) alloys [3]. These systems are well known as magnetic shape memory alloy. Compared with those of the DFT method with generalized gradient approximation, the energy band structure indicates both an energy level shift to the high energy side and a narrow bandwidth in the minority-spin state. Employing the rigid band approximation, the profile of generalized susceptibility was found to indicate the peak positions at some modulation vectors. These modulations may be assigned to the instability of the cubic symmetry phase in the martensitic phase transition observed in the experiment.

(E) Ni_2MnX (X=Al, Mn, In) by QSGW

According to the QSGW, our group has found the Ni e_g orbitals appear just on the Fermi level in the cubic (austenite) phase of Ni_2MnX [4]. This appearance could be lead to martensite phase transition combined by the band Jahn-Teller effect. We investigated the electronic structures of Ni2MnX (X=Al, Ga, In) series using the QSGW [4]. Their narrow bandwidth appearing at the Fermi level in the minority-spin state has not been reproduced by the approaches of DFT and DFT+U methods.

(F) Migration of twin boundary

Migration of the twin boundary in a modulated martensite phase of the magnetic shape memory alloy Ni_2MnGa is significant to understand the magnetic shape memory effects. This work explored the migration mechanism of the nano-twin boundaries among the layers by first-principles calculations. We systematically analyzed intermediate structures throughout the migration path using the DFT approach [5]. We identified some key factors using the systems of 10M and 14M modulated phases. As a result, we obtained a concise barrier energy formula as empirical one. The resulting energy for barriers was found to be enough so low as a permission of the transition by the thermal energy.

References

[1] T. Kotani, J. Phys. Soc. Jpn. **83**, 094711 (2014); *ecalj*: https://github.com/tkotani/ecalj/.

[2] T. Oda *et al.*, submitted in the conference, SCES 2025.

[3] A. Akatov *et al.*, Sci. Rep. Kanazawa Univ. **68**, 83 (2025).

[4] J. Luštinec *et al.*, J. Magn. Soc. Jpn. **48**, 94 (2024).

[5] R. Majumder *et al.*, accepted in the proceedings CCP2023.

Development of Ceramic Protective Coating to Suppress Corrosion and Hydrogen Embrittlement of Metallic Materials

Yuji Kunisada

Center for Advanced Research of Energy and Materials, Faculty of Engineering, Hokkaido University, Sapporo, Hokkaido 060-8628

In order to develop efficient hydrogen permeation barriers, we investigated the formation energies and diffusion properties of hydrogen impurities in the vicinity of the cationic dopants and interfaces between different ceramic materials,[1] with the aid of the first-principles calculation based on the density functional theory (DFT). We also investigated the behaviors of hydrogen impurities at the interface between ceramic and metallic materials.

We investigated the formation energies and diffusion barriers of hydrogen impurities near the cationic dopants in the α-Al_2O_3 and α-Al_2O_3/α-Cr_2O_3 interface using The Vienna Ab initio Simulation Package (VASP). We installed a parallelized VASP with Intel® MPI Library and Intel® Math Kernel Library. We found that hydrogen impurities can form chemical bonds with coordinated oxygen atoms near transition metal dopants in α-Al_2O_3. Such chemical bonds can be observed at the stable sites in the α-Al_2O_3 region as well as in the α-Cr_2O_3 region. Those are because transition metal cations near hydrogen impurities can stably accept excess electrons associated with forming OH bonds.[2] The range in which this stabilization of hydrogen impurities occurs depends on the element of transition metal cation and varies from a few to 15 Å. Therefore, dilute transition metal cation dopants can affect the stability of hydrogen impurities.

We also investigated the behaviors of hydrogen impurities at the interface between ceramic and metallic materials. The behaviors of hydrogen impurities at the interface between ceramics and metallic materials significantly affect the diffusion properties of hydrogen impurities and the exfoliation properties of ceramic coating films. We considered α-Al_2O_3/Fe interfaces. Since the α-Al_2O_3/Fe interface is incommensurate, we revealed that the formation energies of hydrogen impurities vary depending on its site. We also found that hydrogen impurities are more stable in the interface region than in the bulk region.

References

[1] Y. Kunisada, R. Sano, N. Sakaguchi, Int. J. Hydrog. Energy 97 (2025) 1327.

[2] T. Watanabe, Y. Kunisada, N. Sakaguchi, ChemPhysChem 20 (2019) 1369.

First-principles study on electron transport properties of heterostacking of graphene and graphitic carbon nitride

Yoshiyuki EGAMI
Division of Applied Physics, Faculty of Engineering, Hokkaido University
Kita 13, Nishi 8, Kita-ku, Sapporo, Hokkaido 060-8628

Graphene, a typical two-dimensional material, is expected to find a wide range of applications because of its outstanding electrical conductivity, thermal conductivity, and mechanical strength. To apply graphene to electronic and optical devices, a great deal of effort has been devoted to the development of techniques to widen its band gap. Although graphene has many potential applications, the optimum band gap size for each application is often different. Therefore, research into methods that can adjust the band gap after synthesis is highly desirable.

In this study, we investigated the electronic transport properties of heterostructures composed of atomic layer materials. Specifically, we aimed to modulate the electronic structure and transport properties of heterostructures formed by van der Waals stacking (heterostacking) with graphene and graphitic carbon nitride using first principles calculations. First-principles simulations were carried out using the "RSPACE" code based on the real-space finite-difference formalism[1, 2]. Our goal is to design semiconductor materials with low effective mass and tunable band gap in the range of about 0.2 eV to 1.0 eV using graphene and carbon nitride heterostacking. As a method of tuning, the application of an external electric field and mechanical pressure are considered, and the resulting changes in electronic structure and transport properties are simulated.

First, in graphene/C_3N heterostacking, it was found that simple stacking alone has little effect on the respective band structures. However, by applying pressure and an electric field perpendicular to the layers, the band gap size could be continuously controlled in the range of about 0.01 eV to 0.4 eV, while maintaining the small effective mass derived from graphene. On the other hand, in graphene/C_3N_4 heterostacking, continuous bandgap control from about 0.01 eV to 0.75 eV was shown to be possible by simply applying pressure. Furthermore, electron transport calculations reveal that in the AA-stacking model, the applied pressure causes reflection of incident electrons within the heterostructure region, which significantly affects the electron transmission probability and can even lead to a completely OFF state.

References

[1] K. Hirose *et al.*: First-principles calculations in real-space formalism (Imperial College Press, 2005).

[2] Y. Egami, S. Tsukamoto and T. Ono: Phys. Rev. Res. **3**, 013038 (2021).

Molecular dynamics simulations of thermal diffusion field around laser irradiated nanoparticle with LSPR electric field

Kiyoto KAWAI[1], Hiroki GONOME[1]

[1]*Graduate School of Science and Engineering, Yamagata University, Jonan, Yonezawa, Yamagata 992-8510*

Plasmonic nanoparticles (NPs) have attracted enormous attention because of their unique optical, chemical, electric, and catalytic properties. They have been widely applied in various fields including plasmonics, sensing, catalysis, and biomedical fields [1]. For these applications, detailed thermal reaction properties of NPs are important to optimized design. In this study, we evaluate the thermal diffusion field around laser irradiated Au NP by using molecular dynamics simulations. The laser absorbance was set as 1.92 eV/ps on NP. The electric field (EF) distribution was pre-calculated by COMSOL Multiphysics and applied as no EF, static EF, and cyclic EF conditions. Figure 1 shows orientation distribution of water molecules. In the static EF case, weak crystallization of water molecules occurred and enhanced thermal diffusion in water solvent. Figure 2 shows the energy difference between translation and rotation energy of water molecules. In the case of cyclic EF case, the energy difference was smaller than other cases. It suggests the cyclic EF promote conversion translation energy to rotation energy of water molecules. The thermal diffusion in cyclic EF case was enhanced because the rotation motion has more contribution to thermal diffusivity in water solvent than translation motion.

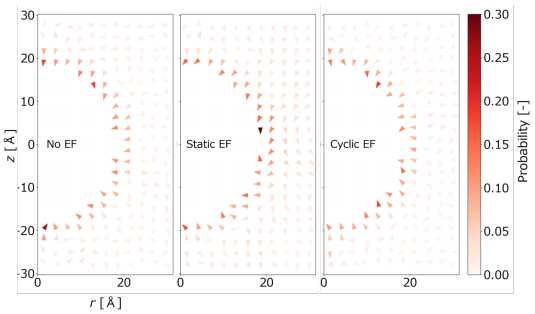


Fig. 1: Orientation of water molecules.

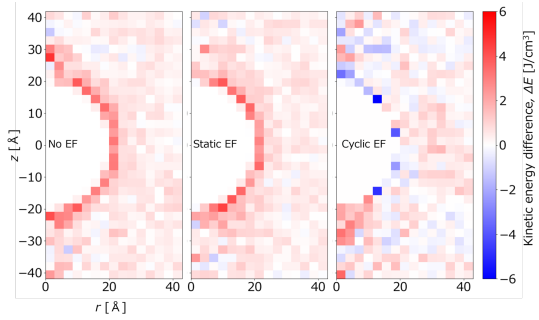


Fig. 2: Kinetic energy difference between translation and rotation of water molecules.

References

[1] J. E. Park, M. Kim, J. Hwang, and J. Nam, Small methods, **1**, 1600032 (2017).

First-principles study of mechanical properties on alloys

Naoki UEMURA

Department of Mechanical and Electrical Systems Engineering,
Faculty of Engineering, Kyoto University of Advanced Science,
18, Yamanouchi-Gotandacho, Ukyo-word, Kyoto, 615-8577

We have studied magnesium alloys with long-period stacking ordered (LPSO) structures by performing first-principles calculations based on density functional theory (DFT) using the VASP code. As a representative material of LPSO-Mg alloys, we calculated the generalized stacking fault energy (GSFE) on the basal and prismatic planes of Mg-Zn-Y alloys with LPSO structure [1]. This year, we investigated the dependence of the GSFE of Mg–Zn–Y with LPSO structure on normal strain and found that the GSFE on the prismatic plane is more sensitive to normal strain than the basal plane [2].

Following the approach proposed by Ogata *et al*. [3], in which the maximum derivative of the GSFE curve is defined as the ideal shear strength, we estimated the ideal shear strengths of both hcp-Mg and the 10H LPSO structure in Mg–Zn–Y alloys based on the tangent at the first inflection point of their respective GSFE curves (Fig. 1). Considering the presence of solute clusters in the LPSO structure, it is reasonable to assume that the ideal shear strength of LPSO is slightly higher than that of hcp-Mg. Experimentally, uniaxial micro-compression and nanoindentation tests along the [0001] axis of single-crystal magnesium have reported stress values ranging from 600 to 1200 MPa [4]. In micropillar tests of single-crystalline 18H LPSO in Mg–Zn–Y alloys, the stress at the first pop-in event was reported to be 750 MPa [5]. Although the ideal shear strength does not account for the nucleation of dislocations, interfaces, or defects and is therefore higher than the experimental values, it serves as an upper limit for the material's intrinsic strength.

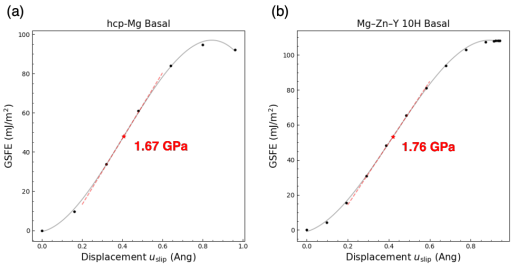


Fig. 1: Ideal shear strengths estimated from the GSFE curves of (a) hcp-Mg and (b) 10H LPSO.

References

[1] N. Uemura *et al*., Mater. Trans. **65** 1080 (2024).

[2] N. Uemura *et al*., in preparation.

[3] S. Ogata *et al*., Science **298** 807 (2002).

[4] S. L. Shang *et al*., Acta. Mater. **67** 168 (2014).

[5] W. S. Chuang *et al*., J. Alloys Compd. **772** 288 (2019).

Analysis of defect structures and ion migration using first-principles calculations and machine learning

Koji SHIMIZU

Research Center for Computational Design of Advanced Functional Materials, National Institute of Advanced Industrial Science and Technology, Umezono, Tsukuba, Ibaraki 305-8568

Understanding the correlation between local structures, including defects, and ion conduction mechanisms in solid electrolytes is essential for advancing all-solid-state battery development. Despite advances in computational techniques and resources enabling the study of more complex models, first-principles calculations based on density functional theory (DFT) remain computationally expensive, which limits large-scale analyses. Machine learning potentials (MLPs) trained on first-principles data offer a promising approach to balance accuracy and computational efficiency.

The author has applied MLPs to investigate the structure and lithium-ion conduction properties of crystalline, glassy, and crystallized glass forms of Li_3PS_4 [1]. This project explores the impact of additive incorporation on the solid electrolyte properties of Li_3PS_4. A diverse set of atomic configurations was generated, and a DFT-based training dataset was constructed. An equivariant graph neural network potential [2] was employed to train the MLP, enabling molecular dynamics (MD) simulations.

Additionally, the author studied the effects of hydrogen incorporation on the fracture behavior of aluminum during tensile MD simulations, revealing hydrogen segregation near grain boundaries and its role in strength degradation and fracture [3]. To explore high-entropy alloys as potential catalysts, a ML model was developed to predict the adsorption energies of hydrogen and carbon monoxide on cluster alloys with various compositions and geometries, demonstrating their potential for catalytic applications through high-throughput screening [4].

References

[1] K. Shimizu, P. Bahuguna, S. Mori, A. Hayashi, and S. Watanabe, J. Phys. Chem. C **128**, 10139 (2024).

[2] Y. Park, J. Kim, S. Hwang, and S. Han. J. Chem. Theory Comput. **20**, 4857 (2024).

[3] Y. Liu, K. Shimizu, and S. Watanabe, submitted.

[4] K. Miyamoto, K. Shimizu, A.K.A. Lu, and S. Watanabe, e-J. Surf. Sci. Nanotechnol. Accepted.

Numerical evaluation of the effect of twist angle on phonon hydrodynamics in twisted 2D materials

Xu Bin

Department of Mechanical Engineering,

The University of Tokyo, 7-3-1, Hongo, Bunkyo-ku, Tokyo 113-8656

Two-dimensional materials, particularly transition metal dichalcogenides (TMDs), are widely used in electronics, photonics, and thermoelectrics due to their exceptional physical and chemical properties. Recently, stacked 2D materials with slight twist angles have shown unique properties, but the effect of twist angle on interfacial thermal conductance remains unclear. Although some simulation studies suggest that thermal conductivity decreases as the twist angle increases, experimental verification is lacking. Therefore, this study aims to systematically investigate the impact of twist angle on thermal conduction in bilayer TMDs through time-domain thermoreflectance (TDTR) experiments and molecular dynamics simulations, providing theoretical support for the design of thermoelectric materials and thermal management systems.

As shown in Fig.1, We employed the TDTR technique to measure the interlayer thermal conductance (TC) of twisted bilayer TMDs ($MoS_2$and WS_2) with varying twist angles. The samples were fabricated using a sequential pick-up method to ensure clean interfaces, and the twist angle was precisely controlled. The TDTR measurements revealed a significant decrease in thermal conductance as the twist angle increased,

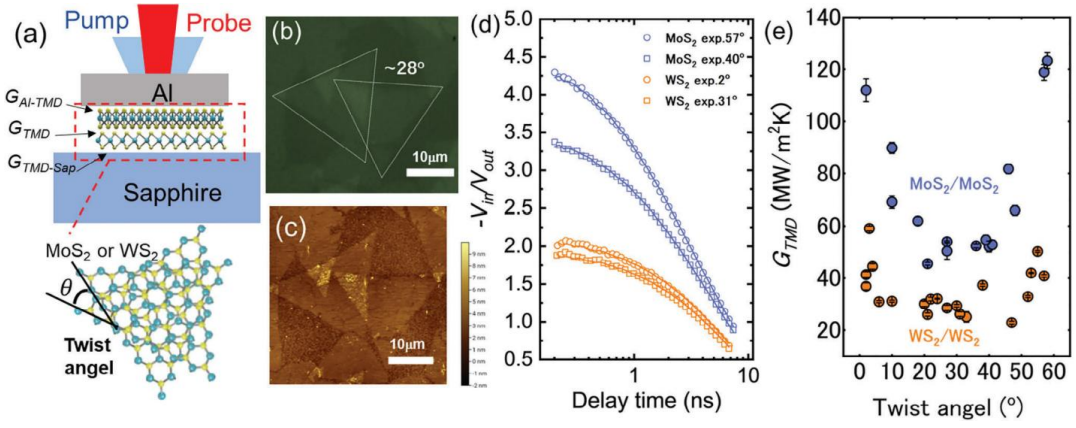


Figure 1. Time-domain thermoreflectance (TDTR) measurement for measuring thermal conductance (TC) of twisted bilayer TMD. a) Schematic of the TDTR system and sample. b) Optical microscopy and c) AFM images of twisted bilayer MoS_2 with a twist angle of 28°. d) Representative temperature decay profile (–Vin/Vout) of twisted bilayer MoS_2 and WS_2. e) TC between bilayers MoS_2 and WS_2 (G_{TMD}) under different twist angles.

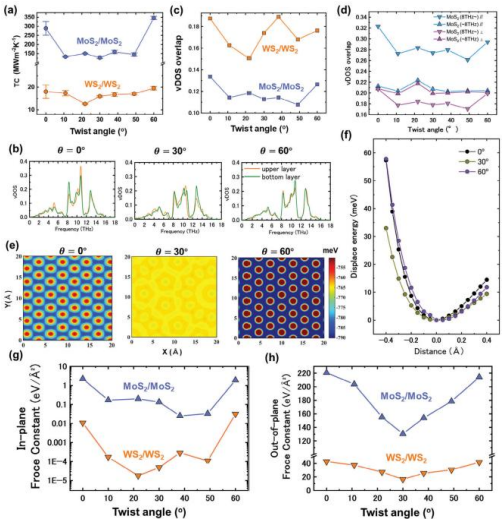


Figure 2. MD simulations of interfacial heat conduction in twisted bilayer TMDs. a) Thermal conductance (TC) of MoS_2 and WS_2 bilayers at different twist angles. b) vDOS of the upper and bottom layers in twisted MoS_2 bilayers. c) vDOS overlap of upper and bottom layers in WS_2 and MoS_2. d) vDOS overlap in low (≈8 THz) and high (8 THz~) frequency ranges for in-plane (//) and out-of-plane (⊥) directions. e) Displacement energy of twisted MoS_2 along in-plane and f) out-of-plane directions. g) Second-order force constant of MoS_2 and WS_2 along in-plane and h) out-of-plane directions across twist angles from 0° to 60°.

with a more pronounced variation observed in MoS_2 compared to WS_2. These experimental findings provided the first direct evidence of twist-angle dependence on TC in bilayer TMDs

Figure 2 investigates the relationship between twist angle and interfacial thermal conductance through molecular dynamics (MD) simulations. The simulation results show that thermal conductance decreases as the twist angle increases, with a more significant variation observed in MoS2, which aligns with the experimental findings. By analyzing the vibrational density of states (vDOS) and interlayer interactions, the study reveals that interfacial heat conduction is closely related to the overlap of interlayer interactions and vibrational frequencies. The simulations further show that the changes in vDOS due to atomic reconstruction in the twisted structure are a key factor affecting thermal conductance.

Reference

[1] B. Xu, M. An, S. Masubuchi, Y. Li, R. Guo, T. Machida, and J. Shiomi, Heat conduction modulation in incommensurate twisted stacking of transition-metal dichalcogenide, Adv. Funct. Materials, 2422761 (2025)

First-principles calculation of optical control on semiconductor transport properties

Shunsuke A. Sato

Department of Physics, Tohoku University, Sendai 980-8578, Japan

We have studied light-induced electron dynamics in semiconductors based on microscopic calculations grounded in quantum mechanics. For this study, we employed two theoretical frameworks. The first is first-principles electron dynamics calculations based on time-dependent density functional theory (TDDFT) [1]. Practical calculations were performed using the SALMON code [2] and the Octopus code [3]. The second method is the quantum master equation approach with a tight-binding Hamiltonian, for which we employed a home-made code [4].

In addition to applications in attosecond science of transition metal dichalcogenides [5], we used first-principles calculations to study the transport properties of bulk silicon in the THz regime under the presence of MIR laser fields. For this purpose, we employed the Wigner distributions of ions to account for phonon scattering contributions through an ab initio approach [6]. Based on this approach, we can investigate the transient optical and transport properties of silicon with phonon-assisted indirect gap transitions. As a result of these calculations, we computed the light-induced anomalous Hall effect in silicon. Currently, we are investigating the microscopic origin of this phenomenon.

Using the quantum master equation approach, we have also investigated light-induced electron dynamics in GaAs, a prototypical wide-gap semiconductor. Based on pump-probe simulations employing two light pulses, we found that the optical and transport properties of GaAs are significantly affected by the coupling between intra- and interband transitions. While the contributions from solely intraband and interband transitions have been investigated separately, the effects of their coupling remain to be clarified. We are currently conducting a microscopic analysis of the induced transient optical and transport properties based on this coupling.

These studies are expected to provide a fundamental understanding of the optical and transport properties of semiconductors in nonequilibrium regimes, advancing technological applications toward optoelectronic devices.

References

[1] Erich Runge and E. K. U. Gross, Phys. Rev. Lett. 52, 997 (1984).

[2] M. Noda, et al., Comput. Phys. Commun. 235, 356 (2019).

[3] N. Tancogne-Dejean, et al., J. Chem. Phys. 152, 124119 (2020)

[4]https://github.com/shunsuke-sato/tight_binding_spds

[5] A. Zong, et al., arXiv:2407.00772 [cond-mat.str-el]

[6] K. Lively, S. A. Sato, G. Albareda, A. Rubio, Aaron Kelly, Phys. Rev. Research 6, 013069 (2024)

Exploration of Stable Structure in $K_2NdTa_5O_{15}$ using First-Principles Phonon Calculations

Hodaka ABE, Sou YASUHARA

School of Materials and Chemical Technology,

Institute of Science Tokyo, Ookayama, Meguroku, Tokyo 152-8550

Antiferroelectrics are promising materials for the next-generation ceramics capacitors because they can exhibit high ε_r under high electric fields due to a field-induced antipolar-to-polar phase transition. Here, we focused on antiferroelectric $K_2NdM_5O_{15}$ (M=Nb^{5+}, Ta^{5+}), which exhibit relatively high permittivity ε_r~800. We have experimentally demonstrated that controlling the Nb/Ta ratio is effective in shifting the phase transition temperature and stabilising the antiferroelectric phase around room temperature, but the microscopic mechanism is still unclear. To elucidate key factors determining the modulation of phase stability by changing the Nb/Ta ratio, we derived the stable structure of $K_2NdTa_5O_{15}$ based on first-principles phonon calculations and compared it with that of $K_2NdNb_5O_{15}$.

In this study, VASP and Phonopy codes were used for density functional calculations and finite difference phonon calculations, respectively. To deduce phase transition pathway from the high-symmetry structure, we first calculated phonon dispersion of $K_2NdTa_5O_{15}$ with the aristotype *P*4/*mbm* structure (Fig.1(a)). Stable structure exploration was carried out by performing structural relaxation for low-symmetry structures with displacements along phonon modes with imaginary frequencies.

Figure 1(b) shows the stable structure of $K_2NdTa_5O_{15}$ derived from the phonon calculations. While $K_2NdNb_5O_{15}$ has two types of structural distortion, NbO_6 octahedral tilting distortion and antipolar distortion due to intraoctahedral displacement of Nb, the stable structure of $K_2NdTa_5O_{15}$ has only tilting distortion of TaO_6 octahedra and the antipolar distortion is inactivated. Suppression of the second order Jahn-Teller effect in the Ta system with higher *d*-level is thought to have caused a such change in the stable structure.

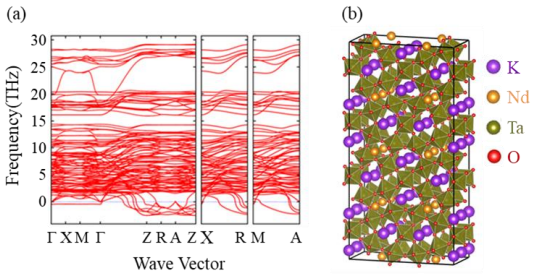


Fig.1 (a) Phonon dispersion curves of $K_2NdTa_5O_{15}$ with the aristotype *P*4/*mbm* structure. (b) The stable structure of $K_2NdTa_5O_{15}$ derived from phonon calculations.

References

[1] H. Abe, S. Yasuhara, T. Tsurumi and T. Hoshina: J. Ceram. Soc. Jpn. **131**[7], 189(2023)

Investigation on single ion motions for a polarization switching in a wurtzite-type $LiGaO_2$

Sou YASUHARA

School of Materials and Chemical Technology,

Institute of Science Tokyo, Ookayama, Meguroku, Tokyo 152-8550

A wurtzite-type materials have gathered much attention since a discovery of ferroelectricity in a wurtzite-type structure of Sc doped AlN in 2019[1]. Exploring new wurtzite-type materials is essential for understanding polarization switching mechanisms. We now focus on $LiGaO_2$ with a distorted wurtzite-type structure, which distortion is originated from a difference of ionic radii between Li^+ and Ga^{3+}. In this study, we carried out first principles calculations for evaluating a polarization switching in $LiGaO_2$ focusing on single ion motions during a polarization switching.

The density functional theory calculations were carried out using the projector augmented wave method as implemented in the VASP. The modified Predew-Burke-Ernzerhof generalized gradient approximation was utilized as an exchange correlation functional. The k-point mesh was 8×8×8. The cutoff energy and convergence energy were 550 eV and 1.0×10^{-7} eV, respectively. The formation energy of $LiGaO_2$ with structural modifications of Li or Ga ion sites was calculated. Li or Ga positions were altered from -0.15 to 0.15 in the atomic position of $LiGaO_2$ structure.

A calculation result as a color map is shown in Fig. 1. As a result, a case of opposite polarization state of Li and Ga ions were unstable. In addition, a promising way to the polarization switching is that both Li and Ga ions move at the same time. We further carried out an evaluation of a Li or Ga motion in a super cell structure (2 x 2 x 1). The energy difference during the movements of Ga and Li were 0.42 eV/f.u. and 0.26 eV/f.u., respectively. This result indicates that single cation movements are less favor for the polarization switching in $LiGaO_2$.

References

[1] S. Fichtner, N. Wolff, F. Lofink, L. Kienle, and B. Wagner, J. Appl. Phys. **125**, 114103 (2019).

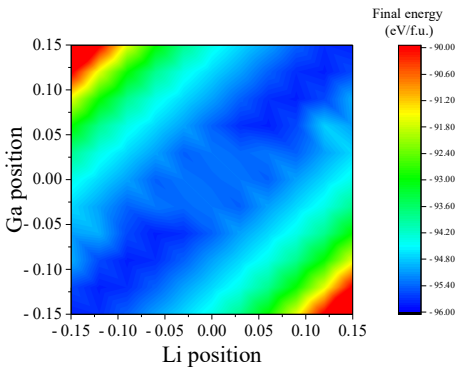


Fig. 1 A color map of calculation results of final energy in $LiGaO_2$ as a function of Ga/Li position.

First-Principles Molecular-Dynamics Study of Structural and Electronic Properties of Disordered Materials under Extreme Conditions

Fuyuki SHIMOJO

Department of Physics, Kumamoto University, Kumamoto 860-8555

Since disordered materials do not exhibit long-range order as observed in crystals, simulations with larger system sizes are required to investigate their static and dynamic properties. For this purpose, machine-learning interatomic potentials (MLIPs) based on artificial neural networks trained on accurate first-principles molecular dynamics (MD) data are useful.

We have developed a method using a robust MLIP that enables stable MD simulations for systems of tens of thousands of atoms under high-temperature and high-pressure conditions for highly covalent materials [1]. In the present study, we apply this method to SiO_2 glass under decompression to simulate the transformation from the sixfold- to fourfold-coordinated structures, which is accompanied by permanent densification. A system consisting of about 30,000 atoms was simulated from 60 to 0 GPa at room temperature with the MLIP. The calculations were performed in steps of 5 GPa down to 20 GPa, and then in steps of 2 GPa thereafter. The simulation time for each pressure was longer than 10 ps. At 14 GPa, where the transformation occurred most significantly, the calculation was extended to 2.7 ns. Figure 1 shows the calculated pressure dependence of the coordination number for Si. A drastic change in the coordination number is observed between 16 and 10 GPa. These results indicate that the MLIP successfully reproduces the structural transformation in SiO_2 glass. The transformation was found to proceed via a relatively unstable fivefold-coordinated state, and the fourfold-coordinated phase grows logarithmically with time.

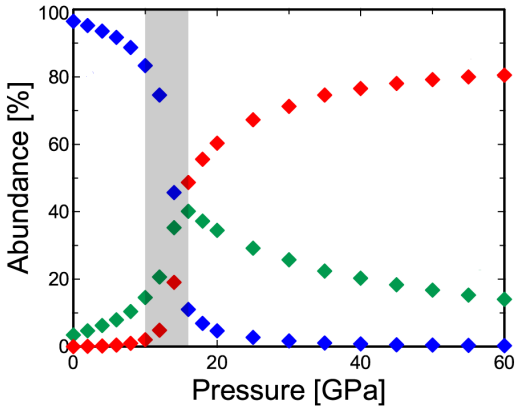


Fig. 1: Pressure dependence of calculation results for distribution of coordination number for Si. The blue, green, and red symbols represent the abundance of fourfold-, fivefold-, and sixfold-coordinated Si atoms, respectively.

References

[1] D. Wakabayashi et al., J. Phys. Soc. Jpn. **92**, 074002 (2023).

GW + BSE photoabsorption spectra of transition metal doped TiO_2 and excited-state TD*GW*-MD simulation of CH_4 + Ni

Kaoru OHNO

Yokohama National University, Tokiwadai, Hodogaya-ku, Yokohama 240-8501

To explore quasiparticle (QP) energy gaps and photoabsorption spectra of rutile TiO_2 with nonmagnetic transition metal (Zr, Mo, Zn, Cd) impurities, we conducted a Γ-point only *GW* + Bethe–Salpeter equation (BSE) calculation on a 72 (or 71) atom supercell using our all-electron mixed basis program, TOMBO [1]. Zn and Cd impurities must coexist with oxygen vacancy to maintain charge neutrality. Mo, Zn, or Cd doped rutile TiO_2 exhibits optical absorption and catalytic activity under visible light (Fig. 1). The resulting QP energy gaps and photoabsorption energies are fairly in good agreement with experimental and theoretical data currently available. As the most important condition for the applicability of the Γ-point only approach in the *GW* + BSE frame-work is that the Γ-point only *GW* calculation should reproduce a reasonable band gap.

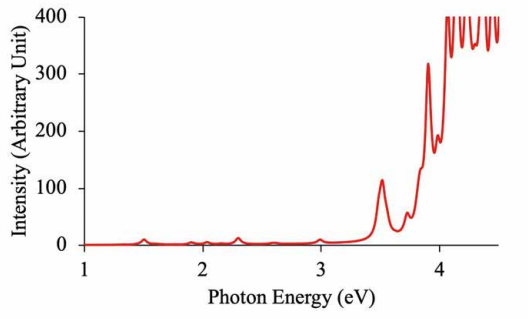


Fig. 1 Photoabsorption Spectra of Mo-doped TiO_2

We have also performed excited-state time-dependent *GW* (TD*GW*) molecular dynamics simulation for the photolysis of CH_4 + Ni using TOMBO [2]. We demonstrated that only the H ejection away from the Ni side (Fig. 2) facilitates the formation of a hydrogen molecule with the quasiparticle level corresponding to it having an energy close to the negative ionization potential of an isolated H_2 molecule. This is achieved at a PAE of 8.4 eV which is lower compared to 10.2 eV of pristine methane without Ni [3].

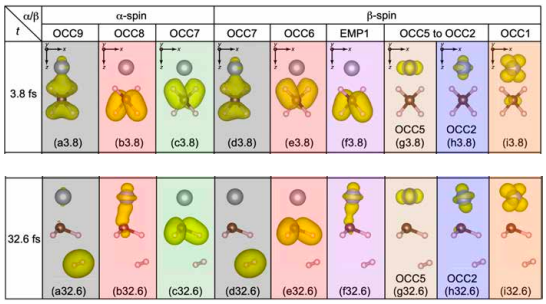


Fig. 2 Density $|\varphi|^2$ of QP levels at 3.8 fs and 32.8 fs.

References

[1] K. Ohno, R. Sahara, T. Nanri, and Y. Kawazoe, Comput. Cond. Matter **41**, e00977 (2024).

[2] A. Manjanath, R. Sahara, Y. Kawazoe, and K. Ohno, Nanomaterials, **14**, 1775 (2024).

[3] A. Manjanath, R. Sahara, K. Ohno, and Y. Kawazoe, J. Chem. Phys. **160**, 184102 (2024).

Understanding Fast Ion Conduction in Inhomogeneous Materials

Shusuke KASAMATSU

Academic Assembly (Faculty of Science),

Yamagata University, Kojirakawa, Yamagata-shi, Yamagata 990-8560

Functional materials including glasses, solid solutions, and their interfaces contain many types of inhomogeneities at the nanoscale that contribute to their performance in various applications. However, quantifying such inhomogeneities from experiments is often challenging because of the lack of nanoscale probes that can characterize local atomistic environments. First-principles quantification of such systems is also often intractable due to limitations in simulation time or the number of configurations that can be calculated within a reasonable amount of time. To overcome this limitation, we have been employing machine learning surrogate models to speed up first-principles calculations. Here, we report examination of (a) intermediate-range order/disorder in the prototypical network glass system GeO_2, and (b) dopant order/disorder in heavily doped perovskite oxides and its impact on proton conduction.

(a) Intermediate range order in GeO_2 glass [1]-- The atomistic structure of glasses have been of fundamental interest for over a century; although short-range order has often been clarified as being similar to crystalline motifs, intermediate-range order whose existence is implied by small-wavevector diffraction peaks is yet to be unambiguously characterized in real space. Although reverse Monte Carlo (RMC) fitting of diffraction data is often used to construct three-dimensional models, its reliability is sometimes questionable because diffraction data only contains two-body correlations which are not enough to fix the three-dimensional structure. Here, we performed melt-quench simulations in a 3240-atom cell using a neural network potential trained on first-principles data to construct a model of vitreous GeO_2. The structure factor calculated from the obtained model is in good agreement with experiment. Intermediate-range features were characterized using ring distributions and persistent homology, and it was found that the simulated model shows a stronger ordering compared to that obtained by RMC modeling. That is, the underlying density functional approximation in first-principles calculations determines the preferred network assembly more strictly than conventional RMC modeling, even when multiple diffraction data is used in the fitting. This shows the promise and necessity of simulations using machine learning potential based on first-principles data

for accurate determination of the glass structure and its physical properties.

(b) Proton conduction in heavily Sc-doped $BaZrO_3$ [2]--Acceptor-doped perovskite oxides are of interest for application in proton ceramic fuel cells. Acceptor doping is necessary for the introduction of protons into the material, but it has been observed that increased doping leads to a decline in the proton conductivity. This is often explained by trapping of protons by the dopant. However, it was recently discovered that Sc doping leads to continuous conductivity increase up to the solubility limit of ~60 atomic percent. Here we performed Monte Carlo simulation using our abICS code to determine the Sc configuration in the material, followed by molecular dynamics simulation to explain how the detrimental effect of proton trapping is avoided. As seen in Fig. 1, our simulations revealed that a conduction path along the network of Sc dopants is formed, enabling long-range diffusion without detrapping from the dopant.

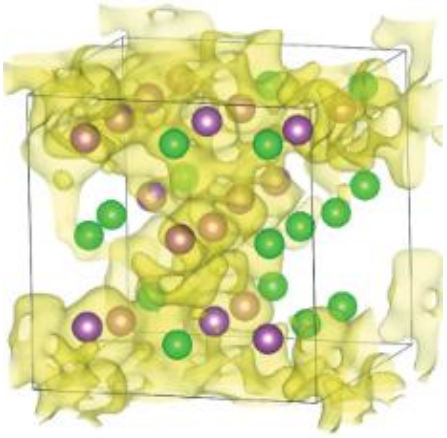


Fig. 1: Proton concentration isosurface in Sc-doped $BaZrO_3$. The Sc and Zr atoms are shown as purple and green spheres, and Ba and O atoms are omitted for clarity. From Ref. [1], reproduced under CC-BY 4.0 license.

References

[1] K. Matsutani et al., J. Chem. Phys. 161, 204103 (2024).

[2] S. Fujii et al., Sci. Technol. Adv. Mater. 25, 2416383 (2024).

Advancement of methods for predicting dielectric properties and structure exploration of materials

Shinji TSUNEYUKI

Department of Physics, The University of Tokyo

Hongo, Bunkyo-ku, Tokyo 113-0033

In preparation for developing electronic and communication devices for the 5G and beyond 5G era, it is necessary to understand and predict the dielectric properties of various materials, including crystals, amorphous materials, and polymers. In particular, the dielectric properties in the sub-terahertz to terahertz (THz) range have recently become possible to measure with high precision. However, these properties are difficult to understand due to the contribution of various physical phenomena such as electronic responses, anharmonic lattice vibrations, molecular rotation, molecular (and intermolecular) polarization, and structural relaxation. The strong anharmonic nature and slow relaxation also make computer simulations extremely challenging.

This study aims to develop and demonstrate the fundamental technology for structural simulation and first-principles simulation of permittivity of molecular materials including polymers which are technically more challenging and strongly demanded by industry. This year, we conducted (1) calculations of highly efficient permittivity calculation methods in the sub-terahertz to terahertz range for molecular liquids with complex structures, large thermal fluctuations, and slow relaxation and (2) data-assimilated structure exploration using X-ray diffraction data from materials composed of multiple crystals.

Permittivity of molecular liquids

The dielectric constant of liquids and polymer materials with large atomic displacements in the THz range can be calculated from the auto-correlation function of the system's dipole moments using molecular dynamics methods (MD). However, to determine the dielectric constant down to the sub-THz range, simulations lasting nanoseconds are required, and performing all of this using first-principles MD is extremely difficult from a cost perspective. On the other hand, fast classical MD using fixed charges cannot accurately evaluate dipole moments. To address this, we have developed a machine learning model of the Wannier center (MLWC), which represents the center of mass of electron distributions corresponding to chemical bonds

and lone pairs, and have developed a method for calculating permittivity using this model.

This year, we applied this method to alcohol [1], propylene glycol, and its polymers [2] and demonstrated that it is possible to perform high-precision calculations of permittivity and light absorption coefficients in the sub-THz to THz range, including temperature dependence. For the latter, we successfully demonstrated the high transferability of the model by applying it to oligomers with higher polymerization degrees using a model learned from propylene glycol dimers.

Data assimilation structure exploration

Structure prediction using simulations has been helpful for discovering new crystals and studying amorphous and liquid materials, which are difficult to analyze by experiments. However, there are limitations due to the combinatorial explosion caused by increased atoms and the slowness of structural relaxation. To address these issues, we have developed a data-assimilated structural exploration method incorporating X-ray or neutron diffraction data into simulations to perform structural exploration efficiently. Since last year, we have been working on extending this method to cases where diffraction experimental samples contain multiple crystals, or prior estimation of lattice parameters is difficult.

This year, we confirmed that by applying the method in multiple stages, we can reproduce all crystal structures, even from powder XRD data containing three polymorphs of SiO_2 [3]. Among these three crystal phases is Coesite, which contains 48 atoms in the unit cell, demonstrating that data-assimilated structure exploration is effective for determining complex crystal structures.

References

[1] T. Amano, T. Yamazaki, and S. Tsuneyuki, Phys. Rev. B 110, 165159 (2024).

[2] T. Amano, T. Yamazaki, N. Matsumura, Y. Yoshimoto, S. Tsuneyuki, arXiv:2410.22718, to appear in Phys. Rev. B.

[3] Y. Kubo, R. Sato, Y. Zhao, T. Ishikawa, and S. Tsuneyuki, J. Chem. Phys. 161, 214113 (2024).

Design and Understanding of the Activity and Stability of Promising Electrocatalysis via Precise Catalysis Theory and AI

HAO LI

Advanced Institute for Materials Research (WPI-AIMR),

Tohoku University, Sendai, 980-8577

We have studied the development of new catalytic theories and ML-based models, as well as the design of effective catalysts for industrially significant reactions, by integrating precise theoretical models, high-level computations, machine learning (ML), and experimental validation.

This year, we utilized supercomputing resources to perform high-throughput density functional theory (DFT) calculations and machine-learning force field (MLFF)-accelerated molecular dynamics (MD) simulations to provide predictive insights into the activity and stability of electrocatalysts. This “theory-experiment-theory” cycle ensures that theoretical predictions not only guide experimental research but are also refined by experimental feedback, making it possible to identify catalyst materials with improved performance efficiently. Beyond this, to relieve the computational burden of DFT and AIMD, novel ML models are designed to learn from high-fidelity theoretical datasets and accurately predict energies and forces for new structures. Leveraging the synergy between physics-based insights and data-driven methods, we aim to develop catalysts that are not only highly active and cost-effective but also robust for long-term operation. Through this integrated approach, the work presented here outlines a path toward optimizing industrially significant electrocatalytic reactions and demonstrates the broader potential of combining fundamental theory with cutting-edge ML techniques.

During the project period, **46 papers** were published in leading journals, including JACS, Angew. Chem., Nature Commun., etc., under this ISSP supercomputer support. Some notable works will be discussed in the following:

1. Why Do Weak-Binding M–N–C Single-Atom Catalysts Possess Anomalously High Oxygen Reduction Activity? (JACS; Hao Li as the Last and Corresponding Author)

In this work, we integrated a pH-field coupled microkinetic model with detailed experimental electron state analyses to verify a novel key step in the oxygen reduction reaction (ORR) pathway of weak-binding SACs - the oxygen adsorption at the metal – nitrogen bridge site (**Fig. 1**). This step significantly altered the adsorption scaling relations, electric field responses, and solvation effects, further

impacting the key kinetic reaction barrier from HOO* to O* and pH-dependent performance. Synchrotron spectra analysis further provides evidence for the new weak-binding M–N–C model, showing an increase in electron density on the antibonding π orbitals of N atoms in weak-binding M–N–C catalysts and confirming the presence of N–O bonds. These findings redefine the understanding of weak-binding M–N–C catalyst behavior, opening up new perspectives for their application in clean energy.

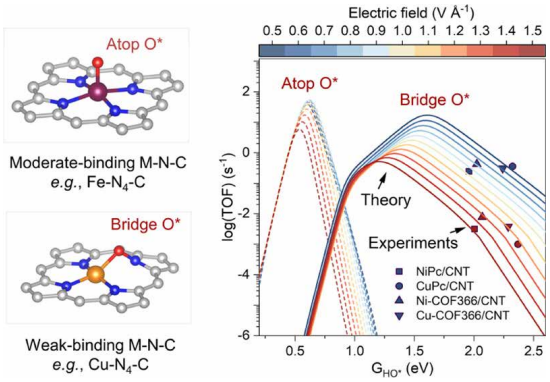


Fig. 1. A pH-field coupled microkinetic model with detailed experimental electron state analyses.

2. Hydrogen Binding Energy Is Insufficient for Describing Hydrogen Evolution on Single-Atom Catalysts (Angewandte Chemie; Hao Li as the Last and Corresponding Author)

We investigate the effects of HO*/O* poisoning and H* coverage on SACs with varied metal centers and coordination environments using pH-dependent surface Pourbaix diagrams at the reversible hydrogen electrode (RHE) scale and microkinetic modeling. Our findings reveal that HO* poisoning, realistic H* adsorption strengths at active metal sites, and the potential HER activity at the coordinating N-sites are crucial factors that should be considered for accurate descriptor development. Experimental validation using a series of M-phthalocyanine/CNT catalysts (M = Co, Ni, Cu) confirms the theoretical predictions, with excellent agreement in exchange current densities and the role of N-sites in Ni/Cu-phthalocyanine/CNT catalysts. This work provides answers to a long-lasting debate on HER descriptors by establishing ΔG_{H^*} and ΔG_{HO^*} as a combined HER descriptor for SACs **(Fig. 2)**, offering new guidelines for catalyst design.

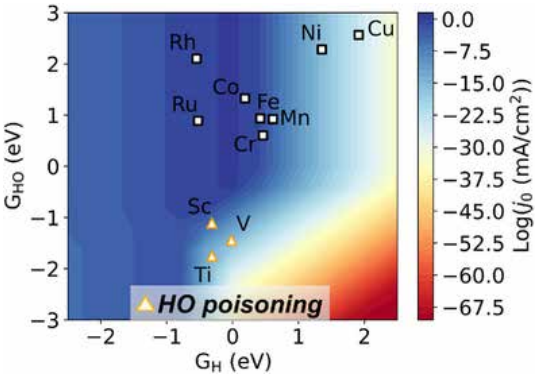


Figure 2. New microkinetic modeling predicts HER at M-N-C SACs.

References

[1] D. Zhang, F. She, J. Chen, L. Wei*, and H. Li*, J. Am. Chem. Soc. **147**, 6076–6086 (2025).

[2] S. Ye, F. Liu, F. She, J. Chen, D. Zhang, A. Kumatani, H. Shiku*, L. Wei*, and H. Li*, Angew. Chem. Int. Ed, e202425402 (2025).

Free-energy evaluation of alloys

Yoshihiro GOHDA
Department of Materials Science and Engineering, Institute of Science Tokyo
J2-22, Nagatsuta-cho 4259, Midori-ku, Yokohama 226-8501, Japan

Aiming construction of first-principles phase diagrams, we are trying to develop methods to evaluate free energies of metallic alloys. The free energy is decomposed into a few contributions, including the phonon effects and the configrational entropy as the most important ones. Moreover, other components and couplings among various contributions significantly affects phase equilibria, e.g., phase transition temperatures. Indeed, the spin-phonon coupling changes the Curie temperature of bcc Fe more than 500 K [1].

In this project, we developed a method to perform first-principles phonon calculations to evaluate Gibbs free energies efficiently [2]. In our volume integral of pressure (VIP) method, multiple phonon calculations with varying the volume are avoided in incorporating the effect of thermal expansion. This feature makes the Gibbs-energy evaluation possible for high-temperature austenite phases that is in general difficult for conventional volume-varied approaches, by combining the VIP method with the self-consistent phonon (SCPh) method [3] implementd in the ALAMODE code [4]. In applications to bcc Ti [2], we demonstrated that the electron-phonon coupling changes the austenite-martensite phase-transition tempearature more than 200 K as shown in Fig. 1. We also applied the VIP method to Ti-Al alloys that require huge computational costs.

Conventional CALPHAD approach largely relies on experimental data. In some cases, mixing enthalpies are additionally evaluated from first principles [5]. Evaluation of free energies from first principles should further expand possible range of Gibbs-energy database to experimentally unavailable cases. As one of approaches to achive the goal above, we also developed a method to include the spin-electron coupling in the evaluation of exchange-coupling parameters [6].

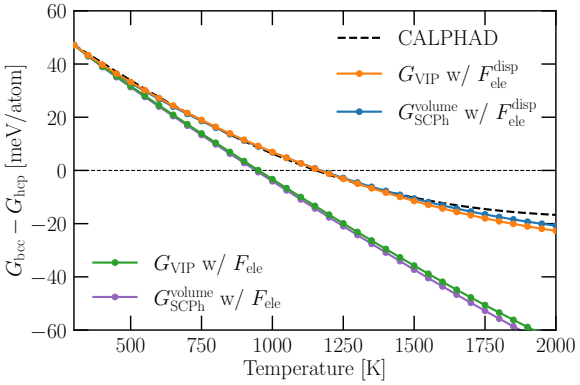


Figure 1: Difference in the Gibbs free energy between bcc and hcp Ti from 300 K to 2000 K. The origin of the DFT calculations is shifted to the CALPHAD data at 300 K, i.e., changes from 300 K are evaluated from first principles. Superscripts "disp" indicate that calculations include the electron-phonon coupling as effects of vibrational atomic displacements.

[1] T. Tanaka and Y. Gohda, npj Comput. Mater. **6**, 184 (2020).
[2] K. Hashimoto, T. Tanaka, and Y. Gohda, arXiv:2405.14823 (2024).
[3] T. Tadano and S. Tsuneyuki, Phys. Rev. B **92**, 054301 (2015).
[4] T. Tadano, Y. Gohda, and S. Tsuneyuki, J. Phys.: Condens. Matter **26**, 225402 (2014).
[5] S. Enomoto, S. Kou, T. Abe, and Y. Gohda, J. Alloys Compd. **950**, 169849 (2023).
[6] T. Tanaka and Y. Gohda, arXiv:2410.11256 (2024).

Development of the optimization method for the long-range correlation factor in the first-principles wave-function theory

Masayuki OCHI
Department of Physics, Osaka University
1-1 Machikaneyama-cho, Toyonaka, Osaka 560-0043

We have developed a first-principles electronic structure calculation software using the transcorrelated (TC) method [1, 2]. The TC method is a many-body wave function theory, where Hamiltonian is similarity-transformed with the Jastrow correlation factor. By this transformation, electron correlation effects are efficiently considered. In particular, one-electron orbitals in the Jastrow-Slater-type wave function can be optimized in the same manner as the Hartree–Fock (HF) method, to say, by solving a one-body self-consistent-field (SCF) equation. It is advantageous that the computational cost for this process is the same order as that for the HF method [3].

We have developed our computational code TC++, which was published on github [4, 5]. One can perform TC calculations using TC++ by reading some output files dumped by DFT calculation using the Quantum-Espresso package [6]. TC++ supports the following functionalities: HF, TC, and biorthogonal TC (BITC) calculations, SCF and band calculations, solids and homogeneous electron gas, a plane-wave-basis set, and norm-conserving pseudopotentials. Calculation is MPI-parallelized for the k-point and band indices.

In this year, we have implemented the interface between TC++ and first-principles quantum-Monte-Carlo code CASINO [7]. By using CASINO, one can optimize the Jastrow correlation factor using the variational Monte Carlo (VMC) method. TC++ can read the optimized Jastrow parameters, and then perform TC++ calculation using those parameters. At present, TC++ can deal with electron-electron Jastrow factors with the RPA-type and polynomial-type. By performing test calculations using ISSP supercomputers, we verified that (1) stable optimization of TC+VMC was achieved and (2) polynomial Jastrow factors improve the accuracy of calculated lattice constants.

References

[1] S. F. Boys and N. C. Handy, Proc. R. Soc. London Ser. A **309**, 209 (1969); *ibid.* **310**, 43 (1969); *ibid.* **310**, 63 (1969); *ibid.* **311**, 309 (1969).

[2] N. C. Handy, Mol. Phys. **21**, 817 (1971).

[3] M. Ochi, K. Sodeyama, R. Sakuma, and S. Tsuneyuki, J. Chem. Phys. **136**, 094108 (2012).

[4] https://github.com/masaochi/TC

[5] M. Ochi, Comput. Phys. Commun. **287**, 108687 (2023).

[6] https://www.quantum-espresso.org/

[7] https://vallico.net/casinoqmc/

First-principles materials design of perovskite semiconductors toward improving photocatalytic performance

Seiichiro L. TEN-NO
Graduate School of System Informatics, Kobe University
Rokkodai-Cho, Nada-Ku, Kobe 657-8501

Divalent cation doping into perovskite photocatalyst $SrTiO_3$ [1]

Perovskite oxide $SrTiO_3$ (STO) is a typical semiconductor photocatalyst for overall water splitting under ultraviolet. The defect control during synthesis is crucial for promoting photocatalytic activities as well as other photocatalysts. The recent experiment [2] shows that Al-doped STO (STO:Al) enables a quantum efficiency of almost unity in the ultraviolet range.

To achieve the materials design using efficient dopants for higher-performance photocatalysts, we have studied the electronic structure and formation energy of doped STO using the first-principles analysis based on the density functional theory (DFT). The supercell method is adopted to describe point defects including oxygen vacancy and substitutional doping, where several supercell models, namely, $2 \times 2 \times 3$, $2 \times 2 \times 4$, $3 \times 3 \times 3$, and $3 \times 3 \times 4$ supercell of the primitive cell of PTO, are considered to take into account the finite size effects. The DFT calculations were performed within the PBE+U functional using PAW method as implemented in VASP [3]. The Hubbard U was set to be $U = 4.36$ eV for the 3d orbitals at the Ti sites, which reproduces the relative position of defect levels to the valence and conduction band. We focus on the oxygen vacancy (V_O) and substitutional doping for the nearest Ti site. Since the V_O works as the n-type doping and introduces 2 electron carriers, we consider divalent and trivalent cations, D^{2+} and T^{3+}, with a similar ionic radius to Ti^{4+} to introduce hole carriers: D = Mg, Ni, Zn, and T = B, Al, Ga, In, Tl, Sc.

The projected density of states (PDOS) for STO:V_O shows that the defect level composed of Ti-3d appears just below the conduction bands as a donor level. This defect level can degrade the photocatalytic activities since it works as a recombination center. On the other hand, D_{Ti} and $2T_{Ti}$ doping can remove the defect level owing to the p-type doping, while the dopant levels composed of Ni-3d appear for Ni_{Ti} doping. Therefore, the photocatalytic degradation is expected to be prevented for D = Mg, Zn, and T = B, Al, Ga, In, Tl, Sc.

Furthermore, we calculated the dopant formation energy for the D_{Ti} and $2T_{Ti}$ doping, which shown in Figure 1. Here each chemical potential is evaluated from the phase equilibrium of STO, and dopant chemical potentials are evaluated from the phase equilibrium of their oxides. Mg/Zn_{Ti} and 2Ga/Sc_{Ti} doping are easy to form according to the formation energy. Therefore, Mg/Zn_{Ti} and 2Ga/Sc_{Ti} doping can be expected to be efficient dopants for high-performance photocatalytic STO. These numerical results are consistent with the experimental ones: the photocatalytic activity of synthesized STO:Mg and Zn samples are enhanced compared to pristine STO sample.

Efficient dopants for perovskite photocatalyst $PbTiO_3$

Perovskite oxide $PbTiO_3$ (PTO) is a photocatalyst for overall water splitting as well as ferroelec-

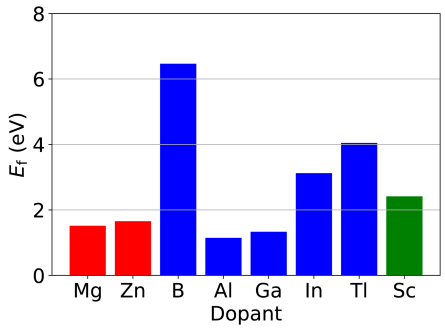


Figure 1: Dopant formation energy for each D_{Ti} and $2T_{\mathrm{Ti}}$ doping.

tric material. Similar to other photocatalysts such as STO:Al, the enhancement of photocatalytic activities is expected by the defect control using efficient dopants [4]. We have investigated the electronic structure of doped PTO using the first-principles calculations based on DFT. The $3\times3\times3$ supercell of the primitive cell of STO is used to describe point defects including oxygen vacancy and substitutional doping. The DFT calculations were performed within the PBE+U functional using PAW method as implemented in VASP [3]. The Hubbard U was set to be U = 4.75 eV for the 3d orbitals at the Ti sites, which reproduces the relative position of defect levels to the valence and conduction band. We also focus on the $\mathrm{V_O}$) and divalent cation (D) substitution of the nearest Ti site. We consider divalent cations D^{2+} with a similar ionic radius to Ti^{4+} to introduce hole carriers: D = Mg, Ni, Zn. The oxygen sites around Ti are distinguished by the apical and in-plane oxygens ($\mathrm{O_{ap}}$ and $\mathrm{O_{in}}$) due to the tetragonal crystal structure.

Figure 2 shows the PDOS for PTO:$\mathrm{V_{Oap}}$ and PTO:Mg. The presence of $\mathrm{V_{Oap}}$ introduces the defect level composed of Ti-3d below the conduction bands. In contrast, the Mg substitution of the nearest Ti ($\mathrm{Mg_{Ti}}$) removes the defect level and the band gap is recovered. This tendency is the same as $\mathrm{V_{Oin}}$, which is not shown here. Therefore, the divalent cation substitution is expected to enhance the photocatalytic activity similar to STO case. The investigation of the other divalent cation substitution and evaluation of the doping formation energy will be future works.

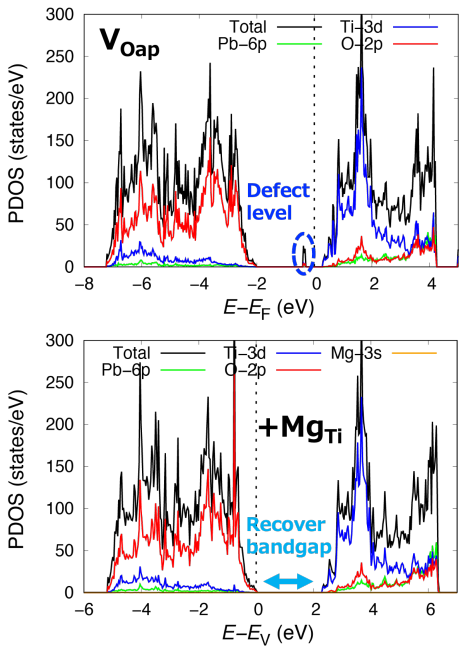


Figure 2: PDOS for PTO:$\mathrm{V_{Oap}}$ and PTO:Mg.

Calculation conditions

We have performed hybrid (MPI+OpenMP) parallel computing using, where the parallelization over bands and k-points is used by VASP version 6.4.2.

References

[1] K. Nishiguchi, T. Takayama, S. Takasuka, Y. Harashima, M. Fujii, and S. L. Ten-no: J. Phys. Chem. Lett. 2025, 16, 11, 2823–2830.

[2] T. Takata *et. al.*: Nature **581**, 413 (2020).

[3] G. Kresse *et. al.*: Phys. Rev. B **47**, 558 (1993); Phys. Rev. B **49**, 14251 (1994); Computational Materials Science **6** (1996) 15–50; Phys. Rev. B **54**, 11169 (1996).

[4] G. Wan *et. al.*: J. Am. Chem. Soc. 2022, 144, 20342–20350.

Microscopic structure of water/CeO_2 interface

Akira NAKAYAMA

Department of Chemical System Engineering,

The University of Tokyo, Tokyo 113-8656, JAPAN

1. Introduction

At interfaces between metal-oxide and water or alcohols, molecules in the liquid phase undergo dissociative adsorption due to acid-base sites on the surface. The ionic species generated by dissociation diffuse via proton hopping and recombine with surface hydroxyl groups. For such complex systems involving bond dissociation and formation, we constructed a neural network potential (NNP) using training data obtained by DFT calculations. Using this NNP, we performed large-scale, long-time molecular dynamics (NNP-MD) simulations to analyze the interfacial structure and dynamics.

2. Results and Discussion

Through NNP-MD simulations of the CeO_2/water interface, we successfully analyzed, with sufficient statistical reliability, the dissociation rate of water molecules at the interface and the diverse proton hopping mechanisms and its frequencies. Furthermore, when attempting to model proton hopping based on kinetics, we found that proton relay at the interface depends on the timescale of the solvent network dynamics. Therefore, it is difficult to construct meaningful kinetic models using reaction rates that ignore this time dependence, i.e., the so-called “memory effect.” To address this, we proposed a semi-Markov model in which the reaction rate is not treated as a constant, but rather depends on the time interval since the previous reaction. This approach idealizes the point of temporal reference for changes in the surrounding environment as the immediately preceding reaction. The fact that the results of kinetic Monte Carlo (KMC) simulations using this rate constant successfully reproduce those of the NNP-MD simulations demonstrates the importance of non-Markovian dynamics at the interface. As a result, we were able to establish a coarse-grained analysis method for the long-time reaction dynamics captured by NNP-MD [1].

In this work, the CP2K program package was used for DFT-MD simulations, and the PLUMED program was employed to perform the enhanced sampling simulations. The DeePMD-kit was used to construct NNPs

References

[1] Kobayashi, T.; Ikeda, T.; Nakayama, *Chem. Sci.* **2024**, *15*, 6816–6832.

Thermal Expansion and Phase Stability of BF_3 (B = Sc, Y, La, Al, Ga, In): A First-Principles Study

Yasuhide MOCHIZUKI

Department of Materials Science and Engineering,

Tokyo Institute of Technology, Ookayama, Meguro-ku, Tokyo 152-8550

Much attention has been paid to ScF3 because of its simple crystal structure and negative thermal expansion (NTE) over a wide temperature range [1]. No other binary trifluoride has the same crystal structure and exhibits NTE in as wide a temperature range as ScF_3. There has hitherto been no sufficient explanation for this reason. Herein, to discuss the phase stability and the NTE behavior of ScF_3, the 6 binary trifluorides BF_3 (B = Sc, Y, La, Al, Ga, In) are thoroughly compared by using the *ab initio* molecular-dynamics (AIMD) calculations with the on-the-fly machine-learning technique [Fig. 1(a–d)], first-principles lattice-dynamics calculations, and electronic-structure analyses based on group-representation theory and the band-unfolding method [Fig. 1(e, f)]. Our calculation results reveal that (i) the $a^-a^-a^-$

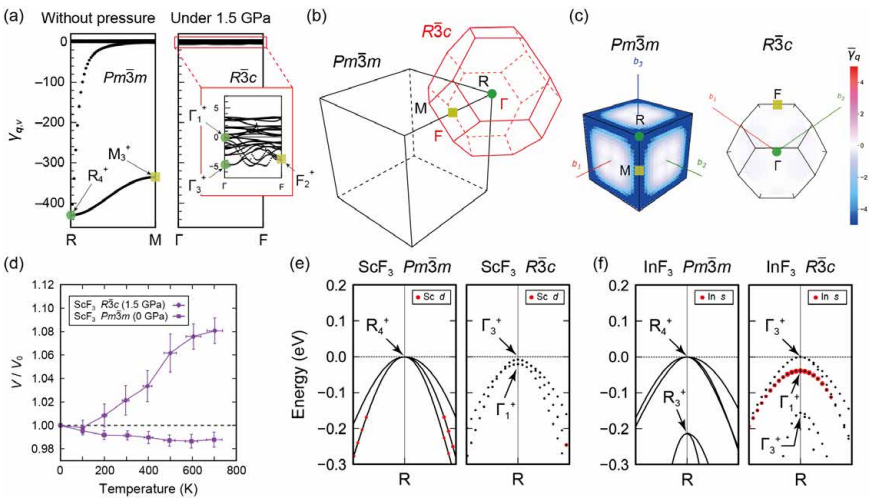


FIG. 1. (a) Dispersions of $\gamma_{\mathbf{q},\nu}$ of the $Pm\bar{3}m$ without pressure and $R\bar{3}c$ phases under 1.5 GPa for ScF_3. (b) The visualized first Brillouin zone of $Pm\bar{3}m$ and $R\bar{3}c$. (c) The distributions of averaged $\gamma_{\mathbf{q},\nu}$ in the first Brillouin zone of $Pm\bar{3}m$ and $R\bar{3}c$ phases. (d) Equilibrium lattice volumes of the $Pm\bar{3}m$ phases without pressure and $R\bar{3}c$ phases under 1.5 GPa for ScF_3 extracted from the AIMD calculations. (e, f) Calculated electronic band structures with and without the octahedral rotational distortions for (e) ScF_3 and (f) InF_3 by using the HSE06 hybrid functional in the vicinity of VBM.

octahedral rotational distortion (ORD) in ScF_3 increases the frequency of the crucial phonons for realizing NTE, leading to a weakening of the NTE behavior under hydrostatic pressure; (ii) the group-representation theory predicts the emergence of ORDs triggered by the second-order Jahn–Teller effect in cubic ScF_3, YF_3, AlF_3, GaF_3, and InF_3; (iii) cubic ScF_3 and YF_3 do not possess ORD without pressure due to their slight orbital overlap between the cations and anions; (iv) ScF_3 has a delicate balance between the repulsive force term and the energy stabilization term, induced by the octahedral rotational phonon modes; and (v) metastable cubic YF_3 and LaF_3 exhibit NTE behaviors. Our findings would provide an understanding of a material-design principle for realizing NTE [2].

Our first-principles calculations were performed by using the computing resources of Research Center for Com- putational Science at ISSP (System B).

References

[1] B. K. Greve, K. L. Martin, P. L. Lee, P. J. Chupas, K. W. Chapman, and A. P. Wilkinson, *J. Am. Chem. Soc.* **132**, 15496 (2010).

[2] H. Koiso, S. Yoshida, T. Nagai, T. Isobe, A. Nakajima, and Y. Mochizuki, *Phys. Rev. B* **110**, 064104 (2024).

Substrate can enhance thermal transport of two-dimensional materials

Jie Sun
Graduate school of Engineering,
The University of Tokyo, Hongo 7-3-1, Bunkyo-ku, Tokyo 113-8656, Japan

Two-dimensional (2D) materials are promising candidates for next-generation electronics, yet their intrinsic thermal conductivity (κ) is often suppressed when supported on substrates due to enhanced phonon scattering. While interface engineering efforts have largely focused on improving heat dissipation, mitigating the loss of intrinsic κ remains an open challenge. In this work, we investigate whether κ can be preserved—or even enhanced—on a substrate by accounting for complex phonon behaviors, including four-phonon (4ph) scattering and wave-like transport effects, which are particularly significant in low-κ materials. Employing machine learning interatomic potentials trained with moment-tensor potentials (MTPs), we simulate anharmonic thermal transport in graphene and germanene with high accuracy and efficiency. Surprisingly, we find that substrate contact can increase κ, albeit through distinct mechanisms in each material.

Thermal conductivity is calculated using the Wigner-Boltzmann transport equation, which captures both particle-like and coherent phonon transport. Accurate structural and vibrational properties are obtained from first-principles DFT calculations, which serve as training data for the MTP models. These models enable efficient extraction of high-order interatomic force constants via HIPHIVE. While substrate interactions are included during training to reflect realistic environments, they are excluded from final IFCs to isolate the intrinsic transport characteristics of the 2D layers.

To minimize lattice mismatch between the two-dimensional (2D) materials and the Au substrate, we constructed supercells with matched in-plane lattice vectors, effectively reducing intralayer strain. Graphene was modeled using a 2×2×1 supercell on Au, resulting in negligible strain (0.042%) and a consistent in-plane lattice constant of 4.92 Å, with an interlayer spacing of 3.36 Å. In contrast, germanene—with its buckled structure and lower symmetry—required a larger √13×√13×1 supercell to maintain stability. This configuration yields minor strains of 0.10% and 0.13% along the a and b directions, respectively, with an in-plane lattice constant of 14.36 Å and a vertical spacing of 2.73 Å. Top views of the relaxed heterostructures are shown in Figures 1(a) and 1(b).

We computed the lattice thermal conductivities of both free-standing and substrate-supported configurations, with the results summarized in Figures 1(c) and 1(d). For graphene at 300 K, the thermal conductivity increases from 1288 W/mK (free-standing) to 1644 W/mK on Au and remains elevated at higher temperatures. This unexpected enhancement challenges the conventional notion that substrates degrade thermal transport in 2D materials. The improved conductivity is attributed to reduced four-phonon scattering in the supported

graphene, stemming from symmetry breaking of the flexural (ZA) phonon mode. When only three-phonon scattering is considered, the substrate shortens phonon lifetimes and reduces κ, as seen in Figure 1(e). However, including four-phonon scattering reveals longer lifetimes in the supported structure (Figure 1(f)), resulting in higher κ. Substrate-induced electron-phonon coupling was found to have a negligible impact on thermal transport.

For germanene, the intrinsic thermal conductivity decreases from 2.45 W/mK (free-standing) to 0.82 W/mK at 300 K when both three- and four-phonon interactions are included, with an additional coherent contribution of 0.3 W/mK. Upon contact with Au, particle-like transport is further suppressed, while coherent conductivity increases significantly—to 1.35 W/mK at 300 K and 1.92 W/mK at 600 K—compared to only 0.77 W/mK in the free-standing case. Figures 1(g) and 1(h) illustrate this mode-dependent enhancement of wave-like phonon transport. These findings point to a promising strategy for thermal management in nanoscale devices by leveraging phonon coherence through substrate interactions.

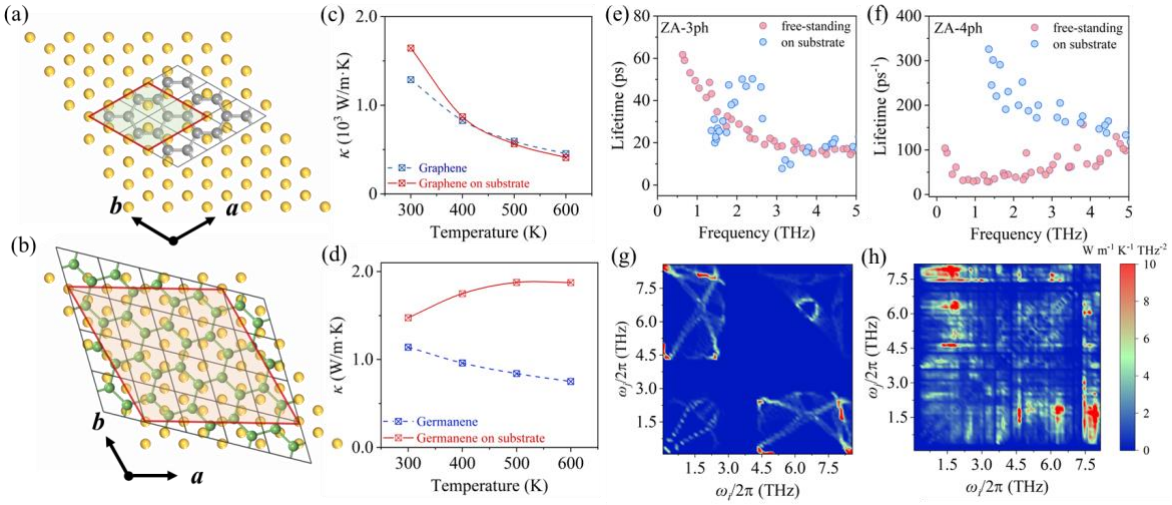


Figure 1. Top views of (a) graphene and (b) germanene on Au substrate. Thermal conductivity of free-standing and on-substrate (c) graphene and (d) germanene. Phonon lifetime of ZA mode from 0-5 THz considering (e) three-phonon and (f) four-phonon scattering in free-standing and on-substrate graphene. Mode-dependent wave-like phonon transport in (g) free-standing and (h) on-substrate germanene.

Theoretical study of grain boundary structures and segregation behavior of impurities

Kazutoshi INOUE
Advanced Institute for Materials Research, Tohoku University
Katahira 2-1-1, Aoba-ku, Sendai, Miyagi 980-8577

A comprehensive understanding of grain boundary (GB) structures is important to control their practical applications. However, the corpus of knowledge concerning GB structures remains limited even in MgO, which is a versatile compound with a high natural abundance.

In this study, we found a transitional structure from symmetric to asymmetric units at the MgO Σ5(210) GB by atomic resolution scanning transmission electron microscopy. In order to reveal the mechanism of the structural transition, we performed theoretical calculations to determine the stable structure of MgO and its variation with the segregation of impurities. It has been demonstrated that the simulated annealing technique using molecular dynamics (MD) simulation is an effective method to explore possible structures by cooling down models from high temperature. In order to screen potential stable and meta-stable atomic configurations by GB energy, the simulated annealing process has been repeated hundreds of times. The Buckingham force field is utilized to account for ionic charges and Coulomb forces. All MD simulations was performed using the LAMMPS package. Then, the pristine and Ca-segregated GB models were computed using the projector augmented wave method implemented in the VASP code using CPU nodes in System B. The generalized gradient approximation is employed for exchange-correlation interactions, with the formulation parameterized by Perdew, Burke, and Ernzerhof. All models were thoroughly optimized with an energy and force convergence threshold of 10^{-5} eV and 0.05 eV/Å. A $1 \times 1 \times 4$ k-point grid and 450 eV for the energy cutoff of plane waves were established after a comprehensive convergence testing. The Nudged Elastic Band (NEB) method was employed to determine the minimum energy path for the structural transition from symmetric to asymmetric units. The NEB and related methods are algorithms that can find the minimum energy pathway between two known states by iteratively optimizing a chain of intermediate structures. Subsequently, the substitution and interstitial energies of Ca were investigated to evaluate the segregation energies.

Theoretical calculations suggested that Ca atoms have a low substitution energy in metastable structures, therefore stabilizing asymmetric structures. Moreover, although there is a favored path in the NEB calculation, the difference in the transition barriar is low, which explains why Ca induces a different structure. This finding is expected to contribute to the development of materials design at the atomic level, which will take advantage of dopant segregation around GBs.

References

[1] Q. Chen, M. Saito, K. Kawahara, A. Nakamura, K. Inoue, Y. Ikuhara, "Grain Boundary Structural Transformation and the Effect of Impurities in MgO", *under review* (2025).

Quantum transport theory based on large-scale first-principles electron transport calculations

NOBUHIKO KOBAYASHI
Department of Applied Physics, University of Tsukuba
1-1-1 Tennodai Tsukuba Ibaraki 305-8573

Quantum transport theory based on large-scale first-principles electron transport calculations is important from the viewpoint of materials science and technology. We have developed the nonequilibrium Green's function (NEGF) method and the O(N) time dependent wave-packet diffusion (TD-WPD) method on the basis of the density functional theory (DFT). We have also developed methods to predict the crystal structures of organic materials, and have applied the methods to the design of organic semiconductors.

Organic semiconductors have attracted much attention for their applications to flexible, printable, lightweight, and low-cost electronic devices. The organic crystals are assemblies of π-conjugated molecules weakly bonded by van der Waals interactions, and it is difficult to predict the crystal structures. We have developed an efficient method based on DFT to predict the crystal structures of organic semiconductors from molecular structural formulas without using experimental data. As a demonstration, we applied this method to high-mobility organic semiconductor molecules, and performed crystal structure analyses for the molecules. We successfully obtained organic crystal structures from the molecular structural formulas. The predicted stable structures agree well with the experimentally observed structures, and the transport properties are accurately estimated. [1]

We have also developed a method to determine the crystal structure of organic semiconductors by incorporating the machine learning technique into PXRD analysis as shown in Fig.1. A machine-learning model that can automatically detect the peak positions from the PXRD pattern was developed by learning the PXRD patterns calculated from the crystals of the organic compounds and their peak positions. The crystal-structure analysis is successfully performed using their peak positions and the initial structure generated from the molecular structure information. [2]

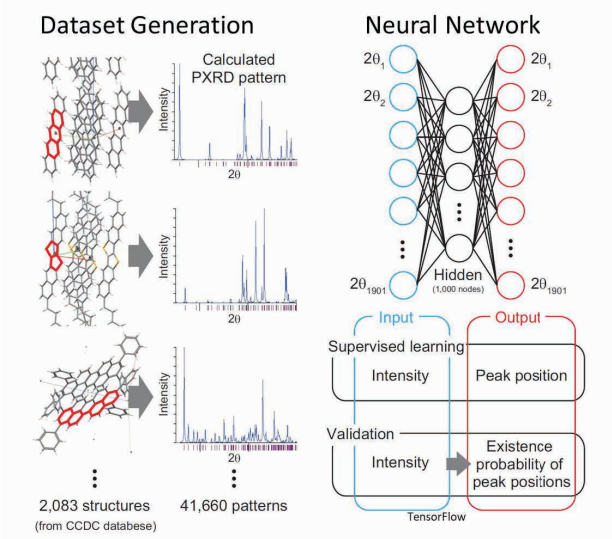


Figure 1: Machine learning model and the dataset generation process.

We have performed first-principles calculations of vertical transport in single-crystalline thin films of organic semiconductors consisting of periodically arranged molecules using a Simulation code for Atomistic Kohn-sham Equation (SAKE) developed by our group based on the DFT and NEGF formalism.[3] The transport properties are compared between single-crystalline thin film and single-molecule systems, and we reveal transport properties reflected by band dispersion and current characteristics due to good contact with organized electrode interface.

We developed the O(N) TD-WPD method for the quantum transport calculation of huge systems of up to 100 million atoms a decade ago, and have also succeeded in O(N) ther-

moelectric transport calculation such as Seebeck coefficient and power factor. Different from a conventional method using the electric conductivity spectrum, it obtains the coefficients directly from the correlation function between heat and electric current based on linear response theory. We apply the methodology to a two-dimensional system and confirm that the calculated results are consistent with those obtained by the conventional method. The proposed methodology provides an effective approach to evaluate the thermoelectric performance of micron-scale materials based on quantum mechanics from an atomistic viewpoint. [4]

References

[1] S. Hakata, H. Ishii, H. Takaki, T. Okamoto, J. Takeya, N. Kobayashi, *Appl. Phys. Express* 17 101001 (2024)

[2] N. Niitsu, M. Mitani, H. Ishii, N. Kobayashi, K. Hirose, S. Watanabe, T. Okamoto, J. Takeya *Appl. Phys. Lett.* 125, 013301 (2024)

[3] H.Takaki, N.Kobayashi, K.Hirose, *J. Phys.: Condens. Matter.* 32 325901(2020)

[4] H. Ishii, N. Kobayashi, K. Hirose *J. Phys. Condens. Matter.* 36 335903 (2024).

Ab initio molecular-dynamics study of CO_2 adsorption mechanisms in cement hydration process

Ikumi KANEMASU and Satoshi OHMURA

1) Premier Institute for Advanced Studies, Ehime University, Matsuyama, Ehime 790-8577

2) Department of Civil and Environmental Engineering

Hiroshima Institute of Technology, Hiroshima, Hiroshima 731-5193

It has been reported that the cement industry is the third or fourth largest emitter of carbon dioxide (CO_2) worldwide. As a result, CO_2 capture technologies in the cement industry have attracted significant attentions. To improve these technologies, detailed research on the CO_2 absorption mechanisms of cement-based materials from an atomistic perspective is required. For this reason, we have investigated the absorption properties of hydrate minerals in the cement using ab initio molecular dynamics simulations. In this study, we focused on the ettringite and tobermorite as a model of calcium silicate hydrate mineral, which formed when water reacts with cement. Figure 1 shows the structural models of ettringite and tobermorite.

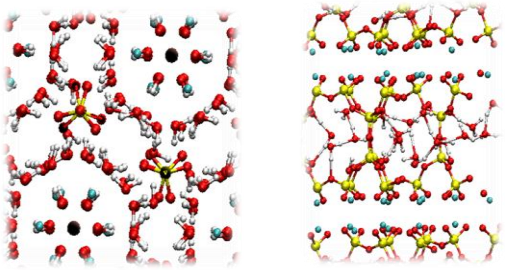


Fig. 1. Atomic configurations of ettringite and tobermorite.

We performed ab initio moelcualr dynamics simulations for these minerals + CO_2 systems. For Ettieigite-CO_2 system, It was found that CO_2 is converted to CO_2-OH (i.e., HCO_3^-), due to the presence of numerous hydroxyl groups (OH^-) in ettringite, which can react with CO_2 molecules through acid-base reactions. On the other hand, since tobermorite contains fewer hydroxyl group compared to ettringite, the formation of (HCO_3^-) is more limited.

.

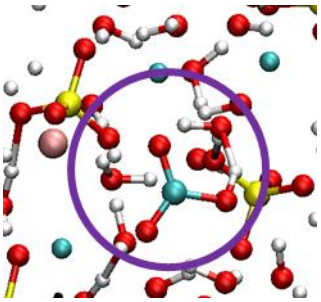


Fig. 2. HCO_3^- observed in the simulation for ettringite

References

[1] I. Kanemas, *et al.*, Cement Science and Concrete Technology **78**, 18-25 (2025).

Computational Design of Novel Functional Materials and Catalysts for Energy-related Applications

Tetsuya TAKETSUGU

Department of Chemistry, Faculty of Science

Hokkaido University, N10W8, Kita-ku, Sapporo 060-0810

The main goal of this project is to develop a number of innovative real functional materials for energy and environment-related applications using a computational approach. The density functional theory (DFT) methods as implemented in the VASP and Quantum Espresso software packages were used. The following main results were achieved:

1) We have modeled the catalytic reaction of ammonia electrooxidation in aqueous solution to produce nitrate and nitrite while generating hydrogen under ambient conditions [1]. Our DFT calculations support experimental observations and reveal the mechanism of the electrochemical oxidation of ammonia to nitrite and nitrate on a nickel oxyhydroxide (NiOOH) type of catalyst formed on the Ni foam. Different reaction pathways leading to formation of nitrate and nitrite and N_2 are studied. This research contributes to the development of a cost-effective and highly efficient catalyst for large-scale ammonia electrolysis, while shedding light on the underlying mechanism of the NiOOH catalyst.

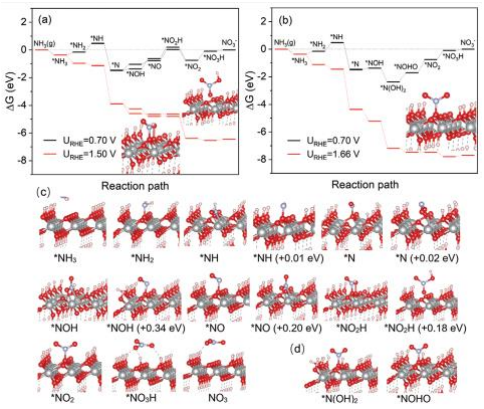


Fig. 1: Free energy diagrams for electrochemical oxidation of ammonia and the most stable structures of the reaction intermediates [1].

2) Using the extensive large-scale DFT and generic force field calculations with periodic boundary conditions (pGFN-FF) calculations we have modeled the formation of the nearly freestanding 2D gold (Au) sheets with triangular nanoscale patterns separated from the Ir(111) surface by embedded B atoms [2]. We have also unveil the structure of the buried B species and their crucial role in forming the nanostructured Au mono- and bilayers. Interfacial B atoms do not form the χ-type borophene typically observed on the

Ir(111) surface but adsorb in the Ir substrate hollow sites. Changes in the Au monolayer's band structure upon substrate decoupling indicate a transition from 3D to 2D metal bonding. The resulting Au films exhibit remarkable stability, making them practical for studying the catalytic activity of 2D gold.

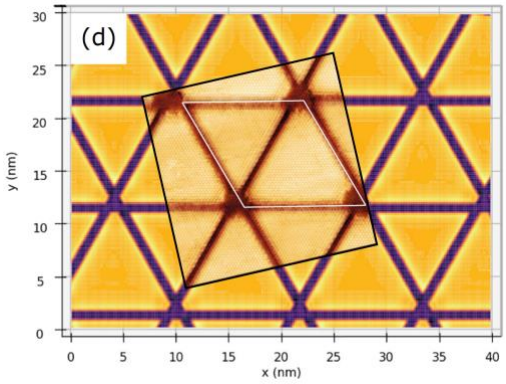


Fig 2: Nanopattern structure of monolayer gold on B/Ir(111) along with the superimposed STM image [2].

3) We performed a systematic investigation on the catalytic activities of high-spin small Fe(III) oxides for efficient hydrogen production through ammonia decomposition, using the artificial force-induced reaction method within the framework of density functional theory with the B3LYP functional. An analysis of NH_3 dehydrogenation and H_2 formation on various Fe(III) oxide sizes identifies the rate-determining steps for each reaction [3]. We found that the rate-determining step for the full NH_3 dehydrogenation on $(Fe_2O_3)_n$ (n = 1–4) is size-dependent, with the $NH* \rightarrow N* + H*$ reaction acting as the limiting step. The obtained results are valuable for designing iron trioxidebased nanosized catalysts by regulating the size of the $(Fe_2O_3)_n$ clusters to enhance H_2 production from the catalytic decomposition of ammonia.

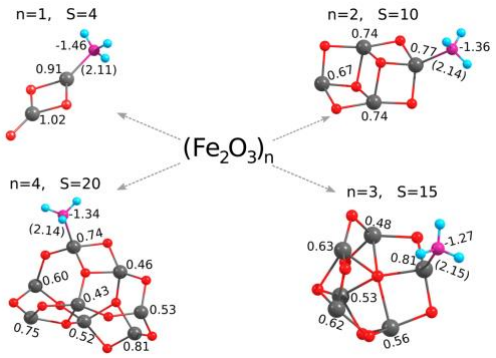


Fig 3: Optimized geometries of NH_3 adsorbed on $(Fe_2O_3)n$ clusters for n = 1–4 [3].

References

[1] H. Liu, C.-J. Yang, C.-L. Dong, J. Wang, X. Zhang, A. Lyalin, T. Taketsugu, Z. Chen, D. Guan, X. Xu, Z. Shao, and Z. Huang, Adv. Energy Mater. **14**, 2401675 (2024).

[2] A. Preobrajenski, N. Vinogradov, D. A. Duncan, T.-L. Lee, M. Tsitsvero, T. Taketsugu, and A. Lyalin, Nat. Commun. **15**, 10518 (2024).

[3] S. Ibragimov, A. Lyalin, S. Kumar, Y. Ono, T. Taketsugu, and M. Bobrowski, J. Chem. Phys. **162**, 054305 (2025).

First-principles study of the Fano resonance in copper phthalocyanine adsorbed on Cu(100)

Yuji HAMAMOTO

Department of Communication Engineering,

Okayama Prefectural University, 111 Kuboki, Soja, Okayama 719-1197

The Fano effect is a ubiquitously observed quantum phenomenon characterized by an asymmetric resonance peak that results from the interference between continuum and discrete levels. Recent experiments based on scanning tunneling spectroscopy (STS) have demonstrated that the Fano resonance also appears in the dI/dV spectra of copper phthalocyanine (CuPc) adsorbed on the Cu(100) surface [1]. The experimental results indicate that the q-parameter, which characterizes the line shape of the Fano resonance, varies dramatically as a function of the position of the STS tip and fluorine substitution of the CuPc molecule, whereas their dependence disagrees with the theoretical expression of the q-parameter.

To elucidate the origin of the discrepancy, we perfume the density functional theory (DFT) calculation of the Fano resonance, using the adsorption structure obtained for CuPc on a slab model of Cu(100) [1] as shown in Fig. 1. The continuum levels of the metal surface are described by the Embedding Green's function method [2], and dI/dV is approximated by the local density of states (LDOS) near the apex of the STS tip [3].

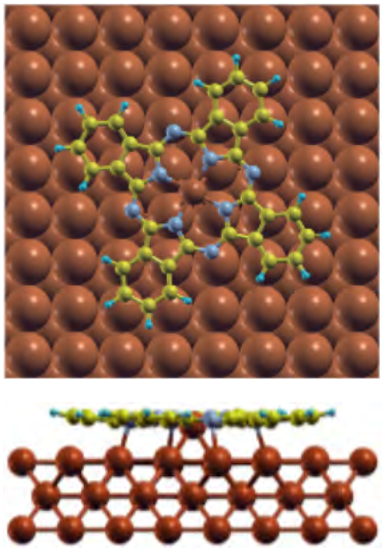


Fig. 1: Top and front views of CuPc adsorbed on Cu(100).

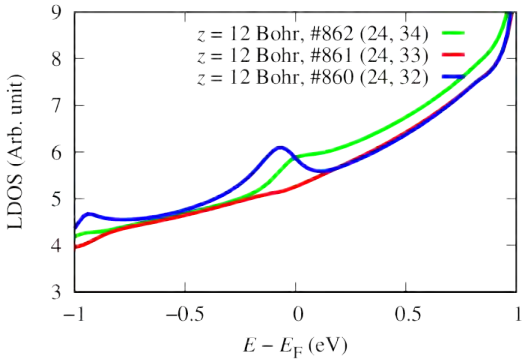


Fig. 2: LDOS obtained near the edge of the CuPc molecule adsorbed on the Cu(100) surface.

Preliminary results for the LDOS obtained

near the edge of the molecule are shown in Fig. 2, where slight signatures of a dip as well as asymmetric peaks can be observed. However, resonance peaks are almost symmetric above the molecule, in disagreement with the experimental results. This might be attributed to the fact that the generalized gradient approximation adopted in the DFT calculation fails to describe the image potential above the molecule, suppressing the interference of the surface states with molecular orbitals. For the future outlook, we plan to perform further calculations taking the image potential into account.

References

[1] H. Okuyama, S. Kuwayama, S. Hatta, T. Aruga, Y. Hamamoto, T. Shimada, I. Hamada, and Y. Morikawa, Appl. Surf. Sci. **643**, 158700 (2024).

[2] J. E. Inglesfield, J. Phys. C: Solid State Phys. **14**, 3795 (1981).

[3] J. Tersoff and D. R. Hamann, Phys. Rev. Lett. **50**, 1998 (1983).

Structure search for germanene on Ag(111) by Gaussian process regression

Yuji HAMAMOTO

Department of Communication Engineering,

Okayama Prefectural University, 111 Kuboki, Soja, Okayama 719-1197

Germanene, a germanium (Ge) analog of graphene, has been drawing growing attention because of its peculiar electronic properties due to the linear dispersions, as well as the potential application in semiconductor nanotechnology. Experimentally, germanene is grown by depositing Ge atoms on the Ag(111) surface, where a transition from Ag_2Ge alloy at low coverage to the striped phase of germanene at 1 ML has been observed. However, the existence of the Ag_2Ge alloy at the early stage casts a doubt on the formation of pure germanene. Theoretically, density functional theory calculations have been performed to analyze the electronic structures of germanene grown on Ag(111), where the formation of pure germanene is assumed in most cases, because of the structural complexity of the AgGe alloy.

To overcome the computational difficulty, we adopt GOFEE, an efficient structure search method based on the Gaussian process regression and an evolutionary algorithm [1], to investigate the possibility of alloy formation. Recently, we have applied the method to silicene on Ag(111) and successfully determined not only the well-known stable structures but also previously unknown metastable structures. We here examine the applicability of GOFEE, taking pure germanene on Ag(111) as an example. The surface is modeled with a periodically repeated $7 \times \sqrt{3}$ surface unit cell of the Ag(111) slab composed of one Ag atomic layer. A typical structure obtained by GOFEE is shown in Fig. 1, where the honeycomb lattice is significantly distorted as compared with a freestanding germanene. For the future outlook, we plan to apply this method to the GeAg alloy on Ag(111) and determine the stable structures for various stoichiometries.

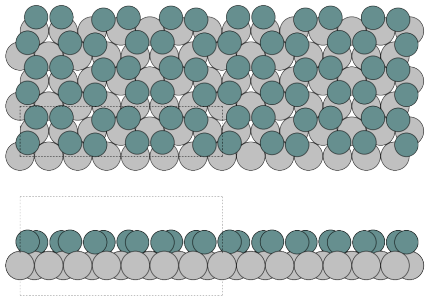


Fig. 1: Top and front views of germanene on Ag(111) obtained by GOFEE. The dotted rectangle indicates the unit cell of the system.

References

[1] M. K. Bisbo and B. Hammer, Phys. Rev. Lett. **124**, 086102 (2020).

Non-perturbative calculation of exchange coupling tensor

Tomonori TANAKA
Department of Materials Science and Engineering, Institute of Science Tokyo
Nagatsuta-cho, Yokohama 226-8501

In recent years, spintronics utilizing complex magnetic interactions found in noncollinear magnetic structures has been rapidly advancing. Meanwhile, first-principles evaluation methods for such complex magnetic interactions are still under development. Although several state-of-the-art evaluation methods exist, they are commonly based on perturbation theory, which presents issues regarding quantitative accuracy.

In this project, we first demonstrated that the non-perturbative evaluation of the exchange coupling parameters J_{ij} in the Heisenberg model [1]. Surprisingly, we find that contributions from changes in the electronic structure—which have been ignored in the perturbative methods—are necessary even in relatively small deviations from the ground magnetic state.

Although the exchange coupling parameters in the Heisenberg model remain important, they are insufficient for describing many magnetic orders and textures. Therefore, we believe that non-perturbative methods for evaluating other types of magnetic interactions are also essential. To achieve this, we have developed an efficient implementation of the spin-cluster expansion (SCE) method [2]. While the original SCE formulation theoretically allows for the description of any type of magnetic interaction within the classical spin model, its initial implementation incurred prohibitively high computational costs and was therefore impractical. We overcame this issue by utilizing constraining local magnetic fields [3].

As a demonstration, we applied the spin-cluster expansion method to a relatively simple ferromagnetic system, $L1_0-$FePt. We performed constrained-noncollinear DFT calculations using the GGA-PBE functional implemented in the VASP package. Thirty different spin configurations near the ferromagnetic state were prepared, and the corresponding total energies were collected. The SCE coefficients were then estimated using the least-squares method. For example, the exchange coupling tensor for the first-nearest-neighbor Fe-Fe pair along the x-direction, $\mathcal{J}_{1\mathrm{NN}}$, was obtained as

$$\mathcal{J}_{1\mathrm{NN}} = \begin{pmatrix} 17.81 & 0 & 0 \\ 0 & 18.30 & 0 \\ 0 & 0 & 17.67 \end{pmatrix} \mathrm{meV}. \quad (1)$$

This method enables the evaluation of non-diagonal components consisting of symmetric and antisymmetric anisotropic exchange couplings from fully self-consistent DFT calculations. We therefore plan to apply our method to systems exhibiting more complex magnetic textures.

References

[1] T. Tanaka and Y. Gohda, arXiv:2410.11256.

[2] R. Drautz and M. Fähnle, Phys. Rev. B **69**, 104404 (2004).

[3] T. Tanaka and Y. Gohda, in preparation.

Boosting Energy Efficiency in Biomass & Fuel Cell Systems: Using Ni Nanoparticles on CeO_2 for Methane Conversion

Takaya FUJISAKI

Faculty of Materials for Energy,

Shimane University, 1060 Nishikawatsu, Matsue, Shimane 690-0823

The global demand for electrical energy continues to grow, prompting significant interest in fuel cells as a highly efficient device for converting chemical energy from hydrogen and oxygen directly into electrical energy without reliance on fossil fuels. Moreover, fuel cells have the capability to utilize biogas (CH_4-based gas), a renewable resource primarily composed of methane, for electricity generation as seen in Fig.1[1][2].

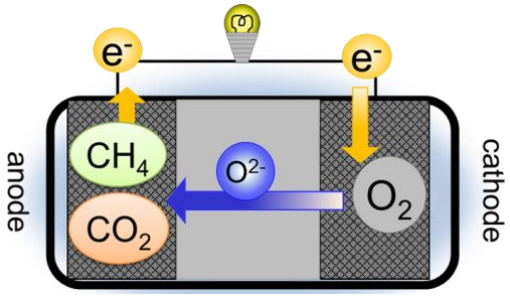


Fig.1 Principle of biogas direct fuel cell. The reforming catalyst in the electrode allows hydrogen to be drawn from methane.

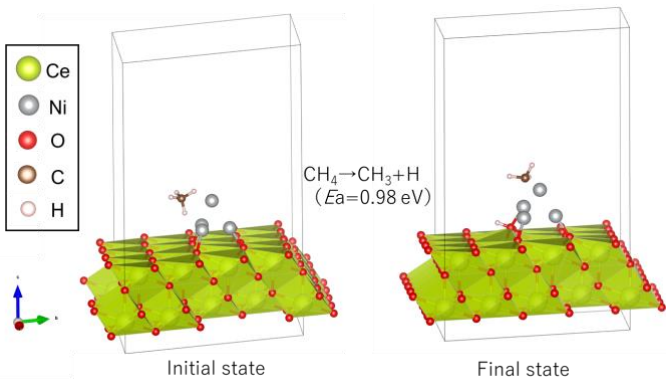
Biogas is produced through the methane fermentation of biomass, a renewable energy source. Hydrogen can be effectively extracted from methane through the Dry Reforming of Methane (DRM) reaction ($CH_4 + CO_2 \rightarrow 2H_2 + 2CO$). Minimizing the activation barriers for the critical steps in DRM, specifically methane dissociation ($CH_4 \rightarrow CH_3 + H$) and carbon dioxide dissociation ($CO_2 \rightarrow CO + O$), is essential for enhancing hydrogen extraction efficiency and thus improving fuel cell efficiency.

My project employed theoretical calculations, specifically density functional theory (DFT), to systematically explore Ni nanoparticle catalysts supported on CeO_2 substrates. I focused on two distinct Ni_4 configurations, designated as "Ni_4 above Ce" and "Ni_4 above O"[3]. My comprehensive computational approach allowed to elucidate the reaction mechanisms at atomic resolution and assess strategies for reducing the activation energy of methane dissociation.

As seen in Fig.2, Results showed that the "Ni_4 above O" structure demonstrated lower activation energy (0.98 eV) compared to the "Ni_4 above Ce" configuration (1.03 eV), suggesting a preferable catalytic configuration. Detailed electron density analyses indicated that a more positively charged Ni_4 cluster, influenced by the electronegativity of substrate atoms beneath the Ni nanoparticles, significantly reduces the activation energy of methane dissociation. Further electronic structure analysis using the projected crystal orbital Hamilton population

(pCOHP) method revealed weaker antibonding interactions between CH_3 and Ni atoms in the "Ni_4 above O" structure, leading to enhanced stability and reduced activation energy.

Fig.2 Before and after methane dissociation of the Ni on above O structure as shown by first-principles calculations.



Experimental validation of the computational predictions was achieved through DRM tests using a specially developed flower-like Ni-supported CeO_2 catalyst (Ce(F)). The experimentally determined activation energy for methane dissociation was 0.69 eV, closely matching our DFT-calculated apparent activation energy (0.80 eV) for the "Ni_4 above O" structure. This experimental confirmation significantly validates our theoretical model, highlighting the reliability of DFT calculations in predicting catalytic behaviors.

In conclusion, this project provides critical insights into optimizing Ni-supported CeO_2 catalysts for the DRM reaction, emphasizing the importance of charge distribution and structural configuration. The study offers a viable strategy for future catalyst design, aiming at achieving high efficiency and sustainability in energy production.

Acknowledgments:

This work was supported by JSPS KAKENHI, Fostering Joint International Research (B), Grant Number 20KK0248. Computational resources were provided by the Research Institute for Information Technology at Kyushu University, the Institute for Solid State Physics at the University of Tokyo, and the Cyberscience Center at Tohoku University. Additional support was received from JSPS KAKENHI Grant Numbers JP21K04996 and JP22H05146 (Grant-in-Aid for Transformative Research Areas (A) “Supra-ceramics”), Tateisi Science and Technology Foundation Grant Number KH-018, and Sumitomo Foundation Environmental Research Projects Grant Number 2340007.

References:

[1] T. Fujisaki, K. Ikeda, A. T. Staykov, H. Setiawan, Y. Shiratori, RSC Adv. 2022.

[2] H. Setiawan, M. Sakamoto, T. Fujisaki, S. M. Lyth, Y. Shiratori, Biomass Bioenergy, 2022.

[3] T. Fujisaki, Y. Tsuji, P. H. Tu, T. C. D. Doan, D. S. Rivera Rocabado, A. T. Staykov, K. Yashiro, Y. Shiratori, Phys. Chem. Chem. Phys. 2024

Designing Impurity Doping in Two-Dimensional Materials by First-Principles Calculations

Soungmin Bae

Institute for Materials Research, Tohoku University, 2-1-1 Katahira, Aoba-ku, Sendai, 980-8577, Japan

Introduction

The critical dimensions of modern semiconductor fabrication have already reached just a few nanometres, and further miniaturization of silicon-based devices is approaching its physical limits. To push integrated circuits into the true nanoscale regime, entirely new device architectures built on two-dimensional (2D) materials are indispensable.

Transition-metal dichalcogenides (TMDCs) with layered crystal structures—most notably MoS_2—retain high electrical conductivity even in monolayer form (< 1 nm), making them strong candidates for next-generation transistor channels. Yet TMDCs suffer from large contact resistance at metal interfaces, so purposeful tuning of their intrinsic properties is essential.

In this study, we systematically explore stable impurity-doped structures and strategies for electrical property control in 2D MoS_2 by means of first-principles calculations.

Computational Methods

To capture the formation of localized polaron states and to evaluate donor/acceptor transition levels with high fidelity, we performed

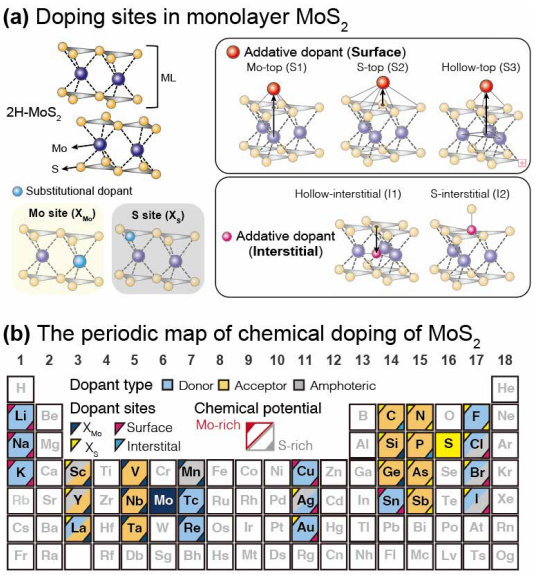


Figure 1. (a) Possible doing sites of 2H-MoS_2 considered in this study. (b) Stable dopant sites predicted for 27 elements from first principles point defect calculations.

exhaustive density-functional-theory (DFT) calculations on impurity-doped MoS_2. Roughly twenty dopant elements from the periodic table were surveyed in three configurations—substitutional, surface-adsorbed, and interstitial—while charge states from −2 to +2 were considered. Thermodynamic stability was assessed under varying chemical potentials and Fermi-level positions.

All calculations employed the Vienna Ab initio

Simulation Package (VASP), and defect-formation energies were post-processed with our in-house pydefect workflow.

Discussion

Figure 1 summarizes the energetically preferred configurations. Elements adjacent to Mo or S in the periodic table tend to substitute for Mo or S, respectively. Alkali metals preferentially adsorb on the surface, while small-radius elements such as C and P are stabilized at interstitial sites. Representative electronic structures for Re_{Mo} and Nb_{Mo} dopants are plotted in Figure 2. In both cases, carriers introduced by Re or Nb localize strongly around the dopant, forming distinct polaronic states. Similar behaviour was observed for all 27 elements examined, implying that charge transport in doped monolayer MoS_2 is dominated by impurity (hopping) conduction. These insights not only aid the rational design of high-performance TMDC-based devices but also advance our fundamental understanding of MoS_2 electronics.

References

[1] Universal Polaronic Behavior in Elemental Doping of MoS_2 from First-Principles, Soungmin Bae, Ibuki Miyamoto, Shin Kiyohara, Yu Kumagai, ***ACS Nano*** 8, 33988–33997(2024).

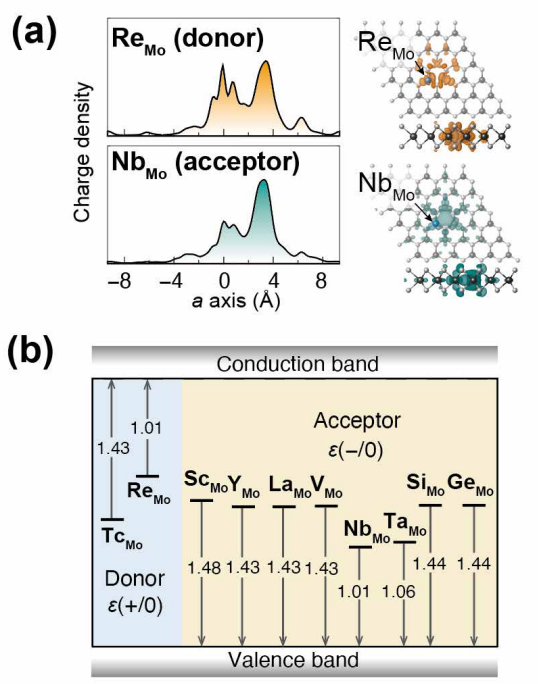


Figure 2. (a) Polaronic (localized) charge distribution of Re_{Mo} (donor) and Nb_{Mo} (acceptor) in monolayer MoS_2. (b) Donor/acceptor charge transition levels of dopants in Mo site in monolayer MoS_2.

Understanding of Spin-splitting Phenomena in Altermagnets

Kunihiko YAMAUCHI

Center for Spintronics Research Network, Osaka University, Toyonaka, Osaka 560-8531, Japan

We have investigated spin-splitting phenomena in altermagnetic materials, building on our research initiated last year on altermagnet MnTe [1]. In practice, a combination of first-principles DFT calculations (using the VASP and Wannier90 codes) and ARPES experiments enables us to reveal the electronic structure and uncover the microscopic mechanisms underlying macroscopic material properties.

RuO_2 was initially proposed as a candidate altermagnet that exhibits spin-split band structures in the antiferromagnetic phase, even in the absence of spin-orbit coupling. However, the antiferromagnetic nature of RuO_2 is currently a subject of intense debate. In this study, we elucidated the band structure of the (100), (110), and (101) surfaces of bulk single-crystalline RuO_2. Regardless of surface orientation, the ARPES-derived band structures show semi-quantitative agreement with bulk calculations in the nonmagnetic phase, but exhibit significant discrepancies with those in the antiferromagnetic phase.

These findings suggest the absence of the altermagnetic spin splitting in RuO_2. Moreover, we identified nodal lines near the Fermi energy that give rise to π Zak phase and the topologically protected surface states in nonmagnetic RuO_2 as shown in the figure below. This work is currently being prepared for publication [3].

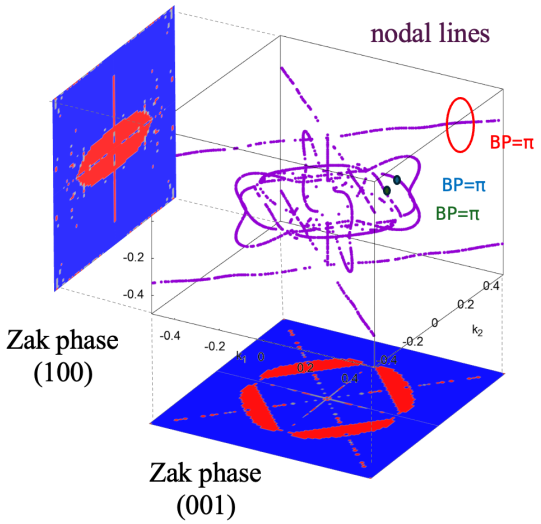


Figure: Nodal-lines and π Zak phase responsible for the topological surface states in nonmagnetic RuO_2.

References

[1] T. Osumi, S. Souma, T. Aoyama, K. Yamauchi, et al., Phys. Rev. B **109**, 115102 (2024).

[2] K. Nakayama, A. Tokuyama, K. Yamauchi, et al., Nature **631**, 54 (2024).

[3] T. Osumi, K. Yamauchi, et al., arXiv:2501.10649 (2025).

First-Principles Calculation on the Adsorption of Ethylene Acrylic Acid Molecules on Chromium Oxide Surfaces

Hiroki IWAI, Yuta TSUJI

Interdisciplinary Graduate School of Engineering Sciences,

Kyushu University, 6-1, Kasuga-koen, Kasuga, Fukuoka, 816-8580, Japan

Hybrid materials that combine metals and polymers are widely utilized across various fields, including aerospace and biomedicine. Specifically, the laminated strips composed of chrome-plated steel and ethylene-acrylic acid (EAA), which are the focus of this study, are employed as protective materials for fiber optic cables. A thorough understanding of the bonding mechanisms between these materials is crucial for improving the long-term stability of the cables. Experimental studies indicate that at the adsorption interface between chrome-plated steel and EAA molecules, two distinct types of coordination bonds, in addition to hydrogen bonding, are formed: (O=)C–O–Cr, which is monodentate, and –C–(O–Cr)$_2$, which is bidentate [1]. In this study, the adsorption energies of EAA molecules on Cr_2O_3 (001) and (012) surfaces, both with a thin layer of chromium hydroxide and without it, were evaluated using density functional theory (DFT). The bonding mechanisms observed in the experiments were corroborated through the DFT calculations at the adsorption interfaces. When coordination bonds were formed, the adsorption interface exhibited greater stability compared to when adsorption occurred solely via hydrogen bonding. However, on the (012) surface with the hydroxide layer, the Cr atoms became coordinatively saturated, preventing the formation of coordination bonds between the EAA molecules and the surface. Furthermore, calculations performed under ferromagnetic conditions, in contrast to antiferromagnetic conditions, revealed minimal differences in the adsorption energy, with negligible structural differences between the two magnetic states. This suggests that the adsorption energy of antiferromagnetic materials can be effectively approximated by that of ferromagnetic materials, with only a minor error.

References

[1] X. Zou, *et al*. *ACS Appl. Mater. Interfaces*, **14**, 27383 (2022).

First-principles study of surface and defect systems for power electronics materials

Kaori SEINO
Department of Materials Science and Engineering, Kyushu Institute of Technology
Sensui-cho 1-1, Tobata, Kitakyushu, Fukuoka 840-8550, Japan

Power device solutions for highly efficient power are a technical challenge directly related to environmental issues. In addition to Si-based power devices, SiC-based and GaN-based power devices have recently been used. Since high efficiency is also required for power devices that replace silicon, it is essential to minimize the effects of defects that may affect device performance. Moreover, diamond has overwhelming advantages over Si, SiC, and GaN in power electronics, although it is not on the market. For these new power devices to perform as expected, their surface and defect characteristics must be understood.

In this project, we have performed first-principles calculations of surface and defect systems for power electronics materials. For GaN, we consider the atomic diffusion of a Mg atom in *p*-type GaN via the vacancy mechanism. As a local structure for atomic diffusion of a Mg atoms in GaN, a defect complex which consists from Ga vacancy (V_{Ga}) and a Mg substitutional to Ga site ($\mathrm{Mg_{Ga}}$) would be a starting configuration of Mg diffusion. Therefore, we first clarify structural and electronic properties of defect systems, V_{Ga}, $\mathrm{Mg_{Ga}}$, and its complex $\mathrm{Mg_{Ga}}$-V_{Ga} by spin-polarized HSE calculations containing 360 atoms using the VASP package [1].

In the case of $\mathrm{Mg_{Ga}}$-V_{Ga}, the removal of a Ga atom results in four N dangling bonds, and substituting the Ga atom with an Mg atom reduces the number of electrons by one. Therefore, in the neutral charge state of $\mathrm{Mg_{Ga}}$-V_{Ga},

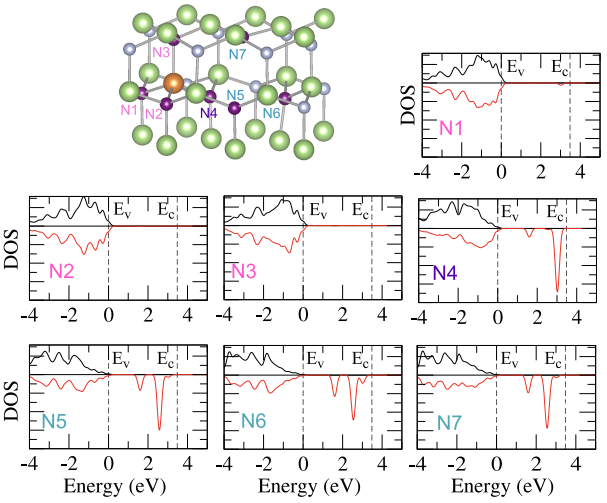


Figure 1: Local atomic configuration of defect complex $\mathrm{Mg_{Ga}}$-V_{Ga} in GaN with pDOS of $2p$ orbitals.

there are one hole derived from the acceptor atom and four N dangling bonds occupied by a total of five electrons, i.e., possibly four defect states. Accordingly, we can consider high- and low-spin configurations with S=2 and S=0, respectively. Furthermore, the position of V_{Ga} is considered perpendicular or parallel to the *c*-axis related to Mg impurity. The local electronic structure near the $\mathrm{Mg_{Ga}}$-V_{Ga} region, in particular near V_{Ga}, is remarkable as shown in Fig. 1.

References

[1] K. Seino, K. Shiraishi, and A. Oshiyama, *in preparation.*

Theoretical evaluation of mechanical properties of nano-carbon device structures

Koichi KUSAKABE
Graduate School of Science, University of Hyogo
Kouto, Kamigori-cho, Ako-gun, Hyogo 678-1297

In this study, we investigated nano-carbon and molecular structures and their dynamical properties, as well as layered material structures relevant for the molecular sensing and spintronics applications.

Our design method created material design of a possible Heisenberg spin chain with spin gap, which was realized in a polymerized hydrocarbon molecule called poly-PTM.[1] We have confirmed realization of a new 2D S=3/2 spin system by certifying material stability of the 2D poly-PTM using the density functional theory (DFT) simulation. The magnetic property was determined by construction of the effective Heisenberg Hamiltonian, where its effective exchange interactions were derived by evaluating a low-energy electron Hamiltonian. The localized zero-modes play relevant roles for both the design step and the realization step giving feasible magnetic exchange interaction strength for a quantum computation device.[2]

Topological insulator Bi_2Se_3, which is a layered Van-der-Waals crystal providing a spin-current device. Surface terminations control is shown to be plausible by having various cleaved surfaces, whose topological electronic states are confirmed by our simulations.[3]

Second harmonic generation of $La_4Ge_3S_{12}$ was observed in a recent experiment, whose electronic structures were directly confirmed by our electronic structure calculations.[4] This result again certified relevance of direct comparison of DFT-based simulations with experiments.

Giant Rashba spin-orbit coupling on light-element polar superlattices were designed by an international collaborative work. This investigation focuses staked ultra-thin material structures, whose spintronics properties are newly confirmed.[5]

Mechanical properties of stacked molecular structures, *i.e.* the amyloid-β protein, are analyzed using the nudged-elastic-band method in the DFT simulation. The dynamical properties of a protein molecule at an edge of the fibril are explored, where steric hindrance is important for an elementary deformation process. The size of a residue and occurrence of extra hydrogen bonding are keys to judge probable dissociation process of the fibril.

References

[1] N. Morishita, *et al.*, Appl. Phys. Express **14**, 121005-1-4 (2021).

[2] K. Komatsu, *et al.*, J. Phys. Soc. Jpn. 94, 044704 (2025).

[3] K. Fukumoto, *et al.*, Sci. Rep. 14, 10537 (2024).

[4] H. Ohtsuki, *et al.*, Z. anorg. allg. Chem. e202500029, (2025).

[5] Y. Wicaksono, *et al.*, Phys. Rev. B **110**, L220408 (2024).

Improving Stability of Molecular Dynamics Simulation using Machine-Learning Interatomic Potentials

Kohei Shimamura

Department of Physics,

Kumamoto University, 2-39-1 Kurokami, Chuo-ku, Kumamoto 860-8555

By training on highly accurate first-principles molecular dynamics (FPMD) data, the development of machine-learning interatomic potentials (MLIPs) that maintain the accuracy of FPMD while enabling large-scale and long-time MD simulations has been advancing. Through improvements in training methods, we have been able to construct robust MLIPs over the series of our projects, and we are actively applying them to the calculation of important physical quantities such as thermal conductivity. However, instabilities can still arise during MD simulations. These instabilities typically manifest when MD simulations are performed on systems larger than those represented in the training data. Since the size of systems treatable by FPMD is limited, supplementing training data for larger systems is challenging. Nevertheless, overcoming this issue is essential for handling more realistic systems.

In this study, we aimed to achieve stable MD simulations for one of the graph neural network-type MLIPs, the Allegro model [1], by adopting the Potential Averaging (PA) that we proposed [2]. The PA method belongs to ensemble learning, where multiple MLIPs are treated as a single predictor, and the "averaged forces" computed by these MLIPs are used in the MD simulations. Furthermore, by utilizing the "standard deviation of the forces," it naturally connects to active learning, which allows efficient collection of training data.

We found that, to implement the PA method in the Allegro model, it is necessary to modify not the main body written in Pytorch, but the interface part developed to link Allegro with the MD code LAMMPS, specifically the file pair_allegro.cpp written in C++. Even when MD simulations are performed using MD codes other than LAMMPS, it was possible to run them by modifying only pair_allegro.cpp.

The code validation was conducted using silver chalcogenide systems, for which we had accumulated sufficient knowledge through previous projects. In addition, we use the code developed in this study for a microscopic-level analysis of the supercooled liquid state of Mg alloys. The results of the study on the Mg alloys were presented at the 2025 Spring Meeting of the Physical Society of Japan.

References

[1] A. Musaelian, *et al.*: Nat. Commun. **14**, 579 (2023). [2] D. Wakabayashi, *et al.*: J. Phys. Soc. Jpn., **92**, 074002 (2023).

Quantitative description of cation-dependent electrode potential shift based on liquid Madelung potential

Atsuo YAMADA

Department of Chemical System Engineering,

The University of Tokyo, Bunkyo-ku, Hongo, Tokyo 113-8656

The electrode potential (E) governs the driving force of redox reactions in any electrochemical system. While the Debye–Hückel theory describes electrostatic interactions in dilute solutions, it fails at higher concentrations. To address this, we introduced the concept of the liquid Madelung potential, which explicitly treats electrostatic interactions in electrolyte solutions and successfully reproduces experimental potential shifts [1]. To further improve accuracy, we developed a thermodynamic framework based on MD simulations that considers not only electrostatic interactions but also van der Waals and entropic contributions to the Gibbs energy. This approach was validated for Na^+ and K^+ systems, in addition to the Li^+ system.

Figure 1a shows experimental potential shifts (open circles) as a function of concentration. Smaller cations deviate more from ideal Nernst behavior (dashed line), while calculated shifts (solid circles) agree well with experiment. These shifts stem from a Coulombic penalty caused by substitution of electron-localized solvent with electron-delocalized anions around the cation, which is more pronounced for smaller cations (Figure 1b). The developed computational approach thus provides a general, quantitative framework for potential shifts across alkali cations.

References

[1] N. Takenaka, S. Ko, A. Kitada, A. Yamada, *Nat. Commun*, **15**, 1319 (2024).

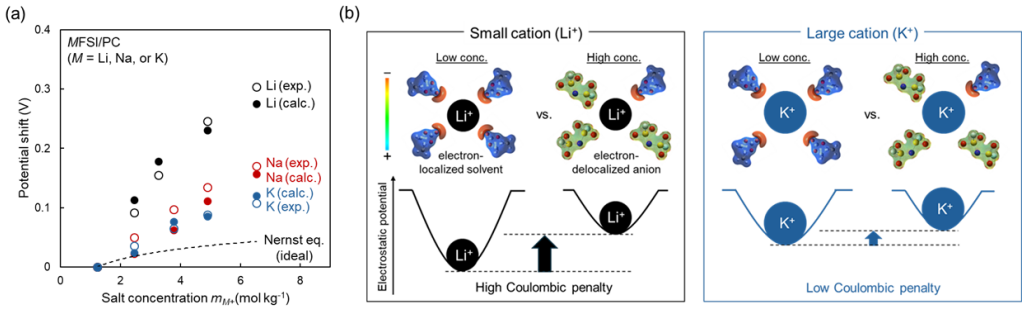


Figure 1 (a) Experimental (open circles) and calculated (solid circles) potential shifts for *M*FSI/PC electrolytes (*M* = Li, Na, or K) as functions of salt concentration (m_{M+}) relative to reference concentration of 1.2 mol kg^{-1}. (b) Schematic illustration explaining the origin of the cation-dependent potential shifts.

Distortion of ultrasmall metal oxides and their electronic state

Akira Yoko

International Center for Synchrotron Radiation Innovation Smart

Tohoku University, Aramaki aza Aoba, 468-1、*Aoba-ku, Sendai, Miyagi, 980-8572, Japan*

Size effect of materials in nanoscale has been attracting many attentions because of its unique physical properties. Recently, ultrasmall metal oxides can be synthesized by continuous flow hydrothermal method [1,2]. Precisely controlled metal oxide nanoparticles can be obtained with large scale synthesis, and it is currently important to study size effects in ultrasmall region (approximately 1~3 nm) to understand and predict the new properties of those ultrasmall particles.

As one example of the nano-size effect, large magnetic moment of cerium oxide (CeO_x) nanoparticles compared to its bulk has been reported [3,4]. Researchers proposed many possibilities of the origin of unusual magnetism. Although excessive oxygen such as oxygen antisites, interstitial, or Ce vacancy [5] can theoretically contribute to the magnetism in bulk structures, the atomistic structural origin of the size-effect is unclear to date. Here, we propose that the peroxidized structure in vertices of $CeO_{2+\delta}$ nanoparticles attribute to the magnetism in nanoparticles by first-principles calculations of the $Ce_{13}O_{32}$ nanocluster and experimental observation of nanoparticles whose diameter is up to 4 nm synthesized using hydrothermal reaction [1].

We employed density functional theory calculation using VASP package. PBE functional with Hubbard U correction for 4f orbitals is applied with on-site potential 5 eV [6]. The electronic density of states (DOS) shows obvious spin splitting in the $Ce_{13}O_{32}$ cluster, which has high symmetry of the arrangement of surface oxygen atoms. It results in a magnetic moment $m = 12.0\ \mu_{\mathrm{N}}$. On the other hand, if we take six oxygen atoms from the cluster and calculate the stoichiometric proper $Ce_{13}O_{26}$ cluster, it does not show any magnetic properties. The results indicate that the surface peroxidization on the nanocluster induce the magnetism.

References

[1] A. Yoko et al., J. Am. Chem. Soc. 146, 16324 (2024).

[2] A. Yoko et al., Precision Chemistry, In press (2025).

[3] M. Coey et al. Nat. Phys., 12, 694 (2016).

[4] K. Ackland and J. M. D. Coey, Phys. Rep. 746, 1 (2018).

[5] A.G. El Hachimi et al., Comput. Mater. Sci. 85, 134 (2014).

[6] M. Nolan et al., Surf. Sci., 576, 217 (2005).

Development of Stretchable Electret Materials for Energy Harvesting with the Aid of Machine Learning

Yuhan Gu, Rui WANG, Kuniko SUZUKI, and Yuji SUZUKI

Department of Mechanical Engineering

The University of Tokyo, Hongo, Bunkyo-ku, Tokyo 113-8656

Electronic devices with skin-like mechanical properties have significant potential in health monitoring and human-machine interface, particularly in wearable and implantable devices [1]. To ensure the overall flexibility of such electronic skin, it is highly desirable to develop intrinsically flexible power sources, such as kinetic energy harvesters using the stretching motions of skin.

Electret is a class of dielectric material with quasi-permanent charges, which can store charges for a long time, even decades [2]. Since electret energy harvesters have a high output power at low frequency with a thinner profile than other principles [3], they are excellent candidates for powering skin electronics.

We recently proposed perfluoro-elastomer FFKM as the base material for stretchable electrets [4]. The cross-linking process is employed for improving the stretchability of elastomer, but it is also used for embedding deep charge traps in the elastomer. By using triallyl isocyanurate (TAIC) as the cross-linking agent, the surface charge density as high as 0.74 C/m^2 has been obtained.

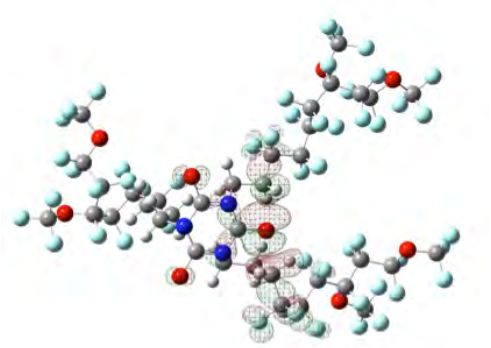


Fig. 1. Preliminary DFT results of cross-linked FFKM with TAIC [4].

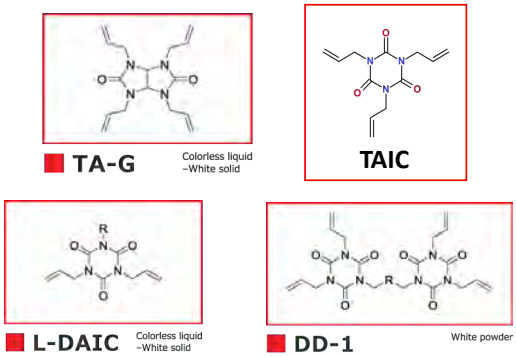


Figure 2. Cross-linking agents studied in this work.

In the present study, we investigate the effect of different cross-linking agents (Fig. 2) on the stretchability and charge stability of cross-linked FFKM.

All the quantum chemical calculations are made with the software GAUSSIAN [5] at the DFT level with the CAM-B3LYP

functional, while PCM is combined for solid-state analysis due to the solvation effect correction. The 6-31+G(d,p) basis set is employed to reduce CPU time

Figure 3 shows the distribution of trapped charges in FFKMs. In pristine FFKM, charges are distributed widely in the molecular structure, indicating shallow charge trap. On the other hand, all the cross-linked FFKMs exhibit deep charge trap, and the charges are concentrated in the cross-linking agent. The ionization potential (IP), which is the index of charging performance [2] of those cross-linked FFKMs are 8.57, 8.55, 8.52, and 7.1 eV for DD-1, L-DAIC, TAIC, and TA-G, while that of pristine FFKM is 11.2 eV.

Therefore, FFKM/TA-G should have the highest charging performance. Our physical experiments actually show that FFKM/TA-G gives the highest surface potential after charging and the highest peak temperature in the TSD (thermally stimulated discharge) spectra [6]. This fact proved that DFT-based screening of cross-linking agents is effective for finding high-performance stretchable electrets using FFKM.

This work was supported by JSPS KAKENHI Grant Number JP24H00306. The computation in this work has partially been done using the Supercomputer Center, the Institute for Solid State Physics, the University of Tokyo (ISSPkyodo-SC-2024-Ca-0002).

References

[1] W. Gao, et al., Nature, 529, pp. 509-514 (2016).

[2] Z. Mao, et al., Adv. Mater., 2303827, (2024).

[3] Y. Suzuki, IEEJ Trans. Electr. Electr. Eng., 6, pp. 101-111 (2011).

[4] R. Wang, et al., PowerMEMS 2022, Salt Lake City, pp. 14-17 (2022).

[5] M. Frisch, et al., “Gaussian 09, Rev. A. 1,” Gaussian, Inc. Wellingford, CT, (2009).

[6] R. Wang et al., Adv. Mater., submitted.

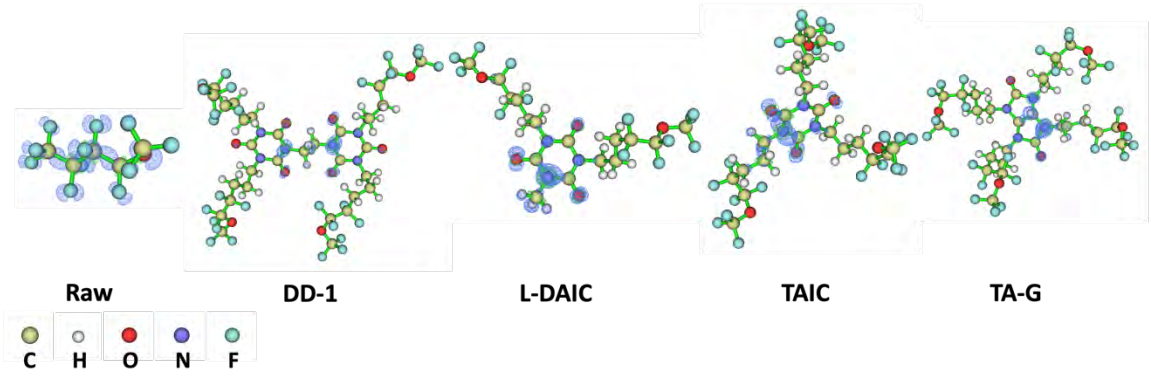


Figure 3. Visualized distribution of trapped charges in FFKMs [6].

Material Design Using Crystal Structure Prediction and First- Principles Calculations

Tomoki YAMASHITA
Department of Electrical, Electronics and Information Engineering,
Nagaoka University of Technology
Kamitomioka-machi, Nagaoka, Niigata, 940-2188

We have studied the structural stability of $Li_xM_{1-x}Cl_{2-x}$ (M = Ca, Mg) that can be a candidate material for solid electrolyte of Li-ion batteries. While the synthesis of $LiCaCl_3$ (x = 0.5) has been reported [1], its crystal structure has not yet been elucidated. A crystal structure prediction simulation for $LiCaCl_3$ was performed using CrySPY [2]. The calculation was performed with 20 atoms, and the structure search was conducted using an evolutionary algorithm with 20 structures per generation up to the 37th generation. Structure optimization and energy evaluation were carried out using the first-principles calculation software VASP. The PBE exchange-correlation functional was employed, and each structure was calculated using a single node. The most stable structure obtained from the search is shown in Fig. 1. The formation energy of this structure, calculated using LiCl and $MgCl_2$ as reference compounds, is –3.2 meV/atom. Although the value is negative, the result indicates that the energy gain is negligible. These results suggest that, rather than stabilizing in a simple ordered phase, $LiCaCl_3$ favors a disordered phase that becomes stable above a certain temperature.

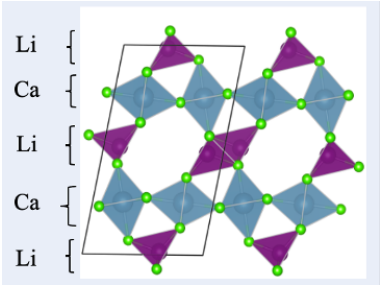


Figure 1: Stable structure of $LiCaCl_3$ obtained by crystal structure prediction.

Another research topic addressed in this study was the investigation of defect formation in the semiconductor material $Cu_2Sn_{0.5}Ge_{0.5}S_3$ (CTGS). Formation energies of various defects in CTGS were calculated using VASP. The HSE06 hybrid functional, which provides a good reproduction of the band gap, was employed for the exchange-correlation treatment. The eFNV correction scheme by Kumagai and Oba [3] was applied to account for defect formation energy corrections, as implemented in the pydefect code [4]. First-principles calculations with the HSE06 functional were performed using 16 compute nodes for each calculation. The Cu vacancy defect was found to have a low formation energy and to be the dominant defect. It is also expected to act as a shallow acceptor level, consistent with experimental observations, indicating that it serves as the primary source of holes. Donor levels were identified within the band gap for the (+1/0) charge transition levels of the Sn_{Cu} and Ge_{Cu} substitutional defects. Although the band gap can be tuned by varying the Sn/Ge ratio, these donor levels become deeper as the band gap increases, indicating that they may contribute

to the reduced power conversion efficiency. In CTGS, the Sn_{Cu} and Ge_{Cu} antisite defects form deeper levels as the band gap increases. This indicates that synthesizing the material with a composition ratio that suppresses the formation of these levels, corresponding to a band gap of approximately one eV, may be one of the key conditions for achieving high conversion efficiency.

References

[1] K. Mahendran, S. Nagaraj, R. Sridharan, and T. Gnanasekaran, Journal of Alloys and Compounds **325**, 78 (2001).

[2] T. Yamashita, S. Kanehira, N. Sato, H. Kino, H. Sawahata, T. Sato, F. Utsuno, K. Tsuda, T. Miyake, and T. Oguchi, Sci. Technol. Adv. Mater. Meth. **1**, 87 (2021).

[3] Y. Kumagai and F. Oba, Phys. Rev. B **89**, 195205 (2014).

[4] Y. Kumagai, N. Tsunoda, A. Takahashi, and F. Oba, Phys. Rev. Mater. **5**, 123803 (2021).

Study on the etching mechanism of Si in catalyst-refereed Etching

Daisetsu TOH, Pho Van BUI, Kiyoto KAYAO, Hiroto YAMASAKI, Kouji INAGAKI, Yoshitada MORIKAWA

Department of Precision Engineering, Graduate School of Engineering, The University of Osaka, Yamada-oka, Suita, Osaka 565-0871

Si has recently been utilized as a substrate material for X-ray mirrors due to its thermal stability and ease of processing. To achieve high reflectivity and focusing performance, the mirror surface must be atomically smooth. To address this requirement, we propose the application of a novel surface fabrication technique, Catalyst-Referred Etching (CARE). In this method, Si surface was etched via hydrolysis reaction enhanced metal catalyst, leading to atomically smooth surface [1]. In fact, surfaces polished by the CARE method exhibit atomically stepped, extremely smooth surfaces. On the other hand, the etching mechanism of the CARE method requires that hydroxyl (OH) groups exhibit nucleophilicity toward step-edge atoms. However, in the case of Si, where the step-edge atoms are not ionized, OH groups cannot approach the step edges, making it difficult to form stable intermediate states and thereby hindering the progress of etching. To address this issue, we propose the following hypothesis: OH groups formed by the dissociative adsorption of water molecules on the catalyst surface replace hydrogen atoms bonded to step-edge Si atoms, resulting in the formation of OH-terminated step edges, as shown in Fig.1. Through this process, the hydrolysis reaction can proceed in the same manner as previously described, as shown in Fig. 2. Thus, density functional theory (DFT) based calculations for Si(100) have been performed in this study. The calculations were performed by the first-principles approach using the STATE-senri program package. The first-principles simulations were based on the generalized gradient approximation (GGA) with the Perdew-Burke-Ernzerhof (PBE) functional. Ion cores were replaced by ultrasoft pseudopotentials for the Si, H, O, and Pt atoms. Valence wave functions and

charge densities were expanded in the plane wave basis sets with cut-off energies of 25 and 225 Ry, respectively. To calculate the reaction pathway, the climbing image nudged elastic band method was adopted. The reaction energy profile for OH termination of step-edge Si atom on Si(100) are shown in Fig. 3. The OH termination required an activation barrier of 0.80 eV, which shows that OH termination proceeds easily. Nest, the height of activation barrier for etching the step edge Si atom via hydrolysis reaction was simulated. The simulation result shown in Fig. 4, indicates that OH termination reduces the potential energy of the intermediate state, lowering the energy barrier from 2.1 eV to 0.52 eV, and thereby promotes the removal of the step-edge Si atom. Our proposed etching mechanism was validated. Furthermore, the simulation results suggest that the presence of a catalyst enables etching of Si even in an environment without dissolved oxygen, leading to the formation of high-precision surfaces, thereby demonstrating the effectiveness of this method.

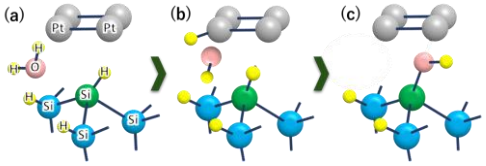


Fig.1 OH terminated step on step-edge Si atom (green marked) on Si(001) surface of (a) intial state, (b) intermediate state and (c) final state

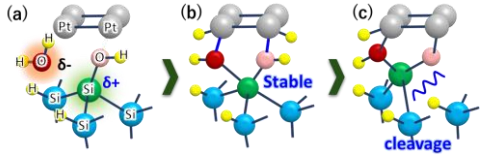


Fig.2 Etcing step on step-edge Si atom teminated by OH of (a) initial state, (b) intermediated state and (c) final state.

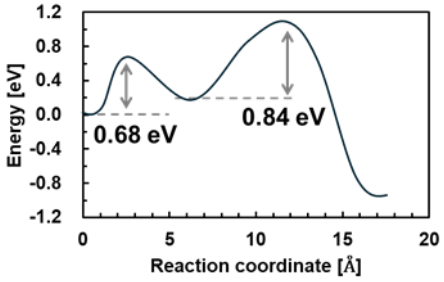


Fig.3 Reaction energy profiles for OH termination on a step-edge Si atom on Si(100)

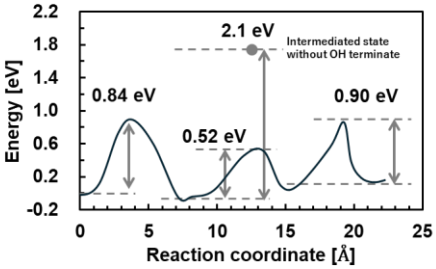


Fig.4 Reaction energy profiles for etching reaction on a step-edge Si atom terminated by OH on Si(100).

References

[1] D. Toh, P. V. Bui, A. Isohashi, N. Kidani, S. Matsuyama, Y. Sano, Y. Morikawa, K. Yamauchi, Rev. Sci. Instrum. Soc. Jpn. **90** 045115 (2019)

Ab Initio Study on Static Structure of White Light Generating Amorphous Molecular Materials

Akihide KOURA

Technical Division, Headquarters for Research and Development Strategy,

Kumamoto University, Kumamoto 860-8555, Japan

In this project, we performed the ab initio molecular dynamics (AIMD) simulations to clarify the static structure of the white light generating amorphous materials [1,2] consisting of $[(RSn)_4S_6]$ clusters, where the substituents R are methyl (Me), phenyl (Ph), and cyclopentadienyl (Cp). In our simulations, we used eight molecules in a cubic supercell, i.e., numbers of atoms were 208 (Me), 432 (Ph), and 400 (Cp).

Firstly, we carried out AIMD simulations for these three targets. Although the obtained structure factors $S(k)$ seem to be in reasonable agreement with the experimental results, statistics of the intermolecular orientation correlations is insufficient because of only eight molecules.

Secondly, we tried to construct the machine learning interatomic potentials (MLIPs) using the Aenet package [3] to perform large-scale simulations. In this training process, we took not only energy but also interatomic forces and virial tensor into account as parameters of the cost function [4].

To validate the accuracy of MLIP, MLIP-MD simulations with the same size as the FPMD were carried out. Figure 1 shows the partial static structure factors $S_{\alpha\beta}(k)$ and partial radial distribution functions $g_{\alpha\beta}(r)$ of amorphous state consisting of $[(PhSn)_4S_6]$ clusters obtained by AIMD (black dashed line) and MLIP-MD (red solid line) simulations. Represented result is not the best but a champion data in recent calculations. Peak positions of $S_{\alpha\beta}(k)$ are comparable between AIMD and MLIP-MD, however, some parts of them have slightly different regions. These wrong

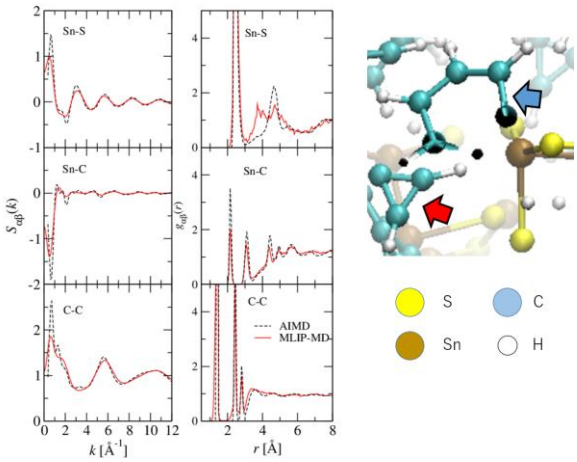


Fig. 1: Partial structure factors $S_{\alpha\beta}(k)$, radial distribution functions $g_{\alpha\beta}(r)$, and a snapshot of $[(PhSn)_4S_6]$ clusters. Carbon atoms (blue ball) indicated with blue and red arrows are correct and broken phenyls, respectively.

results are easily shown in $g_{\alpha\beta}(r)$. The cores of the clusters consisting of Sn_4S_6 are basically kept their shape, however, the second neighbor of Sn-S at approximately $r = 4$ Å obtained by MLIP-MDs has a strange profile in $g_{\mathrm{SnS}}(r)$. Although a correlation function $g_{\mathrm{CC}}(r)$ by MLIP-MD also has similar profile that obtained by AIMD, the first peak of $g_{\mathrm{CC}}(r)$ by MLIP-MD appears at smaller *r* than that obtained by AIMD. This wrong part of the first peak of $g_{\mathrm{CC}}(r)$ is caused by the C-C-C triangle indicated by the red arrow shown in the right panel of Fig. 1. In this study, such carbon triangles have never appeared in the AIMD simulations, i.e., the triangles are considered to be artificial result which should be solved.

To refine the MLIP-MD simulations, we tested various parameters of energy *E*, atomic force *F*, and virial tensor *W* during training. To perform more robust MLIP-MD simulations, we also used the potential averaging method [5], in which number of MLIPs was up to 30 for averaging potentials.

However, this technique did not sufficiently work for the present target as shown in Fig. 1 so far. So, we are planning to employ the active learning (AL) method. One of our group members try to construct MLIP for the liquid state of lactic acid using AL method. In spite of a smaller number of atomic species comparing with [$(PhSn)_4S_6$] clusters, it was needed that times of AL was eight.

It is expected that applying AL method to amorphous [$(PhSn)_4S_6$] clusters will be not easy, however, we plan to continue improving this machine learning technique and clarify the amorphous states of these materials in the future.

References

[1] N.W. Rosemann, *et al.*, J. Am. Chem. Soc. **138**, 16224 (2016).

[2] B.D. Klee, *et al.*, Scr. Mater. **219**, 114851 (2022).

[3] N. Artrith and A. Urban, Comput. Mater. Sci. **114**, 135 (2016).

[4] A. Irie, *et al.*, J. Phys. Soc. Jpn. **90**, 094603 (2021).

[5] D. Wakabayashi, *et al.*, J. Phys. Soc. Jpn. **92**, 074002 (2023).

Interfacial Reaction Study Driven by Mathematical Science, MI and Molecular Dynamics

Ryuhei Sato

Department of Materials Engineering,

The University of Tokyo, 7-3-1 Hongo, Bunkyo-ku, Tokyo 113-8656, Japan

The realization of room-temperature superconductivity is considered one of the holy grails in physics. Polyhydrides with high hydrogen-to-metal (H/M) ratios are among the most promising candidates in terms of superconducting transition temperature (Tc). For instance, CaH_6 exhibits an exceptionally high Tc of 210 K at 160 GPa [1], suggesting that room-temperature superconductivity may be achievable through the exploration of ternary or quaternary compounds within this material class. However, the synthesis of such materials remains a significant challenge. As an example, although CaH_6 was theoretically predicted in 2010 [2], its experimental synthesis was not realized until nearly a decade later [1]. Thus, in addition to predicting stable structures and T_c values, it is crucial to identify feasible synthetic pathways and gain a fundamental understanding of the underlying reaction mechanisms. In this study, we conducted machine learning potential-based molecular dynamics simulations on the CaH_2/H_2 interface to elucidate the reaction mechanism involved in the formation of CaH_6 [3].

During the machine learning potential-based molecular dynamics simulations of the CaH_2/H_2 interface at high pressure and temperature (40 GPa, 1500 K), we observed surface disordering of CaH_2 followed by hydrogen uptake [3]. Upon completion of the reaction, the hydrogen-to-metal ratio in the resulting CaH_x structure converged to approximately 4, and the initially disordered structure was seen to reorganize into an ordered face-centered cubic (FCC) phase. Structural analysis using common neighbor analysis revealed that, during the reaction, the disordered calcium atoms did not exhibit typical crystalline arrangements such as FCC, BCC, or HCP, but rather adopted liquid-like or amorphous configurations. Meanwhile, persistent homology analysis indicated that the hydrogen network around calcium during the reaction closely resembled that of CaH_4. These results suggest that a liquid-phase CaH_4 acts as an intermediate during the hydrogenation process.

This surface-melting hydrogenation reaction ($CaH_2(s) + H_2 \leftrightarrow CaH_4(l)$) can be described by the following free energy relation:

$$\Delta G = \Delta G_{\mathrm{fus}} + \Delta G_{\mathrm{hyd}} + \Delta \gamma_{\mathrm{interface}}$$

Here, ΔG_{fus} denotes the free energy of fusion

for CaH_4 ($CaH_4(s) \leftrightarrow CaH_4(l)$), while ΔG_{hyd} represents the free energy change associated with the CaH_2 hydrogenation ($CaH_2(s) + H_2 \leftrightarrow CaH_4(s)$). γ_{A-B} corresponds to the interfacial energy between phases A and B. According to this relation, the surface-melting-assisted hydrogenation becomes favorable under high-pressure conditions because ΔG_{hyd} becomes negative with increasing pressure. In other words, applying a pressure higher than the equilibrium pressure lowers the activation energy for forming the intermediate liquid-phase CaH_x, thereby promoting the overall reaction [3].

References

[1] H. Wang et. al. PNAS 109 (2012) 6463.
[2] L. Ma et. al. PRL 128 (2022) 167001.
[3] R. Sato et. al. ChemRxiv (2024) DOI: 10.26434/chemrxiv-2024-2v5l6

Sulphur Adsorption on Pt Nanoparticles

Takehiko SASAKI and Kotaro MATSUDA

Department of Complexity Science and Engineering, Graduate School of Frontier Sciences, The University of Tokyo, Kashiwa-no-ha, Kashiwa, Chiba 277-8561

For the use of fuel cells (PEFC) for automobiles, it is important to understand the adsorption states of poisoning speceis on Pt nanoparticles surfaces. Among possible poisoning speceis, sulphur-containing moieties are most important and seeking of removal methods is desired. We are collaborating the research group studying *insitu* measurements of high-energy resolution fluorescence detected X-ray absorption near-edge structure (HERFD-XANES). Various structures of sulphur adsorption states on the surface of platinum nanoparticles were obtained by DFT calculations, where SO_2 is used as the sources of sulphur species.

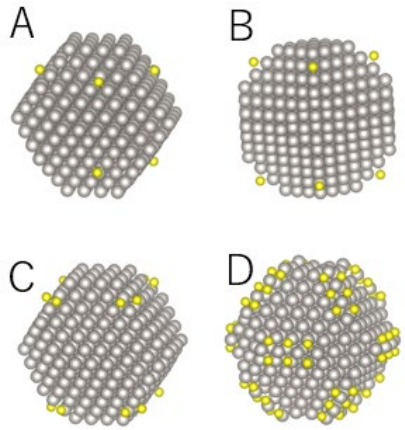


Fig. 1 Sulphur adsorption on Pt nanoparticles. A: hollow site adsorption on (111) terrace. B: Sulphur adsorption on edge. C: Two S atoms on edge. D: Double row- Bridged S atoms.

The Pt nanoparticles are Pt composed of 586 atoms of the cuboctahedron type corresponding to the actual catalyst particle size range of 2.5 nm. DFT calculations were conducted using VASP. The unit cell has a volume of 22.13×44.26×33.19 ($Å^3$) and contains 215 Pt atoms and sulphur atoms. The energy cutoff was 400 eV and the k-point mesh was 3x2x2. After optimization of this unit cell, cuboctahadral nanoparticle is obtained by symmetry operation, as shown in Fig. 1. The model A corresponds to the S adsorption on the hollow site on (111) terrace with the stabilized energy per one species is -6.00 eV. The model B corresponds to the S adsorption on the edge site (-4.49 eV). The model C corresponds to the two S atoms on the edge site (-5.14 eV). The model D corresponds to the Double row-Bridged S atoms on the edge (-5.34 eV). In previous study [1] adsorption states on the flat (111) terrace were obtained but this study revealed the importance of the edge site.

References

[1] M. Happel *et al.* , J. Phys. Chem. C **115**, 479 (2011).

Divergent Activity Shifts of Tin-Based Catalysts for Electrochemical CO_2 Reduction: pH-Dependent Behavior of Single-Atom Versus Polyatomic Structures

XUE JIA

Advanced Institute for Materials Research (WPI-AIMR),

Tohoku University, Sendai, 980-8577

We have studied divergent activity shifts of Tin-based catalysts for electrochemical CO_2 reduction [1], using large-scale parallel computer simulations

This year, we utilized supercomputing resources to perform high-throughput density functional theory (DFT) calculations and machine-learning force field (MLFF)-accelerated molecular dynamics (MD) simulations to investigate the structure–activity relationship of Sn-based catalysts for electrochemical CO_2 reduction reaction (CO_2RR). This study followed a nine-step research process. **Step 1** involved large-scale data mining of experimental literature from the past decade. **Steps 2–4** focused on analyzing structural information transition from single-atom catalysts (Sn−N_4−C SAC) to polyatomic Sn, surface reconstruction, and machine learning force field (MLFF)-accelerated molecular dynamics simulations. **Steps 5–6** examined pH-dependent activity through electric field simulations and ab initio MD (AIMD) simulations, considering *OCHO dipole moments and the potential of zero-charges (PZCs). **Steps 7–8** developed thermodynamic and kinetic models for CO_2RR, validated by comparing theory with experiments. Finally, **Step 9** conducted high-throughput screening to identify promising M–N–C catalysts for formic acid production under various electrochemical conditions.

Finally, we have revealed an interesting pH-dependent activity divergence in Sn−N_4−C SAC and polyatomic Sn in CO_2RR. Our results indicated that Sn−N_4−C and polyatomic Sn catalysts exhibit opposite trends in the response to the electric fields. Due to differences in local structure, *OCHO adsorbed on Sn−N_4−C SAC exhibits a positive dipole moment, making it more stable under a more negative electric filed (corresponding to an alkaline environment). In contrast, *OCHO with negative dipole moment on polyatomic Sn would be destabilized under alkaline conditions. This is the fundamental cause of the opposite volcano shift on the change of pH levels over Sn−N4−C SAC and polyatomic Sn.

References

[1] Y. Wang, D. Zhang, B. Sun, X. Jia, L. Zhang, H. Cheng, J. Fan, H. Li, Angew. Chem. Int. Ed. **64**, e202418228 (2025).

First-principles study on stability of magnetic materials

Yasutomi TATETSU

Meio University, Biimata, Nago, Okinawa 905-8585

Research and development of automation using AI and robots is accelerating towards the realization of a smart society. Since magnetic materials play a crucial role in the power units of many of these electronic devices, the search for novel magnetic materials with decarbonization in mind is an actively researched field. Furthermore, supported by the remarkable progress in computer hardware and software development, expectations are high for materials exploration using computer simulations. In this study, we applied Neural Network Potentials (NNP), which have recently attracted attention for their ability to perform atomic-level physical simulations in a very short time, to magnetic materials containing Fe, and verified their accuracy by comparing the results with those of first-principles calculations.

For multiple magnetic materials, we applied Matlantis and CHGNet [1, 2], in which NNP is implemented, to perform structural optimization and formation energy calculations. Furthermore, to confirm the reliability of the obtained stable structure and formation energy using NNP, we conducted accuracy verification using the first-principles calculation code OpenMX [3].

We compared the formation energies of each material calculated using OpenMX, Matlantis, and CHGNet. The calculation targets are approximately 200 materials containing Fe, including rare earth permanent magnets. In most materials, the NNP method accurately reproduced the trend of the results calculated with OpenMX. However, in some cases, the formation energies calculated with OpenMX did not match those obtained with the NNP method. These discrepancies tend to appear when formation energies are relatively small, which is a region where high-precision first-principles calculations are required anyway. We believe that detailed analysis is necessary regarding the reasons for the discrepancies. While accuracy verification ultimately requires comparison with high-precision first-principles calculations, the results suggest the potential effectiveness of NNP for high-throughput calculations that require a large amount of computation.

References

[1] S. Takamoto, *et al*., Nat Commun 13, 2991 (2022); Matlantis (https://matlantis.com/), software as a service style material discovery tool.

[2] B. Deng, *et al.*, Nature Machine Intelligence **5**, 1031–1041 (2023).

[3] http://www.openmx-square.org

Study on physical properties of structural elementary excitations at solid surfaces and interfaces

Hiroyuki KAGESHIMA
Graduate School of Natural Science and Technology, Shimane University
1060 Nishi-Kawatsucho, Matsue, Shimane 690-8504

In this project, we have been focused on physical properties of structural elementary excitations, such as point defects and precursors, of semiconductor surfaces and interfaces [1, 2, 3]. In this year, we have focused on the physical properties of hexagonal boron nitride (hBN) growth on Cu(111) [4]. The calculations were performed based on the first-principles calculation. Program package PHASE/0 was employed [5].

The growth process of hBN on a Cu substrate is, at first glance, a simple phenomenon, in which B and N precursors just aggregate to form hBN islands. However, since hBN is a two-component material, the island shape can vary depending on the relative supply of B and N, which is governed by their chemical potentials. The energy of an island initially increases with size due to the high edge energy but decreases beyond a certain 'critical size', as the inner energy becomes dominant. Under conditions where the critical size is large, intrinsic nucleation becomes more difficult. Therefore, experimental conditions that lead to a larger critical size, controlled via chemical potentials, are desirable for achieving hBN layers with high crystallinity. To investigate this, we studied the relationship between island size, shape, and chemical potential using first-principles calculations, incorporating van der Waals interactions via the vdW-DF2-b86r functional.

To evaluate the critical size, it is necessary to examine the stability of islands at macroscopic scales. However, first-principles calculations are typically limited to systems of microscopic size. In this study, we aimed for higher accuracy by building upon insights from our previous work [3]. We computed the energies of nanoribbons with various widths, featuring both zigzag and armchair edges, as well as islands with different shapes and sizes. From these calculations, we extracted the energies associated with zigzag-edge B and N atoms, armchair-edge B and N atoms, corner B and N atoms, and inner B and N atoms. Using these atomic energy contributions, we then predicted the stability of hBN islands, over a wide range of sizes, including those approaching macroscopic scales.

We first investigated the relationship between island size, chemical potentials, and the resulting stable island shapes. Islands with zigzag edges are generally more stable than those with armchair edges. As a result, the most stable shapes are equilateral triangles and hexagons composed exclusively of zigzag edges. When the chemical potential shifts from a B-rich/N-poor condition to a B-poor/N-rich condition, the stable shape transitions from an equilateral triangle with zigzag B edges, to a hexagon with mixed zigzag edges, and eventually to an equilateral triangle with zigzag N edges.

Furthermore, we found that zigzag-edged equilateral triangles tend to form at smaller sizes, while zigzag-edged hexagons become more favorable at larger sizes. This size-

dependent shape transition arises because inner atoms are stabilized by van der Waals interactions with the Cu substrate. As the island grows, the proportion of stable inner atoms increases, reducing the relative contribution of edge energy. This behavior is a distinctive feature of hBN grown on a Cu substrate and does not occur in freestanding hBN. Our finding also highlight a limitation in previous theoretical studies, which overlooked the stabilization effect of inner atoms and thus arrived at incorrect conclusions regarding the most stable island shapes.

Next, we investigated the relationship between critical size and chemical potentials. Under B-rich/N-rich conditions, the critical size becomes small, and can even drop below the size of a single atom when the chemical potentials are excessively high. This implies that islands nucleate rapidly whenever B and N atoms adsorb on the Cu surface, leading to the formation of an amorphous hBN layer. Conversely, under extremely B-poor/N-poor conditions, the critical size approaches infinity, meaning that spontaneous island formation becomes impossible. These findings indicate that a moderately B-poor/N-poor chemical potentials is optimal for promoting the growth of high-quality crystalline hBN layers. Such a condition corresponds to high-temperature growth with a limited supply of B and N precursors, aligning well with the experimental conditions commonly used in practice.

In experiments, equilateral triangular islands are frequently observed. Since subsurface B atoms are calculated to be more stable than those adsorbed on the surface, the Cu surface is likely to become N-rich under typical conditions. As a result, triangles with zigzag N-terminated edges are expected to form. In other experiments, hexagonal islands appear when O_2 is introduced into the source gas. This can be attributed to N reacting with O, thereby reducing the N concentration on the Cu surface and shifting the environment toward N-poor conditions. Similarly, hexagonal islands are also observed when the Cu surface pretreated by electrochemical polishing, which likely leads to surface oxidation and a B-rich condition. These observations are well explained by our theoretical framework, which consistently accounts for the experimental variations.

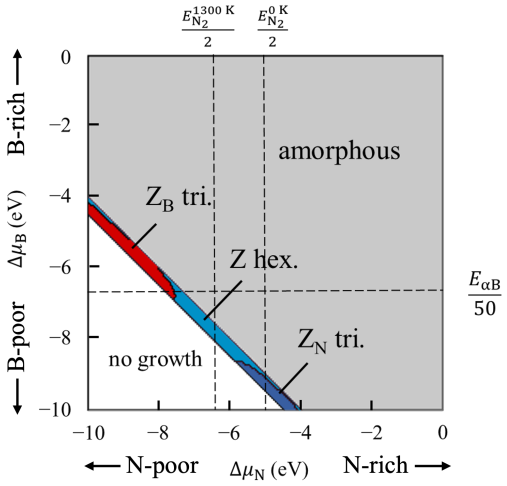


Figure 1: Phase diagram showing the stable shapes of hBN islands at the critical size, as a function of chemical potentials, during growth on the Cu(111) surface.

References

[1] H. Kageshima, T. Akiyama, and K. Shiraishi, Matter. Sci. Semicon. Process. **162** (2023) 107527 (7 pages).

[2] H. Kageshima, T. Akiyama, and K. Shiraishi, Jpn. J. Appl. Phys., 63 (2024) 04SP08 (5 pages).

[3] R. Imamura and H. Kageshima, Jpn. J. Appl. Phys., 63 (2024) 04SP39 (11 pages).

[4] R. Imamura, I. Seo, and H. Kageshima, e-J. Surf. Sci. Nanotechnol. 23 (2025) *advanced online publication* (13 pages).

[5] https://azuma.nims.go.jp

Development of Fast Calculation Codes of Berry Phases in First-principles Calculations and its Application to Energy Conversion Materials

Naoya YAMAGUCHI
Nanomaterials Research Institute (NanoMaRi), Kanazawa University
Kakuma-machi, Kanazawa, Ishikawa 920-1192

This year further development of calculation methods and programs for intrinsic anomalous Hall conductivity (AHC) was carried out. AHC is related to thermoelectric conversion phenomena such as the anomalous Nernst effect, and its intrinsic contribution is based on the Berry curvature of the electronic states of the material. Since the previous year, we have also been developing a computational method for analyzing the layer-by-layer contribution of the AHC by combining the local Berry phase (LBP) method with the hybrid Wannier function method. We have performed applied calculations on various systems such as magnetic topological insulators and magnetic metal thin films and confirmed that the layer-by-layer AHC contribution in magnetic topological insulators and magnetic metal thin films can be analyzed.

On the other hand, in complex material systems, especially those that have defects and impurities, many degenerate points occur due to folding of the electronic band structure in the first Brillouin zone (FBZ), and obtaining the intrinsic AHC is computationally difficult because it requires more k-point sampling than that for perfect crystals. We have developed the LBP method [1] by extending the Fukui-Hatsugai-Suzuki method [2] to metallic systems for intrinsic AHC calculations. In the LBP method, the calculation of the determinant of the overlap matrix that consists of the periodic parts of the Bloch functions between k-points on the edges of the plaquettes is necessary, so basically the occupation numbers within the plaquettes must be the same. When the chemical potential crosses bands, the occupation numbers differ near the intersection point, and they can be approximated by averaging. If there are degenerate points within the plaquette, coarse k-point sampling may result in only one of the bands at a degenerate point contributing to the determinant, leading to numerical instability.

Then, we implemented various methods for calculating determinants in the LBP method using the first-principles calculation code OpenMX [3]. We found that even when degenerate points exist due to the folding of the FBZ, it is possible to evaluate appropriately by successively assessing the properties of overlapping matrices and then providing appropriate minor determinants. We have shown that the proposed method is effective by performing AHC calculations for BCC iron and its supercell systems. In the conventional LBP method, the AHC vibration increased due to the superlattice formation of cells when sampling was performed with the almost same k-point spacing. In the above new method, in BCC iron, it was found that the degree of fluctuation in the results obtained using the primitive cell model, conventional cell model, and supercellized 4-atom model was equivalent, indicating that the AHC vibration, which appears as an error due to superlattice formation of cells, was suppressed. Excessive k-point sampling is no longer necessary, and the required number of k-points can be easily estimated, so it is expected that high-throughput calculations will also be possible. We have developed a new LBP method and have confirmed that the numerical instability can be resolved for various superlattice systems.

References

[1] H. Sawahata, N. Yamaguchi, S. Minami, F. Ishii, Phys. Rev. B **107**, 024404 (2023).

[2] T. Fukui, Y. Hatsugai, H. Suzuki, J. Phys. Soc. Jpn. **74**, 1674 (2005).

[3] http://openmx-square.org.

First-principles calculations of functionalities in Mn_3Sn-based alloys

Katsuhiro Tanaka[1] and Yuta Toga[1,2]
[1]*Department of Physics, University of Tokyo, Bunkyo-ku, Tokyo 113-0033, Japan*
[2]*JSR-UTokyo Collaboration Hub, CURIE, JSR Corporation, Minato-ku, Tokyo 105-8640, Japan*

Several studies have shown that a non-collinear antiferromagnet Mn_3Sn can show physical properties such as the anomalous Hall effect [1] and the tunnel magnetoresistance (TMR) effect [2], which have been observed typically in ferromagnets. In order to pursue the possibility of Mn_3Sn as a material for spintronic devices like thermoelectric devices and magnetic tunnel junctions (MTJs), we have investigated the physical functionalities of Mn_3Sn using first-principles calculations.

Particularly, we have focused on the enhancement of the intrinsic anomalous Hall conductivity (AHC) in Mn_3Sn through elemental substitution in its alloys. We have performed first-principles caluclation of the electronic structure of Mn_3Sn based on the density functional theory (DFT), using the Quantum ESPRESSO package [3]. Based on the results of the DFT calculation, we have constructed a tight-binding model with maximally localized Wannier functions using the Wannier90 package [4]. To calculate the AHC, σ_{xz}, it is needed to integrate the Berry curvature over the Brillouin zone with a dense $\boldsymbol{k}$-point mesh, which often demands a high computational cost.

We have investigated the effects of alloying using the virtual crystal approximation (VCA). In particular, we have simulated the substitutions of In for Sn and Cr for Mn, aiming at achieving the hole doping and tuning the electronic properties. Figure 1 shows the

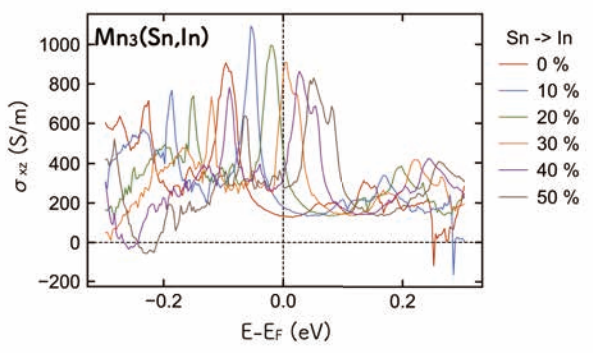


Figure 1: Calculated energy dependence of the anomalous Hall conductivity, σ_{xz}, of $Mn_3(Sn, In)$ alloys for various In ratios.

chemical potential dependence of σ_{xz} for the VCA calculations for $Mn_3(Sn, In)$ alloys. We can see a systematic shift of the main peak in the energy-dependent AHC with the increase of the In concentration. This result suggests that the hole doping via In substitution could potentially lead to a significant enhancement of the AHC near the Fermi energy at some specific In ratio. Furthermore, we have observed a similar systematic change in the AHC features as a function of the Cr ratio in the VCA calculations for $(Mn, Cr)_3Sn$ alloys, as shown in Fig. 2. These VCA results indicate that the hole doping through elemental substitution at both of the Sn and Mn sites will be a possible route for tuning the AHC in Mn_3Sn system. Since the VCA approach has limitations in precisely describing the electronic properties of the materials with element substitutiion, it will be also necessary to employ some other

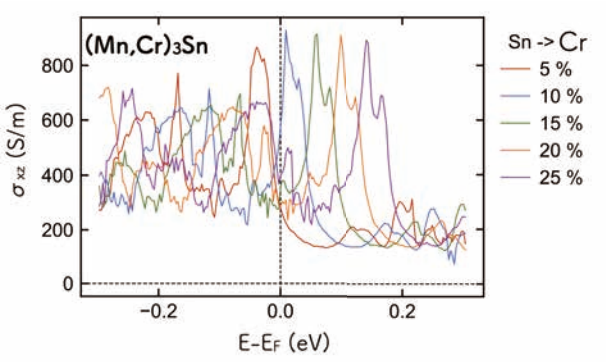


Figure 2: Calculated energy dependence of the anomalous Hall conductivity, σ_{xz}, of $(\mathrm{Mn,Cr})_3\mathrm{Sn}$ alloys for various Cr ratios.

methods like supercell calculations for more quantitative predictions.

Apart from the effect of elemental substition on the AHC, we have also investigated the potential of Mn_3Sn as a magnetic electrode of the MTJs. Constructing the MTJs using Mn_3Sn, we have performed first-principles calculations of the TMR effect as well as the electronic structures of the MTJs.

References

[1] S. Nakatsuji, N. Kiyohara, and T. Higo, Nature **527**, 212 (2015).

[2] X. Chen et al., Nature **613**, 490 (2023).

[3] P. Giannozzi et al., J. Phys.: Condens. Matter **21**, 395502 (2009); P. Giannozzi et al., J. Phys.: Condens. Matter **29**, 465901 (2017).

[4] G. Pizzi et al., J. Phys. Cond. Matt. **32**, 165902 (2020).

Electronic state analysis on molecular thin film surface

Kaori Niki

Graduate school of science

Chiba University, Yayoi-cho, Inage-ku, Chiba 263-8522

Introduction

To reduce CO_2 emissions, catalyst development for CO_2 reduction has been actively pursued. We aimed to realize a CO_2 reduction catalyst using inexpensive metals and investigated the electronic states involved in the conversion process from CO_2 to CO on the ZrO_2 surface.

Method

We performed density functional theory (DFT) calculations using the Vienna Ab initio Simulation Package (VASP) version 6.4.1 [1,2]. The exchange correlation effects were described by the spin-polarized generalized gradient approximation (GGA) within the revised Perdew-Burke-Ernzerhof (RPBE) formalism [3]. We chose the surfaces of monoclinic ZrO_2(001), containing (2*2*2) elemental unit cells, and tetragonal ZrO_2(101), containing (2*1*2) elemental unit cells as slab models.

Results

It was found that the adsorption energy of CO2 on ZrO2 is lowest at oxygen vacancy sites. At this time, CO2 is bended when it is adsorbed as C fills the vacancy site. It was also found that electrons are exchanged between the vacancy sites of CO2 and ZrO2. It was found that the CO2 is separated into CO and OH when hydrogen atoms, which are added in the experiment, are adsorbed. Furthermore, when H is added, OH becomes H2O and is desorbed. At that time, the energy is more stabilized when new CO2 is adsorbed onto the defects than when defects are generated in ZrO2. This clarified at the electronic state level that a cycle of CO reduction is generated.

It was also found that, between a monoclinic surface and a tetragonal surface, more energy is required to generate H2O on the tetragonal surface. This clarified that the reduction cycle does not establish itself on the tetragonal surface, resulting in a smaller amount of reduction [4].

Conclusion

By performing VASP calculations, we clarified the structural changes of CO_2 and the electron transfer processes between CO_2 and the vacancy of ZrO_2.

References

[1] G. Kresse and J. Hafner, Phys. Rev. B **47**, 558 (1993).

[2] G. Kresse and D. Joubert, Phys. Rev. B **59**, 1758 (1999).

[3] J. P. Perdew, K. Burke, and M. Ernzerhof, Phys. Rev. Lett. **77**, 3865 (1996).

[4]A. Omata *et al.*, e-Journal surf. Sci. Nanoteh. **22**, 327 (2024).

First-principles study of surface atomic structure and chemical properties of intermetallic compounds

Kazuki Nozawa

Department of Physics and Astronomy, Kagoshima University,

1-21-35, Korimoto, Kagoshima 890-0065

This fiscal year, we have studied the adsorption structure of Pentacene (Pn) on the Ag-In-Yb quasicrystal (QC) surface, and the hydrogen and acetylene adsorption on the trace-amount Pd-doped $Al_{13}Fe_4$ intermetallic compound surface. These calculations were carried out using the VASP code.

In recent years, quasi-periodic molecular arrangements of Pn have been obtained by depositing Pn on the icosahedral Ag-In-Yb QC surfaces. To get insight into the details of the quasi-periodic Pn layer, we studied the stable adsorption structure of Pn on the two-fold and five-fold surfaces of the Ag-In-Yb QC. The atomic positions of the surface atoms were extracted from the X-ray diffraction experimental data, and the surface was approximated using a disk-shaped cluster with a diameter of 2.2 nm and a thickness of 0.8 nm to be treated within the ordinary DFT calculation. The simulation cell contains about 700 atoms. Because the calculated force acting on the atoms is incorrect, especially at the cluster edge, we identified the stable adsorption positions by manually varying the Pn molecule. We found that Pn is stable in the Yb-rich region. However, some typical motifs observed by STM experiments have not been explained by the calculated stable adsorption sites. We are currently investigating the possibility of a surface point defect at some Yb sites.

$Al_{13}Fe_4$ is a periodic approximant to decagonal QCs. The monoclinic unit cell contains 102 atoms, occupying 20 inequivalent atomic sites: Al(1)-Al(15) and Fe(1)-Fe(5). The surface was modeled by a symmetric slab model composed of seven atomic layers and a 1.55 nm thick vacuum layer. We previously studied the bulk and surface structure of $Al_{13}Fe_4$, where a single Pt atom is introduced per unit cell. This year, we studied the case where the Pd atom was introduced and confirmed that Pd occupying the Fe(1) site is exposed on the surface, as is the case with Pt. We also studied the adsorption of acetylene and hydrogen on this surface. The calculations for acetylene adsorption are almost completed, and the acetylene molecule tends to be stable on the Al_5Fe flower-like motif, which is a fragment of the puckered layer separated by cleavage.

First-principles molecular dynamics simulations for confined water

Tatsuhiko Ohto

Graduate School of Engineering, Nagoya University, Furo-cho, Chikusa-ku, Nagoya, 464-8603 Aichi, Japan

Water plays a crucial role in geological, biological, and technological processes. Nanoscale water confinement occurs in many of these settings, including sedimentary rocks, water channel proteins, and applications like desalination and water purification membranes. The structure and properties of water in nanoconfinement can differ significantly from bulk water, exhibiting, for instance, modified hydrogen bonds, dielectric constant, and phase transitions. Despite the importance of strongly nanoconfined water, experimentally elucidating the nanoconfinement effect on water, such as its orientation and hydrogen bond (H-bond) network, has remained challenging. Here, we study two-dimensionally nanoconfined aqueous electrolyte solutions with tunable confinement from nanoscale to angstrom-scale sandwiched between a graphene sheet and CaF2. We employ heterodyne-detection sum-frequency generation (HD-SFG) spectroscopy, a surface-specific vibrational spectroscopy capable of directly and selective probing water orientation and H-bond environment at interfaces and under confinement. Remarkably, the vibrational spectra of the nanoscale confined water can be described quantitatively by the sum of the individual water surface signals from the CaF2/water and water/graphene interfaces until the confinement reduces to angstrom-scale (< ~8 Å). Ab initio molecular dynamics simulations confirm our experimental observation. These results manifest that interfacial, rather than nanoconfinement effects, dominate the water structure until angstrom-level confinement.

References

[1] Y. Wang et al., arXiv:2310.10354v2

Material search and spin-orbit coupling induced properties at artificial interfaces and multilayers

Kohji NAKAMURA

Graduate School of Engineering, Mie University, Tsu Mie 5148507

Search of promising thin films with desired magnetic properties is an important goal in the field of spintronics. We here report on three examples calculated by using full-potential linearized augmented plane-wave (FLAPW) method [1].

Enhancement of interfacial perpendicular magneto-crystalline anisotropy (iPMA) at Fe/MgO: We demonstrated that large iPMA and low Gilbert magnetic damping constant (α) at Fe/MgO interface are achieved by substituting N-anions at MgO barrier interface. The iPMA is enhanced by four times and the α is reduced by 65% compared to the pristine Fe/MgO. The mechanism is explained by a band realignment at Fermi level (E_F), where the Fe $d_{\pm1}$ orbitals at the interface are pushed above and below E_F but the Fe $d_{\pm2}$ orbitals remain at E_F by the N-anion substitution.

Enhancement of spin Hall conductive (SHC) in Graphene/MoS_2: Generation and controlling of spin current in two-dimensional (2D) materials such as graphene are challenging due to small intrinsic SOC of the 2D materials. We predicted the finite SHC of 25 $\Omega^{-1}cm^{-1}$ in van der Waals heterostructure of graphene/MoS_2. By applying positive external-electric-field, we find that the SHC increase up to 170 $\Omega^{-1}cm^{-1}$ while application of negative external-electric-field hardly affects the SHC. The underlying mechanism is explained in terms of spin Berry curvature in Dirac-cone bands of graphene in the heterostructure, where the size of band gap is modulated sensitively by the magnitude of external-electric-field.

Code development for angle-dependent X-ray magnetic circular dichroism (AD-XMCD): Method to calculate AD-XMCD spectra was successfully developed and applied to $L1_0$-ordered FeX and CoX (X = Ni, Pt) alloys systematically. By changing incident angles and magnetic moments from [001] to [100], we demonstrated the modification of XMCD spectra at the L_2 and L_3 edges. We find that this originates from the changes in magnetic dipole and orbital moments that depend on the angle variation.

References

[1] K. Nakamura et.al., Phys. Rev. B **67**, 014420 (2003).

Prediction of properties of organic ferroelectrics and piezoelectrics by first-principles calculation

Shoji ISHIBASHI
National Institute of Advanced Industrial Science and Technology (AIST)
Tsukuba, Ibaraki 305-8568

In response to the application of an electric field, the refractive index varies linearly for certain class of materials. This effect is known as the Pockels effect and is one of the second-order nonlinear optical effects. In the present study, we simulated the Pockels effect in organic ferroelectric crystals of croconic acid (CRCA) and 5,6-dichloro-2-methylbenzimidazole (DC-MBI) [1].

Simulations were carried out in the following three modes: (1) with a clamped cell and clamped atomic positions (an optimized structure at $E = 0$), (2) with a clamped cell and relaxed atomic positions at E, and (3) with a relaxed cell and relaxed atomic positions at E. In the first mode, the response to electric field application is purely electronic. In the second mode, the ionic response was included. For the third mode, the piezoelectric effect was also added to the electronic and ionic responses. A dielectric constant ε at an electric field of E was evaluated using the formula $\varepsilon = 1 + (1/\varepsilon_0)(\mathrm{d}P/\mathrm{d}E)$, where ε_0 is the vacuum permittivity. Electric polarization values P were calculated at $E, E \pm 0.1, E \pm 0.2$ (MV cm^{-1}). By applying linear regression to the relationship between E and P, $\varepsilon(E)$ values were obtained. Pockels coefficients r_{ijk} were evaluated by applying linear regression to $1/\varepsilon(E)$. For CRCA, E values were sampled as $0, \pm 1, \pm 2$ (MV cm^{-1}) while for DC-MBI, simulations were also carried out at ± 3 (MV cm^{-1}) because its electro-optic response was small. For these organic crystals, the van der Waals interaction is critical, and two types of van der Waals density functionals vdW-DF-cx and rVV10 were used. These functionals reproduce the lattice parameters of CRCA and DC-MBI successfully [2]. All the calculations were performed using the QMAS code.

Table 1: Percentages from piezoelectric, ionic and electronic contributions.

	piezoelectric	ionic	electronic
CRCA*	32.2	57.7	10.1
CRCA†	24.4	61.8	13.8
DC-MBI*	54.1	24.5	21.4
DC-MBI†	58.5	21.0	20.5

* vdW-DF-cx, † rVV10

For CRCA and DC-MBI, the r_{333} values are obtained as 17.0 and 2.7 (pm/V) with the vdW-DF-cx functional while as 12.4 and 2.0 (pm/V) with the rVV10 functional, respectively. Percentages from piezoelectric, ionic and electronic contributions are shown in Table 1. It is shown that the ionic contribution is important particularly for CRCA. These calculated results are reasonable compared with the experimental ones [1].

References

[1] K. Sunami, S. Horiuchi, S. Ishibashi, and J. Tsutsumi: Adv. Electron. Mater. **11**, 2400346 (2025).

[2] S. Ishibashi, S. Horiuchi, and R. Kumai: Phys. Rev. Mater. **5**, 094409 (2021).

Electronic structures of doped carbon nanotubes

Yoshitaka FUJIMOTO
School of Engineering, Kyushu University, Fukuoka 819-0395

Carbon nanotubes (CNTs) are candidate materials for next generation nanoelectronics devices because they show unique and excellent electronic properties such as long mean free path and high carrier mobility. It has been often reported that the doping with heteroatoms can enhance the chemical reactivity of CNTs, and a variety of applicable systems such as catalyst and sensors are proposed using doped CNTs [1]. It has been reported that the boron-doped graphene can strongly bind with harmful NO_x molecules, which suggests the possibility to fabricate the harmful NO_x sensors [2, 3]. The B-doped (10,0) CNTs can adsorbe the toxic CO molecule, and it is revealed that the conductivity of the B-doped CNTs is largely changed by the adsorption of the CO molecule [4, 5]. Pyridine-type nitrogen-doped CNT is another candidate material for development of highly sensitive gas sensors. The adsorption properties of ammonia and water molecules to pyridine-type N-doped graphene have been studied and the ammonia and water molecules are adsorbed strongly to pyridine-type N-doped graphene [6].

We here report the adsorption properties of toxic molecules to the pyridine-type N-doped CNTs for designing high-performance gas sensors. We firstly exmaine the adsorption properties of toxic molecules (CO, NO, and NO_2) on the pyridine-type N-doped (11,0) CNTs. It is found that three kinds of molecules (CO, NO and NO_2) are adsorbed with relatively large adsorption energies of $|E_a| > 2$ eV. Here, the adsorption energy E_a is defined by $E_a = E_{tot} - E_{pyr} - E_{mol}$, and E_{tot}, E_{pyr} and E_{mol} are the total energies of pyridine-type N-doped (11,0) CNT with and without the molecule and of the isolated molecule, respectively. In the case of the adsorption of the CO molecule, the C atom of the CO molecule binds with three N atoms in the pyridine-type N defects, forming tetrahedral coordinations. For the adsorption of NO molecules, the N atom of the NO molecule is adsorbed with the N atom in the pyridine-type defect, whereas for the NO_2 molecule, the desorption takes place at the pyridine-type defect: the NO_2 molecule attached to the N atom in the pyridine-type defect is desorbed as an NO molecule, and the remaining O atom of the NO_2 molecule is adsorbed to the N atom in the pyridine-type defect.

We next study the transport properties of the pristine and pyridine-type N-doped (11,0) CNTs. There is an energy band gap of ~ 1 eV in the pristine (11,0) CNT, and its conductance shows a quantized value at the outsides of the energy gap. When pyridine-type N defects are introduced to the nanotube, the acceptor states emerge around the valence-band maximum and the Fermi energy of the pyridine-type N-doped CNT relatively moves to the edge of the valence bands. As a result, the pyridine-type N-doped CNT should become a p-type semiconductor. When a CO molecule is adsorbed to the pyridine-type N-doped CNT, the conductance spectrum is sizably modified: the conductances overall decrease. We also study the conductance variation at the Fermi energy for adsorption of various molecules. Three kinds of molecules (CO, NO, and NO_2) are distinguishable from one another for the adsorptions to the pyridine-type N defect due to the relatively large changes of the conductance.

In summary, we have examined the effects of the introduction of pyridine-type N defects and the adsorption of molecules on the atomic structures, energetics and transport properties of (11,0) CNTs using the first-principles electronic transport study. The CO, NO, and NO_2

molecules bind to the pyridine-type N-doped (11,0) CNTs with relatively large adsorption energies. The introduction of the pyridine-type defects into semiconducting (11,0) CNT should give rise to a *p*-type transport property. Three kinds of molecules (CO, NO, and NO_2) are distinguishable from one another for the adsorptions to the pyridine-type N defect because of the relatively large changes of the conductance. The pyridine-type N-doped CNT could become a highly sensitive sensor material to detect toxic CO and harmful NO_x molecules.

References

[1] Y. Fujimoto, Micromachine **15**, 1172 (2024).

[2] Y. Fujimoto and S. Saito, Chem. Phys. **478**, 55 (2016).

[3] Y. Fujimoto and S. Saito, Appl. Surf. Sci. Adv. **1**, 100028 (2020).

[4] Y. Fujimoto and S. Saito, J. Electrochem. Soc. **169**, 037512 (2022).

[5] Y. Fujimoto, J. Electrochem. Sci. Eng. **12**, 431 (2022).

[6] Y. Fujimoto and S. Saito, JPS Conf. Proc. **4**, 012002 (2015).

Electronic structure analysis of spin devices using first-principles calculation

Hideo KAIJU, Mizuki MATSUZAKA, Koki HORIGANE, and Chika HASHIMOTO

Faculty of Science and Technology, Keio University

Yokohama, Kanagawa 223-8522, Japan

Magnetic tunnel junction (MTJ), which consists of a thin insulation layer sandwiched by two magnetic layers, exhibits a large tunnel magnetoresistance (TMR) effect [1,2]. The TMR effect strongly depends on not only the materials of an insulation layer and magnetic layers, but also the lattice matching between the insulation layer and magnetic layers. In a recent study, a significant TMR ratio of 631% was achieved in lattice-matched FeCo/MgO/FeCo MTJs at room temperature [3].

In this study, we compare TMR ratios based on the materials of insulation and magnetic layers and the lattice matching, to clarify the mechanism of the TMR effect. We investigate the tunneling transmittance and conductance of electrons, and TMR ratios in good lattice matched MgO-based MTJ, $SrTiO_3$-based MTJ, and InP-based MTJ, in which Fe or FeCo is used for magnetic layers, using first-principles calculations.

We used Quantum ESPRESSO for first-principles calculations. The calculations are performed based on density functional theory, plane wave approximation, and pseudopotential model. First, we performed structural relaxation for each MTJ in parallel magnetization. The supercells of MgO-, $SrTiO_3$-, and InP-based MTJs are shown in Figure 1. Then, we calculated the tunneling transmittance and conductance in parallel and antiparallel magnetizations using the Landauer-Büttiker method. Finally, we calculated the TMR ratio for each MTJ from the obtained conductance. The calculations are MPI-parallelized in each step especially for *k* points.

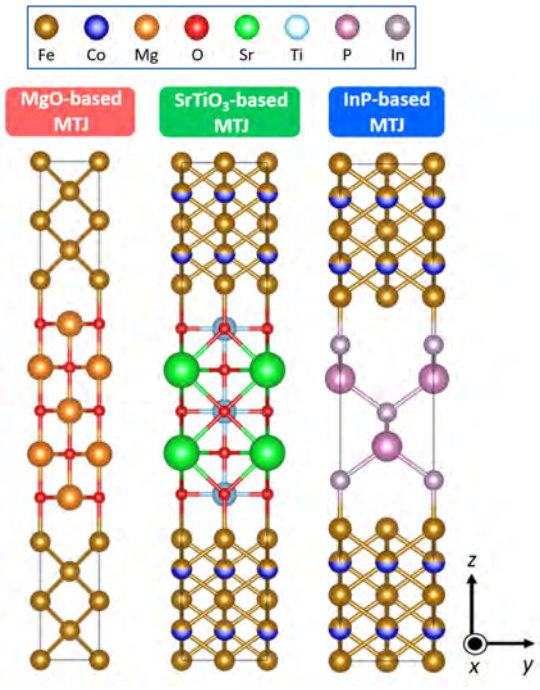


Figure 1: Supercells of MgO-, $SrTiO_3$-, and InP-based MTJs.

Table 1 shows the conductance G_P and G_{AP} in parallel and antiparallel magnetizations, respectively, and TMR ratio for MTJs. We obtain relatively small TMR ratios of 229%, 324%, 100% and 426% in Fe/$SrTiO_3$/Fe, FeCo/$SrTiO_3$/FeCo, Fe/InP/Fe and FeCo/InP/FeCo MTJs, whereas large TMR ratios of 8920% and 6420% in Fe/MgO/Fe and FeCo/MgO/FeCo MTJs, respectively. Figure 2 shows the $k_{\|}$-resolved conduction spectra of majority spins in parallel magnetization. The conductance of majority spins at Γ point is dominant in MgO-based MTJs, in contrast to the conductance of minority spins or at non-Γ point is enhanced in $SrTiO_3$-based and InP-based MTJs. We clarified the robust conduction through the Δ_1 band of majority spins contributes to large TMR ratios in MgO-based MTJs, whereas the suppression of the conduction through the Δ_1 band of majority spins as well as the enhancement of the conduction through other bands leads to the decrease of TMR ratios in $SrTiO_3$-based and InP-based MTJs.

Table 1: Conductance in both parallel and antiparallel magnetizations, respectively, and TMR ratio for MTJs.

MTJs	G_P ($\Omega^{-1}\mu m^{-2}$)	G_{AP} ($\Omega^{-1}\mu m^{-2}$)	TMR ratio
Fe-MgO	0.508	0.00564	8920%
Fe-$SrTiO_3$	51.4	15.7	229%
Fe-InP	64.9	32.6	100%
FeCo-MgO	0.673	0.0103	6420%
FeCo-$SrTiO_3$	20.8	4.92	324%
FeCo-InP	41.5	8.03	416%

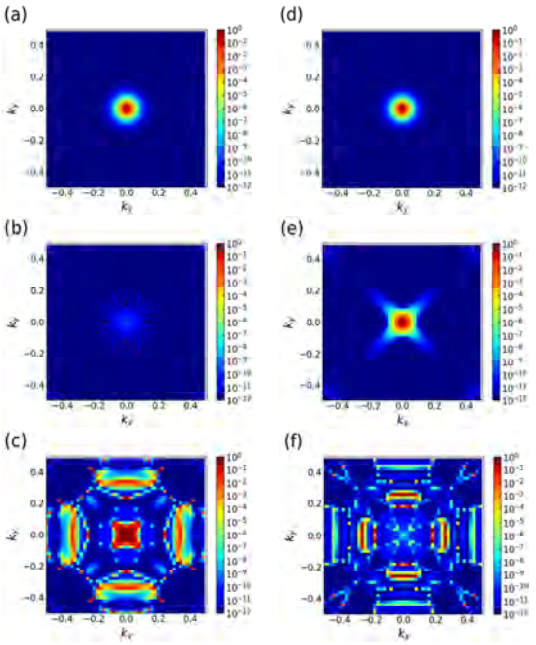


Figure 2: $k_{\|}$-resolved conduction spectra (in units of Ω^{-1}) of majority spins in parallel magnetization for (a) Fe/MgO/Fe, (b) Fe/$SrTiO_3$/Fe, (c) Fe/InP/Fe, (d) FeCo/MgO/FeCo, (e) FeCo/$SrTiO_3$/FeCo, and (f) FeCo/InP/FeCo MTJs.

References

[1] S. S. P. Parkin *et al*., *Nat. Mater.* **3**, 862 (2004).

[2] S. Yuasa *et al*., *Nat. Mater.* **3**, 868 (2004).

[3] T. Scheike *et al., Appl. Phys. Lett.* **112**, 112404 (2023).

Ab initio calculation of the rotation effect of oxygen octahedron in Ca_2MnO_4 on electronic properties

Kazuma NAKAMURA
Quantum Physics Section, Kyushu Institute of Technology
1-1 Sensui-cho, Tobata, Kitakyushu, Fukuoka, 804-8550

Domain walls in transition-metal oxides are expected to have new functions due to their local structure, and have been actively studied in recent years. One example is Ca_2MnO_4 (CMO), which is known to have the freedom to rotate the oxygen octahedron around the c-axis, resulting in the formation of multiple phases. In CMO, the rotation of the octahedron tends to result in domain boundaries. At high temperatures (above 1,050 K), CMO has a highly symmetric structure without oxygen octahedral rotation [$I4/mmm$, Fig. 1(a)], and at low temperatures it is known that it can coexist with multiple phases in which the oxygen octahedron is rotated. The low-temperature phases are classified according to the difference in the stacking pattern in the c-axis direction of the MnO_2 layers composed of oxygen octahedra, and are known to be a structure with in-phase rotation [$Acam$, Fig. 1(b)] and a structure with anti-phase rotation [$I4_1/acd$, Fig. 1(c)]. In this study, we focus on the effect of the oxygen octahedral rotation of CMO on the low-energy electronic properties.

Ab initio spin-polarized density functional calculations were performed using Quantum Espresso [1] for the three structures identified in the experiment shown in Fig.1 (left). These structural models were aligned to a 56-atom superlattice so that the electronic structures could be compared. In addition, several structural models differing in spin arrangement, rotation pattern of oxygen octahedra, and rotation angle are generated, and the band-

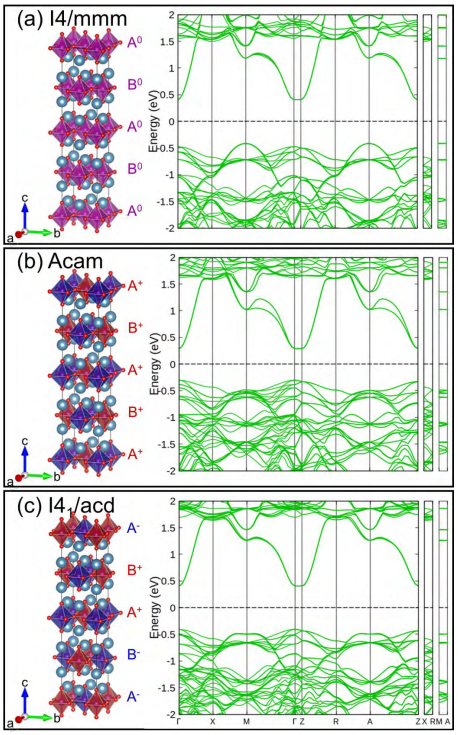


Figure 1: **Three crystal structures (left) and antiferromagnetic band structure (right) of Ca_2MnO_4: (a) $I4/mmm$, (b) $Acam$, (c) $I4_1/acd$. Ca (blue), Mn (purple), O (red). The colors of the oxygen octahedra indicate the rotation state [no rotation (purple), clockwise (blue), counterclockwise (red)].**

structure calculations were performed. Transport properties were calculated using BoltzTraP2 [2].

Figure 1 (right) are the calculated band structures by spin-polarized density functional calculations for the three basic structures. We

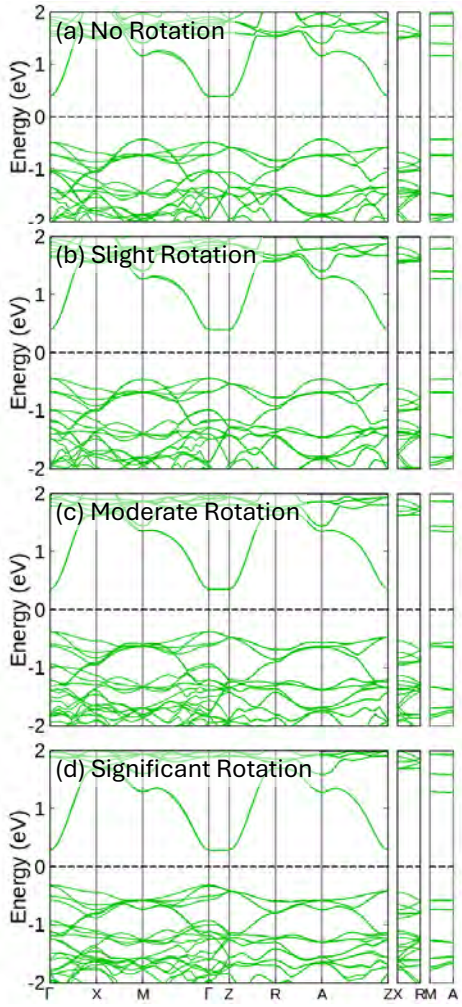


Figure 2: **Antiferromagneitc C-type band structures for structural models (28-atom system) with different rotation angles: (a) 0°, (b) 4.6°, (c) 9.1°, (d) 13.5°.**

found that the C-type (AFC), in which the magnetization of adjacent Mn atoms in the MnO_2 plane is arranged antiferromagnetically, is stable. $I4/mmm$ has an indirect band gap of 0.82 eV between the Γ point and the M point, while $Acam$ and $I4_1/acd$ have a direct band gap at the Γ point, which are 0.59 eV and 0.81 eV, respectively. This result is consistent with the experimental and other calculations. Also, when focusing on the band at the top of the valence band near the M point, $I4/mmm$ and $Acam$ form a parabolic band, while $I4_1/acd$ has a band structure with a flattened parabola. We found that these details are not due to the rotation pattern and result from the rotation angle itself.

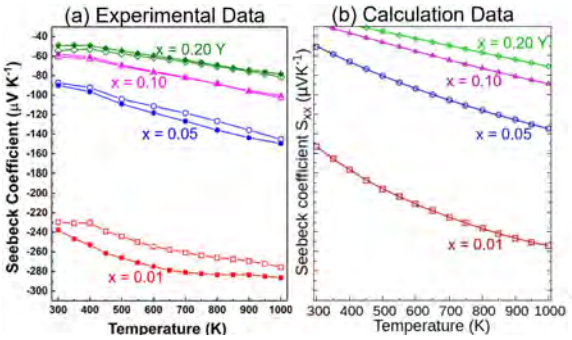


Figure 3: **Temperature dependence of the Seebeck coefficient. (Left) Experimental results for polycrystalline** $Ca_{2-x}Ln_xMnO_4$ **(Ln = La or Y doped). (Right) Theory. The scale of the y-axis is the same.**

Figure 2 compares the AFC band structures for four rotation angles of the oxygen octahedron, (a) 0°, (b) 4.6°, (c) 9.1°, and (d) 13.5°. The band gap at the Γ point decreased (0.88 eV, 0.84 eV, 0.73 eV, and 0.60 eV, respectively), and the shape of the band at the top of the valence band at the M point changed. From the above, we conclude that the electronic structure of CMO is greatly affected by the rotation angle.

The transport properties were investigated: Temperature dependence of the Seebeck coefficient under electron doping is shown in Fig. 3. The Seebeck coefficient decreases with temperature, being insulating behavior. It can be seen that the calculated values in the in-plane direction show a reasonable agreement with the experiment. The different colors in the figure represent the difference in the doping amount. The doping dependence of the Seebeck coefficient is also consistent with the experiment.

References

[1] P. Giannozzi et al. *J. Phys.: Condens. Matter* **21**, 395502 (2009).
[2] G. K. H. Madsen, J. Carrete, and M. J. Verstraete. *Comput. Phys. Commun.* **231**, 140 (2018).

Advances in Catalytic Theory and Predictive Modeling Enabled by Large-Scale Parallel Computing

Di ZHANG

Advanced Institute of Material Research,

Tohoku University, 2 Chome-1-1 Katahira, Aoba Ward, Sendai, Miyagi 980-8577

We utilized the ISSP massive parallel computer system to perform simulations on single-atom and dual-atom M-N-C catalysts, focusing on ORR and OER performance modeling across different pH conditions, spin state simulations, and data-driven catalyst design. VASP software on ISSP was primarily used for DFT calculations and first-principles molecular dynamics simulations. The main achievements are summarized below.

Unlocking New ORR Mechanisms in M–N–C Catalysts with Massive Parallel Simulations: Using the ISSP supercomputer, we performed large-scale first-principles modeling combined with pH-coupled microkinetic simulations and synchrotron spectroscopy to reveal a new ORR pathway in weak-binding M–N–C catalysts.We identified oxygen adsorption at the metal–nitrogen bridge site as a key step (**Fig. 1**), altering scaling relations, electric field responses, and kinetic barriers. These findings redefine the catalytic behavior of weak-binding SACs and open new directions for clean energy applications. [1]

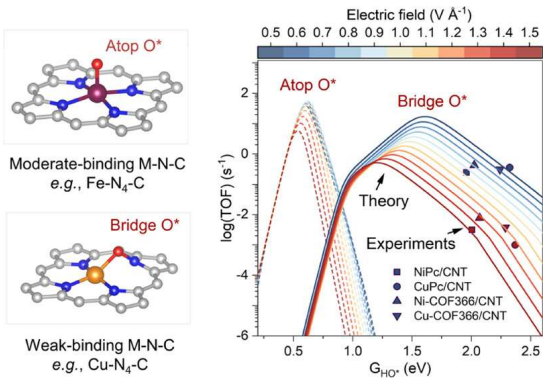


Fig. 1: New ORR Mechanisms on weak-binding M–N–C Catalysts

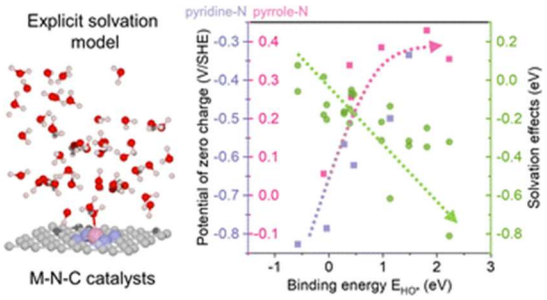


Fig. 2 PZC and solvation effect of M-N-C catalysts

We employed large-scale ab initio molecular dynamics and DFT simulations to reveal how the potential of zero charge (PZC) and solvation effects govern the activity of M–N–C catalysts. Our results show that PZC and solvation vary with metal type and nitrogen coordination, fundamentally impacting key reaction intermediates and pH-dependent behaviors (**Fig. 2**). This work highlights the necessity of including these effects for accurate

modeling and rational catalyst design. [2]

We integrated high-throughput supercomputing with precise synthesis to accelerate the discovery of single-atom catalysts (SACs) for water purification (**Fig. 3**). Large-scale computational screening of 43 metal–N_4 structures enabled the rapid identification of high-performance candidates, leading to the synthesis of an Fe–SAC with record-high Fenton-like activity and outstanding long-term stability. This work demonstrates the power of combining supercomputing-driven prediction with controlled synthesis for next-generation catalyst development.[3]

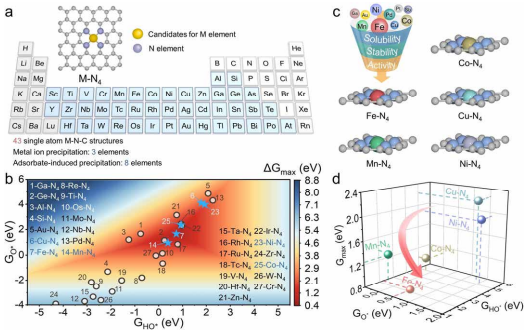


Fig. 3 The discovery of single-atom catalysts (SACs) for water purification.

Using DFT simulations, we elucidated how a built-in magnetic field modulates the spin state of Co centers in molecular M–N–C electrocatalysts, driving major enhancements in ORR and OER performance. Spin-state transitions from low- to high-spin states, validated by computation and experiment, lead to a one-order increase in turnover frequency and 4000% magnetocurrent boost. This approach offers a universal platform for spin-controlled catalyst design.[4]

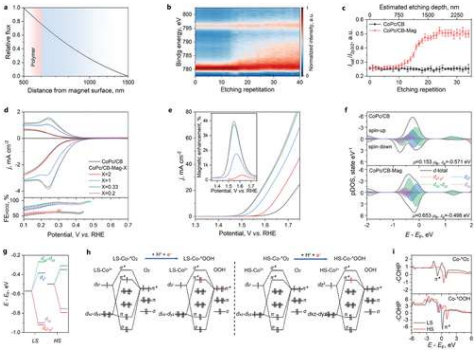


Fig.4 DFT calculations with a magnetic field-integrated electrocatalyst.

References

[1] J. Am. Chem. Soc. 2025, 147, 7, 6076–6086.

[2] J. Mater. Chem. A, 2024, 12, 13742-13750.

[3] Angew. Chem. Int. Ed. 2025, e202500004.

[4] Advanced Materials 2024, 36, 45, 2408461

DFT and Multireference Calculations of Zeolites, High-Entropy Alloys, and Framework Materials

Quan Manh PHUNG

Graduate School of Science, Department of Chemistry

Nagoya University, Furocho, Chikusa, Nagoya, Aichi 464-8601

We have utilized the Supercomputer System B to study various chemical systems, using mainly density functional theory (DFT) and ab initio methods (CASSCF/CASPT2). DFT calculations were performed with VASP and OpenMX, while CASSCF/CASPT2 calculations were done with OpenMolcas. In addition, we perform classical molecular dynamics simulations with GROMACS.

1. Zeolites [1]

We studied the homolytic and heterolytic methane hydroxylation in copper zeolites, $[CuOCu]^{2+} + CH_4 \rightarrow CH_3OH + [Cu\text{-}Cu]^{2+}$. The investigation employed a combination of DFT and CASSCF/CASPT2 calculations to provide detailed mechanistic insight.

2. Mesoporous materials [2]

Various mesoporous materials, particularly high-entropy alloys (HEA), have been studied with DFT. The studies focused on catalytic processes, such as hydrogen evolution reaction (HER), oxygen reduction reaction (ORR), and methanol reduction reaction (MOR).

The catalytic properties of some metal-organic frameworks (MOFs) and covalent-organic frameworks (COFs) have been investigated mainly with DFT and MD simulations.

References

1. M. Han, T. Nagaura, H. N. Nam, Z. Yang, A. Alowasheeir, Q. M. Phung, T. Yanai, J. Kim, S. M. Alshehri, T. Ahamad, Y. Bando, Y. Yamauchi, *Small*, **2025**, Accepted.
2. Q. M. Phung, T. Yanai, D. Plessers, B. F. Sels, R. A. Schoonheydt, K. Pierloot, *ACS Catal.*, **2025**, *15*, 1249.

Materials exploration loop with materials informatics.

Yosuke HARASHIMA
Graduate School of Science and Technology, Nara Institute of Science and Technology
Takayama-cho, Ikoma, Nara 630-0192

In this study [1], we proposed a new materials exploration method called the Covariance Linkage Assimilation method for Unobserved Data Exploration (CLAUDE), which combines a multivariate Gaussian-based data assimilation technique with Bayesian optimization. The goal is to improve the efficiency of finding optimal material properties using limited experimental and simulation data.

Materials informatics often suffers from the scarcity of property-specific experimental data, while simulation data, though abundant, may have systematic errors. Data assimilation techniques have been successful in fields like weather forecasting and are now being adapted for materials science. Bayesian optimization has also become a key tool for efficient material discovery.

The proposed method uses a posterior distribution derived from multivariate Gaussian distribution instead of the conventional Gaussian process regression. It can handle missing data via direct likelihood formulation, enabling the assimilation of multiple datasets. Monte Carlo sampling of the posterior distribution allows Bayesian optimization without requiring full data matching between experiments and simulations.

We demonstrated as follows.
1. Optimization of Example Functions: We tested CLAUDE on example models and demonstrated that the method more efficiently found the maximum value compared to ordinary Bayesian optimization. Incorporating simulation data exploration alongside experimental data exploitation significantly accelerated optimization.
2. Practical Application to Photocatalysts: The method was applied to predict the bandgap of $(Sr_{1-x_1-x_2}La_{x_1}Na_{x_2})(Ti_{1-x_1-x_2}Ga_{x_1}Ta_{x_2})O_3$, an important photocatalytic material. Using a combination of first-principles calculations and limited experimental measurements, the assimilation model accurately predicted bandgap values even at compositions not included in the original dataset. Experimental validation confirmed the predictions, capturing effects like atomic hybridization and non-linear bandgap shifts.

The proposed assimilation method significantly improves search efficiency and prediction accuracy in materials exploration, especially when experimental data are scarce. The successful demonstration with photocatalyst bandgaps highlights the method's practical utility. CLAUDE is positioned as a powerful tool for accelerating materials discovery through intelligent data integration.

References

[1] Y. Harashima, *et al.*: arXiv:2408.08539 (2024);
`https://github.com/yy-harashima/CLAUDE`.

Computational Investigation of Multi-Exciton Generation Mechanism by Large-Scale Excited-State Method

Takatoshi Fujita
National Institutes for Quantum Science and Technology
Anagawa, Inage-ku, Chiba 263-8555

We have been developing the large-scale excited-state methods based on the fragment molecular orbital (FMO) method and the GW/Bethe-Salpeter equation method. Recently, we extended the FMO-based GW/BSE method to calculate the electronic couplings relevant to the singlet fission process. This development enables the first-principles investigation of multi-exciton generation processes in molecular aggregates based on the first-principles calculations.

In parallel, we developed a computational procedure to characterize the excited states in molecular aggregates. Characterizing the excited states is essential for understanding photophysical and photochemical processes. In this study, we propose a method to reconstruct the total transition density matrix (TDM) and natural transition orbitals (NTOs) from the FMO method. By expressing NTOs as linear combinations of fragment molecular orbitals, we introduce novel measures to quantify the extent of collectivity and delocalization of excited states. As an application, we characterized the low-energy excited states in a pentacene cluster. First, we derived the Frenkel exciton and Wannier-Mott exciton states as limiting cases of the FMO-based excited-state Hamiltonian. We compared the wave function obtained from FMO with those of the Frenkel and Wannier-Mott exciton states in terms of collectivity and delocalization. We suggest that the excited states of the pentacene cluster exhibit intermediate properties between the Frenkel and Wannier-Mott exciton states.

Furthermore, as an application of our multi-scale approach [1], we have elucidated the role of charge-transfer (CT) state manifold in the exciton dissociation processes in donor/acceptor blends. Understanding the relationship between the energy levels and the charge photogeneration in donor/acceptor blends is crucial to improving the power conversion efficiency of organic solar cells. Here, we investigate the exciton dissociation dynamics in poly(3-hexylthiophene) (P3HT)/[6,6]-phenyl-C61-butyric acid methyl ester (PCBM) blends by employing the ensemble-averaged wave packet dynamics and the Marcus-Levich-Jortner rate equation. To improve the accuracy of the wave packet dynamics method, we introduced reorganization and temperature corrections and validated these methods against the hierarchical equation of motion method. Our analyses reveal that higher-energy CT states, often overlooked in conventional models, play a significant role in facilitating exciton dissociation. These results highlight the importance of considering the entire CT-state manifold in understanding the charge photogeneration dynamics in donor/acceptor blends.

References

[1] T. Fujita, M. Nozaki, submitted.

Search for high temperature superconductivity in hydrides

Takahiro ISHIKAWA
Department of Physics, The University of Tokyo
7-3-1 Hongo, Bunkyo-ku, Tokyo 113-0033

Lanthanum hydride (La-H) shows superconductivity at 260 K at 170 GPa [1, 2]. Recently, the superconducting critical temperature T_c was reported to increase further to 550 K through repeated cooling and heating of the sample [3]. The large enhancement of the superconductivity has been speculated to be caused by the reaction of La-H with other materials existing in the sample chamber of the diamond anvil cell. Dominant candidates for the materials are nitrogen (N) and boron (B), originating from a hydrogen-source material (NH_3BH_3) used for the synthesis of hydrides, and platinum (Pt), gold (Au), and gallium (Ga), originating from electrodes.

In this study, assuming a reaction between La-H and Pt, we searched for thermodynamically stable phases in the La-Pt-H system at 20 GPa using a high-speed construction method of a formation-enthalpy convex hull (CH) diagram that integrates evolutionary algorithms (EA), first-principles calculations based on the density functional theory (DFT), and universal neural network potential (UNNP) calculations [4]. At each generation for the CH construction, a few thousand structures created by EA are rapidly optimized by the UNNP calculations implemented in Matlantis [5], and only several dozen structures appearing near CH are extracted. Then, the structural optimizatios are performed for the extracted structures using the DFT calculations implemented in the Quantum ESPRESSO (QE) code [6], executed on the ISSP supercomputer, and the convex hull is subsequently updated. For the stable compounds, we calculated the electron-phonon coupling constant λ and the logarithmic averaged phonon frequency $\omega_{\log}$ using the QE code and estimated T_c based on the Allen-Dynes formula [7]. Our exploration revealed that $LaPtH_6$ exhibits the highest Tc of 18.67 K at 20 GPa [8], with no evidence supporting the previously reported superconductivity at 550 K.

References

[1] M. Somayazulu *et al.*: Phys. Rev. Lett. **122**, 027001 (2019).

[2] A. P. Drozdov *et al.*: Nature **569**, 528 (2019).

[3] A. D. Grockowiak *et al.*: Front. Electron. Mater. **2**, 837651 (2022).

[4] T. Ishikawa *et al.*: Phys. Rev. B **109**, 094106 (2024).

[5] Matlantis (https://matlantis.com/), software as a service style material discovery tool.

[6] P. Giannozzi *et al.*: J. Phys.: Condens. Matter **21**, 395502 (2009).

[7] P. B. Allen and R. C. Dynes: Phys. Rev. B **12**, 905 (1975).

[8] T. Ishikawa *et al.*: http://arxiv.org/abs/2502.06821 (2025).

Structural and electronic properties of gold nanotubes

Shota ONO
Muroran Institute of Technology, Muroran, Hokkaido 050-8585, Japan

Carbon nanotubes (CNTs) are created by rolling up the graphene. The chiral vector determines the structure of CNTs and also their electronic properties. The properties of different nanotubes have been investigated by rolling up other 2D materials. Recently, Kashiwaya et al. have reported the creation of goldene, which is 2D gold with a hexagonal structure [1]. The goldene has been expected to be useful for miniaturizing electronic devices to the nanoscale.

In this project, we have studied the structural and electronic properties of gold nanotubes (GNTs). Based on first-principles calculations, we calculated the strain energy $\Delta E(n,m) = E(n,m) - E_{\mathrm{2D}}$, where $E(n,m)$ and E_{2D} are the total energy per atom of the (n,m) GNT and the goldene. The continuum elasticity theory predicts $\Delta E(n,m) \propto R^{-2}$ with the GNT radius R. We have shown that the inverse square law does not hold for GNTs (see Fig. 1). This is due to the enhanced strain energy in specific GNTs. The specific chiralities were identified by imposing the Bloch and geometric boundary conditions to the electronic structure of goldene having a hexagonal shape of the Fermi surface. We also confirmed that the electronic states on the Fermi surface exhibit an in-plane character. These factors result in an increase in the strain energy.

These research findings were reported in Ref. [2]. Another study regarding other 2D materials conducted last year was also completed, and its results were reported in Ref. [3].

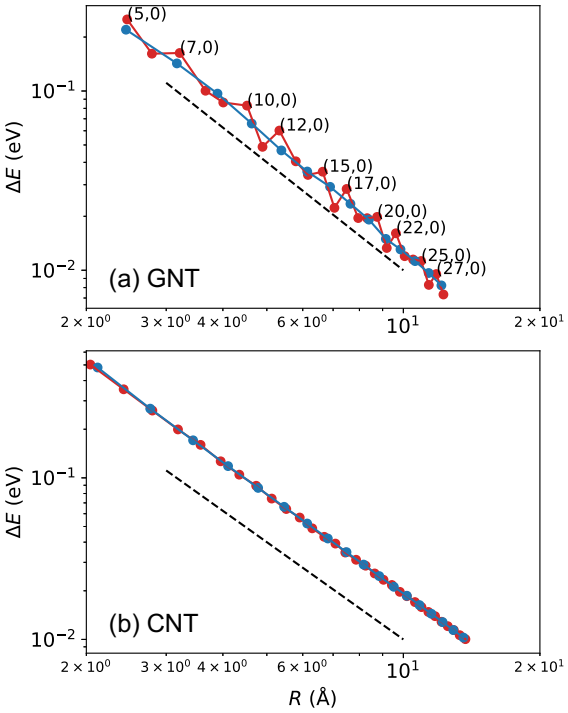


Figure 1: The strain energy $\Delta E(n,m)$ as a function of R for (a) GNTs and (b) CNTs with the chiral indices $(n,0)$ and (n,n).

References

[1] S. Kashiwaya et al., Nat. Synth **3**, 744 (2024).

[2] S. Ono and H. Yoshioka, Phys. Rev. B **111**, 085414 (2025).

[3] S. Ono and R. Pawar, Phys. Rev. Materials **8**, 094002 (2024).

Modeling ultrafast electron dynamics: Case studies of elemental metals and carbon nanostructures

Shota ONO
Muroran Institute of Technology, Muroran, Hokkaido 050-8585, Japan

In the field of ultrafast dynamics, it is still a challenge to interpret the transient optical responses within the femtosecond timescale. In this project, we have studied (i) the transient luminescence of 15 elemental metals [1] and (ii) the transient absorption spectra of few-walled carbon nanotubes (CNTs) [2].

For the case (i), we interpreted the luminescence dynamics of light metals; 3*d*, 4*d*, and 5*d* transition metals; and noble metals [1]. To understand the different decay rate of infrared luminescence among these metals, we calculated the electron-phonon (e-ph) coupling constant by using the density-functional perturbation theory implemented to the Quantum Espresso. Based on the two-temperature model between hot electrons and phonons, we estimated the decay rate of non-equilibrium electrons. We have confirmed that the calculated decay rate agrees with the experiments (see Fig. 1). The disagreement between the theory and experiments for Al and Be will be due to the creation of non-equilibrium phonons during the relaxation.

For the case (ii), we interpreted the absorption dynamics for bundled few-walled CNTs [2]. To understand the anomalously enhanced decay constant at a specific energy, we constructed an analytical model that relates the absorption decay with the electron temperature decay. By considering the van Hove peaks in the electron density-of-states, we have found that our model captures the overall feature of the absorption dynamics. The dimensionality of electron dynamics in bundled few-walled CNTs and van der Waals heterostructures of CNTs covered with boron nitride nanotubes was also investigated.

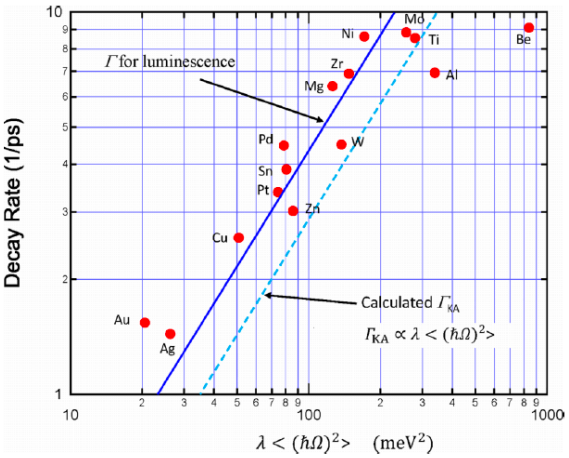


Figure 1: Correlation between the luminescence decay rate at 0.6 eV and the e-ph coupling constant for 15 elemental metals. The blue dashed line represents the values calculated by the temperature model. The values multiplied by 1.5 are shown by a solid line [1].

References

[1] T. Suemoto, S. Ono et al., Phys. Rev. B **111**, 035150 (2025).

[2] G. Noyama et al., Carbon Trends **20**, 100510 (2025).

Theoretical Simulation of Subcycle Reciprocal-Space Images of Electron Density Driven by a Strong Laser Field

Yasushi SHINOHARA[1,2]

[1]*Photon Science Center,*

The University of Tokyo, Hongo, Bunkyo-ku, Tokyo 113-8656.

[2]*NTT Basic Research Laboratories,*

NTT Corporation, 3-1 Morinosato Wakamiya, Atsugi, Kanagawa 243-0198.

We have investigated the response of insulators to strong light fields using time-dependent density functional theory (TDDFT) [1]. When the field strength becomes comparable to the intrinsic electric field within the material, the system exhibits extremely nonlinear responses that cannot be described by perturbative expansions. To accurately capture these dynamics, it is necessary to solve the time-dependent Kohn-Sham equation directly in real time. The SALMON-TDDFT code [2] provides a platform for solving the Kohn-Sham equation for crystalline solids, molecules, and atoms. In this study, we performed simulations using system B at SCC-ISSP.

We conducted TDDFT simulations to obtain subcycle reciprocal-space images of the electron density in monolayer hexagonal boron nitride (hBN) and graphene under an intense electric field. The corresponding real-space electron densities were derived via spatial Fourier transforms. The applied electric field was linearly polarized, with a full width at half maximum (FWHM) duration of 14 fs, a photon energy of 0.4 eV, and a peak intensity of 1 TW/cm².

Under the influence of the peak electric field, the electron distribution becomes significantly distorted. In monolayer hBN, the low-frequency components of the reciprocal-space electron density exhibit oscillations that vary nearly linearly with the applied field strength. Our simulations suggest that these dynamics correspond to electron hopping between two distinct B–N bonds in response to the field. In contrast, graphene does not show such linear field-dependent oscillations.

References

[1] Erich Runge and E. K. U. Gross, Phys. Rev. Lett. 52, 997 (1984).

[2] https://salmon-tddft.jp/, M. Noda, S.A. Sato, et al., Computer Physics Communications. 235, 356 (2019).

Calculation of electronic states for improving characteristics at the channel interface of power MOSFETs

Hironori YOSHIOKA

Advanced Power Electronics Research Center,

National Institute of Advanced Industrial Science and Technology (AIST), Tsukuba, Ibaraki 305-8568

In order to reduce loss in power electronics equipment, it is extremely important to understand and control the electronic state at the channel interface between the gate insulator and the semiconductor of the MOSFETs. For example, in SiC MOSFETs, which have recently been put to practical use, the channel mobility at the SiO_2/SiC interface is very low (10~100 $cm^2V^{-1}s^{-1}$), but the fundamental causes are not fully understood or elucidated.

The fact that channel mobility varies greatly depending on the SiC crystal plane {(0001) or (11-20)} has been a major mystery for 20 years [1]. We have clarified that this is due to the extreme localization of the conduction band wave function at the (0001) interface [2]. Using density functional theory (DFT), we calculated the wave function at the conduction band edge of SiC slabs and found that the wave function of the 4H-SiC (0001) slab is uniquely localized very close to the interface (< 0.5 nm) when an electric field is applied. This is related to the long crystal periodicity specific to the [0001] direction. By comparing the electric field dependence of the distance (z) of the wave function from the interface with the electric field dependence of the mobility obtained experimentally, we showed that the difference in z can explain the difference in mobility between the (0001) and (11-20). In other words, it can be said that the (0001) has smaller z by the unique localization at the interface and then has a lower mobility because of frequent scattering from interface defects.

Conventional simulations based on the effective mass approximation have been used to predict the characteristics of semiconductor devices, but we have shown that the unique localization of the wave function shown by DFT calculations cannot be reproduced by the effective mass approximation. In other words, DFT calculations are essential for predicting the properties of the SiO_2/SiC interface.

DFT calculations were performed using the ISSP supercomputer. Using the RSDFT (Real-space density functional theory) code [3], we applied an electric field of about 1 MV/cm, which is close to the situation for the inversion electrons in MOSFETs, and calculated the wave function attracted to the interface. Norm-

conserving pseudopotentials and GGA by PBE were used. The H/amorphous SiO_2/4H-SiC/H slab structures, which were terminated with H atoms, were used. The (0001) and (11-20) SiC were used as the interface. z was calculated from the expectation value of the position of the wave function.

In [2], DFT calculations were performed with a slab thickness of 3 nm. For this thickness, the confinement effect by the finite thickness slab results in a non-negligible error in the calculation of z, compared to calculations for a sufficiently thick slab. Therefore, in FY2024, re-calculation was performed with a slab thickness of 11 nm (maximum number of atoms: 1,323). In addition, the E-k dispersion was calculated by setting the k-points finely, and the effective mass was calculated from the second derivative.

Even when the slab thickness increased, the qualitative trend did not change, and z was smaller for the (0001) plane. The effective mass did not change significantly from the bulk upon application of an electric field. We were able to quantitatively show that the difference in mobility between the (0001) and (11-20) can be largely explained by the difference in z and the anisotropy of the effective mass. We presented the results at [4] in November 2024.

References

[1] H. Yoshioka, J. Senzaki, A. Shimozato, Y. Tanaka, and H. Okumura, Appl. Phys. Lett. **104**, 083516 (2014).

[2] H. Yoshioka, J. Iwata, and Y. Matsushita, Appl. Phys. Lett. **122**, 222104 (2023).

[3] J. Iwata *et al.*, J. Comp. Phys. 229, 2339 (2010).

[4] H. Yoshioka, J. Iwata, and Y. Matsushita, 先進パワー半導体分科会第 11 回講演会, invited, (2024).

Modeling of the Ammonia Decomposition Reaction and Nitriding on Metal Surfaces

Peijie FENG, Minhyeok LEE, and Yuji SUZUKI

Department of Mechanical Engineering, School of Engineering,

The University of Tokyo, 7-3-1 Hongo, Bunkyo-ku, Tokyo 113-8656

Ammonia is a promising green energy carrier for the next generation, but employing it directly as a fuel is challenging due to its low flammability and potential NOx emissions [1]. Moreover, our previous study [2] showed that ammonia catalytically decomposes on iron-based materials, forming iron nitride, which in turn enhances ammonia decomposition more effectively than pure iron surfaces. To model the dynamics of the nitriding process in conjunction with surface decomposition, understanding the reaction mechanisms at the atomic level is indispensable. Considering both accuracy and computational complexity, we employed a density functional theory (DFT)-based first-principles approach using Vienna Ab-initio Simulation Package (VASP) to calculate the possible underlying surface reactions.

Due to the diversity of iron nitrides, which includes not only solid solutions of α- and γ-iron, but also γ', ε, and ζ iron nitrides, the systematic modeling and computation of these atomic interfaces remain a challenging task. To address this, we embarked on building a framework to systematically explore surface reactions on all possible forms of iron and iron nitrides.

First, the low Miller indices were computed for α-Fe, ε-Fe, γ-Fe, γ'-Fe_4N, and ε-Fe_3N, which include (001), (100), (010), (110), (101), (011), (111), (211), (121), (112), (102), (012), (120), (210), (021), (201), and (221). Table 1 illustrates the results obtained after systematic interface modeling and computation. Based on the most stable facet identified, surface reactions were subsequently computed on these facets.

The catalytic activities of iron and iron nitrides were first examined by comparing the adsorption energy of nitrogen atoms [3], which serves as an indicator of promoting ammonia decomposition. Because modeling the facet

Table 1: Systematic examination of the surface energies of iron and iron nitrides involved in the phase transformations during ammonia-induced nitriding.

	α-Fe	γ-Fe	ε-Fe	γ'-Fe_4N	ε-Fe_3N
Computed Facets	10	11	20	16	48
The most stable facet	(110)	(001)	(001)	(001)	(101)
Surface Energy (eV)	0.163	0.169	0.204	0.125	0.189

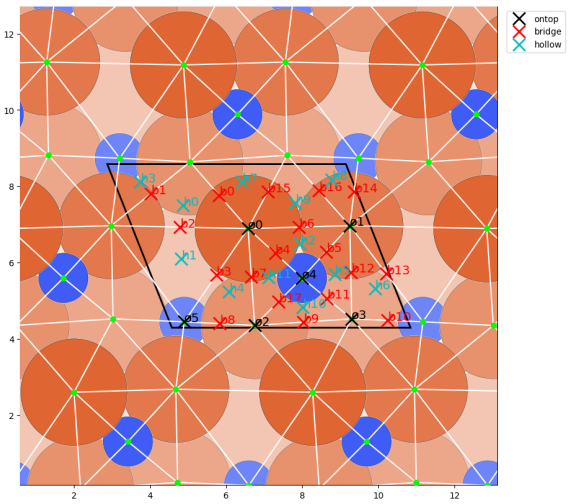


Fig. 1: The identified adsorption sites on ε-Fe_3N, 101 facet. The orange and blue circle represent the Fe and N atoms, respectively, with lighter colors indicating atoms located further from the interface. The black lines illustrate the unit cell and the "x" mark represents the identified adsorption sites in a unit cell.

with adsorbates requires meticulous examination of all possible adsorption sites, we developed a program using the Python Materials Genomics (pymatgen) package [4]. As a result, all possible adsorption sites were identified by considering both the periodicity and symmetry of the facet as shown in Fig. 1. In addition to ε-Fe_3N, adsorption sites were also identified for α-Fe and γ'-Fe_4N. The computational results show that nitrogen atoms preferentially adsorb at hollow sites formed by neighboring iron atoms. For ε-Fe_3N, as shown in Fig. 1, the sites marked h0, h7, and h9 can form stable adsorption configurations. Among these sites, the h0 site exhibits the most stable adsorption, with an adsorption energy of −6.41 eV. A similar computation performed on α-Fe revealed that the adsorption energy is slightly lower than that of ε-Fe_3N, with a value of −6.56 eV. This indicates that ε-Fe_3N may exhibit greater reactivity when iron is nitrided to a certain extent and ε-Fe_3N is formed.

In conclusion, the most stable facets were identified for α-Fe, ε-Fe, γ-Fe, γ'-Fe_4N, and ε-Fe_3N. Subsequently, a program was developed to identify adsorption sites, enabling a systematic examination of the adsorption energies of various adsorbates. The most stable adsorption sites for nitrogen atoms were then determined, and the corresponding adsorption energies were used to estimate their reactivity in catalyzing ammonia decomposition. ε-Fe_3N is predicted to be more reactive than the un-nitrided α-Fe. Future work will include a more detailed investigation of the reaction pathways.

References

[1] M.V. Manna, P. Sabia, R. Ragucci, M. de Joannon, Fuel **264**, 116768 (2020).
[2] P. Feng, M. Lee, D. Wang, Y. Suzuki, Int. J. Hydrog. Energy **48**, 75 (2023).
[3] E. Skúlason et al., Phys. Chem. Chem. Phys. **14**, 1235-1245 (2012).
[4] P. S. Ong. et al., Comput. Mater. Sci. **68**, 314-319 (2013).

First-principles calculation of dielectric constant in oxide-based phosphor

Kenji HIRATA

National Institute of Advanced Industrial Science and Technology (AIST) 807-1, Shuku, Tosu, Saga 841-0052

Recently, it was discovered that $SrAl_2O_4:Eu^{2+}$, which is $SrAl_2O_4$ doped with europium, emits light due to energy generated by static electricity.[1] Since static electricity can cause malfunctions in electronic devices, both in manufacturing environments and in next-generation mobility applications, the development of a general-purpose visualization technique for static electricity is highly desirable. As a result, this material has attracted considerable attention as a potential static electricity visualization material. In this study, the dielectric constant of the oxide phosphor $SrAl_2O_4:Eu^{2+}$ was estimated using first-principles calculations in order to investigate the mechanism underlying its electrostatic emission. Furthermore, calculations were performed on the energy levels of oxygen vacancies, which are deeply involved in the emission mechanism.

A supercell was created by expanding $SrAl_2O_4$ unit cell $2\times1\times2$ times, and one strontium site was replaced with Eu (Fig. 1). The dielectric constant of $SrAl_2O_4:Eu^{2+}$ without oxygen vacancies was estimated to be approximately 5.3, and it was found that the introduction of oxygen vacancies tends to increase this value. The chemical potential of oxygen was calculated in order to determine the energy levels of oxygen vacancies. The phase diagram of the Sr-Al-O system was estimated in chemical potential space, which was consistent with previous reports. [2] The present results will be utilized in future studies to calculate the energy levels of oxygen vacancies with greater accuracy.

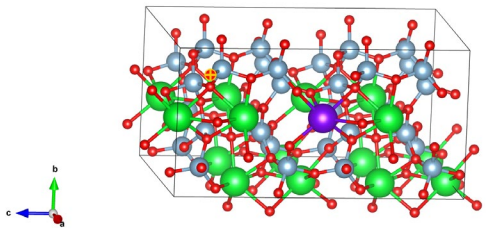


Fig. 1. Supercell model of $SrAl_2O_4:Eu^{2+}$. Purple, green, blue, and red spheres represent Eu, Sr, Al, and O atoms, respectively.

References

[1] K. Kikunaga and N. Terasaki, Sci. Rep. **12**, 8524 (2022).

[2] E. Finley, A. M. Tehrani, and J. Brgoch, J. Phys. Chem. C **122**, 16309 (2018).

Phase transformation and electric state of high entropy alloys

Yoko Yamabe-Mitarai

Frontier Science Graduate School,

The University of Tokyo, Kashiwa-no-ha, Kashiwa, Chiba 277-8561

High-entropy alloys (HEAs) have been attracting attention as new-generation structural and functional materials since this new paradigm was proposed in 2004 [1]. Most HEAs have a single face-centered-cubic (fcc), body-centered-cubic (bcc) structure, or their mixtures. Not many examples of HEAs with the hexagonal-close-packed (hcp) structure have been studied. We are applying to find HEAs with hcp structure experimentally and a few alloys were found to have an hcp structure [2].

Among the hcp-HEAs, equiaxed single-phase hcp phase was successfully developed in TiZrAl, TiZrHf, and TiZrHfAl. The deformation mechanism was investigated using a strain jump test and slip analysis after deformation. The hcp-HEAs indicated high strength compared with conventional Ti alloys, even though the slip system is the same as that of conventional Ti alloys. A strong solid-solution strengthening effect of HEAs was suggested by strong multi-elemental interaction and short-range order from macroscopic analysis. To investigate whether strong multi-elemental interaction or short-range order formation occurs, an electron charge of density was calculated using DFT. A supercell model with 128 atoms was used to indicate the solid solution phase. Special Quasirandom Structure was used to simulate random atomic positions. The internal coordinate was optimized using Quantum Espresso (QE). The electron charge density was calculated on the optimized coordinates. The results indicated that the strong bonding between some specific elements is expected to improve strength [3].

The second topic is the adhesion behavior of the oxide layer on Ni to understand the stability of the protective oxide layer. Some alloying elements drastically decreased interfacial energy, improving the adhesion between Ni and the oxide layer [4].

References

[1] B. Cantor et. al., A. J. B. Vincent, Mater. Sci. Eng. A, **375-377**, 213 (2004).

[2] Y. Yamabe-Mitarai et. al., JALCOM, **911**, 164849 (2022)

[3] S. J. Liang, T. Yoshino, R. Matsumoto, R. Sahara, Y. Toda, S. Matsunaga, G. Miyamoto, Y. Yamabe-Mitarai, Mater. Sci. Eng. A, **929**, 148143 (2025).

[4] M. Negami, R. Morihashi, T. Yoshino, R. Sahara, Y. Yamabe-Mitarai, Corros. Sci, **237**, 112329 (2024).

Theoretical design of bistable functional materials based on calculations for diradical-solid interaction

Kohei TADA

Department of Materials Engineering Science, Graduate School of Engineering Science, Osaka University, Toyonaka, Osaka 560-8531, Japan

Molecules with all paired-electrons are called closed-shell molecules, while other molecules that has unpaired electrons are called open-shell molecules. The highest occupied molecular orbital (HOMO) of closed-shell molecules is generally bonding and the lowest unoccupied molecular orbital (LUMO) is antibonding; therefore, the HOMO-LUMO gap is generally large. As the covalent bonds in the closed-shell molecule weaken, the HOMO-LUMO gap narrows, the electrons are localised on each atom and show the properties of unpaired electrons. These unpaired electrons occupy the degenerate orbitals. Such open-shell molecules are called diradical molecules.

The degree of localisation is featured by diradical character (y value) and the y value is widely used in molecular design [1]. The relationship between y value and electronic properties of the molecules is shown in Fig 1. The variation in localisation will cause magnetism change. The HOMO-LUMO gap is affected by the y-variation, and redox properties will be changed. The design of bistable molecular materials can be achieved by establishing a closed-/open-shell controlling This study aims to establish a theoretical basis for the control by molecule-solid interactions.

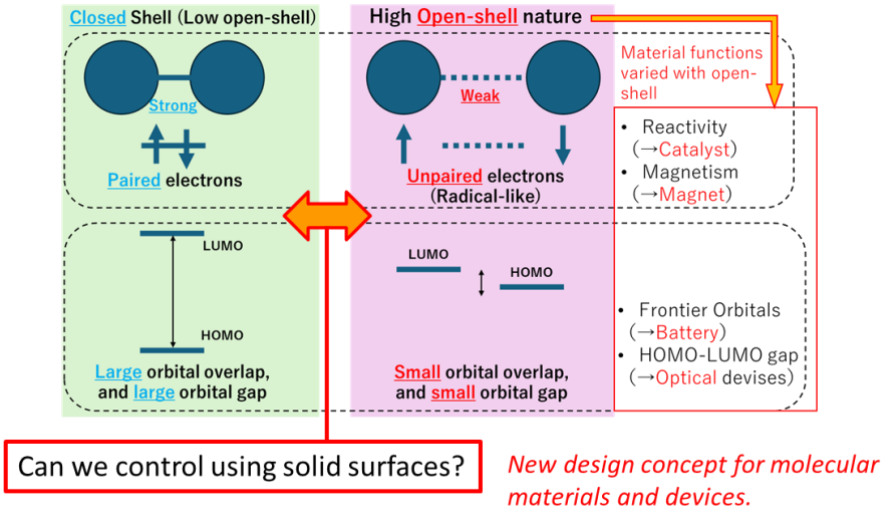


Fig. 1: Schematic view of study concept.

A method to estimate *y*-values of molecule-solid composite systems with realistic costs has been developed by the author (AP-DFT/plane-wave method) [2,3]. Electronic state optimisation via DFT/plane-wave was performed by the VASP code, and the y-values were calculated by the developed code using the optimised electron densities. System B (ohtaka) was used for the investigation of theoretical models, and system C (kugui) was used for the application to real systems.

For "control," it is necessary to find both "increasing" and "decreasing" mechanisms. A systematic study using diatomic adsorption model of Au, Ag, and Cu showed that the oxide surface have (1) a mechanism to increase y-value due to orbital polarisation effect and (2) a mechanism to decrease y-value due to electron transfer; the balance between these two opposing mechanisms determines whether the y-value is increased or decreased by surface adsorption (Fig. 2) [4]. The former effect is dominant in Au adsorption, while the latter effect is dominant in Ag adsorption. This result was selected as an issue cover of *Chemistry*.

As an application to real systems, we investigated metal-organic-framework (MOF) materials based on a Ru binuclear complex (Ru_2-MOF). It was found that the electron distribution around the Fermi level of Ru_2-MOF is strongly dependent on the magnetic state [5]. This indicates that the conductivity would be related with their magnetic properties.

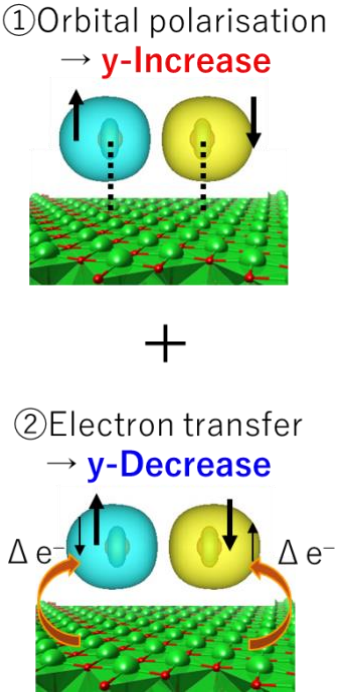


Fig. 2: *y*-Modification effects by oxide surfaces.

References

[1] T. Stuyver, B. Chen, T. Zeng, P. Geerlings, F. De Proft, R. Hoffinann, Chem. Rev. **119**, 11291 (2019).

[2] K. Tada, Y. Kitagawa, T. Kawakami, M. Okumura, S. Tanaka, Chem. Lett. **50**, 392 (2021).

[3] K. Tada, H. Ozaki, K. Fujimaru, Y. Kitagawa, T. Kawakami, M. Okumura, Phys. Chem. Chem. Phys. **23**, 25024 (2021).

[4] K. Tada, K. Masuda, R. Kishi, Y. Kitagawa, Chemistry **6**, 1572 (2024).

[5] N. Amamizu, K. Tada, R. Kishi, W. Kosaka, H. Miyasaka, Y. Kitagawa, Chem. Lett. **53**, upae230 (2024).

Theoretical investigation to design of novel Na-ion battery materials with low environmental impact and high durability

Kohei TADA

Department of Materials Engineering Science, Graduate School of Engineering Science, Osaka University, Toyonaka, Osaka 560-8531, Japan

Sodium-ion battery (SIB) systems are candidates for sustainable energy storage systems. The Na-containing layered transition metal oxide materials can be synthesized easily and have high capacity, making them the most extensively studied materials for cathode materials of SIB systems. Among the layered structures, P2-type $Na_{2/3}(Mn_{2/3}Ni_{1/3})O_2$ (P2-type Na-NMO)is an attractive material because its theoretical capacity and working potential are comparable to those of the cathode materials of lithium-ion battery systems [1]. However, the P2-structure is metastable at higher potential range, and schemes to retain the structure during cycling must be discussed. Recently, it is shown that milling the materials increases durability [2]; however, the mechanism is still unknown. Furthermore, life cycle assessment analysis showed the environmental impact belonging to Ni is high [3]. Hence, to achieve low environmental impact and high durability systems, theoretical investigations is needed.

In this project, density functional theory (DFT) calculations were performed (1) to investigate the mechanism of high durability in milling samples, and (2) to design low Ni-containing materials. The calculations were performed by VASP programme implemented in ohtaka (system B) and kugui (system C).

The P2-type structure transitions to a more stable layered structure (O2 structure) by layer-sliding, and the O2 structure transferred to a rock-salt structure, resulting in redox-inactivation [4]. Our DFT calculations showed that the P2-type structure will quickly transitions to the O2-type structure. Therefore, for clarifying the mechanism of high durability of milling sample, we should investigate not only bulk structure but also other pieces.

Then, I assumed the difference of surface energy would be a reason, and the surface energies of P2- and O2-type NMOs were estimated using the total energies of oxides such as NiO and MnO. The calculated results show a clear difference on the (100) surface energy. The P2-type structure would be stabilized by milling due to the increase of the exposed (100) surface area.

A faster method than DFT calculations, such as machine learning interatomic potential (MLIP) calculation, is needed to study the

change in potential due to the substitution of Ni in NMO with other elements. DFT calculations were performed for several substituents (Mg, Zn, Cu, Sn), and the calculated results were compared with the predicted results of MLIP calculations. From the comparison, I found that the CHGNet potential has good agreement with DFT. Furthermore, the DFT calculation showed that an O-redox mechanism of the P2-structure; it indicates if milling process could introduce the Ni-defects and the defect density could be controlled, the NMO material with low Ni amount and high capacity will be obtained. These results will be presented at Pacifichem2025.

References

[1] N. Yabuuchi, K. Kubota, M. Dahbi, S. Komada, Chem. Rev. **114**, 11636 (2014).

[2] R. Kataoka, N. Taguchi, K. Tada, A. Machida, N. Takeichi, Batteries & Supercaps **6**, e202200462 (2022).

[3] R. Yokoi, R. Kataoka, T. Masese, V. Bach, M. Finkbeiner, M. Weil, M. Baumann, M. Motoshita, Res. Conservation Recycl. **204**, 107526 (2024).

[4] P.-F. Wang, Y. You, Y.-X. Yin, Y.-S. Wang, L.-J. Wan, L. Gu, Y.-G. Guo, Angew. Chem. Int. Ed. **55**, 7445 (2016).

Exploration of photonic hypermaterials with complete-gap

Nayuta TAKEMORI

Department of Physics,

Osaka University, Toyonaka,Osaka 560-0043,JAPAN

In this study, we investigated the formation mechanisms of photonic band gaps in two-dimensional quasiperiodic structures using large-scale parallel computations. We focused on three representative tilings—the Hexagon-Boat-Star (HBS) tiling, the square-triangle tiling [1], and the Ammann-Beenker tiling [2]—and constructed photonic crystal models by placing air cylinders at each vertex on a dielectric background.

The simulations were performed using a custom-built photonic band structure solver based on the plane-wave expansion method. We adopted the Ho method [3] to ensure accurate eigenvalue convergence and employed the MAGMA GPU-based eigensolver to accelerate the diagonalization of large sparse matrices. These techniques enabled us to compute the photonic band structures efficiently across various geometrical configurations and material parameters.

Our results [4] revealed the existence of complete photonic band gaps in the square-triangle and HBS tilings. By introducing secondary air cylinders at the centers of star prototiles, we were able to significantly enhance the gap width. This work paves the way for more efficient designs in photonic technologies, with potential applications in optical sensors and novel laser systems.

References

[1] M. E. Zoorob et al., *Nature* **404**, 740 (2000).

[2] D. T. Roper, D. M. Beggs, M. A. Kaliteevski, S. Brand and R. A. Abram, Journal of Modern Optics **53** 407–416 (2006).

[3] K. M. Ho, C. T. Chan, and C. M. Soukoulis, *Phys. Rev. Lett.* **65**, 3152 (1990).

[4] N. Takemori and A. Yamamoto, *J. Phys.: Condens. Matter, submitted*

Magnetic properties of ferromagnetic Fe lattice induced by He atoms trapped in vacancy

Kazuhito Ohsawa

Institute for Applied Mechanics, Kyushu University,

Kasuga-koen 6-1, Kasuga, Fukuoka 816-8580

Introduction

Iron (Fe) and its alloys are important structural materials in advanced fusion reactors. Vacancies (V) and vacancy type lattice defects are nucleated in the plasma facing materials (PFMs) used in the fusion reactors under the irradiation circumstance. Such vacancy type lattice defects are considered to be remarkable trap sites of helium (He) atoms. According to first-principle calculations, more than 30 He atoms can be accommodated in a single vacancy. So, the effects of the vacancy-helium (V-He) complexes, vacancy trapping one or multiple He, have been investigated in the field of the PFMs for safe operation of the fusion reactors. Rare gas, such as He, does not make chemical bonding with other elements. However, He atoms trapped in a vacancy physically presses the Fe lattice, and it causes stress field. In the present report, we focused on the magneto-volume effect around the V-He complexes, that is, variation of magnetic moment of Fe atoms derived from the stress field owing to the He atoms trapped in a Fe vacancy.

Simulation method

First-principle calculations based on density functional theory are performed by Vienna ab-initio simulation package (VASP) with generalized gradient approximation (GGA) and projector augmented wave method (PAW). We used supercell in which one vacancy was introduced into 128 Fe atoms (4x4x4 bcc lattice). The cut-off energy of plane wave was 500eV. In the present simulations, Fe atoms are supposed to be ferromagnetic elements.

Binding energy E_b between single or multiple He atoms and vacancy was estimated, as follows.

$$E_b = E[\mathrm{Fe}_{m-1}\mathrm{VHe}_n] + nE[\mathrm{Fe}_m] - E[\mathrm{Fe}_{m-1}\mathrm{V}] - E[\mathrm{Fe}_m\mathrm{He}] \quad (1)$$

where E is cohesive energy of supercell. For example, the supercell $\mathrm{Fe}_{m-1}\mathrm{VHe}_n$ is composed of m-1 Fe atoms, one vacancy V, and n He atoms trapped in the Fe vacancy. Similarly, supercell Fe_m is perfect Fe lattice, $\mathrm{Fe}_{m-1}\mathrm{V}$ is supercell including a vacancy. $\mathrm{Fe}_m\mathrm{He}$ represents supercell including a He located at an interstitial lattice site. In the present simulations, the total number of Fe atoms is m=128.

Results and discussion

There are two typical interstitial sites, T-site and O-site, in bcc lattice, as shown in Fig. 1. An interstitial He atom at T-site is more stable than that at O-site. We searched stable structures of single and multiple He atoms trapped in the Fe vacancy, as shown in Fig. 2. In the case of single He, it is located at the center of the Fe vacancy. While, multiple He atoms in the vacancy are located at positions separated from other atoms as far as possible. The reason why such structures are selected is that He is rare gas which does not make chemical bonding.

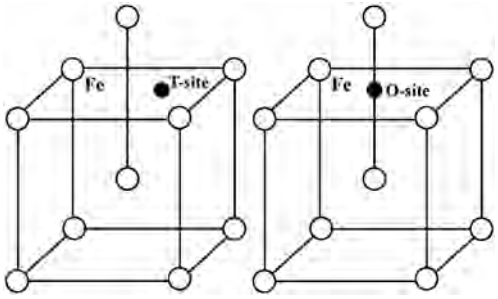


Fig. 1: Schematic view of T-site and O-site in bcc lattice.

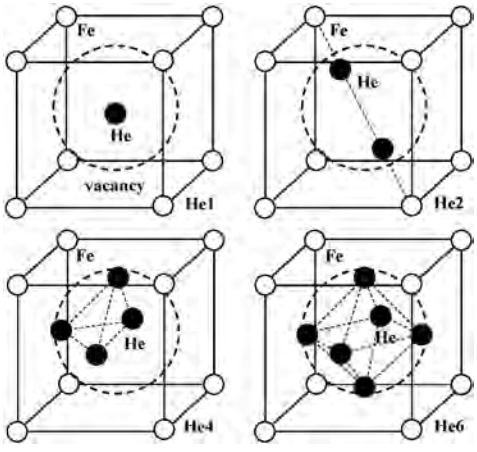


Fig. 2: Schematic view of stable structure of He atoms in Fe vacancy.

Binding energies are shown in Fig. 3, which is almost proportional to the number of He atoms. Fig. 4 shows the relation between average magnetic moment of Fe atoms and volume expansion of Fe lattice. The magnetism of Fe lattice is larger, as the number of He atoms trapped in the Fe vacancy increases. This result indicates that magneto-volume effect is observed around Fe-V complex. We expect that this study will be applied to development of a new non-destructive inspection method to detect He aggregation in ferromagnetic materials

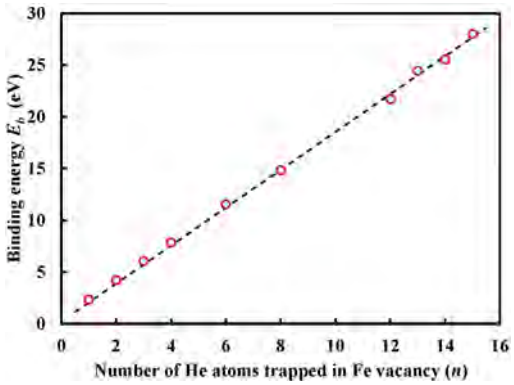


Fig.3: Binding energy for single and multiple He atoms trapped in Fe vacancy.

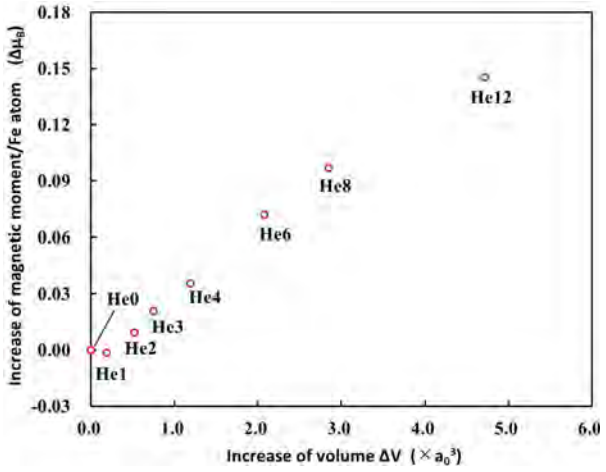


Fig. 4: Relation between average magnetic moment of Fe atoms and volume expansion of Fe supercell.

Evaluation of a New Methodology for Emission Spectra of Light-Element Materials

Masahito Niibe,[a,b] Takeru Nakashima,[c] Yoko Saito,[c] Yasunobu Ando,[c] Teruyasu Mizoguchi,[d] and Iwao Matsuda[a]

[a] *ISSP, The University of Tokyo, 5-1-5Kashiwa-no-ha, Kashiwa, Chiba 277-8581*

[b] *LASTI, University of Hyogo, 3-1-2 Koto, Kamigori, Hyogo 678-1205*

[c] *IIR, Institute of Science Tokyo, Yokohama, Kanagawa 226-8501*

[d] *IIS, The University of Tokyo, Komaba, Tokyo 153-8505, Japan*

X-ray emission spectroscopy (XES) is a method for spectroscopic analysis of X-rays emitted from atoms excited by means such as X-rays, electron beams, and particle beams during the relaxation process of the excitation [1]. XES can directly identify the valence electronic states and track the chemical reactions occurring at the surface. This usability potentially leads to the prediction of new substances and to design functional materials through combinations of material informatics and computational simulations.

Especially, XES is less commonly performed than X-ray absorption spectroscopy (XAS) due to limitations in measurement equipment. Therefore, *ab-initio* simulations play a crucial role; however, there are relatively few *ab-initio* codes designed for simulating XES. We have focused on this difficulty and found the new methodology to simulate XES for light-element materials.

In this study, we evaluate a new methodology for simulating XES of light-element materials

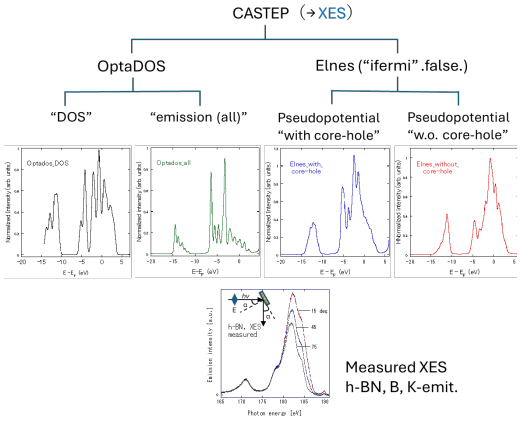


Fig.1: Schematic comparison of the applications of ELNES and OptaDOS for XES, and their treatment of core-hole effects.

through a series of material calculations using the facilities of the Supercomputer Center, ISSP. The methodology involves applying CASTEP's conventional ELNES [2] approach to XES simulations, while neglecting core-hole effects. To verify this approach, we compare the XES results obtained using our methodology with those from OptaDOS [3] and assess the impact of core-hole effects in light-element materials, which is shown schematically in Fig.1. Additionally, we compare both simulation

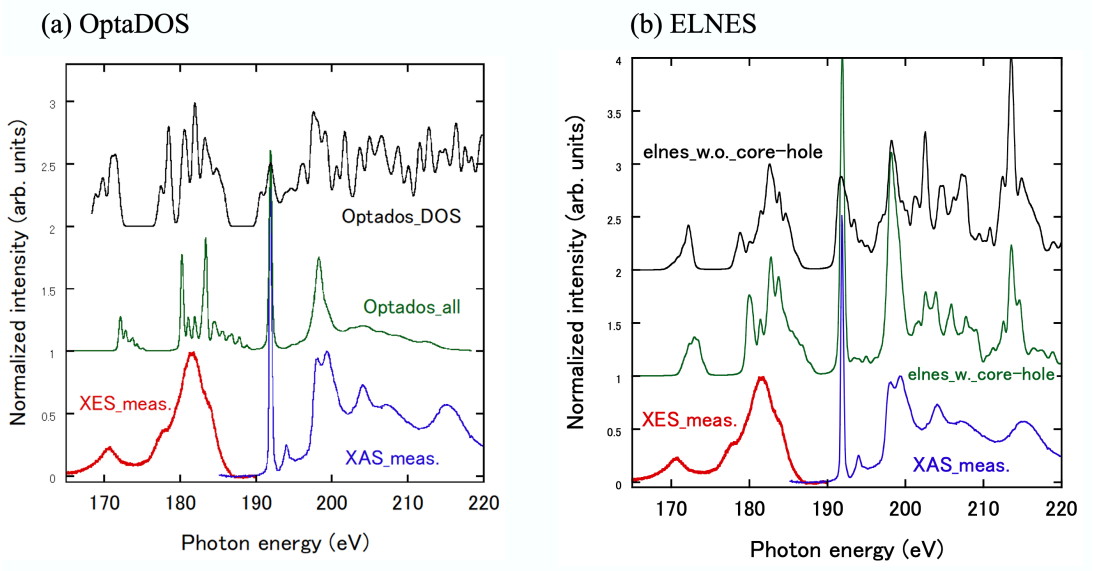


Fig.2: Measured and calculated XES and XAS spectra near the B K-edge of h-BN powder. In both (a) and (b), the red and blue lines indicate the measured XES and XAS, respectively. The green and black lines represent the calculated XES or XAS spectra. (a) shows the simulation results obtained using the OptaDOS method, while (b) shows those using the CASTEP-ELNES method. CASTEP-ELNES method without core-hole effect showed the good agreement with experimental XES spectra. The energy axes of the calculated spectra near the Fermi edge were shifted to almost coincide with the measured spectra.

results with experimental data to evaluate the accuracy and validity of our methodology. For some light-element material, we confirmed that our methodology successfully reproduces the experimental XES spectra. Figure 2 shows the measured and calculated XES and XAS spectra near the B K-edge of h-BN powder as example of our calculations. This study is currently under review [4].

References

[1] A. Meisel, G. Leonhardt, R. Szargan, “X-ray spectra and chemical binding” Springer-Verlag, New York (1989).

[2] M. C. Payne, M. P. Teter, D. C. Allan, *et al.*, Rev. Modern Phys. **64**, 1045 (1992).

[3] A. J. Morris, R. J. Nicholls, C. J. Pickard, and J. R. Yates, Comput. Phys. Commun. **185**, 1477 (2014).

[4] M. Niibe, T. Nakashima, Y Saito, *et al.*, e-J. Surf. Sci. Nanotechnol. *under review.*

Clarification of adhesion mechanism at interface between plasma-treated fluoropolymer and CuO using DFT+U method

Yuji OHKUBO, Kota YAMAGUCHI, and Kouji INAGAKI
Graduate School of Engineering,
Osaka University, 2-1 Yamadaoka Suita, Osaka 565-0871

Polytetrafluoroethylene (PTFE) has very low relative dielectric constant and dielectric loss tangent is considered as a suitable dielectric of high frequency printed wiring boards. However, PTFE has low adhesion property, so adhering PTFE to copper foil is difficult. We have achieved generation of oxygen-containing functional groups and adhesion strength of 0.98 N/mm between PTFE and Cu when PTFE was Helium-plasma-treated at over 200℃ under atmospheric pressure [1]. The adsorption energies of fluorinated molecules with C–OH, C=O, C–OO˙ generated by plasma treatment on Cu(111) surface were calculated to investigate the functional groups that contribute to adhesion improvement [2]. However, X-ray Photoelectron Spectroscopy (XPS) spectra indicates that the copper foil surface is naturally oxidized to CuO by atmospheric oxygen. In this report, we calculate the adsorption energies of fluorinated molecules on the CuO(111) surface, taking into account the natural oxidation of the copper foil, and clarify the functional group that contributes to adhesion improvement.

The calculations were performed using the STATE (Simulation tool for atom technology) code based on Density functional theory (DFT) with plane-wave basis and ultra-soft pseudopotentials. The standard DFT fails to obtain the correct electronic structure of CuO due to the strong electron correlation and antiferromagnetic behavior. Therefore, in this study, we used the DFT+U method, which has been reported to accurately describe the structure of CuO by considering on-site Coulomb repulsion among localized d-d electrons by incorporating an extra energetic penalty for delocalization. The exchange-correlation functional used was the generalized gradient approximation (GGA) based on the Perdew–Burke–Ernzerhof (PBE) formulation. The wave function and the charge density of cutoff energies were 36 Ry and 400 Ry, respectively. K point mesh was 9 × 9 × 9 when CuO bulk is calculated.

The adsorption energy (E_{ads}) per molecule was calculated from the relation

$$E_{ads} = (E_{surf} + E_{mol}) - E_{mol/surf} \quad (1)$$

where E_{surf} is the energy of the naked surface slab; E_{mol} is the energy of the isolated fluorinated molecules; $E_{mol/surf}$ is the total energy of the adsorbate–substrate system.

Transition state energies (E_a) were calculated using the CI-NEB method to determine the activation energies of various adsorption reactions. The activation energies (E_{act}) were calculated using the following equation.

$$E_{act} = E_a - E_{ini} \quad (2)$$

Table. 1. E_{ads} of fluorinated molecules on CuO(111) surface and E_{act} of various reactions.

	E_{ads} [eV]			E_{act} [eV]
	Adsorption site			
molecule	Cu_{3c}	Cu_{4c}	O_{3c}	
CF_3–CF_3	0.00	0.00	0.00	-
CF_3–CF_2–OH	0.08	-	0.50	-
CF_3–CF=O	0.00	0.00	0.00	-
CF_3–CF_2–OO˙	0.65	0.14	0.08	-
CF_3–CF_2˙	-	-	2.37	-
CF_3–CF_2–O˙	1.79	-	-	-
CF_3–CF_2˙ + F	-	-	0.87	2.39
CF_3–CF_2–O˙ + H	1.31	-	-	0.00
CF_3–CF_2–O˙ + O	0.83	-	-	1.15

Table. 2. E_{ads} of fluorinated molecules on nonstoichiometric CuO(111) surface.

molecule	E_{ads} [eV]
CF_3–CF_3	0.00
CF_3–CF_2–O˙ + H	1.66
CF_3–CF=O	0.14
CF_3–CF_2–OO˙	2.29
CF_3–CF_2–O˙	3.23

where E_{ini} is the energy of the initial state.

Table 1 shows the calculated E_{ads} of fluorinated molecules on CuO(111) surface and E_{act} of various reactions. The [+] in **Table 1** indicates that the F, H, or O atoms in the fluorinated molecule dissociated and adsorbed on the CuO(111) surface.

CF_3–CF_3 was not adsorbed at either site (E_{ads} = 0 eV). In addition, when the F atom dissociates from CF_3–CF_3 and CF_3–CF_2˙ adsorbs, the activation energy is very large, indicating that CF_3–CF_3 cannot adsorb on the CuO(111) surface. This is consistent with the experimental result that untreated PTFE cannot adhere to copper foil[1]. The adsorption energies of fluorinated molecules with oxygen-containing functional groups (C–OH, C=O, C–OO˙) introduced by plasma treatment are all lower than 1 eV, indicating that they do not contribute significantly to adhesion. On the other hand, the adsorption energy of CF_3–CF_2–O˙ was as high as 1.79 eV. When the H atom dissociates from CF_3–CF_2–OH or the O atom dissociates from CF_3–CF_2–OO˙ and CF_3–CF_2–O˙ adsorbs, the activation energies are 0.00 eV and 1.15 eV, respectively. These reactions are likely to proceed under the thermocompression conditions (320°C) used to bond the plasma-treated PTFE and copper foil [1]. Therefore, –OH and –OO˙ are thought to contribute to adhesion improvement by dissociating and adsorbing H and O atoms during thermal compression.

The adsorption energy of CF_3–CF_2˙ was the highest at 2.37 eV. The adsorption state of CF_3–CF_2˙ on a stoichiometric CuO(111) surface is equivalent to that of CF_3–CF_2–O˙ on a nonstoichiometric CuO(111) surface with an oxygen vacancy. Since the adsorption energy is expected to increase significantly when oxygen vacancies exist on the CuO(111) surface, the adsorption energy on the nonstoichiometric CuO(111) surface was also calculated.

Table 2 shows that the adsorption energy increases significantly if oxygen vacancies exist on the CuO(111) surface. Oxygen vacancies are thought to be created by diffusion of oxygen atoms into the bulk (Cu or Cu_2O layer) through thermal compression [3].

References

[1] M. Nishino et al., *RSC adv.*, **13** (2023) 25895–25903.

[2] 西野実沙 他, 日本接着学会 第 60 回年次大会講演要旨集 (2022) 50–51.

[3] S. Y. Lee et al., *Appl. Surf. Sci.* **206** (2003) 102–109.

Ab-initio study on phonon localization and phonon-assisted electron transport in multilayer 2D materials

Kenji TSURUTA, Kosuke TAKAHASHI, Ryusei TERASAKA, Yuri FUKAYA, Masaaki MISAWA,[a] and Satoshi OHMURA[b]
Department of Electrical and Electronic Engineering, Okayama University, Okayama 700-8530, Japan
[a] *Department of Intelligent Mechanical Engineering, Fukuoka Institute of Technology, Fukuoka 811-0295, Japan*
[b] *Department of Civil and Environmental Engineering, Hiroshima Institute of Technology, Hiroshima 731-5193, Japan*

The current operating frequency of telecommunication devices is in the GHz band and, with increasing demand for communication, the range expected will be toward THz regime in the future. The objective of this research is thus to investigate and design materials for devices operating in the THz band. Specifically, by introducing defects in a bilayer structure of graphene and boron nitride (BN), we aimed to control the localization of phonons by using defects as channels. We also investigated a phonon-induced electron transport between carbon nanotubes (CNTs) and boron nitride nanotubes (BNNTs) in CNTs and BNNTs heterostructures. Ultrafast photo-induced charge transfer from CNTs to BNNTs through electron channels and the subsequent formation of radial phonons at the interface of van der Waals heterostructures has been demonstrated through ultrafast time-resolved electron diffraction measurements [1].

In this study, first-principles calculations based on density functional theory were performed using the Vienna Ab initio Simulation Package (VASP) and Phonopy [2] to perform phonon analysis. Simulation models of graphene and BN bilayer structures and CNTs and BNNTs heterostructures were created and the phonon dispersion relations were calculated by VASP and Phonopy using these models as inputs to analyze each vibrational mode.

The results of phonon analysis show that the introduction of defects in the graphene resulted in localized phonon modes in the BN layer underneath the defects [3], which may lead to turning on/off the localization of phonon states. In the study of CNT and BNNT heterostructure, we compared the electronic band structure at the ground state with that for the structure where the BNNT layer was displaced according to phonon modes excited with large out-of-plane displacement. We found that by exciting the phonon mode, the electronic band of the BNNT shifts to the lower energy side and overlaps with the near-ultraviolet absorption band of the CNT, allowing electrons to undergo interlayer transition. Also, the wave functions of the shifted bands were found to spatially overlap between CNTs and BNNTs. As a typical case among the transfer mode assisted by the phonon excitations, figure 1 shows a CNT (20,0) – BNNT (29,0) heterostructure subjected to one of the phonon modes as well as the wave function distribution overlapping between CNT and BNNT.

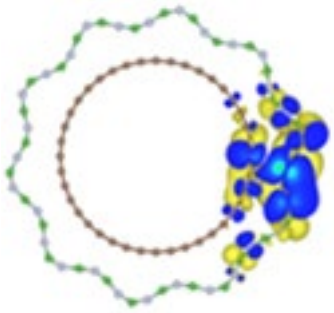


Fig. 1 Wave function in a CNT (20,0) – BNNT (29,0) heterostructure subjected to a phonon mode.

References

[1] Y. Saida *et al.*, *Nat. Commun*. **15**, 4600 (2024).
[2] A. Togo *et al*., *J. Phys.: Condens. Matter* **35** ,353001 (2023)
[3] K. Takahashi *et al.*, in *Abstract Book of the 10th International Symposium on Surface Science (ISSS-10)*, 3P31 (2024).

Structural analysis of metal oxide quasicrystal thin films

Junji YUHARA

School of Engineering, Nagoya University,

Furo-cho, Chikusa-ku, Nagoya, Aichi 464-8603

We have studied metal oxide quasicrystal ultra-thin films [1] using massively parallel computer simulations. This year, we focused on the structural analysis of honeycomb structure ultrathin Ce-Ti-O films on Pt(111) [2]. The density functional calculations were conducted using VAPS 5.4.4.

After deposition of 0.5 ML Ce and 0.8 ML Ti on Pt(111)/sapphire(0001), following with annealing in oxygen atmosphere and vacuum, an arrangement of dodecagonal clusters, which consists of triangles and squares marked in white, were locally observed in STM image (Fig. 1). In addition, there are some purple triangles and green trapezoids which have an unequal distance to the clusters marked in white, leading it to be recognized as OQC-related structure.

For the OQC-related structure of the ultrathin Ce-Ti-O film, Ce corresponds to Ce^{3+}. Titanium appears as Ti^{2+} ions, as the XPS and XAS spectra indicate. The elemental atomic composition was determined based on the experiment, proposing a low-density model, as shown in Fig. 2. This model's stability and STM simulation are calculated using VASP. Surface atomic density is estimated through XPS and Rutherford backscattering spectroscopy.

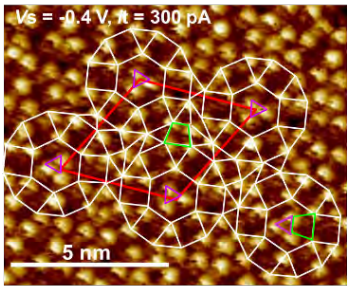


Fig.1: STM image of OQC-related structure of ultra-thin Ce-Ti-O film.

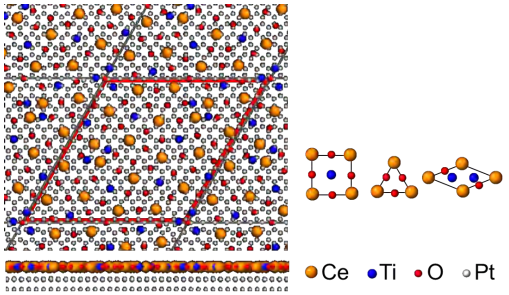


Fig.2: Schematic structural model of OQC-related structure of ultra-thin Ce-Ti-O film.

References

[1] J. Yuhara, K. Horiba, R. Sugiura, X. Li, T. Yamada, Phys. Rev. Mater. **4**, 103402 (2020)

[2] X. Li, S. Yamada, Y. Yamada, M. Yoshida, Y. Hashimoto, T. Matsushita, W. Ma, E. Gaudry, and J. Yuhara, J. Phys. Chem. C **128**, 20238 (2024)

Theoretical study of work function and band gap of double-perovskite

Kazume NISHIDATE
Graduate School of Science and Engineering, Iwate University
4-3-5 Ueda, Morioka, Iwate, 020-8551

In our course of study, we found that the origin of the optical band gap of 1.0 eV of the double perovskite Ba_2PrBiO_6 may originate in its defect structure, namely, Pr_{Bi} surface defect[1]. This year, we mainly focus on the surface electronic state of TiO_2 rutile photocatalyst as a reference, since its work function and electronic structures are fairly well-known compared to those of the double perovskite, and therefore, it gives us a guide to construct the model systems. We employed GGA with U method to suppress the underestimation tendency of the band gap. We constructed (110) surface slab consisting of four 3×3 layers of TiO_2 with the vacuum region of 20 Å.

When we apply the U= 10 eV, the calculated band gap, 2.9 eV, is almost equal to that of the experimental one, 3 eV. However, the crystal field energy splitting of the t_{2g} and the e_g becomes somewhat blurred, consistent with the reported result[2]. Next, we evaluated projected DOS for each atom of layers. We found that the DOS of the topmost surface oxygen shows similar energy distribution as that of the oxygen in the TiO_2 bulk. On the other hand, the 3d state of the topmost Ti is significantly modified due to the lack of the surrounding oxygen atoms breaking its crystal field symmetry. The projected DOS for the Ti at the subsurface shows a similar energy distribution as that of the Ti in the TiO_2 bulk system. Therefore, we can conclude that the electronic structure of (110) TiO_2 slab already becomes bulk-like in the subsurface region. Next, we studied

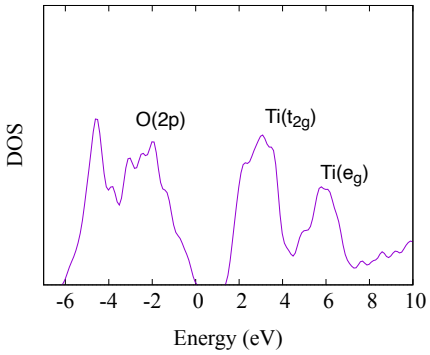


Figure 1: DOS of Rutile (110) surface

surface defects. When we introduce the V_O by subtracting an oxygen atom from the topmost layer, we observed defect-induced states 0.66 eV above the VBM (valence band maximum). The interstitial Ti at the subsurface, Ti_i, creates defect induced states 0.35 eV above the VBM. Adsorption of hydrogen on the topmost oxygen, OH defect, creates an energy state just above the VBM. We are currently inspecting the validity of our findings compared with the reported experimental results.

References

[1] K. Nishidate, M. Matsukawa, A. Matsushita, Y. Li, D.C. Roy, and M. Hasegawa,: Surf. and Int. **24**, 103914 (2024).

[2] M. E. Arroyo-de Dompablo, A. Morales-Garcia, and M. Taravillo, J. Chem. Phys, **135**, 054503 (2011)

Development of a multi-GPU quasiparticle self-consistent *GW* calculation code

Masao OBATA

Institute of Science and Engineering, Kanazawa University, Kanazawa, Ishikawa 920-1192

The quasi-particle self-consistent *GW* (QSGW) method is a powerful approach for first-principles electronic structure calculations, surpassing the one-shot G_0W_0 approach [1]. However, its computational cost is significantly higher due to the requirement for off-diagonal elements of the self-energy Σ, unlike G_0W_0 calculations. Additionally, the self-consistent procedure demands considerable computational time. The main computationally intensive parts are the computation of Σ and screened Coulomb interaction W, which scale with the fourth power of the system size and the square of the k-points.

In this study, we applied a multi-GPU implementation to the QSGW code ecalj [2] to extend its application range by accelerating computation. Our approach utilizes GPU-accelerated math libraries with OpenACC programming. The math libraries are accessed through wrapper functions providing a unified interface for GPU and CPU versions. These wrapper functions, implemented using Fortran module coding and the C preprocessor, enable easy switching between GPU and CPU computations. This implementation avoids code duplication, ensuring that most of the code is common to both CPU and GPU versions. By utilizing math libraries, we have facilitated the implementation of mixed-precision calculations such as TensorFloat-32 (TF32). As a benchmark, for an interface system with 40 atoms (Type II superlattice $(InAs)_{10}/(GaSb)_{10}$), the computation of Σ and W using 4 GPUs was completed in 2.9 hours (0.9 hours with TF32). In comparison, the same calculation on a CPU (512 cores) required 34 hours, achieving a speedup of 12 times and 38 times with TF32. Although QSGW calculations consume significant memory due to the expansion coefficients of W and wavefunction products, the introduction of batch partitioning methods enables robust calculations for large-scale systems.

References

[1] M. van Schilfgaarde et al., Phys. Rev. Lett., 96, 226402 (2006).

[2]ecalj:https://github.com/tkotani/ecalj

Theoretical Study on Electronic Properties in New Nanoscale Surfaces and Interfaces

Katsuyoshi KOBAYASHI
Department of Physics, Ochanomizu University
2-1-1 Otsuka, Bunkyo-ku, Tokyo 112-8610

Recently, there has been a report of spirally grown graphene [1]. This year, we calculated the electronic state and electron transmission properties of spirally structured graphene. Figure 1 shows a structure of a finite-width graphene which changes its direction by 120 degrees. A triangular structure is inserted between two finite-width graphenes. Figure 2 shows an energy band structure of a spiral structure which has this triangular structure as the unit cell. The tight-binding method is used. Only the transfer energy between nearest-neighbor atoms is considered. The unit of energy is the transfer energy. The figure shows the case where the triangular unit cell consists of 9 carbon atoms. This corresponds to the width of 6 atoms of the straight graphene. The energy bands are symmetrical with respect to the zero energy line with a phase shift by π. This result can be understood from the triangular structure in Fig. 1.

The atoms in a triangle are divided into A and B sublattices. We assign the boundary atoms as A sublattices. Inside the triangle, A sublattice atoms have only B sublattice atoms next to them, and vice versa. In a spiral structure, which is a periodic structure of triangles, the boundary A sublattice atoms have adjacent A sublattice atoms in the neighboring triangles. Therefore, in the tight-binding equation, if the sign of the amplitudes of the A sublattice atoms of one triangle and that of the B sublattice atoms of the neighboring triangles are simultaneously inverted, it is also the solution with the energy having the reverse sign. In this case, a phase mismatch arises between the boundary A sublattice atoms of adjacent triangles, which is resolved by the Bloch phase π.

Figure 3 shows the electron transmission property calculated as a function of energy. The transmission probability between two straight graphenes through a spiral graphene is calculated. The rotation angle of the spiral graphene is that of 10 triangular unit cells. The transmission probability is close to zero in the band gap region of the energy bands of the spiral graphene. Outside the band gap, the transmission probability is close to unity. It implies that electrons travel well through the spiral structure. First-principles calculations of wider graphene are found in Ref. [2].

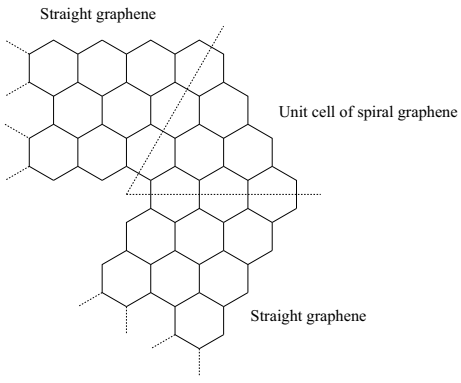


Figure 1: Atomic structure of a graphene spiral structure. The figure shows a triangular unit cell of a spiral graphene connected to two straight graphenes.

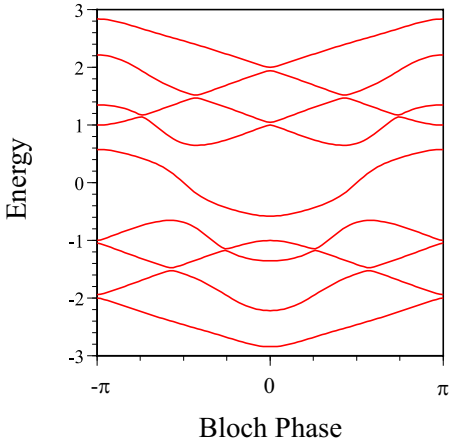


Figure 2: Band structure of a spiral graphene.

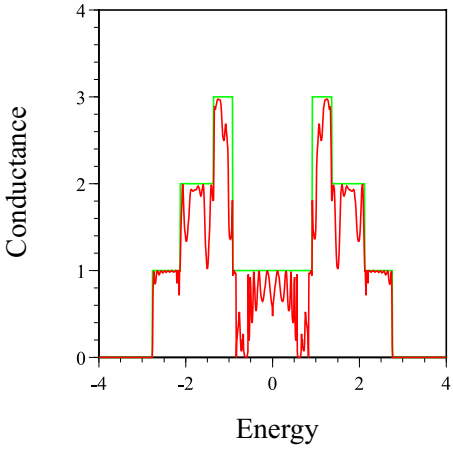


Figure 3: Electrical condunctance through a spiral graphene. The unit of conductance is $2e^2/h$. The green line shows the number of conduction channels.

References

[1] H. Sun, X. Kong, H. Park, F. Liu, Z. Lee, F. Ding, Adv. Mater. **34** (2022) 2107587.

[2] Z. Zhou, L. Yan, X.-M. Wang, D. Zhang, J.-Y. Yan, Results in Phys. **35** (2022) 105351.

Photocatalytic versus Thermal Reaction Pathways of CO_2 Methanation over Single Ru–Ni/ZrO_2 Catalyst Proved by DFT Calculations

Masahito Sasaki, Keisuke Hara, Tomoki Oyumi, and Yasuo Izumi

Graduate School of Science, Chiba University, Yayoi 1-33, Inage-ku, Chiba 263-8522

Photocatalytic CO_2 reduction into fuels and/or valuable chemicals creates new C neutral cycle. Major problem to apply this technique in sustainable society is slow formation rates of fuels and/or value-added chemicals that are governed by photon number of the light reaching the earth [1].

In this report, the formation rates were increased both by increasing irradiated photons and by effective additive to photocatalyst. The effect of irradiated UV–visible light intensity on photocatalysis was evaluated. We previously reported one of the best photocatalytic CO_2 methanation activity using Ni/ZrO_2 photocatalyst: 0.98 mmol h^{-1} g_{cat}^{-1} irradiated by UV–visible light @186 mW cm^{-2} [2]. Therefore, the effect of single Ru doped onto Ni/ZrO_2 photocatalyst on CH_4 formation rate was also evaluated.

In the evaluation, reaction pathway including the activation energy was important based on density functional theory calculations using Vienna Ab Initio Simulation Package code version 6.4.1. The supercomputer of ISSP was ultimately essential for the searches of reaction pathway for each step from CO_2 to CH_4 over the composite surface of the best photocatalyst using climbing-image nudged elastic band method mostly owing to the CPU comprising more than 128 cores at ISSP.

When the UV–visible light intensity was increased from 186 mW cm^{-2} [2] to 713 mW cm^{-2}, the CO_2 methanation rate increased from 0.98 to 2.9 mmol h^{-1} g_{cat}^{-1} using Ni/ZrO_2 photocatalyst. Furthermore, by doping single Ru (1.0 wt %) to Ni/ZrO_2, the CO_2 methanation rate even increased to 8.9 mmol h^{-1} g_{cat}^{-1} @713 mW cm^{-2}.

DFT calculation results were summarized in Schemes 1 and 2 using single Ru–Ni/ZrO_2 photocatalyst (Panels A and B) in comparison to Ni/ZrO_2 photocatalyst (Panel B′). Scheme 1 corresponded to photocatalytic CO_2 methanation irradiated at 186 mW cm^{-2} or photocatalyst cooled in water bath irradiated at 568 mW cm^{-2}. The activation energy was the highest: 1.17 eV from adsorbed CO_2 to OCOH species at O vacancy site at ZrO_2 surface [3] using both single Ru–Ni/ZrO_2 and Ni/ZrO_2 (Scheme 1B and B′). In fact, under these photocatalytic reaction conditions, photocatalytic CO_2 methanation rates were essentially equivalent either using single Ru–Ni/ZrO_2 or Ni/ZrO_2.

Scheme 2 corresponded to photocatalytic CO_2 methanation irradiated by UV–visible light at 713 mW cm^{-2}, without water cooling. Under the reaction conditions, the catalyst was heated by light energy and the charge separation and resulting red-ox reactions over ZrO_2 surface became negligible compared to thermal steps over Ru and/or Ni (Scheme 2A). Under such reaction conditions, single Ru atom on Ni nanocluster lattice adsorbed CO_2 (Scheme 2B(b) and (b′)) and facilitated the dissociation to CO and O (species c), whereas over Ni cluster surface free from Ru, the weakly-adsorbed CO_2 was much more difficult to dissociate (Scheme 2B′(b) and (c)). This accounted for the rate difference of 2.9 mmol h^{-1} g_{cat}^{-1} using Ni/ZrO_2 versus 8.9 mmol h^{-1} g_{cat}^{-1} using single Ru–Ni/ZrO_2 @713 mW cm^{-2}. The reaction pathway illustrated in Scheme 2A and B was also supported by predominantly adsorbed CO species over single Ru–Ni/ZrO_2 under UV–visible light (Scheme 2A(c–e)) observed by FTIR.

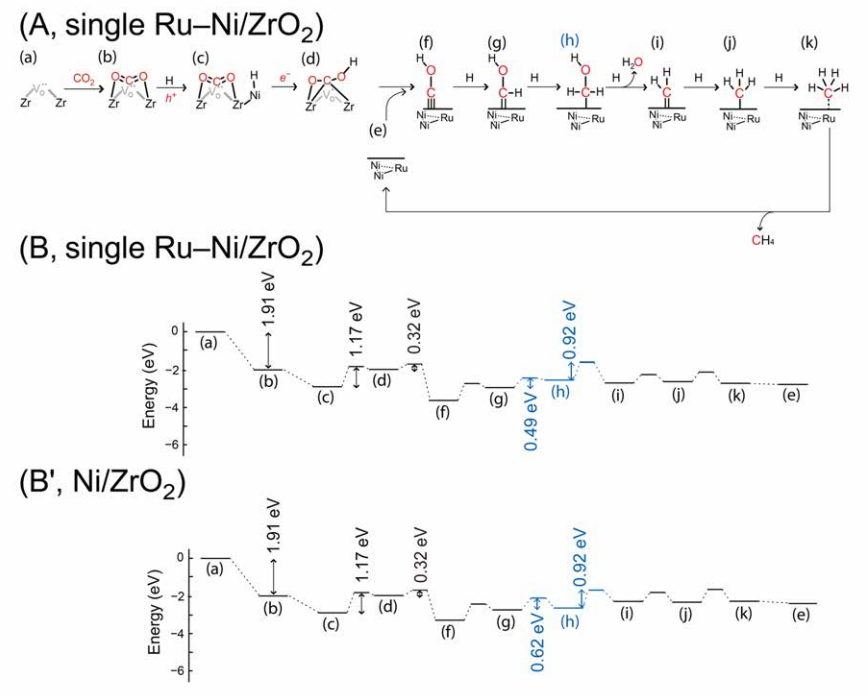
References

[1] T. Loumissi, R. Ishii, K. Hara, T. Oyumi, I. Abe, C. Li, H. Zhang, R. Hirayama, K. Niki, T. Itoi, and Y. Izumi, *Angew. Chem. Int. Ed.* **63**, e202412090 (2024).

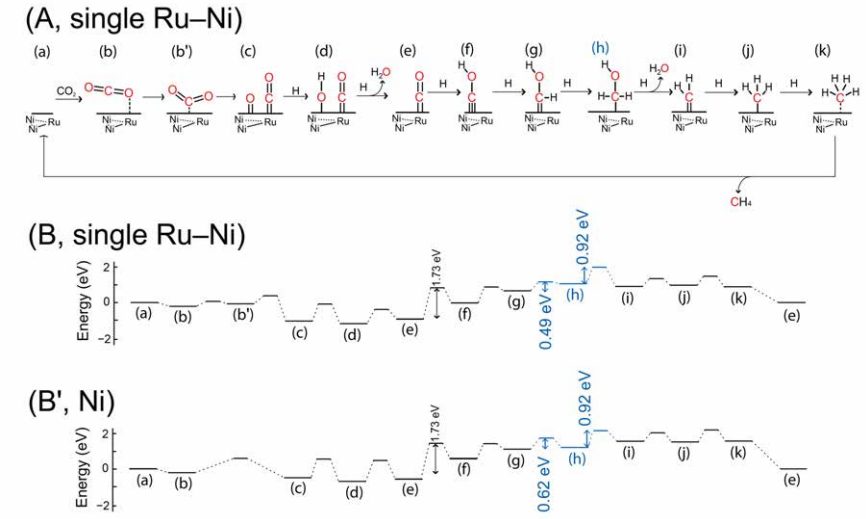
[2] H. Zhang, T. Itoi, T. Konishi, and Y. Izumi, *Angew. Chem. Int. Ed.* **60**, 9045–9054 (2021).

[3] K. Hara, M. Nozaki, T. Hirayama, R. Ishii, K. Niki, and Y. Izumi, *J. Phys. Chem. C*, **127**, 1776–1788 (2023).

Scheme 1. Proposed photocatalytic reaction pathway and corresponding free energy calculations of CO_2 photoreduction to proceed over (A, B) single Ru–Ni/ZrO_2 and (B') Ni/ZrO_2.



Scheme 2. (A) Proposed thermal reaction pathway and corresponding free energy calculations of CO_2 reduction using (B) Ni/ZrO_2 and (B') single Ru–Ni/ZrO_2.



First-principles study of multi-orbital and multi-layer compounds

Hirofumi Sakakibara

Faculty of Engineering, Tottori University, Tottori, Tottori 680-8552

Since the discovery of the Ruddlesden-popper type bilayer nickelate superconductor $La_3Ni_2O_7$ (Fig.1 (a)) [1], related studies and publications have explosively increased. One of this extreme scientific interest may originate the similarity with high-T_c cuprates, because the first example of such cuprates is the single layer Ruddlesden-popper type oxide. A clear similarity is that both compounds are strongly-correlated-electron systems since the main layer is formed by oxidized transition metal (Cu and Ni). On the other hand, the biggest difference is the number of active orbital degrees of freedom, namely, the minimum model of bilayer nickelate may consists of total four orbitals, the $d_{x^2-y^2}$ and $d_{3z^2-r^2}$ orbitals in each layer [2]. Our previous calculation using fluctuation-exchange approximation (FLEX) has shown that the superconducting symmetry in La3Ni2O7 is $s\pm$ with reversed sign between the bonding and anti-bonding bands like as iron-pnictide ones [2]. These bonding is formed by the $d_{3z^2-r^2}$ orbitals facing between the layers.

One of the problems in FLEX calculation is that the incompleteness of the treatment for electron-correlation. A complementary approach is the Density Matrix Renormalization Group (DMRG), in which the numerically exact solution can be obtained. However, DMRG is much consuming about the computational resource, the model should be much simplified compared to our original two-dimensional and multiorbital-multilayer model. To overcome this difficulty, we have derived a one-dimensional ladder model to mimic the bilayer model. In the first paper, we have calculated the two-orbital Hubbard ladder model in which all of the interorbital interactions are omitted (only the intraorbital interaction "*U*" is activated). The conclusion throughout the analysis of spatial pair correlation function is that this model is favorable for the superconductivity. However, although this model may capture the essence of superconducting transition in La3Ni2O7, there remain a simple problem that whether if the interorbital interactions such as Hund's coupling change the conclusion? To clarify this point, we have additionally derived a *t-J* ladder model, having the lower computational costs to include Hund's coupling. The conclusion is that superconductivity is favorable in this model, and the Hund's coupling may stabilize the superconductivity [4].

Another significant problem is how to theoretically predict a new bilayer superconductor. Until now, all of the bulk nickelates need to be pressurized to exhibit superconductivity (exceptions are the thin-film

nickelates, not only the infinite layered ones [5] but also the Ruddlesden-popper type ones [6]). Therefore, to discover a nickelate superconductor free from pressure is a good aim. One well-known empirical rule is that the chemical bonds connecting the NiO2 layer should be straight if the superconductivity occurs. To clarify this hypothesis, we have proposed an oxychloride nickelate $Sr_3Ni_2O_5Cl_2$ (Fig. 1(b))[7] and theoretically evaluated the possibility of supercondutivity. Firstly, we have determined the energetically most stable structure at ambient pressure (= 0 GPa external pressure) using VASP code. The obtained structure has *I*4/*mmm* space group symmetry. Subsequently, we have calculated the phonon dispersion (Fig. 1 (c)) and checked the absence of imaginary mode, which means that the *I*4/*mmm* structure of $Sr_3Ni_2O_5Cl_2$ is dynamically stable at ambient pressure. This theoretical prediction about the symmetry of the crystal structure has been experimentally proven by Yamane *et al.* [8]. We have also constructed a low-energy tight-binding model through the maximally localized Wannier function, including the derivation of onsite interaction parameters using constrained Random Phase Approximation (cRPA) method. We have also applied FLEX approximation to this model to conclude that $Sr_3Ni_2O_5Cl_2$ probably exhibit the superconductivity. Unfortunately, there is still no report that superconductivity is observed in $Sr_3Ni_2O_5Cl_2$. The absence of superconductivity may be because of the stacking faults between layers [8]. The experimentally estimated band gap is much small, implying that $Sr_3Ni_2O_5Cl_2$ is intrinsically metallic, consistent with our first-principles calculation.

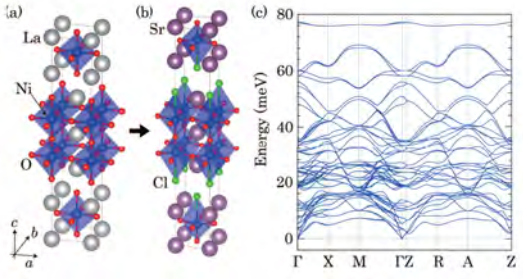


Fig. 1: crystal structure of (a)$La_3Ni_2O_7$ and (b)$Sr_3Ni_2O_5Cl_2$, and phonon dispersion of the latter (cited from Ref. [7]).

References

[1] H. Sun *et al*., Nature (London) **621**, 493 (2023).

[2] H. Sakakibara, N. Kitamine, M. Ohi, and K. Kuroki, Phys. Rev. Lett. **132**, 106002 (2024).

[3] T. Kaneko, H. Sakakibara, M. Ochi, K. Kuroki, Phys. Rev. B **109**, 045154 (2024).

[4] M. Kakoi, T. Kaneko, H. Sakakibara, M. Ochi, and K. Kuroki, Phys. Rev. B **109**, L201124 (2024).

[5] D. Li et al., Nature (London) **572**, 624 (2019).

[6] E. K. Ko et al., Nature (London) **638**, 935 (2025).

[7] M. Ochi, H. Sakakibara, H. Usui, and K. Kuroki, Phys. Rev. B **111**, 064511 (2025).

[8] K. Yamane et al., Acta Cryst. **C81** (2025).

A theoretical study on an oxidation process at a metal surface

Satoshi Hagiwara

Center for Computational Sciences,

University of Tsukuba, Tennodai, Tsukuba 277-8581

Corrosion reaction at the metal/water interface is one of the significant chemical reactions for controlling material lifetimes. During corrosion reaction, the breakdown of protective oxide passivation layers on host materials occurs due to the migration of environmental Cl ions through the passivation layer. The accumulated Cl ions at the interface mechanically break a metal/oxide junction. Therefore, we carried out the DFT calculations using the Al(111)/α-Al_2O_3(0001) interface to reveal the details of the Cl ion insertion [1]. Moreover, we developed the surface stress calculation method under a finite bias voltage using the effective screening medium (ESM) method [2] and applied it to the Al(111) surface [3]. Here, we explain the results of surface stress.

We performed all calculations by using the open-source package QMAS (Quantum MAterials Simulator) code [4]. To simulate the bias-voltage dependence of surface stress, we combined the macroscopic stress and stress density calculation methods with ESM, which is easily done through the Green's function satisfying the Poisson equation. In this study, we used the vacuum/slab/metal boundary condition of ESM.

The result of macroscopic surface stress quadratically depends on the bias-voltage, which agrees with that of thermodynamic Gokhshtein's equation [5]. The local stress analysis using stress density reveals that the outermost layer behaves as a capacitor. The inner layer contribution to the bias-voltage dependence of surface stress cannot be neglected. Thus, enough thickness of the surface slab is necessary to determine the surface stress precisely. This method will be useful to discuss the mechanical effect on the passivation film breakdown.

References

[1] S. Hagiwara, and M. Otani et al., Corr. Sci. under review. [2] M. Otani and O. Sugino, Phys. Rev. B **73**, 115407 (2006). [3] S. Hagiwara, S. Ishibashi, and M. Otani, Phys. Rev. B **110**, 155409 (2024). [4] https://qmas.jp/. [5] A. Y. Gokhshtein, Russ. Chem. Rev. **44**, 921 (1975).

First principles study on the thermoelectric properties of goniopolar compounds

Hidetomo USUI

Department of Applied Physics,

Shimane University, Nishikawatsu-cho, Matsue, Shimane 690-8504

Goniopolar compounds exhibit both p-type and n-type characteristics depending on direction. Due to this anisotropic nature, these compounds have been investigatedas candidates for transverse thermoelectric materials. For example, the goniopolar thermoelectric material Re_4Si_7 exhibits a relatively high figure of merit $Z_{xy}T$ ~ 0.7 [1]. Mg_3Bi_2 is another goniopolar thermoelectric material, which shows $Z_{xy}T$ of 0.06 at 300K [2]. This value is not particularly high, indicating the need for further optimization.

In this study, we analyzed the thermoelectric performance of Mg_3Bi_2 using first-principles calculations to understand the origin of its relatively high performance. The Quantum ESPRESSO package [3] was used to calculate the electronic and phonon structures of Mg_3Bi_2. The electron relaxation time was evaluated by assuming electron-phonon scattering, using the EPW code [4]. We calculated the electrical resistivity, and the Seebeck coefficient within Boltzmann transport theory, using the calculated relaxation time.

The goniopolarity of Mg_3Bi_2 originates from its band dispersion around the Fermi level. Its band structure features both Dirac cone-like valence and conduction bands at the Γ point, as well as multi-valley bands near the L* point. We found that Mg_3Bi_2 exhibits a long relaxation time, which is favorable for thermoelectric performance. However, the Seebeck coefficient is relatively low due to the closed band gap.

We conclude that opening the band gap is essential to enhancing the Seebeck coefficient and improving transverse thermoelectric performance.

References

[1] M. R. Scudder *et al.*, Energy Environ. Sci. **14**, 4009 (2021).

[2] Y. Goto *et al.*, Chem. Mater. **36**, 2018 (2024).

[3] P Giannozzi *et al.*, J.Phys.:Condens.Matter **29**, 465901 (2017).

[4] H. Lee *et al.*, npj Comput. Mater. **9**, 156 (2023).

Impurity control of chalcogenides by surface-modification

Ken-ichi SHUDO

Fac. of Eng/Sci, Yokohama Nat'l Univ.

Tokiwadai 79-5, Hodogaya-ku Yokohama 2408501

We measured electronic states of layered material such as chalcogenides and topological insulators, experimentally by means of ultraviolet photoemission spectroscopy (UPS) and metastable-atom electronic spectroscopy (MAES). While the spectra of the former method involve the density of state near the surface with a few nanometer depth, those of the latter the spectra only reflect the electronic states whose wavefunctions protrude into vacuum. Thus, we calculated the electronic states of MoS_2 with impurity and defects in the top-most layer, and that of Bi_2Se_3. Several layers of those materials stand for the slab model, and the electronic states are obtained using a first-principle density functional package Vienna Ab initio Simulation Package (VASP). The top panel in Fig.1 indicates the slab of $TiSe_2$ with vacuum layer at the right-hand. The local density in each slice parallel to the surface was projected, into energy distribution as shown in main panel of Fig.1. The special localizations specific to the near-surface region and to the vacuum region are both going to be discussed with the basis of the experimental data.

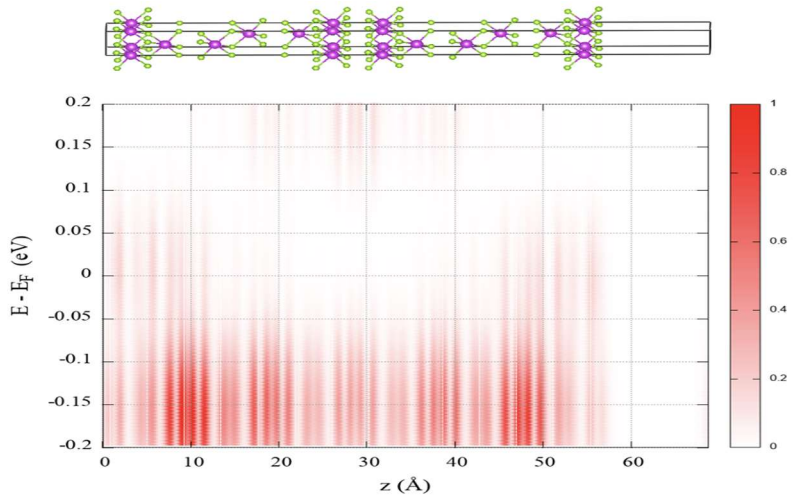


Fig. 1: Spatial distribution of density of state near the surface of Bi_2Se_3. This slab is the case without any defect.

First-principles lattice defects engineering for atomic-scale multiferroics

Takahiro SHIMADA and Susumu MINAMI

Graduate School of Engineering, Kyoto University,

Kyoto daigaku-Katsura, Nishikyo-ku, Kyoto 616-8540

Recent advancements in nanotechnology have driven the need for functional materials that exhibit electromechanical responses at the atomic scale. In this context, this work investigates the electromechanical behavior of an isolated oxygen vacancy in a paraelectric oxide, $BaHfO_3$, using *ab initio* finite electric field calculations based on density functional theory (DFT). Our results unveil a previously unrecognized localized electromechanical phenomenon—negative electrostriction—centered around a single oxygen vacancy.

We models a neutral oxygen vacancy in $BaHfO_3$ using the 5 x 3 x 3 supercell including a relatively large number of atoms up to 225. We simulate the structural and electronic properties under applied finite electric fields up to 15 MV/cm using the VASP code [1] based on the modern theory of polarization [2] with the supercomputers. We explicitly include the effect of electric field on force and stress in order to obtain the equilibrium structure under finite electric fields. The results indicate that, although the pristine $BaHfO_3$ does not exhibit a net polarization, the introduction of an oxygen vacancy leads to a local dipole moment and strain distribution under the electric field. Remarkably, the strain response along the field direction is compressive (negative), a stark contrast to typical positive electrostriction observed in conventional dielectrics.

Further detailed analysis reveals that this negative electrostriction originates from the localized defect states and associated electrons near the vacancy. Under the electric field, these electrons shift in the direction opposite to the field, creating an asymmetric charge distribution. This in turn causes an uneven displacement between the adjacent hafnium atoms, generating localized compressive strain. The calculated electrostrictive coefficients (Q_{11} = −0.040 m^4/C^2, Q_{12} = 0.019 m^4/C^2) further confirm the negative electrostriction nature, and the local dielectric permittivity near the vacancy is estimated to be ~129—substantially larger than the host material (~43).

This work emphasizes the engineering implications of these findings. First, it shows that oxygen vacancies—commonly treated as passive defects—can be reinterpreted as active electromechanical elements at the atomic scale. Second, since oxygen vacancies can be

selectively introduced and manipulated (e.g., via ion irradiation or scanning probe techniques), they present a viable route for constructing ultra-compact and tunable electromechanical devices. Furthermore, unlike conventional materials that require complex processing to achieve miniaturization, the approach demonstrated here relies solely on point defect engineering.

This work has been published in *Journal of Applied Physics* [3].

References

[1] G. Kresse and J. Hafner, Phys. Rev. B **48**, 13115 (1993).

[2] I. Souza, J. Íñiguez, and D. Vanderbilt, Phys. Rev. Lett. **89**, 117602 (2002).

[3] Y. Ikeda, S. Minami, and T. Shimada, J. Appl. Phys. **136**, 214101 (2024).

First-Principles calculation of transverse thermoelectric conductivity in the $D0_3$-type Heusler compound Fe_3Si

Susumu MINAMI, Takahiro SHIMADA

Department of Mechanical Engineering and Science,

Kyoto University, Nishikyo-ku, Kyoto 615-8540

The anomalous Nernst effect (ANE), which generates a transverse voltage from a longitudinal temperature gradient in magnetic materials, has gained renewed interest for energy harvesting applications[1]. The intrinsic component of ANE can be understood through the Berry phase concept, with topological electronic structures such as Weyl nodes and nodal lines inducing large Berry curvature. Fe_3Si is particularly promising due to its high Curie temperature (820 K[2]) and lack of rare or toxic elements. We performed first-principles calculations based on density functional theory using the VASP for the D03-type Heusler compound Fe_3Si. A Wannier function was constructed to calculate the Berry curvature and transverse thermoelectric (TE) properties. The anomalous Hall conductivity (σ_{xy}) and transverse TE conductivity (α_{xy}) were evaluated using Berry curvature formalism with 200×200×200 k-point sampling.

The calculated total magnetic moment was ~5.07 μB/f.u., and σ_{xy} and α_{xy} reached about 500 $\Omega^{-1}cm^{-1}$ and 1.5 $AK^{-1}m^{-1}$ at room temperature, consistent with experimental values[3,4]. With hole doping ($E = E_F$ - 0.22 eV), σ_{xy} exhibited a sharp peak reaching ~1500 $\Omega^{-1}cm^{-1}$, while α_{xy} increased to ~5 $AK^{-1}m^{-1}$. This value is comparable to other well-known ANE materials with topological electronic structures. We identified a clear correspondence between the nodal line network in Fe_3Si and large Berry curvature distribution in the Brillouin zone. The nodal lines form ring shapes on the $k_i = 0$ plane and connect near the X point. Our analysis revealed that the density of states composed of nodal lines (D_{NL}) shows peaks that directly correlate with enhanced transverse TE conductivity, specifically attributable to a "Van Hove singularity" in the D_{NL}.

Our first-principles study demonstrates that Fe_3Si exhibits α_{xy} of 1.5 $AK^{-1}m^{-1}$ at room temperature, which increases to ~5 $AK^{-1}m^{-1}$ with hole carrier doping[5]. From an experimental perspective, tuning the D_{NL} peak to the Fermi energy through chemical doping or external fields could lead to improved ANE performance in Fe_3Si-based materials.

References

[1] M. Mizuguchi and S. Nakatsuji, Sci. Tech. Adv. Mater. **20**, 262 (2019).

[2] Y. Nishino, S.-Y. Inoue, S. Asano, and N. Kawamiya, Phys. Rev. B **48**, 13607 (1993).

[3] Y. Hamada, et al.,, Appl. Phys. Lett. **119**, 152404 (2021).

[4] Y. Wang et al., Appl. Phys. Lett. **125**, 081901 (2024).

[5] S. Minami, S. Hogaki, and T. Shimada, Phys. Rev. Mater. **8**, 075403 (2024).

Atomic-level surface architecture of nanocellulose

Shuji FUJISAWA

Graduate School of Agricultural and Life Sciences ,

The University of Tokyo,Yayoi 1-1-1, Bunkyo-ku, Tokyo 113-8657

The surface molecular structure of nanocellulose has remained poorly understood, primarily due to the hurdles in resolving atomic-level details of its surfaces. Nuclear magnetic resonance (NMR) is a powerful method to unveil the surface structure, but conventional solid-state ^{13}C NMR faces a significant challenge stemming from its low sensitivity at natural abundance. Here, we present first detailed surface architecture of nanocellulose using dynamic nuclear polarization (DNP) enhanced solid-state NMR [1]. DNP-NMR can significantly enhance the detection of surface molecules and their dipolar interactions, enabling detailed analysis of the spatial distribution and substitution positions of the functional groups on the nanocellulose surface. Furthermore, we quantitatively characterized the molecular conformations present in the entire CNF and identified the preferred molecular conformation exhibited specifically on the nanocellulose surface, which was reinforced by molecular dynamics simulations and density functional theory calculations. his combined technique is applicable not only to P-CNF but also to various types of CNF previously reported, such as surface carboxylated- and sulphated-, and aminated-CNFs. Therefore, our approach fills a critical gap in understanding the surface structure and material properties of CNF, and thus can help tailor CNF properties for specific applications in materials science, biotechnology, environmental engineering, and beyond.

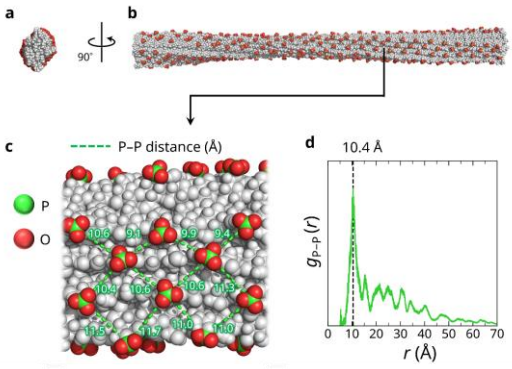


Fig. 1: Distance between phosphorus atoms on the surface of P-CNF. (a,b) Equilibrated structure of a CNF created by MD simulation. (c) enlarged view of the chemical structure (d) Radial distribution function between the phosphorus atoms

References

[1] D. A. Hall et al. Science **276**, 930 (1979)

Revisiting the conventional superconducting theory: Toward nearly uniform electron systems

Ryosuke AKASHI
National Institutes for Quantum Science and Technology

The first-principles calculation of superconducting transition temperatures has long been an intriguing goal in the materials science. Its applicability to phonon-mediated superconductors [1] has been recently improved with the first-principles Eliashberg theory [2, 3, 4] and density functional theory for the superconductors (SCDFT [5, 6, 7]). Its extension to electronic correlation effects such as charge and spin still remains difficult. To include the dynamical charge fluctuation (plasmon) effect one needs to faithfully execute the Eliashberg equation with full dependence of the electron self energy on the wavenumber and frequency, but it is numerically demanding. In the computationally cheaper counterpart, SCDFT, how to properly include the self energy with the formally static DFT is under debate, even in the uniform electron gas [9]. As particular interests are featured in the enhancement of superconductivity in nearly uniform electron systems [11], a efficient code for analyzing the superconducting properties for nearly uniform electrons is needed.

We developed a code to calculate the self energy efficiently for superconducting calculations in the uniform system, aiming at future extension to nearly-uniform cases. The self energy in the GW_0 approximation is defined as follows:

$$\Sigma(\mathbf{k}, i\omega) = -T\sum_{\nu}\int \frac{d\mathbf{q}}{(2\pi)^3} G(\mathbf{k}-\mathbf{q}, i(\omega-\nu))W_0(\mathbf{q}, i\nu), \tag{1}$$

with

$$G(\mathbf{k}, i\omega) = [1 - G_0(\mathbf{k}, i\omega)\Sigma(\mathbf{k}, i\omega)]^{-1} G_0(\mathbf{k}, i\omega),$$
$$G_0(\mathbf{k}, i\omega) = \frac{e^{i0^+\omega}}{i\omega - (k^2 - k_{\mathrm{F}}^2)/2}. \tag{2}$$

Here k_{F} denotes the Fermi wavenumber. To execute the Matsubara summation efficiently, we implemented a method using the intermediate representation [12], thanks to which the number of frequency grid points were reduced from $O(\beta)$ to $O(\log\beta)$ $(\beta = 1/T)$. Figure 1

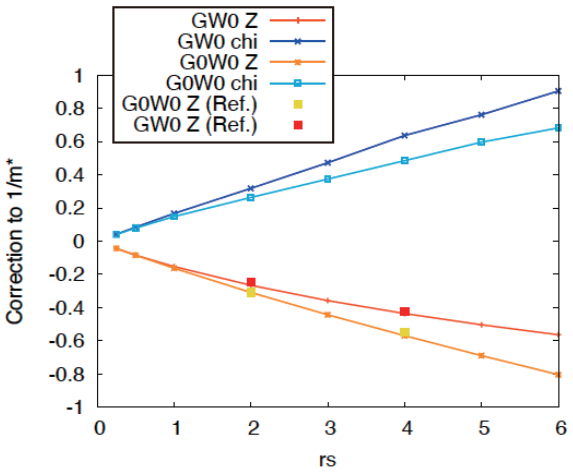


Figure 1: The GW_0 self-energy correction to the inverse effective mass in the uniform electron gas. "Z" and "chi" are contributions coming from the antisymmetric and symmetric parts of the self energy with respect to Matsubara frequency, respectively. The G_0W_0 results are taken from Ref. [9]. "Ref" points are from Ref. [10]

shows the self-energy correction to the electron normal-state effective mass. The application of this GW_0 self energy to the Eliashberg equations [4] at extremely low temperature and extension to nearly uniform systems are under way.

Also, we have recently pointed out a nearly free electron-like character of the electronic states in a pressure-induced high-temperature superconductor H_3S [11]. We deepened the analysis by examining the Kohn-Sham (KS) wavefunctions. We calculated the band structure in the cubic ($Im\bar{3}m$) phase at 200GPa. Figure 2 depicts the accumulated squared norm of the plane-wave coefficients

$$\sum_{|\mathbf{G}'|<|\mathbf{G}|} |c_n(\mathbf{k}+\mathbf{G}')|^2 \qquad (3)$$

for the KS eigenstates $\psi_{n\mathbf{k}}(\mathbf{r}) = \sum_{\mathbf{G}} c_n(\mathbf{k}+\mathbf{G})e^{i(\mathbf{k}+\mathbf{G})\cdot\mathbf{r}}$ The band index n is labeled in ascending order in theKS energy. The steep increase from zero to $\gtrsim 0.95$, which is exhibited by all the bands shown, indicates that the corresponding KS state is dominated by a single plane wave. The same features were also seen in other k points; H, N and the point marked by arrow (not shown). This result shows that in this system, the electronic states indeed lose their atomic-orbital character and are rather well represented by the nearly uniform electron theory [13]. The first-principles calculations were performed using Quantum Espresso [14] with norm conserving pseudopotentials from *Pseudo dojo* [15].

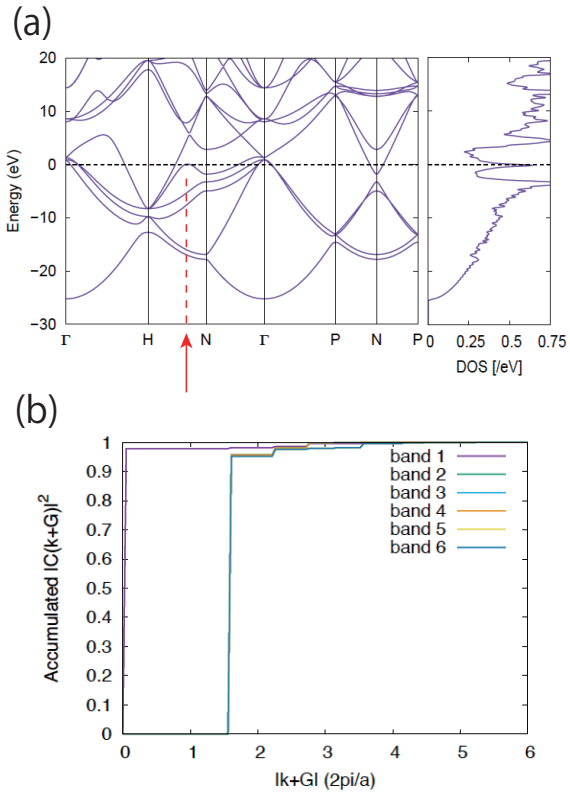


Figure 2: (a) Electronic band structure and density of states (DOS) of H_3S at 200GPa. Dashed horizontal line indicates the Fermi level, whereas vertical line indicates the cut of the van-Hove line that is responsible for the peak in the DOS. (b) Accumulated squared plane-wave coefficients of the KS states at Γ point.

References

[1] J. Bardeen, L. N. Cooper, and J. R .Schrieffer, Phys. Rev. **108** (1957) 1175.

[2] G. M. Eliashberg, Zh. Eksp. Teor. Fiz. **38**, (1960) 966.

[3] A. B. Migdal, Zh. Eksp. Teor. Fiz. **34**, (1958) 1438.

[4] A. Sanna *et al.*, J. Phys. Soc. Jpn. **87**, (2018) 041012.

[5] M. Lüders *et al.*, Phys. Rev. B **72** (2005) 024545.

[6] M. A. L. Marques *et al.*, Phys. Rev. B **72** (2005) 024546.

[7] A. Sanna, C. Pellegrini, and E. K. U. Gross, Phys. Rev. Lett. **125** (2020) 057001.

[8] F. Essenberger *et al.*, Phys. Rev. B **90** (2014) 214504.

[9] R. Akashi, Phys. Rev. B **105** (2022) 104510 .

[10] B. Holm and U. von Barth, Phys. Rev. B **57** (1998) 2108.

[11] R. Akashi, Phys. Rev. Research **6** (2024) 033012.

[12] H. Shinaoka, *et al.*, Phys. Rev. B **96** (2017) 035147.

[13] R. Akashi, in preparation.

[14] P. Giannozzi *et al.*, J. Phys. Condens. Matter **29** (2017) 465901.

[15] G. Pizzi *et al.*, J. Phys. Condens. Matter **32** (2020) 165902.

Ab-initio MD simulation for molten Rb_2AgI_3

Shuta TAHARA

Department of Liberal Arts and Sciences,

Chukyo University, 101-2 Yagoto Honmachi Showa-ku, Nagoya, Aichi 466-8666

We have been carried out experimental and theoretical studies with an interest in the diffusion mechanism of Ag ions diffusing in solids, such as AgI and $RbAg_4I_5$ and its molten phases [1-3]. Although Rb_2AgI_3, the subject of this study, is not a superionic conductor, it is an interesting material for studying the conductive environment of Ag ions in materials by comparing it with $RbAg_4I_5$, which is a superionic conductor in the RbI-AgI system. Since Rb_2AgI_3 and $RbAg_4I_5$ have different structures in the solid state, we thought that comparing the structures and physical properties in the high-temperature molten state would be more appropriate for investigating the effect of differences in composition on the Ag ion conductive environment than comparing the two solid states. In this project, we carried out AIMD simulations of molten Rb_2AgI_3. Figure 1 shows a comparison of our previous experimental data for molten Rb_2AgI_3 with the results of this simulation. We plan to analyze ion diffusion by checking whether the ionic conductivity derived from the ion diffusion coefficient matches the experimental data.

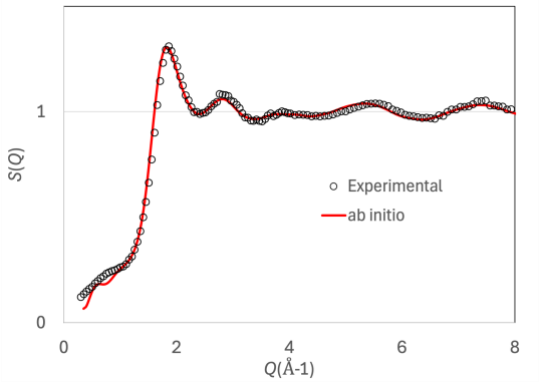


Fig. 1: Structure factors of molten Rb_2AgI_3. Open circles and red curve indicate experimental data and AIMD of this study, respectively.

References

[1] S. Tahara and T. Fukami, J. Phys. Soc. Jpn. **84**, 024602 (2015).

[2] S. Tahara et al., J. Chem. Phys. **143**, 044509 (2015).

[3] S. Tahara, et al., EPJ Web conf. **151**, 03006 (2017).

Optical properties and dielectric functions parameterization in UV-visible spectroscopy data analysis of $LiNbO_2$

Takayuki MAKINO
Graduate School of Engineering, University of Fukui
Bunkyo 3-9-1, Fukui, Fukui 910-8507

Lithium niobate crystallizes into a three-dimensional structure ($LiNbO_3$) or a metastable $LiNbO_2$ modification. Epitaxial growth techniques enable $LiNbO_2$ thin-film growth [1]. This material exhibits intriguing properties, such as superconductivity [2]. Its previously unknown band gap in stoichiometric $LiNbO_2$ was recently quantified by us [3]. However, the optical properties of delithiated $LiNbO_2$ remain unclear. Experimental data conversion from UV-visible spectroscopic data into complex dielectric functions [$\tilde{\epsilon} = \epsilon_1 + i\epsilon_2$ (or the complex index of refraction $\tilde{n} = n + ik$)], is crucial for material analysis. This also plays a significant role in comparative studies with theory using high-performance computers.

Several approaches for the abovementioned conversion are documented [4]. The numerical inversion can estimate dielectric functions at each wavelength but poses challenges as an inverse problem [5]. Using, *e.g.*, the Newton-Raphson method, this approach requires precise knowledge of material properties and layer thickness, risks inaccuracies without these details. Challenges include multiple possible solutions and requires well-chosen initial values for the root search. Recently, a deep learning-based method has been adopted, improving robustness and efficiency [6].

A second approach employs physics-based models to describe optical properties with meaningful parameters. While insightful, this method incurs high computational costs due to complex function structures. A third approach, which we adopt here, parameterizes dielectric functions using Lorentz functions for continuous modeling, avoiding the abovementioned limitations and ensuring smooth interpolation between spectral points.

In the simplest case, by letting us take ℓ thickness of the sample and λ wavelength, measured quantities such as transmission (T) and reflectivity (R) are expressed as functions of n and k as shown below.

$$T = (1-R)^2 \exp(-\frac{4\pi k\ell}{\lambda}),$$

and

$$R = \frac{(n-1)^2 + k^2}{(n+1)^2 + k^2}.$$

Because we now consider the film-on-substrate (two-layer) case, the relevant equations become significantly complicated. Explicit notations of the related equations in two layer model can be found elsewhere [6].

Strictly speaking, the aforementioned Lorentz oscillator (peak) is an equation related to the dielectric constant. However, to avoid the complexity of deriving both the complex refractive index and the complex dielectric constant, the equation for the Lorentz oscillator concerning the complex refractive index is presented here. The related equation reads:

$$\tilde{n} \propto \frac{1}{\omega_j^2 - \omega^2 + i\gamma\omega},$$

where ω, ω_j, γ denotes photon energy, peak energy and a broadening, respectively.

Due to typically broad measured photon energy range, spectroscopic data analysis leads to challenges in optimizing high-dimensional parameter spaces. Its challenge with high-dimensional problems make MCMC (Markov-chain Monte Carlo) method more effective. Tools like STAN offer user-friendly environments for these tasks. Additionally, Likhachev's criteria, such as the information criterion, improve reliability by determining the optimal number of peaks [4].

Photometric spectra were obtained via a UV-visible spectrometer, and numerical computations were performed using STAN (https://mc-stan.org). In implementing the proposed approach, we used 6 peaks. Figure 1 presents the converted result from measured quantities, i.e., complex dielectric function in delithiated $LiNbO_2$ film at room temperature. The delithiation degree is *ca.* 50%.

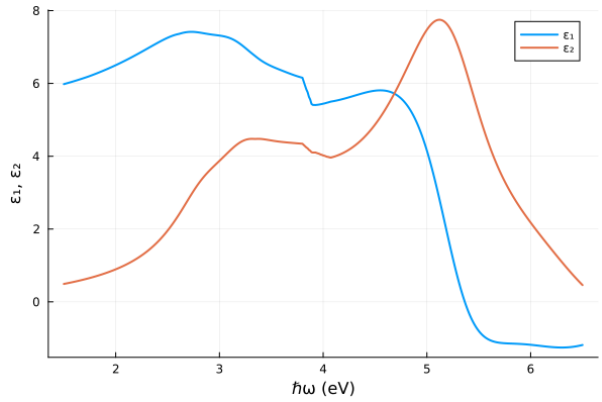


Figure 1: Complex dielectric functions (ϵ_1, ϵ_2) of delithiated $LiNbO_2$ thin film

The transition from stoichiometric to delithiated $LiNbO_2$ induces a blueshift due to the role of delithiation in hole doping, i.e., a degenerate semiconductor with the Burstein effect [7]. Delithiation also causes inhomogeneity-related broadening, more pronounced than in the stoichiometric case.

Comparisons between measured dielectric functions and ab-initio calculations are underway, utilizing density functional theoretical methods via Quantum ESPRESSO to model electronic structures, and RESPACK for many-body effects such as electron-hole correlations [8].

In summary, we have discussed dielectric function parameterization, including measured quantity conversions, introduced three approaches, explained the reasoning behind our selected method, and reported dielectric functions of delithiated $LiNbO_2$.

References

[1] T. Soma, K. Yoshimatsu, and A. Ohtomo: Science Advances **6** (2020) eabb8570.

[2] E. R. Ylvisaker and W. E. Pickett: Phys. Rev. B **74** (2006) 075104.

[3] T. Kurachi, T. Yamaguchi, E. Kobayashi, T. Soma, A. Ohtomo, and T. Makino: Physica B **621** (2021) 413259.

[4] D. Likhachev: Thin Solid Films **636** (2017) 519.

[5] G. E. Jellison and F. A. Modine: Appl. Phys. Lett. **69** (1996) 371.

[6] K. Saeki and T. Makino: Jpn. J. Appl. Phys. **62** (2023) 081002.

[7] E. Burstein: Phys. Rev. **93** (1954) 632.

[8] K. Nakamura, Y. Nohara, Y. Yosimoto, and Y. Nomura: Phys. Rev. B **93** (2016) 085124.

Structural analysis of single layer borophene and boride on Ni surfaces

Takeshi NAKAGAWA

Interdisciplinary Graduate School of Engineering Sciences,

Kyushu university, 6-1 Kasuga koen, Kasuga, Fukuoka 816-8580

We performed a structural search and analysis of boron deposited on Ni(111). Owing to boron's electron deficiency and the structural variability associated with its hexagonal network—particularly with respect to defect concentration—two-dimensional boron films exhibit considerable complexity. Surface boride formation introduces additional challenges for structural characterization. To explore stable configurations, we employed a crystal structure prediction based on particle-swarm optimization (CALYPSO) [1], combined with first-principles calculations using VASP, across a wide range of boron–nickel compositions. Our calculations identify B_{13} overlayer borophene and Ni_7B_3 boride structures as energetically favorable. Among these, the B_{13} structure exhibits better agreement with low-energy electron diffraction (LEED) and scanning tunneling microscopy (STM) results. Phonon dispersion analysis further confirms the dynamical stability of B_{13}, with all phonon modes displaying real (positive) frequencies.

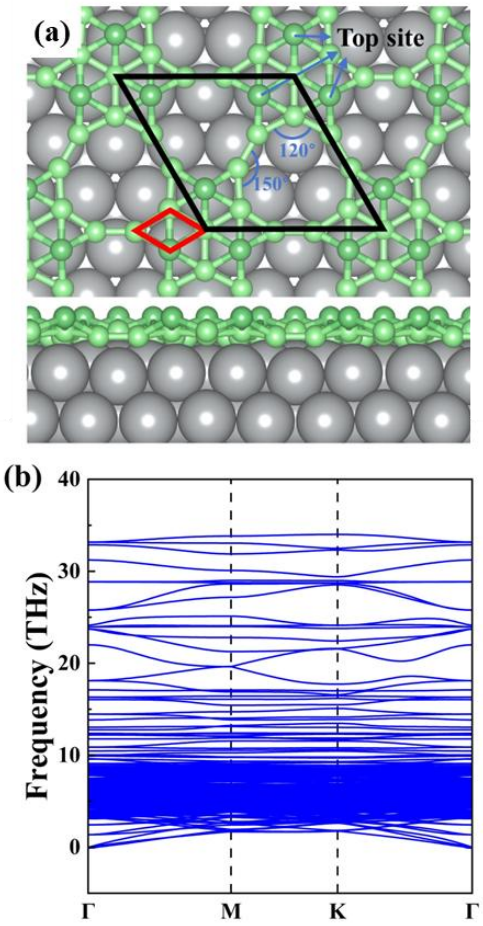


Fig. 1: (a) A predicted structural model of B_{13} on Ni(111). (b) Phonon dispersion for B_{13} on Ni(111).

References

[1] Y. Wang, J. Lv, L. Zhu, Y. Ma, Phys. Rev. B **82**, 094116 (2010).

Interfacial phonon modes at grain boundaries in single-layer graphene/hexagonal boron nitride

Masaaki MISAWA
Department of Intelligent Mechanical Engineering, Fukuoka Institute of Technology
3-30-1 Wajiro-higashi, Higashi-ku, Fukuoka 811-0295

With the development of surface acoustic wave devices, there is a need for more advanced technology to control phonon propagation. To establish a methodology to control ultra-high frequency phonons in the THz band based on nanoscale structures, we conducted a first-principles calculations with the following objectives. (1) Exploring localized phonon modes at grain boundaries (GBs). (2) Controlling phononic properties using vdW heterojunction. All calculations are performed using VASP [1] and PHONOPY [2] codes.

Phonon dispersion relations of the single-layer graphene containing armchair-GB (SLG) and that stacked with hexagonal boron nitride (G/BN) systems were analyzed. In the SLG system, the four interfacial phonon modes (three in-plane and one out-of plane modes) localized at the GB were introduced (Figure 1). On the other hand, in the G/BN system, the nine interfacial phonon modes (seven in-plane and two out-of plane modes) were detected (Figure 2). Some of them, the BN layer oscillates simultaneously with the GB in SLG. These results suggest the possibility of introducing GB-localized phonons in the desired frequency band using stacking structures.

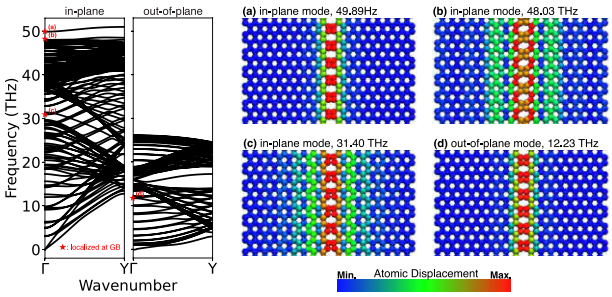


Figure 1: Phonon dispersion relation and atomic displacement of the localized phonon modes in the SLG system.

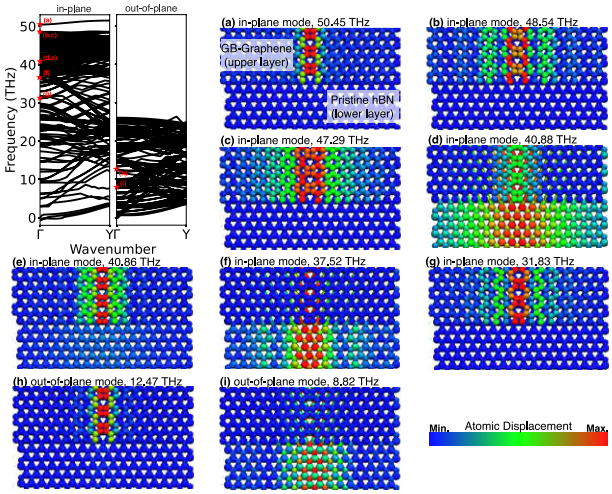


Figure 2: Phonon dispersion relation and atomic displacement of the localized phonon modes in the G/BN system. the upper graphene layer is displayed only in the upper half of the images.

References

[1] G. Kresse and D. Joubert, Phys. Rev. **59**, 1758 (1999).

[2] A. Togo, J. Phys. Soc. Jpn. **92**, 012001 (2023).

First-principles Calculation of Tungsten Alloy

Shoya Kawano

Department of Electrical and Electronic Engineering, Kyushu Institute of Technology, Kitakyushu, Fukuoka, 804-8550

Tungsten is widely used as a heating element, electrode, and electron‐emitting material in X-ray sources and other high-temperature applications. Among these applications, there is growing interest in enhancing heater performance by raising its electrical resistivity. It has been found that adding ruthenium (Ru) to tungsten increases its electrical resistivity fourfold. This demonstrates that alloying tungsten with suitable elements can effectively raise its resistivity. Accordingly, optimizing both the type and concentration of alloying elements in tungsten is essential for industrial applications.

First, we conducted a resistivity simulation for pure tungsten, which crystallizes in the body-centered cubic (bcc) structure. Using Quantum ESPRESSO [1] and Perturbo [2], we calculated the temperature-dependent resistivity of pure tungsten; the results are shown in Fig. 1 (solid line denotes calculated values; dashed line denotes data-book values). The close agreement confirms that first-principles methods can reliably predict tungsten's electrical resistivity. The average electron relaxation time (scattering lifetime) determined from these calculations was 16 fs. Applying the same methodology to Au yields a relaxation time of 24 fs [3], consistent with Au's lower resistivity and validating our pure-W results.

Next, we modeled W–Ru alloys for which experimental resistivity data are available. In these alloys, Ru atoms randomly substitute for W sites within the bcc lattice. To capture this disorder, we generated numerous candidate structures using the cluster-expansion method implemented in ATAT [4] and computed each structure's formation enthalpy. Enthalpy decreases with increasing Ru concentration, indicating favorable Ru dissolution in W and agreeing with experimental observations. When we attempted to compute electron–phonon scattering lifetimes for these structures, however, low-concentration Ru alloys exhibited dynamical instabilities in phonon calculations, preventing a direct calculation of their resistivities.

We therefore approximated the relaxation time in W–Ru alloys as no greater than that of pure tungsten. Under this assumption, we calculated the electrical conductivity of the alloys using BoltzTraP2 [5]. Figure 2 shows the resistivity as a function of

Ru concentration, with black circles for individual configurations and red circles for ensemble averages. The averaged values exhibit a clear upward trend with increasing Ru content. Experimentally, a 4 % Ru alloy has a resistivity of approximately 22 μΩ·cm; our results reproduce this trend, though they slightly underestimate the absolute values because of the constant-lifetime assumption. Nevertheless, our calculations successfully capture the effect of alloying on tungsten's resistivity.

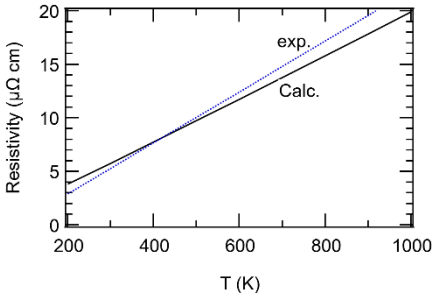


Fig. 1: Electrical resistivity of pure tungsten

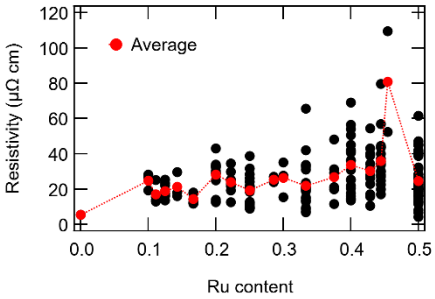


Fig. 2: Electrical resistivity of W-Ru calculated using the relaxation time of pure tungsten ($W_{1-x}Ru_x$, $x \leq 0.5$). Black circles indicate the electrical resistivity of each structure produced, and red circles indicate the average value for each composition.

References

[1] https://www.quantum-espresso.org/

[2] https://perturbo-code.github.io/

[3] J. I. Mustafa et. al., Physical Review B **94** (2016).

[4] A. van de Walle, M. Asta and G. Ceder, Calphad **26** (2002).

[5] https://arxiv.org/abs/1712.07946

Relative stabilities of In-induced surface reconstructions on the Si(111) surface

Tsuneo FUKUDA

Department of Physics and Electronics, Graduate School of Engineering, Osaka Metropolitan University, 1-1 Gakuen-cho, Nakaku, Sakai, Osaka 599-8531

Indium-induced atomic structures on the Si(111) surface were studied by first-principles calculations. Experimental and theoretical studies on In-induced silicon surface have attracted much attention because of the implication of various condensed matter physics, such as charge density waves, Peierls transition, and two-dimensional super-conductivity to name a few. To understand the physics behind the Si-In system, it is crucial to accurately determine the atomic structure and electronic states.

The aim of this project is to determine relative stability of surface atomic structures as a function of In and Si coverages based on first-principles scheme. We used VASP (=Vienna Ab initio Simulation Package) for this project and various calculation parameters that affect the total energies of surface structures were systematically studied in detail for several surface reconstructions and chemical potentials were compared. The parameters and surface reconstruction studied are listed in Table 1.

The lattice parameter of bulk Si was $0.72 \pm 0.01\%$ larger than the experimental parameter extrapolated to 0 K, and that cohesive energy was $1.7\% \pm 0.2\%$ smaller than experimental value, respectively. These errors are due to the cutoff energies and the number of k points.

Table 1:Calculation Parameters and Surface reconstrcutions

Potential	PBE [1]
Cutoff Energy	382-500 eV
Electronic Conver-gence	<1E-6 eV
Structure Convergence	<0.1 eV/nm
Slab layers	3-8 DL
k-points	0.015-0.055 Ang^{-1}
Surface Reconstruction (Superstructure)	$\sqrt{3} \times \sqrt{3}R30°(\sqrt{3}\text{-}\alpha)$ $\sqrt{31} \times \sqrt{31}$R9° $4 \times 1(8\times 2)$ $\sqrt{7} \times \sqrt{7}$ $\sqrt{7} \times \sqrt{3}$-rect

For the In-induced surface structures, all the structures shown in Table 1 were stable. However, the formation energies depended on the number of k points, the cutoff energies, and the number of layers in the slab, and no systematic trend was observed in the range of a few tens of meV. Thus, the relative stability of each structure varies depending on the choice of these calculation parameters. We are currently trying to find a method of selecting correct grand state energies and appropriate for the In-Si system [2].

References

[1] J.P. Perdew, K. Burke, M. Ernzerhof, Phys. Rev. Lett. **77** 3865 (1996).

[2] T. Fukuda, in preparation

DFT calculations of adsorbed molecules captured by metal-organic films on Cu(111)

Noriyuki TSUKAHARA
National Institute of Technology, Gunma College
Toriba-machi, Maebashi, Gunma, 371-8530

In this study, I verified that the porous 2D metal-organic network (2D-MON) film on the metal surface can trap adsorbed atoms and molecules, enabling control of the size of metal clusters and molecular oligomers in the pores.

Element-specific cluster formation in the pore of the 2D-MON.

From STM measurements, when Ag, In, and Pd atoms are deposited on the 2D-MON on Ag(111), indium clusters grow at the center of the pores, while Ag and Pd clusters grow from the 2D-MON. The present DFT calculations show that an In adatom in the pores interact with the 2D-MON repulsively, whereas Ag and Pd adatoms interact attractively. The location where the metal adatoms aggregate is determined by the interaction between the metal adatom and the 2D-MON. [1]

Formation of specific HCOOH oligomer in the pore of the 2D-MON.

HCOOH molecules aggregate one-dimensionally on Cu(111). From STM measurements, when HCOOH molecules are trapped in the present 2D-MON on Cu(111), tetramer chains tend to be selectively formed in the pores, and both ends of the tetramer chain are located at the specific sites in the pore. Figure 1 shows the position dependence of the adsorption energy of a HCOOH molecule in the pore, and attractive interaction occurs between the 2D-MON and the HCOOH molecule. A chain grows from this HCOOH molecule, and the other end of the tetramer chain also interacts attractively with the 2D-MON. [2]

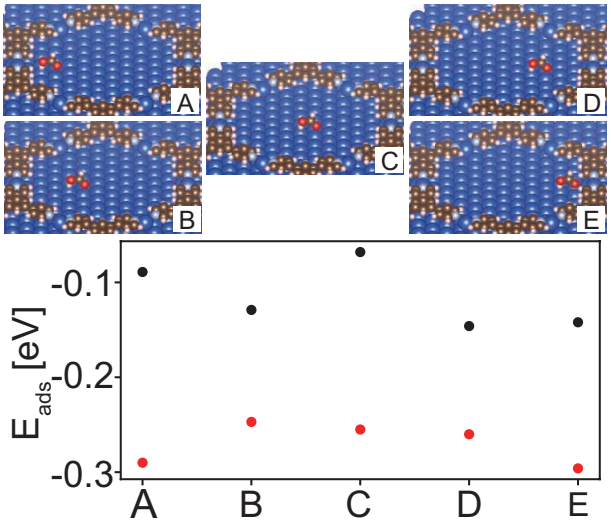


Figure 1: Position dependence of the adsorption energy of a HCOOH molecule in the pore. Black and red dots indicates the calculated results without and with vdW correction, respectively.

References

[1] N. Tsukahara, R. Arafune, and J. Yoshinobu: Jpn. J. Appl. Phys. **63**, 065504 (2024).

[2] N. Tsukahara and J. Yoshinobu: *in preparation*

Search and realization of novel electronic properties of surfaces and interfaces and of nanostructures

Takeshi INAOKA
Department of Physics and Earth Sciences, Faculty of Science, University of the Ryukyus, 1 Senbaru, Nishihara, Okinawa 903-0213

Advances in supercomputers have made it possible to calculate the electronic structure of organic crystals composed of large molecules. Using the van-der-Waals density functional theory, we have been investigating the electronic structure of x-form phthalocyanine (Pc) crystals doped with iodine (I) atomic chains. The Pc is a planar π-conjugated macrocyclic molecule which can include an atom of various species at its center position, such as Si or Li, as mentioned below. The x-form crystal is constituted of a square-lattice arrangement of molecular chains with double period and with molecular planes normal to the stacking direction. Doped I atoms form atomic chains between these molecular chains.

We employ the program package 'Vienna Ab initio Simulation Package' (VASP) [1-4] on system B (ohtaka).

(I) x-SiPcI crystals

In last year's study [5], we found that the SiPc chains act to form equally spaced I atomic chains, while the I atoms try to create trimerized chains. These effects compete with each other, but the trimerization effect is larger. The trimerized I atomic chains are not metallic . However, since the distance between neighboring trimers is not so large compared to the bond length of the trimer, application of uniaxial compression in the stacking direction could create equally spaced I chains and thereby conduction bands. In this study, with a gradual increase in uniaxial compressive strain, we perform structural optimization and trace changes in the electronic structure. Since SiPc molecules are stacked with double period, and I atomic chains are trimerized, we assume an x-form SiPcI crystal with 6-fold period in the stacking direction.

In the stable structure, the lattice constant c_0 of the unit cell in the c-axis direction is 19.12 Å, the bond length of each trimer is 3.00 Å, and the distance between adjacent trimers is 3.55 Å. In order to apply uniaxial compressive strain in the stacking direction, we gradually decrease c_0, and perform structural optimization at each c_0 value. In this process, the bond distance of the trimer almost remains unchanged, but the distance between neighboring trimers decreases, and at c_0=18.00Å, the I atomic chains are equally spaced at 3.00Å. Figure 1 shows the electron density distribution (a) before and (b) after application of uniaxial compressive strain. The compressive strain changes the distribution localized in each trimer to that extending over the entire I chain.

Our band analysis along this process clearly shows how the Peierls gap associated with the trimerized I chains gradually reduces and finally closes above the Fermi level E_F. When I atoms are equally spaced, the structure becomes doubly periodic in the stacking direction. Analysis of band dispersion shows that a band with extremely strong dispersion originating from the p_z orbitals of the I

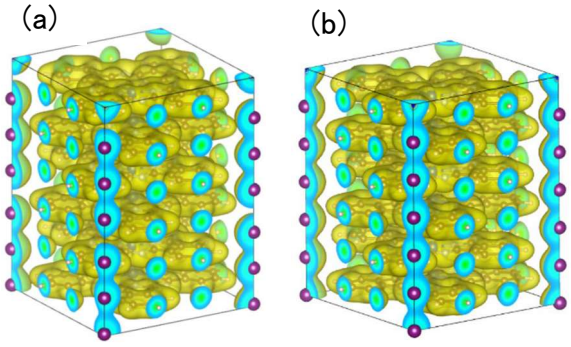


Fig.1 Electron density distribution of x-SiPcI crystals (a) before and (b) after uniaxial compression is applied. This compression changes trimerized I chains to equally spaced ones.

atoms crosses E_F, indicating that the conduction band is formed by uniaxial compressive strain. The effective mass ratio and the one-dimensional electron density are m^*/m_0=0.11 and n_{1D}=1.00 $\times 10^7$/cm, respectively. From the strain dependence of the total energy, the uniaxial compressive stress required for formation of conduction bands is estimated to be about 1.6 GPa.

(II) x-LiPcI crystals

Teruya et al. showed that Mott insulators of x-LiPc can be converted to metals of x-LiPcI and vice versa by chemical I doping and dedoping [6]. Here, we describe the progress of our theoretical study of x-LiPcI crystals.

Figure 2 exhibits the band dispersions on the Γ-Z line in the stacking direction in the Brillouin zone. The dispersive bands near and above E_F originate from p_z-orbital overlapping between neighboring stacked molecular planes. The double period in the stacking direction is reflected in the band structure. A pair of bands b193 and b194 with strong dispersion are formed by band folding at the Z point, and b193 crosses E_F, which indicates that this is a metallic band. Without I doping, the Fermi level E_F comes just at the band folding point of b193 and b194 at the Z point. As stated in last year's report as

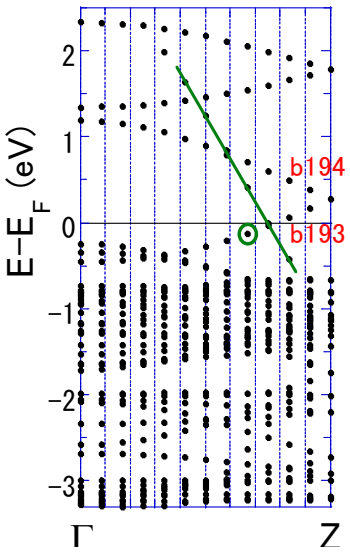


Fig. 2 Band dispersions of x-LiPcI crystal on the Γ-Z line.

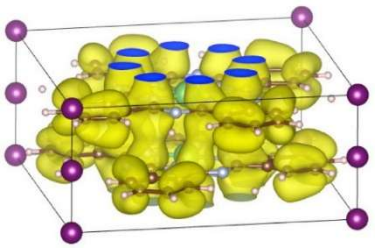


Fig. 3 Electron density distribution (isosurfaces) of the state circled green in Fig. 2.

for a single x-LiPc chain, each of these two degenerate states at the band folding point is occupied by an unpaired electron. This corresponds to the appearance of Mott insulators in x-LiPc. On I doping, since I atomic chains receive electrons from x-LiPc molecular chains, the Fermi level E_F shifts down from the band folding point, and the band b193 becomes metallic. Figure 3 exhibits the electron density distribution of the state on b193 just below E_F circled green in Fig. 2. We can see the p_z orbital overlap between the neighboring stacked molecules at each position of C atoms nearest to the center Li atom. This overlap contributes to electrical conductivity in the stacking direction.

If we consider equally spaced I chains, we have a metallic band originating from I atomic chains, as lined green in Fig. 2. However, Raman spectroscopy analysis indicates that the I chains are in a pentameric arrangement as I_5^-. If we consider ten-fold periodicity in the stacking direction and perform structural optimization, we would find that pentamerized chains are more stable than equally spaced chains, and that the resulting band of I chains is not metallic.

References

[1] G. Kresse and J. Hafner: Phys. Rev. B **47**, 558-561 (1993).
[2] G. Kresse and J. Furthmüller: Comput. Mat. Sci. **6**, 15-50 (1996).
[3] P. E. Blöchl: Phys. Rev. B **50**, 17953 (1994).
[4] J. Klimeš, D. R. Bowler, and A. Michaelides: Phys. Rev. B **83**, 195131 (2011).
[5] T. Inaoka, AIP Advances **14**, 085016 (2024).
[6] R. Teruya et al.: Angew. Chem. Int. Ed. **61**, e202206428 (2022).

Ab initio molecular dynamics study of inorganic polymer

Yoh-ichi Mototake, Yoshifumi Amamoto, Hiroyuki Kumazoe,
Hidetoshi Morita, Hayato Okubo
Graduate School of Social Data Science,
Hitotsubashi University, Chome-1 Naka, Kunitachi, Tokyo, 186-0004

To model, predict and control pattern dynamics involving chemical reactions, such as the formation of SiC polycrystalline ceramics from precursor polymers (Figure), it is necessary to integrate and model phenomena with different chemical bonding states and temporal and spatial scales, such as chemical reactions involving changes in chemical bonds and structure formation of global patterns from atoms and molecules. Although modeling such pattern dynamics must be integrated, no method has yet been established to model such pattern dynamics. Therefore, we aim to develop a machine learning modeling framework to realize it.

The purpose of this project is to generate a simulation-based dataset to develop a machine learning model that reproduces the formation process of SiC polycrystalline ceramic from the precursor polymer.

Originally, we planned to collect a dataset of multi-scale material formation processes involving chemical reactions based on existing simulation methods such as first-principles molecular dynamics calculations using neural potentials. However, we found that it is very difficult to reproduce the formation of thousands of molecules and their networking and crystallization processes using existing methods, no matter how coarse-grained the simulations are. Therefore, we developed an informatics framework to construct an entire dataset by combining partially simulated data. This year, we realized to start creating the dataset based on this framework.

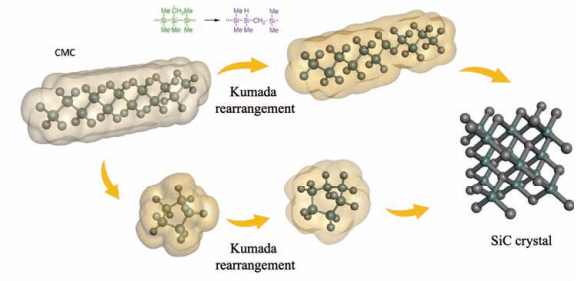


Figure: SiC polycrystal formation process by precursor polymer method [1,2,3].

References

[1] S. Yajima, J. Hayash, and M. Omori, Chem. Lett., 931（1975）.

[2] S. Yajima, J. Hayashi, M. Omori and K. Okamura, Nature, 261, 683（1976）.

[3] K. Shiina and K. Kumada, J. Org. Chem., 23, 139（1958）

First-principles study of Si, Ge, and nanodiamond materials

Hana Pratiwi KADARISMAN

Nanomaterials Research Institute (NanoMaRi), Kanazawa University

Kakuma machi, Kanazawa, Ishikawa 920-1192

1. **The OH-termination on Si and Ge surfaces**

Termination of semiconductor surfaces influences the stability and affects the chemical reactivity of the materials. Previously, we found the persistent spin helix on diamond 111 surface [1] after introducing the OH (hydroxyl termination on its surface. These results motivated us to investigate the impact of OH termination on the other group IV semiconductors, specifically Si and Ge surfaces.

This year, we performed first-principles calculation of OH-terminated Si and Ge surfaces. Our goals are to observe and analyze the electronic properties of the Si and Ge after OH-termination on its surface. Moreover, we also investigate the spin-orbit coupling property of OH-terminated Si, and Ge surfaces. First-principles electronic structure calculations were carried out based on the density functional theory using the OpenMX[2] code. The spin orbit coupling was included in this computation.

The results show that the OH-termination on silicon and germanium surfaces induces spin splitting at the conduction band minimum (CBM) and valence band maximum (VBM), for the silicon and germanium surfaces, respectively. Based on these findings, we discuss the possibility of OH-terminated silicon and germanium for the spintronic application.

2. **NV center in nanodiamond**

We performed the first-principles calculation of NV center in nanodiamond using Openmx [2] code. To simulate the nanodiamond structure, a large number of carbon atoms is required, which demands substantial computational resources. The computational demands of this study were efficiently handled using the ISSP supercomputer. We expect the difference shapes of nanodiamond structure may produce the difference stabilities and electronic properties. To investigate these further, additional calculations and analyses are necessary.

References

[1] H. P. Kadarisman, N. Yamaguchi, and F. Ishii: Appl. Phys. Express **16** (2023) 023001.

[2] http://openmx-square.org

Analyses of semiconductor surface processes by machine-learning based potentials

Kouji INAGAKI

Graduate School of Engineering, Osaka University

Yamadaoka 2-1, Suita, Osaka 565-087

The mechanochemical method, a type of ultra-precision surface processing, uses a synergistic effect of mechanical interaction and chemical reaction processes, but the mechanism is not clear. A proper understanding of the mechanism is essential for efficient improvement of the processing method.

The objective of this study is to establish and apply a method to analyze the mechanism by large-scale Molecular Dynamics (MD) calculations using the Machine Learning Potential (MLP). In contrast to other studies, where MLPs that use structures close to stable atomic structures as training data have been used to search for new materials with metastable structures, this study aims to develop MLPs that employ more training data at the boundaries of bond formation and bond breaking for highly accurate simulations of processing phenomena. In order to collect training data, we proposed a method to collect training data from atomic structures where bond formation/breakage occurs by performing MD calculations at high temperatures using a provisional MLP.

An application was developed to extract structures from trajectories of MD calculations, and the method was evaluated using the example of a diffusion process of H adsorbed on a Si(001) surface. After preparing the initial training data, an iterative MLP refinement process consisting of MLP generation, MD execution, and additional training data was performed. This repetition reduced the frequency of calculation crashes due to non-physical breakdowns caused by imperfections in the MLP during MD, confirming the effectiveness of the method.

However, the occurrence of non-physical breakage could not be reduced to zero, and additional learning data is considered necessary. Furthermore, the learning data collection application we developed required a large amount of storage space, making it difficult to collect learning data on a larger scale. We plan to improve the learning data collection application in the future.

References

[1] K. Inagaki, The 72th JSAP Spring Meeting 2025 14p-K507-9.

Electronic structure of aqueous polymers

Osamu TAKAHASHI, Nanami SHIMA, Risa OKADA, and Yuika WATARI
Graduate School of Science, Hiroshima University, Kagamiyama, Higashi-hiroshima, Hiroshima 739-8526

Membrane technology to produce fresh water from seawater and contaminated water is extremely attractive because it is low energy and simple to implement [1]. Recently, self-assembled liquid crystalline membrane materials with uniform pore size in the nano or sub-nano class have been developed. By controlling the hydrophilic groups in the films, liquid crystalline films with different separation capacities can be produced. In order to develop membranes with more effective separation ability, it is important to understand the nature of water in the pores, i.e., the structure of hydrogen-bonded water in the nanochannel.

Soft X-ray emission spectroscopy (XES) measurements were performed to investigate the structure of water in the pores of liquid crystal films. In the case of liquid crystal membranes (ILCs) with benzyltriethylammonium groups, observed spectra of the water in the membranes resembles that in $MgSO_4$ solution when compared to that in NaCl solution, suggesting that this explains the water permeability [2]. In the present study, we constructed membrane models of two types of liquid crystal membranes with triethylammonium and imidazolium groups (Figure 1) as typical examples of membranes by molecular dynamics (MD) simulations. In addition, X-ray emission spectroscopy (XES) calculations were performed to explore the structure of water in the pores.

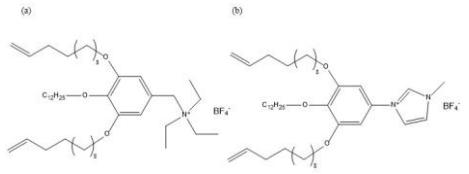


Fig.1 Molecular structure of ILC. (a) benzyl-triethylammonium and (b) benzylimidazorium system.

Structures of model ILCs were constructed by MD simulations using Gromacs [4] following Ref. [3]. Using a snapshot of MD simulations, a water molecule was sampled randomly and surrounding atoms within 6Å were picked up. Dangling chemical bonds were terminated by hydrogen atoms. A geometry at the center water molecule was optimized, and vibrational frequencies were obtained by Hessian matrices. Initial positions and velocities for hydrogen atoms in the water molecule were sampled quantum mechanically. Core-hole induced MD simulations were propagated within 20 fs. For obtained

trajectories XES calculations were performed using density functional theory code deMon2k [5]. XES spectral calculations were performed along with a scheme of semi-classical Kramers-Heisenberg theory [6]. To resolve entanglements of potential energy surface and the transition moment curves genetic algorithm were applied [7].

We focus on the double peaks seen around 528 and 529 eV, which are attributed to the $1b_1$ state of water. In our previous study [8], these peaks originate from two different structures that induce different dynamics. The peak structures differ depending on the type of solution and the membrane structure. In water in the membrane, the relative intensity of the double peaks is independent of the water concentration (experimentally corresponding to the water pressure in the membrane). In the case of the triethylammonium system, the intensity between the double peaks tends to be higher at 3M. This reflects the difference in dynamics resulting from the various hydrogen bonding modes. In the case of the imidazolium system, the spectrum is independent of the water concentration. These differences may reflect differences in the hydrophilicity of the functional groups. The water in the membrane is more similar to that in the $MgSO_4$ solution, providing a qualitative explanation for the permeability of the membrane.

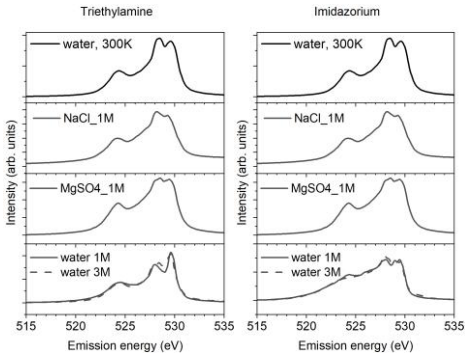


Fig.2: Calculated XES spectra of water, 1M NaCl solution, 1M $MgSO_4$ solution, and ionic liquid crystal with benzyltriethylammonium and imidazorium functionals.

References

[1] M. Henmi et al., Adv. Mater., **24**, 2238 (2012).

[2] R. Watanabe et al., Ang. Chem. Int. Ed., **59**, 23461 (2020).

3) Y. Ishii et al., Sci. Adv., **7**, eabf0669 (2021).

4) M.J. Abraham, et al., SoftwareX, **1-2**, 19 (2015).

5) A. M. Köster et al., deMon2k ver.5 (2018).

6) M. P. Ljungberg et al., Phys. Rev. B, **82**, 245115 (2010).

7) L. G. M. Pettersson et al., Theor. Chem. Acc., 140, 162 (2021).

8) O. Takahashi et al., Phys. Rev. Lett., 128, 086002 (2022).

Machine Learning-based DFT Calculation of Lignin Adsorption and Oxidative Activity on Ni/CeO_2 (111)

TEPPEI NUNOURA and ZHIHE ZHAO

Department of Environment Systems, Graduation School of Frontier Science,

The University of Tokyo, Kashiwa-no-ha, Kashiwa, Chiba 277-8581

To explore the adsorption behavior of lignin on Ni-loaded CeO_2 (111) surfaces, we integrated machine learning techniques to automatically generate and screen over 100 adsorption configurations. Through structural optimization, we identified the most stable adsorption structures and utilized the results to evaluate the oxidative potential of the catalyst toward lignin.1

In this study, we performed ab initio calculations to investigate the lignin adsorption behavior of Ni-loaded CeO_2 (111) surfaces. The theoretical framework was established using the PBE functional within the Vienna Ab initio Simulation Package.

We first identified the thermodynamically stable (111) surface of CeO_2 and modeled Ni cluster loading on this surface. Using a machine learning-assisted workflow, we generated and screened over 100 different lignin adsorption configurations, enabling high-throughput identification of the most stable structures. Among the 300 adsorption configurations, Guaiacol showed the highest oxidative reactivity on the Ni/CeO_2 (111) surface than syringol and p-hydroxyphenol.

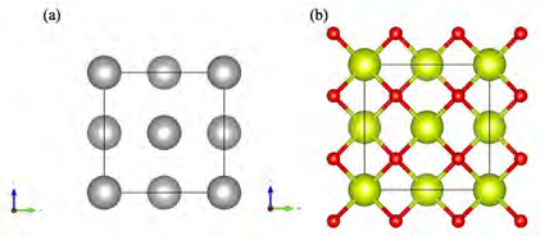


Fig.1 (a) Ni cluster crystal structure is face-centered cubic; (b) CeO_2 crystal cell (before cleavage)

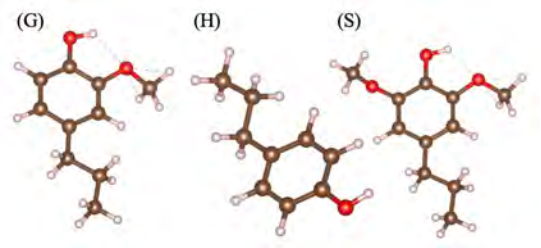


Fig.2 Guaiacyl (G), Hydroxyphenyl (H), and Syringyl (S) unit of lignin.

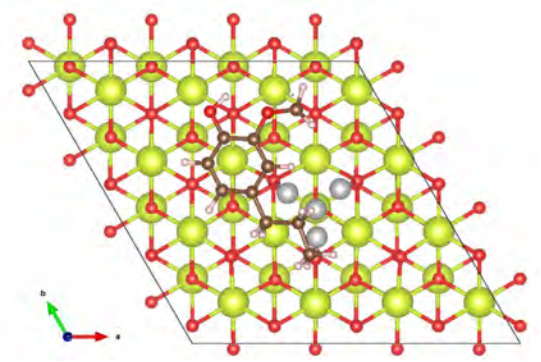


Fig.3 Guaiacyl (G) adsorbed on Ni/CeO_2 (111).

References

[1] Xie, Jin.; et al. *ACS Catal.* **2023**, *13* (14), 9577–9587.

Theoretical Analysis of H-terminated Si Atomic Layer Nanoribbons

Junhuan LI, Kenta ARIMA

Graduate School of Engineering,

The University of Osaka, Yamada-oka, Suita, Osaka 565-0871

Our goal was to predict the electrical and optical properties of silicon atomic layer nanoribbons (SiNRs), which we are attempting to form using our group's unique experimental techniques [1]. Density functional theory calculations were performed using the STATE [2] code with ultrasoft pseudopotentials.

Our computational model starts with bulk silicon as the initial material. Si nanosheets with atomic-layer thickness were generated by cleaving along the Si(111) plane. These sheets were then cut along the armchair direction to form armchair Si nanoribbons (ASiNRs). Examples of hydrogen-terminated ASiNRs are shown in Figure 1. The ribbons in Figures 1(a−c) have different thicknesses but the same width, defined as the number of dimer lines across the ribbon, which is 7 in this case.

Structural optimization was performed for the models, including hydrogen atoms. A plane-wave basis set was used to expand wave functions and charge density with cutoff energies of 36 Ry and 400 Ry, respectively. The Brillouin zone integration was done with a uniform grid of 30 k points along the edge direction. The electronic structures of ASiNRs were simulated using the optimized models. Our preliminary results show that the bandgap of the ribbons is strongly dependent on their thickness and decreases with increasing width.

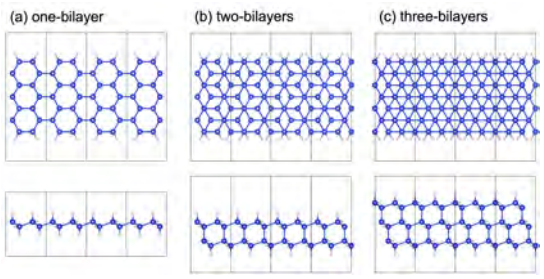


Fig. 1: Three atomic configurations of ASiNRs: (a) one-bilayer, (b) two-bilayers, and (c) three-bilayers.

References

[1] Z. Ma, S. Masumoto, K. Kawai, K. Yamamura, and K. Arima, Langmuir **38**, 3748 (2022).

[2] J. Li, K. Inagaki, and K. Arima, Phys. Rev. Res. **6**, 013252 (2024).

Electronic Structure of WO_3

Takahiro Maehira
Faculty of Science, University of the Ryukyus, Nishihara, Okinawa 903-0213

The monocarbides of transition elements from the group-IVB, -VB, and -VIB columns of the Periodic Table are well known for their great hardness and strength, high melting temperatures, metal-like thermal and electrical resistivities, nonstoichiometry, and superconducting properties [1, 2]. Most experimental and theoretical efforts to understand the fundamental properties of these technologically important materials have focused thus far on the group-IVB and -VB carbides, all of which crystallize with the cubic rocksalt structure. The compound WO_3 has eight phases: a low temperature phase is cubic WO_3. We studied simple cubic WO_3 with a space group of Pm3m which contains one molecule in the unit cell. The lattice parameter a is 3.838 Å, respectively [3]. The calculation for the energy band structures was carried out by using the OpenMX code(`http://www.openmx-square.org/`). First, we discuss the calculated results for WO_3 as shown in Figure 1, in which we depict the energy band structure along the symmetry axes in the Brillouin zone, which is shown in Figure 1, in the energy region from -10.0 to 10.0 eV. The Fermi level E_F is at 0.0 eV. for WO_3 and indicated by dashed lines in Figure 1. With respect to the energy band structure near E_F, we emphasize that there is always hybridization between the W $5d$ and O $2p$ states in WO_3. The total number of holes is equal to that of electrons, which represents that WO_3 is a compensated metal. Since the lowest twelve bands are fully occupied, as shown in Figure 1, the next three bands are partially occupied, while higher bands are empty. This compound is compensated metal because of having two chemical units in the unit cell. We move to discuss the Fermi surface of WO_3. Three bands cross the E_F, therefore WO_3 has three Fermi surfaces in Figure 2. The color on the Fermi surface illustrates the distribution of the Fermi velocity components. Fermi surfaces for WO_3 centered at the Γ points, respectively. The 7th band has one lattice-like hole sheet centered at the each Γ point. Red-shift indicate the increase of the admixture of Fermi velocity components. The Fermi surfaces were calculated with FermiSurfer [4].

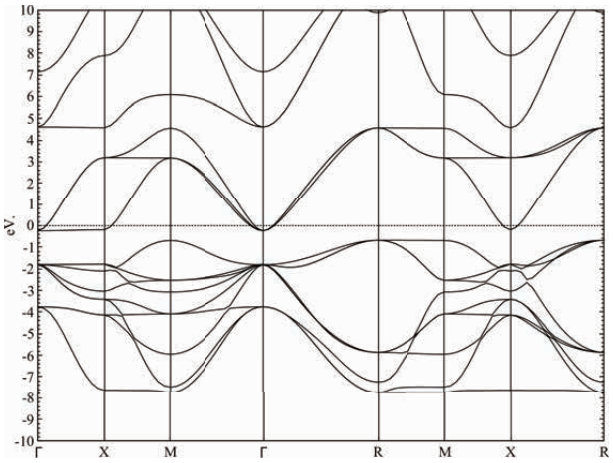


Figure 1: The energy band structure for WO_3, the symmetry points and axis for the simple cubic structure. E_F indicates the position of the Fermi level.

WO_3-type structures can be described as ABX_3 perovskites in which the A-cation site is unoccupied. They therefore have the general composition BX_3, where B is normally a cation and X is a bridging anion. The chemical diversity of such structures is very broad,

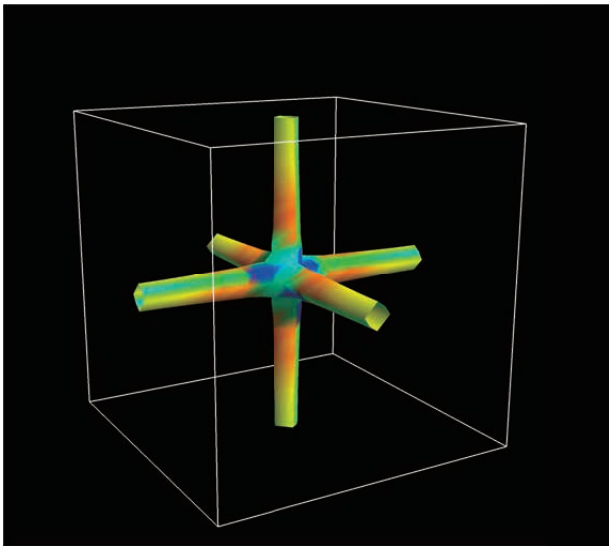


Figure 2: The Fermi surface for WO_3 centered at Γ point. Colors indicate the Fermi velocity components on the Fermi surface.

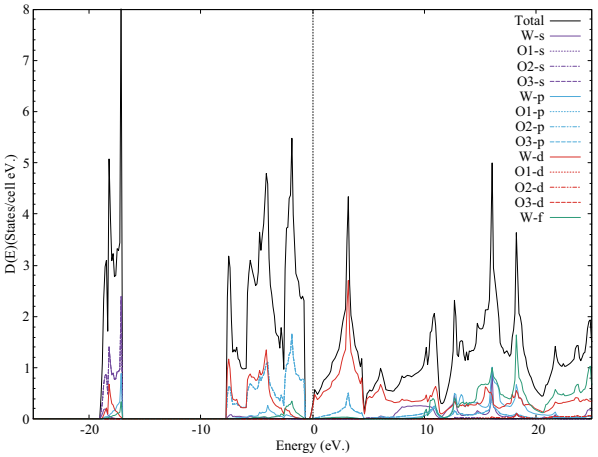


Figure 3: The density of states for WO_3. E_F indicates the position of the Fermi level shown by the dashed line.

ranging from simple oxides and fluorides, such as WO_3 and AlF_3, to more complex systems in which the bridging anion is polyatomic, as in the Prussian blue-related cyanides such as $Fe(CN)_3$ and $CoPt(CN)_6$. The calculated total density of states (DOS) for WO_3 is shown in Figure 3, in the energy region from -10.0 to 10.0 eV. The total density of states for WO_3 is shown by the solid black line and the s, p, d and f states are shown by the solid color lines, respectively. This figure tells us that the DOS of the d states is higher than that of the f states at the Fermi level.

References

[1] L. E. Toth: *Transition Metal Carbides and Nitrides.*, Academic, New York(1971).

[2] E.K. Storms: *The Refractory Carbides.*, Academic, New York(1967).

[3] L.S. Palatnik, O.A. Obol'yaninova, M.N. Naboka, N.T. Gladkikh : Inorg. Mater.(1973)718.

[4] R. Kubo: J. Phys. Soc. Jpn. **12** (1957) 570.

3.3 Strongly Correlated Quantum Systems

Theoretical study of strongly correlated electron systems using quantum many-body simulation and information science

Yukitoshi MOTOME

Department of Applied Physics,

The University of Tokyo, Bunkyo, Tokyo 113-8656

We have theoretically studied a variety of strongly-correlated electron systems by using numerical methods, including first-principles calculations, quantum many-body calculations, and machine learning (project numbers: 2024-Ca-0065 and 2024-Cb-0020). We also made several collaborations with experiments. During the last fiscal year, we have achieved substantial progress on the following topics.

(i) *Kitaev quantum spin liquids and Majorana fermions*: We clarified the origin of a chiral spin liquid state, which we discovered last year in the S=1 Kitaev model with bilinear-biquadratic interactions, by comparative studies of SU(3), O(3), and a discrete spin models [1]. We also studied effects of dissipation in the non-Hermitian Kitaev model under a magnetic field [2]. In addition, we demonstrated that rare-earth magnets can be good candidates for the Kitaev magnets [3,4]. Furthermore, we proposed new experimental platforms in heterostructures composed of van der Waals magnets [5] and ilmenite oxides [6]. Finally, we showed that the spin Seebeck effect can be a good probe of Majorana fermions in the Kitaev spin liquid [7]. The project leader gave a lecture in 物性若手夏の学校 on quantum spin liquids [8].

(ii) *Topological spin crystals and their dynamics*: Extending the research until the last years, we clarified how one-dimensional chiral solitons can penetrate into the system from the edges by using the Landau-Lifshitz-Gilbert dynamics [9]. We also unveiled a peculiar Hall response of magnetic torons ― pairs of hedgehogs and antihedgehogs connected by skyrmion strings, whose Hall angle ranges from zero to infinity [10]. In addition, we proposed a stable superstructure made of magnetic hopfions ― closed rings of twisted skyrmion tubes, by carefully investigating the interactions between magnetic hopfions [11].

(iii) *Topological phase transitions*: By using first-principles calculations, we showed that a monolayer of Co-based shandite exhibits topological transitions by rotating the magnetic field [12]. We also demonstrated that the Haldane model on a 1/6-depleted honeycomb lattice, which we call the Bishamon-kikkou lattice, and its connection to the honeycomb lattice exhibit peculiar topological insulating and metallic states and phase transitions between them [13].

(iv) *Collaborations with experimental groups*: We made fruitful collaborations on experiments for spin-polarized STM measurements of topological spin crystals in $GdRu_2Si_2$ [14], pressure-induced quantum melting of chiral spin order in FeGe [15], and anomalous Hall effects in a *p*-wave magnet with a helical magnetic order, $Gd_3Ru_4Al_{12}$ [16].

(v) *Development of new theoretical methods and their applications*: We proposed a new framework, which we call “physical reservoir probing”, inversely exploiting the framework of quantum reservoir computing [17]. We demonstrate that this framework is powerful to identify quantum critical points in a wide range of quantum phase transitions, even for topological ones [18]. We also applied the inverse Hamiltonian design that we developed to discover new Hamiltonians with maximized quantum entanglement [19].

References

[1] R. Pohle, N. Shannon, and Y. Motome, Phys. Rev. Research **6**, 033077 (2024).

[2] K. Fukui, Y. Kato, and Y. Motome, Phys. Rev. B **110**, 024429 (2024).

[3] S.-H. Jang and Y. Motome, Commun. Mater. **5**, 192 (2024).

[4] S.-H. Jang and Y. Motome, Phys. Rev. B **110**, 155124 (2024).

[5] L. Zhang and Y. Motome, Phys. Rev. B **110**, L241109 (2024).

[6] Y.-F. Zhao, S.-H. Jang, and Y. Motome, preprint (arXiv:2403.09112).

[7] Y. Kato, J. Nasu, M. Sato, T. Okubo, T. Misawa, and Y. Motome, Phys. Rev. X **15**, 011050 (2025).

[8] 求 幸年:第 69 回物性若手夏の学校 講義「スピン液体の物理」.

[9] K. Shimizu, S. Okumura, Y. Kato, and Y. Motome, Phys. Rev. B **111**, 024411 (2025).

[10] K. Shimizu, S. Okumura, Y. Kato, and Y. Motome, Commun. Phys. **8**, 69 (2025).

[11] S. Kasai, K. Shimizu, S. Okumura, Y. Kato, and Y. Motome, preprint (arXiv:2411.00396).

[12] K. Nakazawa, Y. Kato, and Y. Motome, Phys. Rev. B **110**, 085112 (2024).

[13] S. Ikegami, K. Fukui, S. Okumura, Y. Kato, and Y. Motome, Phys. Rev. B **110**, 245107 (2024).

[14] J. Spethmann, Y. Motome *et al.*, Phys. Rev. Materials **8**, 064404 (2024).

[15] Y. Fujishiro, K. Nakazawa, Y. Kato, Y. Motome *et al.*, Phys. Rev. B **110**, L220401 (2024).

[16] R. Yamada, S. Okumura, Y. Motome *et al.*, preprint (arXiv:2502.10386).

[17] K. Kobayashi and Y. Motome, preprint (arXiv:2308.00898).

[18] K. Kobayashi and Y. Motome, preprint (arXiv:2402.07097), to be published in Nat. Commun.

[19] K. Inui and Y. Motome, Phys. Rev. Research **6**, 033080 (2024).

Development of Transformer+PP Wave Function

Yusuke NOMURA

Institute for Materials Research (IMR), Tohoku University,

2-1-1 Katahira, Aoba-ku, Sendai 980-8577

Analyzing quantum many-body problems is one of the central challenges in condensed matter physics. In recent years, there has been a growing interest in utilizing the expressive power of artificial neural networks to approximate quantum many-body wave functions. This line of research began with the seminal work by Carleo and Troyer in 2017, where a restricted Boltzmann machine (RBM) was introduced to represent quantum states [1].

Since then, a variety of neural network architectures have been explored for quantum-state representation. Notably, a transformer-based wave function was recently proposed by Viteritti *et al*., demonstrating high accuracy in capturing ground states of quantum spin systems [2].

The most challenging applications, however, lie in strongly correlated electron (fermionic) systems [3], which serve as a rich platform for exotic phenomena such as high-temperature superconductivity. To apply neural-network wave functions to fermionic systems, it is essential to satisfy the anti-commutation relations inherent to fermions.

One established approach is to combine a symmetric neural network-based wave function with an antisymmetric fermionic wave function, such as a Slater determinant. For example, the RBM combined with a pair-product (PP) wave function has achieved state-of-the-art accuracy in simulating the two-dimensional Hubbard model [4].

Building on this foundation, we are now exploring the combination of transformer-based wave functions with the PP wave function. Given the greater flexibility of transformers compared to RBMs, we expect the transformer+PP wave function to outperform the RBM+PP in terms of accuracy.

We have completed the implementation of a vision transformer for quantum spin systems, along with an efficient parameter-update scheme known as minSR [5]. We are now in the final stages of integrating the vision transformer with the PP wave function, which is an important next step that we aim to complete in the near future.

References

[1] G. Carleo and M. Troyer, Science **355**, 602 (2017).

[2] L. Viteritti *et al*., Phys. Rev. Lett. **130**, 236401 (2023).

[3] D. Wu *et al*., Science **386**, 296 (2024).

[4] Y. Nomura, A. S. Darmawan, Y. Yamaji, and M. Imada, Phys. Rev. B **96**, 205152 (2017).

[5] A. Chen and M. Heyl, Nat. Phys., **20**, 1476 (2024).

Studies on Quantum Many-Body Problem by Machine Learning

Masatoshi IMADA
Physica Division, Department of Engineering and Applied Sciences, Sophia University, 7-1 Kioi-cho, Chiyoda-ku Tokyo, 102-8554

Numerical method to construct ground-state wave functions of strongly interacting quantum many-body systems is one of the grand challenges in physics. Various algorithms have been proposed. Recently, neural network with Boltzmann machine has established an accurate way to approximate ground states of quantum spin systems [1] as well as itinerant fermion systems [2]. These neural networks are constructed by introducing hidden variables that are described by classical degrees of freedom.

In this project, we have explored mapping of the Hubbard model (in general, interacting lattice fermions) to noninteracting multicomponent fermion models in the ground states, from which we have proposed a quantum machine learning algorithm called Fermi machine aiming at an efficient quantum many-body solver [3]. Fermion systems are introduced as the hidden part coupled to the physical system, instead of the classical one such as the Ising spins in the previous neural networks. This algorithm has been designed stimulated by the successful descriptions of strongly correlated electron systems by fractionalized fermions [4, 5]. After showing the exact correspondences of 1- and 2-site Hubbard models to two-component noninteracting fermions, a numerical algorithm of the quantum machine learning for the Hubbard model was proposed. Benchmark for the 4-site systems was successfully presented.

In the conventional variational Monte Carlo method, the fermion Slater determinant or Pfaffian is used as the starting point [6]. A crucial difference of the present Fermi machine is the entanglement with the hidden fermion degrees of freedom hybridizing with the physical (visible) fermions in the physical Hubbard model, which allows the formation of the gap structure in the spectra without spontaneous symmetry breaking, generating zeros of the Green's functions as well as poles as in the case of the genuine Mott insulator.

The project was financially supported by MEXT KAKENHI, Transformative Research Area (Grant No. JP22H05111 and No. JP22H05114). and also supported by MEXT under the grant number JPMXP1020230411.

References

[1] G. Carleo and M. Troyer, Science **355**, 602 (2017).

[2] Y. Nomura, A. S. Darmawan, Y. Yamaji, and M. Imada, Phys. Rev. B **96**, 205152 (2017).

[3] M. Imada. J. Phys. Soc. Jpn. **93**, 104002 (2024).

[4] S. Sakai, M. Civelli, and M. Imada, Phys. Rev. Lett. **116**, 057003 (2016).

[5] M. Imada: J. Phys. Soc. Jpn. **90** (2021) 111009.

[6] T. Misawa *et al.* Comput. Phys. Commun. **235**, 447 (2019).

Massively parallel variational Monte Carlo method for excitation spectra augmented by artificial neural networks

Youhei YAMAJI
Research Center for Materials Nanoarchitectonics, National Institute for Materials Science
Namiki, Tsukuba-shi, Ibaraki 305-0044

We have extended the dynamical variational Monte Carlo (dVMC) method [1, 2] for dynamical structure factors to simulating photoemission/inverse photoemission and resonant inelastic x-ray scattering spectra. In Fig. 1, the charge and spin dynamical structure factors (left panel) and momentum resolved inverse photoemission spectrum (right panel) for a one-dimensional half-filled Hubbard model are shown as examples of the extended dVMC results. By combining the results of the dynamical structure factors and the inverse photoemission, we can obtain the resonant inelastic x-ray scattering spectrum as well.

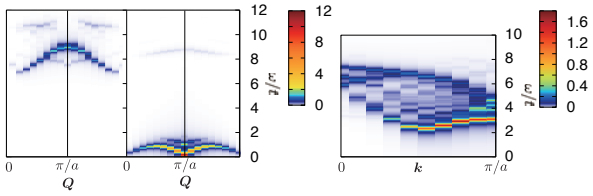


Figure 1: Examples of dVMC results for the one-dimensional Hubbard model at half-filling with 18 sites.

In the present project, we have introduced the quantum number projections [3] omitted in the previous version of the dVMC [2], to improve the accuracy and efficiency of the shared memory parallelization. To further improve the accuracy of the numerical spectroscopy realized by the dVMC method, we also incorporate the restricted Boltzmann machine, which was implemented in the original mVMC [4], and the feed-forward deep neural network, as a part of the generalized Jastrow-Gutzwiller correlation factor.

By further analyzing the resonant inelastic x-ray scattering simulation, we can identify the mutual correlations between single-particle spectral weight and charge and spin excitations. In the one-dimensional Hubbard model, for example, the correlations indeed enable us to identify the spinon and holon branches.

We will apply the method developed in the present project to the low-energy *ab initio* hamiltonians for the cuprate superconductors. To improve the parallelization efficiency of the present dVMC method, the population Monte Carlo that may shorten the warming up process will be useful.

References

[1] T. Li and F. Yang: Phys. Rev. B **81**, 214509 (2010).

[2] K. Ido, *et al.*: Phys. Rev. B **101**, 075124 (2020).

[3] T. Mizusaki and M. Imada: Phys. Rev. B **69**, 125110 (2004).

[4] T. Misawa, *et al.*: Comput. Phys. Commun. **235**, 447 (2019).

Generation of spin model based on machine learning

Satoru Hayami
Graduate School of Science, Hokkaido University, Sapporo 060-0810, Japan

Spin textures that exhibit fundamentally distinct physical properties from those of conventional ferromagnetic and antiferromagnetic systems have been the subject of extensive investigation in both theoretical and experimental contexts. Among these, the magnetic skyrmion, which is characterized by a swirling, topologically nontrivial spin configuration, has served as a focal point in the field of topological magnetism since its initial discovery in 2009. Although skyrmion crystal phases, comprising periodic arrays of magnetic skyrmions, have been experimentally realized in a variety of materials, the precise conditions under which such phases are stabilized, particularly with respect to lattice structures and magnetic interactions, remain to be fully understood. In the project with numbers 2024-Ca-0003 and 2024-Cb-0002, we have undertaken a series of numerical investigations aimed at elucidating the mechanisms responsible for the stabilization of magnetic skyrmion crystal phases under distinct situations. We have presented the main results this year below.

(i) Field-induced transformation between triangular and square skyrmion crystals in a tetragonal polar magnet: We have investigated magnetic field-induced transitions between triangular and square skyrmion crystals in a polar tetragonal magnet [1]. Using simulated annealing of a classical spin model, we have revealed that the competition between Dzyaloshinskii-Moriya and RKKY interactions at multiple wave vectors drives structural transitions in skyrmion lattices. The results demonstrate how magnetic frustration in momentum space can stabilize distinct skyrmion phases, such as distorted-triangular, square, and distorted-square types. These findings provide insight into topological phase transitions and may guide future exploration of skyrmion phenomena in noncentrosymmetric magnets.

(ii) Double-Q and quadruple-Q instabilities at low-symmetry ordering wave vectors under tetragonal symmetry: We have investigated the emergence of double-Q and quadruple-Q magnetic instabilities at low-symmetry wave vectors on a square lattice under tetragonal symmetry [2]. By employing simulated annealing for a classical spin model, we have classified four types of multiple-Q phases depending on the position of the ordering wave vectors. The results reveal that isotropic and anisotropic multiple-Q states can be stabilized without requiring Dzyaloshinskii-Moriya interactions. These findings highlight a novel route to realizing exotic, non-skyrmionic spin textures through momentum-space magnetic frustration.

(iii) Anisotropic skyrmion crystal on a centrosymmetric square lattice under an in-plane magnetic field: We have investigated the stabilization of skyrmion crystals on a centrosymmetric square lattice under an in-plane magnetic field [3]. By performing simulated annealing for an effective spin model, we have demonstrated that the interplay between easy-plane magnetic anisotropy, biquadratic interactions, and high-harmonic wave-vector interactions is essential for stabilizing anisotropic skyrmion crystals. The resulting skyrmion crystal features a vortex-antivortex pair with opposite out-of-plane spin polarizations. We

found that various double-Q phases also emerge, depending on magnetic field strength and anisotropy. These findings reveal new routes for realizing topological spin textures in centrosymmetric magnets with tunable anisotropy under an in-plane magnetic field.

(iv) XXZ-type interlayer exchange interaction in the bilayer triangular-lattice system as a source of multiple skyrmion phases: We have investigated how XXZ-type anisotropic interlayer exchange interactions stabilize various skyrmion crystal phases in a bilayer triangular-lattice spin model with staggered Dzyaloshinskii – Moriya interaction [4]. Through simulated annealing, we have revealed a rich magnetic phase diagram featuring multiple skyrmion crystal phases, including fractional and distorted types, depending on the interlayer anisotropy and external magnetic field. The results highlight how interlayer spin coupling modifies the relative positions of skyrmion cores across layers and facilitates topological spin textures in centrosymmetric systems.

(v) Stabilization mechanisms of magnetic skyrmion crystal and multiple-Q states based on momentum-resolved spin interactions: We have reviewed the theoretical framework for stabilizing magnetic skyrmion crystals and other multiple-Q spin textures using a momentum-resolved effective spin model [5]. We have shown taht the momentum-resolved effective spin model systematically classifies various stabilization mechanisms, such as Dzyaloshinskii – Moriya interaction, biquadratic interaction, anisotropy, and multisublattice effects, across both centrosymmetric and noncentrosymmetric crystals. The model captures diverse topological spin states, including hedgehog, meron-antimeron, and bubble crystals, offering a unified approach to explain experimental phase diagrams and predict novel magnetic phases in quantum materials.

References

[1] S. Hayami, Phys. Rev. B **109**, 184419 (2024).

[2] S. Hayami, Phys. Rev. B **110**, 014404 (2024).

[3] S. Hayami, J. Magn. Magn. Mater. **604**, 172293 (2024).

[4] S. Hayami, J. Magn. Magn. Mater. **619**, 172876 (2024).

[5] S. Hayami and R. Yambe, Mater. Today Quantum **3**, 100010 (2024).

Analyzing Ferromagnetic Order in Multi-Component Fermionic Systems using DMFT

Akihisa Koga
Department of Physics, Institute of Science Tokyo
Meguro, Tokyo 152-8551

Low-temperature properties in correlated fermion systems have attracted much attention since the discovery of high-T_c cuprates. In strongly correlated electron systems, spin degrees of freedom play a crucial role in stabilizing intriguing low-temperature phenomena such as magnetism, superconductivity, and Mott transitions. Orbital degrees of freedom further enrich the emergent behavior in these systems. Recently, optical lattice systems—periodic potentials imposed on ultracold atoms—have emerged as promising platforms for simulating strongly correlated models. In such systems, various parameters such as hopping amplitudes, interaction strengths, and lattice geometries can be precisely controlled. Furthermore, spin and orbital degrees of freedom can be introduced, enabling the realization of multicomponent strongly correlated fermionic systems.

One fundamental question is how symmetry-breaking states emerge in such multicomponent systems. In our previous work [1], we have investigated the half-filled Hubbard model with repulsive interactions to explore the instability toward antiferromagnetic order. By contrast, ferromagnetic instability in SU(N) Hubbard models remains poorly understood, especially beyond the SU(2) case. In the strong-coupling limit of the SU(2) Hubbard model, the motion of a single hole on a closed-loop lattice leads to a fully spin-polarized ground state—a phenomenon known as Nagaoka ferromagnetism. Although similar behavior has been reported in the SU(3) case [2], it remains an open question whether such ferromagnetic order persists at finite doping. In this regime, it is essential to treat strong Coulomb interactions and the low-energy itinerant behavior of electrons on an equal footing.

In this project, we investigate multicomponent fermionic systems described by the SU(N) Hubbard model and examine how ferromagnetic order emerges at low temperatures. To take strong particle correlations into account, we employ dynamical mean-field theory (DMFT) combined with the continuous-time quantum Monte Carlo (CTQMC) method. This approach allows us to treat strong correlations non-perturbatively and access low-temperature regimes relevant to magnetic ordering. Preliminary calculations suggest that ferromagnetic order emerges upon hole doping around one-third filling. Further detailed simulations and analyses are ongoing and will be reported in a forthcoming publication [3].

References

[1] H. Yanatori and A. Koga, Phys. Rev. B 94, 041110 (2016).

[2] H. Katsura and A. Tanaka, Phys. Rev. A 87, 013617 (2013).

[3] J. Fujii, K. Yamamoto and A. Koga, to be submitted.

Theoretical design of candidates for multilayer nickelate superconductors

KAZUHIKO KUROKI
Department of Physics, Osaka University
1-1 Machikaneyama, Toyonaka, Osaka, 560-0043, Japan

Theoretical studies have shown that the superconducting T_c in the bilayer Hubbard model can be higher than that of the d-wave superconducting state in the single-orbital Hubbard model [1, 2]. Hence, a realization of the bilayer Hubbard model in actual materials is a promissing path toward finding new high temperature superconductors. Along this path, we previously proposed that a double layer Ruddlesden-Popper compound $La_3Ni_2O_7$ can be a good candidate for realizing the bilayer Hubbard model that satisfies the abovementioned conditions [3].

Recently, this material $La_3Ni_2O_7$ was found to exhibit high T_c superconductivity with a highest T_c of about 80 K under pressure above 14 GPa [4]. Iinspired by this experiment, we theoretically revisited the possibility of superconductivity in $La_3Ni_2O_7$ by constructing a four-orbital model that takes into account the crystal structure at high pressures, and applying fluctuation exchange approximation to the model. We find that $s\pm$-pairing superconductivity, which is somewhat similar to that of the bilayer Hubbard model, can take place with high T_c that is consistent with the experimental observation[5].

Moreover, we further studied the possibility of superconductivity in a trilayer Ruddlesden-Popper nickelate $La_4Ni_3O_{10}$ under pressure. Since experiments on $La_3Ni_2O_7$ suggest that superconductivity takes place when the crystal structure becomes tetragonal ($I4/mmm$ symmetry) under pressure, it is natural to assume that a similar condition should be necessary for superconductivity to take place in $La_4Ni_3O_{10}$. Through DFT calculations, we found that a structural phase transition from monoclinic to tetragonal takes place around 15 GPa. Using the tetragonal crystal structure, we have theoretically investigated the possibility of superconductivity, where a combination of fluctuation exchange approximation and linearized Eliashberg equation is applied to a six-orbital model constructed from first principles band calculation. The obtained results suggests that $La_4Ni_3O_{10}$ may also become superconducting under high pressure with T_c comparable to relatively low T_c cuprates, although it is not as high as $La_3Ni_2O_7$[6]. This theoretical expectation was confirmed from experiments on polycrystalline samples[6].

There is now growing desire to realize bulk high T_c superconductivity at ambient pressure. In R6

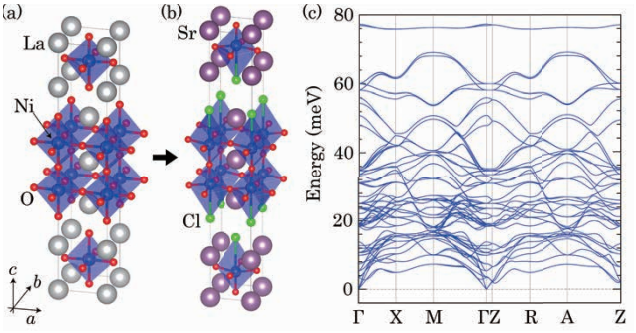


FIG. 1. (a) Crystal structure of $La_3Ni_2O_7$ at high pressure. (b) Crystal structure and (c) phonon band dispersion for $Sr_3Ni_2O_5Cl_2$ without applying pressure. Panels (b) and (c) are shown for the space group of $I4/mmm$. Crystal structures in this paper were depicted using the VESTA software [9]. Phonon dispersions in this paper were depicted in the Brillouin zone of the conventional tetragonal lattice.

fiscal year, we have theoretically designed a new material, $Sr_3Ni_2O_5Cl_2$, for which we predicted that the crystal structure takes $I4/mmm$ symmetry at ambient pressure[7]. Here, we have replaced La by Sr to raise the tolerance factor, and replaced the two outer apical O by Cl to partially compensate the number of electrons in Ni (Fig.1(a)(b)). Our phonon calculation performed for the structure with $I4/mmm$ symmetry at ambient pressure exhibit no imaginary modes (Fig.1(c)), showing that this structure is dynamically stable. Our fluctuation exchange study on this material shows that the T_c can be comparable to pressurized $La_3Ni_2O_7$[7]. Although this material had never been synthesized in the past, quite recently, Takano's group at NIMS succeeded in high pressure synthesis of this material[8], and found that the crystal structure indeed takes $I4/mmm$ symmetry at ambient pressure. Although superconductivity has not been observed at present, certainly more experiments are necessary to understand the nature of this new material.

[1] K. Kuroki, T. Kimura, and R. Arita, Phys. Rev. B **66**, 184508 (2002).
[2] V. Mishra, D. J. Scalapino, and T. A. Maier, Sci.

Rep. **6**, 32078 (2016).
[3] M. Nakata, D. Ogura, H. Usui, and K. Kuroki, Phys. Rev. B **95**, 214509 (2017).
[4] H. Sun, M. Huo, X. Hu, J. Li, Z. Liu, Y. Han, L. Tang, Z. Mao, P. Yang, B. Wang, J. Cheng, D.-X. Yao, G.-M. Zhang, and M. Wang, Nature (2023).
[5] H. Sakakibara, N. Kitamine, M. Ochi, and K. Kuroki, Phys. Rev. Lett. **132**, 106002 (2024).
[6] H. Sakakibara, M. Ochi, H. Nagata, Y. Ueki, H. Sakurai, R. Matsumoto, K. Terashima, K. Hirose, H. Ohta, M. Kato, Y. Takano, and K. Kuroki, Phys. Rev. B **109**, 144511 (2024).
[7] M. Ochi, H. Sakakibara, H. Usui, and K. Kuroki, Phys. Rev. B **111**, 064511 (2025).
[8] K. Yamane, Y. Matsushita, S. Adachi, R. Matsumoto, K. Terashima, T. Hiroto, H. Sakurai, and Y. Takano, Acta Cryst. **C81**, 259 (2025).
[9] K. Momma and F. Izumi, J. Appl. Crystallogr. **44**, 1272 (2011).

Field-driven spin structure and magnetization plateau in a spinel ferrimagnet $MnCr_2S_4$

Hidemaro SUWA
Department of Physics, University of Tokyo, Tokyo 113-0033

Many interesting magnetic materials behave in unexpected ways because the local spins inside them cannot all point in directions that keep every neighbour happy. This situation is called magnetic frustration, and it can lead to exotic states of matter such as spin liquids, multiferroics, or supersolid-like magnets. Spinel crystals whose chemical formula is AB_2X_4 are a playground for such behaviour because their crystal lattice forces the spins on the A and B sites into two different, competing arrangements.

We studied the sulphur spinel $MnCr_2S_4$, in which the A site hosts manganese ions (Mn^{2+}) and the B site hosts chromium ions (Cr^{3+}). At ordinary temperatures the spins point every which way (a paramagnet). On cooling to about 65 K they lock into a ferrimagnetic pattern: the manganese and chromium sublattices point in opposite directions, so the whole crystal keeps a net magnetisation. Cooling further, below ≈ 5 K, the spins tilt away from perfect opposition and form a special canted arrangement known as a Yafet–Kittel (YK) phase.

Things become even richer when we apply very strong magnetic fields. At low temperatures we observed a sequence of five field-driven transitions at roughly 11 T, 25 T, 50 T, 75 T and 85 T. Between 25 T and 50 T the magnetisation plateaus at exactly 6 μB per formula unit—a hallmark of strong coupling between the spins and the crystal lattice (spin-lattice coupling). Theoretical work suggests some of these field-induced phases behave like spin superfluids or supersolids.

Previous neutron studies of $MnCr_2S_4$ were carried out on powdered samples and only in zero field, leaving several open questions: Is the low-temperature YK phase real or an artefact? What exact spin patterns appear in the various high-field phases? How does the interaction between manganese and chromium spins evolve with field?

To answer these questions, we performed a large-scale Monte Carlo simulation of a frustrated spin-lattice model on ISSP System B in the class C project (2024-Ca-0073) in an MPI parallel computation using up to eight nodes simultaneously. We nailed down the spin structre for each phase by comparing our simulation to a neutron-diffraction experiment combining conventional powder measurements and high-resolution single-crystal experiments in magnetic fields up to 35 T. By analysing the data together with mean-field calculations, we determined how the manganese–manganese and manganese–chromium exchange couplings change from one phase to the next and how strongly the lattice participates in those changes. Our results clarified the complete magnetic phase diagram of $MnCr_2S_4$ and provide a solid starting point for future theories of frustrated spin-lattice systems.

References

[1] F. Duc, N. Qureshi, H. Suwa, et al., Phys. Rev. B. **110**, 214416 (2024).

Spin Nematics and Spin Liquids in *S*=1 magnets

Rico Pohle

Creative Science Unit,

Faculty of Science, Shizuoka University, Shizuoka 422-8529

We have studied the thermodynamic and dynamical properties of unconventional magnets composed of atoms with higher spin *S*. In particular, we focused on magnets made of *S*=1 moments due to their connection with spin nematic phases – magnetically ordered states where the order arises not from spin-dipole moments, but from spin-quadrupole moments. To investigate these systems, we have utilized a novel method based on a *U*(3) formalism [1]. This method enables us to compute finite-temperature properties via Monte Carlo simulations (u3MC) and dynamical properties via molecular dynamics simulations (u3MD) for *S*=1 magnets on any type of lattice. Our codes have been efficiently implemented with large-scale CPU parallelization on the ISSP supercomputer. During the fiscal year FY2024, we achieved significant progress on the following topics:

(i) Simulation of gravitational waves from spin nematic phases: Fluctuations away from ferroquadrupolar order in spin nematics can be described by higher-rank tensor fields. In this project, we compared the action governing quadrupolar fluctuations in spin nematics to the action of spacetime fluctuations in flat space, and found that their mathematical structures are closely related. This opens a new avenue for studying gravitational wave physics within a microscopic condensed matter system. We supported this theoretical proposal with numerical simulations of vortex-pair annihilation processes in a spin nematic state, suggesting a potential direction for experimental observation in cold atom systems [2].

(ii) Interplay of spin nematics and spin liquids in *S*=1 Kitaev models: We investigated the interplay between spin nematic phases and spin liquids in the *S*=1 Kitaev model with bilinear-biquadratic (BBQ) interactions using the u3MC and u3MD simulation methods. We discovered that the model stabilizes a chiral spin liquid, which we analyzed further by simplifying the model to a discretized eight-color model [3]. We found that the chiral spin liquid can be interpreted as an example of classical topological order, after mapping it to a Z_2 lattice gauge theory. We confirmed our physical understanding and interpretations through classical Monte Carlo simulations [4].

(iii) *S*=1 BBQ model on the pyrochlore lattice and application to $NaCaNi_2F_7$: We

studied the phase diagram of the S=1 BBQ model on the pyrochlore lattice using u3MC and u3MD simulations. We identified up to seven distinct spin liquid phases and proposed that $NaCaNi_2F_7$ is proximate to a nematic spin liquid, where strong biquadratic interactions drive a finite-temperature transition that breaks spin rotational symmetry while retaining a residual $U(1)$ degree of freedom. We also showed that dynamics of quadrupolar moments reveal a gapless Goldstone mode and proposed a mechanism for the observed spin glass transition based on weak anisotropic spin interactions perturbing the nematic spin liquid state [5].

References

[1] K. Remund *et al.*, Phys. Rev. Research **4**, 033106 (2022).

[2] L. Chojnacki *et al.*, Phys. Rev. B **109**, L220407 (2024) [Editor's suggestion].

[3] R. Pohle, N. Shannon, and Y. Motome, Phys. Rev. Research **6**, 033077 (2024).

[4] H. Yan and R. Pohle, Phys. Rev. Research **7**, L012052 (2025).

[5] R. Pohle and N. Shannon, preprint (arXiv:2503.12776).

Novel Quantum Phases with Current and Spin Current Textures due to Electron Correlation

Takami TOHYAMA
Department of Applied Physics, Tokyo University of Science, Katsushika, Tokyo 125-8585

Unexpected phenomena often emerge in quantum many-body systems, and they are most pronounced when strong quantum fluctuations are present in strongly correlated electron systems. Such phenomena have recently observed in kagome metals AV_3Sb_5 (A=Cs, Rb, K). In these compounds, unconventional superconductivity, time-reversal symmetry breaking, and nematic order have been reported in the presence of charge orders. Based on a single-orbital Hubbard model on a kagome lattice, an inverse star of David-type bond order as well as a charge-loop current order has been proposed theoretically [1]. However, there are few studies that investigate the ground state of the model by unbiased numerical calculations.

In this project, we investigate the ground state properties of the single-orbital kagome Hubbard model using the density-matrix renormalization group (DMRG) method whose computational code has been developed by our group. We use a 76-site rhombus lattice with six triangles along one direction (open boundary condition) and four triangles along the other direction (periodic boundary condition) and the ratio of on-site Coulomb interaction U and nearest-neighbor hopping t to be $U/t = 6$ and 10. The bond dimension of the DMRG procedures is maximally set to be 10,000 and a snake-type geometry is taken for one-dimensional sweeping in DMRG.

The electron-density and bond-density distributions are calculated for $n = 0.95$, 0.84, and 0.74, whose numbers are determined by the fact that the Fermi level of AV_3Sb_5 is close to a van Hove singularity (vHS) point in a non-interacting kagome band structure. We find that the inverse star of David-type bond order is formed only at $n = 0.84$ (close to the vHS point) for both $U/t = 6$ and 10 [3]. At the same time, a charge order is seen in the density profile at $n = 0.84$. We also calculate the spatial distribution of charge and spin currents around a bond to which a pinning field is applied. This method has been applied to several types of Hubbard models and spin loop-current textures have been proposed for a charge-modulated system such as a stripe phase of the Hubbard model on a square lattice [2]. We find that only the $n = 0.84$ case induces charge and spin currents near the bond with a pinning field. These findings indicate that vHS in a kagome lattice under the presence of strong correlation plays a crucial role in generating unexpected quantum phenomena.

References

[1] R. Tazai, Y. Yamakawa, and H. Kontani: Nat. Commun. **14**, 7845 (2023).

[2] K. Shinjo, S. Sota, S. Yunoki, and T. Tohyama: Phys. Rev. B **108**, 195118 (2023).

[3] T. Tohyama *et al.*, in preparation.

Research of Quantum Critical Points in the Vicinity of Three-Channel Kondo Phase

Takashi HOTTA
Department of Physics, Tokyo Metropolitan University
1-1 Minami-Osawa, Hachioji, Tokyo 192-0397

For the purpose to promote our understanding on the emergence of three-channel Kondo effect from Ho ions for the case with Γ_5 triplet ground state [1], we have attempted to investigate quantum critical points around the three-channel Kondo state in the phase diagram on the V_8-V_7 plane, where V_7 and V_8 denote the hybridization of localized Γ_7 and Γ_8 electrons with the conduction bands, respectively.

Let us start our discussion on the exhibition of the model Hamiltonian. First we define one f-electron state by the eigenstate of spin-orbit and crystalline electric field (CEF) potential terms. Under the cubic CEF potential, we obtain Γ_7 doublet and Γ_8 quartet from $j = 5/2$ sextet, whereas we find Γ_6 doublet, Γ_7 doublet, and Γ_8 quartet from $j = 7/2$ octet. Next we include the Γ_7 and Γ_8 conduction electron bands. Note that we consider only the hybridization between the conduction and $j = 7/2$ electrons to consider heavy rare-earth ion such as Ho^{3+}. Then, we obtain the model Hamiltonian as

$$\begin{aligned} H &= \sum_{\boldsymbol{k},\mu,\tau} \varepsilon_{\boldsymbol{k}} c^\dagger_{\boldsymbol{k}\mu\tau} c_{\boldsymbol{k}\mu\tau} + \sum_{\boldsymbol{k},\mu,\tau} V_\mu (c^\dagger_{\boldsymbol{k}\mu\tau} f_{b\mu\tau} + \text{h.c.}) \\ &+ nE_f + \sum_{j,\mu,\tau} (\lambda_j + B_{j,\mu}) f^\dagger_{j\mu\tau} f_{j\mu\tau} \\ &+ \sum_{j_1\sim j_4} \sum_{\mu_1\sim\mu_4} \sum_{\tau_1\sim\tau_4} I^{j_1 j_2, j_3 j_4}_{\mu_1\tau_1\mu_2\tau_2,\mu_3\tau_3\mu_4\tau_4} \\ &\times f^\dagger_{j_1\mu_1\tau_1} f^\dagger_{j_2\mu_2\tau_2} f_{j_3\mu_3\tau_3} f_{j_4\mu_4\tau_4}, \end{aligned} \tag{1}$$

where $\varepsilon_{\boldsymbol{k}}$ denotes the dispersion of conduction electron with wave vector $\boldsymbol{k}$, $c_{\boldsymbol{k}\mu\tau}$ indicates the annihilation operator of a conduction electron, $f_{j\mu\tau}$ is the annihilation operator of a localized f electron in the bases of (j, μ, τ), j denotes the total angular momentum, $j = 5/2$ and $7/2$ are denoted by "a" and "b", respectively, μ distinguishes the cubic irreducible representation, Γ_8 states are distinguished by $\mu = \alpha$ and β, while the Γ_7 and Γ_6 states are labeled by $\mu = \gamma$ and δ, respectively, τ denotes the pseudo-spin, which distinguishes the degeneracy concerning the time-reversal symmetry, V_μ denotes the hybridization between f electron in the μ orbital and conduction electron of the μ band, n is the local f-electron number at an impurity site, and E_f is the f-electron level to control n.

As for the spin-orbit term, we obtain $\lambda_a = -2\lambda$ and $\lambda_b = (3/2)\lambda$, where λ is the spin-orbit coupling of f electron. Here we set $\lambda = 0.265$ eV for Ho ion. Concerning the CEF potential term for $j = 5/2$, we obtain $B_{a,\alpha} = B_{a,\beta} = 1320B^0_4/7$ and $B_{a,\gamma} = -2640B^0_4/7$, where B^0_4 denotes the fourth-order CEF parameter for the angular momentum $\ell = 3$. For $j = 7/2$, we obtain $B_{b,\alpha} = B_{b,\beta} = 360B^0_4/7 + 2880B^0_6$, $B_{b,\gamma} = -3240B^0_4/7 - 2160B^0_6$, and $B_{b,\delta} = 360B^0_4 - 3600B^0_6/7$. In the following calculations, we use the parametrization as $B^0_4 = Wx/15$ and $B^0_6 = W(1 - |x|)/180$ for $\ell = 3$, where x specifies the CEF scheme for the O_h point group, while W determines the energy scale of the CEF potentials. In this work, we set $W = 10^{-3}$ eV and treat x as the parameter to control the CEF ground state.

For the Coulomb interaction terms, we do not show the explicit forms of I here, but they are expressed by the four Slater-Condon pa-

rameters, F^0, F^2, F^4, and F^6. These values should be determined from experimental results, but here we simply set the ratio as $F^0/10 = F^2/5 = F^4/3 = F^6 = U$, where U indicates the Hund's rule interaction among the f orbitals. In this work, we set $U = 1$ eV.

Concerning the electron hybridization, we introduce $V_7 = V_\gamma$ and $V_8 = V_\alpha = V_\beta$ with $V_\delta = 0$. In the previous research, we have considered only the case of $V_7 = V_8$ [1], but in the present research, we treat the general case of $V_7 \neq V_8$ to depict the ground-state phase diagram including the three-channel Kondo state.

We have analyzed the three-band Anderson model by exploiting a numerical renormalization group (NRG) method. We introduce a cut-off Λ for the logarithmic discretization of the conduction band. Due to the limitation of computer resources, we keep M low-energy states. Here we use $\Lambda = 8$ and $M = 5,000$. In the NRG calculation, the temperature T is defined as $T = D\Lambda^{-(N-1)/2}$, where D is half the conduction band width, which is set as 1 eV, and N is the number of renormalization steps.

We briefly explain our previous result [1]. From the NRG calculations for the case of $V_7 = V_8$, we have unveiled the three-channel Kondo effect for the local Γ_5 triplet ground state, characterized by a residual entropy $S_{\rm imp}(0)$ of $\log \phi$ with the golden ratio $\phi = (1+\sqrt{5})/2$.

In order to seek for the relation between the quantum criticality and the emergence of the three-channel Kondo phase, we have attempted to depict the ground-state phase diagram on the V_8-V_7 plane, by repeating the NRG calculations for a thousand of parameter sets (V_8, V_7). To understand the ground-state property, we have checked the temperature dependence of entropy $S_{\rm imp}(T)$ and the change of the energy spectra as functions of NRG steps. The details will be discussed elsewhere [2], but here we show a part of the results.

In Fig. 1, we show the ground-state phase diagram on the V_8-V_7 plane in the region of $0 < V_8 \leq 1.2$ and $0 < V_7 \leq 1$. We note a quantum critical point (QCP) on the line of $V_7 = 0$ around $V_8 \approx 0.8$, characterized by the residual entropy $S_{\rm imp}(0) = \log\sqrt{2}$. This QCP is well known to appear between the Kondo singlet and the CEF singlet phases. Note that in the present case, the Kondo singlet appears for small V_8 from the screening of local Γ_5 triplet.

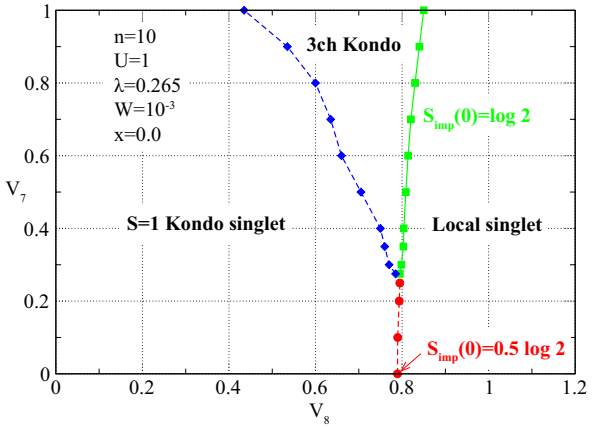


Figure 1: Ground-state phase diagram on the V_8-V_7 plane in the region of $0 < V_8 \leq 1.2$ and $0 < V_7 \leq 1$.

With the increase of the value of V_7 near the QCP, the residual entropy of $\log\sqrt{2}$ is found to disappear, while the sudden change in the energy spectrum still remains, corresponding to the change in the ground state from the Kondo singlet to the local singlet phase. When we further increase V_7 up to 0.3, we encounter the three-channel Kondo phase between the Kondo singlet and the local singlet phases. Note that the boundary between the three-channel Kondo and the local singlet phases is characterized by a residual entropy of $\log 2$ [1]. We have noticed that the three-channel Kondo phase eventually disappears when we further increase V_7, but the final destination will be discussed in the near future [2].

References

[1] T. Hotta, J. Phys. Soc. Jpn. **90**, 113701 (2021).

[2] T. Hotta, in preparation.

Spin fluctuations and superconductivity in f-electron compounds under pressure

Makoto SHIMIZU
Department of Physics, Graduate School of Science, Kyoto University
Kyoto 606-8502, Japan

A heavy-fermion paramagnet UTe_2 has been a strong candidate for a spin-triplet superconductor. Experiments on UTe_2 under pressure have been vigorously conducted, and rich phase diagrams have been suggested. We study the electronic structure of the compound under pressure based on the density functional theory (DFT) with employing structural optimization. For structural optimization, we use VASP installed on the ISSP supercomputers.

As a result, the low-energy band structure and Fermi surfaces are not sensitive to pressure for parameters where itinerant f-electrons are not essential. However, we find a significant pressure dependence for a certain Coulomb interaction U of the GGA+U calculation, where the large weight of f-electrons appears at the Fermi level. An increase in the density of states at the Fermi level is observed under pressure, which is attributed to compressive stress along the [010] crystallographic axis.

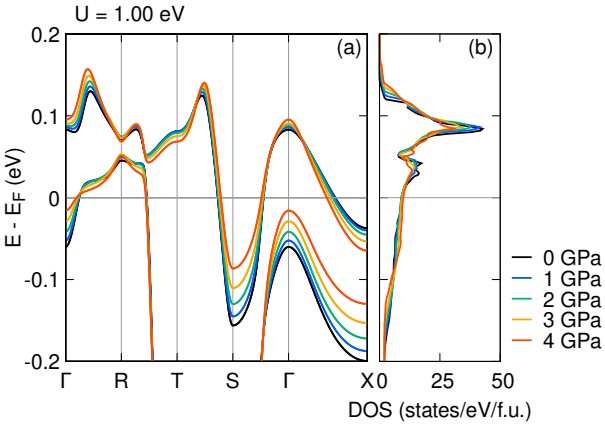


Figure 1: (a) Band structure and (b) density of states of UTe_2 under hydrostatic pressure within GGA+U where $U = 1$ eV.

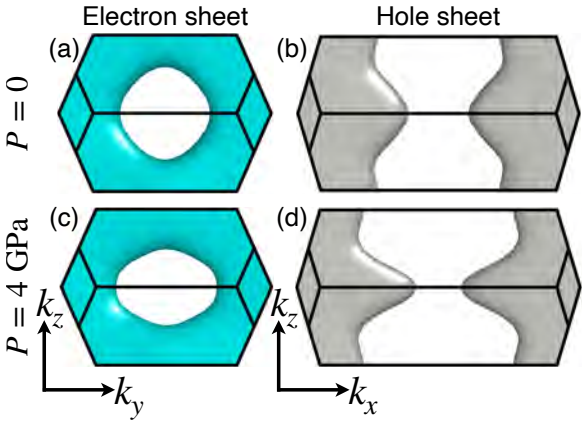


Figure 2: Fermi surface of UTe_2 under hydrostatic pressure within GGA+U where $U = 1$ eV.

References

[1] M. Shimizu, and Y. Yanase, arXiv:2408.04292.

Nonequilibrium phenomena in strongly correlated systems

Robert Peters

Department of Physics

Graduate School of Science, Kyoto University, Kyoto 606-8502

Understanding emergent phenomena in strongly correlated and topologically nontrivial materials requires high-precision numerical simulations that go beyond analytical treatments. Leveraging large-scale computational resources, we investigated (i) nonlinear response functions in magnetic materials and (ii) quantum dynamics in spin systems using neural network quantum states.

Nonlinear Responses in Correlated and Topological Magnetic Systems

In recent years, nonlinear spintronics has emerged as a promising frontier for the control and detection of spin phenomena that goes beyond linear response theory. Using supercomputing resources, we numerically evaluated second-order response functions in strongly correlated systems and magnets, focusing on two key phenomena: the nonlinear Edelstein effect (NEE) and the nonlinear magnetoelectric effect (NMEE).

In the first study [1], we investigated the NEE in a correlated electron system described by a Hubbard model. Our simulations revealed that electron correlations can significantly modify the magnitude of the nonlinear spin response. Specifically, the real part of the electronic self-energy enhances the NEE, while the imaginary part leads to suppression. The NEE was also found to be closely related to optically induced spin currents and the inverse Faraday effect, providing a bridge to nonlinear optical spintronics.

In the second study [2], we explored the NMEE in systems with magnetic octupole order, such as a d-wave altermagnet and a pyrochlore lattice with all-in/all-out magnetic order. We calculated the NMEE tensor using quantum kinetic theory and confirmed its significant magnitude through detailed numerical simulations. Notably, in the magnetic Weyl semimetal phase of the pyrochlore lattice, the NMEE is strongly enhanced near Weyl nodes due to the contribution of the quantum metric in the response tensor. These results provide a pathway for detecting hidden

multipolar orders through nonlinear magneto-optical measurements.

Quantum Dynamics with Neural Network Quantum States

In a separate project, we investigated the real-time dynamics of quantum skyrmions using neural network quantum states (NNQS) [3]. Employing variational Monte Carlo with a restricted Boltzmann machine as the wavefunction ansatz, we first obtained the ground state of a quantum Heisenberg model with Dzyaloshinskii-Moriya interaction. Using the time-dependent variational principle, we simulated the evolution of quantum skyrmions under a magnetic field gradient.

Our results show that field gradients are a powerful tool for controlling skyrmion motion in quantum spin systems. Furthermore, we observed skyrmion decay due to interactions, highlighting the importance of quantum effects in skyrmion dynamics. These calculations demonstrate that NNQS can access quantum real-time dynamics in regimes inaccessible to conventional exact diagonalization.

References

[1] Jun Ōiké and Robert Peters, *Phys. Rev. B* **110**, 165111 (2024).

[2] Jun Ōiké, Koki Shinada, and Robert Peters, *Phys. Rev. B* **110**, 184407 (2024).

[3] Ashish Joshi, Robert Peters, and Thore Posske, *Phys. Rev. B* **110**, 104411 (2024).

Computational Studies of Pressure Effects on Electronic Correlations and Superconductivity in Organic Conductors

Kazuyoshi Yoshimi
Institute for Solid State Physics, University of Tokyo
Kashiwa-no-ha, Kashiwa, Chiba 277-8581

The objective of this research is to estimate detailed crystal structures under pressure and predict functional properties of strongly correlated materials using *ab–initio* calculations. Special attention is given to organic molecular solids, where pressure significantly affects electronic properties, including charge/spin ordering, superconductivity, and topological phenomena. Based on crystal structure data obtained from experimental groups, we derived low-energy effective models under pressure and quantitatively analyzed electronic correlation effects. We also performed first-principles calculations to optimize structures obtained under ambient pressure and verified consistency with experimental results. As a large number of systematic calculations were required for various pressure conditions, scripts were generated for bulk jobs using Moller [4] and exhaustive calculations were carried out for several pressure conditions in order to significantly improve the efficiency of the calculations.

In this study [5], single-crystal X-ray diffraction experiments on the organic conductor $(TMTTF)_2PF_6$ were performed under pressures up to 8 GPa, enabling precise structural determination. Using these structures, we conducted first-principles calculations with Quantum ESPRESSO [1] and derived low-energy effective models using RESPACK [2], based on the calculated band structures and Wannier functions. These models were then analyzed using mVMC [3], thoroughly evaluating the stability of charge and spin ordering under pressure.

As a result of the significant decrease in crystal volume with increasing pressure, the conduction bandwidth is broadened and the screen-Coulomb interaction is dramatically reduced. Additionally, the degree of dimerization in the conduction bands sharply decreased and nearly vanished above 3 GPa, significantly diminishing the strength of electronic correlations. Furthermore, we confirmed a good agreement between experimental resistivity measurements and theoretical analysis. Specifically, the stability of spin-density wave (SDW) and charge ordering (CO), derived from theoretical calculations, was consistent with experimental resistivity data. The CO notably became unstable above approximately 1 GPa, while the SDW persisted at higher pressures. These outcomes clarify the differences between physical and chemical pressures [6] and deepen the understanding of unified phase diagrams.

Additionally, we performed X-ray structural analysis and electronic structure calculations under pressure on the organic superconductor β'-$(ET)_2ICl_2$ [7]. Our findings revealed a Lifshitz transition around 6 GPa, changing the Fermi surface from one-dimensional to two-dimensional. Concurrently, the on-site Coulomb interaction significantly decreased, reaching approximately half its ambient-pressure value around 10 GPa.

These results provide crucial insights into the mechanism of superconductivity under high pressure and elucidate the significant impact of pressure-induced electronic structure changes on superconductivity in organic materials.

References

[1] P. Giannozzi, O. Andreussi, T. Brumme *et al.*, J. Phys. Condens. Matter. **29**, 465901(2017).

[2] K. Nakamura, Y. Yoshimoto, Y. Nomura *et al.*, Comput. Phys. Commun., **261**, 107781 (2021).

[3] T. Misawa, S. Morita, K. Yoshimi *et al.*, Comput. Phys. Commun. **235**, 447 (2019).

[4] https://github.com/issp-center-dev/Moller.

[5] M. Itoi, K. Yoshimi, H. Ma *et al.*, Phys. Rev. Research **6**, 043308.

[6] K. Yoshimi, T. Misawa, T. Tsumuraya, and H. Seo, Phys. Rev. Lett. **131**, 036401 (2023).

[7] T. Kobayashi, K. Yoshimi, H. Ma *et al.*, Phys. Rev. Materials **9**, L021801 (2025).

Studies of the superconductivity and magnetic states in the strongly correlated electron systems using Hubbard models.

Atsushi Yamada
Department of Physics, Chiba University
Chiba 263-8522, Japana, Chiba 277-8581

Strong electron correlations lead to interesting phenomena such as superconductivity with various pairing symmetries and purely paramagnetic insulator (spin liquid) in low dimensional materials. The organic charge-transfer salts κ-(BEDT-TTF)$_2$Cu$_2$(CN)$_3$ [1, 2, 3, 4, 5, 6, 7] is a good example of such materials, whose spin liquid state transits to a superconductor with d_{xy} pairing symmetry at $T_K = 3.9$ K upon applying pressure [5, 6].

The superconductivity(SC) of this material was studied theoretically using the Hubbard model on the isotropic triangular lattice, which is a simple effective Hamiltonian of this material[8] described by the hopping t and the on-site Coulomb repulsion U.

We have studied d-wave superconductivity(SC) in this model at zero temperature and half-filling using the variational cluster approximation[9]. We found that the d_{xy} SC is the ground state below the Mott insulator phase $U/t \lesssim 6$, and the energy of chiral $d + id$ SC is slightly higher than the d_{xy} SC. The energy difference between the normal and d_{xy} states is about $0.02t \sim 0.06t$ for $U/t \simeq 4 \sim 5$. This result is semi-quantitatively consistent with the SC transition temperature $T_K = 3.9$ K of κ-(BEDT-TTF)$_2$Cu$_2$(CN)$_3$, where t is estimated to be about 0.06 eV, and the predicted pairing symmetry d_{xy} agrees with the STM observations. The energy difference between the $d + id$ and d_{xy} is about $0.01t \sim 0.03t$ for $U/t \simeq 4 \sim 5$ so the transition from $d + id$ to d_{xy}, or some effects of $d + id$ in d_{xy} phase may be observed in experiments for κ-(BEDT-TTF)$_2$Cu$_2$(CN)$_3$.

References

[1] S. Lefebvre, P. Wzietek, S. Brown, C. Bourbonnais, D. Jérome, C. Mézière, M. Fourmigué, and P. Batail, Phys. Rev. Lett. **85**, 5420 (2000).

[2] Y. Shimizu, K. Miyagawa, K. Kanoda, M. Maesato, and G. Saito, *et al.*, Phys. Rev. Lett. **91**, 107001 (2003).

[3] F. Kagawa, T. Itou, K. Miyagawa, and K. Kanoda, Phys. Rev. B **69**, 064511 (2004).

[4] Y. Kurosaki, Y. Shimizu, K. Miyagawa, K. Kanoda, and G. Saito, Phys. Rev. Lett. **95**, 177001 (2005).

[5] K. Izawa, H. Yamaguchi, T. Sasaki and Y. Matsuda, Phys. Rev. Lett. **88** 027002 (2001).

[6] K. Ichimura and K. Nomura, J. Phys. Soc. Jpn. **75**, 051012 (2006).

[7] R.S. Manna, M. de Souza, A. Brühl, J.A. Schlueter, and M. Lang, Phys. Rev. Lett. **104**, 016403 (2010).

[8] H. Kino and H. Fukuyama, J. Phys. Soc. Jpn. **65**, 2158 (1996).

[9] A. Yamada, J. Phys. Soc. Jpn. **94**, 044705 (2025).

Electron correlation in strongly interacting electron systems

Takashi YANAGISAWA
National Institute of Advanced Industrial Science and Technology (AIST)
1-1-1 Umezono, Tsukuba, Ibaraki 305-8568, Japan

1 Introduction

In our numerical research, we use the optimized many-body wave functions to study electronic properties of strongly correlated electron systems. The expectation values are evaluated by using the Metropolis Monte Carlo procedure. We carried out parallel computations in Monte Carlo calculations. In order to reduce statistical errors, we performed ~ 500 parallel calculations. Parallel computing is very essential to reduce Monte Carlo statistical errors. The parallelization rate reached 99%.

We use the optimized many-body wave function which is improved by multiplying by off-diagonal exponential operators given by $e^{-\lambda K}$ and P_G where K is the kinetic energy part (non-interacting part) of the Hamiltonian and $P_G = P_G(g)$ is the Gutzwiller operator to control the double occupancy with the variational parameter g[1]. P_G is also written in the form $e^{-\alpha D}$. $\psi^{(1)} \equiv \psi_G = P_G\psi_0$ is the well known Gutzwiller wave function. We consider the many-body wave function given by $\psi^{(2)} \equiv \exp(-\lambda K)P_G\psi_0$, where ψ_0 indicates an initial wave function which is usually taken as the Fermi sea, the BCS wave function or the state with some magnetic (or charge) orders. We can improve the wave function systematically by multiplying by operators P_G and $e^{-\lambda K}$ further.

We can also consider $\psi^{(3)} \equiv P_G(g')\psi^{(2)}$ and $\psi^{(4)} \equiv \exp(-\lambda' K)P_G(g')\psi^{(2)}$ for different variational parameters λ' and g'. The wave function $\psi^{(4)}$ is a very good many-body wave function because the ground-state energy is lowered greatly and the ground-state energy is lower than those that are evaluated by using any other wave functions. We can further proceed to employ $\psi^{(5)}$ and $\psi^{(6)}$. We can also use the Jastrow-type wave function which is written as $\psi_J = P_G P_Q P_J \psi_0$ where P_J indicates a nearest-neighbor number correlation operator and P_Q controls the nearest-neighbor doublon-holon correlation.

2 Strong correlation effect on superconductivity

We have carried out variational Monte Carlo simulations to examine the ground state of the two-dimensional Hubbard model on a square lattice. We here examine the effect of strong correlation on superconductivity. The BCS wave function $\psi_{BCS}(\Delta_s)$ with the gap function Δ_s clearly shows the long-range correlation. In Fig. 1, we show the superconducting correlation function $D_{sc}(\ell) = \langle \Delta^\dagger(i)\Delta(i+\ell)\rangle$ as a function of lattice sites for $N_e = 88$, $U = 18t$ and $t' = 0$ on a 10×10 lattice[5]. Here the pair annihilation operator $\Delta(i)$ at the site i is given by

$$\Delta(i) = \Delta_x(i) + \Delta_{-x}(i) - (\Delta_y(i) + \Delta_{-y}(i)), \quad (1)$$

where $\Delta_\alpha = c_{i\downarrow}c_{i+\hat{\alpha}\uparrow} - c_{i\uparrow}c_{i+\hat{\alpha}\downarrow}$ for $\alpha = x$ and y. $\hat{\alpha}$ indicates the unit vector in the α-th direction. The pair correlation function $D_{sc}(\ell)$ shows that the long-range order of superconductivity indeed exists in the ground state. $D_{sc}(\ell)$ is, however, reduced by strong electron correlation since as shown in Fig. 1 the Gutzwiller projection operator suppresses the pair correlation considerably.

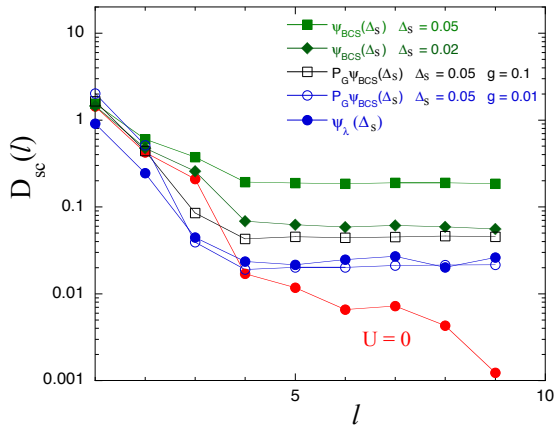


Figure 1: The pair correlation function $D_{sc}(\ell)$ as a function of the lattice site ℓ on a 10×10 lattice with $U = 18t$, $t' = 0$ and $N_e = 88$. The lattice sites ℓ are ℓ=(1,1), (1,2), (1,3), (1,4), (1,5), (2,5), (3,5), (4,5) and (5,5) and the site i is chosen as $i = (1, 1)$. The figure includes $D_{sc}(\ell)$ for $U = 0$, the non-interacting BCS wave function with the gap function $\Delta_s = 0.05$ and 0.02 and the the Gutzwiller projected BCS function with $\Delta_s = 0.05$. The result for ψ_λ indicates $D_{sc}(\ell)$ for the optimized wave function with $\Delta_s = 0.05$.

3 Charge-ordered state

We investigated the stability of charge-ordered state near the 1/8-doping region when $t' = 0$ and U/t is large. The one-particle state ψ_0 with inhomogeneous charge and spin orders are given by the eigenstate of the following Hamiltonian

$$H_{tri} = -\sum_{ij\sigma} t_{ij} c^\dagger_{i\sigma} c_{j\sigma} + \sum_{i\sigma} (\rho_i - \mathrm{sgn}(\sigma) m_i) n_{i\sigma}, \tag{2}$$

with $\rho_i = \rho \cos(\mathbf{Q}_c \cdot (\mathbf{r}_i - \mathbf{r}_0))$ and $m_i = m \sin(\mathbf{Q}_s \cdot (\mathbf{r}_i - \mathbf{r}_0))$. ρ and $m \equiv \Delta_{AF}$ are variational parameters. Here two incommensurate wave vectors $\mathbf{Q}_c$ and $\mathbf{Q}_s$ characterize the charge and spin configurations, respectively. We set $\mathbf{Q}_c = 2\mathbf{Q}_s$. $\mathbf{r}_0$ denotes the position of the domain boundary. The vertical stripe is represented by $\mathbf{Q}_s = (\pi \pm 2\pi\delta, \pi)$ where δ stands for the incommensurability.

We consider the case $t' = 0$. In this case, when U is as large as $U = 18t$, the antiferromagnetic state does not become stable[2] and thus a pure charge-ordered state can be stable in stead of stripes. This charge-ordered state can be called the nematic state. An important question is whether the charge-ordered state without magnetic order exists and then coexists with superconductivity. We indeed found that the charge-ordered state exists without magnetic ordering and this state coexists with superconductivity when the doping rate x is near 1/8 where we set $\delta = 1/8$[4, 5].

4 Summary

We examined the ground state of the two-dimensional Hubbard model by using the advanced optimized variational Monte Carlo method. We presented the d-wave pair correlation function as a function of lattice sites. We can show that the inhomogeneous charge-ordered state without magnetic ordering becomes stable for $t' = 0$ when the doping rate x is near $x = 0.125$. It is also shown that the d-wave superconductivity with a spatially oscillating gap function can coexist with charge ordering.

References

[1] T. Yanagisawa et al., J. Phys. Soc. Jpn. 67, 3867 (1998).
T. Yanagisawa, Phys. Rev. B75, 224503 (2007) (arXiv: 0707.1929).

[2] T. Yanagisawa, J. Phys. Soc. Jpn. 85, 114707 (2016).
T. Yanagisawa, J. Phys. Soc. Jpn. 88, 054702 (2019).
T. Yanagisawa, Condensed Matter 4, 57 (2019).

[3] T. Yanagisawa, Phys. Lett. A403, 127382 (2021).
T. Yanagisawa et al., EPL 134, 27004 (2021).

[4] M. Miyazaki, T. Yanagisawa, Phys. Lett. A448, 128276 (2022).

[5] T. Yanagisawa, High Temperature Materials 1, 10004 (2024).
T. Yanagisawa, preprint.

High harmonic generation in a spin scalar chiral state

Atsushi ONO
Department of Physics, Tohoku University
Sendai 980-8578

High harmonic generation (HHG) has emerged as a powerful tool for investigating ultrafast electron dynamics and reconstructing electronic band structures. Recent studies have demonstrated that HHG can also capture the geometric properties of electronic systems, such as the Berry curvature. However, while HHG in systems with broken spatial inversion symmetry has been extensively explored, studies of systems with broken time-reversal symmetry remain scarce.

In a paper [1], we numerically examined HHG in a spin scalar chiral state, where time-reversal symmetry is broken by the four-sublattice all-in/all-out spin structure, as depicted in Figs. 1(a) and 1(b). We considered the ferromagnetic Kondo lattice model on a triangular lattice, where electrons are driven within a fixed spin texture. Figure 1(c) presents the polarization angle dependence of the fifth harmonic intensity for scalar chiral states with positive (bold red curve) and negative (bold blue curve) chirality. We found that the sign of the scalar chirality significantly affects the harmonic intensity and that this effect predominantly appears in the component parallel to the polarization direction (thin orange and cyan curves), in contrast to the typically observed transverse responses of intraband currents. Our semiclassical analysis revealed that this behavior originates from interband currents induced by the recombination of electron–hole pairs whose real-space trajectories are modulated by the anomalous velocity.

These findings offer new insights into how topological spin textures and the Berry curvature imprint themselves on high harmonic spectra, highlighting the potential of HHG as a probe of geometry in magnetic materials.

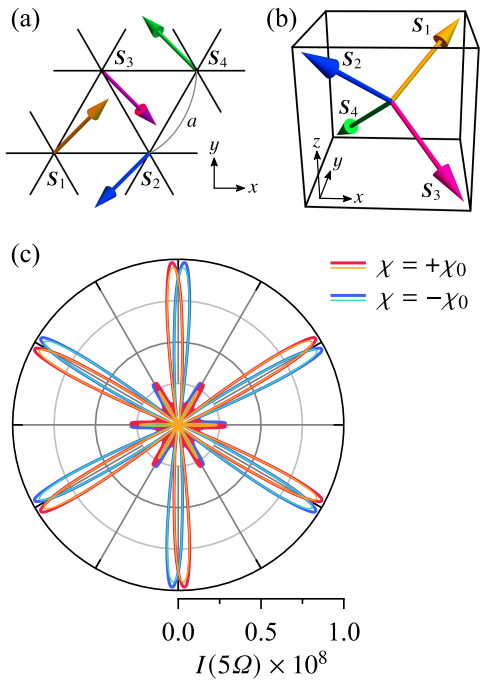


Figure 1: (a) Magnetic unit cell of the four-sublattice spin scalar chiral state, and (b) configuration of the four localized spin vectors. (c) Polarization angle dependence of the fifth harmonic intensity. These figures are adapted from Ref. [1].

References

[1] A. Ono, S. Okumura, S. Imai, and Y. Akagi: Phys. Rev. B **110**, 125111 (2024).

Ferromagnetism in $CeRh_6Ge_4$: A DFT+DMFT study

Junya OTSUKI
Research Institute for Interdisciplinary Science, Okayama University, Okayama 700-8530

$CeRh_6Ge_4$ is a cerium-based compound that exhibits a ferromagnetic transition at $T_c = 2.5$ K. It has attracted significant attention due to the observation of a ferromagnetic quantum critical point under pressure, and associated non-Fermi-liquid behavior. Central to understanding these phenomena is the nature of Ce $4f$ electrons—whether they are localized or itinerant—and the mechanism stabilizing the ferromagnetic order. We investigate the ferromagnetic order in $CeRh_6Ge_4$, applying a recently developed method that succeeded in reproducing the quadrupolar ordering in a prototypical material, CeB_6 [1].

We employ a combination of density functional theory (DFT) and dynamical mean-field theory (DMFT) to investigate the magnetic properties of $CeRh_6Ge_4$. We begin with DFT calculations assuming itinerant $4f$ electrons, then incorporate strong local Coulomb interactions through DMFT, yielding localized $4f$ electrons. These calculations were done using the open-source software `DCore` [2]. With the converged solution in DFT+DMFT, we calculate the momentum-dependent susceptibilities using the strong-coupling-limit (SCL) formula, which was derived by approximating the Bethe-Salpeter equation in the DMFT [3]. We used the FAT node of the system B to treat the system size (the division of the Brillouin zone) up to $24 \times 24 \times 42$.

The results for the momentum-dependent susceptibilities reveal that the nearest-neighbor exchange interaction along the c-axis forms ferromagnetic chains, while weaker and anisotropic interactions in the ab-plane align these chains [4]. The intersite interactions follow an RKKY-like decay and are spin-isotropic along the c-axis but spin-anisotropic within the plane. The calculated transition temperature $T_c \approx 3.2$ K is in reasonable agreement with experiment, though slightly overestimated due to mean-field nature of the DMFT.

This work successfully reproduces the ferromagnetic ground state of $CeRh_6Ge_4$ using a localized $4f$ electron model and elucidates the microscopic origin of the magnetic ordering via intersite exchange interactions. It provides compelling theoretical evidence for the localized nature of $4f$ electrons at ambient pressure and a new insight of weakly interacting ferromgnetic chains. These findings establish a fundamental basis for elucidating pressure-induced quantum criticality in $CeRh_6Ge_4$.

References

[1] J. Otsuki, K. Yoshimi, H. Shinaoka, H. O. Jeschke, Phys. Rev. B **110**, 035104 (2024).

[2] H. Shinaoka, J. Otsuki, M. Kawamura, N. Takemori, K. Yoshimi, SciPost Phys. **10**, 117 (2021).

[3] J. Otsuki, K. Yoshimi, H. Shinaoka, Y. Nomura, Phys. Rev. B **99**, 165134 (2019).

[4] S. Itokazu, A. Kirikoshi, H. O. Jeschke, J. Otsuki, in preparation.

Computational study on spin splitting and x-ray spectroscopy responses in altermagnets using DFT+DMFT method

Atsushi Hariki

Department of Physics and Electronics,

Osaka Metropolitan University, 1-1 Gakuen-cho, Naka-ku, Sakai, Osaka 599-8531, Japan

We conducted a computational study on several candidate altermagnets (MnTe, CrSb, and NiF_2), a newly emerging class of collinear magnets that exhibit time-reversal symmetry-breaking responses despite having a compensated magnetic moment. Using our in-house DFT+DMFT and Hartree-Fock codes, along with the large-scale parallel computing resources provided by ISSP, we analyzed their electronic band structures and computed their optical responses to circularly polarized light in the x-ray regime.

First, we calculated the circular dichroism (CD) in the resonant inelastic x-ray scattering (RIXS) spectra of MnTe using the DFT+DMFT method. By comparing our results with recent experimental data, we demonstrated that the angular dependence of the RIXS-CD signal can be used to distinguish between different domains of the altermagnetic order. Furthermore, based on numerical simulations in both the ordered and normal phases, we showed that the RIXS-CD signal can remain finite even in the normal phase. This effect originates from non-Hermiticity in the Kramers–Heisenberg RIXS cross section, caused by coupling to continuum states involved in the optical propagation during the RIXS process [1].

We also calculated the x-ray magnetic circular dichroism (XMCD) spectra for NiF_2 [2]. A key challenge in identifying altermagnetism is the influence of spin–orbit coupling, which can perturb the altermagnetic order by inducing a small ferromagnetic canting. Based on our numerical simulations, we proposed a method to separate the altermagnetic and ferromagnetic contributions in the experimental XMCD spectra.

In addition, we investigated the electronic structures of $R_3Ni_2O_7$ [3] and $PbCrO_3$ using the DFT+DMFT method.

References

[1] D. Takegami *et al*., arXiv:2502.10809.

[2] A. Hariki *et al*., accepted in npj Quantum Materials.

[3] D. Takegami *et al*., **111**, 165101 (2025).

An inequivalent dimer model to describe compensated ferrimagnetism in organic compounds: Electronic states explored

Akito Kobayashi[a], Kouki Nunota[a], Kazuyoshi Yoshimi[b], Kenichiro Hashimoto[c], and Takahiro Misawa[b]

[a] *Department of Physics, Nagoya University, Nagoya 464-8602*

[b] *Institute for Solid State Physics, University of Tokyo, Kashiwa, Chiba 277-8581, Japan*

[c] *Department of Advanced Materials Science, University of Tokyo, Kashiwa, Chiba 277-8561, Japan*

Traditionally, collinear antiferromagnets, characterized by antiparallel spin alignment, have been considered incapable of exhibiting unconventional transport phenomena, such as the generation of spin currents. However, recent theoretical advancements have unveiled the existence of intriguing antiferromagnetic materials, including altermagnets and compensated ferrimagnets, which demonstrate unique transport properties, such as the anomalous Hall effect and spin current generation [1, 2, 3].

Despite these findings, research on compensated ferrimagnetic materials has largely been confined to inorganic compounds, such as alloys, with limited progress in their practical implementation.

In this study, we introduce a straightforward approach to achieve compensated ferrimagnetism using organic compounds with dimer structures [4]. Specifically, we propose a simple design principle whereby compensated ferrimagnetic materials can be realized if an antiferromagnetic order emerges within organic compounds containing two distinct types of dimers (Fig. 1). We highlight the potential for compensated ferrimagnetism to be realized in the organic compound $(EDO\text{-}TTF\text{-}I)_2ClO_4$ through this mechanism [4].

Furthermore, a theoretical analysis of a two-dimensional inequivalent dimer model employing mean-field theory reveals a diverse range of electronic states, including band insulator/metal, antiferromagnetic insulator/metal, small-spin-splitting insulator/metal, half metal, and compensated ferrimagnetic insulator.

References

[1] M. Naka et al., Nat. Commun. **10**, 1, (2019)

[2] H. van Leuken et al., Phys. Rev. Lett. **74**, 1171 (1995)

[3] S. Semboshi et al., Sci. Rep. **12**, 10687 (2022)

[4] T. Kawamura et al., Phys. Rev. Lett. **132**, 156502 (2024)

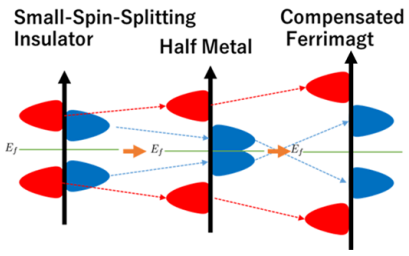


Figure 1: Diverse range of electronic states in the two-dimensional inequivalent dimer model

Quantum Damping of Magnons in Altermagnetism

Masahito MOCHIZUKI

Department of Applied Physics,

Waseda University, Okubo, Shinjuku-ku, Tokyo 169-8555

Altermagnetism is a newly identified class of nonrelativistic collinear magnetism that exhibits even-parity spin splitting, distinct from conventional ferromagnetism and antiferromagnetism. In this project (ID: 2024-Ba-0044), we study the stability of magnons against quantum many-body scatterings across all three classes of nonrelativistic collinear magnets [1].

Using kinematic analysis, nonlinear spin-wave (NLSW) perturbation theory, and density-matrix renormalization group with matrix-product-operator-based time evolutions (DMRG+tMPO), we demonstrate that magnon-magnon interactions universally destabilize the spin-split upper-branch magnons in altermagnets. In particular, in two-dimensional *d*-wave altermagnets, even an infinitesimal altermagnetic splitting opens up a decay phase space, leading to the emergence of a stable lower branch and an unstable upper branch in the long-wavelength limit. Furthermore, we show that NLSW perturbation theory with corrections up to the order $1/S^2$ (S being the spin length) accurately reproduces nonperturbative DMRG+tMPO results, highlighting spin-conserving three-magnon scattering processes [Fig. 1] as the leading quantum correction. We propose organic altermagnets as promising candidates for observing the predicted damped and long-lived magnons. This work sheds light on the potential for unique quantum spin dynamics in altermagnets.

In this project, parts of NLSW calculations are performed by using Ohtaka (System B).

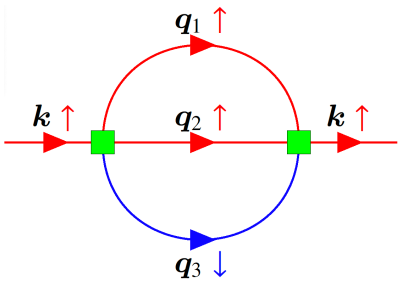


Fig. 1: Three-magnon forward bubble diagram with total spin conservation.

References

[1] R. Eto, M. Gohlke, J. Sinova, M. Mochizuki, A. L. Chernyshev, and A. Mook, preprint, arXiv:2502.20146

Theoretical study of enhancement mechanism of thermoelectric properties with spin fluctuations: A weak-coupling approach

Kazutaka NISHIGUCHI
Graduate School of System Informatics, Kobe University
Rokkodai-Cho, Nada-Ku, Kobe 657-8501

Ferromagnetic fluctuations in Heusler alloy Fe_2VAl

Heusler compound Fe_2VAl is one of the promising thermoelectric materials, which exhibits a large power factor $P = \sigma S^2$ with σ and S being the electrical conductivity and Seebeck coefficient, respectively. On the other hand, the thermal dimensionless figure of merit $ZT = \sigma S^2 T/\kappa$ is not so large yet reflecting its large thermal conductivity κ. Recently, it is experimentally observed in doped Fe_2VAl (i.e., $Fe_2V_{0.9}Cr_{0.1}Al_{0.9}Si_{0.1}$ and $Fe_{2.2}V_{0.8}Al_{1-y}Si_y$) as a weekly ferromagnetic material that ferromagnetic fluctuations enhance the thermoelectric properties such as S and P around the Curie temperature ($T_c = 285$ K). [1] It is not only a desirable property for practical use in realistic (room) temperatures, but also a fundamental and intriguing quantum phenomena where quantum fluctuations and thermoelectric effects are entangled by electron correlations.

Motivated above, we have studied electronic properties of Fe_2VAl using first-principles calculations based on the density functional theory (DFT) within the generalized gradient approximation (GGA). We performed DFT calculations with the Perdew–Burke–Ernzerhof (PBE) exchange-correlation functional for solids (PBEsol) and the projector augmented wave (PAW) method using The Vienna Ab Initio Simulation Package (VASP) [2] and Quantum ESPRESSO (QE) package. [3]

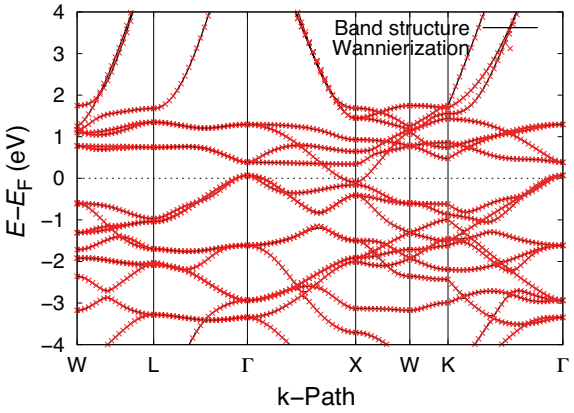


Figure 1: DFT band structure and Wannierization of Fe_2VAl.

Using the maximally localized Wannier functions, we could construct a low-energy effective model from the first- principles bands around the Fermi level. The effective model is composed of the Fe-3d, V-3d, and Al-2sp3 Wannier orbitals, namely, 19 orbitals. The DFT and structure and Wannier orbitals are shown in Fig. 1.

Furthermore, the obtained 19-orbital effective model was investigated using the random phase approximation (RPA). The susceptibilities show that the spin fluctuations are dominant compared to the charge ones. Also, the obtained spin susceptibility has a peak at $q = (0, 0, 0)$, which reflects the ferromagnetic instability. This is consistent with the fact

that Fe_2VAl exhibits the weak ferromagnetism.

Calculation conditions

We have performed the DFT calculations using the hybrid (MPI+OpenMP) parallel computing, where the parallelization over bands and k-points is used by VASP version 6.4.2 and QE version 7.2.

References

[1] N. Tsujii, A. Nishide, J. Hayakawa, and T. Mori: Sci. Adv. **5**, eaat5935 (2019).

[2] G. Kresse *et. al.*: Phys. Rev. B **47**, 558 (1993); Phys. Rev. B **49**, 14251 (1994); Computational Materials Science **6** (1996) 15–50; Phys. Rev. B **54**, 11169 (1996).

[3] P. Giannozzi *et. al.*: J. Phys.: Condens. Matter **21**, 395502 (2009) ; J. Phys.: Condens. Matter **29**, 465901 (2017) ; J. Chem. Phys. **152**, 154105 (2020).

[4] I. Souza, N. Marzari, and D. Vanderbilt: Phys. Rev. B **65**, 035109 (2001) ; A. A. Mostofi *et. al.*: Comput. Phys. Commun. **178** (2008) 685–699; A. A. Mostofi *et. al.*: Comput. Phys. Commun. **185** (2014) 2309–2310; G. Pizzi *et. al.*: J. Phys.: Condens. Matter **32**, 165902 (2020).

Theoretical study of BCS-BEC crossover in strongly correlated electron systems

Hiroshi WATANABE
Department of Liberal Arts and Basic Sciences, College of Industrial Technology, Nihon University
2-11-1 Shin-ei, Narashino, Chiba 275-8576

The BCS-BEC crossover, which smoothly connects Bardeen-Cooper-Schrieffer (BCS) theory with Bose-Einstein condensation (BEC), has attracted significant attention across various fields as a fascinating quantum phenomenon. Recently, in addition to ultracold Fermi gases, the possibility of a BCS-BEC crossover has been discussed in strongly correlated electron systems including the iron-based superconductors, the two-dimensional organic superconductor κ-$(ET)_4Hg_{2.89}Br_8$ (κ-HgBr) [1], and cuprate superconductors. However, identifying the BCS-BEC crossover in such systems is far more challenging than in Fermi gases due to unconventional (non-s-wave) gap symmetry and competition with various magnetic and/or charge orders. Understanding the crossover in this context may offer valuable insights into unconventional pairing mechanism and the interplay with competing quantum phases.

The organic superconductor κ-HgBr is a promising candidate due to its doped spin-liquid-like nature and tunable electron correlations. In this study, we investigate the extended Hubbard model on an anisotropic triangular lattice using the variational Monte Carlo method and discuss the possibility of the BCS-BEC crossover in κ-type organic superconductors [2]. The system size for the calculation is N=24×24=576 unit cells (and thus 576×2=1152 molecules in total) and the calculation has been carried out mainly using system B at the ISSP Supercomputer Center. To enable such large-scale simulations, we employed MPI parallelization, which significantly enhanced computational efficiency and made the extensive parameter space exploration feasible.

As shown in Fig. 1, for hole doping rate δ=0.06, the superconducting correlation function P_{SC} exhibits a dome-shaped dependence on interaction strength U/t, which is a hallmark of the BCS-BEC crossover. Other physical quantities including the superfluid weight, the coherence length, and the chemical potential also display characteristic changes. In contrast, for δ=0 or 0.11, the system undergoes transitions to a Mott insulator or stripe-ordered phase, respectively, and superconductivity is suppressed.

Our results demonstrate that the BCS-BEC crossover can emerge when competing phases are suppressed through appropriate hole doping. These findings provide a clear theoretical criterion for identifying the BCS-BEC crossover in real materials and suggest experimental strategies to realize it in strongly correlated electron systems.

References

[1] Y. Suzuki *et al.*, Phys. Rev. X **12**, 011016 (2022).

[2] H. Watanabe and H. Ikeda, Phys. Rev. B **111**, 085130 (2025).

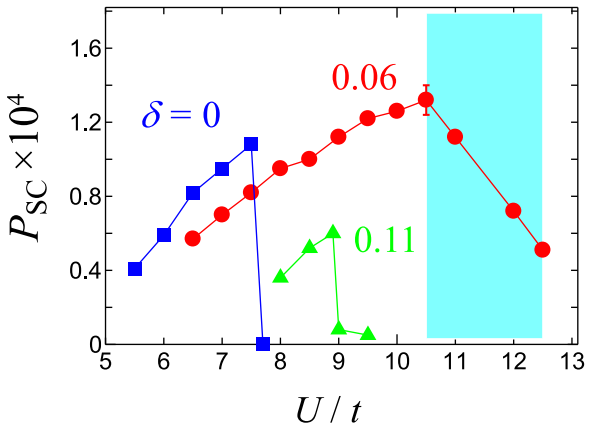


Figure 1: U/t dependence of the superconducting correlation function P_{SC} for the hole doping rate $\delta = 0$, 0.06, and 0.11 [2].

3.4 Cooperative Phenomena in Complex Macroscopic Systems

Molecular Simulation Contributions to Biological Membrane and Energy Materials Research

Wataru SHINODA

Research Institute for Interdisciplinary Science, Okayama University

3-1-1 Tsushima-naka, Kita-ku, Okayama 700-8530

In the past fiscal year, our research group leveraged high-performance computing to tackle fundamental questions in biomembrane dynamics, drug delivery, and energy materials via molecular simulations. Our findings, published in ten peer-reviewed articles, highlight how computational modeling reveals mechanisms that are experimentally challenging to access.

A significant achievement was the extension of the pSPICA coarse-grained force field to include polar water and protein models, enabling accurate simulations of electrostatically sensitive biological events such as membrane pore formation and peptide adsorption. This allowed the reproduction of systems like melittin-induced pores and polyarginine adsorption [1]. In parallel, we combined solid-state NMR and simulations to explore lipid-protein interactions, showing how lipid headgroups modulate membrane structure near bacteriorhodopsin [2]. Another study revealed the structure of Amphotericin B-ergosterol channels using isotope labeling and MD simulations, identifying a stable, seven-membered ion-conducting complex that explains antifungal specificity [3].

We also investigated structural changes in lipid carriers during processing. Time-resolved SAXS and MD simulations showed ethanol-induced transitions from unilamellar to multilamellar liposomes, informing nanoparticle formulation strategies [4]. Building on this, we developed a photoresponsive molecule that induces reversible membrane disruption for intracellular delivery of macromolecules, validated experimentally and through simulations [5].

In energy research, we modeled ether-based electrolytes for lithium–sulfur batteries, identifying how subtle structural changes impact ion transport and polysulfide suppression [6]. Another study screened solvate electrolytes with novel anionic structures, achieving high lithium transference numbers nearing 0.9 [7].

In diagnostics, we developed a nanowire-based device that distinguishes miRNA sources via thermal profiling, offering a new route for cancer-related biomarker analysis [8]. We also designed a ZnO nanowire platform that selectively captures unmethylated DNA, aiding

in epigenetic profiling [9]. Lastly, atomistic simulations of photoswitchable lipid bilayers revealed how light-induced phase transitions modulate membrane properties for controlled drug release [10].

These studies underscore the critical role of molecular simulations, enabled by supercomputing, in advancing both fundamental science and practical applications. In the future, we aim to integrate multiscale modeling and AI-driven simulations to further enhance predictive power and experimental synergy.

References

[1] Y. Miyazaki and W. Shinoda, J. Chem. Inf. Model. **64**, 532 (2024).

[2] Y. Umegawa, S. Kato, S. Sangjae, W. Shinoda, S. Kawatake, S. Matsuoka, and M. Murata, Biophys. Chem. **308**, 107204 (2024).

[3] Y. Umegawa, H. Tsuchikawa, W. Shinoda, M. Murata, Org. Biomol. Chem. **23**, 1233 (2025).

[4] M. Maeki et al., Nanoscale Adv. **6**, 2166 (2024).

[5] W. Huo et al., J. Mater. Chem. B, **12**, 4138 (2024).

[6] T. Ishikawa et al., Faraday Discuss. **253**, 385 (2024).

[7] F. Philippi et al., Chem. Sci. **15**, 7342 (2024).

[8] K. CHattrairat et al., Device, **2**, 100363 (2024).

[9] M. Musa et al., Lab Chip, **25**, 1637 (2025).

[10] K. A. Alberto, MN. H. Begam, H. Xiong, W. Shinoda, P. A. Slesinger, Z. Qin, S. O. Nielsen, Nanoscale, **17**, 2032 (2025).

Low-rank tensor ring decomposition and its application to renormalization group

Naoki KAWASHIMA

Institute for Solid State Physics,

The University of Tokyo, Kashiwa-no-ha, Kashiwa, Chiba 277-8581

Artificial intelligence and machine learning has started deeply influencing our daily lives. Compression of tensor-type data is one of the core parts of machine learning. Being closely related to information extraction and classification, it is a technological element with a very high social need. Recently, it has been widely acknowledged that the data compression can be essential also in extracting the critical information from the tensor network representation of various field theoretical models in both continuous and discrete spaces. Numerical methods based on the tensor network representation are now developing a bridge between condensed matter theory and information science.

In [1], we generalized our own method for computing the elementary excitation. The same task had been carried out by extremely cumbersome book-keeping that required a lot of human time and often leads to programming errors. We applied the new method to the S=1/2 J1-J2 model to obtain the dynamical properties of the putative gapless spin liquid phase. This opens up a new avenue of lattice model studies directly comparable to real experiments.

In [2], we studied the model system of cold atoms characterized by the dipole-dipole interaction. We discovered many distinct phases with various spatial patters, e.g., the stripe and kinked phases. There are multiple candidates for the spatial patterns in the classical level. Some of the phases emerge from the quantum "order-by-disorder" effect that lifts the classical degeneracy by the quantum fluctuation.

The information-compression efficiency of the tensor network methods are best represented in their application to real-space renormalization group method. In [3], we revisited the nature of the real-space renormalization group mappings. We focused on the question whether the common real-space RG really retains the fundamental critical information of the system. It is well-known that the fixed-point system of the decimation map is the trivial. On the other hand, the fixed point system of the majority map is not trivial. However, it had not been known whether this fixed point has the same universality as the original model. In [3], we found that the majority map is faithful, i.e., by its repeated application, the system transforms to a fixed

point system that retains all the critical information as the original one.

In [4], we directly addressed the problem of efficient low-rank decomposition of given tensors. In the previous works aiming at a similar goal, such as the loop-TNR and GILT, the redundant representation is compressed through repeated application of contractions and decompositions guided by the intuition based on the physical picture of "redundant loops". In [3], we adopted the nuclear norm regularization, developed in the field of the data science. It was surprizing to see that the new methods based on very different guiding principles produced the results with the same level of the accuracy.

In [5], we investigated the finite-temperature phase diagram of the classical J_1 - J_2 XY model on a square lattice using a tensor network method. Our study reveals an emergent intermediate phase, which is characterized by a Z_2 long-range stripe order without phase coherence in the XY spins, sandwiched by two transitions; a higher-temperature Ising transition and a lower-temperature Berezinskii-Kosterlitz-Thouless (BKT) transition. We also observed that, in smaller J_2 region, two transitions merge into a single first-order phase transition, which had not been predicted before.

In [6], we propose a multi-impurity method for the bond-weighted tensor renormalization group (BWTRG) to compute the higher-order moments of physical quantities in two dimensions. We demonstrate that the accuracy of the proposed method is much higher than the conventional tensor renormalization group for the Ising model and the five-state Potts model. We found that BWTRG with the optimal hyperparameter is more efficient in terms of computational time than alternative approaches based on the matrix product state in estimating the critical temperature.

References

[1] Wei-Lin Tu, Laurens Vanderstraeten, Norbert Schuch, Hyun-Yong Lee, Naoki Kawashima, and Ji-Yao Chen: Physical Review X Quantum 5, 010335 (2024)

[2] Huan-Kuang Wu, Takafumi Suzuki, Naoki Kawashima, Wei-Lin Tu: Physical Review Research 6, 023297(1-12) (2024)

[3] Katsuya O. Akamatsu and Naoki Kawashima: Journal of Statistical Physics 191, 109 (2024)

[4] Kenji Homma, Tsuyoshi Okubo, Naoki Kawashima: Physical Review Research 6, 043102 (1-9) (2024)

[5] Feng-Feng Song, Hanggai Nuomin, and Naoki Kawashima: Physical Review B 111, 104428 (2025)

[6] Satoshi Morita and Naoki Kawashima: Physical Review B 111, 054433 (2025)

Molecular dynamics analysis of ultrasound cavitation

Yuta Asano

Faculty of Global Nursing

Iryososei University, 1-3-4, Koaota, Kashiwa, Chiba 277-0803

When a liquid is irradiated with ultrasound waves, bubbles are generated due to local depressurization. The bubble formation phenomenon is called ultrasound cavitation. Ultrasonic cavitation is a safe and environmentally friendly technology that is applied in various fields, including not only engineering but also food processing, and medical care [1-3]. However, the analysis of ultrasound cavitation is challenging because of the complexity of the multiscale-multiphysics phenomenon. A direct analysis of the interaction between the phase transition and the sound field under non-equilibrium conditions is essential for understanding ultrasonic cavitation. We have been studying the mechanism of ultrasonic cavitation generation and its physical and chemical effects using molecular dynamics (MD) simulations.

Effective transportation of bubbles is necessary for efficient use of the physical and chemical effects of ultrasound cavitation [4]. In FY2024, we performed MD simulations of vortex rings involving cavitation bubbles. Because vortex rings have a propulsive force in the axial direction of the ring, the bubble ring efficiently transports cavitation bubbles. In this study, the bubble ring is generated by large-scale MD simulations, and the formation process is analyzed. In addition, the stability and moving behavior of the bubble ring were also investigated.

The system is composed of monatomic molecules, and the intermolecular interaction is the Lennard-Jones potential. The dimension of the system is $L_x \times L_y \times L_z = 5000\sigma \times 2000\sigma \times 2000\sigma$, where σ is the molecular diameter. The number of liquid atoms in the system is 11,986,332,544, and the liquid is equilibrated near the boiling point. The two walls were placed at $x = 0$ and 5000σ, respectively. For the bubble ring formation, an orifice plate with a hole whose diameter is $D = 800\sigma$ is placed at $x = 250\sigma$. When the wall at $x = 0$ moves toward the positive x-direction, the vortex ring and phase transition occur due to the jet. Bubble rings appear when the vortex ring entrains the cavitation bubbles.

Figures 1(a) and 1(b) show density fields near the bubble rings generated at low and high amplitudes, respectively. Cavitation bubbles generated when passing through the orifice plate are entrained in the vortex ring. The bubble ring then appears. The size of the bubble

ring increased with increasing amplitude. In addition, the shape is distorted for the larger amplitude. The bubble ring moved at an almost constant velocity. We found that a stable bubble ring is generated by the MD simulation containing 10 billion atoms.

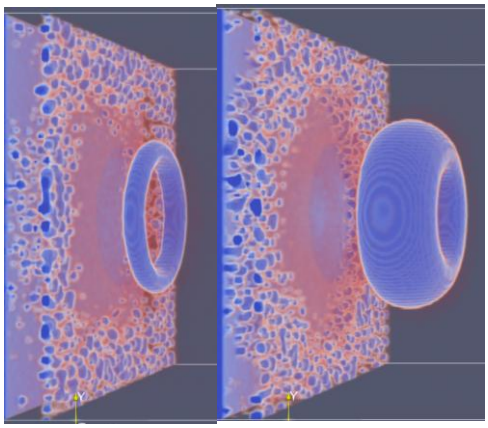


Fig. 1: Density fields of bubble ring simulations.

References

[1] Y. Yao, Y. Pan, and S. Liu, Ultrason. Sonochem. **62**, 104722 (2020).

[2] S. Kentish and H. Feng, Annu. Rev. Food Sci. Technol. **5**, 263 (2014).

[3] Z. Izadifar, P. Babyn, and D. Chapman, J. Med. Biol. Eng. **39**, 259 (2019).

[4] Z. Wang, Z. Shi, L. Liu, Chem. Eng. J. 465 143070 (2023).

Looking at bare transport coefficients in fluctuating hydrodynamics

Hiroyoshi NAKANO
Institute for Solid State Physics, University of Tokyo
Kashiwa-no-ha, Kashiwa, Chiba 277-8581

The Navier-Stokes equation quantitatively describes macroscopic fluid motion, accurately predicting behaviors ranging from streamlined flow over airplane wings to complex turbulence. However, at the mesoscopic scale, significant fluctuations necessitate incorporating noise terms for an accurate description. This leads to the framework of fluctuating hydrodynamics [1].

The fundamental equations of fluctuating hydrodynamics in d dimensions are:

$$\frac{\partial \rho}{\partial t} = -\nabla \cdot (\rho \boldsymbol{v}) \tag{1}$$

$$\rho \left[\frac{\partial \boldsymbol{v}}{\partial t} + (\boldsymbol{v} \cdot \nabla)\boldsymbol{v} \right] = -\nabla p + \eta_0 \nabla^2 \boldsymbol{v} + \left[\zeta_0 + \left(1 - \frac{2}{d} \right) \eta_0 \right] \nabla(\nabla \cdot \boldsymbol{v}) - \nabla \cdot \boldsymbol{\Pi}^{\mathrm{ran}} \tag{2}$$

Here, $\rho(\boldsymbol{r}, t)$, $\boldsymbol{v}(\boldsymbol{r}, t)$, and $p(\boldsymbol{r}, t)$ are the density, velocity, and pressure fields, respectively. The pressure p is a function of density and temperature, $p = p(\rho, T)$, determined by thermodynamics. $\boldsymbol{\Pi}^{\mathrm{ran}}(\boldsymbol{r}, t)$ is the stochastic momentum flux representing thermal fluctuations due to the random motion of constituent particles (e.g., atoms or molecules). Without $\boldsymbol{\Pi}^{\mathrm{ran}}(\boldsymbol{r}, t)$, Eq. (2) reduces to the standard Navier-Stokes equation. $\boldsymbol{\Pi}^{\mathrm{ran}}(\boldsymbol{r}, t)$ is typically modeled as Gaussian white noise with the correlation:

$$\left\langle \Pi_{ij}^{\mathrm{ran}}(\boldsymbol{r}, t) \Pi_{mn}^{\mathrm{ran}}(\boldsymbol{r}', t') \right\rangle = 2 k_B T \Delta_{ijmn} \delta^d(\boldsymbol{r} - \boldsymbol{r}') \delta(t - t') \tag{3}$$

with

$$\Delta_{ijmn} = \eta_0 \left(\delta_{im}\delta_{jn} + \delta_{in}\delta_{jm} \right) + \left(\zeta_0 - \frac{2}{d}\eta_0 \right) \delta_{ij}\delta_{mn} \tag{4}$$

Fluctuating hydrodynamics is characterized by the noise term $\boldsymbol{\Pi}^{\mathrm{ran}}(\boldsymbol{r}, t)$ and the associated bare transport coefficients (η_0, ζ_0), which govern mesoscopic dissipation and transport. The bare coefficients differ fundamentally from the macroscopic transport coefficients found in the deterministic Navier-Stokes equation. For instance, in two-dimensional (2D) fluids, macroscopic coefficients are known to exhibit logarithmic divergence with increasing system size [2]. In contrast, the bare coefficients (η_0, ζ_0) are expected to be constants determined by microscopic properties such as atomic structure, temperature, and density (or pressure).

Fluctuating hydrodynamics provides the fundamental framework for describing the coupling between fluid flow and thermal fluctuations. However, major challenges remain: how do the bare transport coefficients manifest in macroscopic observables, and how can their values be determined using practical methods? To date, obtaining precise values for these bare coefficients has proven challenging.

To address this challenge, we performed numerical simulations of the fluctuating hydrodynamic equations, Eqs. (1) and (2) [3]. Our simulations focus on a two-dimensional fluid confined between two parallel walls moving in opposite directions (Fig. 1(a)), creating shear

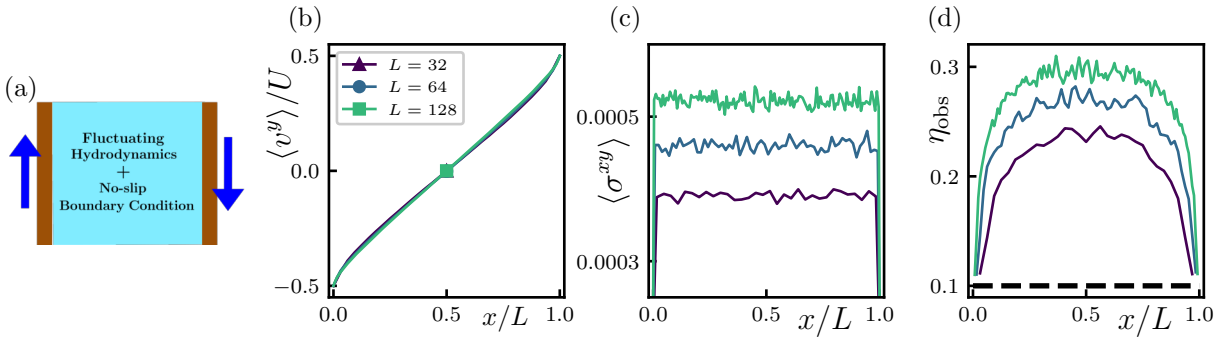


Figure 1: Simulation results for the system-size dependence of observables for Couette geometry in fluctuating hydrodynamics. Colored lines represent simulation results for different system sizes: $L = 32$ (purple), $L = 64$ (blue), and $L = 128$ (green). (a) Scaled velocity profiles $\langle v^y(x) \rangle / U$ as a function of the scaled position x/L. (b) Shear stress profiles $\langle \sigma^{xy}(x) \rangle$ as a function of x/L. (c) Observed viscosity profiles $\eta_{\rm obs}(x)$ as a function of x/L. Parameters are fixed at $\rho_0 = 0.765$, $T = 1.0$, $\eta_0 = 0.10$, $U/L = 0.002$, and $\zeta_0 = 1.0$. The pressure is given as the relation $p = c_T^2 \rho$ with $c_T^2 = 1000$ (approximating an incompressible fluid).

flow. Standard no-slip boundary conditions were applied at the walls ($x = 0, L$):

$$v^x = 0 \tag{5}$$

$$v^y = \mp U/2 \tag{6}$$

$$\partial_x \rho = 0 \tag{7}$$

Here, U is the relative wall velocity.

Figure 1(b)-(d) shows the simulation results (parameters are summarized in the figure caption). Figure 1(b) presents the time-averaged steady-state velocity profile $v^y(x)$ while Fig. 1(c) displays the corresponding shear stress profile $\langle \sigma^{xy}(x) \rangle$. In these plots, the coordinate x is normalized by the system size L, and the velocity $v^y(x)$ is normalized by $U/2$. As shown in Fig. 1(c), the shear stress $\langle \sigma^{xy}(x) \rangle$ is spatially uniform, consistent with force balance requirements.

Interestingly, Fig. 1(b) reveals that the velocity profile deviates from the linear shape expected for ideal uniform shear flow (Couette flow). This deviation from linearity can be characterized by an observed viscosity $\eta_{\rm obs}$, defined locally as:

$$\eta_{\rm obs}(x) := \frac{\langle \sigma^{xy} \rangle}{\partial_x \langle v^y(x) \rangle} \tag{8}$$

This quantity is plotted in Fig. 1(d). The figure shows that $\eta_{\rm obs}$ varies with the distance from the walls, increasing away from them. Far from the walls (in the bulk), $\eta_{\rm obs}$ exhibits system-size dependence; this bulk value is often interpreted as the macroscopic viscosity.

Remarkably, near the walls, $\eta_{\rm obs}$ closely approaches $\eta_0 = 0.10$, the input value for the bare viscosity in our simulations. This key finding suggests that the bare viscosity directly governs the fluid dynamics near the walls. We attribute this observation to the strong suppression of hydrodynamic fluctuations by the no-slip walls. Notably, similar behavior has been observed in atomic-level simulations.

Thus, our results confirm that fluctuating hydrodynamics incorporating the bare viscosity is essential for accurately predicting fluid motion near solid boundaries.

References

[1] L. D. Landau and E. M. Lifshitz, Fluid Mechanics: Volume 6 (Elsevier, 1959)

[2] D. Forster, D. R. Nelson, and M. J. Stephen, Phys. Rev. A 16, 732 (1977).

[3] H. Nakano, Y. Minami, and K. Saito, arXiv:2502.15241 (2025).

Fluctuation of a Bilayer Composed by Amphipathic Molecules

Shunta KIKUCHI and Hiroshi WATANABE
Faculty of Science and Technology, Keio University
Yokohama, Kanagawa 223-8522, Japan

We investigated the thermal fluctuation properties of bilayers composed of amphipathic molecules using molecular dynamics simulations [1]. To model these molecules, we employed a simple diatomic structure and constructed bilayers in a solvent environment. Our main objective was to analyze how membrane fluctuations depend on temperature by examining the Fourier spectrum of the membrane surface. We found that at high temperatures, the fluctuation spectrum is dominated by a q^4 dependence. This suggests that bending elasticity primarily governs the restoring force. At lower temperatures, we observed a crossover from q^4 to q^2 behavior, which indicates that interfacial tension becomes the dominant restoring force in this regime. This result complements our previous findings for monolayer membranes, where a transition from q^2 to q^4 was observed as the interfacial tension decreased [2].

To further understand the bilayer structure, we calculated radial distribution functions of the amphipathic molecules. We discovered that the molecular arrangement within the bilayer depends on temperature in the horizontal direction but remains mostly unchanged in the vertical direction. This means that bilayers preserve their membrane structure even under thermal agitation, allowing increased fluctuations primarily in-plane.

Our results highlight the distinct roles of elasticity and interfacial tension in regulating bilayer fluctuations. At high temperatures, membranes are flexible and their shape is stabilized by bending elasticity. At low temperatures, however, the membrane becomes stiffer due to the influence of interfacial tension. This temperature-dependent crossover deepens our understanding of membrane mechanics and provides a useful framework for analyzing bilayer behavior.

We also emphasize the effectiveness of using a coarse-grained model. Although all-atom simulations offer detailed insights, they are computationally demanding. Our approach achieves a balance between physical realism and computational efficiency, allowing us to focus on the essential characteristics of amphipathic self-assembly and fluctuation.

In summary, we demonstrated that the fluctuation properties of bilayers depend strongly on temperature and that the restoring forces can shift from elasticity to interfacial tension depending on the regime. We also showed that the membrane maintains structural stability while allowing enhanced fluctuations in-plane. These findings contribute to the broader understanding of bilayer dynamics and stability, which is relevant to both biological and synthetic membrane systems.

References

[1] S. Kikuchi and H. Watanabe, J. Phys. Soc. Jpn. **93**, 114601 (2024).

[2] S. Kikuchi and H. Watanabe, J. Chem. Phys., **158**, 124901 (2023).

Tensor network study on frustrated magnets

Tsuyoshi OKUBO
Institute for Physics of Intelligence, University of Tokyo
7-3-1 Hongo, Bunkyo-ku, Tokyo, 113-0033

Frustrated magnets are among the most interesting subjects in condensed matter physics. One striking effect is the emergence of a nontrivial ground state due to frustration. Typical examples are spin-liquid states, which are characterized by the absence of long-range magnetic order. Such a spin liquid state appears in the Kitaev model on the honeycomb lattice, which has a nontrivial ground state called the Kitaev spin liquid [1, 2]. The Hamiltonian of the Kitaev model is given by $\mathcal{H} = \sum_\gamma \sum_{\langle i,j\rangle_\gamma} \left(S_i^\gamma S_j^\gamma\right)$, where γ is the direction of the interaction, and $\langle i,j\rangle_\gamma$ denotes the nearest neighbor sites in the γ direction. Another example is the Kagome lattice Heisenberg model, for which the possibility of a spin-liquid ground state in zero magnetic field has been widely discussed. In addition, under the applied magnetic field, several magnetization plateaus are stabilized [3, 4]. Among them, the plateau with 1/9 of the total magnetization has been actively discussed recently.

In our project this year, we investigated properties of such frustrated spin models on two-dimensional lattices. We mainly considered two models: the $S = 1$ Kitaev model with Heisenberg and symmetric off-diagonal interactions, and the Kagome lattice Heisenberg model under magnetic fields with weak Dzyaloshinskii-Moriya (DM) interaction.

For the $S = 1$ Kitaev model with bilinear-biquadratic interactions, we have recently reported the ground state phase diagram calculated using the infinite projected entangled pair states (iPEPS) method [5]. We showed that when the Heisenberg and biquadratic interactions are properly balanced, the spin-liquid state remains stable. This balance can be interpreted as effective interactions between quadrupole degrees of freedom. Furthermore, we found that under these conditions, a direct phase transition occurs between the spin-liquid phase and a quadrupolar ordered phase —a state that lacks conventional magnetic order but exhibits a different type of symmetry breaking. This year, we extended our calculations to include the symmetric off-diagonal interaction, called Γ interaction, defined as

$$\mathcal{H}_\Gamma = \Gamma \sum_\gamma \sum_{\langle i,j\rangle_\gamma} \left(S_i^\mu S_j^\nu + S_i^\nu S_j^\mu\right), \qquad (1)$$

where (μ,ν,γ) is a cyclic permutation of (x,y,z), for example, $(\mu,\nu,\gamma) = (y,z,x)$ for the x-bond. Using the iPEPS method with bond dimensions D up to $D = 8$, we determined the phase diagram of the $S = 1$ Kitaev model with weak Γ and Heisenberg interactions to reveal the stability of the Kitaev spin liquid. We found that in the case of the Kitaev spin liquid with antiferromagnetic Kitaev interaction, the spin-liquid phase is more stable against the Γ interaction, indicating the possibility of finding the antiferromagnetic Kitaev spin-liquid state in the real compounds [6].

For the Kagome lattice Heisenberg model with weak DM interaction, we calculated finite temperature properties of a finite-size cluster using the matrix product operator (MPO) representation of the density matrix. We optimized the density operator at the inverse temperature $\beta = 1/T$ by exponential tensor renormalization group (XTRG) method [7]. In

the XTRG method, we compute the finite-temperature density matrix $\rho(\beta)$ by iteratively applying $\rho(\beta) = \rho(\beta/2)\,\rho(\beta/2)$ starting from $\beta \sim 10^{-7}$. We determined the finite-temperature states below $T \simeq 0.1$ for the Kagome lattice Heisenberg model with a weak DM interaction under several magnetic fields using the XTRG method. We confirmed that the 1/9, 1/3, 5/9, and 7/9 magnetization plateaus are stabilized at sufficiently low temperatures. We also calculated the temperature dependence of the thermal Hall conductivity around the magnetization plateaus [8]. Our preliminary results suggest that the thermal Hall conductivity exhibits characteristic temperature dependence, notably including a sign change, depending on the magnetic field. The understanding of the relationship between the thermal Hall conductivities and the nature of the plateau states is an important topic for future study.

References

[1] A. Kitaev, Ann. Phys. **321** (2006) 2.

[2] Y. Motome and J. Nasu, J. Phys. Soc.Jpn. **89** (2020) 012002.

[3] S. Nishomoto, N. Shibata, and C. Hotta, Nat. Commun. **4** (2013) 2278.

[4] R. Okuma, D. Nakamura, T. Okubo, A. Miyake, A. Matsuo, K. Kindo, M. Tokunaga, N. Kawashima, S. Takeyama and Z. Hiroi, Nat. Commun. **10** (2019) 1229.

[5] T. Mashiko and T. Okubo, Phys. Rev. Research **6** (2024) 033110.

[6] T. Mashiko and T. Okubo, in preparation.

[7] H. Li, D.-W. Qu, H.-K. Zhang, *et al.* Phys. Rev. Research **2** (2020) 043015.

[8] Y. Nakanishi, K. Ido, S. Morita, Y. Yamaji, and T. Okubo, in preparation.

Ground-state phase diagram of frustrated itinerant magnets

Kota IDO

Institute for Solid State Physics,

The University of Tokyo, Kashiwa-no-ha, Kashiwa, Chiba 277-8581

The Kitaev spin liquid has drawn attention as a platform for non-Abelian anyons, expected to be a source for topological quantum computation [1]. α-$RuCl_3$ is a promising candidate for realizing the Kitaev spin liquid because it is reported that half-integer quantized thermal Hall conductivity, expected for the Kitaev spin liquid under magnetic fields, has been observed [2]. However, this quantization appears only within a limited magnetic field range, stimulating further research for proposing other candidates and methods to realize the Kitaev spin liquid more robustly.

One strategy is the use of heterostructures. Combining Kitaev spin liquid candidates with other layered materials may enhance Kitaev interactions through strain and potentially induce novel phenomena via hybridization between conduction electrons and localized spins. Recently, heterostructures of α-$RuCl_3$ and graphene have been realized, spurring rapid progress in both experimental and theoretical studies [3, 4].

In this study, we investigated the ground state of the Kitaev-Kondo model [4], where a Kitaev spin model is coupled to a conduction electron layer via the Kondo coupling, using the variational Monte Carlo method. As the trial wave function, we employed a pair-product wave function with many-body correlation factors [5]. This wave function can accurately describe the Kitaev spin liquid. In addition, it incorporates the hybridization effect between conduction electrons and localized spins while accounting for many-body correlations beyond mean-field approximation. Our results reveal the emergence of rich ground states, including a fractionalized Fermi liquid, a magnetic ordered phase, and a Kondo insulating state. Further investigation has been ongoing, which will be reported elsewhere.

References

[1] A. Kitaev, Ann. Phys. **321**, 2 (2006).

[2] Y. Kasahara et al., Nature **559**, 227 (2018).

[3] S. Mashhadi et al., Nano Lett. **19**, 4659 (2019), B. Zhou et al., Phys. Rev. B **100**, 165426 (2019), Y. Wang et al., Nano Lett. **20**, 8446 (2020).

[4] U. F. P. Seifert, T. Meng, and M. Vojta, Phys. Rev. B **97**, 085118 (2018), W. Choi et al.,, Phys. Rev. B **98**, 155123 (2018).

[5] T. Misawa et al., Comput. Phys. Comm. **235**, 447 (2019).

Fracture process of semicrystalline polymers using large-scale simulation

Yuji HIGUCHI
Research Institute for Information Technology, Kyushu University
Motooka Nishi-ku, Fukuoka 819-0395

By molecular simulations, we have revealed the fracture processes of semicrystalline polymers [1], water dynamics around osmolytes [2], and water dynamics on the phospholipid membrane [3]. This year, we studied the delamination process of semicrystalline polymers from fillers by coarse-grained molecular dynamics simulations on systems B and C.

Semicrystalline polymers are used in automobile parts by adding fillers to improve their rigidity. On the other hand, a decrease in impact strength is a problem to be solved. The impact fracture occurs when voids are generated and grow from the interfacial delamination between the polymer and the filler. However, the delamination process is still unclear at the molecular level. We study the delamination process between the lamellae, which is a basic structure of semicrystalline polymer, and the filler by coarse-grained molecular dynamics simulations. Figure 1 shows the delamination process. In the edge-on model, where the polymer chains are oriented parallel to the filler surface, the voids grow perpendicular to the stretching direction. In the flat-on model, where the polymer chains are oriented perpendicular to the filler surface, voids grow parallel to the stretching direction. The maximum stress against the stretching is higher in the edge-on model than that in the flat-on model. The flat-on model shows that more polymer is adsorbed at high strains. We clarify the effect of differences in the orientation direction of the interfacial polymer on the delamination.

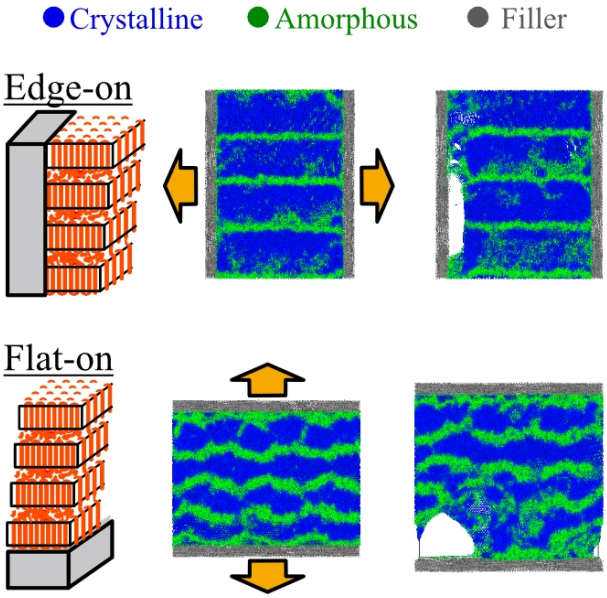


Figure 1: Coarse-grained molecular dynamics simulations on the interfacial delamination between a semicrystalline polymer and a filler in the edge-on and flat-on models.

References

[1] Y. Higuchi and G. Matsubai: Macromol. Chem. Phys. **225**, 2400076 (2024).

[2] Y. Higuchi, M. A. Saleh, T. Anada, M. Tanaka, and M. Hishida: J. Phys. Chem. B **128**, 5008 (2024).

[3] M. K. Rahman, T. Yamada, N. L. Yamada, Y. Higuchi, and H. Seto: J. Phys. Chem. B **129**, 3998 (2025).

Design of Multi-walled CNT Yarns for High-Performance CNT Yarn Composites

Go Yamamoto and Redha A. Ramadhan

Department of Aerospace Engineering, Tohoku University,

6-6-01 Aramaki-Aza-Aoba, Aoba-ku, Sendai 980-8579, Japan

We conducted simulations on approximately 180 multi-walled carbon nanotube yarn (CNTY) models using molecular dynamics (MD) simulations combined with Python-based input scripts [1]. The simulations were conducted on Supercomputer system C at ISSP. From the simulations, we obtained the nominal tensile strength of the CNTY structure with different structural parameters—The number of CNTs in the yarn was set to 3 and 7, and the number of walls ranged from 2 to 5. Both armchair and zigzag chirality were considered. The twist angle was investigated by varying the yarn twist from 0° to 30° in 5° increments. The interwall crosslink density was varied from 0% to 2.0% in 0.2% increments.

The parametric study revealed that the optimal CNTY structure is characterized by the armchair configuration, a small inner tube diameter, a large number of walls, a crosslink density exceeding 1% between each wall, and a low twist angle [1]. To verify these findings, we conducted a series of optimizations of the CNTY structural parameters using machine learning. The primary objective of the optimization was to maximize the nominal tensile strength of the CNTY. The optimization results are presented in Figure 1. Based on the optimization, the structural parameters that yield the highest nominal tensile strength correspond to the armchair-type CNTY, featuring a small inner wall diameter with a [6,6] index, only three CNTs in the yarn, and a near-zero twist angle. The optimized model consists of just two walls with no crosslink density between them.

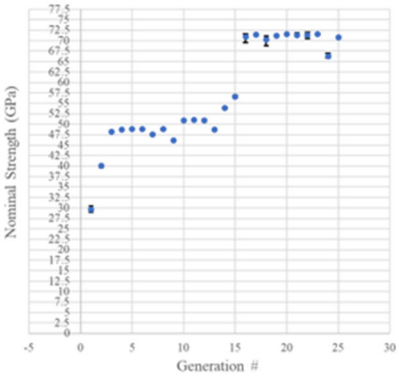


Fig. 1: Plot of the optimization generation vs the nominal strength of CNTY.

The results of this study will be reported in a manuscript. Next, we will conduct an optimization of the CNTY, focusing on the 5-wall CNTY group, with particular emphasis on crosslink density. Optimization of the 10-degree CNTY is also in progress.

References

[1] R.A. Ramadhan, C. Yu, A. Kunitomo, N. Shigemitsu, T. Shindo, G. Yamamoto, Structure-Mechanical Property Relationships in Carbon Nanotube Yarns, Solid State Phenomena 364 (2024) 3–9.

Prediction and Design of Protein Folding and Function

Masataka YOSHIMURA[1], Shunji SUETAKA[1], Koji OOKA[2], Runjing LIU[1], Shinya INOUE[1], Sae KATO[1], Shun NAGAI[3], Shunya OKADA[1], Atsuya WATANABE[1], and Munehito ARAI[1,2,3]

[1]Department of Life Sciences, Graduate School of Arts and Sciences, [2]College of Arts and Sciences, and [3]Department of Physics, Graduate School of Science, The University of Tokyo, Komaba, Meguro, Tokyo 153-8902

Proteins exert their functions after folding into specific three-dimensional structures. Therefore, elucidation of protein folding mechanisms is one of the most important issues in basic life sciences. In recent years, protein structure prediction based on deep learning methods has emerged, such as AlphaFold [1], and the development of AlphaFold was awarded the Nobel Prize in Chemistry in 2024. However, even AlphaFold cannot predict protein folding processes. We have recently developed a statistical mechanical theory called the WSME-L model that can predict folding processes for various types of proteins [2]. To investigate the applicability of this model, we applied it to various proteins to predict folding processes. In the calculations, contact energies between amino acid residues were obtained using the AMBER software [3], and the free energy landscape was calculated using in-house software written in C++ and Python. We compared the predicted results with experimental results in detail and modified the prediction methods to further improve the prediction accuracy and speed. We also tried to extend the theory to predict binding reactions between proteins.

Our WSME-L model can predict the folding reaction processes of various mutant proteins using their structures predicted by AlphaFold (LocalColabFold) [4]. We selected mutant proteins that were predicted to have a different folding pathway than the wild type. We are now investigating the folding processes of the designed proteins experimentally to verify the validity of the predictions.

Aldehyde deformylating oxygenase (ADO) is an enzyme that can synthesize alkanes equivalent to diesel oil and is expected to be useful for biofuel production; however, its activity is low and the mechanism of its function remains unresolved [5]. ADO binds to its upstream enzyme, acyl-ACP reductase (AAR), and efficiently receives aldehyde as substrate from AAR. Previous studies have proposed that ADO synthesizes alkanes upon dissociation from AAR, and the product exits through the substrate entrance [6]. To test this

hypothesis, we investigated whether the alkane product can dissociate from ADO while the AAR and ADO remain bound. Molecular dynamics (MD) simulations with the GROMACS software [7] using the Parallel Cascade Selection (PaCS) MD method [8] revealed that ADO can release the alkane product without dissociation of AAR [9]. Thus, we proposed a new model in which ADO can efficiently produce alkanes while remaining bound to AAR.

Increasing the activity of enzymes is important for the mass production of industrially useful substances. We have previously proposed a universal protocol to rationally increase the activity of enzymes using the physics-based Rosetta software [10]. In this study, we have attempted to use deep learning-based methods to improve the activities of several enzymes based on our protocol. The designed proteins were produced using *Escherichia coli* and experimental verification of their activities is ongoing.

References

[1] J. Jumper, et al.: Nature, **596**, 583-589 (2021).

[2] K, Ooka, and M. Arai: Nat. Commun. **14**, 6338 (2023).

[3] D. A. Case, et al.: AMBER 2022. University of California, San Francisco (2022)

[4] M. Mirdita, K. Schütze, Y. Moriwaki, L. Heo, S. Ovchinnikov, and M. Steinegger: Nat. Methods, **19**, 679-682 (2022).

[5] Y. Hayashi, and M. Arai: Microbial Cell Factories, **21**, 256 (2022).

[6] Y. Gao, et al.: Nat. Commun. **11**, 1525 (2020).

[7] S. Pall, C. J. Smith, B. Hess, E. Lindah: SoftwareX, **1–2**, 19-25 (2015).

[8] S. Ikizawa, et al: J. Phys. Chem. B, **128**, 3631-3642 (2024).

[9] M. Yoshimura, and M. Arai: Biophys. Physicobiol. **22**, e220003 (2025).

[10] J. K. Leman, et al.: Nat. Methods, **17**, 665 (2020).

Creating a quantum computing database for sensor materials

Wataru Mizukami

Center for Quantum Information and Quantum Biology, Osaka University, Osaka 560-0043, Japan

Quantum computers with more than a hundred qubits are now available, and the need for practical algorithms and data sets is growing. Recently, the first tests of quantum error correction on real devices have begun, which is an important step towards building useful quantum computers. Our research focuses on the development of hybrid quantum-classical methods for materials simulation, in particular for sensor materials. We are working on ways to make effective use of current quantum devices, despite their noise problems, by creating new hybrid approaches.

This year we created a quantum circuit dataset for the QM9 molecular database using Automatic Quantum Circuit Encoding (AQCE). This method allows us to convert molecular electronic structure information from exact diagonalisation into quantum circuits. By converting wave function data into quantum circuit format, we have created a useful resource for quantum machine learning with real chemical data.

We have also developed a new method called Quantum Selected Configuration Interaction (QSCI) with Auxiliary Field Quantum Monte Carlo (AFQMC), QSCI-AFQMC for short. QSCI uses quantum computers to find a key subspace and then diagonalises the electronic structure Hamiltonian in that subspace on classical computers. QSCI-AFQMC uses the QSCI wave function as the trial wave function for AFQMC calculations. We tested this method on several molecules, including H_2O and N_2, and achieved chemical accuracy on real superconducting quantum computers at Osaka University and RIKEN.

We also created a local surface energy (LSE) descriptor using neural network potentials to speed up the screening of high-entropy alloy catalysts. By applying both classical and quantum machine learning to this problem, we significantly reduced computation times while maintaining high accuracy, allowing faster exploration of possible catalysts. These advances show how quantum methods can help with practical materials research.

Thermal effects on quantum frustrated magnets

Tokuro Shimokawa
Okinawa Institute of Science and Technology Graduate University, Onna 904-0495, Japan

The properties of quantum frustrated magnets at finite temperatures remain largely unexplored, and there has been a continuous demand for advancements in research based on large-scale numerical calculations. In recent years, with the development in the field of quantum information, several quantum entanglement measures that can be experimentally measured have attracted attention. In this research project, we focused on several quantum entanglement measures that can be witnessed in experiments, and attempted to apply them to a long-standing problem of distinguishing between quantum spin liquid (QSL) and random singlet (RS) states.

As a representative example, we focused on the physics in the S=1/2 random-bond Heisenberg spin chain and J_1-J_2 random-bond triangular-lattice Heisenberg antiferromagnet. We numerically investigated the behaviors of several quantum entanglement measures such as one-tangle, two-tangle, concurrence, and quantum Fisher information, which could be measured by using inelastic neutron scattering experiments. To evaluate the quantum Fisher information at finite temperatures, we developed our non-biased numerical code based on thermal pure quantum state method to calculate the dynamical spin structure factor via real time evolution of thermal pure quantum state [1, 2]. We also have accelerated our computational code using MPI parallelization techniques, and especially, we were able to evaluate the temperature dependence of Quantum Fisher information and dynamical spin structure factor through large-scale parallel computing using F144cpu partitions. Our numerical calculations provided deep insight for understanding the entanglement natures, and qualitative difference in the temperature dependence of the quantum Fisher information could be useful to solve the identification problem in both 1D [3] and 2D [4] cases.

We also tried to study the scaling collapse in the finite-temperature dynamical spin structure factor near quantum critical point for S=1/2 J_1-J_2 triangular lattice magnet, and it's critical exponent for a triangular-lattice material, $KYbSe_2$ [5]. We succeeded in getting semi-quantitative good agreement with experiments [4].

References

[1] H. Ikeuchi, H. De Raedt, S. Bertaina, and S. Miyashita, Phys. Rev. B **92**, 214431 (2015).

[2] H. Endo, C. Hotta, and A. Shimizu, Phys. Rev. Lett. **121**, 220601 (2018).

[3] S. Sabharwal, T. Shimokawa and N. Shannon, arXiv:2407.20797.

[4] T. Shimokawa, S. Sabharwal and N. Shannon, in preparation.

[5] A. O. Scheie et al, Nat. Phys. **20**, 74 (2024).

Dynamic Modes in Active Potts Model

Hiroshi NOGUCHI
Institute for Solid State Physics, University of Tokyo

Various spatiotemporal patterns have been observed in nonequilibrium active systems. Many phenomena are well-captured by a description in terms of nonlinear but deterministic partial differential equations. However, noise effects are not understood so far. We focused on the effects of thermal fluctuations, since they are significant on a molecular scale.

We simulated the nonequilibrium dynamics of Potts models with three and four states, in square lattices [1–3] and meshless membranes [4]. A cyclic flipping energy is introduced in addition to usual nearest-neighbor interactions. Under the cyclically symmetric conditions, the cyclic changes in the dominant phases (called homogeneous cycling) and the spatial coexistence of the all phases are obtained at low and high flipping energies, respectively. In the three-state Potts model, the domains of three states form spiral waves, while waves do not have centers in the four-state Potts model. At a medium flipping energy, two modes temporally coexist, as shown in Fig. 1.

Compared with three-state cycling, the significant characteristics of four-state cycling is that there are no direct flips between the diagonal states ($s = 0$ and 2 or $s = 1$ and 3). Domains in the diagonal-state phase have a long lifetime, and the circular domains slowly shrink to reduce the domain boundary length. This spatial pattern steadily exists under asymmetric conditions. In the homogeneous cycling mode, these long-lived diagonal domains can cause the dominant phase to skip and return to the previous dominant phase. Thus, non-cyclic one-phase modes are formed through growth failure in the four-state cycling, whereas through nucleation failure in the three-state cycling.

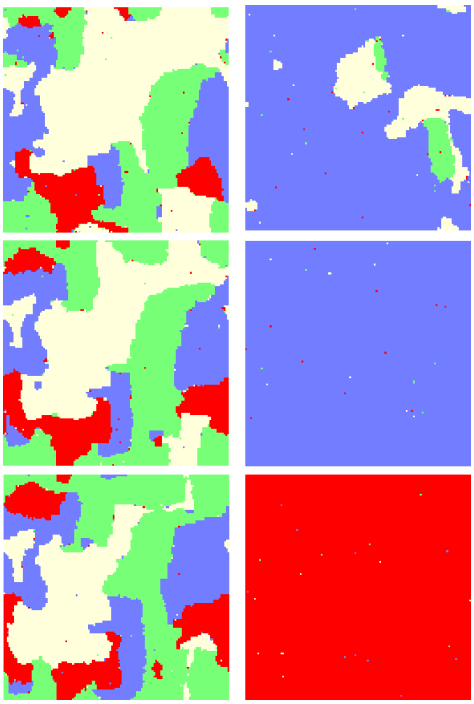


Figure 1: Sequential snapshots of the temporal coexistence of two modes in active four-state Potts model [3]. Each state is represented by a different color. Four states spatially coexist in the first three snapshots, while homogeneous cycling mode emerges in the last two snapshots.

References

[1] H. Noguchi, F. van Wijland, and J.-B. Fournier, J. Chem. Phys. 161, 025101 (2024).

[2] H. Noguchi and J.-B. Fournier, New. J. Phys. 26, 093043 (2024).

[3] H. Noguchi, Sci. Rep. 15, 674 (2025).

[4] H. Noguchi, Soft Matter 21, 1113 (2025).

Dynamical scaling study of three-dimensional XY spin glass

Y. Ozeki and Y. Terasawa

Graduate School of Informatics and Engineering, The University of Electro-Communications

We verified a method for obtaining a high-precision dynamical exponent z from the correlation length in the nonequilibrium relaxation (NER))process to analyze the $\pm J$ XY spin-glass (SG) in three dimensions. Since the Binder parameter exhibits no algebraic divergence in this system, we applied a method to estimate z by using scaling laws for the dynamical correlation function in conjunction with Gaussian process regression [1]. The obtained z yielded consistent and highly accurate results in previous studies for relatively well-studied models—specifically, the three-dimensional (3D) ferromagnetic Ising model and the 3D $\pm J$ Ising model. Building on these previous studies, we obtained highly precise critical temperatures and exponents. These findings support the spin chirality decoupling picture, explaining the experimental spin-glass phase transition.

We calculated the SG susceptibility and chiral grass (CG) susceptibility dynamically with n replicated systems. The calculations were performed with $L = 91$, $n = 256$, and 5 samples. As a result, we obtained $T_{\rm SG} = 0.396(1)$ and $T_{\rm CG} = 0.4460(6)$. In addition, the product of critical exponents $\gamma/z\nu$ and $z\nu$ were estimated as scaling parameters. For $\chi_{\rm SG}$, $\gamma/z\nu = 0.3660(4)$ and $z\nu = 7.67(5)$ were obtained; for $\chi_{\rm CG}$, $\gamma/z\nu = 0.3214(6)$ and $z\nu = 5.70(1)$ were obtained. These results are compared with those reported in previous studies in Table 1 and Table 2. The obtained transition temperature appeared to show good accuracy compared with previously reported values. The results confirmed that the SG transition temperature is lower than the CG transition temperature, supporting the spin chirality decoupling picture in SG systems [2].

Before applying the dynamical correlation method to the present model, we demonstrated the method applying to ferromagnetic (FM) transition in the 3D FM Ising model and SG transition in the 3D $\pm J$ Ising model. We note that the reliability of z obtained from the correlation length estimated by the dynamical scaling law has been established. On the basis of this result, the original objective of analyzing the 3D $\pm J$ XY model was achieved. Using the transition temperatures obtained from the dynamical scaling above, we compute the correlation length. As a result, the value of z is evaluated as $z = 5.86(1)$ for the SG case and $z = 5.24(7)$ for the CG case. These results are compared with those of previous studies in Tables 1 and 2. The obtained results show improved accuracy for both the transition temperature and the critical exponents compared with previously reported findings. The dynamical exponent z was found to be lower in the CG case than in the SG case.

Table 1: Results of the SG transition compared with those in previous studies.

Reference	$T_{\rm SG}$	z	ν
[3]	0.39(2)	4.4(3)	1.2(2)
[4]	0.455(15)	5.6(6)	0.85(8)
[5]	0.435(15)	5.0(1)	1.25(15)
Present work	0.396(1)	5.86(1)	1.30(4)

Table 2: Results of the CG transition compared with those in previous studies.

Reference	$T_{\rm CG}$	z	ν
[6]	0.39(3)	7.4(20)	1.2(2)
[4]	0.467(10)	6.3(5)	0.74(4)
[5]	0.445(15)	5.1(2)	1.05(10)
Present work	0.4460(6)	5.24(7)	1.08(4)

References

[1] T. Nakamura, *Phys. Rev.*E**93** 011301 (2016); **99** 023301 (2019).

[2] H. Kawamura *Phys. Rev. Lett.* **68** 3785 (1992).

[3] E. Granato, *Phys. Rev.*B**69** 012503 (2004).

[4] T. Yamamoto, T. Sugashima and T. Nakamura, *Phys. Rev.*B**70** 0184417 (2004).

[5] T. Nakamura, unpublished.

[6] H. Kawamura and M. S. Li, *Phys. Rev. Lett.* **87** 187204 (2001).

Temperature dependence of specific heat in an extended Kitaev model on a honeycomb lattice

Takafumi SUZUKI
Graduate School of Engineering,
University of Hyogo, Shosha 2167, Himeji, Hyogo 670-2280

Realization of Kitaev spin liquid has been one of challenging tasks in condensed matter physics. As demonstrated by Jackeli and Khaliullin [1], transition metal oxides may have a potential to provide stages for studying the Kitaev spin liquid. So far, α-$RuCl_3$ has been much focused on as a candidate material from both theoretical and experimental aspects. Many effective models for α-$RuCl_3$ have been proposed for this decade, and it is expected that the Kitaev interaction (K) and Γ interaction between the nearest neighbor spins work as the dominant interactions. The details of the ground states in the S=1/2 Kitaev-Γ model has been much investigated by several numerical methods such as numerical exact diagolization, tensor-network scheme, and variational Monte Carlo.

In previous project, we have investigated thermal properties of the S=1/2 Kitaev-Γ model on a honeycomb lattice with the coupling amplitude on the z bond changed (Figure 1) [2]. We found that the two-peak structure in the temperature dependence of the specific heat is confirmed near $d \sim 1$ with the negative K and positive Γ. When $d = 0$, the system is equivalent to the Kitaev-Γ spin chain, where the specific heat shows a single peak structure. This single peak becomes the high-temperature peak in the two-peak structure at $d \sim 1$; the energy scale of the low-temperature peak does not correspond to that of the z bond coupling constant.

In this project, we have focused on the S=1 case. First, we have investigated the ground-state phase diagram by numerical exact diagonalization. We find that the ground-state phase diagram for the S=1 case is similar to that for the S=1/2 case; the isotropically interacting Kitaev-Γ model is located on the phase boundary when $K < 0$ and $\Gamma > 0$ [2], as shown in Figure 2. The different point is that the gapless phase related to the Tomonaga-Luttinger liquid, which appears in the S=1/2 spin chain limit, is replaced by the Haldane gap phase in the S=1 case. Secondary, we have calculated the temperature dependence of the specific heat in the Haldane gap phase by using the thermal pure quantum state [3]. Even in the S=1 case, the two-peak structure also appears at $d \sim 1$. However, the two-peak structure seems to be fragile against the increase of Γ. We find that the single peak in the spin chain limit corresponds to the high-temperature peak.

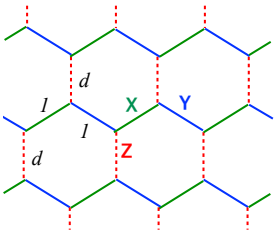


Fig. 1: Anisotropically interacting Kitaev-Γ model. The coupling strength on the X/Y bond is unity, and d is the ratio of the coupling strength on the Z bond against that on the X/Y bond.

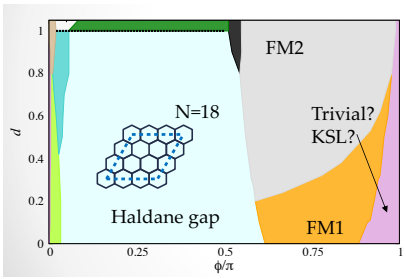


Fig. 2: Ground-state phase diagram for the S=1 anisotropically interacting Kitaev-Γ model. The horizontal axis corresponds to the coupling ratio between the Kitaev interaction and the G interaction; K=-cos ϕ and Γ=sin ϕ. All phase boundaries are decided from the second-derivative of the energy.

References

[1] G. Jackeli and G. Khaliullin, Phys. Rev. Lett. **102**, 017205 (2009).
[2] M. Gohlke, J. C. Pelayo, and T. Suzuki, Phys. Rev. B **109**, L220410; in preparasion.
[3] S. Sugiura, and A. Shimizu, Phys. Rev. Lett. **108**, 240401 (2012).

Level statistics and critical phenomena in non-Hermitian systems

TOMI OHTSUKI[1]
TOHRU KAWARABAYASHI[2]
KEITH SLEVIN[3]
1) Dept. Phys., Sophia University, Chiyoda-ku, Tokyo 102-8554, Japan
2) Dept. Phys., Toho University, Miyama 2-2-1, Funabashi 274-8510, Japan
3) Dept. Phys., Osaka University, Toyonaka, Osaka 560-0043, Japan

Our research over the past year centered on the symmetry classification and spectral statistics of random quantum systems, with a particular emphasis on non-Hermitian Hamiltonians.

We investigated the consequences of relaxing Hermiticity ($H \neq H^\dagger$) on the established tenfold symmetry classification of Hermitian random matrices (which includes three Wigner-Dyson,three Gade-Wegner, and four Altland-Zirnbauer classes). Non-Hermiticity expands the classification framework to 38 classes due to the distinct roles of transposition and complex conjugation.

A key activity was the numerical study of eigenvalue statistics in non-Hermitian systems. While eigenvalues are typically complex, certain symmetry classes permit real eigenvalues. We analyzed the level statistics of these real eigenvalues embedded within the complex spectrum, uncovering novel level repulsion behaviors [1].

Additionally, we studied the singular value statistics of non-Hermitian Hamiltonians. Recognizing that singular values offer different information compared to eigenvalues, we explored their statistical distributions within relevant non-Hermitian symmetry classes [2].

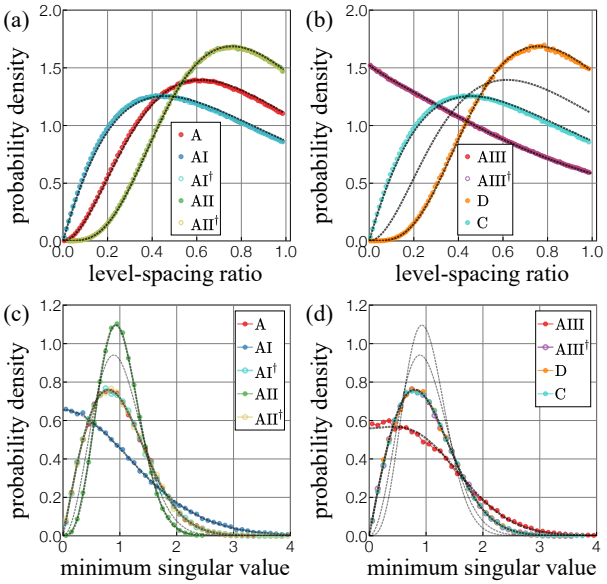


Figure 1: Singular-value statistics of non-Hermitian random matrices. (a, b) Level-spacing-ratio distributions of singular values in classes (a) A, AI, AI†, AII, AII†, (b) AIII, AIII†, D, and C. The black dashed curves are the analytical results for small random matrices. (c, d) Distributions of the minimum singular value $s_{\min}$ in classes (c) A, AI, AI†, AII, AII†, (d) AIII, AIII†, D, and C. The probability distribution functions are normalized such that their averages $\langle s_{\min} \rangle$ are 1. The black dashed curves are the analytical results for small random matrices. Taken from Ref. [2].

References

1. Z. Xiao, K. Kawabata, X. Luo, T. Ohtsuki, R. Shindou, Physical Review Research **4**, 043196 (2022).
2. K. Kawabata, Z. Xiao, T. Ohtsuki, R. Shindou, PRX Quantum **4**, 040312 (2023).

Understanding scrambling dynamics in quantum many-body systems towards realizing the dynamics in quantum computers

Masaki TEZUKA

Department of Physics, Kyoto University, Kitashirakawa, Sakyo-ku, Kyoto 606-8502

The Sachdev-Ye-Kitaev (SYK) model is a model of fermions with independently random all-to-all four-point interactions obeying the Gaussian distribution. The model is solvable, in the sense of random coupling average in the limit of large number of fermions. At low temperatures, the Lyapunov exponent, defined by the out-of-time ordered correlation functions, realizes the universal upper bound.

We previously studied a "sparse" version of the SYK model, in which the number of non-zero interaction terms is reduced to the order of the number of fermions. The sparse model with Gaussian random couplings had been known to reproduce essential features of the original SYK model [1]. In [2], we analyzed the spectral statistics of a further simplification, in which the magnitude of the nonzero couplings is a constant. Towards quantum simulation of such models, in [3] we studied another simplification of the SYK model: a model of Pauli spin operators with all-to-all four-spin interactions. We observed a striking quantitative coincidence between this spin model and the SYK model. In [4], we studied the quantum error correction (QEC) capabilities of the unitary time evolution according to various time-independent Hamiltonians by the Hayden-Preskill protocol. We compared the error estimate, obtained by the decoupling approach, against the one for random unitary evolutions obeying the circular unitary (Haar) ensemble. For the sparse SYK model, the QEC error estimate approaches the Haar value within a short time if the number of remaining couplings is sufficient for a random-matrix like spectral statistics. In contrast, for quantum spin chains often studied in the context of chaotic dynamics, scrambling is not observed in this sense, with the QEC error estimate remaining large.

To better elucidate the conditions for scrambling behavior, we have studied two classes of quantum models with two-local interactions, namely interactions between two distant locations of the system, unlike four in the models studied in [2] and [3]. In the first model, we consider two-local interactions between SU(d) generators. Simulations of this class of models might be accessible with qudit-based quantum devices. In the second model, we consider restricting the interactions in the SYK models to those between two clusters of fermions. By our numerical analysis, we find that these models also show strongly chaotic features. Details will be reported elsewhere.

References

[1] S. Su *et al.*, arXiv:2008.02303; A. M. Garcia-Garcia *et al.*, Phys. Rev. D **103**, 106002 (2021).

[2] M. Tezuka, O. Oktay, E. Rinaldi, M. Hanada, and F. Nori, Phys. Rev. B **107**, L081103 (2023).

[3] M. Hanada, A. Jevicki, X. Liu, E. Rinaldi, and M. Tezuka, J. High Energ. Phys. **2405**, 280 (2024).

[4] Y. Nakata and M. Tezuka, Phys. Rev. Research **6**, L022021 (2024).

Large-Scale Computation for Spin Glasses Using Extended-Ensemble Methods

Koji HUKUSHIMA
Department of Basic Science, University of Tokyo
3-8-1 Komaba, Meguro-ku, Tokyo 153-8902

Markov-chain Monte Carlo (MCMC) methods are the workhorse for sampling high-dimensional probability distributions. However, for systems with rugged, multi-modal energy landscapes –such as spin glasses– standard MCMC suffers from exponentially slow relaxation. Extended ensemble methods, such as Exchange Monte Carlo (or parallel tempering), partially resolve this problem by simulating multiple replicas at different temperatures and allowing configuration exchanges.

On modern supercomputers with $10^4 - 10^6$ cores, however, parallel tempering faces significant scalability issues: to fully utilize available cores, the number of replicas must grow accordingly. In practice, an excessive number of replicas is not only unnecessary but also harmful, at it increases round-trip time in temperature space and degrading sampling efficiency.

To address this issue, we explore Simulated Tempering (ST) as an alternative framework. ST jointly samples configurations and temperatures using a single replica, eliminating the need for inter-replica communication. Once the appropriate temperature weights are learned, independent ST simulations can be launched across thousands of compute nodes, making it well-suited for massively parallel environments.

To further improve ST, we introduce Lifted Simulated Tempering (Lifted ST), which accelerates temperature-space mixing by violating detailed balance in the temperature updates. This method augments the system with a binary lifting variable that indicates the direction of temperature change. Rather than proposing random temperature updates, Lifted ST deterministically continues in the same direction until a rejection occurs, at which point the direction flips. This reduces diffusive backtracking in temperature space and significantly reduces round-trip times.

An additional advantage is that Lifted ST is formulated in the continuous temperature limit, allowing smoother sampling and the use of thermodynamic observables such as the expected energy to guide temperature updates. This continuous formulation also eliminates the need to manually discredited temperature levels.

We applied Lifted ST to the three-dimensional Ising spin glass model as a benchmark. Using this method, we successfully computed the required temperature weights for system sizes up to $N = 64^3$. While equilibrium simulations are currently feasible up to 32^3, our benchmarks suggest that simulations of 48^3 spins are within reach on the ISSP supercomputing platforms. These results demonstrate the practical advantages of Lifted ST over traditional methods, particularly in massively parallel environments where conventional tempering methods struggle to scale.

In summary, Lifted ST offers a promising direction for large-scale sampling in complex systems by combining the strengths of extended ensemble methods with improved parallelized and faster convergence.

Multiscale simulations for complex flows

Yohei MORII and Toshihiro KAWAKATSU

Department of Physics,

Tohoku University, Sendai, Miyagi 980-8578

Macroscopic complex viscoelastic flows usually originate from the microscopic molecular processes such as entanglements of polymer chains or deformations of molecular aggregates. To simulate such complex flows, it is essential to combine macroscopic flow simulation with microscopic molecular simulations to generate local stress field. We are developing a platform for multiscale simulations on complex flows named MSSP (Multi-Scale Simulation Platform for complex flows), where a macroscopic flow simulator based on smoothed particle hydrodynamics (SPH) and microscopic molecular dynamics simulators embedded in each of SPH particles are coupled [1]. In our previous ISSP-supercomputer project (2023-Ca-0111), we studied the Marangoni effect of surfactant adsorbed on an oil/water interface using MSSP. For such a purpose, we implemented an evaluation method of surface tension and a diffusion process of microscopic molecules between adjacent SPH particles. In the present project, we use the above implementation to systematically explore the behavior of an oil droplet shape floating in an aqueous micellar solution.

Figure 1 shows simulation results using 10,000,000 micelles on MSSP. By changing the micellar extensibility (viscoelastic effect) and the surfactant affinity to the oil/water interface, various droplet shapes are observed [2].

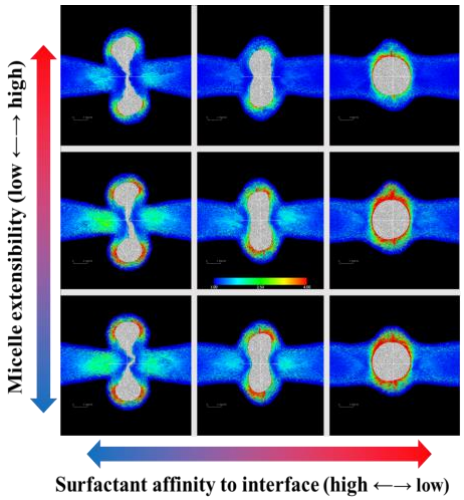


Fig.1 Oil droplet shapes for various conditions of micellar extensibility and surfactant affinity to the oil/water interface.

Acknowledgement

The computation in this work has been done using the facilities of the Supercomputer Center, the Institute for Solid State Physics, the University of Tokyo.

References

[1] Y.Morii and T.Kawakatsu, Phys. Fluids, **33**, 093106 (2021).

[2] Y.Morii and T.Kawakatsu, *in preparation*

Molecular dynamics simulation of protein aggregation

Hisashi Okumura

Exploratory Research Center on Life and Living Systems,
Institute for Molecular Science, Okazaki, Aichi 444-8585

Protein aggregates such as oligomers and amyloid fibrils cause more than 40 diseases. For example, Alzheimer's disease is caused by aggregated amyloid-β (Aβ) peptides. Aβ peptide usually consists of 40 or 42 amino acid residues. Aβ peptide with 40 residues is referred to as Aβ40, and that with 42 residues is referred to as Aβ42. We have performed molecular dynamics (MD) simulations to understand the aggregation and disaggregation mechanisms of Aβ peptides, including dimerization, oligomerization, amyloid fibril structure in bulk solution, conformations at the air-water interface, oligomer structure on the membrane surface, interaction with ganglioside and polyphenols, and disruption by ultrasonic wave and infrared laser irradiation.

During the last few fiscal years, we performed large-scale MD simulations of Aβ peptide aggregation using the supercomputer in ISSP. We have performed all-atom MD simulations of 32 Aβ40 and Aβ42 peptides in explicit water solvent for 2.0 μs. We observed Aβ peptides aggregated with repeating aggregation and disaggregation. They finally formed large oligomers, such as 20-mer and 32-mer. We revealed structural changes in the aggregation process, in particular focusing on the aspect ratio of the oligomers and secondary structure.

We observed that Aβ42 aggregated relatively faster than Aβ40 and formed larger oligomers than Aβ40. This observation is consistent with experimental fact. We revealed the mechanism of this phenomenon. We found that the formation of intramolecular β-sheet structures promotes the formation and aggregation of intermolecular β-sheet structures. In both Aβ40 and Aβ42, Glu22 and Lys28 form hydrogen bonds and the space between them tends to become a loop region. However, in Aβ42, the negatively charged C-terminus comes close to the positively charged Arg5, stabilizing the β-hairpin structure. On the other hand, in Aβ40, the β-hairpin structure is two residues shorter and is less stabilized. Therefore, Aβ42 is easier to take the β-hairpin structure and aggregate.

We also found that small oligomers are relatively spherical, but tend to extend in one way as they get larger. This tendency is also similar to experimental facts. We are currently analyzing this phenomenon in more detail.

Efficient sampling simulation of the soft modes significantly contribute to protein properties

Duy Tran, Wijaya Tegar, Bai Zhen, Sari Hagimoto, Hiroshi Kono, Tatsuki Hori, Masaki Mukaiyama, Yusei Ito, Vi Toan Lam, Yoshito Hasegawa, Reiya Hayashi, Akio Kitao

School of Life Science and Technology,

Institute of Science Tokyo, Ookayama, Meguro-ku, Tokyo 152-8550

Bacterial motility is primarily driven by the rotation of flagella—helical filaments that extend from the cell surface. This rotary motion is powered by a highly efficient, ion-driven molecular motor embedded in the bacterial cell membrane. The stator of this motor consists of a complex formed by five MotA monomers and two MotB monomers [1]. In Escherichia coli and many other bacteria, the MotA/MotB complex acts as the stator unit of the flagellar motor, harnessing the proton motive force (H^+ gradient) to generate torque.

MotA forms a transmembrane channel and contains cytoplasmic domains that interact with the rotor protein FliG, while MotB anchors the stator to the peptidoglycan layer of the cell wall via a conserved peptidoglycan-binding domain. The interaction between MotA and MotB facilitates proton translocation across the membrane, which in turn drives flagellar rotation. MotA contains transmembrane helices and cytoplasmic loops critical for torque generation, whereas MotB possesses a plug domain that regulates ion flow and secures the stator to the cell wall. Despite differences in ion selectivity and environmental adaptation, the MotA/MotB complex represents a remarkable example of convergent evolution, effectively converting electrochemical energy into mechanical motion. Studying this system not only enhances our understanding of microbial motility but also offers insights into bioenergetics and the design of synthetic nanomachines.

In this study, we investigated the ion permeation pathway of the Bacillus subtilis MotA/B complex, focusing on sodium ions. We performed relaxation simulations of the MotA/B structure embedded in a POPE/POPG membrane, using the structure from PDB ID 6YSL [1]. We then calculated the interaction frequency between sodium ions and residues within the MotA/B complex.

Our results revealed that the intracellular regions of MotA exhibit a high propensity for interacting with sodium ions (Figure 1a), while the extracellular regions showed fewer interactions. Among the residues with frequent sodium contact, Ser26, Ser28, and Asn32 were particularly prominent. Additionally, we found that sodium ions are trapped by Thr156 of both MotA1 and MotA2 (Figure 1b, c), located at the interface between MotA and MotB.

We further analyzed the pore architecture of the MotA/B complex using MOLEonline [2]. Two distinct pores were identified: one discontinuous pore extending from the periplasmic domain to the membrane region, and a continuous pore bridging the periplasmic and cytoplasmic domains. Notably, the continuous pore was found to be highly hydrophobic from the periplasmic side down to a bottleneck region within the membrane. This narrowest point, measuring approximately 2.7 Å in diameter, is formed by Ile183 and Phe187 of MotA and Val35 of MotB. Beyond the bottleneck, the pore widens and becomes solvent-accessible.

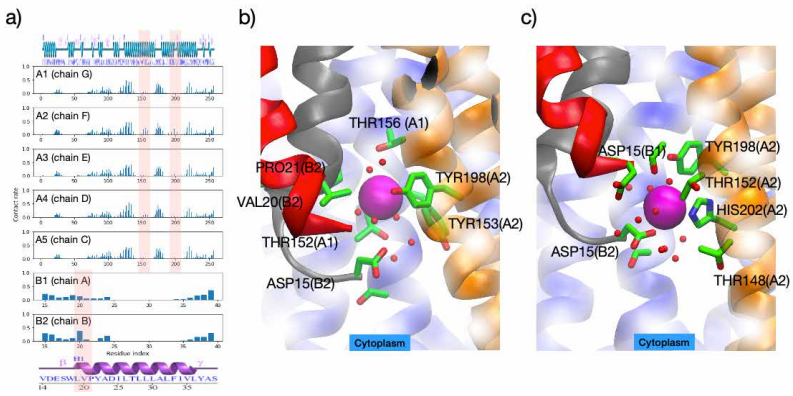


Figure 1. The sodium ions in contact with the residues on MotA, MotB proteins. a) the contact rates. b) the zoom-in of the sodium ion (in purple) in contact with MotA1, MotA2, MotB2. Water molecules are represented by the red spheres.

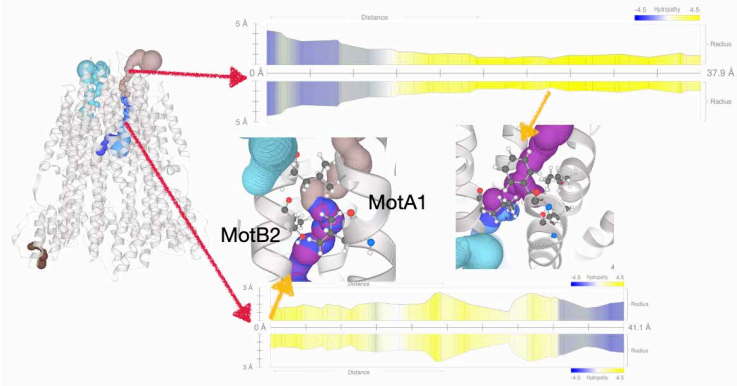


Figure 2. The pores are formed between the interfaces of MotA and MotB proteins of the *Bacillus subtilis* MotA/B complex.

Reference

[1] Deme et al, Nat MicroBiol 5, 1553 (2020)

[2] Pravda et al, Nucleic Acids Res 46, W368 (2018)

Fast free-energy estimation using simulated tempering with Wang-Landau-type feedback

Yoshihiko NISHIKAWA
Department of Physics, Kitasato University
Sagamihara, Kanagawa, Japan, 252-0373

Simulated tempering (ST) [1] is an extended-ensemble Monte Carlo technique that dynamically changes control parameters of the system with maintaining equilibrium at any time. ST can accelerate decorrelation and equilibration of complex systems with rugged free-energy landscapes, by changing temperature (or any other intensive parameters) to bypass the slow dynamical pathways. However, unlike parallel tempering (PT), also known as Exchange Monte Carlo [2], ST needs the free energy of the system to achieve an efficient sampling for a given temperature range. This complicates practical use of ST, since precisely estimating the free energy is in general an exhausting task.

The extended partition function for ST with a set of temperature points $\{\beta_i\}$ ($\beta_1 < \beta_2 < \cdots < \beta_M$) is

$$\mathcal{Z}(\{\beta_i\}_{i=1,2,\cdots,M}) = \sum_{i=1}^{M} Z(\beta_i)\exp(g(\beta_i)), \quad (1)$$

with $Z(\beta)$ the partition function of the system at inverse temperature β and $g(\beta)$ a bias function that controls the marginal distribution of β:

$$\pi(\beta) = \frac{Z(\beta)\exp(g(\beta))}{\mathcal{Z}(\{\beta_i\})} = \frac{\exp(-\beta F(\beta) + g(\beta))}{\mathcal{Z}(\{\beta_i\})}. \quad (2)$$

If we could set $g(\beta) = -\beta F(\beta)$, where $F(\beta)$ is the free energy of the system, then the marginal distribution is flat over $\{\beta_i\}$. ST is thus optimal with $g(\beta) = \beta F(\beta)$ as it can sample from the entire temperature range with equal probability. However, estimating the free energy of a given system needs extensive simulations. One could run PT simulations to estimate the free energy beforehand [3], whereas ST simulations are not needed anymore as PT itself generates equilibrium samples if one employs this approach. Others have proposed on-the-fly estimation algorithms [4, 5], which rely on the naive thermodynamic integration and suffer from slow dynamical relaxation at low temperatures.

Here, we propose an efficient irreversible Monte Carlo algorithm to estimate the free energy of the system. Our algorithm iteratively updates an instantaneous free-energy estimate with the Wang-Landau-type feedback [6, 7], and eventually converges to the true free energy in the long-time limit. We further incorporate a simple yet maximally irreversible dynamical rule in the algorithm. The dynamical rule implements a *lifted* Markov chain [8], which can drastically accelerate the convergence.

Our algorithm needs two additional ingredients compared to conventional ST simulations: A histogram $H(\beta)$ recording the number of visits to each β_i and a parameter f that controls the precision of the free-energy estimate. Suppose the system is currently at $\beta = \beta_i$ and has an energy E. We first sample a *lifting parameter* $v \in \{\pm 1\}$ with equal probability, and propose a change β to β_{i+v} with probability 1. The change is accepted

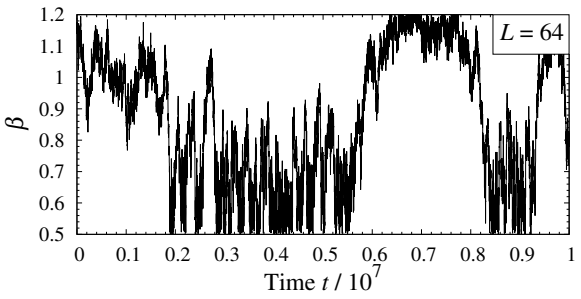


Figure 1: Typical trajectory in the β space during an equilibrium ST simulation for $L = 64$.

with a probability satisfying the balance condition, e.g. the simple Metropolis probability, and update $i \leftarrow i + v$ and $\beta = \beta_i$. We keep proposing the change i to $i + v$ as long as it is accepted. When rejected, we update $v \leftarrow -v$, and repeat the same until the number of attempts reaches a predetermined number ℓ, which is set to $M/2$ in our study. During the β updates, we accumulate the histogram $H(\beta_i)$ and update the current free-energy estimate $g(\beta_i) \leftarrow fg(\beta_i)$. From time to time, we check if the histogram is sufficiently *flat*, and if it is, we reduce f to $\sqrt{f}$ and reset the histogram to zero. Here, we consider the histogram is flat if $\min_i H(\beta_i) > 0.8 \sum_i H(\beta_i)/M$. We stop the estimation when $\log f$ becomes small enough, e.g. 10^{-6}, and can seamlessly move on to production runs using the estimated free energy.

We apply this algorithm to the three-dimensional Edwards-Anderson (EA) spin glass model with Gaussian couplings on a periodic cubic lattice of linear length L. The number of temperature points $M = 401$ and $\beta_i = 0.5 + 0.7(i-1)/(M-1)$ $(i = 1, 2, \cdots, M)$, where the unit of temperature is the standard deviation of the Gaussian couplings. In numerical study of spin glass models, an average of any physical quantity over many random realizations needs to be taken, requiring large-scale numerical resource. We took an advantage of the ISSP supercomputer to perform large-scale parallelized simulations of the model for 512 independent random instances with up to $L = 64$. We numerically find that the mean convergence time τ_c of the algorithm defined as the timescale to reach the optimal performance grows algebraically with L as $\tau_c \sim L^4$. For $L = 64$, our algorithm converges the slowest, most difficult instance within a month, whereas most of the instances take about two weeks. This is in strong contrast with a conventional algorithm [4, 5], which we find takes an exponentially long time to converge. After the convergence of the free-energy estimation, we have run equilibrium ST simulations with fixing the bias function. Fig. 1 shows a typical trajectory in the β space for $L = 64$. Clearly, the system can wander between $\beta_1 = 0.5$ and $\beta_M = 1.2$, indicating our algorithm has precisely estimated the free-energy estimation even with this large L.

This work was done in collaboration with A. C. Maggs and Koji Hukushima.

References

[1] E. Marinari and G. Parisi, EPL **19**, 451 (1992).

[2] K. Hukushima and K. Nemoto, J. Phys. Soc. Jpn. **65**, 1604 (1996).

[3] A. Mitsutake and Y. Okamoto, Chem. Phys. Lett. **332**, 131 (2000).

[4] S. Park and V. Pande, Phys. Rev. E **76**, 016703 (2007).

[5] P. H. Nguyen, Y. Okamoto, and P. Derreumaux, J. Chem. Phys. **138**, 1 (2013).

[6] F. Wang and D. P. Landau, Phys. Rev. Lett. **86**, 2050 (2001).

[7] C. Zhang and J. Ma, Phys. Rev. E **76**, 036708 (2007).

[8] F. Chen, L. Lovász, and I. Pak, Lifting Markov chains to speed up mixing, in Proceedings of the Thirty-first Annual ACM Symposium on Theory of Computing (ACM, New York, 1999), pp. 275 – 281.

Defect structures and their transport properties in thermoelectric chalcogenides

Susumu FUJII
Department of Materials, Faculty of Engineering, Kyushu University
Motooka, Fukuoka 819-0395
Nanostructures Research Laboratory, Japan Fine Ceramics Center
Mutsuno, Atsuta, Nagoya 456-8587

Thermoelectric materials can directly convert heat into electricity. To improve their conversion efficiency, it is necessary to enhance the Seebeck coefficient and the electrical conductivity while simultaneously reducing the lattice thermal conductivity. In recent recent years, strategies such as introducing lattice deffects and nanostructures, as exemplified by nanocrystalline materials, have been actively pursued to effectively reduce lattice thermal conductivity without deteriorating electronic properties [1]. However, the impact of intrinsic point defects, dopants, dislocations, and grain boundaries (GBs) on thermoelectric properties remain unclear at least in a quantitative manner.

In this study, we investigated the effects of intrinsic point defects and GBs on the thermal conductivity of PbTe, a representative thermoelectric material, using MD simulations. We employed an artificial neural network (ANN) potential for the interatomic interactions and also evaluated its accuracy [2]. Most of the computational resources were devoted to the long-time ANN-MD simulations. These calculations were performed using an MD code implemented by a collaborator, with additional codes for perturbed MD for thermal conductivity calculations developed by the author.

First, we examined the reproducibility of phonon properties and lattice thermal conductivity of bulk PbTe using the ANN potential. The ANN potential was found to accurately reproduce the harmonic phonon dispersions, the frequency shifts due to anharmonicity, the linear thermal expansion coefficient, and the temperature dependence of the lattice thermal conductivity. Furthermore, it was confirmed that the ANN potential sufficiently reproduces the energies of intrinsic point defects (such as vacancies, antisites, and interstitials) and grain boundaries, as well as the atomic forces in their vicinity, in good agreements with density functional theory (DFT) calculations.

Using the ANN potential, we calculated the lattice thermal conductivity in the vicinity of point defects. The thermal conductivity was suppressed with a trailing effect behind the point defects (Fig. 1). The extent of the suppression varied depending on the type of point defect, with interstitials causing the significant reduction of thermal conduction. Frequency analysis revealed that the nature of phonons scattered by the defects differed depending on the defect type. The atom-resolved thermal conductivity was found to be strongly correlated with the changes in phonon frequencies induced by the introduction of defects, reflecting alterations in the local potential energy surface [2].

Approximately 20 symmetric tilt GB models of PbTe were also constructed using the ANN potential. Except for the twin boundary, these grain boundaries exhibited relatively

similar GB excess energies. In contrast, the GB excess volumes varied significantly depending on the GB misorientation. The GB thermal resistance among these models differed by up to several times. While the GB thermal resistance showed a correlation with both the GB excess energy and volume, the correlation was weaker compared to the trends observed in MgO and $SrTiO_3$ [3, 4]. The factors governing lattice thermal conduction at PbTe GBs are expected to be elucidated through future structural and phonon analyses.

This study demonstrates that by utilizing highly accurate machine learning potentials, it is becoming possible to quantitatively and microscopically elucidate the effects of lattice defects on thermoelectric properties.

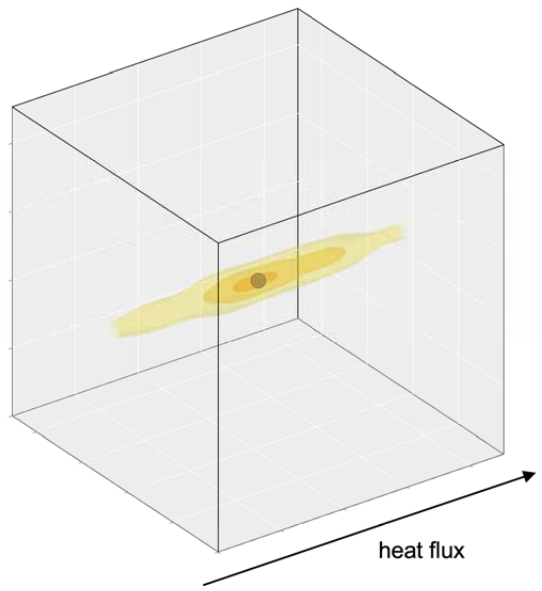


Figure 1: Suppression of lattice thermal conduction near Pb vacancy in PbTe. Black circle indicates the position of the Pb vacancy. The regions where the thermal conductivity is reduced are shown with colored shading, with darker colors indicating greater reductions.

References

[1] K. Biswas, J. He, I.D. Blum et al., Nature **489**, 414-418 (2012).

[2] T. Yokoi, S. Fujii, Y. Ogura, K. Matsunaga, under review.

[3] S. Fujii, T. Yokoi, C.A.J. Fisher et al.m Nat. Commun. **11**, 1854 (2020).

[4] S. Fujii, H. Isobe, W. Sekimoto, M. Yoshiya, Scr. Mater. **258**, 116524 (2025).

Molecular Dynamics Simulation for Studying Polymer Infiltration Process in Nanoporous Materials

Nobuhiko HOSONO

Department of Applied Chemistry, Graduate School of Engineering

The University of Tokyo, Hongo, Bunkyo-ku, Tokyo 113-8656

Metal-organic frameworks (MOFs) are crystalline compounds possessing numerous nano-sized pores, capable of encapsulating molecules ranging from small gas molecules to extremely long polymers, as demonstrated by previous research [1]. Recently, we experimentally discovered that the rate of polymer infiltration and the diffusion pathways within the pores significantly vary depending on the chemical structure and functional groups within the polymer chains, leading to differences in adsorption capacity into the MOFs [2].

From the previous year, we performed all-atom MD simulations of this polymer diffusion process, aiming to gain molecular-level insights into the mechanism behind these phenomena. For this study, we employed the LAMMPS package, which is specialized for large-scale parallel computing of molecular dynamics.

To study how polymer microstructures affect MOF infiltration dynamics, we prepared polyethylene glycol (PEG) chains possessing a xylene unit at the center of their main chain. We modeled three types of PEG chains, which are different in the substitution position at the central xylene unit, namely, *ortho* (***o*-PEG**), *meta* (***m*-PEG**), or *para*-substituted (***p*-PEG**). The molecular weights and other structural characteristics are set to be constant for the three model PEGs. The structure of a MOF was generated based on its single-crystal X-ray diffraction data. Fifteen PEG chains of each type (either ***o*-PEG**, ***m*-PEG**, or ***p*-PEG**) were placed in the simulation box and structurally relaxed. Subsequently, initial structures were obtained by placing the PEG chains in contact with the (001) plane of the MOF. By conducting MD simulations at 393 K for 100 ns each on these structures with MPI processes, we tracked the infiltration and diffusion behavior of the PEGs within the nanopores of the MOF. The center of mass (COM) of the PEG chains was plotted as a function of time, showing infiltration kinetics of the PEG into the MOF nanopores (**Figure 1**). It became evident that differences in conformation due to the positional isomerism significantly influence the infiltration and diffusion behavior (**Figure 1**). This MD-based observation well supported the experimental results that ***o*-PEG** shows significantly slow infiltration kinetics compared to ***m*-PEG** and ***p*-PEG** [3].

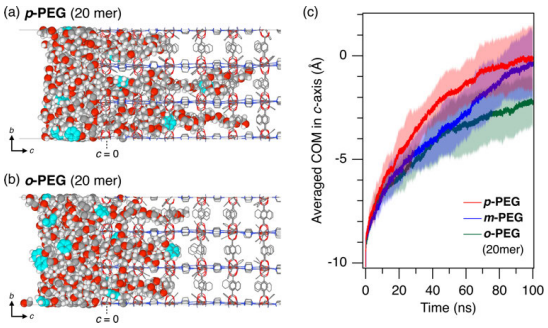


Figure 1. Representative MD snapshots of (a) ***p*-PEG** and (b) ***o*-PEG**. (c) Time evolution of the averaged COM in the c-axis in MOF. Averaged data from the five MD simulation runs are plotted as solid lines with shaded error bands of σ ($N = 5$).

In this study, we also investigated the reverse process using steered molecular dynamics (SMD) simulation. Non-substituted PEG (***n*-PEG**) with methyl group termini was arranged in the nanopores of MOF, then the external force was applied to the terminal C atom near the MOF surface after the 5-ns structural relaxation run, inducing the pullout of the PEG chain (**Figure 2**). It was carried out by "smd" command, pre-installed in LAMMPS. The required force during the pulling event was recorded, which successfully generated a force curve. All the MD run was executed at room temperature (298 K) in the *NVE* condition, and constant pulling speeds of 0.5 m/s or 2 m/s were applied. Interestingly, the force curve obtained by the SMD simulation reproduced the experimental force curve measured by single-molecule force spectroscopy analysis.

We also conducted the same SMD simulation for ***p*-PEG** to see the effect of the xylene unit on the force signals. Interestingly, a characteristic force signal was observed at a certain length in the force curve, which corresponds to the xylene substitution point on the ***p*-PEG** chain.

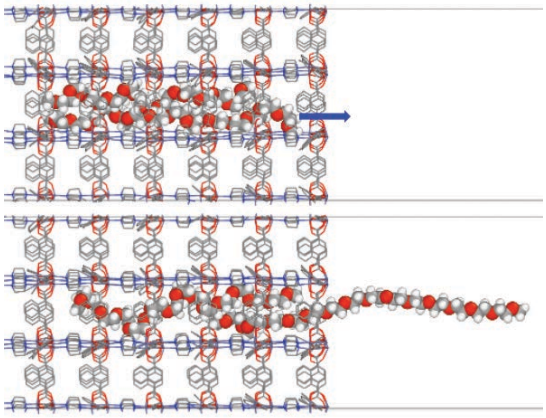


Figure 2. Representative MD snapshots of pulling ***n*-PEG**. The PEG chain was progressively extracted along the *c*-axis.

In summary, we successfully revealed the effect of polymer structure on both infiltration and forced-extraction behaviors in MOF nanopores at the molecular level using the large-scale parallel computing resources.

References

[1] N. Oe, N. Hosono, and T. Uemura, *Chem. Sci.* **12**, 12576 (2021).

[2] N. Mizutani *et al.*, *J. Am. Chem. Soc.* **142**, 3701 (2020).

[3] N. Hosono, Y. Kono, N. Mizutani, D. Koga, and T. Uemura, *Chem. Commun.* **60**, 13690 (2024)

Free energy and phase coexistence in various boundary conditions

Naoko NAKAGAWA
Department of Physics, Ibaraki University
2-1-1 Bunkyo, Mito, Ibaraki 310-8512

We investigate the thermodynamics of simple fluids to describe liquid-gas coexistence under weak gravity during heat conduction.

First, we focused on isothermal systems under weak gravity without heat conduction [1]. We theoretically constructed a global thermodynamic framework incorporating gravitational effects, derived from equilibrium statistical mechanics. The inhomogeneity induced by gravity is summarized by a new intensive variable, mgL, representing the difference in gravitational potential energy between the top and bottom of the container. Consequently, the thermodynamic description is extended from the standard (T, V, N) ensemble to (T, V, N, mgL). The extended free energy exhibits non-analyticity at $g = 0$, which can be interpreted as a first-order phase transition related to the liquid-gas configuration. The Maxwell relations derived from this global thermodynamics predict the behavior of the Virial pressure (the spatial average of the local pressure) as a function of the mean density N/V. We then performed molecular dynamics simulations using LAMMPS for one-component Lennard-Jones fluids. The theoretical predictions align well with the numerical observations, such as the dependence of the Virial pressure on N/V or g.

Next, we drove the system into heat conduction states by connecting heat baths with temperatures T_1 and T_2 to the top and bottom walls of the container, respectively. The heat flow direction was set opposite to gravity, with the top plate colder than the bottom $(T_1 < T_2)$. Thermally, the colder temperature (T_1) favors the liquid phase locating near the top wall above the gas. However, gravity pulls the denser liquid phase towards the bottom. This simple setup leads to rich system behavior. Since the system is conducting heat and thus out of equilibrium, established equilibrium statistical mechanics and thermodynamics do not directly apply. Molecular dynamics simulations provide a means to explore novel phenomena in such non-equilibrium systems, potentially guiding theoretical developments in nonequilibrium thermodynamics. This approach helps circumvent simplifying assumptions that might obscure the system's true behavior. For instance, standard theories might assume local equilibrium or neglect detailed interfacial physics, whereas simulations directly model particle interactions without these constraints.

Gravity and heat flux are the respective mechanical and thermal drivers of inhomogeneity in the system. We define a dimensionless parameter

$$\chi = \frac{k_{\mathrm{B}}(T_2 - T_1)}{mgL}, \tag{1}$$

representing the ratio between the thermal energy difference across the system and the gravitational potential energy difference. This parameter χ quantifies the relative strength of heat conduction versus gravity.

Through careful and elaborate numerical experiments, particularly under non-equilibrium conditions, the observed phenomena were

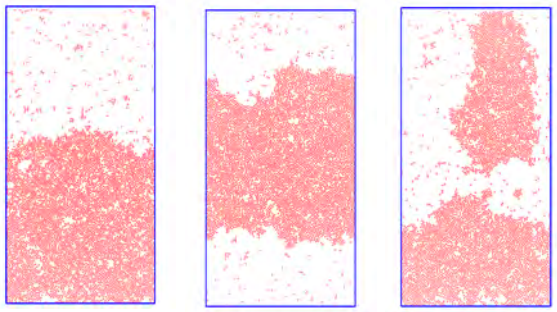


Figure 1: Phase coexistence of liquid and gas in heat conduction under gravity. See text.

found to be highly sensitive to the specific system setup, potentially more so than to the precise value of χ. We focused on the case with 'dry' walls, where the interaction between fluid particles and the top/bottom walls is described by the purely repulsive Weeks-Chandler- Andersen (WCA) potential [2]. When χ is small (i.e., gravity dominates over the thermal gradient effect), the bulk liquid resides at the bottom (Fig. 1, left). For $\chi > 10$, the bulk liquid forms a layer hovering above a gas layer near the bottom (Fig. 1, middle). If gravity is sufficiently weak (corresponding to very large χ), the liquid floats to the top. Furthermore, it was observed that the gas located above the liquid layer (e.g., in the hovering state) becomes supercooled, while the gas below the liquid remains in a normal (non-supercooled) state.

Finally, we changed the wall properties from dry (repulsive) to 'wet' (attractive). With sufficiently attractive (wet) walls, the system's behavior changes significantly; for instance, the hovering state observed with dry walls is no longer found. Instead, the liquid preferentially wets the top wall, residing above the gas, even for χ values as small as 2.0, where thermal effects are comparable to gravity. Furthermore, for slightly smaller χ values (around 1), the system exhibits dynamic behavior: the liquid moves towards the top wall, detaches, and falls back down (Fig. 1, right).

References

[1] N. Nakagawa, S.-i. Sasa, T. Hirao, T. Shiina, K. Tachi, and A. Yoshida, Global Thermodynamics for Isothermal Fluids under Weak Gravity, arXiv 2412.19643.

[2] A. Yoshida, N. Nakagawa, and S.-i. Sasa: Heat-Induced Liquid Hovering in Liquid-Gas Coexistence under Gravity, *Phys. Rev. Lett.* **113**, 117101 (2024)

All-atomic molecular dynamics simulation for vitrimers

Yutaka Oya

Department of Materials Science and Technology,

Tokyo University of Science, Niijuku, Katsushika-ku, Tokyo 125-8585

This study aims to elucidate the damage repair mechanism of vitrimers by molecular simulations. The target material is the reaction-cured product of bisphenol A diglycidyl ether (DGEBA) and 4-aminophenyl disulfide (AFD), which has a dense crosslinked network structure. When the cured product is deformed by external forces, the mechanical properties deteriorate due to the dissociation of numerous covalent bonds that constitute the cross-linked structure, as well as the disulfide bonds contained in AFD. Subsequently, it is considered that the disulfide bonds recombine through thermal pressing, leading to the recovery of mechanical properties.

In this study, the above-mentioned mechanism is reproduced through the integration of quantum chemical (QC) calculations and All-atomic molecular dynamics (MD) simulations. Specifically, quantum chemical (QC) calculations are first conducted to elucidate the recombination pathways of dissociated disulfide bonds. Subsequently, molecular dynamics (MD) simulations incorporating the identified mechanism are performed to derive stress–strain curves and evaluate the degree of mechanical property recovery.

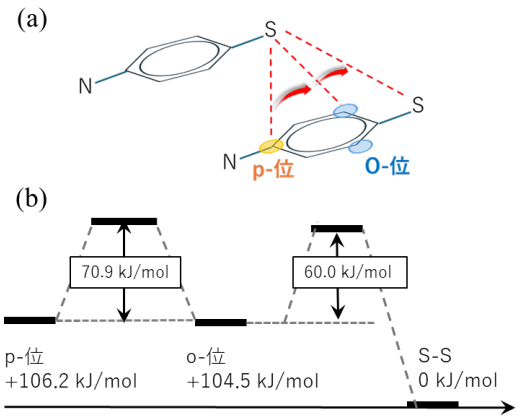


Fig. 1: (a) Stable structures identified by QC calculations, and (b) activation energies associated with disulfide bond reformation.

Reaction pathway searches based on QC were performed using the Global Reaction Route Mapping (GRRM) algorithm [1]. This algorithm interfaces with the quantum chemistry software Gaussian and enables automated exploration of the potential energy surface. As a result, it facilitates efficient identification of transition states even in complex multi-electron systems such as polymers. Furthermore, all molecular dynamics (MD) simulations—including crosslink formation, covalent bond dissociation, and self-healing processes—were carried out using LAMMPS software [2].

Quantum chemical (QC) calculations

revealed two stable structures associated with the reformation of disulfide bonds. As illustrated in Figure 1(a), these structures correspond to configurations in which the carbon atom at either the ortho or para position of the benzene ring bonded to one sulfur atom forms a bond with the second sulfur atom. The activation energies between these three stable structures are shown in Figure 1(b). These activation energies are significantly lower than the previously reported value for disulfide bond exchange (about 192 kJ/mol [3]), indicating that the reactions can readily occur under thermal compression.

To evaluate the impact of the disulfide bond repair mechanism identified by QC on the recovery of mechanical properties in a condensed system, MD were performed. A uniaxial tensile simulation was first conducted on a crosslinked network to induce complete dissociation of all disulfide bonds, followed by compression and relaxation simulations. When the QC-derived repair mechanism was incorporated, approximately 70% of the disulfide bonds were successfully reformed. In contrast, when only direct recombination between sulfur atoms was allowed, the recovery ratio remained around 40%. These results indicate that the reaction pathway identified in this study plays a critical role in enhancing bond reformation.

Finally, the stress–strain curves corresponding to each structure are shown in

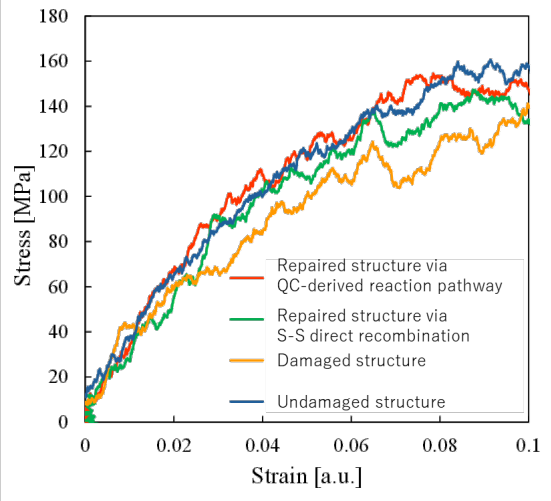


Fig. 1: Stress-strain curves obtained by MD simulations.

Figure 2. The structure repaired via the QC-derived reaction pathway (red) exhibits improved mechanical properties compared to the structure repaired by direct sulfur–sulfur recombination (green) and the fully dissociated disulfide network (yellow). Notably, its mechanical performance comparable to that of the undamaged crosslinked structure (blue), indicating a substantial recovery of properties through the proposed repair mechanism.

References

[1] S. Maeda, K. Ohno, and K. Morokuma, Phys. Chem. Chem. Phys., **15** (11), 3683 (2013).

[2] Large-scale Atomic/Molecular Massively Parallel Simulator, open source code: http://lammps.sandia.gov/ (Last accessed date: 2025/04/30.)

[3] Y.-M. Yang, H.-Z. Yu, X.-H. Sui, and Z.-M. Dang, J. Phys. Org. Chem. **29**, 6-13 (2016).

First-Principles Elucidation of Conducting Mechanisms in OligoEDOT Complexes: Towards Molecular Design Guidelines for High Conductivity

Tomoko FUJINO

Institute for Solid State Physics,

The University of Tokyo, Kashiwa-no-ha, Kashiwa, Chiba 277-8581

Organic conductors are broadly divided into two categories: low-molecular-weight materials and polymers. Low-molecular-weight materials possess well-defined structures but offer limited control over their conductivities. Conductive polymers, on the other hand, feature highly conjugated systems but are challenging to control due to their structural inhomogeneity. To bridge this gap, oligomer-based conductors have been developed as intermediate materials. These conductors, based on oligo(3,4-ethylenedioxythiophene) (oligoEDOT), are modeled after the doped PEDOT family [1–5].

In this study, we systematically investigated the influence of end-cap substituents [6] and the stacking structure in donor–acceptor alternatingly mixed-stack complexes [7]. The effects of these structural factors were quantitatively evaluated using first-principles calculations (QUANTUM ESPRESSO, RESPACK, and H-wave packages; performed at Ohtaka, Supercomputer Center, ISSP). Our calculations revealed that the magnitude of the Coulomb repulsion between carriers, $\boldsymbol{U_{\mathrm{eff}}}$, is the dominant factor determining conductivity. Based on these theoretical findings, we provided electronic insights explaining the superior conductivity of mixed stack complexes compared to previously reported complexes [7]. This work thereby offers a new molecular design guideline for developing highly conducting charge-transfer salts and mixed-stack complexes.

References

[1] R. Kameyama, T. Fujino*, H. Mori*, et al. Chem. Eur. J. **27**, 6696 (2021).

[2] R. Kameyama, T. Fujino*, H. Mori*, et al. Phys. Chem. Chem. Phys. **24**, 9130 (2022).

[3] R. Kameyama, T. Fujino*, H. Mori*, et al. J. Mater. Chem. C **10** (9), 7543 (2022).

[4] K. Onozuka, T. Fujino*, H. Mori*, et al. J. Am. Chem. Soc. **145**, 15152 (2023).

[5] T. Fujino*, H. Mori*, et al. Faraday Discuss. **250**, 348 (2024).

[6] K. Onozuka, T. Fujino*, H. Mori* et al. Higher conductivity in, J. Mater. Chem. C, **12**, 13956 (2024).

[7] T. Fujino*, H. Mori*, et al. Nature Commun. **15**, 3028 (2024).

Field-Induced Spin Liquid Phase of Quantum Spin Chain with Biquadratic Interaction

Tôru SAKAI[1,2], Hiroki NAKANO[1], Masaru HASHIMOTO[1], Tomohide KAWATSU[1], Haruto SUZUKI[1], Tomoki HOUDA[1]Rito FURUCHI[1], and Tokuro SHIMOKAWA[3]
[1]*Graduate School of Science, University of Hyogo, Kouto, Kamigori, Hyogo 678-1297, Japan*
[2]*National Institute for Quantum Science and Technology, SPring-8, Kouto, Sayo, Hyogo 679-5148, Japan*
[3]*Theory of Quantum Matter Unit, Okinawa Institute of Science and Technology Graduate University, Onna-son, Okinawa 904-0495, Japan*

1 Introduction

The quantum spin chains exhibit various interesting phenomena in the magnetization process, for exmaple, the magnetization jump, plateau, and spin nematic state, etc. The density matrix renormalization group analysis of the S=1 antiferromagnetic chain with the biquadratic exchange interaction indicated that the spin nematic liquid phase appears in the magnetization process[1]. It was also supported by the numerical diagonalization and the conformal field theory analysis[2, 3]. In the present work, the magnetization processes of the S=3/2 and S=2 antiferromagnetic chains with the biquadratic exchange interaction are investigated using the numerical diagonalization of finite-size clusters. It is found that the magnetization jump appears just before the saturation magnetization, as well as the classical spin system. This behavior is different from the S=1 chain. In addition it is indicated that the magnetization process where each magnetization step is $2S$ appears for sufficiently large biquadratic interaction. Namely the three-magnon and four-magnon bound states are realized for the S=3/2 and S=2 chains, respectively. In the case of the S=1 chain, the two-magnon bound state corresponding to the spin nematic phase occurs. Thus in general it can be predicted that the 2S-magnon bound state would be induced by the biquadratic exchange interaction in the magnetization process of the spin-S antiferromagnetic chain. The phase diagrams with respect to the biquadratic interaction and the magnetization are also presented for S=3/2 and S=2 antiferromagnetic chains. The three- and four-magnon bound states are expected to correspond the triatic and quatic Tomonaga-Luttinger liquid phases, respectively[4].

2 Model

The systems under the magnetic field are descibed by the Hamiltonian

$$\begin{aligned} \mathcal{H} &= \mathcal{H}_0 + \mathcal{H}_Z \\ \mathcal{H}_0 &= J\sum_{j=1}^{L} \vec{S}_j \cdot \vec{S}_{j+1} + J_{\rm BQ}\sum_{j=1}^{L} (\vec{S}_j \cdot \vec{S}_{j+1})^2 \\ \mathcal{H}_Z &= -H\sum_{j=1}^{L} S_j^z. \end{aligned} \tag{1}$$

Now we consider the cases of $S = 3/2$ and 2, respectively, for $J_{\rm BQ} < 0$ and fix $J = 1$.

3 Results

The $S = 3/2$ and $S = 2$ antiferromagnetic chains with the negative biquadratic interaction are investigated using the numerical diagonalization of the finite-size cluster ($L = 12$). It is found that for sufficiently large negative $J_{\rm BQ}$, the field-induced spin triatic and quatic TLL phases appear in the $S = 3/2$ and $S = 2$ chains, respectively, instead of the spin nematic TLL phase in the $S = 1$ chain. Probably it is expected that the spin-S chain with sufficiently large negative $J_{\rm BQ}$ exhibits the field-induced 2^{2S}-pole TLL phase. In addition it is found that the magnetizaiton jump up to the saturation magnetization occurs for intermediate $J_{\rm BQ}$ in the case of $S > 1$.

References

[1] S. R. Manmana, A. M, Lauchli, F. H. L. Essler and F. Mila, Phys. Rev. B **83**, 184433 (2011).

[2] T. Sakai, AIP Advances 11, 015306 (2021).

[3] T. Sakai, H. Nakano, R. Furuchi and K. Okamoto, J. Phys.: Conf. Ser. 2164, 012030 (2020).

[4] T. Sakai, AIP Advances 14, 015332 (2024).

Spin Nematic Phase of 2D Ferromagnetic Dimer System

Toru SAKAI[1,2], Hiroki NAKANO[1], Masaru HASHIMOTO[1], Tomohide KAWATSU[1], Haruto SUZUKI[1], Tomoki HOUDA[1], Rito FURUCHI[1]

[1]*School of Science, University of Hyogo,, Hyogo 678-1297*

[2]*National Institutes for Quantum Science and Technology, Hyogo 679-5148*

1. Introduction

he spin nematic state is one of interesting topics in the field of magnetism. It is the quadrupole order of spins. It is characterized by the long-range four spin correlation and the two-magnon bound state. In most previous theoretical works, the mechanism of the spin nematic order has been based on the biquadratic interaction[1,2] or the spin frustration[3]. In the recent numerical study on the S=1/2 spin ladder system with the anisotropic ferromagnetic rung interaction, a new mechanism based on the easy-axis anisotropy and the external magnetic field was proposed and the field-induced spin nematic phase was predicted to appear at higher magnetization region[4]. On the other hand, the spin nematic phase was also been predicted for several two-dimensional quantum spin systems. The spin nematic order due to the mechanism based on the anisotropic ferromagnetic interaction proposed in the previous work would be expected to appear even in two dimensional systems. In the present paper, as an example, we focus on a magnetic system on the Shastry-Sutherland lattice, which includes the isotopic antiferromagnetic interaction and the anisotropic ferromagnetic one under magnetic field. Using the numerical diagonalization of finite-size clusters, we investigate the possible field-induced spin nematic phase.

2. Model and Calculation

We consider a spin-1/2 model on the Shastry-Sutherland lattice under magnetic field in Fig. 1. The Hamiltonian is given by the following forms

$$H_{\mathrm{tot}} = H_0 + H_Z$$

$$H_0 = J_1 \sum_{\langle i,j \rangle} \left[S_i^x S_j^x + S_i^y S_j^y + \lambda S_i^z S_j^z \right] + J_2 \sum_{\langle i,j \rangle} \overrightarrow{S_i} \cdot \overrightarrow{S_j}$$

$$H_z = -H \sum_j S_j^z$$

we consider ferromagnetic J_1 and antiferromagnetic J_2, We investigate this model using the numerical diagonalization of the 24-spin cluster under the periodic boundary condition, shown in Fig. 1

3. Results

The S=1/2 spin system on the Shasry-Sutherland lattice with the

anisotropic ferromagnetic interaction under magnetic field is investigated using the numerical diagonalization of the finite-size (24 spins) cluster. It indicates that .the possible field-induce spin nematic phase, which is characterized by the two-magnon bound state, appears at higher magnetization region than m=1/2. Since the numerical study is performed for only one system size in this paper, it would be important to try some other sizes to confirm the present conclusion in the thermodynamic limit. In addition the spin correlation function corresponding to the nematic order should be calculated to reveal the real spin configuration in the future work.

References

[1] H. H. Chen and P. M. Levy, Phys. Rev. Lett. 27, 1383 (1971)

[2] A. V. Chubukov, J. Phys.: Condens. Matter 2, 1593 (1990).

[3] T. Hikihara, L. Kecke, T. Momoi and A. Furusaki, Phys. Rev. B 78, 144404 (2008)

[4] T. Sakai, R. Nakanishi, T. Yamada, R. Furuchi, H. Nakano, H. Kaneyasu, K. Okamoto and T. Tonegawa, Phys. Rev. B 106, 064433 (2022).

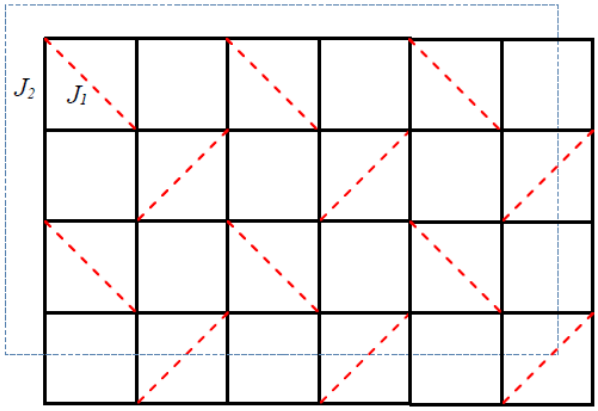


Fig. 1: 24-spin cluster the Shastry-Sutherland lattice under the periodic boundary condition.

Effects of deficit on quantum spin systems

Chitoshi YASUDA
Department of Physics and Earth Sciences, Faculty of Science, University of the Ryukyus, Okinawa 903-0213, Japan

In relation to spin-Peierls materials, the dilution effect of the ground state in a square-lattice antiferromagnetic Heisenberg model with bond-alternating chains of spin size $S = 1/2$ is studied using a quantum Monte Carlo method [1-4]. In the antiferromagnetic long-range ordered phase of the system without bond alternation, the finite staggered magnetization decreases monotonically with increasing the concentration of site dilution, and reaches zero at the percolation threshold. On the other hand, in the dimer phase, the finite staggered magnetization is induced by dilution. Interestingly, near the parameter where a quantum phase transition between the dimer and antiferromagnetic long-ordered phases is driven in the pure system, it has been reported that the staggered magnetization does not decrease due to site dilution but increases once, even though the phase is antiferromagnetic long-ordered phase [1]. It is already known that the spin correlations increase around the diluted site, but the details of this phenomenon and its relation to the magnetization are not clear.

In this project, we investigate deficit effects of the ground state in the antiferromagnetic Heisenberg model consisting of bond-alternated chains on a square lattice using quantum Monte Carlo and exact diagonalization methods. First, we confirmed that the same increase in staggered magnetization is observed in the bond diluted system for the parameters where the increase in staggered magnetization occurs as reported for the site diluted system. Next, the correlation functions at nearest bonds of the diluted bond were examined in the one- and two-dimensional systems, and it was confirmed that the magnitudes of the correlation functions increase in both systems compared to the system without diluted bonds. The increase is larger for the bond alternation parameter close to the phase-transition point to the dimer phase. Furthermore, the correlation functions on the bonds around the diluted bond increase significantly as the bond with the larger exchange integral is diluted. In small-size system with one diluted bond, the ground state itself was investigated by the exact diagonalization method. The ground state consists of a basis with zero eigenvalues for all spin operators, and the weights of the basis, where there is 'no staggeredness' and the spin state on the bond with an enhanced correlation function is antiferromagnetic, are increased due to dilution. Finally, in order to investigate the relationship between the staggered magnetization and the correlation function regarding increase, we examined the change in the distribution of the correlation function with dilution in a randomly diluted bond system. The results show that the change in the correlation function of the nearest-neighbor bond due to dilution contributes significantly to the change in the staggered magnetization.

References

[1] C. Yasuda, S. Todo, M. Matsumoto, and H. Takayama, Phys. Rev. B **64**, 092405 (2001).

[2] C. Yasuda, S. Todo and H. Takayama, J. Phys. Soc. Jpn. **75**, 124704 (2006).

[3] C. Yasuda and S. Miyara, J. Phys. Soc. Jpn. **87**, 014704 (2018).

[4] S. Miyara and C. Yasuda, J. Phys. Soc. Jpn. **87**, 104702 (2018).

Magnetism in the multiple-spin exchange model on a honeycomb lattice

Chitoshi YASUDA
Department of Physics and Earth Sciences, Faculty of Science, University of the Ryukyus, Okinawa 903-0213, Japan

New quantum spin liquid is experimentally observed in the solid ^{3}He layer. This layer is a first monolayer of graphite coated with a bimolecular layer of deuterated molecular hydrogen. It was suggested that there exists a quantum spin liquid with novel dependences of the heat capacity and the magnetic susceptibility on temperature at low density of ^{3}He. This quantum spin liquid has a different behavior from that of conventional two-dimensional solid ^{3}He and is expected to provide new insights into quantum spin liquids. Compared to solid helium thin films that form a triangular lattice, the commensurate solid layer is stabilized at a lower density, suggesting that ^{3}He atoms may form a honeycomb lattice. A commensurate solid layer in conventional two-dimensional solid ^{3}He is well described by the spin-1/2 multiple-spin exchange model on a triangular lattice, and theoretical researches have been done using various methods [1,2,3].

In this project, we research the multiple-spin exchange model with the two-spin and six-body ring exchange interactions on a honeycomb lattice using numerical methods. Ground states are investigated within the mean-field approximation, quantum fluctuations are neglected, and spin operators are treated as a unit vector. Thus, the problem becomes that of minimalization of the classical ground-state energy. The ground-state phase diagram parametrized by the two-spin exchange integral and the external magnetic field with respect to the six-spin exchange integral is investigated using the conjugate gradient (CG) method. In this method, calculations are performed in finite-size systems with a periodic boundary condition. In the CG method, the lowest energy state can be found by continuously searching for spin states from a given initial state. We prepared approximately 500–1000 random spin states as the initial states in addition to some expected states. Thus, we could find unexpected phase transitions by the CG method.

In the region where the contribution of the six-body exchange interaction is large, the eight-sublattice structure with only one nearest-neighbor correlation function and a finite sublattice scalar chirality is stabilized as the ground state in the zero magnetic field system. When the applied magnetic field is increased, the eight-sublattice structure changes to the 5u1d state via the intermediate state. In the 5u1d state, five of the six spins at vertices of a hexagon are parallel to and one is antiparallel to the magnetic field. The phase transition lines between the intermediate and eight-sublattice structure phases and between the intermediate and 5u1d phases depend on the system size. In this project, we examined the dependences of the intermediate phases on the system size in the details.

References

[1] C. Yasuda, D. Kinouchi, K. Kubo, J. Phys. Soc. Jpn. **75**, 104705 (2006).

[2] C. Yasuda, Y. Uchihira, S. Taira, K. Kubo, J. Phys. Soc. Jpn. **87** 104704 (2018).

[3] S. Taira, C. Yasuda, T. Momoi, K. Kubo, J. Phys. Soc. Jpn. **88** 014701 (2019).

Superconducting critical temperature and gap structure of kappa-type BEDT-TTF superconductors

Harald JESCHKE
Research Institute for Interdisciplinary Science, Okayama University
3-1-1 Tsushima-naka, Kita-ku, Okayama 700-8530

We have performed calculations for BEDT-TTF based superconductors with different anions using the fluctuation exchange approximation. The results are not yet fully analyzed, though, and will be reported in a later report. In parallel, we have obtained very good results for the ferromagnet $CrGeTe_3$. Initially, we tried to apply spin fluctuation theory to its sister compound $CrSiTe_3$ to investigate the reported superconducting phase under pressure. However, due to conflicting reports on the high pressure crystal structure, these calculations are incomplete. We investigated the pressure-induced evolution of the electronic and magnetic properties of $CrGeTe_3$. Using density functional theory (DFT) and dynamical mean-field theory (DMFT), we explored the transition from a low-temperature semiconducting ferromagnet to a near room-temperature metallic ferromagnet under pressure (Xu *et al.*, Phys. Rev. B **108**, 125142 (2023)). This was achieved using DCore on System B. We complement our calculations with experimental optical conductivity data, which trace the evolution of electronic correlations through the insulator-to-metal transition. As pressure increases, a distinct mid-infrared (MIR) feature emerges in the optical conductivity, signaling the development of strong orbital-selective correlations. In combination, our results reveal that the double-exchange mechanism plays a key role in stabilizing near room-temperature ferromagnetism in $CrGeTe_3$ [1]. Additionally, we explore the anomalous Hall effect (AHE) in $CrGeTe_3$ [2]. There, a discrepancy between calculations and experiment arises. We conclude that the AHE is primarily driven by extrinsic mechanisms and outline potential scenarios for these extrinsic contributions.

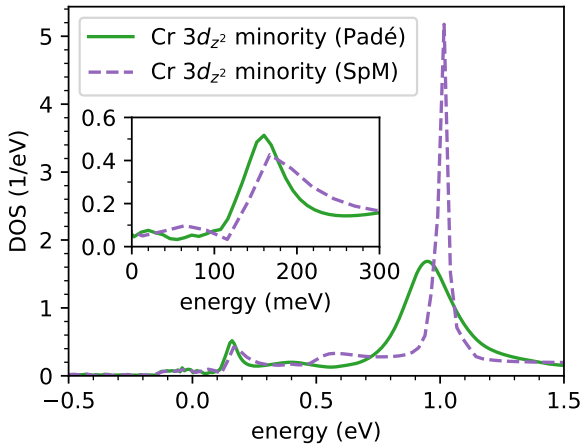


Figure 1: DFT+DMFT spectral function for the minority spin Cr $3d_{z^2}$ orbital of $CrGeTe_3$ at $T = 100\,\mathrm{K}$, $P = 5\,\mathrm{GPa}$ in the ferromagnetic state, explaining the mid-infrared feature.

References

[1] J. Ebad-Allah, D. Guterding, M. Varma, M. Diware, S. Ganorkar, H. O. Jeschke, and C. A. Kuntscher: Phys. Rev. B **111**, L140402 (2025).

[2] G. Scharf, D. Guterding, B. Hen, P. M. Sarte, B. R. Ortiz, G. Kh. Rozenberg, T. Holder, S. D. Wilson, H. O. Jeschke, and A. Ron: Phys. Rev. Res. **7**, 013127 (2025).

Information analysis of complex system with a tensor network formalism

Kenji HARADA
Graduate School of Informatics, Kyoto University
Kyoto 606-8501, Japan

Building on the tensor tree network framework combined with the Born machine approach [1], we propose a general method for constructing a generative model that expresses the target distribution as the amplitude of a quantum wave function represented by a tensor tree [2]. The core idea is to optimize the tree structure to minimize bond mutual information dynamically. This method enhances performance and reveals hidden relational structures within the target data.

Our results indicate that this generative model outperforms conventional methods, particularly in scenarios where the data structure is unknown. Moreover, following the learning and optimization process, the optimized tree structure provides valuable insights into the sometimes obscured relational data structure.

For example, the Global Industry Classification System categorizes stocks into 11 sectors. In our analysis, we input the stock price data of S&P 500 companies into the generative model without prior knowledge of these sector classifications. Figure 1 depicts the optimized network structure with a bond dimension 5. In the figure, the color of each circle represents the sector to which the corresponding company belongs. Companies within the same sector tend to cluster closely, forming predominantly single-colored sub-trees. Importantly, the sector information was not utilized in the learning process; the observed clustering is purely a result of the model's learning.

Therefore, the proposed method automatically learns the hidden relational target data structure and reflects it in the network structure, making it a powerful tool for data analysis even without prior knowledge of the information structure.

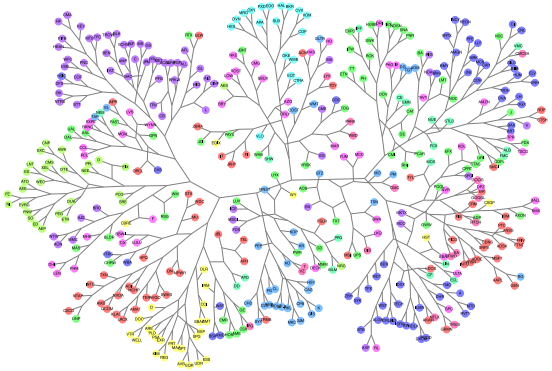


Figure 1: Optimized network structure of S&P 500 companies. The color of each circle indicates the sector to which the corresponding company belongs.

References

[1] Zhao-Yu Han, Jun Wang, Heng Fan, Lei Wang, and Pan Zhang. Unsupervised Generative Modeling Using Matrix Product States. *Phys. Rev. X*, 8(3):031012, 2018.

[2] Kenji Harada, Tsuyoshi Okubo, and Naoki Kawashima. Tensor tree learns hidden relational structures in data to construct generative models. *Machine Learning: Science and Technology*, 6(2):025002, 2025.

Physical properties of crosslinked polymer networks through network topology analysis

Katsumi HAGITA,[1] and Takahiro MURASHIMA[2]

[1]*Department of Applied Physics, National Defense Academy, Yokosuka 239-8686*

[2]*Department of Physics, Tohoku University, Sendai 980-8578*

To elucidate the topological effect on the physical/mechanical properties of the tetra-arm end-link gel/rubber, it is desirable to establish model approaches using coarse-grained MD (CGMD) simulations of the Kremer-Grest model with bond breakage. Here, the bond breakage has a critical importance to describe the behaviors of inhomogeneous networks under stretching.

In this project, the quartic function (1) was used as the bond potential instead of the FENE potential in Kremer-Grest model.

$$U_O(r) = K(r - R_c)^2(r - R_c - C_1)(r - R_c - C_2) + U_0 \quad (1)$$

We performed systematic reparameterization for this quartic function bond in order to realize tunable bond breakage strength (For details on the parameters, see reference [1].) as shown in Fig. 1.

First, we investigated the stress-strain (SS) curves of the diamond lattice with bimodal length between neighboring crosslink points [1]. Figure 2 shows the SS curve for the networks with ($N_s - N_b$, $N_s + N_b$) = (25, 25), (20, 30), (15, 35), (10, 40), and (5, 45). For larger N_b, the SS curve becomes more collapsed shape due to larger the network inhomogeneity.

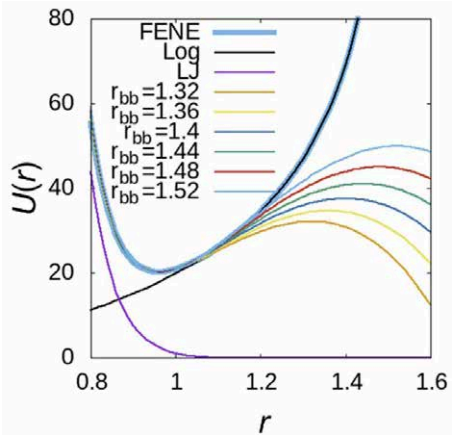


Fig. 1: Bond potential for Kremer-Grest model with bond breakage. r_{bb} is a parameter to characterize the bond breakage strength.

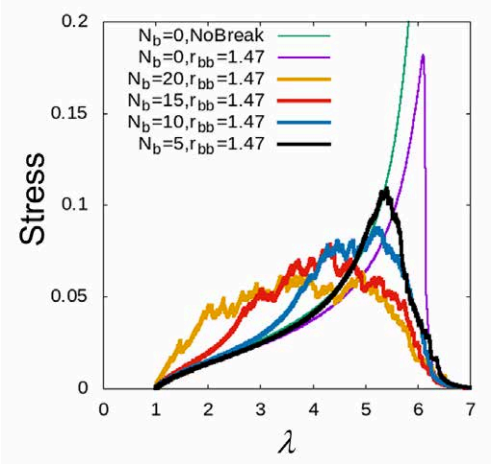


Fig. 2: Stress-strain curves for the networks with ($N_s - N_b$, $N_s + N_b$) = (25, 25), (20, 30), (15, 35), (10, 40), and (5, 45).

Second, we investigate SS curves of AB type tetra-arm gel for various reaction polymer concentrations [2]. For comparison, we obtained the various tetra-functional networks through pseudo reaction process for various pre-polymers. As a result, it was found that when the reaction polymer concentration was lower than the overlapping concentration, the [AB] type had superior toughness compared to the others, as shown in Fig. 3.

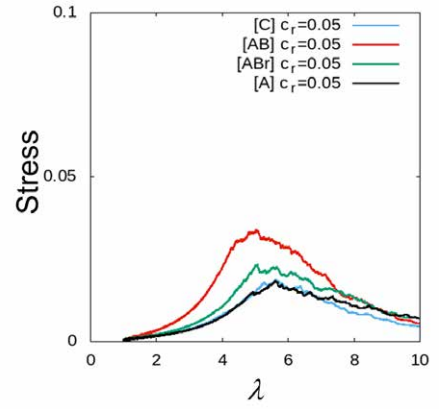


Fig. 3: Stress-strain curves of the various tetra-functional networks.

Thirdly, to study abnormal butterfly patterns of stretched inhomogeneous networks, we evaluated small angle behaviors of two-dimensional scattering patterns (2DSPs) [3]. We studied the calculation method of 2DSPs by using the ISSP supercomputer. Notably, these simulations were performed by using the supercomputer FUGAKU because the huge system size is required for sufficient resolution of 2DSPs. For future basic science, the ISSP supercomputer is used to investigate the basic characteristics of the smaller system size.

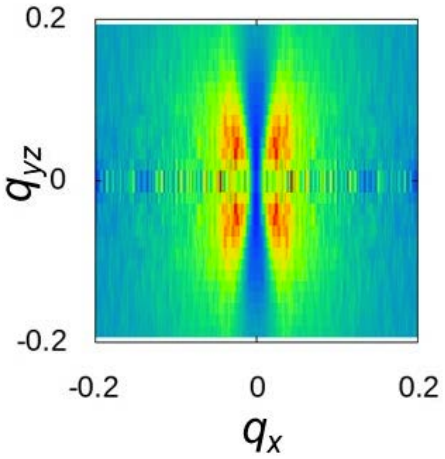


Fig. 4: 2DSP of the AB-type tetra-arm network stretched at the strain of 5.0.

In this project, we aim to quantitatively relate the KG model with the All-atom model in order to improve the connectivity between the KG model and the real world. In order to efficiently measure the correspondence, we have also considered the Martini coarse-grained force field, keeping in mind that large-scale all-atom calculations will be required for the analysis.

References

[1] K. Hagita, T. Murashima, Macromolecules, **57**, 10903–10911 (2024).

[2] K. Hagita, T. Murashima, Macromolecules, in revision.

[3] K. Hagita, T. Murashima, Macromolecules, (2025) doi:10.1021/acs.macromol.5c00207

Study of magnetic excitations in Cuprates and Iridates using MPS-based simulations

Matthias GOHLKE, Jiahui BAO
Theory of Quantum Matter Unit, Okinawa Institute of Science and Technology
1919-1 Tancha, Onna-son, Okinawa 904-0495

Cuprate materials, such as La_2CuO_4, are prototypical examples of two-dimensional antiferromagnetic Mott insulators and serve as parent compounds for high-temperature superconductors [2, 3]. The magnetism in these systems is governed by strong electron correlations, and their low-energy excitations are well described by spin models derived from the Hubbard model in the large-U limit [4, 5]. The basic picture begins with a Heisenberg antiferromagnetic model, but experimental evidence, particularly from inelastic neutron scattering (INS) and resonant inelastic x-ray scattering (RIXS), reveals features such as magnon dispersion along the Brillouin zone boundary and high-energy continua that cannot be captured by simple models alone [6, 7]. These observations have motivated more sophisticated approaches incorporating cyclic four-spin exchange and beyond-linear spin wave corrections.

In our work [1], we have revisited an effective spin model used to describe magnons in cuprate materials such as La_2CuO_4, $CaCuO_2$, as well as the iridate Sr_2IrO_4, which exhibit strong spin-orbit coupling. Although previous works already include higher-order terms such as ring-exchange when deriving an effective spin model from the one-band Hubbard model, these studies are based on linear spin wave theory (LSWT), which is known to have limitations when quantum fluctuations are significant. Here, we instead use the matrix product state (MPS) framework and time domain variational principle (TDVP) to compute the dynamical spin structure factor of an effective spin model that includes cyclic ring exchange and interactions up to third-nearest neighbors. In comparing to LSWT and LSWT with $1/S$ corrections, we are able to quantify the discrepancy of LSWT and estimates based thereon.

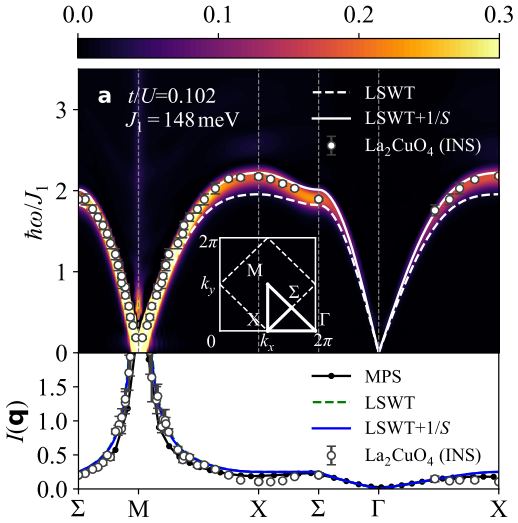


Figure 1: Magnon spectra of La_2CuO_4 compared with LSWT and LSWT+$1/S$ results of an effective spin model derived from a one-band Hubbard model.

Our key findings are: (i) MPS-based calculations provide more accurate predictions for magnon dispersion and intensities, showing very good agreement with experimental data for La_2CuO_4. (ii) LSWT and its variants systematically overestimate exchange parameters and the ratio t/U of Hubbard hopping t and potential U. (iii) We propose an empirical

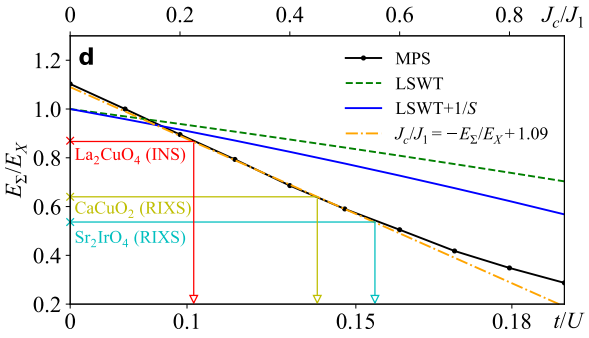


Figure 2: Ratio of excitation energies at $\mathbf{q}_\Sigma = (\pi/2, \pi/2)$ and $\mathbf{q}_X = (\pi, 0)$, showing their scaling with $J_c/J_1 \sim t^2/U^2$.

relation to estimate t/U from experimentally observed magnon energies at high-symmetry points.

Moreover, we find that while the effective spin model, if treated fully quantum, describes the magnon spectrum, it fails to capture the high-energy continuum found in experiments at $q_X = (\pi, 0)$. We argue that this discrepancy is due to limitations of the effective spin model and the underlying one-band Hubbard model. Additional physical phenomena (e.g., higher-order charge fluctuations, spin-phonon coupling, etc.) might be required to explain the observed continuum in cuprate antiferromagnets.

This work has relied heavily on the open source MPS and DMRG package *TenPy* [8] providing parallelization of matrix operations within a single node through optimized LAPACK and BLAS packages.

References

[1] J. Bao, M. Gohlke, J. G. Rau and N. Shannon, PRR **7** L012053 (2025).

[2] J. G. Bednorz and K. A. Müller, Zeitschrift für Physik B **64** 189 (1986).

[3] P. W. Anderson, Science **235** 1196 (1987).

[4] M. Takahashi, J. Phys. C: Solid State Phys. **10** 1289 (1977).

[5] A. H. MacDonald, S. M. Girvin, and D. Yoshioka, PRB **37** 9753 (1988).

[6] R. Coldea et al., PRL **86** 5377 (2001).

[7] N. S. Headings, S. M. Hayden, R. Coldea, and T. G. Perring, PRL **105** 247001 (2010).

[8] J. Hauschild, and F. Pollmann, SciPost Phys. Lect. Notes 5 (2018).

RIXS spectrum of CuO_2 spin chain

Hiroaki ONISHI
Advanced Science Research Center, Japan Atomic Energy Agency, Tokai, Ibaraki 319-1195

Frustrated quantum magnets often exhibit non-trivial ground states that do not have a classical analogue. The spin nematics, which is characterized by spin quadrupoles, is a prominent example. We have studied the excitation dynamics of a spin nematic liquid state in a spin-1/2 J_1-J_2 chain with ferromagnetic J_1 and antiferromagnetic J_2 in a magnetic field using dynamical DMRG [1]. We find gapless longitudinal and gapped transverse spin excitation spectra, in accordance with quasi-long-range longitudinal and short-range transverse spin correlations, respectively. The quadrupole channel exhibits gapless excitations, signaling quasi-long-range antiferro-quadrupole correlations. These properties are useful to identify the spin nematic liquid state by experiments. However, conventional magnetic probes are usually insensitive to spin quadrupoles. In this context, we expect that resonant inelastic x-ray scattering (RIXS) would provide a route to detect spin quadrupole excitations [2].

In this study, we introduce an effective t-J model for an edge-shared CuO_2 spin chain, which gives the J_1-J_2 chain such as $LiCuVO_4$, and analyze RIXS spectra based on the Kramers-Heisenberg formula by Lanczos diagonalization. Parallel computations with OpenMP were done on the system B of the ISSP supercomputer.

In Fig. 1, we present the intensity plot of oxygen K-edge RIXS spectra at zero field. We find excitation continuum above a sinusoidal mode dispersing from $q = \pi/2$, which corresponds to the des Cloizeaux-Pearson mode of the spin excitation. Moreover, we find spectral

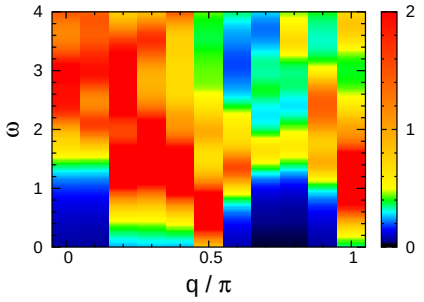


Figure 1: Oxygen K-edge RIXS spectra of the CuO_2 spin chain, by Lanczos calculations with 20 sites, $J_1 = -1$, and $J_2 = 1$ at zero field.

weight in a wide range of ω at $q = \pi$, which is not due to the spin excitation but attributed to spin quadrupole excitations. If we increase the magnetic field, the gapless position of q moves toward zero, while the spectral weight at $q = \pi$ remains large (not shown). These suggest that the RIXS spectra would contain characteristics of both spin and spin quadrupole excitations. To analyze large system sizes, the coding of a dynamical DMRG program is in progress.

References

[1] H. Onishi, J. Phys. Soc. Jpn. **84**, 083702 (2015); J. Phys.: Conf. Ser. **592**, 012109 (2015); Physica B **536**, 346 (2018); J. Phys.: Conf. Ser. **2207**, 012045 (2022).

[2] M. W. Haverkort, Phys. Rev. Lett. **105**, 167404 (2010); L. Savary and T. Senthil, arXiv:1506.04752.

Kinetics of phase transition and polyamorphism

Kazuhiro FUCHIZAKI
Department of Physics, Ehime University, Matsuyama 790-8577

Extensive studies on polyamorphism have been carried out following an astonishing discovery of the liquid-liquid transition (LLT) of black phosphorus (bP) upon increasing pressure [1]. Efforts dedicated to understanding water polyamorphism started in the last century have been a driving force. A first-principles molecular dynamics study predicted that the LLT is a pressure-induced molecular-to-polymerized liquid [2].

Although the thermodynamic understanding of the water-type polyamorphism has been solidified [3], further experimental verification regarding bP's LLT has never been performed. The discovery of the LLT was expected because of bP's unusual melting feature, i.e., a melting maximum [4]. However, a melting maximum is not necessary for exhibiting an LLT. Instead, a singularity at which the slope of a melting curve abruptly changes could be a triple point between two liquid and crystalline phases [5]. Indeed, the most recent experimental research unveiled that the bP's melting curve does not have a maximum but such a singularity. Although the crystalline structures for the ambient- and high-pressure phases have been resolved to be known as A17 and A7 structures, respectively [6], the relationship between those crystalline- and liquid-phase structures has not been clarified yet.

Our research aims to establish the expected relationship between polymorphism and polyamorphism in bP and clarify the melting aspects of crystalline phases. For this aim to be achieved, a system consisting of one component, i.e., P, may be appropriate. The first task should be constructing reliable models that reproduce the A17 and A7 structures. Those models can also determine the phase boundary and the melting curves, which are to be compared with experimentally known results [7] to ensure the reliability of the models.

In FY2024, we aimed to establish the force-field models that can predict the A17–A7 phase boundary as a machine-learning (ML) potential. Such an ML potential is extensively discussed in physics, chemistry, and materials science. Here, considering the high compatibility of the Behler-Parrinello (BP) symmetric functions [8], carrying the intra- and intermolecular interactions, with subsequent molecular dynamics (MD) or Monte Carlo (MC) simulations, we adopted the high-dimensional neural network potential [8], abbreviated as BPNN in the following.

We first carried out the first-principles calculations to prepare a set of learning data using Quantum Espresso installed in System B.

For the A17 structure, we thus obtained the ground state energies for the structures in a pressure range between 0.10 and 6.05 GPa using available CIF files [9]. A combination of the hybrid functionals [10] and PAW [11], giving rise to -55 Ry ($\simeq -750$ eV)/atom, which was almost pressure-independent, was employed for the calculations. In order to obtain the potential energy surface (PES), the BPNN consisting of 24 symmetry functions was trained 2000 times using the QE-based energies calculated for a set of 9720 unit cells, which were made to be compatible with the experimentally found equation of state, as input. The process almost converged at around 1000 times of learning, giving rise to ~ 0.16 eV

per phosphorus atom for the loss function.

Similar QE calculations were also made for the A7 structure in a pressure range between 6.05 and 10.23 GPa using two kinds of CIF files available [12]. However, a pressure at which the energy becomes comparable with that of A17 was not found. Therefore, we constructed the symmetry-adapted A7 structures "by hand" to recalculate the energies. The lattice constants were assumed to vary linearly according to pressure. We could then find the A7 structure, whose energy equals that of A17 at ~ 5 GPa. This pressure almost agrees with the pressure when the experimentally known A17–A7 phase boundary [13] is extended to zero temperature. Thus, we prepared 9882 unit cells around the structure at 5 GPa to be provided to QE to obtain their energies. These energies were input to the BPNN to assess the A7 PES. The result again converged halfway through the whole 2000 processes of learning. The maximum loss was 0.13 eV per phosphorus atom.

Having thus established the PESs for the A17 and A7 structures in terms of BP symmetry functions [8], we are now ready to carry out classical MD or MC simulations to achieve the aim mentioned at the beginning.

Finally, it should be mentioned that we quantum chemically [14] examined the polymerization process of P_4 tetrahedral molecules [15] in the low-density liquid (LDL) phase upon the pressure-induced LLT to the high-density liquid (HDL) phase. The energy barrier for a P_4 molecule to break up a single bond to be radically polymerizable is ~ 4 eV per molecule. Polymerized $(P_4)_n$ is energetically stable and costs negligible energy for polymerization beyond $n = 3$. Therefore, once P_4 molecules are polymerized, the reverse reaction would not occur at around 1500 K, the LLT temperature. Thus, the LDL and HDL comprise not a pseudo-binary but a binary system. Four radical P_4 molecules form, as the energetically stable state, a layered structure, which must share the structural feature with A7.

References

[1] Y. Katayama *et al.*: Nature **403**, 170 (2000).

[2] T. Morishita: Phys. Rev. B **66**, 054204 (2002).

[3] M. A. Anisimov *et al.*; Phys. Rev. X **8**, 011004(2018).

[4] E. Rapoport: J. Chem. Phys. **46**, 2891 (1967).

[5] K. Fuchizaki: J. Chem. Phys. **139**, 244503 (2013).

[6] Y. Akahama *et al.*: Phys. Rev. B **61**, 3139 (2000).

[7] V. L. Solozhenko and V. Turkevich: J. Phys. Chem. C **127**, 6088 (2023).

[8] J. Behler and M. Parrinello: Phys. Rev. Lett. **98**, 146401 (2007).

[9] J. B. Herbert *et al.*: J. Appl. Cryst. **49**, 277 (2016).

[10] J. P. Perdew *et al.*: J. Chem. Phys. **105**, 9982 (1996).

[11] F. Jollet *et al.*: Comput. Phys. Commun. **185**, 1246 (2014).

[12] C. R. Groom *et al.*: Acta Crystallogr. B: Struct. Sci. Cryst. Eng. Mater. **72**, 171 (2016).

[13] D. Scelta *et al.*: Chem. Commun. **54**, 10554 (2018).

[14] M. J. Frisch et al.: GAUSSIAN 09 Revision E.01, Gaussian, Inc., Wallingford, CT, 2009.

[15] P. Ballone and R. O. Jones: J. Chem. Phys. **121**, 8147 (2004).

Mathematical crystal chemistry

Ryotaro Koshoji
Institute for Solid State Physics, University of Tokyo
Kashiwa-no-ha, Kashiwa, Chiba 277-8581

I have developed the algorithm to design structural prototypes of inorganic crystals. The huge coordination space of the spatial order of atoms makes it difficult to predict crystal structures from chemical compositions. While many researchers have pursued the numerical techniques such as mathine learning methods to accelerate the discovery of the most stable structure, I focus on the inorganic structural chemistry that describes the structural principles of inorganic molecules and solids. In 1929, Pauling summarizes the principles of determining the structures of inorganic crystals. As George *et al.* showed that oxides satisfying all the Pauling's rules simultaneously are minority [J. George *et al.*, Angewandte Chemie International Edition **59**, 7569 (2020)], the predictive power of the Pauling rules is limited, but the rules offer the basic concepts for inorganic structural chemistry.

The goal of mathematical crystal chemistry is to give the definite rules to design the structural prototypes of inorganic crystals in place of the Pauling rules [1,2]. The concept is shown in Fig. 1. The rules are mathematically formalized by equality or inequality constraints in mathematical optimization problem, which has the form

$$\begin{aligned} \text{minimize} \quad & f_0(\boldsymbol{x}) \\ \text{subject to} \quad & f_i(\boldsymbol{x}) \leq 0 \quad i = 1, \cdots n \\ & h_j(\boldsymbol{x}) = 0 \quad j = 1, \cdots m \end{aligned}$$

Here the vector $\boldsymbol{x}$ is the optimization variable of the problem. The form of mathematical optimization problem suits to the expression of crystal structures that are the global optimum satisfying all the constraints corresponding to the competitive rules.

The first rule of mathematical crystal chemistry is the definition of interatomic forces. Since interatomic forces stabilize a crystal structure by keeping all the interatomic distances within the stable ranges, they are defined as the geometrical constraint G that constrains the feasible interatomic distance as

$$d_{ij\boldsymbol{T}}^{(G)} \leq |\boldsymbol{x}_j + \boldsymbol{T} - \boldsymbol{x}_i| \leq D_{ij\boldsymbol{T}}^{(G)}, \tag{1}$$

where $d_{ij\boldsymbol{T}}^{(G)}$ and $D_{ij\boldsymbol{T}}^{(G)}$ are the minimum and maximum distances between atom i and atom j in lattice $\boldsymbol{T}$, respectively, with $\boldsymbol{x}_i$ and $\boldsymbol{T}$ being the cartesian coordinate of atom i in the original cell and the lattice vector, respectively. The second rule is the definition of $d_{ij\boldsymbol{T}}^{(G)}$ and $D_{ij\boldsymbol{T}}^{(G)}$. Since inorganic structural chemistry estimates a chemical bonding distance as the sum of atomic radii, mathematical crystal chemistry defines the minimum and maximum interatomic distances as

$$d_{ij\boldsymbol{T}}^{(G)} = r_i^{(G)} + r_j^{(G)}, \tag{2}$$

$$D_{ij\boldsymbol{T}}^{(G)} = R_i^{(G)} + R_j^{(G)}, \tag{3}$$

where $r^{(G)}$ and $R^{(G)}$ are the minimum and maximum atomic radii depending on the type of the geometrical constraint G, respectively. The third rule describes how to create chemical bonds between atoms, for exaple, an ionic bond is formed if the interatomic distance between an anion and a cation satisfies the inequality constraint of Eq. (1). The previous study [2] introduces the creatability function

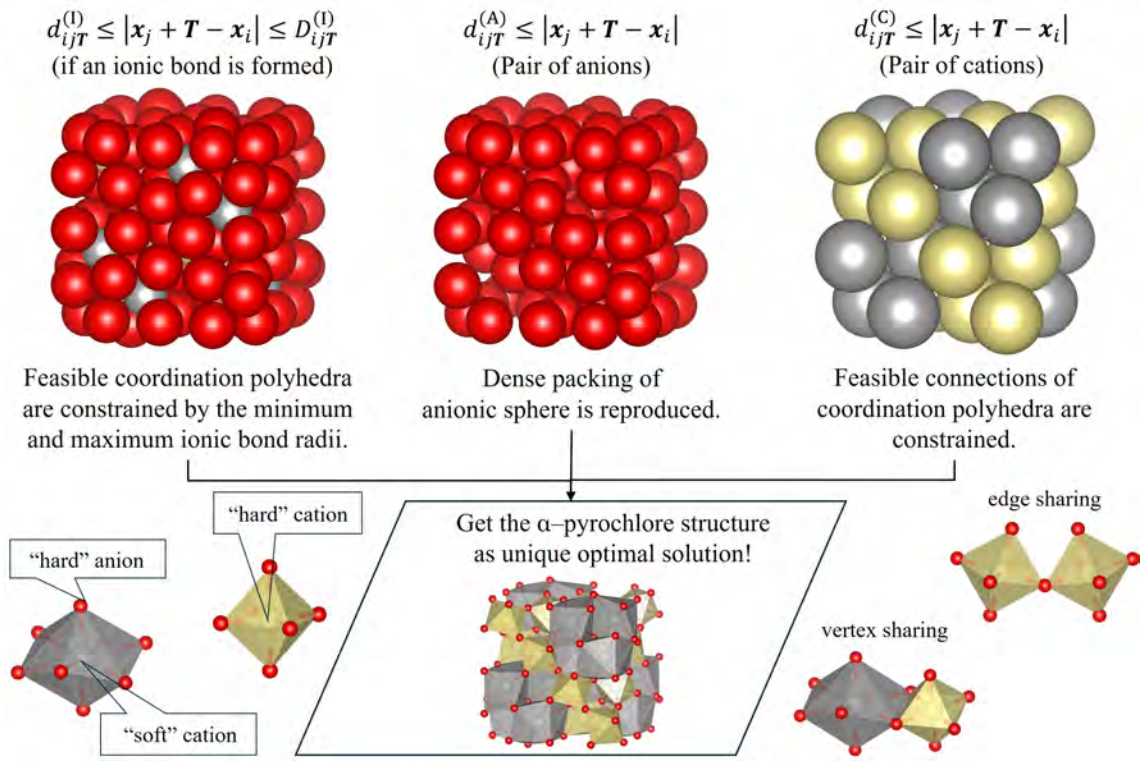


Figure 1: Concept of mathematical crystal chemistry.

$\Lambda_{ij\boldsymbol{T}}^{(\mathrm{G})}$ that returns one or more if the geometrical constraint G is creatable. Accordingly, the putative mathematical optimization problem [1,2] to design structural prototypes of inorganic crystals are given by

$$
\begin{aligned}
\text{minimize} \quad & \Omega \\
\text{subject to} \quad & (1-\varepsilon)\, d_\sigma \le x_\sigma \le (1+\varepsilon)\, D_\sigma \\
& d_\sigma = \max_G \left[n_\sigma^{(G)} \left(r_i^{(G)} + r_j^{(G)} \right) \right] \\
& D_\sigma = \min_G \left[n_\sigma^{(G)} \left(R_i^{(G)} + R_j^{(G)} \right) \right]. \\
& \sum_G n_\sigma^{(G)} = 1 \\
& n_\sigma^{(G)} \in \{0, 1\} \\
& n_\sigma^{(G)} \le \Lambda_\sigma^{(G)} (\boldsymbol{\Phi}, \varepsilon)
\end{aligned}
$$

Additionally, in the previous study [1,2], the coordination number of each cation is fixed as

$$\sum_{j,\boldsymbol{T}} \chi_j^{(\mathcal{E})} n_\sigma^{(\mathrm{I})} = N_{i\mathcal{E}}^{(\mathrm{I})}. \tag{4}$$

First, supercomputer Ohtaka was mainly used to apply the mathematical model to crystal structure prediction. As a result, it identified unique optimal solutions corresponding to the structures of spinel, pyrochlore (α and β), pyroxene, quadruple perovskite, cuprate superconductor $YBa_2Cu_3O_{7-x}$, and iron-based superconductor LaFeAsO. Second, oxide crystals registered in ICSD are analyzed whether they can be the optimal solutions. Notably, up to 95% of oxide crystal structure types in ICSD align with the optimal solutions preserving experimental structures despite the discretized feasible atomic radii. The successful results strongly imply that the mathematical optimization problem deserves to be the mathematical foundation of the principles determining the structures of inorganic crystals.

References

[1] R. Koshoji and T. Ozaki: Phys. Rev. Mater. **8**, 113801 (2024).

[2] R. Koshoji: arXiv:2503.20273 (2025).

Analyses on the Potential-dependent Dynamics of Ionic Liquid Electrolytes Forming Electric Double Layers Facing the Electrodes

Ken-ichi FUKUI

Department of Materials Engineering Science, Graduate School of Engineering Science, Osaka University, Machikaneyama, Toyonaka, Osaka 560-8531

Ionic liquids (ILs) are promising electrolytes for electrochemical devices such as secondary battery, capacitor, etc., due to their high chemical stability with negligible vaporization. Structuring and dynamics of the interfacial IL faced to charged graphite electrodes have been analyzed by molecular dynamics (MD) calculations [1], but the transport of Li^+ ion inside EDL formed at negatively charged electrode is not apparent because Li^+ coordinated with anions has negative charge in total. In the present study, we have analyzed the transport of Li^+ ion inside EDL of BMIM-TFSI electrolyte at the negatively charged graphite electrode by MD calculations, which is closely related to charging process of Li-ion battery composed of these components.

All MD simulations were conducted by classical MD package of LAMMPS. A simulation cell in Fig. 1(a) contains 650 ion pairs of BMIM-TFSI with randomly distributed 150 pairs of Li-TFSI ($9\times8\times11$ nm^3) sandwiched with 5-layer graphite electrodes from top and bottom separated with vacuum layer. Same amounts of positive and negative charges were assigned to the top and bottom electrode, respectively at the graphene layer faced to the electrolyte reproducing the electrified interfaces. Two different applied potential sequences were compared in the present study; (i) firstly stabilized the interface structure by annealing the cell at the surface charge equivalent to ±1.8 V and then the surface charge equivalent to ±3.5 V was applied (lower case in Fig. 1(b)) and (ii) the surface charge equivalent to ±3.5 V was directly applied (upper case in Fig. 1(b)). 10 ns MD trajectories at 350 K were analyzed.

Apparent difference was found for the interface structure at the electrode potential of -3.5 V depending on the applied potential sequences (Fig. 1(b)). By the sequence (ii), no Li^+ was present at the electrode. By analyzing the MD trajectories, it was due to the dense BMIM cation layers already formed by equilibrium at -1.8 V, which prevent the exchange of Li^+ at least during 10 ns. In the sequence (i), the interface is rather randomized and provide the chance for some Li^+ to be attach to the electrode by deforming the coordination with TFSI anions in 10 ns.

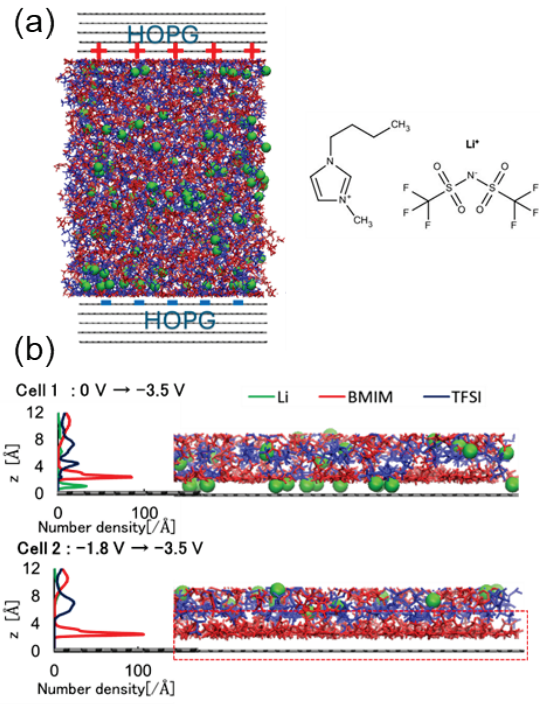


Fig. 1 (a) Simulation cell. (b) Interface structure at -3.5 V vs. PZC depending on the deferent applied potential sequences.

Reference

[1] H. Miyamoto, Y. Yokota, A. Imanishi, K. Inagaki, Y. Morikawa, K. Fukui, *Phys. Chem. Chem. Phys.* **20**, 1940 (2018).

Calculation of high dimensional systems at finite temperature using random quantum states of general variational wavefunctions

Toshiaki IITAKA

Center for Computational Science,

RIKEN, 2-1 Hirosawa, Wako, Saitama, 351-0198 JAPAN

Calculation of the thermal average of an observable of a closed quantum many-body system in its thermal equilibrium at an inverse temperature has two major computational difficulties. The number of quantum states to be included and the dimension of each quantum state vector both exponentially increase as the temperature and the system size increases, respectively. Each difficulty has been independently attacked using *random state method* [1, 2] and *variational wave function*, respectively.

Thermal average of observable *A* at inverse temperature β is calculated using *random state* $|\Phi\rangle$ as

$$\langle A\rangle = \frac{tr[e^{-\beta H}A]}{Z} = \frac{\langle\langle\langle\Phi|A|\Phi\rangle\rangle\rangle}{Z}$$

where

$$Z(\beta) = tr[e^{-\beta H}] = \langle\langle\langle\Phi|\Phi\rangle\rangle\rangle$$

is the *partition function* and the double bracket indicates statistical average over random states. The *thermal state* is defined by the imaginary time evolution of the random state.

$$|\Phi(\beta)\rangle = e^{-\beta H/2}|\Phi\rangle$$

Thermal energy E and specific heat C are expressed as $E(\beta) = \langle H\rangle$ and$C(\beta) = \frac{dE(\beta)}{dT}$, respectively.

Variational wave function is a point on a manifold embedded in the Hilbert space,

$$|\psi(w)\rangle = \sum_{\boldsymbol{\sigma}} c(w,\boldsymbol{\sigma})|\boldsymbol{\sigma}\rangle$$

which is parameterized with variational parameters, $w = \{w_i\}$, whose number is much less than the dimension of the Hilbert space.

Thermal variational wave function has been introduced

$$|\Psi(\beta;w)\rangle = e^{-\beta H/2}|\Psi(w)\rangle$$

where $|\Psi(w)\rangle$ is a *linear* variational wave functions such as product state,

MPS, PEPS [3-6] String-Bond States and Entangled Plaquette States [7].with random parameters w. The imaginary time evolution was calculated with stochastic reconfiguration[8, 9]. The program is written with NetKet [10] as well as JAX[11] and Python.

In this project, the formulation has been extended to the product of a random variational wavefunction and a generic variational wavefunction (see Fig. 1).

Scaling up of the calculation up to around 10x10 lattice is planned.

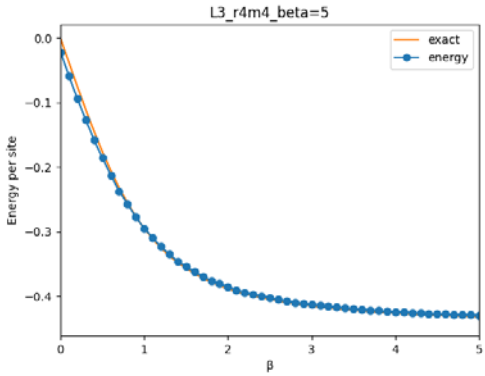


Fig 1. Inverse temperature dependency of the energy of 3x3 square lattice Heisenberg model calculated with 16 samples of the product of restricted Boltzmann machine (α =4) and random phase product states[3].

References

[1] T. Iitaka, and T. Ebisuzaki, Phys. Rev. Lett. **90**, 047203 (2003).

[2] T. Iitaka, and T. Ebisuzaki, Phys. Rev. E **69**, 057701 (2004).

[3] T. Iitaka, arXiv:2006.14459 (2020).

[4] S. Garnerone, T. R. de Oliveira, and P. Zanardi, Phys. Rev. A **81**, 032336 (2010).

[5] A. Iwaki, A. Shimizu, and C. Hotta, Phys. Rev. Res. **3**, L022015 (2021).

[6] S. Goto, R. Kaneko, and I. Danshita, Phys. Rev. B **104**, 045133 (2021).

[7] I. Glasser *et al.*, Physical Review X **8**, 011006 (2018).

[8] S. Sorella, Phys. Rev. Lett. **80**, 4558 (1998).

[9] K. Takai *et al.*, J Phys Soc Jpn **85**, 034601 (2016).

[10] G. Carleo *et al.*, SoftwareX **10**, 100311 (2019).

[11] JAX, https://docs.jax.dev/en/latest/.

Polarized Spin Magnetization Accumulation on Semiconductor Surfaces Under Intense Light Irradiation

Tomohiro Tamaya

Institute for Solid State Physics,

The University of Tokyo, Kashiwa-no-ha, Kashiwa, Chiba 277-8581

This study aims to elucidate the fundamental principles governing polarized spin magnetization that accumulates on semiconductor surfaces under intense terahertz irradiation. Recent progress in high-intensity terahertz sources has reignited interest in strong-field light–matter interactions in semiconductors. The applicant has developed a theoretical framework that concurrently treats intraband and interband transitions of Bloch electrons, uncovering nonlinear optical mechanisms in the nonperturbative regime [1–4]. A central insight is that Bloch electrons, when driven by terahertz fields, remain in a coherent superposition of valence and conduction bands—a quantum pure state—that gives rise to ultrafast, frequency-dependent electric polarization. Unlike conventional spintronics, which typically involves thermally mixed spin states subject to scattering, this approach enables spin magnetization originating from quantum coherence and free from thermal relaxation. This research seeks to clarify and demonstrate the nature and controllability of such quantum-driven spin magnetization through real-space simulations.

To pursue this objective, we conducted large-scale simulations on a representative semiconductor, GaAs, with open boundary conditions imposed along one spatial direction. A strong terahertz electric field was applied, and

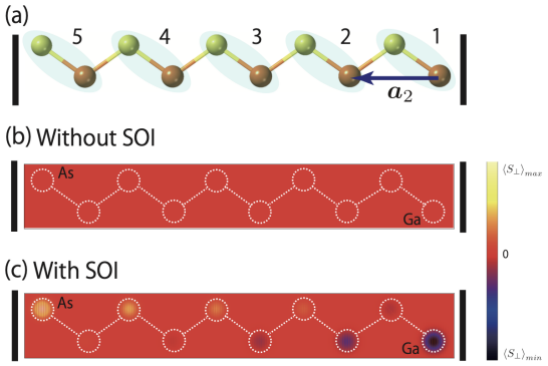


Fig.1: (a) Schematic illustration of the simulation model with five unit cells along the open boundary directions. Orange and green spheres represent As and Ga atoms, respectively. (b) Spatial distribution of spin magnetization at each atomic site without spin–orbit interaction (SOI). (c) Spatial distribution of spin magnetization with SOI.

the resulting spin magnetization accumulation was computed. Figures 1(a)–(c) illustrate: (a) a schematic of the model comprising five unit cells along the open boundary direction; (b) the spatial distribution of spin magnetization at atomic sites in the absence of spin–orbit interaction (SOI); and (c) the corresponding distribution in the presence of SOI. These results reveal that spin magnetization clearly accumulates at the GaAs surface when SOI is present, indicating the emergence of a light-induced spin Hall effect. Additionally, Figure 2 shows the time evolution of spin magnetization components in each unit cell. The observed ultrafast temporal dynamics, synchronized with the incident terahertz field, confirm the generation of dynamically induced polarized spin magnetization.

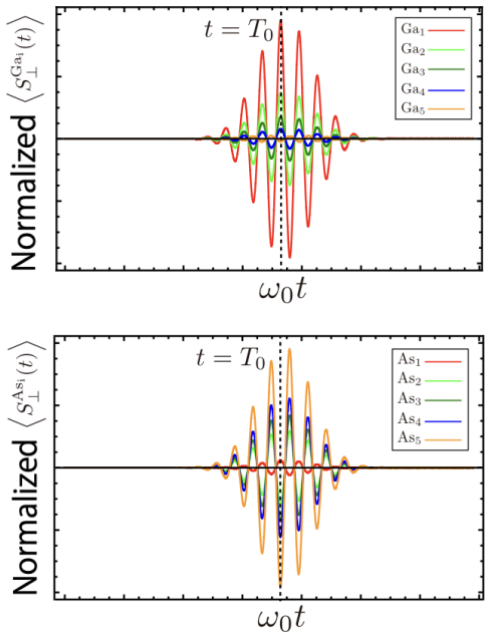


Fig.2: Time evolution of the normalized spin magnetization at each Ga and As atomic site for i=1–5 along the direction with open boundary conditions.

Building upon these results, further analysis reveals that the light-induced spin magnetization directly reflects the material's nonlinear optical response in the spin channel. These findings open the door to novel spintronic functionalities driven by polarized spin magnetization, which we intend to explore in future simulation studies.

References

[1] T. Tamaya and T. Kato, Phys. Rev. B 100, 081203(R) (2019).

[2] N. Yoshikawa, T. Tamaya, and K. Tanaka, Science 356, 736 (2017).

[3] T. Tamaya, A. Ishikawa, T. Ogawa, and K. Tanaka, Phys. Rev. B 94, 241107(R) (2016).

[4]. T. Tamaya, A. Ishikawa, T. Ogawa, and K. Tanaka, Phys. Rev. Lett, 116, 016601 (2016).

Numerical study on low-energy states of quantum spin systems

Hiroki NAKANO
Graduate School of Science, University of Hyogo
Kouto, Kamigori, Hyogo 678-1297, Japan

The many-body problems that researchers encounter in condensed matter physics pose a challenge in accurately estimating physical quantities. The problem of quantum spin systems is a typical one. In the study of a quantum spin system, numerical approaches have been widely and effectively utilized. Valueful information about the target systems has been provided by computational studies.

In the field of quantum spin systems, three methods have been successfully employed. The numerical-diagonalization method is the standard and traditional method. The second method is based on quantum Monte Carlo (QMC) simulation. The density matrix renormalization group (DMRG) method is the third method. Even though there are benefits to each of these methods, they also have drawbacks. QMC simulations are able to handle systems that are significantly bigger, regardless of their spatial dimensions. On the other hand, this approach faces the negative sign problem when we try to accurately evaluate physical quantities in frustrated systems. Regardless of whether or not the target system has frustration, the DMRG method is quite useful when its spatial dimension is one. Regrettably, this method is still being developed for cases where the spatial dimension exceeds one. The numerical diagonalization method can be utilized in various systems regardless of spatial dimension or the presence of frustrations. However, the method can only be used to treat systems that are very small. To overcome this drawback of the numerical diagonalization method, we developed a hybrid-type parallel code for Lanczos diagonalization[1]. By using this code, we can treat various large systems that have not been treated yet. We use this method to analyze various quantum spin systems as our primary approach in this project.

In 2024, this project reported our achievement concerning the spin-S Heisenberg antiferromagnet on the orthogonal dimer lattice [2] in addition to our previous studies of spin-1/2 case[3]. In this study, we successfully carried out Lanczos diagonalizations of this system 16 and 20 sites for $S = 1$ and $S = 3/2$ cases. It is for the first time that within Lanczos-diagonalization studies, numerical results of this model had been presented for $S = 1$ and $S = 3/2$ cases to the best of our knowledge. We clarified the change of the behavior of this model when the ratio of two interaction amplitudes denoted by $r = J_2/J_1$, where J_1 denotes the amplitude of the Heisenberg interaction at the orthgonal dimer and J_2 denotes the amplitude of interaction forming the square lattice. Consequently, we successfully captured the edge of the exact-dimer phase. At the same time, we also detected the edge of the Néel-ordered phase at a different r from the edge of the exact-dimer phase. We confirmed that differences between systems of the 16 and 20 sites are small in our results with respect to the values of r corresponding each of the edges. Our results strongly suggest that the existence of

an intermediate phase between both the edges irrespective of spin-S. Our studies contribute greatly to our deeper understanding of quantum magnetism. Further investigations would shed light on the nontrivial quantum effects in these systems.

References

[1] H. Nakano and A. Terai: J. Phys. Soc. Jpn. **78**, 014003 (2009).

[2] H. Nakano and T. Sakai: J. Phys.: Condens. Matter **36**, 455805 (2024).

[3] H. Nakano and T. Sakai: JPS Conf. Proc. **38**, 011166 (2023).

Universality of Johari-Goldstein relaxation in supercooled liquids and glasses

Takeaki ARAKI[a] and Makina SAITO[b]

[a]*Department of Physics, Kyoto University, Sakyo-ku, Kyoto 606-8502*

[b]*Department of Physics, Tohoku University, Sendai Miyagi 980-8578*

Johari-Goldstein (JG) relaxation, also known as slow β-relaxation, is a relaxation phenomenon observed in supercooled liquids and glasses [1–2]. It plays a crucial role in determining various properties of these materials-particularly their impact strength below the glass transition temperature. Despite its significance, the precise physical mechanism underlying JG relaxation remains unclear, primarily due to the challenges associated with both experimental observation and numerical simulation.

By combining microscopic experiments with molecular dynamics simulations of the ionic glass $CaKNO_3$, we discovered that most particles contribute to the JG process through unexpected, collective non-jumping motions involving angstrom-scale displacements. These subtle movements are activated by the jumping motions of a small fraction of particles [3].

To verify the universality of this physical picture of the JG mode, we conducted molecular dynamics simulations with LAMMPS on metallic glasses ZrCuAl and LaCeNiP, both of which are known to exhibit JG relaxation.

For ZrCuAl, we utilized an embedded atom method (EAM) potential. In contrast, since a suitable EAM potential was not available for LACeNiP, we developed a machine learning potential. We first performed ab initio molecular dynamics simulations on a small atomic system using Quantum ESPRESSO, and subsequently trained a deep learning potential using DeepMD-kit.

Our results revealed that both metallic glasses exhibit fundamentally the same JG relaxation behavior as observed in $CaKNO_3$, supporting the universality of the proposed mechanism.

References

[1] G. P. Johary and M. Goldstein, J. Chem. Phys. **53**, 2327 (1970).

[2] K. L. Ngai, Relaxation and diffusion in complex systems, Springer, Berlin, 2011.

[3] M. Saito, T. Araki, Y. Onodera, K. Ohara, M. Seto, Y. Yoda and Y. Wakabayashi, Acta Materialia **284**, 120536 (2025).

The Physical Origin of the Emerging Ferroelectric Nematic Phase

Matheus DE MELLO and Takeaki ARAKI

Department of Physics,

Kyoto University, Kitashirakawa-oiwake-cho, Sakyo-ku, Kyoto 606-8502

The century-long search for the ferroelectric nematic liquid-crystalline phase reached a major milestone when Nishikawa *et al.* [1] and Mandle *et al.* [2] independently discovered this phase using two distinct rodlike, low-molecular-weight compounds: DIO and RM734, respectively. This novel phase of matter exhibits exceptionally high dielectric permittivity, nonlinear electro-optical properties, and fluidity—making it a promising alternative to conventional ferroelectric solids for advanced technological applications.

This study explores the influence of charge distribution and molecular shape on the stability of ferroelectric nematic liquid crystalline phases through atomistic simulations of 1024-2048 DIO molecules by using GROMACS. We found the role of dipole–dipole interactions and molecular shape in achieving polar ordering by simulating charged and chargeless topologies and analyzing positional and orientational pair-distribution functions. The charged DIO molecules exhibit head-to-tail and side-by-side parallel alignments conducive to long-range polar order, whereas the chargeless molecules show no polar ordering. The 2D x–y cross-section of the correlation pair-distribution function shows that lateral local dipoles in the molecular structure are critical for the formation of the ferroelectric phase.

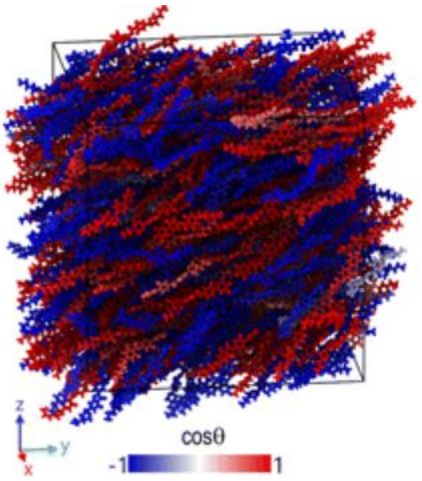


Fig. 1: Configuration snapshot at T = 330 K of the charged DIO.

References

[1] H. Nishikawa, *et al*. Advanced Materials **29**, 1702354 (2017).

[2] R. J. Mandle, *et al.*, Chem. Eur. J. **23**, 14554 (2017).

[3] M. de Mello, M. R. Wilson, and T. Araki, Soft Matter, **21**, 1479 (2025)

Calculating entanglement dynamics in free boson systems by random sampling

Ryui KANEKO
Physics Division, Sophia University
Chiyoda, Tokyo 102-8554, Japan

We analyze the time evolution of entanglement in bosonic systems and explore how quantum information propagates within these systems. This entanglement evolution can be experimentally measured in ultracold atom systems in optical lattices [1, 2]. However, accessible sizes are small in experiments. Comparing experimental results with numerical simulations on classical computers is essential for future experiments to validate the findings. Unfortunately, numerical simulations for the long-time evolution of soft-core boson systems are challenging. Conventional methods, such as exact diagonalization and matrix-product-state methods, can typically compute dynamics for only about 10 sites [3].

Recently, we provided a formal analytical solution for the time evolution of Rényi entanglement during a quench to a noninteracting boson system with a product initial state [4]. Even with this approach, calculations are restricted to around 50 sites at half-filling [4–7], and the computation time grows exponentially with the matrix size n as $\mathcal{O}(n \times 2^n)$. To extend our calculations to larger systems, we employ a random sampling method and investigate how the propagation of quantum information changes with dimensionality.

We specifically focus on the Bose-Hubbard model on a chain and a square lattice and calculate the time evolution of the Rényi entanglement $S_2(t)$ after quenching the system to a noninteracting parameter point $U = 0$, starting from a $010101\cdots$-type charge-ordered state at half-filling. S_2 is given by

$$S_2(t) = -\ln \mathrm{perm} A(t), \tag{1}$$

$$A(t) = \begin{pmatrix} Z(t) & I - Z(t) \\ I - Z(t) & Z(t) \end{pmatrix}, \tag{2}$$

where I is the identity matrix, and $Z(t)$ is a matrix calculated from the time-dependent single-particle correlation functions obtained from the noninteracting Hamiltonian [4]. We evaluate S_2 using the random sampling method up to 100 sites.

According to previous studies [8, 9], the permanent is evaluated as $\mathrm{perm} A = \mathbb{E}\left[\prod_{i=1}^{n} r_i^* \left(\sum_{j=1}^{n} a_{ij} r_j\right)\right]$ using independent and identically distributed random variables r_i with a mean of 0 and a variance of 1. Here, a_{ij} is the (i, j) component of the matrix A. Therefore, the permanent can be calculated by evaluating the expectation value as

$$\mathrm{perm} A \approx \frac{1}{N_{\mathrm{smp}}} \sum_{m=1}^{N_{\mathrm{smp}}} p^{(m)}, \tag{3}$$

$$p^{(m)} = \prod_{i=1}^{n} r_i^{(m)*} \left(\sum_{j=1}^{n} a_{ij} r_j^{(m)}\right), \tag{4}$$

which is the sum of samples for N_{smp} random numbers $\boldsymbol{r}^{(m)}$. Note that, when the entanglement follows the volume-law scaling, the permanent decreases exponentially with the size, and thus the required number of samples increases exponentially with the size. However, when the entanglement satisfies the area-law scaling, the permanent is closed to 1, and thus

the sampling cost is lower than the straightforward computational cost. Although the computational cost of the permanent is still exponential using the random sampling method, it can be reduced to $\mathcal{O}(2^{\alpha n})$ with $\alpha \ll 1$.

We successfully calculate the time evolution of the Rényi entanglement entropy $S_2(t)$ for one-dimensional and two-dimensional systems up to 100 sites by using the number of samples $N_{\rm smp} = 2^{0.2N_{\rm s}+12}$ with $N_{\rm s}$ being the number of sites [10]. The coefficient 0.2 is determined by the scaling of the statistical error of the permanent with the number of samples and the system size. It is found to be universal for both one-dimensional and two-dimensional systems that we studied. After the long-time evolution, the entanglement entropy density approaches a constant value, which is consistent with the volume-law scaling of the entanglement entropy. Remarkably, the entanglement entropy density is independent of the dimensionality and converges to ≈ 0.3 for both one-dimensional and two-dimensional systems. Although performing sufficiently large-scale quantum simulations in experiments is challenging, it is valuable to compare the results of quantum simulations with our numerical results, which can be used to validate the accuracy of the quantum simulations.

References

[1] R. Islam et al., Nature **528**, 77 (2015).

[2] A. M. Kaufman et al., Science **353**, 794 (2016).

[3] S. Goto and I. Danshita, Phys. Rev. B **99**, 054307 (2019).

[4] D. Kagamihara et al., Phys. Rev. A **107**, 033305 (2023).

[5] A. Neville et al., Nat. Phys. **13**, 1153 (2017).

[6] J. Wu et al., Natl. Sci. Rev. **5**, 715 (2018).

[7] P.-H. Lundow and K. Markström, J. Comput. Phys. **455**, 110990 (2022).

[8] D. G. Glynn, Eur. J. Comb., **31**, 1887 (2010).

[9] R. Berkowitz, P. Devlin, Isr. J. Math. **224**, 437 (2018).

[10] R. Kaneko, D. Kagamihara, and I. Danshita, Phys. Rev. A **111**, 032412 (2025).

Dynamic mode decomposition of time-series data in quantum many-body systems

Ryui KANEKO
Physics Division, Sophia University
Chiyoda, Tokyo 102-8554, Japan

Predicting the dynamics of quantum many-body systems over long timescales is a significant challenge. For instance, when using time-dependent variational Monte Carlo methods or tensor network methods to analyze the quench dynamics of isolated quantum many-body systems, calculations often break down within a short time, roughly on the order of the inverse of the energy scale multiplied by Planck's constant $\hbar$ [1–5].

In contrast, instead of trying to determine the wave function at each time step during dynamics calculations, one may predict the long-time dynamics of specific physical quantities by relying solely on accurate short-time time-series data. One such method is dynamic mode decomposition (DMD) [6–9], initially used in fluid dynamics, which has recently proven effective for the dynamics of quantum many-body systems [10–12].

DMD can forecast long-time dynamics up to approximately an order of magnitude longer than the input time-series data [12]. Furthermore, the latest time-dependent variational Monte Carlo methods can compute dynamics for about $100\hbar$ times the inverse of the energy scale [13]. Combining both approaches would make it possible to predict dynamics for durations up to about 1000 times longer than what is achievable with conventional methods applied to quantum many-body systems.

In this study, we have explored the potential of applying DMD to short-term time series data derived from the state-of-the-art time-dependent variational Monte Carlo methods [14] motivated by simulations of superconductivity dynamics under laser irradiation [15]. We trained our model on simulation results of the time evolution of superconducting correlations, utilizing data up to approximately time 200, where we define the time unit as the inverse of the hopping parameter multiplied by $\hbar$. Our predictions successfully extended to time around 400, twice the duration of the input data. We are investigating whether we can achieve high-precision predictions over longer timescales.

References

[1] G. Carleo *et al.* Sci. rep. **2**, 243 (2012).

[2] G. Carleo *et al.* Phys. Rev. A **89**, 031602(R) (2014).

[3] A. Kshetrimayum *et al.*, Nat. Commun. **8**, 1291 (2017).

[4] P. Czarnik *et al.*, Phys. Rev. B **99**, 035115 (2019).

[5] C. Hubig and J. I. Cirac, SciPost Phys. **6**, 31 (2019).

[6] P. J. Schmid and J. Sesterhenn, 61st Annual Meeting of the APS Division of Fluid Dynamics (2008).

[7] C. W. Rowley *et al.*, J. Fluid Mech. **641**, 115 (2009).

[8] P. J. Schmid, J. Fluid Mech. **656**, 5 (2010).

[9] J. H. Tu *et al.*, J. Comput. Dyn. **1**, 391 (2014).

[10] I. A. Luchnikov *et al.*, Phys. Rev. Res. **4**, 043002 (2022).

[11] J. Yin *et al.*, J. Comput. Sci. **64**, 101843 (2022).

[12] R. Kaneko *et al.*, Phys. Rev. Research **7**, 013085 (2025).

[13] K. Ido *et al.*, Phys. Rev. B **97**, 045138 (2018).

[14] T. Misawa *et al.*, Comp. Phys. Commun., **235**, 447 (2019).

[15] K. Ido *et al.*, Sci. Adv. **3(8)**, e1700718 (2017).

Screening in concentrated electrolytes

Takamichi TERAO

Department of Electrical, Electronic and Computer Engineering,

Gifu University, Yanagido 1-1, Gifu, 501-1132

Recently, concentrated electrolyte solutions have attracted considerable attention. In recent studies, surface force measurements have demonstrated that the screening length in concentrated electrolytes becomes considerably large [1], which contradicts the prediction of the Debye–Hückel theory. A theoretical analysis has been performed based on the physical intuition that concentrated electrolytes are analogous to ionic crystals. Because it is difficult to experimentally obtain detailed information on the spatial configurations of ions, molecular dynamics (MD) simulations have been performed as an effective method for clarifying these problems. The results were compared with previously reported experimental studies on the screening length in concentrated electrolytes. To date, the agreement between simulation and experimental results remains under debate.

In this study, MD simulations of aqueous NaCl solutions based on the all-atom model were performed to quantitatively clarify the configuration of monovalent cations and anions in concentrated electrolytes (Fig. 1). Some cations and anions were clustered together by a heteroaggregation process [2]. The results demonstrated that, in concentrated electrolytes, as the electrolyte concentration increased, the fraction of isolated ions diffusing without clustering decreases, whereas the density of isolated ions did not change significantly. Because the total charge of clustered ions approached neutral, these clustered ions may contribute less to the screening effect than isolated ions. These results suggest that, in contrast to dilute electrolytes, the screening length does not change significantly with increasing electrolyte concentration.

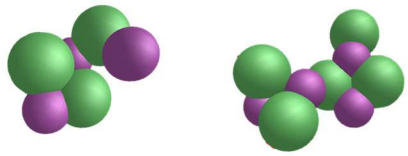


Fig. 1: A snapshot of ions in a system with an electrolyte concentration of 3.8 M. The purple and green spheres represent sodium and chloride ions, respectively.

References

[1] A.M. Smith, A.A. Lee, and S. Perkin, J. Phys. Chem. Lett. **7**, 2157 (2016).

[2] K. Komori and T. Terao. Chem. Phys. Lett. 825, 140627 (2023).

Simulations of polar active fluids under geometrical confinements

Hiroki MATSUKIYO, Jun-ichi FUKUDA

Department of Physics, Kyushu University, Motooka 744, Nishi-ku, Fukuoka 819-0395

We have studied the behavior of polar active fluids under geometrical confinements (The part of the study already mentioned in the previous report has been published in 2024 [1]). The behavior of polar active fluids can be described by a continuum equation, called the Toner-Tu-Swift-Hohenberg (TTSH) equation. In previous studies using the TTSH equation, the nonslip boundary condition was employed. However, the nonslip boundary condition cannot describe the edge current (i.e. edge-localized flow of active fluids observed in several experiments). In ref. [1], we have proposed a new numerical method to calculate the TTSH equation under a slip boundary condition and successfully realized the edge current. Furthermore, we have discovered the temporal oscillation of the edge current direction.

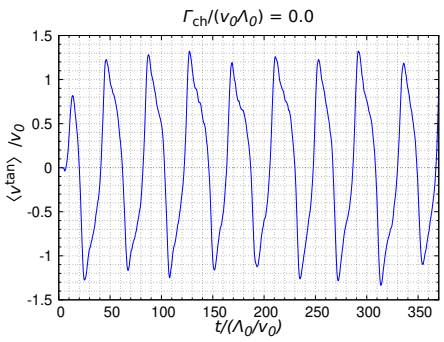
As a further development of this study, we have added a chiral term to the TTSH equation and investigated the behavior of the "chiral TTSH equation" by means of the numerical simulation. The chiral term made the edge current oscillation asymmetric (Fig.1). (We had an oral presentation on this study in the 79th Annual Meeting (2024) of the Physical Society of Japan.)

Throughout the above studies, we have performed simulations for many sets of parameter values, using System B, Ohtaka. The large number of threads of Ohtaka made it possible for us to perform the simulations in parallel for large number of combinations of parameter values, keeping the computing performance.

References

[1] Matsukiyo, H., & Fukuda, J. (2024) Oscillating edge current in polar active fluid. *Physical Review E*, *109*(5), 054604.

(a)



(b)

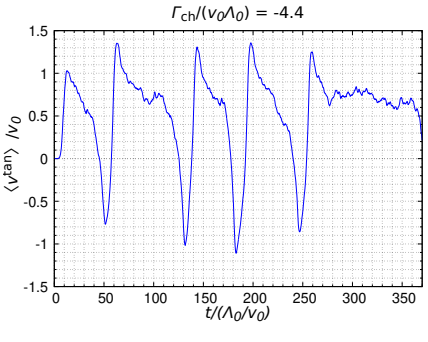


Fig.1. An example of the time evolution of the edge current direction ($\langle v^{\tan}\rangle/v_0$) in the TTSH simulation (a)without and (b)with a chiral term.

Numerical Study of One Dimensional Frustrated Quantum Spin Systems

Kazuo HIDA
Professor Emeritus, Division of Material Science,
Graduate School of Science and Engineering,
Saitama University, Saitama, Saitama 338-8570

1 Model

We investigate the ground-state phases of $(1/2, 1/2, 1)$ mixed diamond chains with single-site anisotropy described by the following Hamiltonian:

$$\mathcal{H} = \sum_{l=1}^{L} \Big[(1+\delta)\boldsymbol{S}_l(\boldsymbol{\tau}_l^{(1)} + \boldsymbol{\tau}_{l-1}^{(1)}) + (1-\delta)\boldsymbol{S}_l(\boldsymbol{\tau}_l^{(2)} + \boldsymbol{\tau}_{l-1}^{(2)}) + \lambda \boldsymbol{\tau}_l^{(1)}\boldsymbol{\tau}_l^{(2)} + D\tau_l^{(2)z2} \Big], \quad (1)$$

where $\boldsymbol{S}_l, \boldsymbol{\tau}_l^{(1)}$ and $\boldsymbol{\tau}_l^{(2)}$ are spin operators with magnitudes $S_l = \tau_l^{(1)} = 1/2$ and $\tau_l^{(2)} = 1$, respectively. The number of unit cells is denoted by L. The lattice structure is depicted in Fig. 1. We consider the region $\lambda \geq 0$ and $1 \geq \delta \geq -1$. The isotropic case ($D = 0$) is investigated in [1].

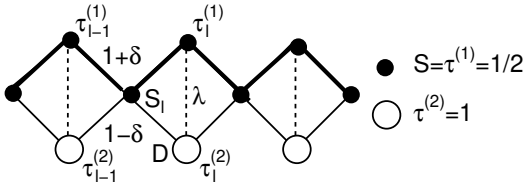


Figure 1: Structure of the diamond chain investigated in this work.

2 Limiting Cases

2.1 $\lambda = 0$

The system is unfrustrated. In the isotropic case $D = 0$, the ground state is the quantized ferrimagnetic (QF) phase with spontaneous magnetization $m_{\rm sp} = 1$ per unit cell according to the Lieb-Mattis (LM) theorem.[1, 2] In the presence of easy-axis anisotropy $D < 0$, this state remains as the QF phase with $m_{\rm sp}^z = 1$. This phase is called the LM1 phase. On the other hand, in the presence of easy-plane anisotropy $D > 0$, the XY component of the magnetization cannot order due to U(1) symmetry. Hence, the ground state turns into the nonmagnetic Tomonaga-Luttinger liquid (TLL) phase.

2.2 $\delta = 1$

If $\lambda > 0$, the system is unfrustrated. The ground state in the isotropic case is the QF phase with $m_{\rm sp} = 1$ according to the LM theorem.[1, 2] For $D < 0$, this state remains as the QF phase with $m_{\rm sp}^z = 1$. We call this phase is the LM2 phase to distingush from the LM1 phase with a different spin configuration. On the other hand, for $D > 0$, the XY component of the magnetization cannot order due to U(1) symmetry. Hence, the ground state turns into the TLL phase.

2.3 $\delta = -1$

The system is unfrustrated and the ground state in the isotropic case is the nonmagnetic phase with $m_{\rm sp} = 0$ according to the LM theorem.[1, 2] This phase is expected to be the TLL phase as discussed in [1]. For $D < 0$, this

parameters	$\mathcal{H}^{\rm eff}$	GS
$\delta > \delta_c, D > 0$	XY-like	TLL
$\delta_c > \delta > 0, D > 0$	Ising-like AF	Néel
$\delta < 0, D > 0$	XY-like	TLL
$\delta > \delta_c, D < 0$	Ising-like F	LM2
$\delta_c > \delta > 0, D < 0$	XY-like	TLL
$\delta < 0, D < 0$	Ising-like AF	Néel

Table 1: Ground-state (GS) phases in the large λ limit. $\delta_c = 0.6(1 + 2D/5\lambda)$. F and AF stand for ferromagnet and antiferromagnet, respectively.

state turns into the Néel phase. On the other hand, for $D > 0$, the ground state remains in the nonmagnetic TLL phase.

2.4 $\lambda \gg 1$

The spins $\boldsymbol{\tau}_l^{(1)}$ and $\boldsymbol{\tau}_l^{(2)}$ are strongly coupled to form a single spin $\boldsymbol{T}_l$ with magnitude 1/2. The effective Hamiltonian for $\boldsymbol{S}_l$ and $\boldsymbol{T}_l$ is a spin-1/2 XXZ Hamiltonian given by

$$\mathcal{H}^{\rm eff} = \sum_{l=1}^{L} \Big\{ J_{\rm eff}^{z} \hat{T}_l^z (S_l^z + S_{l+1}^z) + \frac{1}{2} J_{\rm eff}^{xy} \left[\hat{T}_l^+ (S_l^- + S_{l+1}^-) + \text{h.c.} \right] \Big\} \quad (2)$$

with

$$J_{\rm eff}^{z} \simeq 1 - \frac{5\delta}{3}\left(1 - \frac{32D}{45\lambda}\right) \quad (3)$$

$$J_{\rm eff}^{xy} \simeq 1 - \frac{5\delta}{3}\left(1 - \frac{4D}{45\lambda}\right) \quad (4)$$

within the lowest order in λ^{-1}. Considering that the ferromagnetic ground state of (2) corresponds to the LM2 ferrimagnetic state in (1), the ground states in the large λ limit are classified as tabulated in Table 1.

3 Numerical Results

We have carried out the numerical exact diagonalization (NED) calculation for $L = 6$ to obtain the ground-state phase diagram of Fig. 2 for $D = 1$ and $D = -1$. For $D = 1$, an extremely narrow Néel region is found within the TLL phase. It is not clear whether this phase remains in the thermodynamic limit. For $D = -1$, the Néel phase in the shaded region of Fig. 2(b) shrinks with the system size comparing the present data and those for $L = 4$. The preliminary NED calculations for $L = 8$ also support this tendency. Hence, in the thermodynamic limit, we expect that this region will be replaced by the partial ferrimagnetic (PF) phase with $0 < m_{\rm sp} < 1$ as in the isotropic case.[1]

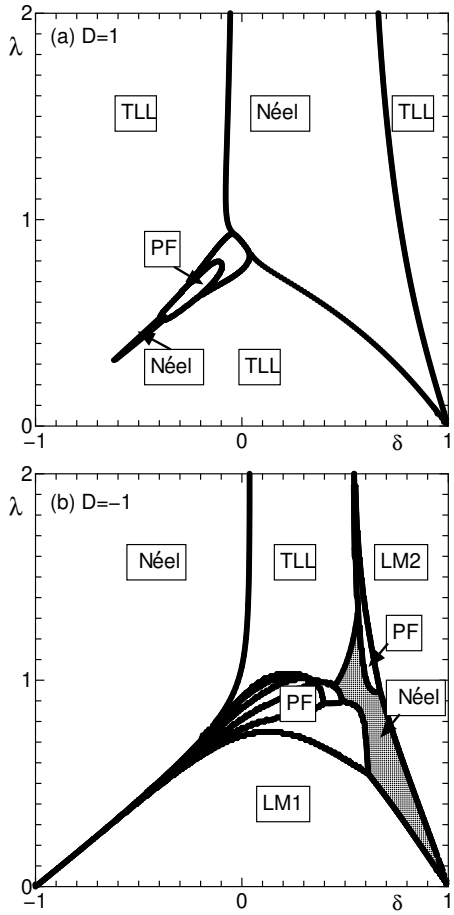


Figure 2: Ground-state phase diagrams based on the NED data with $N = 18$ for (a) $D = 1$ and (b) $D = -1$.

References

[1] K. Hida, J. Phys. Soc. Jpn. **93**, 044703 (2024).

[2] E. Lieb and D. Mattis, J. Math. Phys. **3**, 749 (1962).

Investigation of efficient methods for introducing long-range interactions in the cluster expansion method

Yoshiyuki Fukumoto
Department of Physics and Astronomy, Faculty of Science and Technology, Tokyo University of Science, 2641 Yamazaki, Noda, Chiba 278-8510

In spin-1/2 frustrated systems with magnetic order, the observation of spinon excitations, in addition to magnon excitations, has attracted much interest [1]. The dispersion relation of the magnon excitations provides important information for identifying the spin model, and the linear spin-wave theory (LSWT) is often used for the analysis. However, the application of LSWT is not always justified in frustrated systems because of the smallness of the magnetization. In this case, the series expansion method based on the linked cluster algorithm [2] is useful, and has been successfully applied to the triangular lattice model [3] and the kagome lattice model with Dzyaloshinskii-Moriya interaction [4].

In practical analyses, we often encounter situations where interactions between sites beyond nearest neighbors play some role to determine the shape of magnon dispersion relations. In the LSWT, it is not difficult to introduce such interactions. However, in the series expansion method, the introduction of the such interactions is accompanied by the difficulty of an explosive increase in the number of clusters.

In this study, we performed a series expansion in a stacked triangular lattice system realized in $Ba_3CoSb_2O_9$, where the interlayer interaction is expected to be about 10% of the in-plane interaction [1]. The introduction of three-dimensionality rapidly increases the number of clusters, but to deal with this, we set an order for the clusters and perform the search for them using a binary search algorithm to speed up the process.

When calculating the nth order series exactly, we have to treat all connected clusters with up to n perturbation links. On the other hand, in order to reduce the total number of clusters, it is also possible to restrict the cluster and obtain an approximate series. We previously performed such calculations for a two-dimensional triangular lattice by restricting the total number of sites contained in a cluster to an upper limit of $n+1$ sites. We set $n \leq 8$ and confirmed that we could obtain the same level of accuracy as previous research [3].

In the present study on stacked triangular lattice systems, calculations were first performed using clusters with up to 6 links and 7 sites. As a result, it was found that the excitation energy was negative in part of the wavenumber space. To address this, the number of sites was increased by one and calculations were performed considering clusters with up to 6 links and 8 sites. Then, we found that the problem of negative excitation energy was resolved. Using the latter clusters, calculations were performed for all paths in the experiment and a comparison was made with the experiment. Although some discrepancies were observed in the fine structure, good agreement was obtained for all paths, including the interlayer direction.

[1] S. Ito *et al.*, Nat. Commun. 8, 235, 2017.
[2] M. P. Gelfand *et al.*, JSP 59, 1093, 1990.
[3] W. Zheng *et al.*, PRB 74, 224420, 2006.
[4] S. Kogure *et al.*, JPSJ 92, 113703, 2023.

Analysis for absorption- and fluorescence-spectra of seMpai by quantum chemical calculations, Analysis for *in situ* absorption spectra in firefly bioluminescence by quantum chemical calculations

Miyabi HIYAMA
Gunma University
Tenjin-cho, Kiryu, Gunma 376-8515

Because firefly bioluminescent substrate analogs are attracting attention as next-generation luminescent probes for *in vivo* imaging techniques of animal tissues and cells, the analogs have been developed. seMpai is a soluble chemical species and one of firefly bioluminescent substrate analogs, of which bioluminescence color is red[1].

In this year, the quantum chemical calculations for seMpai were performed to elucidate the absorption and fluorescence property of this compound. Using these calculation results, the experimental absorption and fluorescence spectra of seMpai in aqueous solutions of pH 2-10 were assigned.

The ground-state structures of seMpai and its conjugate acids and bases expected to exist in aqueous solution were obtained using the density functional theory (DFT) method. The excitation energies, oscillator strengths, and free energies of these species were estimated from the time-dependent (TD) DFT calculations.

Using these free energies the relative concentrations in the aqueous solutions at various pH values were obtained. The excitation energies and oscillator intensities of the most abundant chemical species at each pH solutions revealed the assignments of experimental absorption spectrum. The fluorescence energies of these chemical species were determined using TDDFT calculations. The fluorescence pathways of seMpai at each pH solutions were elucidated by the assignments of the experimental spectra.

Quantum chemical calculations of the firefly bioluminescence substrate analog, AkaLumine and its emitter (oxy-AkaLumine) were carried out for the analysis of experimental absorption spectra. The optimized ground state, the oscillator strength and excitation energies at this ground state were obtained for not only the single molecule, but also its dimer using DFT and TDDFT methods. Comparison of the peaks of the experimental absorption spectrum with these excitation energies indicates that there would be the effect of other compounds than those considered in this study.

The computational chemistry software package, Gaussian16, was used for DFT and TDDFT calculations. All calculations were performed on system B of Super Computer Center in ISSP.

References

[1] R. Saito, T. Kuchimaru, S. Higashi, S. W. Lu, M. Kiyama, S. Iwano, R. Obata, T. Hirano, S. Kizaka-Kondoh, and S. A. Maki: Bull. Chem. Soc. Jpn.. **92**, 608 (2019).

Multifractality and topology in monitored quantum dynamics

Yohei FUJI
Department of Applied Physics, University of Tokyo, Tokyo 113-8656

Quantum many-body systems subject to repeated measurements of local observables exhibit measurement-induced phase transitions (MIPTs) [1, 2]. An example of MIPT is the entanglement transition, across which the entanglement entropy of steady states changes from the volume law to area law. Despite its intrinsic nonequilibrium nature, the MIPT bears a close resemblance with equilibrium phase transitions, as it shows critical phenomena with emergent conformal invariance. In this project, we have demonstrated that two other important concepts in equilibrium phase transitions, multifractality and topology, are also revealed in measurement-induced phenomena. To do so, we have used supercomputing facilities (System B) at ISSP, which allow us to perform massive parallel sampling of measurement outcomes required to access measurement-induced phenomena.

First, we considered a single quantum particle evolved under repeated measurements of occupation numbers at random locations [3]. We found that the measurements generally induce multifractality of the single-particle wave function, which is quantified by the scaling properties of moments of the wave-function amplitudes (inverse participation ratios) averaged over measurement outcomes, in analogy with Anderson transitions in disordered systems. Furthermore, we found that a transport property of the particle (diffusive or ballistic) in the absence of measurements qualitatively affects the multifractal properties. It turns out that similar multifractality can also be found

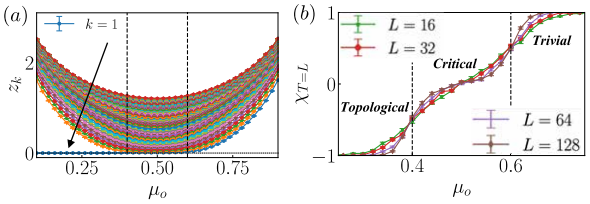


Figure 1: (a) Lyapunov exponents obtained for the monitored Majorana chain of the length $L = 128$ under the open boundary condition. (b) Topological invariant computed at time $T = L$.

for stochastic dynamics of a single classical particle subject to repeated measurements or stochastic resettings, which allows us to obtain some analytical results for measurement-induced multifractality of a diffusive quantum particle.

Second, we considered a monitored version of the famous Kitaev chain [4], a paradigmatic model hosting a topological phase in equilibrium quantum systems. Here, the system is evolved under repeated weak measurements of the fermion parities of neighboring Majorana pairs at every bond. By varying the measurement strengths of even and odd bonds, we can achieve three measurement-induced entanglement phases: topological and trivial area-law entangled phases and a critical phase with subvolume-law entanglement. We showed that the topological area-law phase has a bulk gap and gapless edge spectrum quantified by Lyapunov exponents, as a consequence of Majorana zero modes [see Fig. 1 (a)]. We also constructed a topological invari-

ant to detect the topological area-law phase through the total fermion parity obtained with twisted measurement outcomes at the boundary [see Fig. 1 (b)]. We further showed that a critical phase has gapless bulk Lyapunov spectrum and a vanishing topological invariant at any time $T \leq O(L)$. This study thus establishes the bulk-edge correspondence for measurement-induced topological phases, which certainly goes beyond the equilibrium paradigm.

References

[1] A. C. Potter and R. Vasseur, *Entanglement Dynamics in Hybrid Quantum Circuits*, in Entanglement in Spin Chains: From Theory to Quantum Technology Applications, edited by A. Bayat, S. Bose, and H. Johannesson (Springer International Publishing, Cham, 2022) pp. 211-249.

[2] M. P. A. Fisher, V. Khemani, A. Nahum, and S. Vijay, *Random Quantum Circuits*, Ann. Rev. Condens. Matter Phys. **14**, 335 (2023).

[3] K. Yajima, H. Oshima, K. Mochizuki, and Y. Fuji, *Multifractality in monitored single-particle dynamics*, Phys. Rev. Res. **6**, 043049 (2024).

[4] H. Oshima, K. Mochizuki, R. Hamazaki, and Y. Fuji, *Topology and Spectrum in Measurement-Induced Phase Transitions*, arXiv:2412.11097.

Study on hybrid algorithms for Ising machines

Shu Tanaka

Department of Applied Physics and Physico-Informatics, Keio University

Hiyoshi, Yokohama, Kanagawa, 223-8522

In recent years, Ising machines, which are computers specialized in metaheuristic methods such as quantum annealing, have been actively developed as highly efficient solution methods for combinatorial optimization problems.

In this research project, we have developed a new algorithm that maximizes the hardware performance of Ising machines based on insights from statistical mechanics. This research is expected to provide fundamental technology for the development of existing Ising machine software, as well as contribute to the research and development of new Ising machines based on novel concepts and internal algorithms. Quantum annealing is a promising algorithm for solving combinatorial optimization problems. It searches for the ground state of an Ising model that corresponds to the optimal solution of a given combinatorial optimization problem. The basic principle of quantum annealing is the adiabatic theorem of quantum mechanics. This theorem guarantees that the system remains in the ground state of the Hamiltonian if the time evolution is sufficiently slow. According to the adiabatic theorem, the execution time required for quantum annealing to satisfy adiabaticity is inversely proportional to the square of the minimum energy gap between the ground state and the first excited state during the time evolution. As a result, when the energy gap is small, the search for the ground state becomes extremely difficult, which is a major bottleneck in quantum annealing. Enlarging the energy gap is one strategy to improve the performance of quantum annealing, but its implementation on real hardware remains a difficulty. In this study, we propose a method to efficiently solve instances with small energy gaps by introducing additional local terms into the Hamiltonian and exploiting adiabatic transitions that remain in small energy gaps. The proposed method achieves an approximately quadratic speedup in solution time compared to conventional quantum annealing. Furthermore, we have investigated the transferability of the parameters obtained by the proposed method [1].

References

[1] T. Hattori and S. Tanaka, arXiv:2503.15244 (2025).

Elucidation of critical phenomena by parallelized higher dimensional tensor network RG

Haruki SHIMIZU
Institute for Solid State Physics, University of Tokyo
Kashiwa-no-ha, Kashiwa, Chiba 277-8581

The study of critical systems which lie at the boundary of two distinct phases is crucial in addressing the classification of the phases of matter, which is a central issue of condensed matter physics. By focusing on universality, we can understand the critical behavior of a system, which is characterized by the divergence of correlation length and the emergence of scale invariance.

Conformal field theory (CFT) is a powerful theoretical framework for describing universality, especially for one-dimensional quantum systems and two-dimensional classical systems. It is an important task to identify the underlying CFT of a given critical system. While the central charge plays an important role in CFT, it alone cannot always distinguish between different CFTs. Recent studies of CFT on nonorientable surfaces revealed that the partition function of CFT defined on the Klein bottle contains a universal quantity other than the central charge, so-called Klein bottle entropy, providing an additional tool for discerning different CFTs [1]. Furthermore, the Klein bottle entropy is a universal function of some dimensionless coupling parameter at the region near criticality with its off-critical behavior being useful in extracting the conformal weight of the perturbation operators [2].

Recently, we have proposed a tensor network method for studying critical phenomena on nonorientable surfaces [3]. The key idea involves representing the nonorientable surface topology with the interconnection structure of the tensor network. To be specific, the partition functions on the Klein bottle and real projective plane can be computed by representing the crosscap and rainbow boundaries with renormalized tensors obtained through the higher-order tensor renormalization group (RG) procedure. Our numerical results are consistent with the theoretical predictions.

In this project, we have extended our method to the off-critical regime. Adding thermal and magnetic perturbations to the two-dimensional classical Ising model at criticality, we successfully reproduce the off-critical behavior of the Klein bottle entropy through effectively parallelized calculationss [4]. Our method thus enables efficient computation of the Klein bottle entropy for both critical and off-critical systems, with potential for extension to higher genus surface. Further applications to other models and higher dimensions are in progress.

References

[1] Z.-Q. Li, L.-P. Yang, Z. Y. Xie, H.-H. Tu, H.-J. Liao, and T. Xiang, Phys. Rev. E **101**, 060105(R) (2020).

[2] Y. Zhang, A. Hulsch, H.-C. Zhang, W. Tang, L. Wang and H.-H. Tu, Phys. Rev. Lett. **130**, 151602 (2023).

[3] H. Shimizu and A. Ueda, e-print arXiv:2402.15507 (2024).

[4] H. Shimizu and A. Ueda, in preparation

Numerical Simulation of Anyons in Fractional Quantum Hall Systems

Takeo Kato
Institute for Solid State Physics, University of Tokyo
Kashiwa-no-ha, Kashiwa, Chiba 277-8581

We numerically evaluated the microwave response of edge states in a system composed of a droplet in the fractional quantum Hall state (Laughlin state) coupled to a microwave waveguide. The system considered in this study was theoretically proposed in a previous work [1] as a setup capable of observing the anyonic statistics of excitations in the edge states. Our numerical results are expected to enable detailed comparisons with future experimental results. The effective action of the system was derived by assuming a circular droplet and employing bosonization. The response function to be calculated involves the correlation function of the bosonic field describing the edge states. Since this correlation function cannot be obtained analytically, we performed numerical calculations using the path-integral quantum Monte Carlo method. Large-scale parallel computations were carried out. We numerically evaluated the response functions for two cases: a fractional quantum Hall droplet with Landau level filling factor $\nu = 1/3$, and an integer quantum Hall droplet with $\nu = 1$, for which analytical theoretical construction is possible. In the numerical simulations, we performed 30,000 Monte Carlo steps for thermalization, followed from 1×10^6 to 1.2×10^6 steps for measuring the correlation functions.

The results of our numerical calculations are presented below. Figure 1 shows the temperature dependence of the response function for the case of Landau level filling factor $\nu = 1/3$.

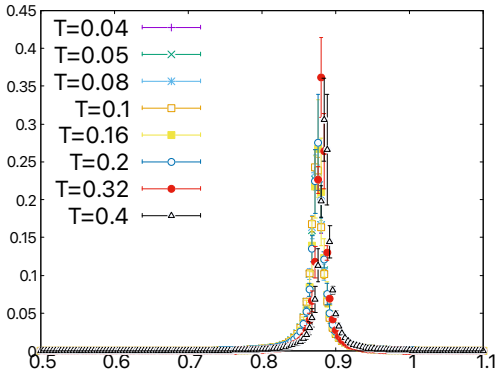


Figure 1: Temperature dependence of the imaginary part of the response function for $\nu = 1/3$ filling.

The results reveal that the peak position shifts and the peak width changes as the temperature varies. This behavior has not been reported in previous studies, including Ref. [1], and thus represents a novel finding. The data shown in Fig. 1 correspond to a quasiparticle tunneling strength of $V = 1.024$. Fig. 3 shows the dependence of the response function on the coupling strength for the integer quantum Hall state with $\nu = 1$. In this case, analytical theoretical calculations are feasible, and the observed peak shift agrees well with the theoretically predicted shift toward lower energies, as shown in the left panel of Fig. 3.

Furthermore, in the case of $\nu = 1$, the peak width shows no significant dependence on the coupling strength and remains nearly constant, as shown in the right panel of Fig. 3. This behavior is consistent with expectations from the theory of chiral Luttinger liquids. Based

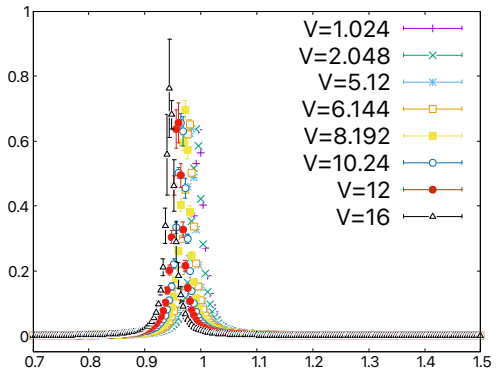


Figure 2: Tunneling-strength dependence of the imaginary part of the response function for $\nu = 1$ filling.

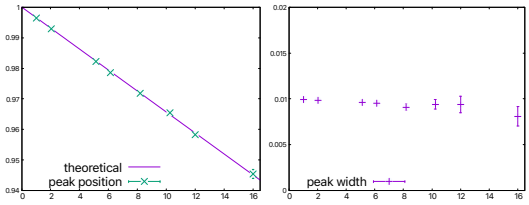


Figure 3: The peak shift (the left panel) and width (the right panel) in the response function for $\nu = 1$ as a function of the quasiparticle tunneling strength.

on these results, we conclude that our numerical calculations successfully reproduce the theoretical predictions for the $\nu = 1$ case.

In the future, we plan to numerically evaluate the microwave response for Laughlin states with filling factors other than $\nu = 1/3$, as well as for droplets with non-circular geometries. At the same time, we aim to improve the numerical accuracy of our simulations and to investigate the detailed temperature dependence of the response functions in Laughlin states.

References

[1] J. Cano, A. Doherty, C. Nayak, D. Reilly. Microwave absorption by a mesoscopic quantum Hall droplet. *Phys. Rev. B*, Vol. 88, p. 165305, 2013.

Tensor learning approaches to computational physics

Hiroshi Shinaoka
Department of Physics, Saitama University, Saitama 338-8570

We have studied quantum impurity problems using physics-informed neural networks (PINNs) [1]. This year, we focused on developing a PINN model that can efficiently predict the self-energy of Anderson impurity models (AIMs) based on the Lehmann representation. The calculations were conducted using the GPU nodes of System C.

The main achievement of this research is the development of a PINN model that combines deep learning techniques with the Lehmann representation and sparse modeling techniques [2]. The model was specifically designed to predict the self-energy of single-orbital AIMs (SAIMs) for noninteracting electron baths with semicircular density of states. As shown in Fig. 1, the key features of our approach include:

- Implementation of physical constraints through the Lehmann representation, which significantly improves the model's accuracy at both high and low Matsubara frequencies
- Use of sparse grids in Matsubara-frequency and real-frequency spaces, reducing the computational cost while maintaining accuracy
- Development of a non-negative projection that ensures the auxiliary spectral function satisfies physical constraints

The PINN model was trained across a wide range of onsite Coulomb interactions U and hybridization strengths V. The results demonstrate high accuracy in both U-V and Matsubara-frequency spaces. For example, the Lehmann representation allows the PINN model to reduce the maximum test error in electron filling by a factor of approximately 7.8.

The calculations were performed using the GPU nodes of System C, which provided the necessary computational resources for training the neural network models.

This research opens up new possibilities for efficient quantum impurity calculations, which are essential for studying strongly correlated electron systems through dynamical mean-field theory (DMFT). The developed PINN model could potentially be extended to more complex systems and integrated into self-consistent DMFT calculations.

References

[1] F. Kakizawa, S. Terasaki, and H. Shinaoka: arXiv:2411.18835 (2023).

[2] J. Li, M. Wallerberger, N. Chikano, C.-N. Yeh, E. Gull, and H. Shinaoka: Phys. Rev. B **101**, 035144 (2020).

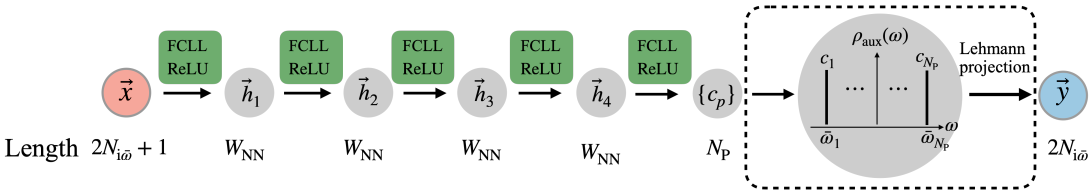


Figure 1: Schematic of the PINN model for predicting the self-energy of Anderson impurity models. The model combines deep learning techniques with the Lehmann representation and sparse modeling techniques to ensure physical constraints are satisfied.

Analysis of Ising model in statistical-mechanical informatics

Yuya SEKI

Graduate School of Science and Technology, Keio University, Kanagawa 223-8522

We have studied properties and performance of factorization machine with annealing (FMA) [1], which is a combinatorial optimization method using simulated annealing (SA) or quantum annealing (QA) combined with factorization machine (FM), a machine learning model whose model equation is in the quadratic form. FMA is a promising approach for combinatorial black-box optimization problems including integer-variable optimization problems [2]. To formulate a Hamiltonian for black-box optimization problems, which is not given analytically, FM is used to estimate interaction coefficients between variables. Then SA or QA is applied to find a low-energy state of the estimated Hamiltonian. Since the Hamiltonian estimated by FM is equivalent to an Ising model, we can apply methods that are developed in the field of condensed matter physics to analyze the properties and the performance of FMA. This year, we have conducted a study to improve the performance of FMA, and that to analyze the performance of FMA for an application to explore a stable structure of crystals.

First, we focused on another surrogate model derived from FM, where interactions between variables are sparsely constrained. Sparse interaction is a common property of actual annealing machines such as D-Wave annealers. In addition, the sparse interaction allows SA to update spin variables with less computation time. Hence, developing the FMA method for a surrogate model with sparsely restricted interactions has the potential to improve the optimization performance. Although this study is still ongoing, we have obtained valuable data, e.g., performance of FMQA for given structures of interactions between spin variables, via parallel computing on the supercomputer.

Second, we studied the performance of FMA for predicting grand canonical crystal structures [3]. In this study, we investigated a wide range of configurations to explore the most stable crystal structure with FMA. By using the supercomputer, we have identified the appropriate configuration.

References

[1] K. Kitai *et al.*: Phys. Rev. Research **2** (2020) 013319.

[2] Y. Seki *et al.*: arXiv:2209.01016 (2022).

[3] Y. Couzinié *et al.*: J. Phys. Soc. Jpn. **94** (2025) 044802.

Scaling law of the partition function ratio

Satoshi MORITA
Graduate School of Science and Technology, Keio University
Yokohama, Kanagawa 223-8522

Tensor network (TN) methods are attracting much attention as powerful tools in various fields including quantum many-body physics, quantum computation, and machine learning. In the classical statistical physics, the state sum in the partition function can be represented in the form of TN. However, the contraction of a large TN still requires an exponentially large computational effort. The tensor renormalization group (TRG) method and its variants calculate a coarse-grained tensor by information compression using the singular value decomposition [1]. Adachi, Okubo and Todo have proposed the bond-weighted TRG (BWTRG) method, which improves the accuracy of TRG by introducing a bond weight and distributing it appropriately [2]. We have proposed the finite-size scaling analysis using TRG results [3]. Our recent study showed that the critical temperature and critical exponent are improved from the previous method by calculating the magnetization using BWTRG [4].

In this study, we consider the ratio of partition functions proposed by Gu and Wen [5], This ratio extracts the structure of the fixed-point tensor in the thermodynamic limit and detects the phase transition. This ratio is a dimensionless quantity and its jump indicates the phase transition, which is similar to the Binder parameter frequently used in Monte Carlo methods. We predict that the finite-size scaling of this ratio is similar to the Binder parameter,

$$X_1 \equiv \frac{Z(L,L)^2}{Z(2L,L)} \sim f(L^{1/\nu}\, t).$$

We demonstrate that this scaling actually holds in a wide size range from $L = 2^10$ to 2^20 by high-precision partition function calculations using BWTRG. We investigate the bond dimension dependence of the critical exponent and critical temperature, and show that it converges to the exact value faster than the method using TRG or matrix product states. Furthermore, we derive that the universal value of X_1 at criticality by the discussion of conformal field theory

$$X_1 = \frac{\left(\sum_\alpha e^{-2\pi x_\alpha}\right)^2}{\sum_\alpha e^{-4\pi x_\alpha}},$$

where x_α is the scaling dimension of the scaling operator ϕ_α, and show that our numerical results are accurately consistent with this [4]. It is known that the partition function can be calculated directly by TRG, and its accuracy is higher than that of the magnetization. We believe that this new scaling law will play an important role in the study of phase transitions using tensor network methods.

References

[1] M. Levin and C. P. Nave, Phys. Rev. Lett. **99**, 120601 (2007).

[2] D. Adachi, T. Okubo, and S. Todo, Phys. Rev. B **105**, L060402 (2022).

[3] S. Morita and N. Kawashima, Comput. Phys. Commun. **236**, 65 (2019).

[4] S. Morita and N. Kawashima, Phys. Rev. B **111**, 054433 (2025).

[5] Z. C. Gu and X. G. W, Phys. Rev. B **80**, 155131 (2009).

A molecular dynamics simulation study for immiscible polymer blends

Takeshi SATO
Advanced Manufacturing Technology Institute, Kanazawa University
Kanazawa, Ishikawa 920-1192

Polymer blends, which are commonly used in polymeric products, are known to exhibit phase-separated structures under specific temperatures and compositional conditions. Thus, from both fundamental and engineering viewpoints, it is critical to understand the phase-separation dynamics and the mechanical properties exhibited by the resulting phase-separated structures. Although these two aspects are closely related to the dynamics of the individual component chains, the detailed mechanisms underlying these relationships have not yet been fully elucidated. This problem occurs because it is difficult to evaluate the dynamics of component chains in detail experimentally. Thus, this project conducted a numerical investigation with a coarse-grained molecular dynamics (CGMD) model. CGMD simulations provide microscopic insights into the dynamics of (CG) polymer chains in blends by directly tracking the motion of chains.

This study employed the Kremer-Grest CGMD model, [1] in which CG beads bonded by finitely extensible nonlinear elastic (FENE) springs represent a polymer chain. A Lennard-Jones (LJ) potential was applied between all bead pairs within a certain cutoff distance. We also incorporated an angle potential to introduce a contrast in the glass transition temperatures of polymers. This study addressed several binary blends of unentangled polymers with different glass transition temperatures. We generated a microscopically phase-separated (PS) structure by varying the LJ interaction strength between beads of the same polymer species. [2] We reset the interaction strength to the standard value after forming the PS structure for simplicity. We also prepared polymer blend systems in a uniformly mixed (UM) state without altering the interaction strength. The systems were thermally equilibrated at a temperature between the glass transition temperatures of the two polymers. We then investigated their shear rheological properties. All CGMD simulations were conducted with LAMMPS.

We computed transient shear viscosity η^+ and the first normal stress coefficient Ψ_1^+ of the prepared blends for several different shear rates. PS and UM blends exhibited a distinct overshoot in η^+ before reaching a steady state. We found that the UM system exhibited larger values of η^+ and Ψ_1^+ compared to the PS system with the same composition as the UM system. Moreover, the shear rheological properties of the PS system corresponded closely to the weighted sum of those of the individual components that consist of the blend at the same temperature. These findings serve as an essential stepping stone for numerically investigating the rheology of blends with PS structures.

References

[1] K. Kremer and G. S. Grest: J. Chem. Phys. **92**, 5057 (1990).

[2] W. Peng, R. Ranganathan, P. Keblinski, and R. Ozisik: Macromolecules **50**, 6293 (2017).

A study of the dynamics of thermal equilibrium and nonequilibrium FFLO states using the nonequilibrium Green's function technique

Taira KAWAMURA
Department of Physics, College of Science and Technology, Nihon University
Tokyo 101-8308, Japan

Among various pairing mechanisms beyond the BCS theory, the Fulde-Ferrell-Larkin-Ovchinnikov (FFLO) state is notable for its unique feature of Cooper pairs with nonzero center-of-mass momentum. It can be realized under an external magnetic field, where Zeeman splitting of the energy bands leads to a thermal-equilibrium FFLO state. Recent studies have also proposed a nonequilibrium counterpart, driven by nonequilibrium quasiparticle distributions [1].

In this project, we studied the dynamics of a superconductor driven out of equilibrium by quasiparticle injection from normal-metal electrodes under an external magnetic field, focusing on the interplay between the equilibrium and nonequilibrium FFLO states [2]. To describe this, we derived a time-evolution equation using the nonequilibrium Green's function technique.

The resulting integro-differential equation includes memory terms, making direct real-space simulations challenging. To overcome this computational difficulty, we developed a method to transform it into a set of coupled ordinary differential equations. We then implemented a parallelized solver using OpenMP on the ISSP supercomputing system, enabling us to track the long-time real-space dynamics following a voltage quench.

From these simulations, we obtained the phase diagram shown in Fig. 1. Notably, we identified a novel reentrant mechanism: while moderate quasiparticle injection destroys the thermal-equilibrium FFLO state, stronger injection gives rise to the nonequilibrium FFLO state. These results highlight the potential for controlling quantum states via coordinated manipulation of band structures and distribution functions.

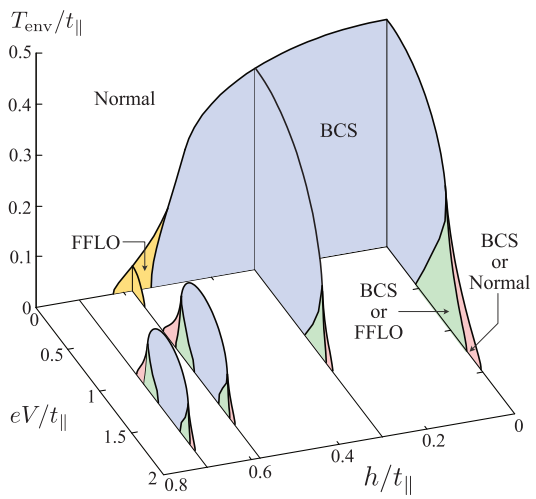


Figure 1: Phase diagram of a superconductor under an external magnetic field h and a bias voltage V [2].

References

[1] T. Kawamura, Y. Ohashi, and H.T.C. Stoof, Phys. Rev. **109**, 104502 (2024).

[2] T. Kawamura and Y. Ohashi, arXiv:2503.04179.

Athermal Simple Shear of Colloidal Gels

Vishnu V. KRISHNAN
RCAST, University of Tokyo
4–6–1 Komaba, Meguro-ku, Tokyo 153–8904

Through our work we aimed to study the mechanical response of colloidal gels to repetitive mechanical deformations. We performed athermal quasistatic shear (AQS) simulations of models of phase-separating colloidal systems in order to probe the evolution of the solid network of the gel. Such a setting models highly overdamped systems at intermediate shear rates where the particles relax to their minima faster than the deformation changes them.

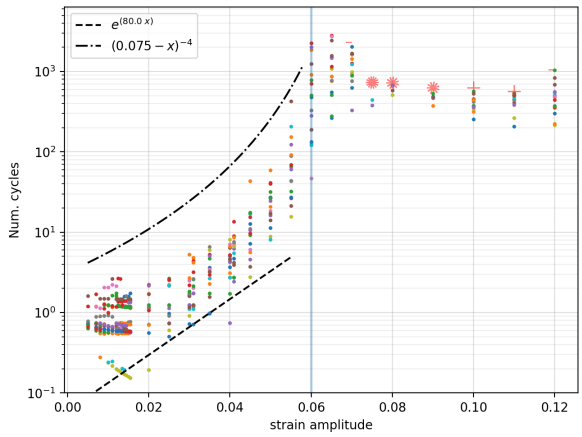


Figure 1: Number of cycles required to achieve steady-state absorption into limit cycles, under *symmetric* AQS. Each color indicates one of 16 distinct samples.

In order to gain a complete understanding of the properties of disordered materials such as gels, one must first comprehend the underlying energy landscape which mediates and dictates both the stable structures and the modes of transformation between them. A crucial feature of amorphous model systems is the existence of limit cycles in this landscape, under AQS deformations. These have been previously utilized, in glasses, to study mechanical properties like yielding. We have made use of similar techniques to better understand corresponding mechanisms in networked materials.

In Figs. 1 & 2 we show the number of strain cycles required by each sample to reach an absorbing state, elucidating the complexity of the energy landscape at each strain amplitude. While the simulations are still on-going, we perceive a maximum in the plots, signifying the existence of a yielding transition in gels. Of even more importance is the existence of absorbing states *after* yield, suggesting the significant role of networks in self-healing.

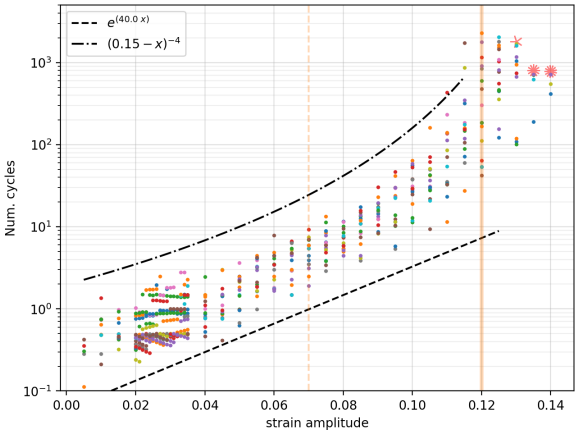


Figure 2: Number of cycles required to achieve steady-state absorption into limit cycles, under *asymmetric* AQS. The spokes in red indicate the number of samples that are yet to be absorbed.

The ISSP infrastructure allowed us to perform extended parallelized simulations using the LAMMPS software.

Performance of uncertainty-based active learning in materials science

Ryo TAMURA
International Center for Materials Nanoarchitectonics,
National Institute for Materials Science,
1-1 Namiki, Tsukuba, Ibaraki, 305-0044

In materials science, materials are synthesized based on information necessary for materials development, such as composition, structure, and processing conditions, and their properties are subsequently measured. This process can be regarded as a function that maps material information as input to material properties as output. This function is called a black-box function because it cannot be described analytically. To optimize a black-box function, black-box optimization methods are developed[1], and most famous one is Bayesian optimization[2]. But, here, we focus on the prediction performance of a black-box function. This is because that obtaining a precise approximation of a black-box function is crucial for understanding and evaluating innovative materials.

Active learning aims to improve such approximations with a limited amount of training data. In this study, we investigate whether uncertainty sampling-based active learning can enable efficient approximation of black-box functions in regression tasks using various materials databases[3]. As materials database, first, we focus on ternary liquidus surfaces where the input space is uniformly distributed and defined in a relatively low-dimensional space. The results demonstrate that uncertainty-based active learning can yield superior black-box functions with higher prediction accuracy compared to random sampling. Furthermore, in cases where the inputs are discretely distributed and imbalanced in a high-dimensional feature space, datasets extracted from inorganic materials, small molecules, and polymer databases are considered. It is shown that uncertainty-based active learning can sometimes be inefficient. Based on the dependence on material descriptors, when the descriptor dimensionality is small, active learning tends to produce better black-box functions than random sampling. The results indicate that active learning is occasionally inefficient in obtaining a better black-box function in materials science.

References

[1] K. Terayama, M. Sumita, R. Tamura, and K. Tsuda, Acc. Chem. Res. **54**, 1334-1346 (2021).

[2] Y. Motoyama, R. Tamura, K. Yoshimi, K. Terayama, T. Ueno, and K. Tsuda, Comput. Phys. Commun. **278**, 108405 (2022).

[3] A. Koizumi, G. Deffrennes, K. Terayama, and R. Tamura, Sci. Rep. **14**, 27019 (2024).

Mechanism of Size Segregation in Granular Media under Vibration: Analysis Based on Effective Interparticle Forces

Fumiaki NAKAI
Department of Earth and Space Science, Osaka University
1-1 Machikaneyama, Toyonaka 560-0043, Japan

When a bidisperse granular mixture is vibrated, particles segregate by size, with particles of similar diameter clustering together—a phenomenon known as size segregation. Several mechanisms have been proposed to account for this behaviour—including convection-driven circulation, void-filling (sinking), depletion-like entropic forces, and segregation caused by gradients in granular temperature (kinetic energy)—yet a comprehensive physical picture has not been established [1]. In this study, we investigated how the steady-state patterns that emerge in a quasi-two-dimensional vibrated bed depend on four key parameters: the partial packing fractions of large and small particles, the size ratio, the acceleration (Γ), and the horizontal system size. The principal results have been published in Granular Matter [2]. We also performed rheological behaviors of a structured granular media [3].

Discrete-element-method (DEM) simulations were carried out with the granular package of LAMMPS. Preliminary test runs were executed on the "i8cpu" partition of the System B supercomputer (Ohtaka) to validate input parameters and estimate computational cost. Production simulations were subsequently carried out on the "F1cpu" partition, using a single compute node with 128 MPI ranks to execute separate runs for each of the 210 distinct parameter sets.

In this study, we investigated a bidisperse granular mixture consisting of 3 mm and 1 mm spheres with a size dispersion of 20 %. The particles were confined between two parallel plates to create a quasi-two-dimensional cell. Structures that developed under vertical vibration were quantified by the radial-distribution

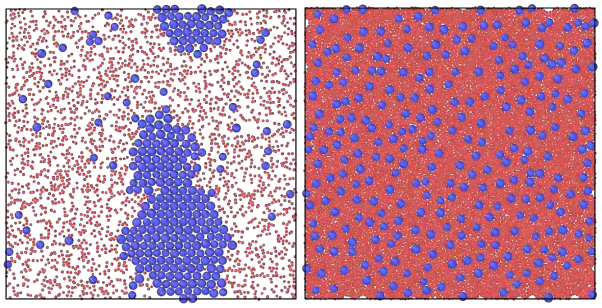


Figure 1: Snapshots of bidisperse granular mixtures in which the packing fraction of large particles (blue) is constant while that of small particles (red) is varied. When the small-particle fraction is dilute (left), the large particles segregate strongly; in contrast, segregation disappears once the small-particle fraction becomes dense (right). This newly observed suppression of segregation is robust across a wide range of size ratios, vibration accelerations, and system dimensions. All segregation simulations were executed on the System B supercomputer (Ohtaka); full details are given in Ref. [2], and related simulations on dislocation-mediated rheology are reported in Ref. [3].

function, the static structure factor, and the hexagonal order parameter over a range of packing fractions. We found that increasing the packing fraction of small particles (ϕ_s) suppresses the segregation of large particles, as illustrated in Fig. 1. This suppression remains robust when the particle-size ratio, system dimensions, or vibration acceleration are varied. The radial-distribution analysis further shows that the effective interaction between large particles depends systematically on ϕ_s: at low ϕ_s an attractive component—reported previously—emerges, whereas at high ϕ_s the interaction becomes predominantly repulsive. The present results have been published in Ref. [2]; a detailed study of the underlying physical mechanism is now in progress.

References

[1] A. D. Rosato and C. Windows-Yule *Segregation in vibrated granular systems*, Academic Press (2020)

[2] F. Nakai and K. Yishii: Granul. Matter **27**, 7 (2025).

[3] F. Nakai, T. Uneyama, Y. Sasaki, K. Yoshii, and H. Katsuragi: arXiv:2410.20308, (2025).

A Large-Scale Molecular Dynamics Simulation Study on the Melt Growth Mechanism of High-Pressure Ice III

Hiroki NADA

Faculty of Engineering, Tottori University, 4-101 Koyama-Minami, Tottori 680-8552

Ice III is one of ice crystal phases that form at high pressure and low temperature conditions. A recent experimental study reported that unknown water, which was different from bulk water, was formed at the interface of ice III during its growth [1]. Thus, in this project, a molecular dynamics (MD) simulation was conducted to elucidate the growth mechanism of ice III from water.

The simulation was performed at 230 K and 315 MPa for a system in which a (100) plane of ice III was in contact with a water phase (Fig. 1). The interaction between pairs of water molecules was calculated using the TIP4P/Ice model. Following a previous study [2], the simulation was carried out with DL_POLY 2.20 using System C of ISSP Supercomputer Center.

The results of the present MD simulation for ice III, which were compared with published results for hexagonal ice (I_h) [3], were summarized as follows. The growth rate was larger for ice III than for I_h. The growth of ice III occurred by a collected molecule process, like in the case for the growth of I_h. The interface for ice III had a diffuse structure, like the interface for I_h. However, the width of the interface was smaller for ice III than for I_h.

Notably, the difference in the density between ice and water was smaller for ice III than for I_h. We speculated that this density difference is correlated with the difference in the growth rate between ice III and I_h. To confirm it, the MD simulation for the growth of ice III was also performed at 400, 500, and 700 MPa. At 400 MPa, the density difference between ice III and water became the smallest, and the growth rate became the largest.

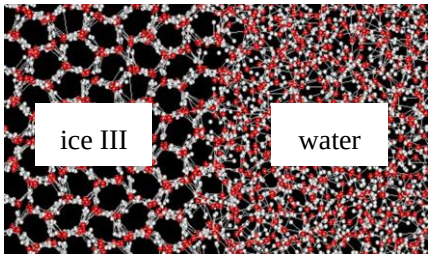


Fig. 1: Snapshots of water molecules near the interface in the simulation system.

References

[1] H. Niinomi, T. Yamazaki, H. Nada, T. Hama, A. Kouchi, T. Oshkiri, M. Nakagawa, and Y. Kimura, J. Phys. Chem. Lett. **15**, 659 (2024).

[2] H. Nada, J. Chem. Phys. **38**, 136 (2022).

[3] P. Montero de Hijes, J. R. Espinosa, C. Vega, and E. Sanz., J. Chem. Phys. **151**, 044509 (2019).

Two variants of discrete-time quantum walk

Manami YAMAGISHI
Department of Physics, The University of Tokyo
Kashiwa-no-ha, Kashiwa, Chiba 277-8581

Naomichi HATANO
Institute of Industrial Science, The University of Tokyo
Kashiwa-no-ha, Kashiwa, Chiba 277-8581

We have considered two non-trivial variants of discrete-time quantum walk. First, we proposed a minimal model of a quantum active particle [1] as a building block of a quantum version of active matter. Active matter is a component that takes up energy from the environment, stores it inside, converts the internal energy into kinetic energy, and thereby moves, or a collection of such components. The introduction of the idea of classical active matter enabled us to unify a variety of studies outside conventional classes of dynamics, dynamics without energy or momentum conservation, that had been investigated separately before and to understand their commonalities and universalities. Some researchers very recently tried to introduce the concept of active matter into quantum systems. Starting with a paper by Adachi *et al.* [2], the research field of quantum active matter is expanding [1, 3, 4, 5, 6, 7].

We proposed a quantum active particle using non-unitary quantum walks in one and two spatial dimensions (1D and 2D). We have observed similarities to a classical active Brownian particle [8] and distinct quantum features at the same time. As a similarity, we observed that dynamics of our quantum active walker becomes more active in a non-trivial way when a non-Hermiticity parameter g, which corresponds to the energy take-up in classical active Brownian particles, becomes larger. As quantum features, we observed ballistic propagation of peaks (1D), particle staying on the constant energy surface (2D) and resonant transition between two energy levels (1D and 2D).

Second, in the hope of eventually proposing quantum active matter in which quantum active walkers interact with each other, we are trying to introduce the Kondo-type interaction [9] between two quantum walkers. We first formulate the standard quantum walk as a massless Dirac particle propagating through a continuum time-space with a series of periodically located delta potentials. This new formulation lets us define the Kondo-type interaction in the following way. We update a delta potential at the origin to one with the inner degree of freedom of a spin. We then introduce a Heisenberg-type interaction between the magnetic impurity spin and the inner degree of freedom of a quantum walker, namely the left-moving and right-moving components.

When we have more than one quantum walker, each quantum walker interacts with the rest through the magnetic impurity spin; which is the Kondo physics. A unique feature of our model is that the inner degree of freedom of the quantum walker is strongly coupled to the spatial movement of the walker, because the left-moving component is shifted to the left in the next time step and the right-moving component to the right. In other words, there is a strong spin-orbit coupling in each quantum walker. This makes the dynamics due to the

Kondo-type interaction quite distinctive from the dynamics of the standard Kondo model.

We have found an exact solution of the bound state of one walker to the magnetic impurity. We then simulated an impact of a second walker colliding to the first walker bounded to the impurity. We discovered that the first walker keeps bounded to the impurity even after the collision of the second walker, which reminds us of the Kondo screening.

We utilized the Supercomputer at ISSP to numerically diagonalize our time-evolution operator, whose maximum size was $(70 \times 70 \times 8)^2$ in two dimensions as well as the case of two interacting quantum walkers. By allocating arrays dynamically, we allowed our system to reach the spatial size of 70×70 (one in the x direction and the other in the y direction).

References

[1] M. Yamagishi, N. Hatano, and H. Obuse: Proposal of a quantum version of active particles via a nonunitary quantum walk, Sci. Rep. **14**, 28648 (2024).

[2] K. Adachi, K. Takasan, and K. Kawaguchi: Phys. Rev. Res. **4**, 013194 (2022).

[3] Y. Zheng, A.P. Antonov, B. Liebchen, and H. Löwen: arXiv:2305.16131 (2023).

[4] R. Khasseh, S. Wald, R. Moessner, C.A. Weber, and M. Heyl: arXiv:2308.01603 (2023).

[5] K. Takasan, K. Adachi, and K. Kawaguchi: Phys. Rev. Research **6**, 023096 (2024).

[6] T. Nadolny, C. Bruder, and M. Brunelli: Phys. Rev. X **15**, 011010 (2025).

[7] A.-G. Penner, L. Viotti, R. Fazio, L. Arrachea, and F. con Oppen: arXiv:2503.07751 (2025).

[8] F. Schweitzer, W. Ebeling, and B. Tilch: Phys. Rev. Lett. **80**, 5044 (1998).

[9] J. Kondo: Prog. Theor. Phys., **32**, 37 (1964).

Deep learning glassy dynamics by graph neural networks

Hayato SHIBA
Department of Information Science, University of Hyogo
Minatojima-Minatomachi, Chuo-ku, Kobe, Hyogo 650-0027

Over the past two decades, the relationship between structure and dynamics in glass-forming liquids has been a subject of intensive discussion. As atomic motion slows down drastically near the glass transition, localized domains of particles that are more likely to undergo rearrangement begin to grow. Recently, machine learning (ML) methodologies have enabled the prediction of where such domains are likely to emerge based on the initial particle configurations. A number of ML models have been proposed for this task, achieving significant improvements in prediction accuracy over the years. The most recent models show comparable performance, though they differ in the details of their predictions. These developments are reviewed in a recent review [1], where the models are compared largely based on a common datasets including that created by our group.

In FY2024, we developed a graph neural network (GNN) model tailored for predicting the dynamics of athermal glasses under quasi-static shear deformation. For training, we used our own simulation dataset of a 3D Kob-Andersen Lennard-Jones mixture, prepared in FY2022. Since external shear breaks the system's rotational symmetry, the resulting deformation evolves anisotropically. To accommodate this, we modified our existing GNN model, BOTAN [2], so that it outputs three-dimensional displacement vectors rather than scalar displacement magnitudes. Inhereting the merit of BOTAN of having another output, changes in inter-particle distances, the model succeded in partially capturing collective motions of particles. We are continuing our efforts to improve the model's prediction accuracy and its consistency with physical aspects highlighted in the direct simluations (training data).

References

[1] G. Jung, R. M. Alkemade, V. Bapst, D. Coslovich, L. Filion, F. P. Landes, A. J. Liu, F. S. Pezzicoli, H. Shiba, G. Volpe, F. Zamponi, L. Berthier, and G. Biroli: Nat. Rev. Phys. **7**, 91-104 (2025).

[2] H. Shiba, M. Hanai, T. Suzumura, and T. Shimokawabe: J. Chem. Phys: **158**, 084503 (2023).

Local structure analysis and non-equilibrium phase transition in self-propelled hard polygon systems

Masaharu ISOBE
Nagoya Institute of Technology
Gokiso-cho, Showa-ku, Nagoya, 466-8555

Hard disk/sphere systems, representing the most fundamental models in statistical mechanics, have been extensively investigated through molecular simulations for both equilibrium and non-equilibrium phenomena [1]. In this project, we investigate the equilibration processes and non-equilibrium phase transitions in self-propelled hard polygon model systems utilizing state-of-the-art computational techniques, specifically Event-Chain Monte Carlo (ECMC)[2, 3], Newtonian Event-Chain Monte Carlo (NECMC)[4], and Event-Driven Molecular Dynamics (EDMD) [5].

Simple and efficient methods for local structural analysis in polydisperse hard disk systems [6]

In nonequilibrium statistical physics, quantifying nearest (and higher-order) neighbors and free volumes of particles is crucial for understanding macroscopic collective phenomena in many-body systems. Conventional techniques using fixed-distance cutoffs or Voronoi constructions have significant limitations, particularly when applied to nonequilibrium, inhomogeneous, and polydisperse systems. These limitations have hindered comprehensive analysis of complex phenomena such as glass/granular jamming transitions and active matter behavior. In this study, we implement several efficient approaches for local structure analysis in nonequilibrium, inhomogeneous, and polydisperse hard disk systems. Through systematic evaluation, we identified limitations in conventional analytical methods when applied to these complex configurations, and confirmed that our "2D SANNex" algorithm effectively overcomes these traditional constraints. Furthermore, we established rigorous mathematical formulations for evaluating higher-order neighbors. We also implemented the neighbors for enclosing local free area ("NELF-A") methodology, which enables precise quantification of local free areas and local pressure in densely packed polydisperse systems. These methodologies provide substantial analytical tools for examining essential local structural information in many-body systems, thereby elucidating slow relaxation dynamics and enabling precise identification and characterization of hopping motion between metastable states in highly packed systems.

Microscopic mechanisms of diffusion dynamics : a comparative efficiency study of event-chain Monte Carlo variants in dense hard disk systems [7]

In molecular simulations, efficient methods for investigating equilibration and relaxation processes in high-density systems are critically important yet challenging. This study examines the diffusional characteristics of monodisperse hard disk systems at equilibrium, comparing novel methodologies of event-chain Monte Carlo methods [3], specifically the Newtonian event-chain [4] and straight event-chain algorithms [2]. We systematically analyze both event-based and CPU time-based efficiency in liquid and solid phases, aiming to elucidate the microscopic mechanisms un-

derlying structural relaxation. Our results demonstrate that NEC frequently exhibits superior efficiency in terms of diffusion coefficient per event and CPU time among ECMC variants, while SEC-xy shows better CPU-time efficiency in certain chain length regimes due to its simplified implementation. The diffusion coefficients display a three-stage behavior with respect to chain length or duration, attributed to increased collision events relative to simple accepted displacements (as in MCMC) and reducible sampling due to finite system size effects. Notably, NEC's diffusion coefficient remains independent of chain duration time in the infinite limit and increases logarithmically with system size, suggesting potential divergence in the thermodynamic limit. These findings provide valuable insights into the optimization of slow equilibrium dynamics in high-density and large-scale systems, particularly for reducing practical computational costs in molecular simulations.

Recursive algorithm to the centroid of free area for inherent structure and hopping motion in deeply supercooled binary hard disk systems [8]

Inherent structures, obtained by removing thermal fluctuations from complex trajectories, reveal fundamental mechanisms of structural relaxation in dense glassy systems. For hard disk/sphere systems, determining these structures is challenging due to discontinuous inter-particle potentials and flat energy landscapes. We introduce the Recursive Centroid of Free Area algorithm (ReCFA), inspired by steepest descent methods, to compute inherent structures in hard disk systems. Our comparative analyses between ReCFA and conventional techniques focused on string-like hopping motions in supercompressed binary hard disks. ReCFA effectively captures entropic contributions and produces physically reasonable particle displacements that identify hopping motions between metastable basins in jammed states. This approach enhances our understanding of relaxation dynamics in highly compressed glassy systems and provides a robust analytical tool for investigating structural characteristics.

Self-organized spatial inhomogeneity in self-propelled quasi-elastic hard disk systems [9]

The freely cooling process in inelastic hard sphere systems has been extensively studied as a fundamental model of granular gases. Here, we investigate the emergence of self-organized spatial inhomogeneities in quasi-elastic hard disk systems through large-scale molecular dynamics simulations. By systematically varying the packing fraction in high-density regimes near the Alder transition point, we identify novel dynamical behaviors and intriguing self-organized spatial patterns not previously reported.

References

[1] M. Isobe: Mol. Sim. **42** (2016) 1317.

[2] E. P. Bernard, W. Krauth, and D. B. Wilson: Phys. Rev. E **80** (2009) 056704.

[3] W. Krauth: Front. Phys. **9** (2021) 229.

[4] M. Klement and M. Engel: J. Chem. Phys. **150** (2019) 174108.

[5] M. Isobe: Int. J. Mod. Phys. C **10** (1999) 1281.

[6] D. Mugita, K. Souno, H. Koyama, T. Nakamura, and M. Isobe: J. Chem. Phys. **160** (2024) 174104.

[7] D. Mugita and M. Isobe: J. Chem. Phys, **161** (2024) 154508.

[8] D. Mugita , K. Souno, and M. Isobe: J. Phys. Soc. Jpn. **94** (2025) 024002.

[9] R. Kitagawa, D. Mugita, N. Murase, and M. Isobe: Proceedings of the 30th Symposium on Traffic Flow and Self-driven Particles, **30** (2024) 9. (in Japanese)

Energy exchange and fluctuations between a dissipative qubit and a monitor under continuous quantum measurement

Tsuyoshi YAMAMOTO

Institute of Pure and Applied Sciences,

University of Tsukuba, Tsukuba, Ibaraki 305-8577, Japan

Quantum measurement can change the state of the measured system, an effect known as *measurement backaction*. Along with this state change, energy can be exchanged between the system and the measurement apparatus. This energy exchange is referred to as quantum heat [1], and it plays a crucial role in the development of quantum thermodynamics and the design of quantum thermal devices.

However, little is known about energy exchange in the presence of dissipation. It has been shown that energy does not flow from the measured system to the measurement apparatus under continuous measurement in the case of a qubit [2]. Nonetheless, the statistical properties remain to be explored.

In this study [3], we focus on the power spectrum, which characterizes the fluctuations in energy flow between a dissipative qubit and a monitor under continuous measurement (see Fig. 1). By solving the stochastic quantum master equation numerically and taking ensemble averaging over 10-100 million trajectories using parallel computation, we find that the fluctuations are unique features of continuous quantum measurement. Notably, the fluctuations can be decomposed into two contributions: quantum jumps and dynamics of measurement backaction. In particular, the latter is a hallmark of continuous measurement and leads to sub-Poisson statistics.

Our findings are expected to guide future developments in measurement-based thermal machines and provide a deeper understanding of quantum thermodynamics in open quantum systems.

This work was supported by the JST Moonshot R&D- MILLENNIA Program Grant No. JPMJMS2061.

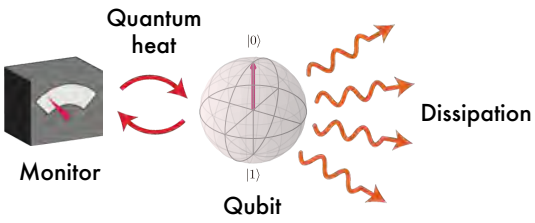


Fig. 1: Schematic of the quantum measurement setup. A measurement apparatus continuously monitors a dissipative qubit.

References

[1] C. Elouard *et al.*, Phys. Rev. Lett. **118**, 260603 (2017).

[2] T. Yamamoto and Y. Tokura, Phys. Rev. Research **6**, 013300 (2024).

[3] T. Yamamoto and Y. Tokura, SciPost Phys. Core **8**, 016 (2025).

Theoretical study of magnetic properties in atomically thin materials

Toshikaze KARIYADO

Research Center for Materials Nanoarchitectonics,

National Institute for Materials Science, Namiki, Tsukuba, Ibaraki 305-0044

We have mainly worked on (1) phonon properties of double wall carbon nanotubes (DWNT) and (2) spin-spin interactions in graphene nanoflakes with decorated edges. The supercomputer is used to perform the first-principles density functional theory (DFT) calculations to analyze structural, electronic, and magnetic properties of DWNT and nanoflakes. We have used Quantum Espresso [1] package for DFT and used Phonopy [2] package for the phonon analysis. Quantum Espresso is well parallelized, and we were able to take advantage of the massive computational resources in the supercomputer.

DWNTs have rich variety in their structures coming from variety in combination of chiralities for inner and outer shells. Experiments show that in some specific combinations of chiralities, there appear new Raman peaks that cannot be explained by superposing Raman spectra from inner and outer shells [3]. Amongst the structures showing new Raman peak, one has relatively small unit cell where the first-principles methods can be applicable. Then, we calculated eigenfrequencies and eigenmodes, and found a mode showing strong hybridization between the inner and outer shells at the frequency of the new Raman peak [3]. The theory suggests that the strong hybridization occurs when the ratio of the radii of the inner and outer shells is close to some simple rational number (in this specific case, 3/5). This well explains the experimental findings.

It is well known that graphene zigzag edges can host magnetism, and it is sensitive to the edge shapes. Then, edge decorated graphene nanofrakes form a promising playground for nanosized spin devices. In this study, we theoretically/numerically proposed a way to have localized spins in nanoflakes, and a way to control the spin-spin interaction between them [4], showing potential of nanoflakes as a foundation for nanoscale spintronics devices.

References

[1] https://www.quantum-espresso.org

[2] https://phonopy.github.io/phonopy/

[3] S. Sun *et al.*, Phys. Rev. Lett., accepted (2025).

[4] T. Kariyado, Materials Today Quantum, accepted (2025).

Dissipative effects on quantum computation

Tatsuhiko Shirai
Waseda Institute for Advanced Study, Waseda University
Nishi Waseda, Shinjuku-ku, Tokyo 169-0051

Thermalization of isolated many-body quantum systems is a fundamental problem in non-equilibrium statistical physics. Although their dynamics follow unitary time evolution, the expectation values of local observables generally relax to those of equilibrium states in the thermodynamic limit. This relaxation can be understood in terms of operator spreading, where a local observable in the Heisenberg picture becomes increasingly delocalized over time, rendering local measurements insensitive to the initial state.

Here, we explore the connection between operator spreading and quantum computation on noisy quantum computers. In recent work [1], we observed that autocorrelation functions in bulk-dissipated many-body quantum systems exhibit accelerated decay during a transient regime before reaching the long-time asymptotic regime. Since noisy quantum computers can effectively be modeled as dissipative many-body systems, we expect this accelerated decay to be observable in such platforms. To investigate this, we consider two-point measurement of a local observable at times $t = 0$ and $t = 2T$, wth the system evolving under noise for the total duration $2T$. The coherent parts of the forward and backward processes (for $0 \leq t \leq T$ and $T \leq t \leq 2T$, respectively) are represented by unitary operators U and $U^\dagger$. We find that the resulting correlation function exhibits the accelerated decay as a function of T. These findings were verified through numerical simulations using OpenMPI (see Fig. 1).

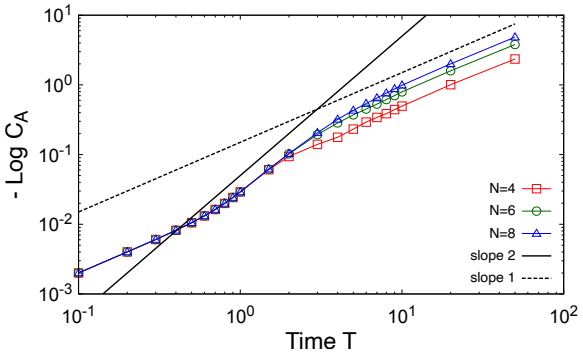


Figure 1: Dependence of the correlation function on execution time T for various system sizes. Accelerated decay is observed in the range $1 \leq T \leq 2$, and the duration of this transient regime increases with system size.

References

[1] T. Shirai, T. Mori: Phys. Rev. Lett. **133**, 040201 (2024).

Long-term reliability assessment of reinforced concrete structures with a surface polymer barrier layer.

T. Ishida[1)], F. Nakai[2)]

1) Department of Materials Physics, Graduate School of Engineering, Nagoya University, Furo-cho, Chikusa, Nagoya 464-8603, Japan

2) Department of Earth and Space Science, Osaka University, 1-1 Machikaneyama, Toyonaka 560-0043, Japan

Low-molecular species (Cl^-, CO_2, O_2, etc.) diffuse through the polymer barrier and concrete cover to reach steel reinforcement and initiate corrosion, which governs the service life of RC structures. To predict the onset of corrosion realistically, we must account for long-term degradation of the polymer coating and model molecular transport through the heterogeneous cementitious matrix. In this project we use coarse-grained molecular dynamics and kinetic Monte Carlo methods to (1) simulate nonequilibrium ageing of the polymer barrier and (2) compute diffusion of low-molecule penetrants in cementitious media, integrating these results to estimate the effective lifetime of coated RC elements.

For polymer degradation simulations, we investigated how the diffusivity of free radicals generated during polymer degradation affects the progression of aging using LAMMPS. The results showed that while low radical diffusivity slightly enhances heterogeneous degradation, its overall impact on the degradation scenario is limited. slightly amplifies localized (heterogeneous) degradation and has a minimal impact on the overall degradation pathway [1].

For the diffusion of penetrants in cement paste, we found that, within a certain short-time regime, the displacement distributions of gas molecules deviate from the Gaussian form, exhibiting heavy tails. The duration of this non-Gaussian behavior depends on both the gas species and the porosity, as shown in Fig. 1 [2].

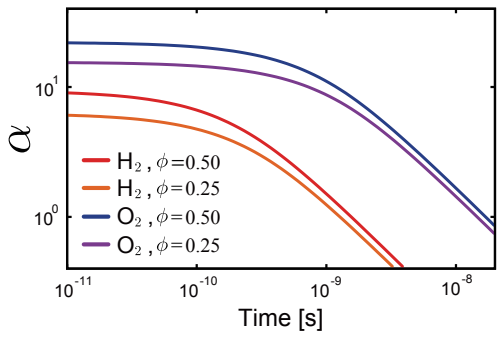


Fig. 1 Duration of the Non-Gaussian Parameter

References

[1] T. Ishida, etal. Polym. J., **56**, 1069–1078 (2024).

[2] F. Nakai, T. Ishida, J Soc Rheol Jpn, **52**(2), 83-89 (2024).

Spin dynamics in J_1-J_3 antiferromagnets on kagome lattices

Kazushi AOYAMA
Department of Earth and Space Science, Graduate School of Science, Osaka University
Machikaneyama-cho, Toyonaka, Osaka 560-0043

Real-space structures of magnetic orders are often reflected in spin dynamics. In this work, we theoretically investigate the spin dynamics in three different types of triple-**Q** states emerging in J_1-J_3 antiferromagnets on the breathing kagome lattice whose Hamiltonian is given by

$$\mathcal{H} = J_1 \sum_{\langle i,j\rangle_S} \mathbf{S}_i \cdot \mathbf{S}_j + J_1' \sum_{\langle i,j\rangle_L} \mathbf{S}_i \cdot \mathbf{S}_j + J_3 \sum_{\langle\langle i,j\rangle\rangle} \mathbf{S}_i \cdot \mathbf{S}_j, \quad (1)$$

where $\mathbf{S}_i$ is a classical Heisenberg spin, J_1 (J_1') is the exchange interaction for the site pair on small (large) triangles, and $J_3 > 0$ is the third nearest neighbor interaction along the bond direction. For strong J_3, a 12-sublattice triple-**Q** state characterized by the three ordering vectors $\mathbf{Q}_1 = \frac{\pi}{2}(-1, -\frac{1}{\sqrt{3}})$, $\mathbf{Q}_2 = \frac{\pi}{2}(1, -\frac{1}{\sqrt{3}})$, and $\mathbf{Q}_3 = \frac{\pi}{2}(0, \frac{2}{\sqrt{3}})$ is favored. It takes a noncoplanar, coplanar, or collinear structure depending on the breathing parameter J_1'/J_1 and temperature T [1]. The noncoplanar state possesses nonzero net chirality $\chi^T \neq 0$, and energetically degenerate two spin configurations can be distinguished by the sign of χ^T.

By numerically integrating the spin-dynamics equation

$$\frac{d\mathbf{S}_i}{dt} = \mathbf{S}_i \times \mathbf{H}_i^{\rm eff}, \quad \mathbf{H}_i^{\rm eff} = -\sum_j J_{ij}\mathbf{S}_j, \quad (2)$$

we calculate the dynamical spin structure factor $S(\mathbf{q},\omega) = |\frac{1}{t_0}\int dt\, \frac{1}{3L^2}\sum_i \mathbf{S}_i e^{-i(\mathbf{q}\cdot\mathbf{r}_i - \omega t)}|^2$ for $t_0 = 1000/J_1$ and $L = 288$, where the initial equilibrium spin configurations are prepared by using Monte Carlo simulations. Although in the collinear and coplanar states, $S(\mathbf{q},\omega)$ is symmetric with respect to the Γ point, it becomes asymmetric in the nonccoplanar case with $\chi^T \neq 0$ (see Fig. 1), suggesting that nonreciprocal spin waves emerge in the chiral phase. It is also found that such an asymmetry flips when the chirality χ^T flips. By further performing the spin-wave expansion, we find that the asymmetry or nonreciprocity microscopically originates from geometric phases acquired in the spin-wave propagation processes [2].

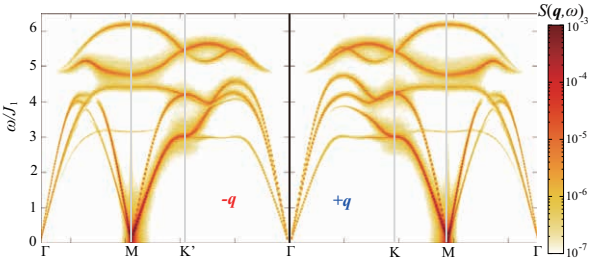


Figure 1: $S(\mathbf{q},\omega)$ obtained in the noncoplanar state for $J_1'/J_1 = 0.8$ and $T/J_1 = 0.08$ [2].

References

[1] K. Aoyama and H. Kawamura: Phys. Rev. B **105**, L100407 (2022); J. Phys. Soc. Jpn. **92**, 033701 (2023).

[2] K. Aoyama and H. Kawamura: Phys. Rev. B **111**, 144413 (2025).

Modeling for interaction between gas-phase reaction with pattern formation and solid surface

Takaki AKIBA

Department of Mechanical Engineering,

The University of Tokyo, Hongo, Bunkyo-ku, Tokyo 113-8656

To understand the coupled physics of gas-solid interactions in reacting flows, methods for chemical reaction simulation were developed.

Three-dimensional combustion models with two variables of temperature and fuel concentrations were designed for GPU acceleration (Fig. 1). Previously the simulation was designed for MPI with multi-node CPU clusters. With the use of GPU resources at ISSP C system through CUDA SDK with a Fortran interface, we achieved comparable performance using a single GPU chip, matching the computing speed of over 2000 MPI processes on CPUs.

Another framework was developed for chemical reaction simulations for quantum computing. As quantum computers can only handle problems described by linear algebra, while the chemical reaction inherently involves non-linearities due to collisions and temperature-dependent reaction rates, we applied Carleman linearization to bridge this gap. Carleman linearization transforms nonlinear systems into high-dimensional linear systems that preserve essential nonlinear behavior. However, the resulting linear systems are often too large to solve efficiently. In this project, the linearization pre-process was performed on CPU, while the solution of the large linear system was accelerated using the CUDA SDK with a C++ interface on GPU. This hybrid approach achieved over a tenfold speedup compared to a CPU-only implementation (Fig. 2).

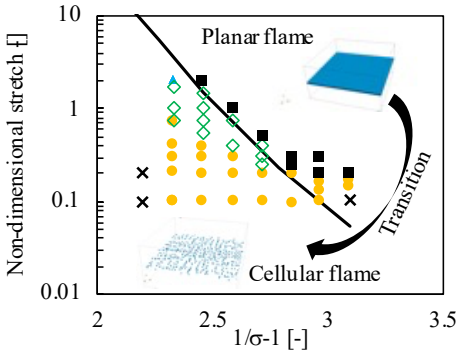


Fig. 1 Flame transition with three-dimensional combustion simulation

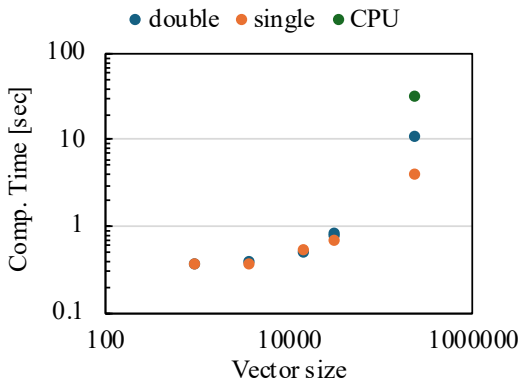


Fig. 2 GPU acceleration for chemical reaction problems with Carleman linearization.

Solitons and phase transitions in quantum chiral spin model in tilted magnetic field

Yusuke MASAKI
Department of Applied Physics, Tohoku University
Sendai, Miyagi 980-8579

Classical spin models of monoaxial chiral magnets predict a continuous phase transition (CPT), known as the Dzyaloshinskii transition, driven by chiral solitons under magnetic fields perpendicular to the helical axis (nucleation-type CPT, Fig. 1). In tilted magnetic fields, two multicritical points, T and M (Fig. 1), emerge, leading to discontinuous phase transitions (DPTs) in intermediate angular regions due to attractive soliton interactions. Recent theoretical investigations of the corresponding quantum spin models (which we call quantum monoaxial chiral magnets) have revealed novel phenomena, such as spin parity effects in small systems with periodic boundary conditions and quantum tunneling across surface barriers in magnetization processes. However, how quantum nature of spins modifies classical phase transitions, such as DPTs and the Dzyaloshinskii transitions in Fig. 1, remains unexplored.

This year, we have numerically investigated magnetization process and phase transitions in quantum monoaxial chiral magnets under tilted magnetic fields using the density matrix renormalization group (DMRG) and tensor renormalization group (TRG). Our DMRG calculations suggest that the first-order behavior persists for $S \geq 1$, but transitions become continuous for $S = 1/2$. DMRG results on the surface-spin modulation indicate attractive soliton interactions, which can explain the origin of the DPTs, consistent with classical results. However, for $S = 1/2$, the order of

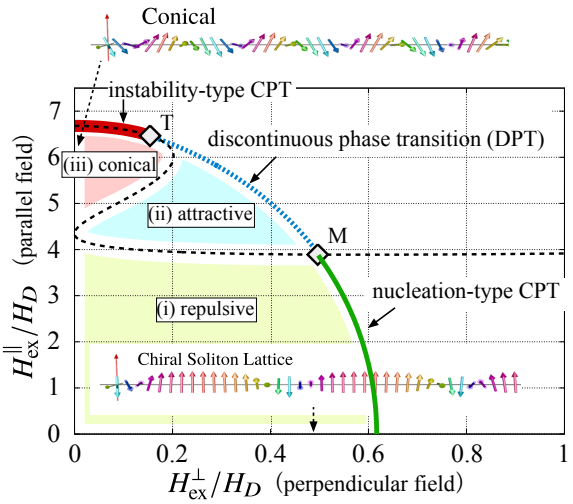


Figure 1: Phase diagram of a classical spin model for a monoaxial chiral magnet under a tilted magnetic field.

the phase transitions is altered probably due to quantum tunneling. We have also studied phase transitions through magnetization curves and energy gaps using tensor network methods, specifically the higher-order TRG, enabling precise calculations for large systems with periodic boundary conditions. Our results identify a distinct point on the CPT line for S=1/2, at which the nature of the CPT changes, while the whole phase boundary remains continuous. This structure is reminiscent of the finite-temperature phase diagrams, where thermal fluctuations compress the DPT region into a single critical point.

Density of States for Selenium Chains Confined in Carbon Nanotubes Through First-Principles Calculations

Md Saiful ISLAM and Hiroyuki IKEMOTO
Department of Physics, University of Toyama, Toyama, 930-8555, Japan

Selenium (Se) is a group 16 element in the periodic table that belongs to the chalcogen family and exhibits unique structural properties. As a chalcogen, selenium naturally forms a hierarchical structure, where the primary structure is a three-turn helical chain and these chains further assemble to form the trigonal selenium (t-Se) crystal structure. Isolated selenium chains are interesting because they are one dimensional system and lack the inter-chain interactions present in the bulk. Our X-ray absorption fine structure measurements showed a temperature-dependent drop in the coordination number of selenium confined in single-walled carbon nanotubes (Se@SWCNT), suggesting a possible Peierls transition—a metal-to-semiconductor phase transition associated with splitting of the covalent bond into two types [1].

We conducted ab-initio calculations employing the Quantum ESPRESSO package, which is based on density functional theory (DFT) with plane-wave basis sets and pseudopotentials. We used the generalized gradient approximation (GGA) with the Perdew–Burke–Ernzerhof (PBE) exchange-correlation functional. Self-consistent field (SCF) calculations were performed to optimize the energy and k-point meshes for each system. The electronic density of states (DOS) was then computed for SWCNT, Se@SWCNT, and various isolated selenium chains including a three-turn helical chain, two collinear chains, and a planar zigzag chain.

Figure 1 compares the DOS of candidate selenium chain structures within SWCNT. The first candidate is a three-turn helical chain, as it is the primary structure for bulk t-Se; the second one is two collinear chains, which was suggested by electron spectroscopy [1], and the third one is a planar zigzag conformation which was expected in sulfur case [2]. According to Figure 1, while the three-turn helical chain exhibits semiconducting behavior, both the two collinear chains and the planar zigzag chain display metallic characteristics. These findings indicate that the electronic properties of selenium are highly sensitive to its structural conformation.

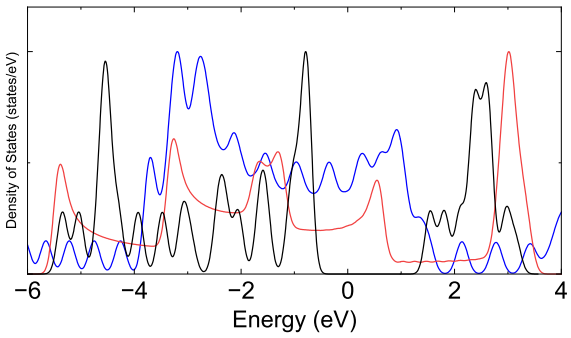


Figure 1: DOS for selenium structures: three turn helical chain (black), two collinear chains (blue), and a planar zigzag chain (red).

We are performing photoemission spectroscopy (PES) measurements on single-wall CNT (SWCNT) and Se@SWCNT to obtain DOS of the selenium confined in single-wall CNTs (SWCNT). PES signals are sensitive to

surface material, so PES of Se@SWCNT was very close to SWCNT. At this stage, we obtained the PES for confined selenium chains by subtracting the PES spectrum of Se@SWCNT from that of SWCNT. However, this method may oversimplify the actual spectral contributions. Therefore, to assess the validity of this approach, theoretical calculations are crucial.

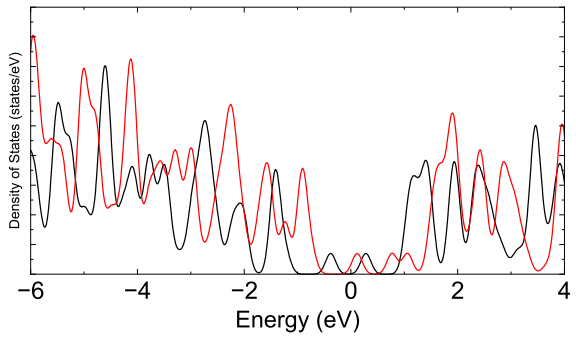


Figure 2: The DOS of SWCNT (black), and Se@SWCNT (red).

Figure 2 presents the DOS of the SWCNT, and the combined Se@SWCNT system. The obtained DOS were clearly different from each other, which was different from PES signal. The difference may come from two reasons, one is that PES signals are sensitive to the surface, and the other is the precision of the calculations.

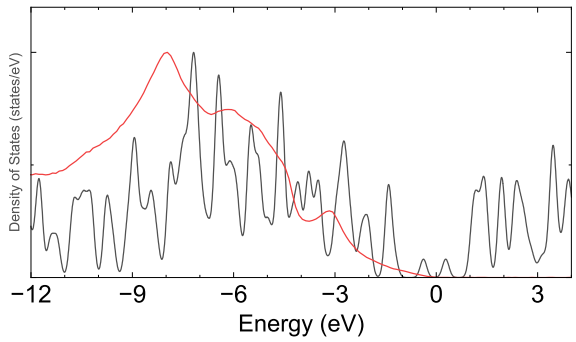


Figure 3: Comparison of the theoretical (black) and experimental (red) DOS of SWCNT.

Figure 3 compares the theoretical and experimental DOS for SWCNTs. The theoretical DOS exhibits sharper features compared to the broad peaks seen experimentally. This discrepancy could be due to differences in chirality, and diameter of the SWCNT model, or insufficient broadening in the theoretical model. Alternatively, it may indicate that the computational parameters require reconsideration.

Therefore, to obtain DOS of confined selenium chain in SWCNT, we have to first focus on improving our calculations. After reconsidering the calculation model and parameters, we will perform new calculations and carry out a detailed comparison with the experimental data to gain deeper insights into the structural–electronic correlations in confined selenium systems.

References

[1] H. Ikemoto, T. Fujimori, T. Miyanaga, R. Kawaguchi, K. Urita, and M. Tabuchi, *Structures of Se chains encapsulated in single-walled carbon nanotubes*, J. Phys. Chem. Solids **185**, 111737 (2024).

[2] T. Fujimori, A. Morelos-Gómez, Z. Zhu, H. Muramatsu, R. S. Sinha, M. Terrones, M. Endo, and K. Kaneko, *Conducting linear chains of sulphur inside carbon nanotubes*, Nature Communications, **4**, 2162 (2013).

Friction law for macroscopic objects driven at high speed

Michio OTSUKI

Graduate School of Engineering Science,

The University of Osaka, Machikaneyama, Toyonaka, Osaka 560-8531

In sliding contact of viscoelastic material, it is known that hysteresis friction occurs due to the delay in deformation caused by viscosity. However, many aspects remain unexplored regarding the behavior of hysteresis friction at high sliding velocities near the elastic wave velocity, such as those observed in airplane tires during landing.

In this study, we investigate hysteresis friction on a rigid indenter in sliding contact with a viscoelastic substrate using finite element simulations. The computational size is 1,000,000 nodes and 100,000,000 time steps. The calculation takes 12 hours using our in-house code compiled with the Intel Fortran compiler and 300 MPI processes on the CPU servers. Here, the Young's modulus of the viscoelastic substrate is E, the density is ρ, and the viscosity coefficient is $\tilde{\eta}$.

As shown in Fig. 1, the friction coefficient μ depends on the sliding velocity V and has a peak at a certain velocity that depends on the viscosity coefficient $\tilde{\eta}$. Furthermore, we find that the friction coefficient μ changes dramatically at sliding velocities near the elastic wave velocity scale $c = \sqrt{E/\rho}$ due to a singular deformation [1].

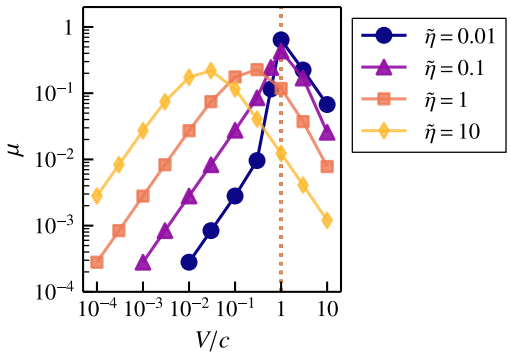


Fig. 1: Dependence of friction coefficient μ on sliding velocity V/c for various viscosity coefficients $\tilde{\eta}$. The vertical dashed line represents the elastic wave velocity scale $V/c = 1$.

References

[1] W. Iwashita and M. Otsuki, The 4th Malaysian International Tribology Conference (MITC2024), 69 (2024).

On the microstructure and loading behavior of graphene-nanospacer structure with molecular dynamics simulation

Mingda Ding, Taiki Inoue, Yoshihiro Kobayashi

Department of Applied Physics, The University of Osaka, Yamadaoka, Suita, Osaka 565-0871

This year, we studied the microstructure of graphene (Gr) stacking structures with nanodiamond (ND) nanospacer and the effect of carbon nanotube (CNT) spacers on the mechanical behavior of using molecular dynamics (MD) simulations. The insertion of nanospacers between Gr layers effectively modulates the interlayer distance and interlayer interaction [1]. The insertion of CNTs can also change the mechanical response of multilayer Gr [2]. By adjusting the inter-spacer distance and the size of CNTs, we gain insight into the deformation mechanisms and energy variations in these nanostructures.

MD simulations were conducted using the open-source software LAMMPS (Large-scale Atomic/Molecular Massively Parallel Simulator). The system sizes ranged from 10,000 to 800,000 atoms, depending on the lateral size of the Gr layers. The AIREBO potential was used to describe the short-range interactions, while the Lennard-Jones (LJ) potential was employed for interlayer van der Waals interactions. Dynamic relaxation was performed using the velocity-Verlet algorithm to obtain energy-minimized structures.

Computational resources were allocated across different systems based on the complexity of the simulation. Large-scale graphene and nanodiamond (Gr-ND) simulations were primarily conducted on System B (Ohtaka) with 2–4 nodes, requiring a computational time of 16–72 hours per simulation. In contrast, the graphene and carbon nanotube (Gr-CNT) stacking structures, which typically required smaller system sizes, were simulated on System C (Kugui) using 1–2 nodes with a computational time of 5–24 hours per simulation.

The MD simulations focused on two types of stacking structures: Gr-ND (Figure 1a) and Gr-CNT (Figure 1b). By applying periodic boundary conditions, systems with different areal densities of NDs and CNTs were examined. Additionally, simulations were performed with various diameters of nanospacers to analyze their influence on the transition between Gr layer separation and interlayer adhesion. The results showed that a decrease in nanospacer areal density led to a transition from Gr layer separation to interlayer adhesio, consistent with our experimental

observations. Moreover, larger nanospacers required a higher critical areal density to maintain suspension. Energy analysis revealed that the difference between deformation energy and adhesion energy of the separation and adhesion structure governs the stability of different configurations [1].

modulation of multilayer Gr structures via nanospacer insertion. The findings contribute to the functional enhancement of multilayer Gr for potential applications in flexible electronics, coatings, and energy storage devices.

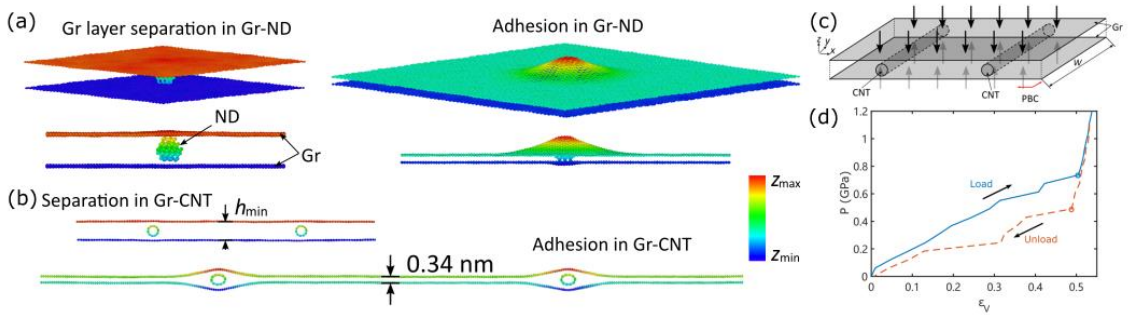


Figure 1 (a) Deformed configuration obtained by MD simulation of graphene (Gr) and nanodiamond (ND) stacking structure (Gr-ND) with Gr layer separation (shorter inter-ND distance) and adhesion (larger inter-ND distance). (b) Gr and carbon nanotube (CNT) stacking structure (Gr-CNT) with Gr layer separation (shorter inter-tube distance) and adhesion (larger inter-tube distance). (c) The schematic of the loading press of Gr-CNT stacking structure. (d) Loading-unloading curve of the Gr-CNT stacked structure with hysteresis.

Then, the loading-unloading pressure (Figure 1c) is imposed on the Gr-CNT system [2]. The hysteresis force curve is observed, which means the loading and unloading curves are inconsistent (Figure 1d). The hysteresis is the symbol of energy dissipation. The energy dissipation is verified by experiment and has application in lightweight damping and energy absorption structures.

Our study provides fundamental insights and mechanism exploration into the mechanical

References

[1] M. Ding, T. Inoue, J. I. Enriquez, H. H. Handoko, Y. Ogawa, Y. Taniyasu, Y. Hamamoto, Y. Morikawa, Y. Kobayashi, Carbon **229**, 119464 (2024).

[2] M. Ding, N. Sakurai, T. Inoue, T. Matsuzaki, T. Mizuno, K. Suzuki, J. I. Enriquez, H. H. Halim, Y. Hamamoto, H. Yoshikawa, Y. Morikawa, Y. Kobayashi, (In preparation).

Development of integrated interface of eigensolvers Rokko and application to quantum spin systems

Tatsuya Sakashita
Department of Physics, The University of Tokyo
7–3–1 Hongo, Bunkyo-ku, Tokyo 113–0033

To establish universal exact diagonalization package for quantum lattice models including the Heisenberg–Kitaev model, we focused on developing integrated interfaces for eigensolvers, "Rokko" [1].

In Rokko, we implemented the integrated interfaces for the following types:

- Serial solvers for dense matrices (Eigen3, LAPACK)
- MPI parallelized solvers for dense matrices (EigenExa [2], ELPA [3], Elemental [4], ScaLAPACK)
- MPI parallelized solvers for sparse matrices (Anasazi in Trilinos [5], SLEPc [6]) to cover matrix representations below:
  - CRS (Compressed Row Storage)
  - Matrix-free method (the method to give matrix-vector product routines to solvers)

Rokko has the following features:

- Integrated interfaces for eigensolvers and matrices, independent of individual eigensolver libraries
- Rokko's interfaces are implemented by utilizing factory. It enables the user to dynamically select a solver.
- C, Fortran, and Python bindings of Rokko
- Automatically detecting libraries by using CMake in building Rokko
- Unit and integrated test programs by GoogleTest
- Install scripts of eigensolvers for various architectures

We prepare a paper to report design policy, software structure, and usage examples of Rokko.

References

[1] T. Sakashita, R. Igarashi, Y. Motoyama, T. Okubo, and S. Todo. Repository of Rokko. `https://github.com/t-sakashita/rokko.git`, 2012.

[2] T. Imamura, T. Hirota, and T. Fukaya. EigenExa web page. `https://www.r-ccs.riken.jp/labs/lpnctrt/projects/eigenexa/`, 2021.

[3] ELPA Consortium. ELPA (Eigenvalue soLvers for Petaflop Applications web page). `https://elpa.mpcdf.mpg.de/`, 2013.

[4] J. Poulson. Distributed-memory dense linear algebra Elemental web page. `https://github.com/elemental/Elemental`, 2013.

[5] M. A. Heroux, R. A. Bartlett, and V. E. Howle. Trilinos Project web page. `https://trilinos.github.io`, 2003.

[6] V. Hernandez, J. E. Roman, and V. Vidal. SLEPc web page. `http://slepc.upv.es`, 2002.

Structure analysis of atomic layer alloy with Rashba effect studied by TRHEPD

R. Takahashi[A], L. Konermann[A], I. Mochizuki[B], K. Wada[B], T. Hyodo[B] and A. Takayama[A,C]

[A]*Department of Physics, Waseda University, Ohkubo, Shinjuku-ku, Tokyo 169-8555*

[B]*IMSS, KEK, Oho, Tsukuba, Ibaraki 305-0801*

[C]*IMRAM, Tohoku University, Katahira, Sendai, Miyagi 980-8577*

Introduction

The superconducting phenomenon that occurs in the spin-split electronic state due to the Rashba effect is theoretically predicted to be an unconventional superconducting state where *s*-wave and *p*-wave superconductivity coexist (Rashba-SC). In order to investigate the details of this Rashba-SC, material exploration and research on its electronic states are being actively conducted. Previous studies have shown that (Bi, Pb) single-atom layer (SAL) alloys on Ge(111) and Si(111) substrates are predicted to exhibit Rashba-type spin-split bands due to the strong spin-orbit coupling of Pb and Bi [1]. We revealed several metallic electronic states exhibit with spin-splitting in the (Bi, Pb)-Ge(111)-2×2 structure by angle- and spin-resolved photoemission spectroscopy.

In this study, we performed structural analysis of several SAL structures exhibiting the Rashba effect in order to discuss the details of the Rashba effect in SAL structures from a structural perspective, using by total-reflect high-energy positron diffraction (TRHEPD). Here, we report mainly on structural analysis of Bi/Ge(111), Pb/Ge(111), and (Bi, Pb)/Ge(111).

Experiments and analysis methods

The TRHEPD measurements were performed at the Slow Positron Facility, KEK. The TRHEPD experiment involves measuring a series of diffraction patterns for a fixed incident azimuthal direction at various glancing angles (θ). In this context, the rocking curve (RC) is defined as the diffraction intensity of the (00) spot plotted as a function of θ.

In the structural analysis, the experimental rocking curves are compared with those calculated for various structural models. The locking curves for each structure were calculated and compared with experimental results using the structural analysis program ODAT-SE (2DMAT) [2]. Specifically, large-scale calculations were performed on supercomputers, including: (i) long-period structure induced by the striped-incommensurate (SIC) phase in Pb/Ge(111), and (ii) structural analysis with multiple parameters set for (Bi, Pb) SAL structure with unclear structural model.

Results and discussion

Figure 1(a) shows the results of structural analysis for Pb/Ge(111)-√3×√3 structure. The RC calculated from the structural model proposed by Otsubo *et al*. [3] reproduced the experimental results relatively well. In this study, structural optimization was performed using Nelder-Mead method, and we concluded that the structural model shown in Fig. 1(a) is the most reliable. Additionally, rocking curves were

calculated for a long-period structure incorporating the SIC phase, which revealed that there were no significant changes in the calculation results. Structural analysis was also performed on Bi/Ge(111)- √3×√3 structure, as shown in Fig. 1(b). The RC calculated from the structural model proposed in previous study [4] reproduced the experimental results very well. In both structures, it was found that there was almost no structural relaxation of Ge in the out-of-plane direction. Furthermore, we also found that slight differences in the in-plane positions of Pb (T_4 site) and Bi (T_1 site) atoms greatly affect the shape of RC.

Figure 2 shows the RCs of (Bi, Pb)/Ge(111)-2×2 structure and the RCs calculated from the structural model proposed in previous studies. The calculated RC from the 2×2 structure model proposed by Mihalyuk *et al*. [1] does not match the experimental RC. Currently, we are performing structural analysis following two different approaches. The first approach is structural optimization based on the Mihalyuk model. In this approach, the structure can be determined by varying the distances and configurations between atoms. The second proposal addresses the fact that the ratio of Bi and Pb in the 2×2 unit cell has not yet been determined. To investigate this, we will investigate structural models by adjusting the atomic densities of Pb and Bi as parameters.

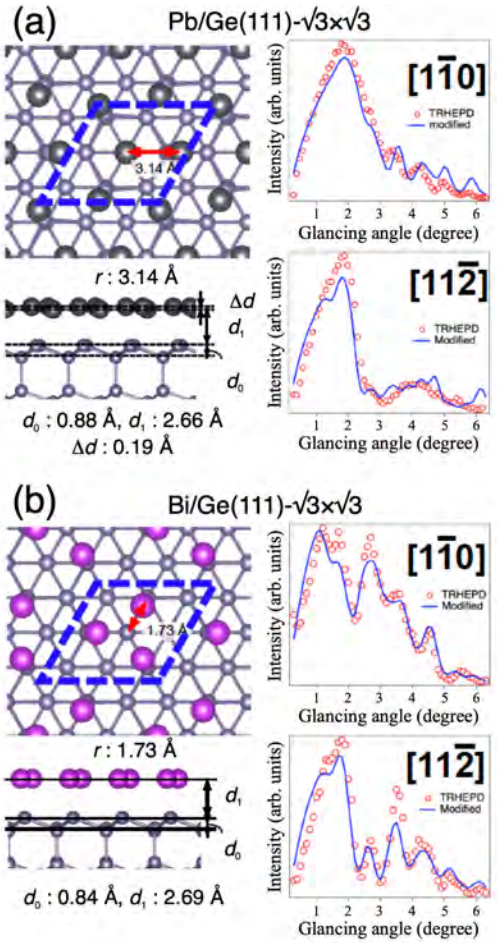


Fig. 1: Results of structural analysis by TRHEPD of (a) Pb/Ge(111)-√3×√3 and (b) Bi/Ge(111)-√3×√3. (left) Determined structural model. (right) RCs with calculated curves under many-beam conditions.

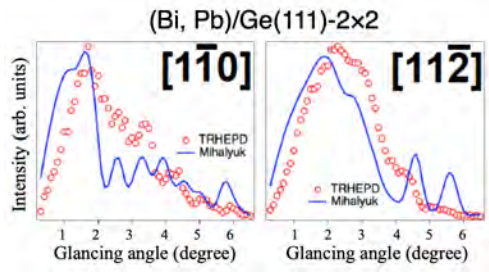


Fig. 2: RCs under many-beam conditions for (Bi, Pb)/Ge(111)-2×2 structure with calculated curves from proposed structural model in previous study [1].

References

[1] A. Mihalyuk, *et al*., Front. Mater. **9**, 882008 (2022).
[2] Y. Motoyama, *et al*., Computer Physics Communications, **280** (2022) 10846.
[3] Y. Ohtsubo, *et al*., J. Phys.: Condens. Matter., **23**, 435001 (2011).
[4] Y. Ohtsubo, *et al*., J. Phys.: Condens. Matter., **21** 405001 (2009).

Molecular spin dynamics study on the multiple-Q orders in Hubbard models

Takashi UCHIDA
Hokkaido University of Science
4-1, 7-15, Maeda, Teine-ku, Sapporo 006-8585

Recently, the magnetic structures of multiple-Q states have attracted attention since the topologically protected magnetic structures such as magnetic skyrmions emerge as 3Q helical orders in the Dzyaloshinskii-Moriya (DM) interaction driven systems under magnetic field. The topologically nontrivial multiple-Q orders can also be realized in centrosymmetric systems where the DM interaction is absent [1]-[3]. The stabilization mechanism of multiple-Q orders in the latter systems, however, is not unique and still under investigation.

The purpose of the present research is to investigate the stability of multiple-Q orders in the centrosymmetric triangular-lattice single-band Hubbard model by means of the molecular spin dynamics (MSD) method [4]. The present formulation of the MSD adopts the static approximation to the functional integral method and the isothermal molecular dynamics technique, and reduces to the generalized Hartree-Fock approximation at the ground state.

In the present MSD scheme, the most time-consuming process in the numerical calculations is the magnetic force calculation at each time step, where the local electronic structures are calculated in real space by means of the recursion method [4]. We have adopted the MPI parallel calculation scheme and found it effective in saving both computing time and CPU resources.

In the present work, we have included the 3rd neighbor hopping integral t_3 in addition to the nearest neighbor hopping integral t_1 in the Hubbard model. We have performed magnetic structure calculations on a hexagonal supercell with 972 lattice points, which is embedded in a large cluster consisting of 6 such supercells, each of which are connected by the periodic boundary condition. Under zero magnetic field and the fixed value of the temperature $T/t_1 = 0.0005$, we have explored the magnetic structures changing the Coulomb interaction strength U/t_1, the hopping integral ratio t_3/t_1, and the electron number n. For $t_3/t_1 = -0.40$, $n = 1.21$ and $U/t_1 = 7.0$, the dominant magnetic order was found to be a 3Q noncoplanar order with commensurate wave vectors $\boldsymbol{Q_1} = (2\pi/a)(1/3, 0)$, $\boldsymbol{Q_2} = (2\pi/a)(-1/6, \sqrt{3}/6)$ and $\boldsymbol{Q_3} = (2\pi/a)(-1/6, -\sqrt{3}/6)$ (a being the lattice constant). The electronic density of states becomes zero in the vicinity of the Fermi energy E_{F}, opening a gap at E_{F}. This suggests that the Fermi surface nesting occurs for the wave vectors $\boldsymbol{Q_1}$, $\boldsymbol{Q_2}$ and $\boldsymbol{Q_3}$, stabilizing the 3Q orders.

References

[1] T. Okubo, S. Chung, and H. Kawamura: Phys. Rev. Lett. **108** (2012) 017206

[2] Y. Kakehashi: J. Phys. Soc. Jpn. **89** (2020) 094710.

[3] K. Kobayashi and S. Hayami: Phys. Rev. B**106** (2022) L140406.

[4] Y. Kakehashi, S. Akbar, and N. Kimura: Phys. Rev. B**57** (1998) 8354.

Proposal of novel superconducting states coexisting/competing with higher-order magnetic multipole order or helical magnetism

Shuntaro SUMITA
Department of Basic Science, The University of Tokyo, Meguro, Tokyo 153-8902

We have theoretically studied a variety of intriguing topological phenomena in strongly correlated electron systems by using numerical methods including first-principles calculations, quantum many-body calculations, and machine learning (project number: 2024-Ba-0030). During the last fiscal year, we have achieved some progress on the following topics.

(1) Superconducting states coexisting with altermagnetism

We conducted a study on spatially non-uniform superconducting states coexisting with altermagnetism [1], which is known as a higher-order magnetic multipole order exhibiting anisotropic spin splitting in the energy bands despite a conventional collinear antiferromagnetic structure. Focusing on the organic salt κ-$(ET)_2X$, a candidate material for altermagnetism, we constructed an effective two-sublattice tight-binding model (cf. Ref. [2]) and performed many-body calculations incorporating a molecular field representing the magnetic order. Specifically, assuming an onsite repulsive Hubbard interaction, we analyzed the linearized Eliashberg equation based on the random phase approximation. In this analysis, we employed the Matsubara Green's function method and utilized the `SparseIR.jl` package [3], which is based on the intermediate representation [4] and the sparse sampling [5], to reduce memory usage and computation time. As a result, we demonstrated that Fulde–Ferrell–Larkin–Ovchinnikov (FFLO) superconductivity, a spatially non-uniform state characterized by a finite center-of-mass momentum, can be stabilized by altermagnetism, obtaining results consistent with several previous theoretical studies [6–10].

Next, to understand this spatially non-uniform state from the perspective of phenomenological parameters, we conducted an analysis based on Ginzburg–Landau (GL) theory. Specifically, within the microscopic tight-binding model, we numerically determined the coefficients of the GL free energy, assuming a superconducting mean-field theory with a d-wave order parameter. Our analysis revealed that as the molecular field of altermagnetism increases, the coefficient κ of the second-order gradient term changes its sign from positive to negative, while the coefficient β of the fourth-order uniform term remains positive. Consequently, the FF state, in which only the *phase* of the order parameter is spatially modulated, is stabilized.

(2) Magnetic resonance peaks in UTe_2

We studied the magnetic resonance peaks in the heavy-fermion superconductor UTe_2 [11], which was discovered in late 2018. Based on a mixed-dimensional periodic Anderson model that reproduces the antiferromagnetic fluctuations observed near $\boldsymbol{q}_{\mathrm{AFM}} = (0, \pi, 0)$ in this material [12], we assumed a spin-triplet superconducting order parameter and calculated the dynamical spin susceptibility within the random phase approximation to investigate the presence of resonance peaks by examining its imaginary part. As a result, we demonstrated that when the order parameter belongs to the B_{2u} representation that changes its sign upon momentum transfer of $\boldsymbol{q}_{\mathrm{AFM}}$, a magnetic resonance peak appears at an energy corresponding to the su-

perconducting gap. Furthermore, we found that while the order parameter belonging to the A_u representation also exhibits a sign change, it vanishes in the $\boldsymbol{k}$-space region that dominantly contributes to the spin susceptibility, thereby preventing the emergence of a resonance peak.

References

[1] S. Sumita, M. Naka, and H. Seo, in preparation.

[2] M. Naka *et al.*, Nat. Commun. **10**, 4305 (2019).

[3] M. Wallerberger, *et al.*, SoftwareX **21**, 101266 (2023); T. Wang *et al.*, Phys. Rev. B **102**, 134503 (2020).

[4] H. Shinaoka *et al.*, Phys. Rev. B **96**, 035147 (2017).

[5] J. Li *et al.*, Phys. Rev. B **101**, 035144 (2020).

[6] S. Sumita *et al.*, Phys. Rev. Research **5**, 043171 (2023).

[7] S.-B. Zhang *et al.*, Nat. Commun. **15**, 1801 (2024).

[8] D. Chakraborty and A. M. Black-Schaffer, Phys. Rev. B **110**, L060508 (2024).

[9] G. Sim and J. Knolle, arXiv:2407.01513.

[10] K. Mukasa and Y. Masaki, arXiv:2409.08972.

[11] K. Shimura, S. Sumita, and Y. Kato, in preparation.

[12] R. Hakuno *et al.*, Phys. Rev. B **109**, 104509 (2024).

Analysis of phase transition in languages based on Combinatory Categorial Grammar

Takehito SUZUKI
Department of Human Science, Takachiho University
2-19-1, Omiya, Suginami-ku, Tokyo 168-8508

Language has been attracted the interests of researchers in the field of physics (e.g., [1, 2, 3]). However, grammar for natural language has not been considered there. We employ the combinatory categorial grammar (CCG) to deal with natural languages mathematically. The definition of CCG is as follows. First, we consider ground categories noun (N), noun phrase (NP), and sentence (S). We also employ operators / and \. These operators combine two categories into a single category. Let us consider two categories A and B. The combination A/B indicates that if the category B emerges just after this category, the category is merged into the category A. The combination A\B indicates that if the category B emerges before this category, the category is merged into the category A. For example, let us write intransitive verb with CCG. If the noun phrase comes before the intransitive verb, the sentence is completed. We therefore conclude that the intransitive verb is a category S\NP. An additional example involves the use of the adjective, which can be expressed as N/N with CCG. Notably, the operators can be utilized recursively. With this framework, all categories are represented by the combinations of N, NP, S, /, and \. The categories other than the ground categories are called syntactic categories.

Actually, we need other rules for representing natural sentences. We write the sequence for the categories A and B as A+B. We require the following rules,

$$\mathrm{A/B} + \mathrm{B/C} \to \mathrm{A/C}, \tag{1}$$

$$\mathrm{B\backslash C} + \mathrm{A\backslash B} \to \mathrm{A\backslash C}, \tag{2}$$

where A, B, and C are categories. Equations (1) and (2) are called forward and backward functional composition rules, respectively. For example, if we employ the rule (1), the sequence with the auxiliary verb ((S\NP)/(S\NP) with CCG) and the transitive verb ((S\NP)/NP) is merged into (S\NP)/NP, which is the same as the transitive verb.

We also assume the following rules.

$$\mathrm{A} \to \mathrm{T/(T\backslash A)}, \tag{3}$$

$$\mathrm{A} \to \mathrm{T\backslash(T/A)}, \tag{4}$$

where A is a category and T is a categorical variable. Any category can be substituted for T. Both the rules (3) and (4) are called the forward and backward type raising rules, respectively.

We now treat CCG mathematically. First, we define W_i^l as the combined category C_i from the beginning of the sentence to the lth word, where l is an arbitrary integer, $i = 1, 2, \cdots, N_C$, and N_C is a number of the categories. We found that $N_C = 19$ for English sentences (see Table 1). Note that the end of the sentence is defined as the category $C_Q = C_{12}$. We then define the category vector, $\boldsymbol{W}^l$, as

$$\boldsymbol{W}^l \equiv (W_1^l \;\; W_2^l \;\; \cdots \;\; W_{N_C}^l). \tag{5}$$

Table 1: All categories

Index	Category	Part-of-speech
1	N	noun
2	NP	noun phrase
3	S	sentence
4	S\NP	intransitive verb
5	(S\NP)/NP	transitive verb
6	N/N	adjective
7	(S\NP)\(S\NP)	adverb
8	(S\NP)/(S\NP)	auxiliary verb
9	(S\NP)\(S\NP)/NP	proposition (adverb-like)
10	(NP\NP)/NP	proposition (adjective-like)
11	NP/N	article
12	Q	-
13	S/NP	-
14	S/(S\NP)	-
15	NP/NP	-
16	NP\NP	-
17	S/N	-
18	(S\NP)\(S\NP)/N	-
19	(NP\NP)/N	-

Using this vector, we found that $\boldsymbol{W}^{l+1}$ and $\boldsymbol{W}^{l}$ are related via the equation

$$\boldsymbol{W}^{l+1} = \boldsymbol{W}^{l} G, \tag{6}$$

where G is a matrix, whose components are categories, not real numbers. Moreover, using Eq. (6) recursively leads to the equation

$$\boldsymbol{W}^{l+1} = \boldsymbol{W}^{1} G^{l}. \tag{7}$$

We now assume that the sentence begins with an article. Therefore, we have

$$\boldsymbol{W}^{1} = (0\ 0\ 0\ 0\ 0\ 0\ 0\ 0\ 0\ 0\ C_{11}\ 0\ 0\ 0\ 0\ 0\ 0\ 0\ 0). \tag{8}$$

Using Eq. (7), we can obtain all patterns consisting of L categories, where L is an integer. We can regard L as the sentence length. In particular, the 12th component of $\boldsymbol{W}^{L+1}$ gives such all patterns; note again that the sentence ends with C_{12}.

Moreover, using G, we can also obtain the probability that the sentence length is L. Therefore, we can obtain the average value of L, $\langle L \rangle$. Though the convergence is found to be slow, we can conclude with numerical calculations that $\langle L \rangle$ takes almost 10, which is near but a little smaller than the observed values. This discrepancy could be attributed to the exclusion of certain representations, such as parallel representations, from the analysis. This study is a basis for the future study related to the phase transition observed in natural languages.

References

[1] E. De Giuli: J. Phs. A: Math. Theor. **52**, 504001 (2019).

[2] T. Yamamoto, S. Yamada, and T. Mizuguchi: Eir. Phys. J. B **94**:200 (2021).

[3] K. Nakaishi, and K. Hukushima: Phys. Rev. Res. **4**, 023156 (2022).

Entanglement analysis for cyclic polymers

Takahiro MURASHIMA

Department of Physics, Tohoku University,

Aramaki-aza-Aoba, Aoba-ku, Sendai, Miyagi, 980-8578

Recent advances in synthetic technology have produced polymers with complex topologies. In particular, the physical properties of complex polymers with many rings have attracted much attention. We have so far clarified the physical properties of linear polymers penetrating into cyclic polymers. On the other hand, there is no easy analytical method for the penetration between cyclic polymers, so a clear relationship with the physical properties has not been clarified. In this study, coarse-grained molecular dynamics simulations were carried out on the ISSP supercomputer to obtain many equilibrium structures, and a method for analysing equilibrium structures was investigated.

The N-dependence of the diffusion coefficient was investigated by determining the mean-square displacement of cyclic polymers using the multiple tau method reported last year[1], and it was found that the power exponent of the N-dependence of the diffusion coefficient decreases around a chain length N above 400. Increased entanglement and penetration between cyclic polymers is to be expected as N increases, but when normal primitive path analysis is performed, the cyclic polymers converge to a single point and the penetration state cannot be correctly captured. Therefore, an attempt was made to carry out primitive path analysis[2] in sequence by fixing all but one ring of interest and scrinking only the ring of interest. Figure 1 shows the penetrated rings resulting from this new primitive path analysis method. It was found that this method can be used to obtain the appearance of rings penetrating each other. A method to automatically determine which rings penetrate which rings needs to be developed.

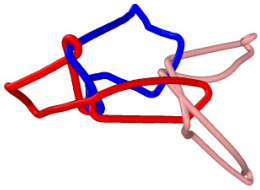


Fig. 1: Three interpenetrating cyclic polymers

References

[1] T. Murashima, ISSP Activity Report 2023, 298.

[2] https://github.com/t-murash/LAMMPS-PPA

General algorithm of calculating the SU(N) symmetry coefficients for a generic N

Masahiko G. YAMADA
Department of Physics, School of Science, University of Tokyo
Hongo, Bunkyo-ku, Tokyo 113-0033

We have studied a general algorithm of calculating the SU(N) symmetry coefficeints. This is problematic in the case N is large, for example $N > 4$. The sophisticated algorithm is necessary and the previous method based on Clebsch-Gordan coeffcients is not efficient enough for a large-scale simiulation, e.g. for the density matrix renormalization group (DMRG).

The calculation of F-symbols (6j-symbols for SU(2)) or R-symbols is done by the method discussed in Chen's textbook [1] based on subduction coefficients. This method is specifically suitable for the case $N > 4$ and the calculation is easily parallelized and made fast by many nontrivial techniques. Calculations for SU(5) and SU(6) are ongoing. SU(5) and SU(6) Heisenberg models are especially interesting for the emergence of many complicated orders, or quantum phases.

The calculation supports MPI parallelization, and suitable for a large-scale computation in the ISSP supercomputers.

References

[1] J. Q. Chen: Group representation theory for physicists (2nd edition) (2002).

3.5 SCCMS Projects

Estimation of Hamiltonians of quantum magnets using Bayesian optimization

Takahiro Misawa
Institute for Solid State Physics, University of Tokyo
Kashiwa-no-ha, Kashiwa, Chiba 277-8581

Determination of spin Hamiltonians in magnetic compounds has been recognized as a crucial step in elucidating their magnetic properties. A commonly adopted approach involves the derivation of a Hubbard-type Hamiltonian via *ab initio* downfolding [1], followed by the application of a strong-coupling expansion to obtain an effective spin model. Although this method has been successfully applied to various materials, the absence of a systematic criterion for determining the required order of perturbative expansion has been noted as a limitation. In addition, the Liechtenstein formula [2] has been widely employed to evaluate exchange interactions between classical spins, where the energy variation caused by infinitesimal rotations of magnetic moments around a given magnetic order is computed. Despite its widespread use, the applicability of classical spin models derived from this approach to quantum magnetic systems remains unclear.

Among quantum magnets, α-$RuCl_3$ has been regarded as a prototypical system in which the determination of the spin Hamiltonian continues to be debated. This compound has been intensively investigated as a promising candidate for realizing the Kitaev quantum spin liquid [3]. In conventional approaches, the estimated parameters of the spin Hamiltonian in α-$RuCl_3$, such as the Kitaev interaction (K), off-diagonal terms (Γ, Γ'), and the Heisenberg interaction (J), have been shown to vary significantly depending on the computational method employed [4].

In this project, an alternative strategy is used for determining the spin Hamiltonian of α-$RuCl_3$ through the formulation of an inverse problem constrained by experimental data [5]. Bayesian optimization is employed to identify the parameter set that best reproduces the observed magnetization process. We focus the model that has five essential parameters: the Kitaev interaction (K), the off-diagonal interactions (Γ and Γ'), the Heisenberg interaction (J), and the g-factor along the c-axis (g_c). In the actual calculations, the magnetization curves are computed using the exact diagonalization method implemented in $\mathcal{H}\Phi$ [6] and the Bayesian optimization is performed using Physbo [7]. As a result, we obtain the following optimal parameter set: $K = -6.0$, $\Gamma = 7.5$, $\Gamma' = -0.3$, $J = -1.75$ (in meV), and $g_c = 2.3$. We confirm that this set is found to well reproduce the experimental magnetization curves as well as othe physical quantities such as the specific heat and the spin correlations.

We also peform a similar Bayesian optimization for the spin Hamiltonian of azurite, which is a well-studied one-dimensional quantum magnet. As a result, we also find that the parameters set that well reproduces the experimental magnetization curve. Through these applications, we have demonstrated that the Bayesian optimization provides a systematic and efficient approach for determining spin Hamiltonians in quantum magnets.

References

[1] M. Imada, T. Miyake, J. Phys. Soc. Jpn. **79**, 112001 (2010).

[2] A. I. Liechtenstein, M. Katsnelson, V. Antropov, V. Gubanov, Journal of Magnetism and Magnetic Materials **67**, 65 (1987).

[3] A. Kitaev, Annals of Physics **321**, 2 (2006).

[4] P. A. Maksimov, A. L. Chernyshev, Phys. Rev. Res. **2**, 033011 (2020).

[5] T. Misawa, K. Yoshimi, R. Tamura, Y. Yamaji, in preparation.

[6] K. Ido, M. Kawamura, Y. Motoyama, K. Yoshimi, Y. Yamaji, S. Todo, N. Kawashima, T. Misawa, Comp. Phys. Commun. **298**, 109093 (2024).

[7] Y. Motoyama, R. Tamura, K. Yoshimi, K. Terayama, T. Ueno, K. Tsuda, Computer Physics Communications **278**, 108405 (2022).

Theoretical study on proton transfer with nuclear quantum effect in condensed systems

Tomomi Shimazaki

Graduate School of Nanobioscience,

Yokohama City University, 22-2 Seto, Kanazawa, Yokohama 236-0027

There are two primary mechanisms for proton transport. One is the vehicular mechanism, in which protons move via diffusion, and the other is the Grotthuss mechanism, where protons are transferred through hydrogen-bond network rearrangement and hopping. Since proton hopping is a type of chemical reaction, a quantum chemical approach based on first-principles calculations is required to investigate the Grotthuss mechanism in detail. In this year, we have investigated fundamental behaviors of several condensed systems. We have also studied simulation methodologies to handle such phenomena. [3] However, even with today's advanced computational power, it remains challenging to apply only first-principles or quantum chemical methods to handle entire interesting materials. Therefore, this research project employs a QM/MM approach. In the developed QM/MM program, the MM region utilizes "MDYLAS," enabling highly efficient molecular dynamics (MD) simulations even on the Fugaku supercomputer. For the QM region, the Multi-Component Density Functional Theory (MC-DFT) method is used to consider proton quantum effects. In QM-based MD simulation with the quantum effect are considered, a proton more frequently takes the Zundel structure, where it is located between two oxygen atoms, compared to conventional quantum chemical calculations based on the Born–Oppenheimer approximation. This is likely because nuclear quantum effects lower the reaction barrier for proton transfer, making the Zundel structure more favorable. In the future, we plan to investigate various systems, such as carbon-based fuel cell materials and covalent organic frameworks (COFs), to analyze proton transport behavior. In these materials, the proton transfer plays essential roles.

References

[1] E, Kino and T. Shimazaki, *Phys. Chem. Chem. Phys*., **27**, 7429 (2025).

[2] T. Wakahara, T. Shimazaki, et al, *Carbon*, 233, 119838 (2025).

[3] T. Shimazaki and M. Tachikawa, *J. Chem. Phys.*, **161**, 014107 (2024).

High-throughput calculations for magnetic materials with configurational and structural disorders

Tetsuya FUKUSHIMA
CD-FMat, National Institute of Advanced Industrial Science and Technology (AIST)
1-1-1 Umezono, Tsukuba, Ibaraki 305-8568, Japan

The purpose of Data Creation and Utilization-Type Material Research and Development Project (Digital Transformation Initiative Center for Magnetic Materials) is to find new functional permanent magnets, soft magnets, and spintronics materials by data-driven approaches.

In this year, we proceed with two research topics using first-principles calculations: (1) data creation of the magnetic anisotropic energies of $Nd_2Fe_{14}B$ and (2) high-throughput calculations of the magnetic damping constants for FeCoNi alloys.

In the first research topic, we systematically investigate the magnetocrystalline anisotropy of $Nd_2Fe_{14}B$ under lattice distortions. The calculations are performed using the all-electron full-potential Korringa–Kohn–Rostoker (KKR) Green's function method. Spin-orbit coupling is included as the $l_z s_z$ term. The neodymium $4f$ orbitals are treated within the open-core approximation, where the $4f$ electrons are considered as core-like states, and their occupations are not explicitly included in the self-consistent calculations. The distortions are introduced by altering the lattice constant a of the tetragonal crystal structures.

Figure 1 shows the calculated values of the magnetocrystalline anisotropy constant K_u and magnetization J_S for $Nd_2Fe_{14}B$ as a function of the distortion δa in the ab-plane. When there is no distortion ($\delta a = 0$), the calculated value of K_u is 4.2 MJ/m^3, which is close to the experimental value of approximately 5 MJ/m^3 reported in previous studies. Additionally, J_S = 1.89 T is in good agreement with the experimental value of 1.85 T at 4.2 K.

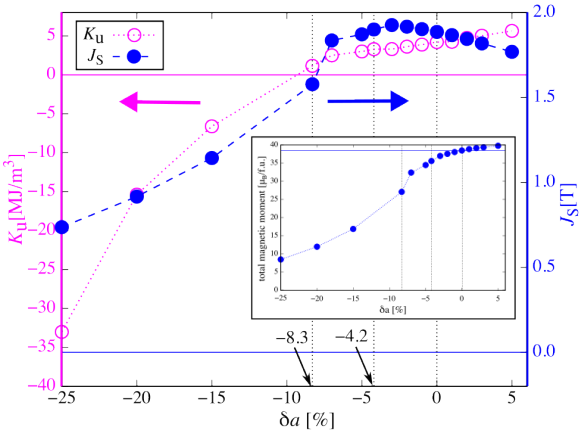


Figure 1: Calculated values of K_u and J_S for $Nd_2Fe_{14}B$ with δa. $\delta a = 0$ corresponds to the experimental lattice constant. The inset figure shows the calculated total magnetic moment as a function of δa.

K_u decreases monotonically with in-plane compression. The $5d$ electron cloud of Nd extends and hybridizes with Fe/B ions within the plane. In-plane compression increases the degree of hybridization, causing the $5d$ orbitals to expand further in the plane. To avoid this $5d$ electron cloud, the $4f$ electrons of Nd ions, which have an oblate shape, spread in the out-of-plane direction, resulting in a reduction of the anisotropy. Furthermore, K_u changes from positive to negative around $\delta a = -8.3$ %. With further compression, the absolute value of K_u

becomes larger and negative. Such extreme compression is observed in strain at interfaces, suggesting that K_{u} becomes negative in these regions.

For J_{S}, no monotonic decrease with respect to δa is observed. However, by examining the total magnetic moment shown in the inset figure of Fig.1, a monotonic decrease is confirmed. Therefore, the reason for the maximum of J_{S} around $\delta a = -4$ % is that the decrease in the crystal volume compensates for the reduction in magnetization. Similarly to K_{u}, J_{S} decreases as δa decreases. Thus, in regions with significant in-plane distortion (such as at interfaces), both K_{u} and J_{S} decrease simultaneously, suggesting that the impact on coercivity is minimal.

The second research topic is for the high-throughput calculations for magnetic damping constants (α), which characterize magnetization dynamics. α strongly affects the operating current and power consumption of spintronics devices; thus, the theoretical approaches to design α are highly desired. However, α exhibits non-monotonic temperature dependence. The conventional frameworks that ignore the temperature effects are insufficient for the practical evaluations. To address this problem, we propose an evaluation framework[1] that incorporates temperature effects into electronic structures via the disordered local moment (DLM) state within first-principles calculations. In this study, we apply this framework to FeCoNi alloys. We systematically calculate α and analyze the magnetic damping mechanisms from an electronic structure perspective.

To evaluate the magnetic damping constant at finite temperatures, the electronic structure calculations are performed using the tight-binding linear muffin-tin orbital method. The local spin density approximation functional is employed, and atomic configuration averaging is incorporated using the coherent potential approximation (CPA). For the evaluation of α, the torque correlation method proposed by Kamberský[2] and Gilmore et al.[3] is adopted. This framework evaluates the intrinsic α due to spin-orbit interaction. The temperature effects are incorporated into the spin fluctuations using the DLM-CPA method, and the effect of these fluctuations is accounted for by evaluating the thermodynamic potential via the electronic structure calculations. The calculations are performed for the FeCoNi alloys with BCC and FCC structures.

Analyzing the calculated data, we confirm that the composition with the minimum α depends on the temperatures. In the BCC structure, the composition with the minimum α is $Fe_{0.75}Co_{0.25}$ from 0 K to 500 K, while at temperatures above 1200 K, the minimum *alpha* is achieved in the pure-Fe. These results are consistent with the previous experiments. Furthermore, from the analysis of the electronic structures, a strong correlation is confirmed between α and the density of states at the chemical potential. With increasing temperature, the correlation becomes stronger. These results are quite useful for the design of spintronic materials with small magnetic damping constants.

References

[1] R. Hiramatsu, D. Miura, and A. Sakuma, Appl. Phys. Express **15**, 013003 (2021).

[2] V. Kamberský, Phys. Rev. B **76**, 134416 (2007).

[3] K. Gilmore, Y. U. Idzerda, and M. D. Stiles, Phys. Rev. Lett. **99**, 027204 (2007).

[4] M. A. W. Schoen, D. Thonig, M. L. Schneider, T. J. Silva, H. T. Nembach, O. Eriksson, O. Karis, and J. M. Shoaw, Nat. Phys. **12**(9), 839 (2016).

All-atom analysis of the solubilities of polypeptides

Kazuo YAMADA and Nobuyuki MATUBAYASI
Division of Chemical Engineering, Graduate School of Engineering Science, Osaka University, Toyonaka, Osaka 560-8531

Artificial polypeptides, synthesized from amino acids, have garnered increasing interest as promising candidates for biopharmaceutical applications due to their biodegradability and tunable functionality. They are particularly being investigated as alternatives to PEGylated protein-based drugs, offering intrinsic biodegradability and a lower risk of long-term side effects. Additionally, they are viewed as potential medium-molecular-weight peptide therapeutics. The chemical diversity of artificial polypeptides is remarkably vast. Even with only the 20 canonical amino acids, the number of possible sequences is immense. The incorporation of non-natural amino acids further expands the chemical space, enabling the design of peptides with improved stability, specificity, and bioavailability. This versatility supports the development of peptide-based drugs with reduced off-target effects compared to conventional small-molecule therapeutics.

Among their physicochemical properties, aqueous solubility and partition coefficients are particularly important, as they directly influence pharmacokinetic properties including absorption, distribution, metabolism, and excretion (ADME). Therefore, a systematic understanding of how amino acid sequence affects solubility is essential for rational peptide drug design.

To address this challenge, we developed a computational framework to predict the aqueous solubility of peptide-based drugs. As a key physicochemical descriptor, we use the solvation free energy, $\Delta\mu$, which quantifies the free energy change when transferring a solute from vacuum to a solvent. $\Delta\mu$ reflects the specificities of the solute-solvent interactions sensitively. Solvation free energies were calculated using all-atom molecular dynamics (MD) simulations combined with the energy representation (ER) method, implemented via ERmod software [1]. The ER method estimates $\Delta\mu$ from the distribution of solute–solvent interaction energies, using only two endpoint states: the fully coupled solute–solvent system and a decoupled reference state. This approach circumvents the need for intermediate coupling states required by conventional methods such as thermodynamic integration (TI) or free energy perturbation (FEP), significantly reducing computational cost while maintaining chemical accuracy. We computed $\Delta\mu$ for 15 different homo-tetrapeptides in both single-component pure solids and in aqueous solutions at infinite

dilution. The difference between the two solvation free energies, denoted as $\Delta\Delta\mu$ = $\Delta\mu$(water) − $\Delta\mu$(pure solid), directly represents the magnitude for dissolution into water. MD simulations were performed using GROMACS 2024 [2] on GPU nodes for equilibration and sampling, while ERmod calculations were conducted on CPU nodes [1].

To elucidate the molecular factors governing peptide solubility, we decomposed the calculated $\Delta\mu$ values into interaction components. Figure 1 shows that the excluded-volume contribution, $\Delta\Delta\mu^{excl}$, exhibits the strongest correlation with peptide solubility (correlation coefficient r = 0.86). This component represents the free energy penalty associated with displacing solvent molecules from the volume occupied by the solute.

In contrast, the correlation between peptide solubility and the direct interaction energy between solute and solvent molecules, defined as the energy difference $\Delta\epsilon = \epsilon(\text{peptide} - \text{water}) - \epsilon(\text{peptide} - \text{peptide})$, was weakly negative ($r = -0.13$). These results suggest that excluded-volume effects, which are strongly related to molecular size and steric occupancy, exert a greater influence on aqueous solubility than specific interactions such as hydrogen bonding. In other words, the spatial footprint of a peptide in solution contributes more significantly to its solubility than the strength of its direct interactions with the solvent. Overall, the excluded-volume component represents the free energy cost associated with peptide insertion into the solvent matrix, increasing with molecular size. These findings underscore that, beyond hydrophilic/hydrophobic balance, molecular size and steric effects are key determinants of peptide solubility in aqueous environments.

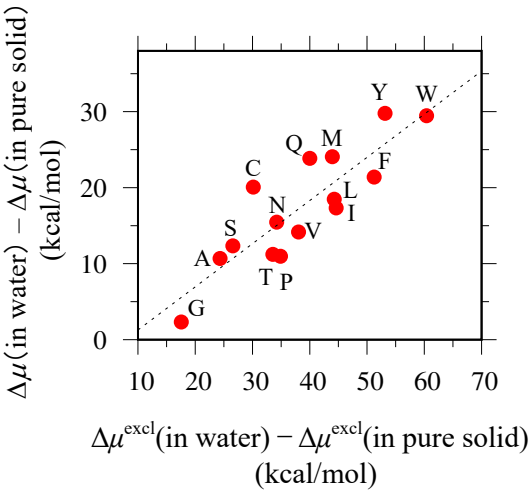


Figure 1: Correlation between ΔΔμ and $\Delta\Delta\mu^{excl}$ for 15 homo-tetrapeptides, where each is defined as the difference between values in the water solvent and in the pure solid. A strong correlation is observed with a correlation coefficient r = 0.86.

References

[1] S. Sakuraba and N. Matubayasi: J. Comput. Chem. **35** (2014) 1592-1608

[2] Abraham, M. et. al., "GROMACS 2024 Manual", Zenodo., (2024)

High-throughput first-principles exploration of stable Heusler alloys

Terumasa TADANO
National Institute for Materials Science
Sengen 1-2-1, Tsukuba, Ibaraki 305-0047

Heusler alloys have attracted significant attention due to their exceptional magnetic and multifunctional properties such as high saturation magnetization, large magnetocrystalline anisotropy, high T_c, notable magnetocaloric effects, and promising thermoelectric performance, which have prompted high-throughput (HTP) computational studies. However, previous HTP screenings have focused mostly on thermodynamic stability and omitted dynamical stability. Since unstable phonon modes can lead to structural phase transitions that may affect performance, our study incorporates phonon stability as an additional crucial metric of stable Heusler alloys.

Our HTP screening encompasses 27,864 Heusler compositions, including regular and inverse Heusler compounds with the X_2YZ composition, half-Heusler compounds with the XYZ composition, and X_3Z compounds (where $X = Y$). Initial structures are generated using primitive cells with lattice parameters taken from the Open Quantum Materials Database (OQMD) when available, or estimated from averages of related compounds. These structures are optimized using density functional theory (DFT) with the Vienna *ab initio* Simulation Package (VASP) under the generalized gradient approximation (GGA). Multiple magnetic configurations, including high-spin and low-spin states as well as various alignment patterns, are tested to determine the magnetic ground state.

Thermodynamic stability is determined by the following two criteria: The formation energy (ΔE) must be negative relative to the elemental reference states, and the energy above the convex hull (ΔH) must be less than 0.3 eV/atom. Only compounds meeting these criteria are then assessed for dynamical stability via phonon calculations, carried out within the harmonic approximation using the ALAMODE package. A compound is considered dynamically stable if all phonon frequencies at commensurate q points are nonnegative. The magnetic transition temperature T_c is calculated within the mean-field approximation using exchange constants from the spin-polarized relativistic Korringa-Kohn-Rostoker (SPRKKR) code.

Out of 106,235 computed structures (including both ground states and metastable states), our workflow identifies 8,191 compounds that satisfy the thermodynamic stability criteria. Phonon calculations were successful for 8,180 compounds, of which 4,011 are dynamically stable (Fig. 1). This indicates the effectiveness of considering the phonon stability for a robust prediction of stable Heusler compounds.

Among the dynamically stable compounds, 1,356 are magnetic. When filtered by $T_c > 300$ K, 631 promising candidates are identified, which include 47 low-moment compensated ferrimagnets. The identified list includes not only Mn-based Heuslers but also Cr-, Ti-, and V-based Heuslers, whose anomalous Hall conductivity can be larger than $250\,\mathrm{S\,cm^{-1}}$.

Our analysis also reveals clear correlations

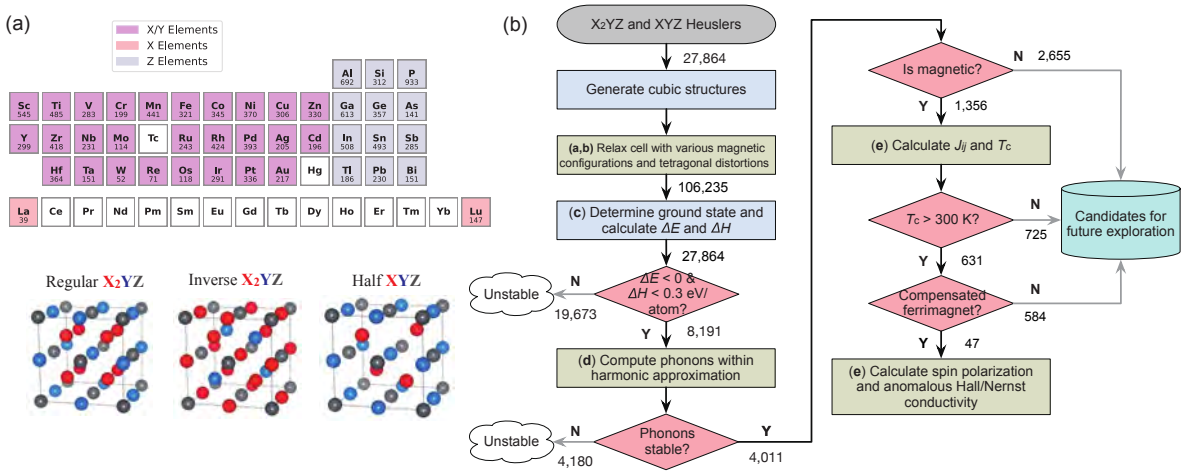


Figure 1: (a) The compositions covered in the high-throughput search and distribution of stable compositions. (b) Workflow of the high-throughput search for stable Heusler compounds. Adapted from Ref. [1].

between stability and atomic properties. In X_2YZ compounds, stability is enhanced when the Z element has a small atomic radius and low ionization energy. For half-Heusler compounds, a necessary condition for stability is that the atomic radius of X is smaller than that of Y. These trends offer useful guidelines for selecting elemental combinations.

In summary, our high-throughput study identifies 631 stable magnetic Heusler compounds with promising functional properties, including 47 candidates of low-moment compensated ferrimagnets. These findings, combined with the comprehensive dataset generated in this work, will contribute significantly to the discovery of next-generation materials for spintronic and energy-harvesting applications and provide a valuable resource for future machine-learning efforts in materials design.

This study was supported by MEXT Program: Data Creation and Utilization-Type Material Research and Development Project (Digital Transformation Initiative Center for Magnetic Materials) Grant Number JPMXP1122715503 and as "Program for Promoting Researches on the Supercomputer Fugaku" (Data-Driven Research Methods Development and Materials Innovation Led by Computational Materials Science, JPMXP1020230327). This study used computational resources of supercomputer Fugaku provided by the RIKEN Center for Computational Science (Project ID: hp240223), the computer resources provided by ISSP, U-Tokyo under the program of SCCMS, and the computer resources at NIMS Numerical Materials Simulator.

References

[1] E. Xiao and T. Tadano, arXiv:2502.17946.

3.6 Software Advancement Projects and Workshop Support

ChiQ: Momentum-dependent susceptibilities in dynamical mean-field theory

Junya OTSUKI[1], Hiroshi SHINAOKA[2], Kazuyoshi YOSHIMI[3],
Yuichi MOTOYAMA[3], Tatsumi AOYAMA[3], Osamu SUGINO[3]
[1]*Research Institute for Interdisciplinary Science, Okayama University, Okayama 700-8530*
[1]*Department of Physics, Saitama University, Saitama 338-8570*
[3]*Institute for Solid State Physics, University of Tokyo, Kashiwa-no-ha, Kashiwa 277-8581*

In the 2017 project supported by the Project for Advancement of Software Usability in Materials Science (PASUMS), we developed an open-source software, `DCore`, which implements the dynamical mean-field theory (DMFT) [1, 2]. DMFT accounts for dynamical correlations arising from strong electron-electron repulsion. Combined with density functional theory (DFT), DMFT yields the electronic structure of strongly correlated materials, which can be compared with angle-resolved photoemission spectroscopy (ARPES) experiments. `DCore` accepts inputs from DFT programs via the Wannier90 format and offers interfaces to various advanced quantum impurity solvers, including quantum Monte Carlo and exact diagonalization methods.

In the subsequent 2024 project, we developed additional features to enhance the applicability of `DCore`, notably the momentum-dependent dynamical susceptibility $\chi(\boldsymbol{q}, i\omega)$. Its dynamical component, $\omega \neq 0$, describes spin excitations that are comparable with inelastic neutron scattering (INS) experiments, while its static component, $\omega = 0$, reflects the tendency toward phase transitions involving magnetic, charge, and orbital ordering. We released an open-source software, `ChiQ` [3], which functions as a post-processing tool for `DCore`.

`ChiQ` provides the following four calculation modes:

- **BSE**: Bethe-Salpeter equation,
- **RPA**: Random phase approximation,
- **RRPA**: Renormalized random phase approximation, and
- **SCL**: Strong-coupling-limit formula.

BSE is the standard approach for calculating the dynamical susceptibility within the DMFT. It requires the computation of the two-particle vertex functions and is therefore computationally costly. The SCL formula, an approximation to BSE, does not require vertex calculations [4, 5] and yields reasonable results in the strong-correlation regime. In the following, we present several examples, which are described in greater detail in the online documentation [6].

Figure 1 shows the static susceptibilities $\chi(\boldsymbol{q}, 0)$ obtained from `ChiQ`. The spin susceptibility exhibits enhancement at the M point, $\boldsymbol{q} = (\pi, \pi) \equiv \boldsymbol{Q}$, indicating the antiferromagnetic fluctuations. Figure 2 shows the temperature dependence of the inverse antiferromagnetic susceptibility, $\chi_{\mathrm{AF}} \equiv \chi(\boldsymbol{Q}, 0)$. The value $1/\chi_{\mathrm{AF}}$ vanishes at $T_{\mathrm{N}} \approx 0.467$, indicating the divergence of χ_{AF}. This allows us to identify the second-order phase transition to an antiferromagnetic state.

It is also possible to estimate the intersite exchange interactions $I(\boldsymbol{r}_{ij})$ in an effective Heisenberg model. $I(\boldsymbol{r}_{ij})$ is evaluated from $\chi(\boldsymbol{q}, 0)$ in the BSE mode, while it is directly computed from the DMFT results in the SCL

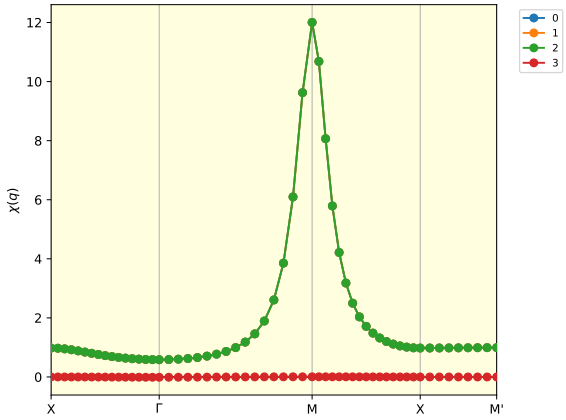


Figure 1: Static susceptibilities $\chi(\boldsymbol{q}, 0)$ for the square-lattice Hubbard model at half filling, calculated using `ChiQ` with the BSE mode. Parameters are $U = 8$ and $T = 0.5$, in units where the nearest-neighbor hopping $t = 1$. The first three modes (labels 0–2) represent spin fluctuations, while the last mode (label 3) represents a charge fluctuation.

mode. Figure 3 presents $I(\boldsymbol{r}_{ij})$ as a function of the distance $\boldsymbol{r}_{ij}$ between two sites, calculated in the BSE mode. The large negative value at $|\boldsymbol{r}_{ij}| = 1$ indicates a strong antiferromagnetic interaction between nearest-neighbor sites. This result converges to the well-known value $-J/2$ with $J = 4t^2/U$ in the strong-coupling limit.

In summary, the open-source software `ChiQ` computes the momentum-dependent susceptibilities $\chi(\boldsymbol{q}, i\omega)$ and the effective interactions $I(\boldsymbol{r}_{ij})$ within the DFT+DMFT framework. The combination `DCore` + `ChiQ` enables the calculation of two-particle responses in realistic materials.

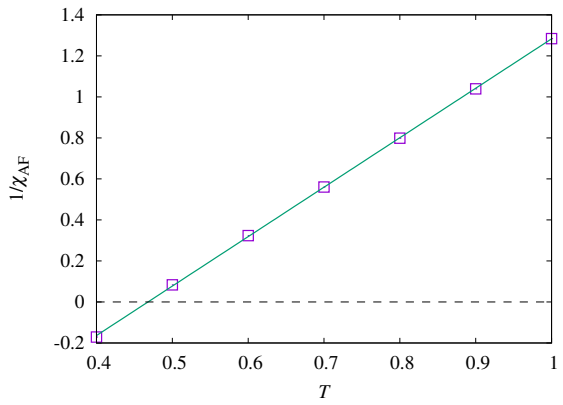


Figure 2: Temperature dependence of the inverse antiferromagnetic susceptibility, $1/\chi_{\mathrm{AF}}$.

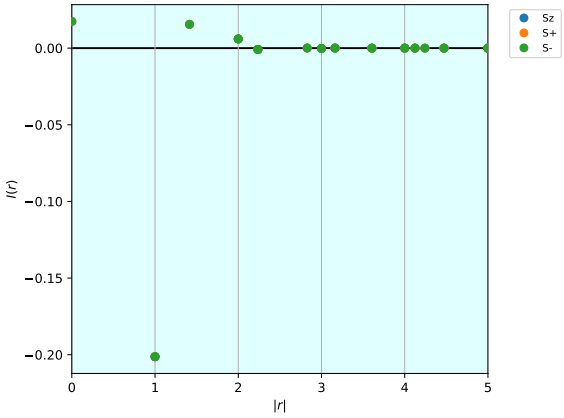


Figure 3: Intersite exchange interactions $I(\boldsymbol{r}_{ij})$ as a function of the distance $\boldsymbol{r}_{ij}$ between two sites. Positive (negative) values indicate ferromagnetic (antiferromagnetic) interactions. The parameters are the same as in Fig. 1. The lattice constant is set to $a = 1$.

References

[1] H. Shinaoka, J. Otsuki, M. Kawamura, N. Takemori, K. Yoshimi, SciPost Phys. **10**, 117 (2021).

[2] `https://github.com/issp-center-dev/DCore`

[3] `https://github.com/issp-center-dev/ChiQ`

[4] J. Otsuki, K. Yoshimi, H. Shinaoka, Y. Nomura, Phys. Rev. B **99**, 165134 (2019).

[5] J. Otsuki, K. Yoshimi, H. Shinaoka, H. O. Jeschke, Phys. Rev. B **110**, 035104 (2024).

[6] `https://issp-center-dev.github.io/ChiQ/`

Report of CCMS hands-on sessions in the 2024 fiscal year

Kota IDO

Institute for Solid State Physics,

The University of Tokyo, Kashiwa-no-ha, Kashiwa, Chiba 277-8581

In the 2024 fiscal year, Center for Computational Materials Science (CCMS) in the Institute for Solid State Physics (ISSP) held 5 hands-on sessions where the ISSP supercomputer was used [1-4]. In this report, we briefly summarize them.

Table 1 shows the list of the hands-on sessions in the 2024 fiscal year. There are 5 hands-on sessions were held. In the last hands-on session, we introduced 5 software related to the *ab initio* downfolding method: Quantum ESPRESSO, RESPACK, H-wave, HΦ and mVMC. Development of the software except for ALAMODE and Quantum ESPRESSO was supported by "Project for advancement of software usability in materials science" (PASUMS) [6].

Features of each software are as follows. ALAMODE is open-source software for calculating phonon properties such as harmonic/anharmonic force constants and lattice thermal conductivity [7]. moller is a tool for generating a job script for performing high-throughput calculations [8]. abICS is open-source software for performing configurational sampling in disordered systems such as alloys [9]. 2DMAT is a software package to search optimal results of given optimization problems by using search algorithms combined with direct-problem solvers [10]. Quantum ESPRESSO is a software package for *ab initio* calculations based on the pseudo potential method using the plane-wave basis [11]. RESPACK is open-source software for the *ab initio* downfolding method [12]. H-wave, HΦ and mVMC are software for analyzing quantum many-body systems using the mean-field approximation, exact diagonalization methods, and the variational Monte Carlo method, respectively [13-15].

Table 1: List of CCMS hands-on sessions where the ISSP supercomputer was used in the 2024 fiscal year.

Date	Lecturer	Software	# of applicants
Aug. 5	T. Tadano et al.	ALAMODE [7]	30
Oct. 18	T. Aoyama et al.	moller[8]	20
Nov. 7	S. Kasamatsu et al.	abICS[9]	14
Dec. 2	T. Hoshi et al.	2DMAT[10]	26
Feb. 6-7	T. Koretsune, T. Misawa et al.	Quantum ESPRESSO [11], RESPACK [12], H-wave [13], HΦ[14], mVMC [15]	28

In all of the hands-on sessions, lecturers explained the basics of each software and gave its tutorial. Materials of some hands-on sessions are available on each official page.

References

[1] https://ccms.issp.u-tokyo.ac.jp/event/6904
[2] https://ccms.issp.u-tokyo.ac.jp/event/6947
[3] https://ccms.issp.u-tokyo.ac.jp/event/6980
[4] https://ccms.issp.u-tokyo.ac.jp/event/7002
[5] https://ccms.issp.u-tokyo.ac.jp/event/7027
[6] https://www.pasums.issp.u-tokyo.ac.jp/en/
[7] http://ttadano.github.io/alamode/
[8] https://www.pasums.issp.u-tokyo.ac.jp/htp-tools/en/
[9] https://www.pasums.issp.u-tokyo.ac.jp/abics/en/
[10] https://www.pasums.issp.u-tokyo.ac.jp/2dmat/en/
[11] https://www.quantum-espresso.org
[12] https://sites.google.com/view/kazuma7k6r
[13] https://www.pasums.issp.u-tokyo.ac.jp/h-wave/en/
[14] https://www.pasums.issp.u-tokyo.ac.jp/hphi/en/
[15] https://www.pasums.issp.u-tokyo.ac.jp/mvmc/en/

Supercomputer course of Computational Materials Design (CMD®) workshop

Masaaki GESHI[1], Yoshitada MORIKAWA[2], Tomoya ONO[3]

[1]*R^3 Institute for Newly-Emerging Science Design,*
Osaka University, Machikaneyama, Toyonaka, Osaka 560-0043

[2] *Department of Precision Engineering, Graduate School of Engineering,*
Osaka University, Yamada-oka, Suita, Osaka 565-0871

[3]*Graduate School of Engineering,*
Kobe University, Rokkodai-cho, Nada, Kobe 657-8501

The 45th Computational Materials Design (CMD®) workshop (CMD45) was held from September 1st to September 5th, and the 46th CMD® workshop (CMD46) took place from February 17th to February 21st. Both were held online. In this workshop, we offer the supercomputer course to train human resources for advancing research using the System B supercomputer at the Institute for Solid State Physics (ISSP), the University of Tokyo.

In CMD45, three participants took the supercomputer course and followed a tutorial on STATE-Senri developed by Y. Morikawa. After an introductory lecture on large-scale computing and an explanation of how to use the supercomputer of ISSP by M. Geshi, the participants started constructing computational models for their own research subjects with the help of the lecturers. Then they carried out calculations using supercomputers. Specific themes included molecular adsorption and reactions on solid surfaces, atom doping bulk Si, and materials desing using generative models. The participants performed calculations and examined their results.

In CMD46, two participants took the supercomputer course and used the supercomputer of ISSP. They got a tutorial on RSPACE developed by T. Ono. After giving the introductory lecture of large-scale computing by M. Geshi and introducing the calculation method of electronic structures and electron-transport property using RSPACE by T. Ono, Y. Egami, and M. Uemoto, the exercises instructed in the textbook were carried out. Then, electronic structure calculations were carried out for various molecules, and the electronic density distribution was visualized. The attendees also performed massively parallel calculations to confirm the efficiency for parallel computing. Finally, the electronic structures of the bulks and interfaces were investigated using large scale models.

4 PUBLICATION LIST

Example:

LASTNAME, Firstname [project class; # points (B), # points (C)] (Page #)

— *Project title*

1. First paper
   Names of Authors, etc.
2. Second paper
   ...

□ ISSP Joint Research Projects

○ B–E classes

AKASHI, Ryosuke [B class; 400 (B), 80 (C)] (188)

— *Revisiting the conventional superconducting theory: Toward nearly uniform electron systems*

1. Illuminating the Bragg intersections as roots of Dirac nodal lines and high-order van Hove singularities
   Ryosuke Akashi Physical Review Research **6**, 033012 (2024)
   DOI:10.1103/PhysRevResearch.6.033012

AKIBA, Takaki [B class; 300 (B), 70 (C)] (350)

— *Modeling for interaction between gas-phase reaction with pattern formation and solid surface*

AN, MENG [B class; 400 (B), 90 (C)] ()

— *Machine learning-assisted computational design of Ionic thermoelectric materials*

ANDO, Yasunobu [B class; 800 (B), 0 (C)] (167)

— *First-principles calculation for building boron-compounds library*

AOYAMA, Kazushi [B class; 300 (B), 80 (C)] (349)

— *Spin dynamics in J1-J3 antiferromagnets on kagome lattices*

1. Spontaneous chirality selection and nonreciprocal spin wave in breathing-kagome antiferromagnets at zero field
   K. Aoyama and H. Kawamura Phys. Rev. B **111**, 14413 (2025).
   DOI:10.1103/PhysRevB.111.144413

ARAI, Munehito [C,D class; 8520 (B), 0 (C)] (261)

— *Accurate prediction of protein folding mechanisms by statistical mechanical models*

— *Development of a novel protein design method for medical and industrial applications*

1. Product release and substrate entry of aldehyde deformylating oxygenase revealed by molecular dynamics simulations
   M. YOSHIMURA, and M. ARAI Biophys. Physicobiol. **22**, e220003 (2025).
   DOI:10.2142/biophysico.bppb-v22.0003

ARAKI, Takeaki [B,C class; 4100 (B), 430 (C)] (310, 311)
— *The Physical Origin of the Emerging Ferroelectric Nematic Phase*
— *Universaliry of Johari-Goldstein relaxation in supercooled liquids and glasses*

1. Discovery of collective nonjumping motions leading to JohariGoldstein process of stress relaxation in model ionic glass
   M. Saito, T. Araki, Y. Onodera, K. Ohara, M. Seto, Y. Yoda, Y. Wakabayashi Acta Materialia **284**, 120536 (2025).
   DOI:10.1016/j.actamat.2024.120536

2. Formation dynamics of branching structure in the slippery DLCA model
   K. Hirata and T. Araki J. Chem. Phys. **160**, 234901 (2024).
   DOI:10.1063/5.0197122

3. Mechanical properties and cooperative motion of aerogels under isotropic expansion
   K. Hirata and T. Araki Soft Matter (submitted)

4. Impact of charge distribution on the stability of ferroelectric nematic liquid crystals
   M. de Mello, M. R. Wilson, and T. Araki Soft Matter, **21**, 1479 (2025)
   DOI:10.1039/D4SM01292E

ARIMA, Kenta [B class; 300 (B), 0 (C)] (208)
— *Detailed analysis of etching at functional graphene/semiconductor interface*

1. First-principles simulations of scanning tunneling microscopy images exhibiting anomalous dot patterns on armchair-edged graphene nanoribbons
   J. Li, K. Inagaki, and K. Arima Phys. Rev. Res. **6**, 013252 (2024).
   DOI:10.1103/PhysRevResearch.6.013252

ASANO, Yuta [E class; 15000 (B), 1850 (C)] (251)
— *Molecular dynamics analysis on ultrasonic cavitation*
— *Molecular dynamics simulation of ultrasonic cavitation*

BAE, Soungmin [C class; 3400 (B), 350 (C)] (107)
— *Doping strategy design for two-dimensional materials from first principles*

BIN, Xu [C class; 4800 (B), 550 (C)] (72)
— *Modulation of Phonon Heat Transport in Van der Waals Heterostructures Utilizing Machine Learning Potentials*
— *Modulation of the phonon hydrodynamic in 2D materials*

DEKURA, Shun [B class; 400 (B), 0 (C)] ()
— *First-principles prediction of structural changes by vapor sorption in HOFs with dynamic skeleton*

EGAMI, Yoshiyuki [C class; 6400 (B), 700 (C)] (68)
— *First-principles study on electron transport properties in heterostructures made of 2-dimensional materials with honeycomb lattice*
— *First-principles study on strain dependence of carrier transport properties in two-dimensional layered materials*

1. GPU acceleration of overbridging boundary matching method without Green's functions based on real-space finite-difference method
   T. Akamatsu, M. Uemoto, Y. Egami, and T. Ono Computer Physics Communications **312**, 109585 (2025).
   DOI:10.1016/j.cpc.2025.109585

2. Wide regime of Efros-Shklovskii variable-range-hopping in $La_{1-x}Ce_xNiO_2$
M. Kouda, K. Osame, H. Nobukane, S. Shimoda, Y. Egami, and M. Sakoda Journal of Physics: Condensed Matter, submitted.

FUCHIZAKI, Kazuhiro [C class; 1800 (B), 350 (C)] (299)
— *Kinetics of phase transition and polyamorphism*

FUJI, Yohei [B class; 600 (B), 0 (C)] (322)
— *Universality in monitored systems with symmetry*
1. Multifractality in monitored single-particle dynamics
K. Yajima, H. Oshima, K. Mochizuki, and Y. Fuji Phys. Rev. Res. **6**, 043049 (2024).
DOI:10.1103/PhysRevResearch.6.043049

2. Topology and Spectrum in Measurement-Induced Phase Transitions
H. Oshima, K. Mochizuki, R. Hamazaki, and Y. Fuji arXiv:2412.11097 (submitted)

FUJII, Susumu [C class; 3400 (B), 0 (C)] (277)
— *Defect structures and their transport properties in thermoelectric chalcogenides*
1. Lone Pair Induced 1D Character and Weak Cation-Anion Interactions: Two Ingredients for Low Thermal Conductivity in Mixed-Anion Metal Chalcohalide $CuBiSCl_2$
X. Shen, K. Pal, P. Acharyya, B. Reveau, P. Boullay, O.I. Lebedev, C. Prestipino, S. Fujii, C.-C. Yung, I.-Y. Tsao, A. Renaud, P. Lemoine, C. Candolfi, and E. Guilmeau J. Am. Chem. Soc., 146, 42, 29072-29083 (2024).
DOI:10.1021/jacs.4c10520

2. Emerging computational and machine learning methodologies for proton-conducting oxides: materials discovery and fundamental understanding
S. Fujii, J. Hyodo, K. Shitara, A. Kuwabara, S. Kasamatsu, Y. Yamazaki Sci. Technol. Adv. Mater., 25, 1, 2416383 (2024).
DOI:10.1080/14686996.2024.2416383

FUJIMOTO, Yoshitaka [C class; 1800 (B), 0 (C)] (139)
— *Electronic structures of doped carbon nanotubes*
— *First-principles study of Impurity-doped carbon nanotubes*
1. First-Principles Theoretical Design of Graphene-Based Field Effect Transistors
Y. Fujimoto Advanced Nanoscale MOSFET architectures: Current Trends and Future Perspectives, ed. K. Biswass, A. Sarkar (Wiley-IEEE press, USA 2024), Chapter 10, pp.201-220.

2. Electronic transport mechanism for nitrogen doping and detection of harmful molecules in carbon nanotubes
Y. Fujimoto submitted.

FUJINO, Tomoko [C class; 2600 (B), 400 (C)] (285)
— *Elucidation of the Origin of Dimerization Fluctuations in Highly Conductive Oligomeric Charge Transfer Complexes*
1. Orbital hybridization of donor and acceptor to enhance the conductivity of mixed-stack complexes
T. Fujino, R. Kameyama, K. Onozuka, K. Matsuo, S. Dekura, T. Miyamoto, Z. Guo, H. Okamoto, T. Nakamura, K. Yoshimi, S. Kitou, T. Arima, H. Sato, K. Yamamoto, A. Takahashi, H. Sawa, Y. Nakamura, and H. Mori Nature Commun. **15**, 3028 (2024).
DOI:10.1038/s41467-024-47298-1

2. Higher conductivity in doped ethylenedioxythiophene (EDOT) dimers with chalcogen-substituted end groups
K. Onozuka, T. Fujino, T. Miyamoto, T. Yamakawa, H. Okamoto, H. Akiba, O. Yamamuro, E. Kayahara, S. Yamago, H. Oike, and H. Mori J. Mater. Chem. C **12**, 13956-13965 (2024).
DOI:10.1039/D4TC02346C

FUJISAKI, Takaya [C class; 3400 (B), 350 (C)] (105)
— *Exploring the optimal composition of reforming catalysts for improving the efficiency of fuel cells using methane*

FUJISAWA, Shuji [B class; 400 (B), 80 (C)] (187)
— *Structural analysis of a single nanocellulose from wood*

FUJISHIRO, Hiroki [C class; 3000 (B), 0 (C)] ()
— *Strained Band-Structure Engineering for Antimonide-Based Terahertz Transistors*

FUJITA, Takatoshi [C class; 1400 (B), 0 (C)] (149)
— *Computational Investigation of Multi-Exciton Generation Mechanism by Large-Scale Excited-State Method*

FUKAYA, Yuri [B class; 300 (B), 0 (C)] ()
— *Theory of local density of states and transport properties in superconductor junctions*

FUKUDA, Jun-ichi [B class; 750 (B), 160 (C)] (317)
— *Calculation of ordered structures dynamics and optical properties of soft materials*
1. Oscillating edge current in polar active fluid
H. Matsukiyo and J. Fukuda Physical Review E **109**, 054604 (2024).
DOI:10.1103/PhysRevE.109.054604

FUKUDA, Masahiro [B class; 400 (B), 70 (C)] (15)
— *Prediction of AFM images of material surfaces by local density quantities*
1. Atomic Observation on Diamond (001) Surfaces with Near-Contact Atomic Force Microscopy
R. Zhang, Y. Yasui, M. Fukuda, T. Ozaki, M. Ogura, T. Makino, D. Takeuchi, and Y. Sugimoto Nano Letters **25**, 1101 (2025).
DOI:10.1021/acs.nanolett.4c05395
,
2. Dimer ribbon structures on diamond (001) surfaces revealed with atomic force microscopy
R. Zhang, Y. Yasui, M. Fukuda, M. Ogura, T. Makino, D. Takeuchi, T. Ozaki, and Y. Sugimoto Phys. Rev. Res. **7**, 023036 (2025).
DOI:10.1103/PhysRevResearch.7.023036

Data Repository
C001_dimer_ribbon_AFM
https://isspns-gitlab.issp.u-tokyo.ac.jp/masahiro.fukuda/C001_dimer_ribbon_AFM
DOI:10.1103/PhysRevResearch.7.023036

C001_dimer_chain_AFM
https://isspns-gitlab.issp.u-tokyo.ac.jp/masahiro.fukuda/C001_dimer_chain_AFM
DOI:10.1021/acs.nanolett.4c05395

FUKUDA, Tuneo [C class; 400 (B), 0 (C)] (198)
— *First-principles Study of In-induced Superstructures on the Si(111) surface*

FUKUI, Ken-ichi [C class; 1800 (B), 100 (C)] (303)
— *Analyses on the Potential-dependent Dynamics of Ionic Liquid Electrolytes Forming Electric Double Layers Facing the Electrodes*

FUKUMOTO, Yoshiyuki [B class; 700 (B), 0 (C)] (320)
— *A series expansion study of magnon dispersion relations in S=1/2 frustrated spin systems*
— *Investigation of efficient methods for introducing long-range interactions in the cluster expansion method*

1. Six magnetization plateau phases in a spin-1/2 distorted kagome antiferromagnet: Application to $Y_3Cu_9(OH)_{19}Cl_8$
   Kazu Bodaiji, Katsuhiro Morita, and Yoshiyuki Fukumoto Phys. Rev. B 110, 104431 (2024).
   DOI:10.1103/PhysRevB.110.104431

GOHDA, Yoshihiro [C class; 4400 (B), 400 (C)] (86)
— *Free-energy evaluation of alloys*

1. Artificial multiferroic heterostructures - electric field effects and their perspectives
   T. Taniyama, Y. Gohda, K. Hamaya, and T. Kimura Sci. Technol. Adv. Mater. **25**, 2412970 (2024).
   DOI:10.1080/14686996.2024.2412970

2. Magnetic-anisotropy modulation in multiferroic heterostructures by ferroelectric domains from first principles
   A.M. Yatmeidhy and Y. Gohda Sci. Technol. Adv. Mater. **25**, 2391268 (2024).
   DOI:10.1080/14686996.2024.2391268

3. Prediction of $NdFe_{16}$-based permanent-magnet compounds with high magnetization
   I. Seo, S. Tanaka, M. Endo, and Y. Gohda Appl. Phys. Express **17**, 075502 (2024).
   DOI:10.35848/1882-0786/ad5fd9

GOHLKE, Matthias [C class; 2000 (B), 300 (C)] (296)
— *Tensor network study of an effective spin model for cuprates*

1. Proximate Tomonaga-Luttinger liquid in an anisotropic Kitaev-Gamma model
   M. Gohlke, J. C. Pelayo, T. Suzuki Phys. Rev. B **109** L220410 (2024).
   DOI:10.1103/PhysRevB.109.L220410

2. Magnon spectra of cuprates beyond spin wave theory
   J. Bao, M. Gohlke, J. G. Rau, N. Shannon Phys. Rev. Research **7** L012053 (2025).
   DOI:10.1103/PhysRevResearch.7.L012053

GONOME, Hiroki [C class; 5800 (B), 650 (C)] (69)
— *Study of the principle of photothermal conversion by ab initio calculations*

HAGITA, Katsumi [C class; 2000 (B), 400 (C)] (294)
— *Physical properties of crosslinked polymer networks through network topology analysis*

1. Coarse-grained molecular dynamics model of AB diblock copolymers composed of blocks with different Lennard-Jones parameters forming lamellar structures
   K. Hagita and T. Murashima Polymer **304**, 127132 (2024).
   DOI:10.1016/j.polymer.2024.127132

2. Coarse-grained molecular dynamics model of conformationally asymmetric AB diblock copolymers forming lamellar structures

K. Hagita and T. Murashima Comput. Mater. Sci. **243**, 113105 (2024).
DOI:10.1016/j.commatsci.2024.113105

3. Critical Importance of Both Bond Breakage and Network Heterogeneity in Hysteresis Loop on StressStrain Curves and Scattering Patterns
K. Hagita and T. Murashima Macromolecules **57**, 1090310911 (2024).
DOI:10.1021/acs.macromol.4c01996

HAGIWARA, Satoshi [B class; 500 (B), 0 (C)] (181)
— *A theoretical study on an oxidation process at a metal surfaces*

1. Bias-dependent surface stress by density functional theory combined with the effective screening medium method
S. Hagiwara, S. Ishibashi, and M. Otani Phys. Rev. B **110**, 155409 (2024).
DOI:10.1103/PhysRevB.110.155409

2. Anion Adsorption-induced Charge Separation at the Alumina/Aluminum Interface
S. Hagiwara, T. Murata, and M. Otani Corr. Sci. under review.

HAMADA, Ikutaro [C,D class; 9400 (B), 1000 (C)] (51)
— *Density functional theory study of adsorption and reaction of molecules on solid surfaces and interfaces*
— *Density functional theory study of adsorption and reaction of molecules on solid surfaces and interfaces: cases of two-dimensional materials*

1. Interplay of hydrogen boride sheets with water: an insight into edge stability
K. I. M. Rojas, Y. Morikawa, and I. Hamada Phys. Rev. Materials **8**, 114004 (2024).
DOI:10.1103/PhysRevMaterials.8.114004

2. Interlayer hydrogen recombination from hydrogen boride nanosheets elucidated by isotope labeling
S-i Ito, K. I. M. Rojas, Y. Yasuda, N. Noguchi, K. Fukuda, M. Hikichi, Z. Kang, M. Yuan, R. Tsuji, O. Oki, S. Roy, Y. Hikita, I. Matsuda, M. Miyauchi, I. Hamada, T. Kondo J. Phys. Chem. Lett. **15**, 10965-10976 (2024).
DOI:10.1021/acs.jpclett.4c01975

3. Isotope-dependent site occupation of hydrogen in epitaxial titanium hydride nanofilms
T. Ozawa, Y. Sugisawa, Y. Komatsu, R. Shimizu, T. Hitosugi, D. Sekiba, K. Yamauchi, I. Hamada, K. Fukutani Nat. Commun. **15**, 9558 (2024).
DOI:10.1038/s41467-024-53838-6

4. Atomic Precision Control of Plasmon-Induced Single-Molecule Switching in a Meta- Semiconductor Nanojunction
Y. Park, I. Hamada, A. Hammud, E. W. Meijer, M. Wolf, T. Kumagai, and A. Shiotari, Nat. Commun. **15**, 6709 (2024).
DOI:10.1038/s41467-024-51000-w

HAMAGUCHI, Satoshi [C class; 7400 (B), 750 (C)] ()
— *Analysis of plasma-material interactions by Machine-Learning-based MD simulation*
— *Dynamical analyses of plasma-surface interactions*

HAMAMOTO, Yuji [C,D class; 3800 (B), 0 (C)] (101, 103)
— *First principles study of the Fano resonance in Copper phthalocyanine adsorbed on Cu(100)*
— *Numerical study of the Fano effect in CuPc adsorbed on the Cu(100) surface using the embedding Green function method*

— *Structure search for germanene on Ag(111) thin films by Gaussian process regression*

HARADA, Kenji [C class; 2000 (B), 400 (C)] (293)
— *Information analysis of complex system with a tensor network formalism*

1. Tensor tree learns hidden relational structures in data to construct generative models
   Kenji Harada, Tsuyoshi Okubo, and Naoki Kawashima Machine Learning: Science and Technology **6**, 025002 (2025).
   DOI:10.1088/2632-2153/adc2c7

HARASHIMA, Yosuke [C class; 1400 (B), 0 (C)] (148)
— *Materials exploration loop with materials informatics.*

1. Data-Driven Approach Considering Imbalance in Data Sets and Experimental Conditions for Exploration of Photocatalysts
   W. Takahara, R. Baba, Y. Harashima, T. Takayama, S. Takasuka, Y. Yamaguchi, A. Kudo, and M. Fujii ACS Omega **10**, 14626-14639 (2025).
   DOI:10.1021/acsomega.4c06997

2. Covariance Linkage Assimilation method for Unobserved Data Exploration
   Y. Harashima, T. Miyake, R. Baba, T. Takayama, S. Takasuka, Y. Shigeta, Y. Yamaguchi, A. Kudo, and M. Fujii submitted to Phys. Rev. Materials.
   DOI:10.48550/arXiv.2408.08539

HARIKI, Atsushi [B class; 550 (B), 0 (C)] (239)
— *Computational study on spin splitting and x-ray spectroscopy responses in altermagnets using DFT+DMFT method*

1. Valence, charge transfer, and orbital-dependent correlation in bilayer nickelates $Nd_3Ni_2O_7$
   Daisuke Takegami, Takaki Okauchi, Edgar Abarca Morales, Koto Fujinuma, Mizuki Furo, Masato Yoshimura, Ku-Ding Tsuei, Grace A Pan, Dan Ferenc Segedin, Qi Song, Hanjong Paik, Charles M Brooks, Julia A Mundy, Takashi Mizokawa, Liu Hao Tjeng, Berit H Goodge, Atsushi Hariki Phys. Rev. B **111**, 165101 (2025).
   DOI:10.1103/PhysRevB.111.165101

2. Magnetic Dichroism in Rutile NiF_2: Separating Altermagnetic and Ferromagnetic Effects
   A Hariki, K Sakurai, T Okauchi, J Kunes npj Quantum Materials in Press

HARUYAMA, Jun [C class; 7000 (B), 850 (C)] (59)
— *Electrochemical reaction analysis using density functional calcula- tion + implicit solvation model 6*
— *Electrochemical reaction analysis using density functional calculation + implicit solvation model 6-2*

1. Effects of chainchain interaction on the configuration of short-chain alkanethiol self-assembled monolayers on a metal surface
   C.-L. Liao, S. M. Faizanuddin, J. Haruyama, W.-S. Liao, and Y.-C. Wen J. Chem. Phys. **160**, 214711 (2024).
   DOI:10.1063/5.0214261

2. Correction to “Effect of Nitrogen Doping and Oxygen Vacancy on the Oxygen Reduction Reaction on the Tetragonal Zirconia(101) Surface ”
   S. Muhammady, J. Haruyama, S. Kasamatsu, and O. Sugino J. Phys. Chem. C **128**, 10248 (2024).
   DOI:10.1021/acs.jpcc.4c03502

3. Elucidation of CO Oxidation and CO2 Desorption Dynamics on Pt(111) by van der Waals DFT Calculations: Hyperthermal Kinetic Energy, Sharp Desorption Angle, and Excited Vibrational

States
H. Li, Y. Kataoka, S. Tanaka, J. Haruyama, O. Sugino, and J. Yoshinobu J. Phys. Chem. C **128**, 15393 (2024).
DOI:10.1021/acs.jpcc.4c03538

HATANO, Naomichi [B class; 500 (B), 0 (C)] (339)
— *Numerical Simulation of Kondo Walk*

HAYAMI, Satoru [C class; 5400 (B), 800 (C)] (218)
— *Efficient search of magnetic skyrmion crystal by using machine learning*
— *Generation of spin model based on machine learning*

1. Classification of Multi-Orbital Superconducting State based on Augmented Multipoles
   A. Kirikoshi and S. Hayami Physical Review B **109**, 174510 (2024).
   DOI:10.1103/PhysRevB.109.174510

2. Field-induced transformation between triangular and square skyrmion crystals in a tetragonal polar magnet
   S. Hayami Physical Review B **109**, 184419 (2024).
   DOI:10.1103/PhysRevB.109.184419

3. Linear and nonlinear spin-current generation in polar collinear antiferromagnets without relativistic spin-orbit coupling
   S. Hayami Physical Review B **109**, 214431 (2024).
   DOI:10.1103/PhysRevB.109.214431

4. Double-Q and quadruple-Q instabilities at low-symmetry ordering wave vectors under tetragonal symmetry
   S. Hayami Physical Review B **110**, 014404 (2024).
   DOI:10.1103/PhysRevB.110.014404

5. Anisotropic skyrmion crystal on a centrosymmetric square lattice under an in-plane magnetic field
   S. Hayami Journal of Magnetism and Magnetic Materials **604**, 172293 (2024).
   DOI:10.1016/j.jmmm.2024.172293

6. XXZ-type interlayer exchange interaction in the bilayer triangular-lattice system as a source of multiple skyrmion phases
   S. Hayami Journal of Magnetism and Magnetic Materials **619**, 172876 (2024).
   DOI:10.1016/j.jmmm.2025.172876

7. Stabilization mechanisms of magnetic skyrmion crystal and multiple-Q states based on momentum-resolved spin interactions
   S. Hayami and R. Yambe Materials Today Quantum **3**, 100010 (2024).
   DOI:10.1016/j.mtquan.2024.100010

HIDA, Kazuo [B class; 700 (B), 140 (C)] (318)
— *Numerical Study of One Dimensional Frustrated Quantum Spin Systems*

1. Ground-State Phase Diagram of (1/2, 1/2, 1) Mixed Diamond Chains
   Kazuo Hida, J. Phys. Soc. Jpn. **93**,044703 (2024).
   DOI:10.7566/JPSJ.93.044703

HIGUCHI, Yuji [C class; 8200 (B), 800 (C)] (259)
— *Crystal structure and mechanical properties of polymers with helical structure*
— *Fracture process of semicrystalline polymers using large-scale simulation*

1. Rotational Dynamics of Water near Osmolytes by Molecular Dynamics Simulations
   Yuji Higuchi, Md. Abu Saleh, Takahisa Anada, Masaru Tanaka, and Mafumi Hishida J. Phys. Chem. B **128**, 5008 (2024).
   DOI:10.1021/acs.jpcb.3c08470

2. Reversibility of Semicrystalline Polymers in Creep Testing by Coarse-Grained Molecular Dynamics Simulations
   Yuji Higuchi and Go Matsuba Macromol. Chem. Phys. **225**, 2400076 (2024).
   DOI:10.1002/macp.202400076

3. Hydration Water Dynamics in Zwitterionic Phospholipid Membranes Mixed with Charged Phospholipids
   Md. Khalidur Rahman, Takeshi Yamada, Norifumi L. Yamada, Yuji Higuchi, and Hideki Seto J. Phys. Chem. B **129**, 3998 (2025).
   DOI:10.1021/acs.jpcb.4c07371

HIRATA, Kenji [C class; 1000 (B), 0 (C)] (158)
— *First-principles calculation of dielectric constant in oxide-based phosphor*

HIRATSUKA, Masaki [B class; 400 (B), 70 (C)] ()
— *Calculation of vibrational spectra using graph neural network force field*

HIYAMA, Miyabi [B class; 650 (B), 0 (C)] (321)
— *Analysis for absorption- and fluorescence-spectra of seMpai by quantum chemical calculations*
— *Analysis for in situ absorption spectra in firefly bioluminescence by quantum chemical calculations*

HO, Ngoc [C class; 1800 (B), 300 (C)] ()
— *Pt-based high entropy alloys for fuel cell applications from multiscale simulations and machine learning method*

HOSHI, Takeo [C class; 4600 (B), 400 (C)] (37)
— *HPC-based fusion of simulation experiment analysis and data-driven science*

HOSONO, Nobuhiko [C class; 3000 (B), 300 (C)] (279)
— *Molecular Dynamics Simulation of Polymer Extraction Process from Nanopores*

1. Detecting Single-Point Isomeric Differences in Polymer Chains by MOF Column Chromatography
   N. HOSONO, Y. KONO, N. MIZUTANI, D. KOGA and T. UEMURA Chem. Commun. **60**, 13690 (2024).
   DOI:10.1039/D4CC04902K

HOTTA, Chisa [B,C class; 4200 (B), 400 (C)] ()
— *Analysis on the critical phases using quantum Glauber dynamics*
— *Disorder and dynamics of strongly correlated elecron in a multi-orbital systems*

HOTTA, Takashi [C class; 3400 (B), 0 (C)] (227)
— *Research of quantum critical points in the vicinity of three-channel Kondo phase*

HUKUSHIMA, Koji [C class; 4200 (B), 0 (C)] (270)
— *Large scale computation for spin glasses using extended ensemble methods*

IDO, Kota [C class; 8600 (B), 850 (C)] (258)
— *Ground-state phase diagram of extended Kondo lattice models*
— *Ground-state phase diagram of frustrated itinerant magnets*

1. Many-body Chern insulator in the Kondo lattice model on a triangular lattice
   Kota Ido, Takahiro Misawa Phys. Rev. B **109**, 245114 (2024).
   DOI:10.1103/PhysRevB.109.245114

IITAKA, Toshiaki [C class; 1600 (B), 250 (C)] (304)
— *Calculation of high dimensional systems at finite temperature using random quantum sates of general variational wave functions*

IKEMOTO, Hiroyuki [B class; 300 (B), 60 (C)] (352)
— *Structures of Sulphur Confined in Carbon Nanotubes*

IMADA, Masatoshi [E class; 12000 (B), 1100 (C)] (216)
— *Studies on Quantum Many-Body Problem by Machine Learning*

1. Dome structure in pressure dependence of superconducting transition temperature for HgBa2Ca2Cu3O8: Studies by ab initio low-energy effective Hamiltonian
   Jean-Baptiste Morée, Youhei Yamaji, and Masatoshi Imada Phys. Rev. Res. , **6** (2024) 023163
   DOI:10.1103/PhysRevResearch.6.023163

2. Fermi Machine — Quantum Many-Body Solver Derived from Correspondence between Noninteracting and Strongly Correlated Fermions
   Masatoshi Imada J. Phys. Soc. Jpn., **93** (2024) 104002
   DOI:10.7566/JPSJ.93.104002

3. Variational Benchmarks for Quantum Many-Body Problems
   Dian Wu, Masatoshi Imada, Yusuke Nomura, Rico Pohle, Michael Schmid, iuseppe Carleo *et al.*
   Science, **386**, (2024) 6719
   DOI:10.1126/science.adg9774

4. Forecasting long-time dynamics in quantum many-body systems by dynamic mode decomposition
   Ryui Kaneko, Masatoshi Imada,Yoshiyuki Kabashima, and Tomi Ohtsuki Phys. Rev. Res. , **7** (2025) 013085
   DOI:10.1103/PhysRevResearch.7.013085

INAGAKI, Kouji [B class; 300 (B), 60 (C)] (204)
— *Analyses of semiconductor surface processes by machine-learning based potentials*

INAOKA, Takeshi [B class; 300 (B), 70 (C)] (200)
— *Search and realization of novel electronic properties of surfaces and interfaces and of nanostructures*

1. First principles study of electronic structure of x-form phthalocyanine crystals doped with one-dimensional iodine atomic chains
   T. Inaoka AIP Advances **14**, 085016 (9 pages) (2024).
   DOI:10.1063/5.0216635

INOUE, Kazutoshi [C class; 4000 (B), 200 (C)] (95)
— *Theoretical exploring of the functionalities in ceramics interfaces*

1. Grain Boundary Structural Transformation and the Effect of Impurities in MgO
   Q. Chen, M. Saito, K. Kawahara, A. Nakamura, K. Inoue, Y. Ikuhara under review (2025).

2. Modeling and Epitaxial Matching of Incoherent and Heterointerfaces

K. Inoue, M. Saito, K. Kawahara, Q. Chen, M. Kotani, Y. Ikuhara under review (2025).

ISHIBASHI, Shoji [C class; 1800 (B), 0 (C)] (138)
— *Prediction of properties of organic ferroelectrics and piezoelectrics by first-principles calculations*

1. Unveiling high electro-optic performance in a proton-π-electron-coupled ferroelectric crystal
   K. SUNAMI, S. HORIUCHI, S. ISHIBASHI, and J. TSUTSUMI Adv. Electron. Mater. **11**, 2400346 (2025).
   DOI:10.1002/aelm.202400346

ISHIDA, Kunio [B class; 1100 (B), 190 (C)] ()
— *Coherent dynamics of strongly coupled electron-phonon-photon systems*

ISHIDA, Takato [B class; 400 (B), 0 (C)] (348)
— *Long-term Reliability Assessment of Reinforced Concrete Structures with Polymer Barrier Layers on the Surface*

1. Coarse-grained Molecular Dynamics Simulation of Oxidative Aging of Polymers - Effect of free radical diffusivity -
   T. Ishida, Y. Doi, T. Uneyama, and Y. Masubuchi Polymer Journal, 56, 10691078 (2024).
   DOI:10.1038/s41428-024-00942-5

2. Analysis of non-Gaussian diffusion of Hydrogen and Oxygen in Cement Paste Using a Two-State Fluctuating Diffusivity Model
   F. Nakai, and T. Ishida Nihon Reoroji Gakkaishi (J Soc Rheol Jpn) , 52(2), 83-89 (2024).
   DOI:10.1678/rheology.52.83

ISHII, Fumiyuki [C class; 10400 (B), 900 (C)] (47)
— *Development and application of computational programs for spin conversion physical properties using first-principles methods*
— *Development of a first-principles computational method for thermoelectric effects in thin film systems and application to van der Waals systems*

ISHIKAWA, Takahiro [C class; 1200 (B), 100 (C)] (150)
— *Search for high temperature superconductivity in hydrides*

ISOBE, Masaharu [B class; 400 (B), 70 (C)] (342)
— *Local structure analysis and non-equilibrium phase transition in self-propelled hard polygon systems*

1. Simple and efficient methods for local structural analysis in polydisperse hard disk systems
   D. Mugita, K. Souno, H. Koyama, T. Nakamura, and M. Isobe, J. Chem. Phys. **160**, 174104 (2024).
   DOI:10.1063/5.0194873

2. Microscopic mechanisms of diffusion dynamics : a comparative efficiency study of event-chain Monte Carlo variants in dense hard disk systems
   D. Mugita and M. Isobe, J. Chem. Phys. **161**, 154508 (2024).
   DOI:10.1063/5.0226246

3. Recursive algorithm to the centroid of free area for inherent structure and hopping motion in deeply supercooled binary hard disk systems
   D. Mugita , K. Souno, and M. Isobe, J. Phys. Soc. Jpn. **94**,024002 (2025).
   DOI:10.7566/JPSJ.94.024002

4. Self-organized spatial inhomogeneity in self-propelled quasi-elastic hard disk systems

R. Kitagawa, D. Mugita, N. Murase, and M. Isobe, Proceedings of the 30th Symposium on Traffic Flow and Self-driven Particles, **30**, 9 (2025).

IZUMI, Yasuo [B class; 450 (B), 90 (C)] (177)

— *Clarification of the Activation Principle of Photocatalyts by Doping Metal Atom*

1. Exchange of CO2 with CO as Reactant Switches Selectivity in Photoreduction on CoZrO2 from C13 Paraffin to Small Olefins
   T. Loumissi, R. Ishii, K. Hara, T. Oyumi, I. Abe, C. Li, H. Zhang, R. Hirayama, K. Niki, T. Itoi, and Y. Izumi Angew. Chem. Int. Ed. **63**, e202412090 (2024).
   DOI:10.1002/anie202412090

2. Light intensitydirected selective CO2 photoreduction using iron(0)zirconium dioxide photocatalyst
   T. Oyumi, I. Abe, M. Sasaki, and Y. Izumi Chem. Commun. **61**, submitted on March 3 2025 and under review (2025).

3. The Role of Oxygen Vacancy on the Carbon Dioxide Photoreduction Using Monoclinic and Tetragonal-phase Zirconium Oxide
   Ayana Omata, Keisuke Hara, Tomoki Oyumi, Rento Ishii, Yasuo Izumi, and Kaori Niki e-J. Surf. Sci. Nanotechnol. **22**, 327-333 (2024).
   DOI:10.1380/ejssnt.2024-032

JESCHKE, Harald [C class; 2600 (B), 0 (C)] (292)

— *Superconducting critical temperature and gap structure of kappa-type BEDT-TTF superconductors*

1. Pressure tuning of intrinsic and extrinsic sources to the anomalous Hall effect in $CrGeTe_3$
   G. Scharf, D. Guterding, B. Hen, P. M. Sarte, B. R. Ortiz, G. Kh. Rozenberg, T. Holder, S. D. Wilson, H. O. Jeschke, and A. Ron Phys. Rev. Res. **7**, 013127 (2025).
   DOI:10.1103/PhysRevResearch.7.013127

2. Near room-temperature ferromagnetism from double exchange in the van der Waals material $CrGeTe_3$: Evidence from optical conductivity under pressure
   J. Ebad-Allah, D. Guterding, M. Varma, M. Diware, S. Ganorkar, H. O. Jeschke, and C. A. Kuntscher Phys. Rev. B **111**, L140402 (2025).
   DOI:10.1103/PhysRevB.111.L140402

3. $CuAg(SO_4)_2$: A doubly strongly correlated altermagnetic three-dimensional analog of the parent compounds of high-Tc cuprates
   H. O. Jeschke, M. Shimizu, and I. I. Mazin Phys. Rev. B **109**, L220412 (2024).
   DOI:10.1103/PhysRevB.109.L220412

JIA, Xue [C class; 2200 (B), 0 (C)] (127)

— *Designing low-cost Metal Oxide Heterostructure catalysts for oxygen evolution reaction through High-Throughput Calculations*

1. Divergent Activity Shifts of Tin - Based Catalysts for Electrochemical CO2 Reduction: pH - Dependent Behavior of Single - Atom Versus Polyatomic Structures
   Y. Wang, D. Zhang, B. Sun, X. Jia, L. Zhang, H. Cheng, J. Fan, and H. Li Angew. Chem. Int. Ed. **64**, e202418228 (2025).
   DOI:10.1002/anie.202418228

2. Origin of the Activity of Electrochemical Ozone Production Over Rutile PbO2 Surfaces
   J. Jiang, Z Guo, S. Deng, X. Jia, H. Liu, J. Xu, H. Li, L. Cheng ChemSusChem **17**, e202400827

(2025).
DOI:10.1002/cssc.202400827

JIE, Sun [C class; 3800 (B), 400 (C)] (93)
— *High-order phonon database and high-performance thermal switch of two-dimensional materials*

KADARISMAN, Hana [B class; 300 (B), 60 (C)] (203)
— *Spin-splitting calculation of Si Ge and Diamond materials*

KAGESHIMA, Hiroyuki [C class; 1800 (B), 300 (C)] (129)
— *Study on physical properties of structural elementary excitations at solid surfaces and interfaces*

1. First-principles Study of Intrinsic hBN Island Nucleated During CVD Initial Growth on Cu(111)
   R. Imamura, I. Seo, and H. Kageshima, e-J. Surf. Sci. Nanotechnol. 23 (2025) *advanced online publication* (13 pages).
   DOI:10.1380/ejssnt.2025-018

KAIJU, Hideo [B class; 1450 (B), 270 (C)] (141)
— *Electronic structure analysis of Heusler-alloy-based magnetic tunnel junctions using first-principles calculation*
— *Electronic structure analysis of half-metal based magnetic tunnel junctions using first-principles calculation*
— *Electronic structure analysis of organic spin valve devices using first-principles calculation*

KANEKO, Ryui [B class; 900 (B), 170 (C)] (312, 314)
— *Calculating entanglement dynamics in free boson systems by random sampling*
— *Dynamic mode decomposition of time-series data in quantum many-body systems*

1. Entanglement entropy dynamics of non-Gaussian states in free boson systems: Random sampling approach
   R. Kaneko, D. Kagamihara, and I. Danshita Phys. Rev. A **111**, 032412 (2025).
   DOI:10.1103/PhysRevA.111.032412

2. Forecasting long-time dynamics in quantum many-body systems by dynamic mode decomposition
   R. Kaneko, M. Imada, Y. Kabashima, and T. Ohtsuki Phys. Rev. Research **7**, 013085 (2025).
   DOI:10.1103/PhysRevResearch.7.013085

3. Ground-state phase diagram of the SU(4) Heisenberg model on a plaquette lattice
   R. Kaneko, S. Goto, and I. Danshita Phys. Rev. A **110**, 023326 (2024).
   DOI:10.1103/PhysRevA.110.023326

KARIYADO, Toshikaze [B class; 400 (B), 50 (C)] (346)
— *Theoretical study of magnetic properties in atomically thin materials*

1. Strongly hybridized phonons in one-dimensional van der Waals crystals
   S. Sun, Q. Lin, Y. Li, D. Kozawa, H. Wu, S. Maruyama, P. Moon, T. Kariyado, R. Kitaura, and S. Zhao Phys. Rev. Lett, accepted (2025).

2. Spin interactions in decorated graphene nanoflakes with two localized spin-1/2 entities
   T. Kariyado Materials Today Quantum, accepted (2025).

KASAMATSU, Shusuke [C class; 4600 (B), 400 (C)] (80)

— *Understanding Fast Ion Conduction in Inhomogeneous Materials*

1. Comparison of intermediate-range order in GeO2 glass: Molecular dynamics using machine-learning interatomic potential vs reverse Monte Carlo fitting to experimental data
   Kenta Matsutani, Shusuke Kasamatsu, and Takeshi Usuki, J. Chem. Phys. **161**, 204103 (2024).
   DOI:10.1063/5.0240087

2. Emerging computational and machine learning methodologies for proton conducting oxides: materials discovery and fundamental understanding
   Susumu Fujii, Junji Hyodo, Kazuki Shitara, Akihide Kuwabara, Shusuke Kasamatsu, and Yoshihiro Yamazaki, Sci. Technol. Adv. Mater., 25, 1, 2416383 (2024).
   DOI:10.1080/14686996.2024.2416383

3. Defect Segregation, WaterLayering, and Proton Transfer at Zirconium Oxynitride/Water Interface Examined Using Neural Network Potential
   Akitaka Nakanishi, Shusuke Kasamatsu, Jun Haruyama, and Osamu Sugino, J. Phys. Chem. C **129**, 2403-2420 (2025).
   DOI:10.1021/acs.jpcc.4c05857

KATO, Takeo [B class; 500 (B), 90 (C)] (326)
— *Numerical Simulation of Anyons in Fractional Quantum Hall Systems*

KATOW, Hiroki [B class; 400 (B), 0 (C)] ()
— *Development of Numerical methods for Light-Matter Interaction*

KAWAKATSU, Toshihiro [C class; 4000 (B), 0 (C)] (271)
— *Multiscale simulations for complex flows*

KAWAMURA, Hikaru [C class; 600 (B), 0 (C)] ()
— *Novel order in frustrated magnets*

KAWAMURA, Taira [B class; 450 (B), 90 (C)] (333)
— *A study of the dynamics of thermal equilibrium and nonequilibrium FFLO states using the nonequilibrium Green's function technique*

1. Engineering nonequilibrium superconducting phases in a voltage-driven superconductor under an external magnetic field
   T. Kawamura, and Y. Ohashi arXiv:2503.04179
   DOI:10.48550/arXiv.2503.04179

2. Nonequilibrium electron distribution function in a voltage-biased metal wire: A nonequilibrium Green ' s function approach
   T. Kawamura, and Y. Kato arXiv:2503.05141
   DOI:10.48550/arXiv.2503.05141

KAWANO, Shoya [B class; 400 (B), 0 (C)] (196)
— *first-principles calculation of tungsten alloy*

KAWASHIMA, Naoki [E class; 29500 (B), 0 (C)] (249)
— *New low-rank approximation by tensor ring decomposition and its application to critical phenomena*

1. Generating Function for Projected Entangled-Pair States
   Wei-Lin Tu, Laurens Vanderstraeten, Norbert Schuch, Hyun-Yong Lee, Naoki Kawashima, and Ji-Yao Chen Physical Review X Quantum 5, 010335 (2024).
   DOI:10.1103/PRXQuantum.5.010335

2. Programmable Order by Disorder Effect through Quantum Simulator
Huan-Kuang Wu, Takafumi Suzuki, Naoki Kawashima, Wei-Lin Tu Physical Review Research 6, 023297 (2024).
DOI:10.1103/PhysRevResearch.6.023297

3. Faithfulness of Real-Space Renormalization Group Maps
Katsuya O. Akamatsu and Naoki Kawashima Journal of Statistical Physics 191, 109 (2024).
DOI:10.1007/s10955-024-03323-7

4. Nuclear norm regularized loop optimization for tensor network
Kenji Homma, Tsuyoshi Okubo, Naoki Kawashima Physical Review Research 6, 043102 (2024).
DOI:10.1103/PhysRevResearch.6.043102

5. Emergent intermediate phase in the J 1-J 2 XY model from tensor network approaches
Feng-Feng Song, Hanggai Nuomin, and Naoki Kawashima Physical Review B 111, 104428 (2025).
DOI:10.1103/PhysRevB.111.104428

6. Multi-impurity method for the bond-weighted tensor renormalization group
Satoshi Morita and Naoki Kawashima Physical Review B 111, 054433 (2025).
DOI:10.1103/PhysRevB.111.054433

Data Repository
Monte Carlo database on quantum spin models
https://isspns-gitlab.issp.u-tokyo.ac.jp/kawashima/monte-carlo-database-on-quantum-spin-models

KEIJI, Yashiro [B class; 500 (B), 100 (C)] ()
— *Study of hydrogen sulfide adsorbent for high efficiency of fuel cells with direct biogas supply*

KITAO, Akio [C class; 3400 (B), 350 (C)] (273)
— *Efficient sampling simulation of the soft modes significantly contribute to protein properties*

KOBAYASHI, Akito [B class; 400 (B), 80 (C)] (240)
— *Elucidation of novel order induced by electronic correlation in organic conductors and related anomalous properties*

1. Compensated Ferrimagnets with Colossal Spin Splitting in Organic Compounds
Taiki Kawamura, Kazuyoshi Yoshimi, Kenichiro Hashimoto, Akito Kobayashi, and Takahiro Misawa Phys. Rev. Lett. 132, 15, 156502 (2024).
DOI:10.1103/PhysRevLett.132.156502

2. H-wave - A Python package for the Hartree-Fock approximation and the random phase approximation
Tatsumi Aoyama, Kazuyoshi Yoshimi, Kota Ido, Yuichi Motoyama, Taiki Kawamura, Takahiro Misawa, Takeo Kato, Akito Kobayashi Computer Physics Communications 298, 109087 (2024).
DOI:10.1016/j.cpc.2024.109087

KOBAYASHI, Katsuyoshi [B class; 500 (B), 80 (C)] (175)
— *Theoretical study on electronic properties of new nanoscale surfaces and interfaces*

KOBAYASHI, Nobuhiko [C class; 3800 (B), 350 (C)] (96)
— *Quantum transport theory by large scale first-principles electron transport calculations*

1. The efficient method for searching stable structures in herringbone-phase organic semiconductors using density functional theory
S. Hakata, H. Ishii, H. Takaki, T. Okamoto, J. Takeya, N. Kobayashi Appl. Phys. Express 17

101001 (2024).
DOI:10.35848/1882-0786/ad7f21

2. Order-N calculations for thermoelectric power factor based on linear response theory
H. Ishii, N. Kobayashi, K. Hirose J. Phys.: Condens. Matter 36 335903 (2024).
DOI:10.1088/1361-648X/ad4a15

KOBAYASHI, Yoshihiro [B class; 250 (B), 70 (C)] (355)
— *Molecular dynamics simulation of graphene-nanosapcer stacking structure*

1. Experimental and Theoretical Investigation of Nanodiamond Insertion on the Interlayer Interaction in Multilayer Stacking Graphene
M. Ding, T. Inoue, J. I. Enriquez, H. H. Handoko, Y. Ogawa, Y. Taniyasu, Y. Hamamoto, Y. Morikawa, Y. Kobayashi Carbon **229**, 119464 (2024).
DOI:10.1016/j.carbon.2024.119464

KOGA, Akihisa [C,D class; 4600 (B), 600 (C)] (220)
— *Analyzing Ferromagnetic Order in Multi-Component Fermionic Systems using DMFT*
— *Numerical analysis of the dissipation-induced superfluidity in non-Hermitian SU(N) Hubbard model*

KOSHOJI, Ryotaro [C class; 1400 (B), 350 (C)] (301)
— *Mathematical Crystal Chemistry*

1. Mathematical crystal chemistry: A mathematical programming approach to crystal structures of inorganic compounds
R. Koshoji and T. Ozaki Phys. Rev. Materials **8**, 113801 (2024).
DOI:10.1103/PhysRevMaterials.8.113801

2. Mathematical crystal chemistry II: Random search for ionic crystals and analysis on oxide crystals registered in ICSD
R. Koshoji arXiv:2503.20273
DOI:10.48550/arXiv.2503.20273

KOURA, Akihide [C class; 2600 (B), 0 (C)] (122)
— *Ab Initio Study on Static Structure of White Light Generating Amorphous Molecular Materials*

1. Intermolecular Correlations in Liquid Lactic Acid Based on ab initio Molecular Dynamics Simulations Combined with High-Energy X-ray Diffraction Measurements
Kai Ito, Hironori Shimakura, Shuta Tahara, Koji Ohara, Akihide Koura, Kohei Shimamura, and Fuyuki Shimojo Journal of Physical Society of Japan **93**, 054601 (2024).
DOI:10.7566/JPSJ.93.054601

2. Thermal Conductivity Calculation using Homogeneous Non-equilibrium Molecular Dynamics Simulation with Allegro
K. Shimamura, S. Hattori, K. Nomura, A. Koura, and F. Shimojo International Journal of Heat and Mass Transfer **234**, 126106 (2024).
DOI:10.1016/j.ijheatmasstransfer.2024.126106

3. Phase Behavior and Atomic Dynamics in Rb_xNa_{1-x}: Insights from Machine Learning Interatomic Potentials based on Ab Initio Molecular Dynamics
A. Irie, Akihide Koura, Kohei Shimamura, and Fuyuki Shimojo Journal of Physics: Condensed Matter **37**, 065401 (2025).
DOI:10.1088/1361-648X/ad9071

4. Intermolecular Correlations in Liquid Racemic Lactic Acid: A Comparison with Liquid L-Lactic

Acid
Kai Ito, Hironori Shimakura, Shuta Tahara, Koji Ohara, Akihide Koura, Kohei Shimamura, Fuyuki Shimojo Journal of the Physical Society of Japan, accepted for publication, (2025).

KUNISADA, Yuji [C class; 7400 (B), 0 (C)] (67)
— *Development of Ceramic Protective Coating for High Corrosion Resistance of Metallic Materials*
— *Development of Ceramic Protective Coating to suppress hydrogen embrittlement of metallic materials*

1. Unveiling the origin of diffusion suppression of hydrogen isotopes at the α-$Al_2O_3(0001)/\alpha$-$Cr_2O_3(0001)$ interfaces
   Y. Kunisada, R. Sano, and N. Sakaguchi, International Journal of Hydrogen Energy **97**, 1327 (2025).
   DOI:10.1016/j.ijhydene.2024.12.027

KUROKI, Kazuhiko [C class; 4800 (B), 0 (C)] (221)
— *Theoretical search for new high T_c nickelate superconductors based on structural and phonon DFT analysis*

KUSAKABE, Koichi [C class; 3200 (B), 0 (C)] (112)
— *Theoretical evaluation of mechanical properties of nano-carbon device structures*

1. Surface terminations control charge transfer from bulk to surface states in topological insulators
   K. Fukumoto, S. Lee, S. Adachi, Y. Suzuki, K. Kusakabe, R. Yamamoto, M. Kitatani, K. Ishida, Y. Nakagawa, M. Merkel, D. Shiga, and H. Kumigashira Sci. Rep. **14**, 10537 (2024).
   DOI:10.1038/s41598-024-61172-6

2. Giant Rashba spin-orbit coupling on light-element polar superlattices
   Y. Wicaksono, J.-Y. You, B. Gu, A. Evseev, I. Piyanzina, K. Kusakabe, S. Yunoki, and S. Maekawa Phys. Rev. B **110**, L220408 (2024).
   DOI:10.1103/PhysRevB.110.L220408

3. Designing a Polymerized Phenalenyl Tessellation Molecule to Realize a Super-honeycomb Antiferromagnetic S = 3/2 Spin System
   K. Komatsu, N. Morishita, M. Kitatani, and K. Kusakabe J. Phys. Soc. Jpn. **94**, 044704 (2025).
   DOI:10.7566/JPSJ.94.044704

4. Synthesis, crystal and electronic structures, and second harmonic generation of La4Ge3S12
   H. Ohtsuki, S. Nakata, Y. Yamane, R. Takahashi, K. Kusakabe, and H. Wadati Z. anorg. allg. Chem. e202500029, (2025).
   DOI:10.1002/zaac.202500029

LEE, Minhyeok [C class; 800 (B), 250 (C)] (156)
— *Modeling of the Ammonia Decomposition Reaction and Nitriding on Metal Surfaces*

LI, Hao [C class; 4800 (B), 0 (C)] (84)
— *Understanding Hydrogen Energy Materials by Ab Initio Calculations and Multiscale Modeling and Simulations*

LUONG, HuuDuc [C,D class; 7800 (B), 600 (C)] ()
— *Investigation of promising cathode material for Na-ion battery.*
— *Investigation on positive electrodes applicable for Na-ion batteries*

MAEHIRA, Takahiro [B class; 200 (B), 50 (C)] (209)
— *Electronic Structure of WO_3*

MAKINO, Takayuki [B class; 400 (B), 70 (C)] (192)
— *Excitonic properties of delafossite-type cuprates*

MASAKI, Yusuke [B class; 300 (B), 70 (C)] (351)
— *Solitons and phase transitions in quantum chiral spin model in tilted magnetic field*

MATSUKAWA, Hiroshi [C class; 2800 (B), 300 (C)] ()
— *Physics of Friction*

MATSUSHITA, Katsuyoshi [C class; 600 (B), 0 (C)] ()
— *Stability Analysis of Collective Cell Movement due to Different Polarity Symmetry*
— *The Investigation of Effects of Cell Polarity Symmetries on Motion Order of Cells*

MATSUSHITA, Yu-ichiro [E class; 16000 (B), 1950 (C)] (43)
— *Emergence of new functions by controlling atomic structures in wide-gap semiconductors based on first-principles calculations*
— *Identification of Killer Defects in SiC-MOS Devices by First-Principles Calculations*

1. Optimized synthesis of circuits for diagonal unitary matrices with reflection symmetry
   Xinchi Huang ,Taichi Kosugi ,Hirofumi Nishi ,and Yu-ichiro Matsushita J. Phys. Soc. Jpn. **93**, 054002 (2024).
   DOI:10.7566/JPSJ.93.054002

2. Channel attention for quantum convolutional neural networks
   Gekko Budiutama, Shunsuke Daimon, Hirofumi Nishi, Ryui Kaneko, Tomi Ohtsuki, Yu-ichiro Matsushita Phys. Rev. A **110**, 012447(2024).
   DOI:10.1103/PhysRevA.110.012447

3. Orbital-free density functional theory with first-quantized quantum subroutines
   Yusuke Nishiya, Hirofumi Nishi, Taichi Kosugi, Yu-ichiro Matsushita arXiv:2407.16191(2024).
   DOI:10.48550/arXiv.2407.16191

4. A probabilistic imaginary-time evolution quantum algorithm for advection-diffusion equation: Explicit gate-level implementation and comparisons to quantum linear system algorithms
   Xinchi Huang, Hirofumi Nishi, Taichi Kosugi, Yoshifumi Kawada, Yu-ichiro Matsushita arXiv:2409.18559v2(2024).
   DOI:10.48550/arXiv.2409.18559

5. Qubit encoding for a mixture of localized functions
   Taichi Kosugi, Shunsuke Daimon, Hirofumi Nishi, Yu-ichiro Matsushita Phys. Rev. A **110**, 062407(2024).
   DOI:10.1103/PhysRevA.110.062407

6. Tensor decomposition technique for qubit encoding of maximal-fidelity Lorentzian orbitals in real-space quantum chemistry
   Taichi Kosugi, Xinchi Huang, Hirofumi Nishi, Yu-ichiro Matsushita arXiv:2501.07211(2024).
   DOI:10.48550/arXiv.2501.07211

7. Encoded probabilistic imaginary-time evolution on a trapped-ion quantum computer for ground and excited states of spin qubits
   Hirofumi Nishi, Yuki Takei, Taichi Kosugi, Shunsuke Mieda, Yutaka Natsume, Takeshi Aoyagi, Yu-ichiro Matsushita Phys. Rev. Applied **23**, 034016(2025).
   DOI:10.1103/PhysRevApplied.23.034016

8. Approximate real-time evolution operator for potential with one ancillary qubit and application to first-quantized Hamiltonian simulation

Xinchi Huang, Taichi Kosugi, Hirofumi Nishi, Yu-ichiro Matsushita Quant. Inf. Proc. **24**, 85(2025).
DOI:10.1007/s11128-025-04697-7

9. Machine Learning Supported Annealing for Prediction of Grand Canonical Crystal Structures
Yannick Couzinie, Yuya Seki, Yusuke Nishiya, Hirofumi Nishi, Taichi Kosugi, Shu Tanaka, Yu-ichiro Matsushita J. Phys. Soc. Jpn. **94**, 044802(2025).
DOI:10.7566/JPSJ.94.044802

MINAMI, Susumu [B class; 400 (B), 80 (C)] (186)
— *First-principles study for anomalous Nernst effect in topological magnets*

MISAWA, Masaaki [B class; 400 (B), 0 (C)] (195)
— *Computational study of surface and interface phenomena and mechanical properties of functional materials based on atomic-scale structures*

MISAWA, Takahiro [E class; 13500 (B), 1150 (C)] (366)
— *Study of correlated topological insulators using the ab initio method for correlated electron systems*

MITARAI, Yoko [B class; 850 (B), 90 (C)] (159)
— *Phase transformation and electric state of high entropy alloys*

1. Effect of reactive elements in MCrAlX bond coat for durability improvement of thermal barrier coatings
M. Negami, R. Morihashi, T. Yoshino, R. Sahara, Y. Yamabe-Mitarai Corrosion Science 237, 112329 (2024).
DOI:10.1016/j.corsci.2024.112329

2. Deformation mechanisms of hexagonal close-packed-multi-principal element alloys (HCP-MPEAs) with equiaxed structures
S. J. Liang, T. Yoshino, R. Matsumoto, R. Sahara, Y. Toda, S. Matsunaga, G. Miyamoto, Y. Yamabe-Mitarai Materials Science and Engineering A 929, 148143 (2025).
DOI:10.1016/j.msea.2025.148143

MIZUKAMI, Wataru [C class; 7600 (B), 400 (C)] (263)
— *Creating a quantum computing database for sensor materials*

1. Comparative study on compact quantum circuits of hybrid quantum-classical algorithms for quantum impurity models
Rihito Sakurai, Oliver J. Backhouse, George H. Booth, Wataru Mizukami, Hiroshi Shinaoka, Phys. Rev. Research 6, 023110 (2024).
DOI:10.1103/PhysRevResearch.6.023110

2. Universal neural network potentials as descriptors: Towards scalable chemical property prediction using quantum and classical computers
Tomoya Shiota, Kenji Ishihara, Wataru Mizukami, Digital Discovery 3, 1714 (2024).
DOI:10.1039/D4DD00098F

3. Ab initio extended Hubbard model of short polyenes for efficient quantum computing
Yuichiro Yoshida, Nayuta Takemori, Wataru Mizukami, J. Chem. Phys. 161, 084303 (2024).
DOI:10.1063/5.0213525

4. Hunting for quantum-classical crossover in condensed matter problems
Nobuyuki Yoshioka, Tsuyoshi Okubo, Yasunari Suzuki, Yuki Koizumi and Wataru Mizukami, npj Quantum Information 10, 45 (2024).

DOI:10.1038/s41534-024-00839-4

5. Lowering the exponential wall: accelerating high-entropy alloy catalysts screening using local surface energy descriptors from neural network potentials
Tomoya Shiota, Kenji Ishihara, Wataru Mizukami, Digital Discovery 4, 738 (2025).
DOI:10.1039/D4DD00303A

6. Taming Multi-Domain, -Fidelity Data: Towards Foundation Models for Atomistic Scale Simulations
Tomoya Shiota, Kenji Ishihara, Wataru Mizukami, arXiv.2412.13088
DOI:10.48550/arXiv.2412.13088

7. Enhancing quantum computations with the synergy of auxiliary field quantum Monte Carlo and computational basis tomography
Viktor Khinevich, Wataru Mizukami, Wataru Mizukami, arXiv.2502.20066
DOI:10.48550/arXiv.2502.20066

MOCHIZUKI, Masahito [B class; 400 (B), 40 (C)] (241)
— *Theoretical study on the correlation effects of magnon-band topology and their optical detections*

MOCHIZUKI, Yasuhide [C class; 4000 (B), 400 (C)] (91)
— *Elucidation of negative thermal expansion behavior based on the first-principles molecular-dynamics calculations using machine-learning potential*

MOID, Mohammad [E class; 800 (B), 0 (C)] ()
— *Heterogeneous nucleation of water droplet*

MORIKAWA, Yoshitada [E class; 24000 (B), 2300 (C)] (41)
— *Theoretical study on chemical reaction processes at surfaces and interfaces using density functional theory and machine learning methods*

1. Stabilization of oxygen vacancy ordering and electrochemical-proton-insertion-and-extraction-induced large resistance modulation in strontium iron cobalt oxides $Sr(Fe,Co)O_y$
Y. Isoda, T. N. Pham, R. Aso, S. Nakamizo, T. Majima, S. Hosokawa, K. Nitta, Y. Morikawa, Y. Shimakawa, and D. Kan, Nature Communications **16**, 56 (2025).
DOI:10.1038/s41467-024-55517-y

2. Origin of the Surface Facet Dependence in the Thermal Degradation of the Diamond (111) and (100) Surfaces in Vacuum Investigated by Machine Learning Molecular Dynamics Simulations
J. I. G. Enriquez, H. H. Halim, T. Yamasaki, M. Michiuchi, K. Inagaki, M. Geshi, I. Hamada, Y. Morikawa Carbon **226**, 119223 (2024).
DOI:10.1016/j.carbon.2024.119223

3. Identification of Chemical Species on Plasma-treated Polytetrafluoroethylene Surface by Ab-initio Calculations of Core-energy-level Shift in X-ray Photoelectron Spectra
M. Nishino, K. Inagaki, Y. Morikawa, K. Yamamura, and Y. Ohkubo Appl. Surf. Sci. **655**, 159369 (2024).
DOI:10.1016/j.apsusc.2024.159369

4. Origin of the Surface Facet Dependence in the Oxidative Etching of the Diamond (111) and (100) Surfaces from First-Principles Calculations
J. I. G. Enriquez, T. Yamasaki, M. Michiuchi, K. Inagaki, M. Geshi, I. Hamada, Y. Morikawa J. Phys. Chem. C **128**, 6294-6308 (2024).
DOI:10.1021/acs.jpcc.3c08378

5. Stability of Pd_xO_y Particles Supported on Strontium Titanate Perovskite under Three-Way Catalyst Operating Conditions: Implications for Sintering Resistance
T. N. Pham, B. A. Choi Tan, Y. Hamamoto, K. Inagaki, I. Hamada, and Y. Morikawa ACS Catal. **14**, 1443-1458 (2024).
DOI:10.1021/acscatal.3c05673

MORITA, Satoshi [B class; 500 (B), 80 (C)] (331)
— *Bond-weight optimization in tensor network renormalization groups*

1. Optimization of conveyance of quantum particles by moving potential-well
S. Morita, Y. Teranishi, and S. Miyashita Phys. Rev. Research **6**, 043329 (2024).
DOI:10.1103/PhysRevResearch.6.043329

2. Multi-impurity method for the bond-weighted tensor renormalization group
S. Morita and N. Kawashima Phys. Rev. B **111**, 054433 (2025).
DOI:10.1103/PhysRevB.111.054433

Data Repository
Multi-impurity method for the bond-weighted tensor renormalization group
https://datarepo.mdcl.issp.u-tokyo.ac.jp/repo/49

MOTOME, Yukitoshi [C,D class; 20000 (B), 1400 (C)] (212)
— *Numerical study of extended Kitaev models in three dimensions by the pseudo-fermion functional renormalization group method*
— *Theoretical study of strongly correlated electron systems using quantum many-body simulation and information science*

1. SP-STM study of the multi-Q phases in $GdRu_2Si_2$
J. Spethmann, N. D. Khanh, H. Yoshimochi, R. Takagi, S. Hayami, Y. Motome, R. Wiesendanger, S. Seki, and K. von Bergmann Phys. Rev. Materials **8**, 064404 (2024).
DOI:10.1103/PhysRevMaterials.8.064404

2. Inverse Hamiltonian design of highly-entangled quantum systems
K. Inui and Y. Motome Phys. Rev. Research **6**, 033080 (2024).
DOI:10.1103/PhysRevResearch.6.033080

3. Eight-color chiral spin liquid in the $S = 1$ bilinear-biquadratic model with Kitaev interactions
R. Pohle, N. Shannon, and Y. Motome Phys. Rev. Research **6**, 033077 (2024).
DOI:10.1103/PhysRevResearch.6.033077

4. Magnetic field effects on the Kitaev model coupled to environment
K. Fukui, Y. Kato, and Y. Motome Phys. Rev. B **110**, 024429 (2024).
DOI:10.1103/PhysRevB.110.024429

5. Topological transitions by magnetization rotation in kagome monolayers of the ferromagnetic Weyl semimetal Co-based shandite
K. Nakazawa, Y. Kato, and Y. Motome Phys. Rev. B **110**, 085112 (2024).
DOI:10.1103/PhysRevB.110.085112

6. Exploring rare-earth Kitaev magnets by massive-scale computational analysis
S.-H. Jang and Y. Motome Commun. Mater. **5**, 192 (2024).
DOI:10.1038/s43246-024-00634-w

7. Exchange interactions in rare-earth magnets A_2PrO_3 (A= alkali metals)
S.-H. Jang and Y. Motome Phys. Rev. B **110**, 155124 (2024).

DOI:10.1103/PhysRevB.110.155124

8. Topological phase diagram of the Haldane model on a Bishamon-kikko–honeycomb lattice
S. Ikegami, K. Fukui, S. Okumura, Y. Kato, and Y. Motome Phys. Rev. B **110**, 245107 (2024).
DOI:10.1103/PhysRevB.110.245107

9. Pressure-induced quantum melting of chiral spin order and subsequent transition to a degenerate semiconductor state in FeGe
Y. Fujishiro, C. Terakura, A. Miyake, N. Kanazawa, K. Nakazawa, N. Ogawa, H. Kadobayashi, S. Kawaguchi, T. Kagayama, M. Tokunaga, Y. Kato, Y. Motome, K. Shimizu, and Y. Tokura Phys. Rev. B **110**, L220401 (2024).
DOI:10.1103/PhysRevB.110.L220401

10. Possible realization of Kitaev spin liquids in van der Waals heterostructures of α-$RuCl_3$ and CrX_3 (X=Cl and I)
L. Zhang and Y. Motome Phys. Rev. B **110**, L241109 (2024).
DOI:10.1103/PhysRevB.110.L241109

11. Altermagnetic perovskites
M. Naka, Y. Motome, and H Seo npj Spintronics **3**, 1 (2025).
DOI:10.1038/s44306-024-00066-9

12. Soliton penetration from edges in a monoaxial chiral magnet
K. Shimizu, S. Okumura, Y. Kato, and Y. Motome Phys. Rev. B **111**, 024411 (2025).
DOI:10.1103/PhysRevB.111.024411

13. Current-induced motion of nanoscale magnetic torons over the wide range of the Hall angle
K. Shimizu, S. Okumura, Y. Kato, and Y. Motome Commun. Phys. **8**, 69 (2025).
DOI:10.1038/s42005-025-01970-0

14. Spin Seebeck Effect as a Probe for Majorana Fermions in Kitaev Spin Liquids
Y. Kato, J. Nasu, M. Sato, T. Okubo, T. Misawa, and Y. Motome Phys. Rev. X **15**, 011050 (2025).
DOI:10.1103/PhysRevX.15.011050

15. Quantum reservoir probing: an inverse paradigm of quantum reservoir computing for exploring quantum many-body physics
K. Kobayashi and Y. Motome, submitted to Sci. Post.

16. Quantum reservoir probing of quantum phase transitions
K. Kobayashi and Y. Motome accepted for publication in Nat. Commun.

17. Spin-Orbit Coupled Insulators and Metals on the Verge of Kitaev Spin Liquids in Ilmenite Heterostructures
Y.-F. Zhao, S.-H. Jang, and Y. Motome submitted to Phys. Rev. B

18. Three-dimensional Topological Superstructure of Magnetic Hopfions Threaded by Meron Strings in Easy-plane Magnets
S. Kasai, K. Shimizu, S. Okumura, Y. Kato, and Y. Motome submitted to Phys. Rev. X

19. Gapping the spin-nodal planes of an anisotropic p-wave magnet to induce a large anomalous Hall effect
R. Yamada, M. T. Birch, P. R. Baral, S. Okumura, R. Nakano, S. Gao, Y. Ishihara, K. K. Kolincio, I. Belopolski, H. Sagayama, H. Nakao, K. Ohishi, T. Nakajima, Y. Tokura, T. Arima, Y. Motome, M. M. Hirschmann, and M. Hirschberger submitted to Nature

MOTOTAKE, Yoh-ichi [B class; 300 (B), 60 (C)] (202)
— *Ab initio molecular dynamics study of inorganic polymer*

MURASHIMA, Takahiro [C class; 4000 (B), 400 (C)] (365)
— *Elongational Flow Simulation of Polymers*

NADA, Hiroki [B,C class; 4500 (B), 0 (C)] (338)
— *A Large-Scale Metadynamics Simulation Study on the Mechanism of Habit Change of NaCl Crystal by Additives*
— *A Large-scale Molecular Dynamics Simulation Study on the Melt Growth Mechanism of High-Pressure Ice III*

1. Unknown crystal-like phases formed in an imidazolium ionic liquid: A metadynamics simulation study
   H. Nada J. Chem. Phys. **160**, 204501 (2024).
   DOI:10.1063/5.0206020

2. Multiple freezing-melting pathways of high-density ice at room temperature
   Y.-H Lee, J. K. Kim, Y.-J. Kim, M. Kim, Y. C. Cho, R. J. Husband, E. Ehrenreich-Petersen, R. Bauer, F. Lehmkuhler, H.-P. Liermann, C. Strohm, K. Appel, M. Tang, Z. Konopkova, T. Eklund, K. Amann-Winkel, E. F. O ' Bannon, Z. Jenei, C.-. Yoo, H. Marquardt, H. Nada, and G. W. Lee Nat. Mater., Submitted

NAKAGAWA, Naoko [C class; 3000 (B), 200 (C)] (281)
— *Free energy and phase coexistence in various boundary conditions*

1. Heat-Induced Liquid Hovering in Liquid-Gas Coexistence under Gravity
   A. Yoshida, N. Nakagawa, and S.-i. Sasa Phys. Rev. Lett. 133, 117101 (2024).
   DOI:10.1103/PhysRevLett.133.117101

NAKAGAWA, TAKESHI [B class; 350 (B), 80 (C)] (194)
— *Structural analysis of single layer borophene and boride on Ni surfaces*

NAKAI, Fumiaki [B class; 500 (B), 0 (C)] (336)
— *Mechanism of Size Segregation in Granular Media under Vibration: Analysis Based on Effective Interparticle Forces*

NAKAMURA, Kazuma [C class; 1600 (B), 0 (C)] (143)
— *Ab initio Material Design for Solar Absorption Films*
— *Ab initio calculation of the rotation effect of oxygen octahedron in Ca2MnO4 on electronic properties*

1. Reflectance spectral studies of spark plasma sintered tungsten carbide pellet
   T. Chono, H. Tokutomi, K. Nakamura, K. Miyazaki Jpn. J. Appl. Phys. **64**, 010905 (2025).
   DOI:10.35848/1347-4065/ad9a43

2. Tc and resistivity variation induced by external bending strain in flexible film of strain-sensitive (La,Sr)2CuO4
   T. Horide, T. Maekawa, T. Aikawa, T. Kitamura, K. Nakamura Phys. Rev. Materials **8**, 094802 (2024).
   DOI:10.1103/PhysRevMaterials.8.094802

NAKAMURA, Kohji [C class; 1800 (B), 0 (C)] (137)
— *Material search and spin-orbit coupling induced properties at artificial interfaces and multilayers*

1. Magnon dispersion and terahertz antiferromagnetic resonance frequencies in 3d transition-metal monoxides
   A. Gumarilang, K. Nawa, K. Nakamura Journal of Magnetism and Magnetic Materials **610**, 172499 (2024).
   DOI:10.1016/j.jmmm.2024.172499

2. Effect of change in number of electrons to optical properties and surface plasmon resonance of noble metals
   M. Riswan, M. Arifin, I. Santoso, K. Nawa, K. Nakamura, E. Suharyadi Computational Materials Science **247**, 113519 (2024).
   DOI:10.1016/j.commatsci.2024.113519

3. Spin direction, quantum size effects, layer stacking, and microstructure of ultrathin Co films on W(110)
   M. Suzuki, K. Nakamura, T. Yasue, T. Koshikawa, E. Bauer Physical Review B **111**, 054405 (2025).
   DOI:10.1103/PhysRevB.111.054405

4. Band engineering for large perpendicular magnetocrystalline anisotropy and low magnetic Gilbert damping constant by anion substitution at Fe/MgO interface
   Y. N. Apriati, K. Nawa, K. Nakamura Applied Physics Letters **126**, 082403 (2025).
   DOI:10.1063/5.0248379

NAKANO, Hiroki [C class; 1200 (B), 200 (C)] (308)
— *Numerical study on low-energy states of quantum spin systems*

1. The spin-S Heisenberg antiferromagnet on the orthogonal-dimer lattice
   H. Nakano and T. Sakai, J. Phys.: Condens. Matter 36 455805 (2024).
   DOI:10.1088/1361-648X/ad6522

NAKANO, Hiroyoshi [C,E class; 11600 (B), 1500 (C)] (253)
— *A comprehensive numerical investigation of suppression of fluctuations near solid wall*
— *Development of a numerical solver for fluctuating hydrodynamics and its applications*

1. Power-law correlation in the homogeneous disordered state of anisotropically self-propelled systems
   K. Adachi, H. Nakano Phys. Rev. Research **6**, 033234 (2024).
   DOI:10.1103/PhysRevResearch.6.033234

2. Long-Range Correlations under Temperature Gradients: A Molecular Dynamics Study of Simple Fluids
   H. Nakano, K. Yokota Phys. Rev. E (accepted)
   DOI:10.48550/arXiv.2411.04416

3. Looking at bare transport coefficients in fluctuating hydrodynamics
   H. Nakano, Y. Minami, K. Saito arXiv.2502.15241
   DOI:10.48550/arXiv.2502.15241

4. Energy diffusion in the long-range interacting spin systems
   H. Nishikawa, K. Saito arXiv.2502.10139
   DOI:10.48550/arXiv.2502.10139

NAKAYAMA, Akira [C class; 4000 (B), 400 (C)] (90)
— *Multiscale simulation for liquid/oxide interface based on first-principle calculations*

NASU, Joji [C class; 3400 (B), 400 (C)] (23)
— *Creation mechanism of non-Abelian anyons in quantum spin liquids*
— *Driving non-Abelian anyons by external fields in quantum spin liquids*

1. Effects of Magnetic Fields and Orbital Angular Momentum on Excitonic Condensation in Two-Orbital Hubbard Model
   R. Koga and J. Nasu J. Phys. Soc. Jpn. 93, 054703 (2024).
   DOI:10.7566/JPSJ.93.054703

2. Thermal Hall effect incorporating magnon damping in localized spin systems
   S. Koyama and J. Nasu Phys. Rev. B 109, 174442 (2024).
   DOI:10.1103/PhysRevB.109.174442

3. Real-time control of non-Abelian anyons in Kitaev spin liquid under energy dissipation
   C. Harada, A. Ono, and J. Nasu Phys. Rev. B 110, 214426 (2024).
   DOI:10.1103/PhysRevB.110.214426

4. Spin Seebeck Effect as a Probe for Majorana Fermions in Kitaev Spin Liquids
   Y. Kato, J. Nasu, M. Sato, T. Okubo, T. Misawa, Y. Motome Phys. Rev. X 15, 011050 (2025).
   DOI:10.1103/PhysRevX.15.011050

NGUYEN, Thi [C class; 2600 (B), 300 (C)] ()
— *Quantum anomalous Hall effect in 2D transition metal halides*

NIKI, Kaori [C class; 1600 (B), 400 (C)] (134)
— *Development of photoelectron intensity calculation method for organic molecular thin films*

1. The Role of Oxygen Vacancy on the Carbon Dioxide Photoreduction Using Monoclinic and Tetragonal-phase Zirconium Oxide
   A. Omata, K. Hara, T. Oyumi, R. Ishii, Y. Izumi, and K. Niki e-J. Surf. Sci. Nanotech. **22**(4), 327-333 (2024).
   DOI:10.1380/ejssnt.2024-032

2. Establishment of a Calculation Method for Investigating Surface Characteristics Using Light
   K. Niki, H. Shimokawa, and A. Nakato e-J. Surf. Sci. Nanotech., **22**(4), 334-341 (2024).
   DOI:10.1380/ejssnt.2024-033

3. Exchange of CO2 with CO as Reactant Switches Selectivity in Photoreduction on Co − ZrO2 from C13 Paraffin to Small Olefins
   T. Loumissi, R. Ishii, K. Hara, T. Oyumi, I. Abe, C. L. H. Zhang, R. Hirayama, K. Niki, T. Itoi, and Y. Izumi Angew. Chem Int. Ed., **63**(51), e202412090 (2024).
   DOI:10.1002/anie.202412090

NISHIDATE, Kazume [C class; 600 (B), 0 (C)] (173)
— *Theoretical study of work function and band gap of double-perovskite*
Data Repository
Computer Simulation with C
http://web.cc.iwate-u.ac.jp/ nisidate/main.pdf

NISHIGUCHI, Kazutaka [B class; 300 (B), 70 (C)] (242)
— *Theoretical study of enhancement mechanism of thermoelectric properties with spin fluctuations: A weak-coupling approach*

NISHIKAWA, Yoshihiko [C class; 3600 (B), 0 (C)] (275)
— *Numerical study of the dynamical transition near the glass transition in the s ensemble*

NOGUCHI, Hiroshi [C class; 5800 (B), 500 (C)] (265)
— *structure formation of biomembrane*

NOGUCHI, Yoshifumi [C class; 7200 (B), 750 (C)] (58)
— *Beyond GW: Development of second-order exchange term*
— *Development of first-principles GW*
Gamma method

1. All-electron first-principles GWΓ simulations for accurately predicting core-electron binding energies considering first-order three-point vertex corrections
   K. Yoneyama, Y. Noguchi, and K. Ohno J. Chem. Phys., **161**, 154102 (2024).
   DOI:10.1063/5.0227580

NOMURA, Yusuke [E class; 12000 (B), 1100 (C)] (214)
— *Variational Ansatz based on Vision Transformers*

1. Ab initio study on heavy-fermion behavior in LiV_2O_4: Role of Hund ' s coupling and stability
   Steffen Backes, Yusuke Nomura, Ryotaro Arita, and Hiroshi Shinaoka Phys. Rev. B **111**, L041102 (2025).
   DOI:10.1103/PhysRevB.111.L041102

NOZAWA, Kazuki [C class; 1400 (B), 550 (C)] (135)
— *First-principles study of surface atomic structure and chemical properties of intermetallic compounds*

1. First-principles Study of Adsorption of Atomic Oxygen on PdZn(111) Surface
   K. Iwamura, Y. Otani, Y. Takahashi, Y. Ishii, and K. Nozawa Materials Transactions, ¥bf 65, 1126 (2024).
   DOI:10.2320/matertrans.MT-M2024060

NUNOURA, Teppei [B class; 300 (B), 0 (C)] (207)
— *Study on catalytic hydrothermal liquefaction of kraft lignin with carbon-nanofiber-supported Ni/CeO2*

OBATA, Masao [B class; 500 (B), 90 (C)] (174)
— *First-principles investigation on magnetic shape memory*

1. Comparative Study of Electronic Structure in Ferromagnetic Heusler Alloys Ni_2MnX (X = Al, Ga, In) Using the Quasi-Particle Self-Consistent GW Method
   J. Lutinec, M. Obata, R. Majumder, K. Hyodo, T. Kotani, L. Kalvoda, and T. Oda J. Magn. Soc. Jpn. 48(6), 94107 (2024).
   DOI:10.3379/msjmag.2411r001

2. Effect of excess Mn on the electronic structure of magnetic shape memory Ni-Mn-Ga alloy via GGA+U and quasiparticle self-consistent GW approaches
   M. Obata, L. Straka, O. Heczko, T. Kotani, T.Oda Proceedings of CCP2023-34th IUPAP Conference on Computational Physics, in press

OCHI, Masayuki [C class; 4600 (B), 0 (C)] (87)
— *Accuracy verification of structural optimizaiton using first-principles wave function theory*

1. Efficient electron doping into $KTaO_3$ by hydrogen ion beam
   S. Hirata, G. Lim, T. Ozawa, M. Wilde, K. Fukutani, M. Ochi, Y. Takagi, H. Kitagawa, and M. Maesato Phys. Rev. Mater. **9**, 025002 (2025).
   DOI:10.1103/PhysRevMaterials.9.025002

2. Theoretical study of the crystal structure of the bilayer nickel oxychloride $Sr_3Ni_2O_5Cl_2$ and analysis of possible unconventional superconductivity
M. Ochi, H. Sakakibara, H. Usui, and K. Kuroki Phys. Rev. B **111**, 064511 (2025).
DOI:10.1103/PhysRevB.111.064511

3. First-principles Study of Metallic-atom Diffusion in Thermoelectric Material Mg_3Sb_2
M. Ochi, K. Nishiguchi, C. H. Lee, and K. Kuroki J. Phys. Soc. Jpn. **94**, 024704 (2025).
DOI:10.7566/JPSJ.94.024704

4. Nonreciprocal charge transport in polar Dirac metals with tunable spin-valley coupling
M. Kondo, M. Kimata, M. Ochi, T. Kaneko, K. Kuroki, K. Sudo, S. Sakaguchi, H. Murakawa, N. Hanasaki, and H. Sakai Phys. Rev. Res. **7**, 013041 (2024).
DOI:10.1103/PhysRevResearch.7.013041

5. Theoretical study of spin-fluctuation-mediated superconductivity in two-dimensional Hubbard models with an incipient flat band
T. Aida, K. Matsumoto, D. Ogura, M. Ochi, and K. Kuroki Phys. Rev. B **110**, 054516 (2024).
DOI:10.1103/PhysRevB.110.054516

6. Pair correlations of the hybridized orbitals in a ladder model for the bilayer nickelate $La_3Ni_2O_7$
M. Kakoi, T. Kaneko, H. Sakakibara, M. Ochi, and K. Kuroki Phys. Rev. B **109**, L201124 (2024).
DOI:10.1103/PhysRevB.109.L201124

7. Theoretical analysis on the possibility of superconductivity in the trilayer Ruddlesden-Popper nickelate $La_4Ni_3O_{10}$ under pressure and its experimental examination: Comparison with $La_3Ni_2O_7$
H. Sakakibara, M. Ochi, H. Nagata, Y. Ueki, H. Sakurai, R. Matsumoto, K. Terashima, K. Hirose, H. Ohta, M. Kato, Y. Takano, and K. Kuroki Phys. Rev. B **109**, 144511 (2024).
DOI:10.1103/PhysRevB.109.144511

ODA, Masato [B class; 150 (B), 0 (C)] ()
— *Vibrational mode analysis of GaN crystals containing a large size of defects*

ODA, Tatsuki [C class; 6800 (B), 600 (C)] (65)
— *Analyses on electronic structure and magnetic anisotropy in high-performance spintronics magnetic materials and parallelization development/application in quasi-particle self-consistent GW*
— *Analyses on electronic structure and magnetic anisotropy in high-performance spintronics magnetic materials and parallelization development/application in quasi-particle self-consistent GW code*

1. Comparative study of electronic structure in ferromagnetic Heusler alloys Ni2MnX (X = Al, Ga, In) using the quasi-particle self-consistent GW method
J. Lutinec, M. Obata, R. Majumder, K. Hyodo, T. Kotani, L. Kalvoda, T. Oda J. Magn. Soc. Jpn.**48**, 94 (2024).
DOI:10.3379/msjmag.2411R001

2. Electronic structures in magnetic shape memory alloys Fe_3X (X=Pd, Pt) by quasi-particle self-consistent GW approach
A. Akatov, M, OBATA, T. Oda Sci. Rep. Kanazawa Univ. **68**, 83 (2025).

OHKOSHI, Shin-ichi [C class; 3400 (B), 0 (C)] ()
— *Theoretical studies on the physical properties of novel functional phase transition materials*

OHKUBO, Yuji [B class; 650 (B), 60 (C)] (169)
— *Clarification of adhesion mechanism at interface between plasma-treated fluoropolymer and CuO using*

DFT+U method -Influence of oxygen vacancy diffusion in CuO layer-
— Clarification of adhesion mechanism at interface between plasma-treated fluoropolymer and copper oxide using first-principles calculations

OHMURA, Satoshi [C class; 4000 (B), 0 (C)] (98)
— Ab initio molecular-dynamics study of CO_2 adsorption mechanisms in cement hydration process
1. 第一原理分子動力学法による 1.1-nm トバモライトが有する層状構造の力学特性
I. Kanemasu, S. Ohmura, N. Takeda, F. Shimojo セメント・コンクリート論文集、**78**, 18-25, (2025).
DOI:10.14250/cement.78.18

OHNISHI, Masato [E class; 8500 (B), 1550 (C)] (53)
— Development of anharmonic phonon property database using first-principles calculations
— Development of database of anharmonic phonon properties using first-principles calculation
1. Enhancing thermoelectric performance of Si-based clathrates via carrier optimization considering finite temperature effects
M. Ohnishi, T. Yamamoto, K. Fujimura, H. Shimizu, K. Yamamoto, and J. Shiomi ACS Chemistry of Materials 36, 10595 (2024).
DOI:10.1021/acs.chemmater.4c02098

2. Optimally Suppressed Phonon Tunneling in van der Waals GrapheneWS2 Heterostructure with Ultralow Thermal Conductivity
W. Ding, Z-Y Ong, M. An, B. Davier, S. Hu, M. Ohnishi, and J. Shiomi Nano Letters 24, 13754 (2024).
DOI:10.1021/acs.nanolett.4c03930

3. Database and deep-learning scalability of anharmonic phonon properties by automated brute-force first-principles calculations
Masato Ohnishi, Tianqi Deng, Pol Torres, Zhihao Xu, Terumasa Tadano, Haoming Zhang, Wei Nong, Masatoshi Hanai, Zhiting Tian, Ming Hu, Xiulin Ruan, Ryo Yoshida, Toyotaro Suzumura, Lucas Lindsay, Alan J. H. McGaughey, Tengfei Luo, Kedar Hippalgaonkar, and Junichiro Shiomi arXiv:2504.21245

OHNO, Kaoru [C class; 4600 (B), 400 (C)] (79)
— Improvement and application of all-electron mixed basis program
1. Optical properties of rutile TiO_2 with Zr, Mo, Zn, Cd impurities
K. Ohno, R. Sahara, T. Nanri, and Y. Kawazoe Comput. Cond. Matter **41**, e00977 (2024).
DOI:10.1016/j.cocom.2024.e00977

2. Non-adiabatic excited-state time-dependent $\boldsymbol{GW}$ (TD$\boldsymbol{GW}$) molecular dynamics simulation of nickel-atom aided photolysis of methane to produce hydrogen molecule
A. Manjanath, R. Sahara, Y. Kawazoe, and K. Ohno Nanomaterials **14**, 1775 (2024).
DOI:10.3390/nano14221775

OHSAWA, Kazuhito [C class; 800 (B), 0 (C)] (165)
— Study of interaction between radiation damage and lattice defect

OHTO, Tatsuhiko [C class; 1800 (B), 0 (C)] (136)
— First-principles molecular dynamics simulations for confined water

OHTSUKI, Tomi [C class; 4800 (B), 100 (C)] (268)
— Level statistics and critical phenomena in non-Hermitian systems
1. Negative longitudinal resistance of monolayer graphene in the quantum Hall regime

A.A. Kaverzin, S. Daimon, T. Kikkawa, T. Ohtsuki, E. Saitoh Applied Physics Letters, **124**, 203103(2024).
DOI:10.1063/5.0207235

2. Channel attention for quantum convolutional neural networks
G. Budiutama, S. Daimon, H. Nishi, R. Kaneko, T. Ohtsuki, Y. Matsushita Physical Review A **110**, 012447(2024).
DOI:10.1103/PhysRevA.110.012447

3. Forecasting long-time dynamics in quantum many-body systems by dynamic mode decomposition
R. Kaneko, M. Imada, Y. Kabashima, T. Ohtsuki Physical Review Research **7**, 013085 (2025).
DOI:10.1103/PhysRevResearch.7.013085

4. Universal Stochastic Equations of Monitored Quantum Dynamics
Z. Xiao, T. Ohtsuki, K. Kawabata arXiv:2408.16974 (2024), to appear in PRL.
DOI:10.48550/arXiv.2408.16974

OKUBO, Tsuyoshi [C class; 10200 (B), 900 (C)] (256)
— *Finite temperature property of frustrated spin systems*
— *Tensor network study of quantum spin models on the honeycomb lattice*

1. Hunting for quantum-classical crossover in condensed matter problems
N. Yoshioka, T. Okubo, Y. Suzuki, Y. Koizumi, and W. Mizukami npj Quantum Information **10**, 45 (2024).
DOI:10.1038/s41534-024-00839-4

2. Quantum phase transition between spin liquid and spin nematics in spin-1 Kitaev honeycomb model
T. Mashiko and T. Okubo Phys. Rev. Research **6**, 033110 (2024).
DOI:10.1103/PhysRevResearch.6.033110

3. Nuclear norm regularized loop optimization for tensor network
K. Homma, T. Okubo, and N. Kawashima Phys. Rev. Research **6**, 043102 (2024).
DOI:10.1103/PhysRevResearch.6.043102

4. Spin Seebeck Effect as a Probe for Majorana Fermions in Kitaev Spin Liquids
Y. Kato, J. Nasu, M. Sato, T. Okubo, T. Misawa, and Y. Motome Phys. Rev. X **15**, 011050 (2025).
DOI:10.1103/PhysRevX.15.011050

OKUMURA, Hisashi [C class; 3400 (B), 350 (C)] (272)
— *Molecular dynamics simulation of protein aggregation*

ONISHI, Hiroaki [C class; 2200 (B), 0 (C)] (298)
— *RIXS spectrum of CuO_2 spin chain*

1. Magnetic ground states of highly doped two-leg Hubbard ladders with a particle bath
H. Onishi and S. Miyashita Submitted to Phys. Rev. B.

Data Repository
Data for "Magnetic ground states of highly doped two-leg Hubbard ladders with a particle bath"
https://jaea.repo.nii.ac.jp/records/2000057
DOI:10.60427/0002000057

ONO, Atsushi [B class; 600 (B), 90 (C)] (237)
— *High harmonic generation and subcycle dynamics in magnetically ordered systems*

1. High harmonic generation from electrons moving in topological spin textures
   A. Ono, S. Okumura, S. Imai, and Y. Akagi, Phys. Rev. B **110**, 125111 (2024).
   DOI:10.1103/PhysRevB.110.125111

ONO, Seishiro [B class; 400 (B), 90 (C)] ()
— *Circuit complexity and tensor network*

ONO, Shota [B,C class; 1050 (B), 190 (C)] (151, 152)
— *Freestanding cubic crystals in the monolayer limit*
— *Nonequilibrium electron dynamics based on Boltzmann equation: Application to carbon nanotubes*

1. Fluorite-type materials in the monolayer limit
   S. Ono and R. Pawar Phys. Rev. Materials **8**, 094002 (2024).
   DOI:10.1103/PhysRevMaterials.8.094002

2. Comprehensive study of the luminescence properties of elemental metals
   T. Suemoto, S. Ono, A. Asahara, T. Okuno, T. Suzuki, K. Okazaki, S. Tani, and Y. Kobayashi Phys. Rev. B **111**, 035150 (2025).
   DOI:10.1103/PhysRevB.111.035150

3. Anomalous chirality dependence of strain energy in gold nanotubes
   S. Ono and H. Yoshioka Phys. Rev. B **111**, 085414 (2025).
   DOI:10.1103/PhysRevB.111.085414

4. Ultrafast dynamics of carrier relaxation determining the quasi-1D and non-1D electronic behaviors in carbon nanostructures
   G. Noyama, T. Gauthier, Y. Arashida, Y. Iwasaki, R. Nagao, Y. Saida, N. Godin, G. Privault, H. Suzuki, Y. Hayashi, S. Ono, R. Bertoni, and M. Hada Carbon Trends **20**, 100510 (2025).
   DOI:10.1016/j.cartre.2025.100510

ONO, Tomoya [C class; 10400 (B), 950 (C)] (49)
— *Computational investigation of carrier-transport property at device interface*

1. Insertion of methylene groups into functional molecules for high thermal stability and superior functionality of single-molecule transistors: a first-principles study,
   M. Furushima, M. Uemoto, D. Yin, S. Izawa, R. Shintani, Y. Majima, and T. Ono New J. Chem. **48**, 16008 (2024).
   DOI:10.1039/D4NJ02610A

2. GPU acceleration of overbridging boundary matching method without Green's functions based on real-space finite-difference method
   T. Akamatsu, M. Uemoto, Y. Egami, and T. Ono Comput. Phys. Commun. **312**, 109585 (2025).
   DOI:10.1016/j.cpc.2025.109585

OPDAM, Joeri [C class; 0 (B), 350 (C)] ()
— *Impact of electrostatic interactions on colloidal gelation*

OSHIKAWA, Masaki [B class; 500 (B), 90 (C)] (325)
— *Elucidation of critical phenomena by parallelized higher-dimensional tensor network renormalization group*

1. Finite-size corrections to the energy spectra of gapless one-dimensional systems in the presence of boundaries

Yifan Liu, Haruki Shimizu, Atsushi Ueda, Masaki Oshikawa SciPost Phys. 17, 099 (2024).
DOI:10.21468/SciPostPhys.17.4.099

OSHIYAMA, Atsushi [E class; 7000 (B), 650 (C)] (63)
— *Clarification of Microscopic Mechanisms of Semiconductor Epitaxial Growth and Device-Interface Formation by Large-Scale Quantum-Theory-Based Computations*

1. Passivation mechanisms of oxygen-vacancy-induced hole traps by Mg acceptor atoms at GaN/SiO2 interface
   S. Hattori, A. Oshiyama, and K. Shiraishi Appl. Phys. Lett. 125, 161601 (2024).
   DOI:10.1063/5.0223569

2. Boron as a passivating dopant of oxygen-vacancy-induced hole traps at GaN/SiO2 interface
   Y. Zhao, A. Oshiyama and K. Shiraishi Appl. Phys. Express, submitted (2025).

3. First-Principles Study of Recombination-Enhanced Migration of an Interstitial Magnesium in Gallium Nitride
   Y. Zhao, K. Shiraishi, T. Narita, and A. Oshiyama Phys. Rev. B **110**, L081201 (2024).
   DOI:10.1103/PhysRevB.110.L081201

4. Space-induced floating electronic states in non-stoichiometric amorphous silicon nitride for memory devices applications
   M. Boero, K. Shiraishi, T. Nagahashi, F. Nanmataki, and A. Oshiyama Phys. Rev. Mat. submitted (2025).

OTSUKI, Junya [B class; 550 (B), 100 (C)] (238, 378)
— *Study of multipolar properties in strongly correlated electron systems by dynamical mean-field theory*

OTSUKI, Michio [C class; 0 (B), 350 (C)] (354)
— *Friction law for macroscopic objects driven at high speed*

1. Roles of waviness and groove in control of stiction and slip nucleation
   W. IWASHITA, M. CASTELLANO, and D.S. KAMMER The 26th International Conference of the Theoretical and Applied Mechanics (ICTAM 2024), ThSM0220 (2024).

2. Dependence of hysteresis friction in viscoelastic material on velocity and viscosity
   W. IWASHITA and M. OTSUKI The 4th Malaysian International Tribology Conference (MITC2024), 69 (2024).

OYA, Yutaka [C class; 2800 (B), 300 (C)] (283)
— *All-atomic molecular dynamics simulation for vitrimers*

1. Molecular Dynamics Simulation of Cumulative Microscopic Damage in a Thermosetting Polymer under Cyclic Loading
   N. Yamada, M. Morita, M. Takamura, Y. Oya and J. Koyanagi Polymers **16**(13), 1813 (2024).
   DOI:10.3390/polym16131813

OZEKI, Yukiyasu [C,E class; 5200 (B), 600 (C)] (266)
— *Confirmations of critical univarsality by improved analysis for relaxations of fluctuations*
— *High-precision evaluation of critical universality by relaxation analysis of fluctuations using Gaussian process regression*

1. Imporvement of analysis for relaxation of fluctuations by the use of Gaussian process regression and extrapolation method
   Y. Osada and Y. Ozeki J. Phys. Soc. Jpn **93**, 114001 (2024).

DOI:10.7566/JPSJ.93.114001

PETERS, Robert [C class; 2600 (B), 400 (C)] (230)
— *Nonequilibrium phenomena in strongly correlated systems*

1. Impact of electron correlations on the nonlinear Edelstein effect
Jun Ōiké and Robert Peters Phys. Rev. B **110**, 165111 (2024).
DOI:10.1103/PhysRevB.110.165111

2. Nonlinear magnetoelectric effect under magnetic octupole order: Application to a d-wave altermagnet and a pyrochlore lattice with all-in/all-out magnetic order
Jun Ōiké, Koki Shinada, and Robert Peters Phys. Rev. B **110**, 184407 (2024).
DOI:10.1103/PhysRevB.110.184407

3. Hinge non-Hermitian skin effect in the single-particle properties of a strongly correlated f-electron system
Robert Peters and Tsuneya Yoshida Phys. Rev. B **110**, 125114 (2024).
DOI:10.1103/PhysRevB.110.125114

4. Quantum skyrmion dynamics studied by neural network quantum states
Ashish Joshi, Robert Peters, and Thore Posske Phys. Rev. B **110**, 104411 (2024).
DOI:10.1103/PhysRevB.110.104411

5. Two-particle correlation effects on nonlinear optical responses in the one-dimensional interacting Rice-Mele model
Akira Kofuji and Robert Peters † Phys. Rev. B **109**, 155111 (2024).
DOI:10.1103/PhysRevB.109.155111

PHUNG, Manh [C class; 1400 (B), 0 (C)] (147)
— *Studying C-H bond activation in zeolite using DFT and highly accurate multi-reference theory*

1. Selective Design of Mesoporous Bi2Se3 Films with Orthorhombic and Rhombohedral Crystals
M. Han, T. Nagaura, H. N. Nam, Z. Yang, A. Alowasheeir, Q. M. Phung, T. Yanai, J. Kim, S. M. Alshehri, T. Ahamad, Y. Bando, and Y. Yamauchi Small, Accepted (2025).

2. Homolytic versus Heterolytic Methane Hydroxylation in Copper Zeolites
Q. M. Phung, T. Yanai, D. Plessers, B. F. Sels, R. A. Schoonheydt, K. Pierloot ACS Catal., 15, 1249 (2025).
DOI:10.1021/acscatal.4c06246

POHLE, Rico [C class; 3200 (B), 350 (C)] (224)
— *Emergent Quantum Spin Liquids on the Pyrochlore lattice*

1. Gravitational wave analogs in spin nematics and cold atoms
L. Chojnacki, R. Pohle, H. Yan, Y. Akagi, and N. Shannon Phys. Rev. B 109, L220407 (2024).
DOI:10.1103/PhysRevB.109.L220407

2. Eight-color chiral spin liquid in the $S = 1$ bilinear-biquadratic model with Kitaev interactions
R. Pohle, N. Shannon, and Y. Motome Phys. Rev. Research 6, 033077 (2024).
DOI:10.1103/PhysRevResearch.6.033077

3. Classical $\mathbf{Z}_2$ spin liquid on the generalized four-color Kitaev model
H. Yan and R. Pohle Phys. Rev. Research 7, L012052 (2025).
DOI:10.1103/PhysRevResearch.7.L012052

4. Abundance of spin liquids in the $S = 1$ bilinear-biquadratic model on the pyrochlore lattice, and its application to $NaCaNi_2F_7$
   R. Pohle and N. Shannon preprint (arXiv:2503.12776).

RAEBIGER, Hannes [C class; 3200 (B), 350 (C)] ()
— *Chemical doping of Mott insulators*

SAKAGUCHI, Norihito [C class; 8800 (B), 0 (C)] (57)
— *Reduction of Rare Metals in Fuel Cell and Formic Acid Decomposition Catalysts*

1. Stability and Oxygen Reduction Reaction Activity of Pt Single-Atom Catalysts on Heteroatom-Doped Graphene
   Y. Kunisada and N. Sakaguchi, 触媒 (Catalysts and Catalysis) **66**, 259 (2024).

2. Structure identification of CO monolayer on Ag(111) using atomic force microscopy
   M. Kimura, Y. Kunisada, and Y. Sugimoto, Advanced Materials Interfaces, in press.
   DOI:10.1002/admi.202400904

SAKAI, Toru [C class; 2600 (B), 300 (C)] (286, 288)
— *Field-Induced Spin Liquid Phase of Quantum Spin Chain with Biquadratic Interaction*

1. The spin-S Heisenberg antiferromagnet on the orthogonal-dimer lattice
   Hiroki Nakano, Toru Sakai Journal of Physics: Condensed Matter 36, 455805 (2024).
   DOI:10.1088/1361-648x/ad6522

2. Magnetization process of antiferromagnetic quantum spin chains with the biquadratic exchange interaction
   Toru Sakai AIP Advances 14, 015332 (2024).
   DOI:10.1063/9.0000656

3. Collapsing Behavior of the Ferrimagnetic Ground State of the S = 1/2 Heisenberg Antiferromagnet on the Lieb Lattice due to Frustration
   Rito Furuchi, Hiroki Nakano, Toru Sakai Journal of the Physical Society of Japan 93, 115002 (2024).
   DOI:10.21468/scipostphysproc.1

4. Translational-Symmetry-Broken Magnetization Plateaux of the $S = 3/2$ Anisotropic Antiferromagnetic Chain
   Tomohide Kawatsu, Haruto Suzuki, Masaru Hashimoto, Koki Doi, Tomoki Houda, Rito Furuchi, Hiroki Nakano, Kiyomi Okamoto, Toru Sakai to appear in Journal of the Physical Society of Japan

5. Translational Symmetry Broken Magnetization Plateau of the S=1/2 Anisotropic Spin Ladder with Ferromagnetic Rung Interaction
   Toru Sakai, Koki Doi, Kiyomi Okamoto, Kouichi Okunishi, Masaru Hashimoto, Tomoki Houda, Rito Furuchi, and Hiroki Nakano to appear in Journal of Physics: Conference Series

6. Magnetization Plateau of the S=1/2 Distorted Diamond Spin Chain with Ferromagnetic Interaction
   Masaru Hashimoto, Koki Doi, Tomoki Houda, Rito Furuchi, Hiroki Nakano, Kiyomi Okamoto, Toru Sakai to appear in Journal of Physics: Conference Series

SAKAKIBARA, Hirofumi [B class; 500 (B), 0 (C)] (179)
— *First-principles study of multi-orbital and multi-layer compounds*

1. Pair correlations of the hybridized orbitals in a ladder model for the bilayer nickelate $La_3\ Ni_2\ O_7$

M. Kakoi, T. Kaneko, H. Sakakibara, M. Ochi, and K. Kuroki Phys. Rev. B 109, L201124 (2024).
DOI:10.1103/PhysRevB.109.L201124

2. Theoretical study on the crystal structure of a bilayer nickel-oxychloride $Sr_3Ni_2O_5Cl_2$ and analysis on the occurrence of possible unconventional superconductivity
M. Ochi, H. Sakakibara, H. Usui, and K. Kuroki Phys. Rev. B 111, 064511 (2025).
DOI:10.1103/PhysRevB.111.064511

SAKASHITA, Tatsuya [B class; 150 (B), 160 (C)] (357)
— *Development of integrated interface of eigensolvers Rokko and application to quantum spin systems*

SASAKI, Ryoma [B class; 550 (B), 100 (C)] ()
— *Microscopic investigation of Li-ion conduction mechanism on grain boundary of organic solid electrolyte*

SASAKI, Takehiko [C class; 2000 (B), 350 (C)] (126)
— *Study on poisoning states of platinum nanoparticles*

SATO, Ryuhei [C class; 2400 (B), 0 (C)] (124)
— *Interfacial Reaction Study Driven by Mathematical Science MI and Molecular Dynamics*
1. Hydrogen Absorption Promoted by Surface Melting: Thermodynamic Criteria for High-Pressure Polyhydride Synthesis
Ryuhei Sato and Lewis Conway and Di Zhang and Chris Pickard and Kazuto Akagi and Kartik Sau and Hao Li and Shin-ichi Orimo, accepted in Proc. Natl. Acad. Sci. USA.

2. Data-assimilated crystal growth simulation for multiple crystalline phases
Yuuki Kubo and Ryuhei Sato and Yuansheng Zhao and Takahiro Ishikawa and Shinji Tsuneyuki, The Journal of Chemical Physics, 214113, 161, 2024
DOI:10.1063/5.0223390

3. Unraveling the Complexity of Divalent Hydride Electrolytes in Solid-State Batteries via a Data-Driven Framework with Large Language Model
Qian Wang and Fangling Yang and Yuhang Wang and Di Zhang and Ryuhei Sato and Linda Zhang and Eric Jianfeng Cheng and Yigang Yan and Yungui Chen and Kazuaki Kisu and Shin-ichi Orimo and Hao Li, Angew. Chem. Int. Ed, accepted
DOI:10.1002/anie.202506573

Data Repository
Dataset for MLP-MD simulation of high pressure Ca-H system including
https://doi.org/10.5281/zenodo.14807586
DOI:10.5281/zenodo.14807586

SATO, Shunsuke [B,C class; 5300 (B), 0 (C)] (74)
— *First-principles analysis on optical-control of current in solids*
— *First-principles calculation of optical control on semiconductor transport properties*
1. Core-level signature of long-range charge-density-wave order and short-range excitonic correlations probed by attosecond broadband spectroscopy
Alfred Zong, Sheng-Chih Lin, Shunsuke A Sato, Emma Berger, Bailey R Nebgen, Marcus Hui, BQ Lv, Yun Cheng, Wei Xia, Yanfeng Guo, Dao Xiang, Michael W Zuerch arXiv:2407.00772 [cond-mat.str-el]
DOI:10.48550/arXiv.2407.00772

SATO, Takeshi [B class; 450 (B), 90 (C)] (332)
— *A molecular dynamics simulation study for immiscible polymer blends*

SAU, Kartik [C class; 800 (B), 0 (C)] ()
— *Developing Advanced Hydride Materials using Theoretical Simulation Toward Next-Generation All-Solid-State-Battery Heat/cooling Management Systems and Hydrogen Storage application.*

SEINO, Kaori [C class; 3000 (B), 400 (C)] (111)
— *First-principles study of surface and defect systems for power-electronics materials*

SEKI, Yuya [B class; 500 (B), 80 (C)] (330)
— *Analysis of Ising model in statistical-mechanical infomatics*

1. Black-box optimization for integer-variable problems using Ising machines and factorization machines
   Y. Seki, R. Tamura, and S. Tanaka arXiv.2209.01016
   DOI:10.48550/arXiv.2209.01016

2. Machine Learning Supported Annealing for Prediction of Grand Canonical Crystal Structures
   Y. Couzinié, Y. Seki, Y. Nishiya, H. Nishi, T. Kosugi, S. Tanaka, and Y. Matsushita J. Phys. Soc. Jpn. **94**, 044802 (2025).
   DOI:10.7566/JPSJ.94.044802

SHIBA, Hayato [B class; 400 (B), 80 (C)] (341)
— *Deep learning glassy dynamics by graph neural networks*

SHIMADA, Takahiro [B class; 400 (B), 80 (C)] (184)
— *First-principles lattice defects engineering for atomic-scale multiferroics*

SHIMADA, Toshihiro [B class; 600 (B), 100 (C)] ()
— *Analysis of reaction mechanism and physical properties of molecular crystals that undergoes polymerization under high pressure*

SHIMAMURA, Kohei [C class; 2800 (B), 300 (C)] (113)
— *Improving Stability of Molecular Dynamics Simulation using Machine-Learning Interatomic Potentials*

1. Thermal conductivity calculation using homogeneous non-equilibrium molecular dynamics simulation with Allegro
   Y. Shimamura, S. Hattori, K. Nomura, A. Koura, and F. Shimojo: Int. J. Heat Mass Transf. **234** 126106 (2024).
   DOI:10.1016/j.ijheatmasstransfer.2024.126106

SHIMIZU, Koji [C class; 4600 (B), 450 (C)] (71)
— *Analysis of defect structures and ion migration using first-principles calculations and machine learning*

1. Investigating the atomic structures and electronic properties of WS2 thin films with sulfur vacancies via a neural network potential-aided first-principles study
   R. Otsuka, K. Shimizu, H. Wakabayashi, and S. Watanabe Appl. Phys. Express **17**, 115501 (2024).
   DOI:10.35848/1882-0786/ad8b0c

2. Construction of machine learning potentials toward the exploration of alloy cluster catalysts
   K. Miyamoto, K. Shimizu, A.K.A. Lu, and S. Watanabe e-J. Surf. Sci. Nanotechnol. accepted.

3. Charge States of Ions around Σ 5(310)/[001] Grain Boundary in Cubic-ZrO2 Revealed by First-

Principles Calculations
S. Arai, K. Shimizu, A.K.A. Lu, H. Masuda, H. Yoshida, S. Watanabe e-J. Surf. Sci. Nanotechnol. under review.

4. Hydrogen embrittlement; Aluminum; Molecular dynamics; Density functional theory; Machine learning potentials
Y. Liu, K. Shimizu, S. Watanabe Acta Mater. under review.

SHIMIZU, Makoto [C class; 3000 (B), 0 (C)] (229)
— *Spin fluctuations and superconductivity in f-electron compounds under pressure*

1. Electronic Structure of UTe_2 under pressure
M. Shimizu, and Y. Yanase arXiv.2408.04292
DOI:10.48550/arXiv.2408.04292

SHIMOJO, Fuyuki [C class; 4800 (B), 400 (C)] (78)
— *First-Principles Molecular-Dynamics Study of Structural and Electronic Properties of Disordered Materials under Extreme Conditions*

1. Intermolecular Correlations in Liquid Lactic Acid Based on ab initio Molecular Dynamics Simulations Combined with High-Energy X-ray Diffraction Measurements
K. Ito, H. Shimakura, S. Tahara, K. Ohara, K. Shimamura, A. Koura, and F. Shimojo J, Phys. Soc. Jpn. **93**, 054601 (2024).
DOI:10.7566/JPSJ.93.054601

2. Thermal Conductivity Calculation using Homogeneous Non-equilibrium Molecular Dynamics Simulation with Allegro
K. Shimamura, S. Hattori, K. Nomura, A. Koura, and F. Shimojo Int. J. Heat Mass Transfer **234**, 126106 (2024).
DOI:10.1016/j.ijheatmasstransfer.2024.126106

3. Photoinduced negative differential resistance at a graphene/silicon interface: a nonadiabatic quantum molecular dynamics study
H. Hokyo, K. Ito, R. K. Kalia, R. Kapadia, A. Nakano, K. Shimamura, F. Shimojo, and P. Vashishta J. Phys. Chem. Lett. **15**, 9226-9232 (2024).
DOI:10.1021/acs.jpclett.4c02272

4. Thermoelectric Grain-Boundary Superlattice in Monolayer MoS_2
A.Irie, A. Aditya, K. Nomura, S. Fukushima, S. Hattori, R. K. Kalia, A. Nakano, V. Rodin, F. Shimojo, S. Tomiya, and P. Vashishta J. Phys. Chem. C **128**, 16172-16178 (2024).
DOI:10.1021/acs.jpcc.4c04339

5. Phase Behavior and Atomic Dynamics in Rb_xNa_{1-x}: Insights from Machine Learning Interatomic Potentials based on Ab Initio Molecular Dynamics
A.Irie, A. Koura, K. Shimamura, and F. Shimojo J. Phys.: Condens. Matter **37**, 065401 (2025).
DOI:10.1088/1361-648X/ad9071

SHIMOKAWA, Tokuro [C class; 6000 (B), 700 (C)] (264)
— *Multipartite entanglement in quantum frustrated magnets*
— *Thermal effects on quantum frustrated magnets*

SHINAOKA, Hiroshi [B class; 500 (B), 80 (C)] (328)
— *Tensor learning approaches to computational physics*

1. Physics-informed neural network model for quantum impurity problems based on Lehmann rep-

resentation
F. Kakizawa, S. Terasaki, and H. Shinaoka arXiv:2411.18835.
DOI:10.48550/arXiv.2411.18835

SHINODA, Wataru [E class; 30500 (B), 2550 (C)] (247)
— *Large-scale Molecular Simulation of Soft Materials using All-Atom and Coarse-Grained Model*

1. Proteinlipid acyl chain interactions: Depth-dependent changes of segmental mobility of phospholipid in contact with bacteriorhodopsin
Yuichi Umegawa, Sho Kato, Sangjae Seo, Wataru Shinoda, Satoshi Kawatake, Shigeru Matsuoka, Michio Murata Biophys. Chem. **308**, 107204 (2024).
DOI:10.1016/j.bpc.2024.107204

2. pSPICA Force Field Extended for Proteins and Peptides
Yusuke Miyazaki, Wataru Shinoda J. Chem. Inf. Model. **64**, 532-542 (2024).
DOI:10.1021/acs.jcim.3c01611

3. Understanding the effects of ethanol on the liposome bilayer structure using microfluidic-based time-resolved small-angle X-ray scattering and molecular dynamics simulations
Masatoshi Maeki, Niko Kimura, Yuto Okada, Kazuki Shimizu, Kana Shibata, Yusuke Miyazaki, Akihiko Ishida, Kento Yonezawa, Nobutaka Shimizu, Wataru Shinoda, Manabu Tokeshi Nanoscale Adv. **6**, 2166-2176 (2024).
DOI:10.1039/D3NA01073B

4. Light-controllable cell-membrane disturbance for intracellular delivery
Wenting Huo, Koji Miki, Huiying Mu, Takashi Osawa, Harumi Yamaguma, Yuuya Kasahara, Satoshi Obika, Yoshimasa Kawaguchi, Hisaaki Hirose, Shiroh Futaki, Yusuke Miyazaki, Wataru Shinoda, Shuji Akai, Kouichi Ohe J. Mater. Chem. B **12**, 4138-4147 (2024).
DOI:10.1039/D3TB02956E

5. Linear ether-based highly concentrated electrolytes for Li-sulfur batteries
Toru Ishikawa, Shohei Haga, Keisuke Shigenobu, Taku Sudoh, Seiji Tsuzuki, Wataru Shinoda, Kaoru Dokko, Masayoshi Watanabe, Kazuhide Ueno Faraday Discuss. **253**, 385-406 (2024).
DOI:10.1039/D4FD00024B

6. Evolving Better Solvate Electrolytes for Lithium Secondary Batteries
Frederik Philippi, Maleen Middendorf, Keisuke Shigenobu, Yuna Matsuyama, Oriele Palumbo, David Pugh, Taku Sudoh, Kaoru Dokko, Masayoshi Watanabe, Monika Schnhoff, Wataru Shinoda, Kazuhide Ueno Chem. Sci. **15**, 7342-7358 (2024).
DOI:10.1039/D4SC01492H

7. Discrimination of extracellular miRNA sources for the identification of tumor-related functions based on nanowire thermofluidics
Kunanon Chattrairat, Akira Yokoi, Min Zhang, Mikiko Iida, Kosuke Yoshida, Masami Kitagawa, Ayuka Niwa, Masatoshi Maeki, Takeshi Hasegawa, Takeshi Yokoyama, Yoshikazu Tanaka, Yusuke Miyazaki, Wataru Shinoda, Manabu Tokeshi, Kazuki Nagashima, Takeshi Yanagida, Hiroaki Kajiyama, Yoshinobu Baba, Takao Yasui Device **2**, 100363 (2024).
DOI:10.1016/j.device.2024.100363

8. Fully atomistic molecular dynamics modeling of photoswitchable azo-PC lipid bilayers: structure, mechanical properties, and drug permeation
Kevin A Alberto, MN Hasna Begam, Hejian Xiong, Wataru Shinoda, Paul A Slesinger, Zhenpeng Qin, Steven O Nielsen Nanoscale **17**, 2032-2042 (2025).
DOI:10.1039/D4NR02509A

9. NMR and molecular simulation studies on the structure elucidation of the amphotericin B ion channel using 13 C and 19 F labelling
Yuichi Umegawa, Hiroshi Tsuchikawa, Wataru Shinoda, Michio Murata Org. Biomol. Chem. **23**, 1233-1252 (2025).
DOI:10.1039/D4OB01468E

10. Selective adsorption of unmethylated DNA on ZnO nanowires for separation of methylated DNA
Marina Musa, Zetao Zhu, Hiromi Takahashi, Wataru Shinoda, Yoshinobu Baba, Takao Yasui Lab Chip **25**, 1637-1646 (2025).
DOI:10.1039/D4LC00893F

SHINOHARA, Yasushi [C class; 1200 (B), 0 (C)] (153)
— *First-principles simulations for photoelectron spectra via extremely nonlinear processes*

SHIOMI, Junichiro [E class; 8000 (B), 900 (C)] (55)
— *Analysis of phonon transport properties in disordered systems*

1. The efficient method of lattice dynamics calculation: Monte Carlo integration with importance sampling
Michimasa Morita, Junichiro Shiomi J. Phys.: Condens. Matter 37, 135902 (2025).
DOI:10.1088/1361-648X/adb231

SHIRAI, Tatsuhiko [B class; 400 (B), 0 (C)] (347)
— *Dissipation effects on quantum algorithm*

1. Accelerated decay due to operator spreading in bulk-dissipated quantum systems
T. Shirai, and T. Mori Phys. Rev. Lett. **133**, 040201 (2024).
DOI:10.1103/PhysRevLett.133.040201

SHIRAISHI, Kenji [C class; 7800 (B), 0 (C)] (61, 62)
— *Clarification of Hole Trap at GaN/SiO2 Interfaces and Fabrication of GaN-MOSFET*
— *Theoretical Studies on New Types of Electron Trap Defects Origninated from Localized Floating States in a-SiN towards Flash Memories Application*

1. Theoretical investigation of NH3 nitridation on Cl-terminated Si(100)-2x1 surfaces
T. Nagahashi, H. Karasawa, R. Horiike, and K. Shiraishi Surface Science **753**, 1222655 (2025).
DOI:10.1016/j.susc.2024.122655

2. Theoretical study of the influence of GaOx interfacial layer on the GaN/SiO_2 interface property
S. Hattori, A. Oshiyama, K. Shiraishi J. Appl. Phys. **135**, 175303 (2024).
DOI:10.1063/5.0204285

3. Passivation mechanisms of oxygen-vacancy-induced hole traps by Mg acceptor atoms at GaN/SiO_2 interface
S. Hattori, A. Oshiyama, K. Shiraishi Appl. Phys. Lett. **125**, 161601 (2024).
DOI:10.1063/5.0223569

SHUDO, Ken-ichi [B class; 400 (B), 80 (C)] (183)
— *Impurity control of chalcogenides by surface-modification*

SUGIHARA, Kaori [B class; 400 (B), 90 (C)] ()
— *Investigating the Molecular Mechanisms Behind the Synergistic Antibacterial Actions of LL-37 and HNP1 Peptides Through Molecular Dynamics Simulations*

SUGINO, Osamu [E class; 6000 (B), 650 (C)] ()
— *Computational study of the material property of metals and oxides*

SUMITA, Shuntaro [B class; 200 (B), 0 (C)] (361)
— *Proposal of novel superconducting states coexisting/competing with higher-order magnetic multipole order or helical magnetism*

SUMIYA, Yosuke [B class; 450 (B), 90 (C)] ()
— *Elucidation of adhesion mechanism of adhesive polymer materials based on first-principle calculations*

SUWA, Hidemaro [C class; 3200 (B), 350 (C)] (223)
— *Magnetic field-induced phases emerging from frustrated spin systems coupled to multiple degrees of freedom*

1. Electronic Raman scattering of antiferromagnetic excitonic insulators
   Hidemaro Suwa, Shang-Shun Zhang, and Cristian D. Batista arXiv:2410.13715
   DOI:10.48550/arXiv.2410.13715

SUZUKI, Takafumi [B,C class; 4800 (B), 520 (C)] (267)
— *Ground state phase diagram of an extended Kitaev model on a honeycomb lattice*
— *Supersolid in Bose-Hubbard model with tilted dipole interactions*

1. Programmable order by disorder effect and underlying phases through dipolar quantum simulators
   Huan-Kuang Wu, Takafumi Suzuki, Naoki Kawashima, Wei-Lin Tu Phys. Rev. Research **6**, 023297 (2024).
   DOI:10.1103/physrevresearch.6.023297

2. Proximate Tomonaga-Luttinger liquid in an anisotropic Kitaev-Gamma model
   Matthias Gohlke, Jose Carlos Pelayo, Takafumi Suzuki Phys. Rev. B **109**, L220410 (2024).
   DOI:10.1103/physrevb.109.l220410

SUZUKI, Takehito [B class; 150 (B), 40 (C)] (363)
— *Analysis of phase transition generated by context-sensitive grammar*
— *Analysis of phase transition in languages based on Combinatory Categorial Grammar*

SUZUKI, Yuji [C class; 2800 (B), 0 (C)] (116)
— *Development of Stretchable Electret Materials for Energy Harvesting with the Aid of Machine Learning*

TADA, Kohei [B class; 700 (B), 160 (C)] (160, 162)
— *Theoretical design of bistable functional materials based on calculations for diradical-solid interaction*
— *Theoretical investigation to design of novel Na-ion battery materials with low environmental impact and high durability*

1. Systematic Investigation on Surface Diradicals Using Theoretical Models: 2M/MgO and 2M/BaO (M = Cu, Ag, and Au)
   K. Tada, K. Masuda, R. Kishi, Y. Kitagawa Chemistry **6**, 1572 (2024).
   DOI:10.3390/chemistry6060095

2. Difference in spin structure of magnetic metal-organic frameworks between cluster model and periodic system
   N. Amamizu, K. Tada, R. Kishi, W. Kosaka, H. Miyasaka, Y. Kitagawa Chemistry Letters **53**, upae230 (2024).
   DOI:10.1093/chemle/upae230

TAHARA, Shuta [B class; 400 (B), 70 (C)] (191)
— *Study on Ag conducting mechanism by comparison between $RbAg_4I_5$ and Rb_2AgI_3*

TAKAHASHI, Osamu [B class; 300 (B), 0 (C)] (205)
— *Electronic structure of aqueous polymers*

TAKAYAMA, Akari [B class; 300 (B), 0 (C)] (358)
— *Structure analysis of atomic layer alloy with Rashba effect studied by TRHEPD*

TAKEMORI, Nayuta [C class; 600 (B), 200 (C)] (164)
— *Exploration of photonic hypermaterials with complete-gap*

TAKETSUGU, Tetsuya [C class; 3600 (B), 350 (C)] (99)
— *Ab initio study on the structure and functions of nanomaterials*

1. Electrocatalytic Ammonia Oxidation to Nitrite and Nitrate with NiOOH-Ni
   H. Liu, C.-J. Yang, C.-L. Dong, J. Wang, X. Zhang, A. Lyalin, T. Taketsugu, Z. Chen, D. Guan, X. Xu, Z. Shao, and Z. Huang Adv. Energy Mater. **14**, 2401675 (2024)
   DOI:10.1002/aenm.202401675

2. Boron-induced transformation of ultrathin Au films into two-dimensional metallic nanostructures
   A. Preobrajenski, N. Vinogradov, D. A. Duncan, T.-L. Lee, M. Tsitsvero, T. Taketsugu, and A. Lyalin Nat. Commun. **15**, 10518 (2024)
   DOI:10.1038/s41467-024-54464-y

3. Theoretical design of nanocatalysts based on $(Fe_2O_3)_n$ clusters for hydrogen production from ammonia
   S. Ibragimov, A. Lyalin, S. Kumar, Y. Ono, T. Taketsugu, and M. Bobrowski J. Chem. Phys. **162**, 054305 (2025).
   DOI:10.1063/5.0242310

TAMAYA, TOMOHIRO [D class; 1000 (B), 500 (C)] (306)
— *Research on quantum spin currents induced by high-intensity terahertz light*

TAMURA, Ryo [B class; 500 (B), 0 (C)] (335)
— *Development of black-box optimization method for materials exploration*

1. Performance of uncertainty-based active learning for efficient approximation of black-box functions in materials science
   Ai Koizumi, Guillaume Deffrennes, Kei Terayama, and Ryo Tamura Sci. Rep. **14, 27019 (2024). DOI:10.1038/s41598-024-76800-4**

TANAKA, Katsuhiro [B,C class; 1850 (B), 190 (C)] (132)
— *First-principles exploration of physical properties of antiferromagnets and its application to magnetic tunnel junction*
— *First-principles study on tunnel magnetoresistance effect using antiferromagnetic metals*

TANAKA, Shu [B class; 500 (B), 90 (C)] (324)
— *Study on hybrid algorithms for Ising machines*

1. Machine Learning Supported Annealing for Prediction of Grand Canonical Crystal Structures
   Yannick Couzinie, Yuya Seki, Yusuke Nishiya, Hirofumi Nishi, Taichi Kosugi, Shu Tanaka, Yuichiro Matsushita J. Phys. Soc. Jpn. **94**, 044802 (2025).
   DOI:10.7566/JPSJ.94.044802

TANAKA, Tomonori [C class; 3400 (B), 350 (C)] (104)
— *Non-perturbative calculation of exchange coupling tensor*

1. Nonperturbative calculation of exchange coupling parameters
   T. Tanaka and Y. Gohda arXiv:2410.11256
   DOI:10.48550/arXiv:2410.11256

2. Efficient first-principles approach to Gibbs free energy with thermal expansion
   K. Hashimoto, T. Tanaka, and Y. Gohda arXiv:2410.11256
   DOI:10.48550/arXiv.2410.11256

TATETSU, Yasutomi [C class; 1800 (B), 300 (C)] (128)
— *First-principles study on stability of nano particles and permanent magnets*

TEN-NO, Seiichiro [C,D class; 9000 (B), 500 (C)] (88)
— *First-principles analysis of perovskite semiconductors toward improving photocatalytic performance*
— *First-principles materials design of perovskite semiconductors toward improving photocatalytic performance*

1. Divalent Cation Doping into $SrTiO_3$ for Enhancing the Photocatalytic Performance of Water Splitting
   K. Nishiguchi, T. Takayama, S. Takasuka, Y. Harashima, M. Fujii, and S. L. Ten-no J. Phys. Chem. Lett. **16**, 11, 2823 (2025).
   DOI:10.1021/acs.jpclett.5c00070

TERAO, Takamichi [B class; 800 (B), 150 (C)] (316)
— *Screening in concentrated electrolytes*

1. Order-Parameter-Free Analysis of Soft Matter: Applications of Machine Learning via Image Recognition
   Terao, and M. Kondo Ann. Phys. (Berlin) **537**, 2400197 (2024).
   DOI:10.1002/andp.202400197

TEZUKA, Masaki [C class; 3800 (B), 400 (C)] (269)
— *Understanding scrambling dynamics in quantum many-body systems and realizing the dynamics in quantum computers*

1. A model of randomly-coupled Pauli spins
   Masanori Hanada, Antal Jevicki, Xianlong Liu, Enrico Rinaldi, and Masaki Tezuka, J. High Energy Phys. **2405**, 280 (2024).
   DOI:10.1007/JHEP05(2024)280

2. Hayden-Preskill Recovery in Hamiltonian Systems
   Yoshifumi Nakata and Masaki Tezuka, Phys. Rev. Research **6**, L022021 (2024).
   DOI:10.1103/PhysRevResearch.6.L022021

TODO, Synge [C class; 4600 (B), 400 (C)] ()
— *Development of tensor-network Markov-chain Monte Carlo and application to quantum many-body systems*

TOH, Daisetsu [C class; 2600 (B), 0 (C)] (120)
— *Study on the etching mechanism of Si in catalyst-referred etching*

TOHYAMA, Takami [C class; 3400 (B), 0 (C)] (226)
— *Novel quantum phases with current and spin current textures due to electron correlation*

1. Keldysh crossover in one-dimensional Mott insulators
   K. Shinjo and T. Tohyama APL Mater. **12**, 041109 (2024).
   DOI:10.1063/5.0198384

TONEGAWA, Takashi [B class; 300 (B), 0 (C)] ()
— *Numerical Study of the One-Dimensional Quantum Spin Systems*

TRAN, Ba [E class; 3000 (B), 700 (C)] ()
— *Computational material design for hydrogen liquefaction*

TSUJI, Yuta [C class; 3000 (B), 550 (C)] (110)
— *Theoretical study of carbon dioxide reduction catalysts using first-principles calculations*
— *Theoretical study of ceria-based composite catalysts using first-principles calculations*

1. Electronic Interaction of Epoxy Resin with Copper at the AdheredInterface
   S. Saeki, D. Kawaguchi, Y. Tsuji, S. Yamamoto, K. Yoshizawa, and K. Tanaka Langmuir **40**, 9725 (2024).
   DOI:10.1021/acs.langmuir.4c00711

2. Mechanistic and Electronic Insights into Efficient Carbon DioxideReduction Driven by Visible Light Using a Coordination Polymer
   Y. Tsuji, S. Yamamoto, Y. Kamakura, C. Suppaso, D.Tanaka, and K. Maeda ACS Appl. Energy Mater. **7**, 4472 (2024).
   DOI:10.1021/acsaem.4c00408

3. Effect of Condensed Water at an Alumina/Epoxy Resin Interface onCuring Reaction
   S. Yamamoto, Y. Tsuji, R. Kuwahara, K. Yoshizawa, and K. Tanaka Langmuir **40**, 12613 (2024).
   DOI:10.1021/acs.langmuir.4c01081

4. Giant anisotropic thermal expansion of copper-cyanido flat layers with flexible copper nodes
   Y. Iwai, M. Nakaya, Y. Tsuji, B.L. Ouay, M.Ohba, and R. Ohtani Chem. Commun. **60**, 6512 (2024).
   DOI:10.1039/d4cc01232a

5. Effects of Curing Agents on the Adhesion of Epoxy Resin to Copper:A Density Functional Theory Study
   Y. Kawashima, and Y. Tsuji Langmuir **40**, 12622 (2024).
   DOI:10.1021/acs.langmuir.4c01093

6. Density Functional Theory Study of Adhesion Mechanism betweenEpoxy Resins Cured with 4,4′-Diaminodiphenyl Sulfone and 4,4′-Diaminodiphenylmethane and Carboxyl Functionalized CarbonFiber
   A. Shrestha, Y. Sumiya, K. Okazawa, Y. Tsuji, and K. Yoshizawa Langmuir **40**, 21573 (2024).
   DOI:10.1021/acs.langmuir.4c02473

7. σ Interference: Through-Space and Through-Bond Dichotomy
   Y. Tsuji, K. Okazawa, T. Tatsumi, and K. Yoshizawa J. Am. Chem. Soc. **146**, 32506 (2024).
   DOI:10.1021/jacs.4c09771

8. Investigating Ni nanoparticles on CeO2 for methane dissociation: a comparative study of theoretical calculations and experimental insights
   T. Fujisaki, Y. Tsuji, P.H. Tu, T.C.D. Doan, D.S.R. Rocabado, A.T. Staykov, K. Yashiro, and Y. Shiratori Phys. Chem. Chem. Phys. **27**, 5024 (2025).

DOI:10.1039/d4cp01324g

9. Van der Waals interactions between nonpolar alkyl chains and polar oxide surfaces prevent catalyst deactivation in aldehyde gas sensing
K. Nakamura, T. Takahashi, T. Hosomi, W. Tanaka, Y. Yamaguchi, J. Liu, M. Kanai, Y. Tsuji, and T. Yanagida Nat. Commun. **15**, 9211 (2024).
DOI:10.1038/s41467-024-53577-8

10. Experimental and Theoretical Investigation of Anisotropic ProtonConduction in Two-Dimensional Metal − Organic Frameworks
Y. Shi, S. Kimura, Y. Iwai, Y. Tsuji, B.L. Ouay, M. Ohba, and R. Ohtani Inorg. Chem. **63**, 22194 (2024).
DOI:10.1021/acs.inorgchem.4c03816

11. Rectified Water Migration Behavior in the NoncentrosymmetricChannels of a Ferroelectric Proton Conductor
Y. Tsuji, and R. Ohtani Inorg. Chem. **64**, 3868 (2025).
DOI:10.1021/acs.inorgchem.4c05053

12. Solvato/Vapochromism-Based Alcohol Sensing throughMetalOrganic Framework Thin Films with CoordinativelyUnsaturated Metal Sites
Y. Toki, K. Okada, A. Fukatsu, Y. Tuji, and M. Takahashi Small Sci. **8**, 2400634 (2025).
DOI:10.1002/smsc.202400634

TSUKAHARA, Noriyuki [B class; 300 (B), 70 (C)] (199)
— *DFT calculations of adsorbed molecules captured by metal-organic films on Cu(111)*

1. Element-specific cluster growth on the two-dimensional metalorganic network
N. Tsukahara, R. Arafune, and J. Yoshinobu Jpn. J. Appl. Phys. 63, 065504 (2024).
DOI:10.35848/1347-4065/ad50b3

TSUMURAYA, Takao [C class; 1200 (B), 200 (C)] ()
— *First-Principles Study on the Origin of Mechanical Properties on Magnesium based Alloys*

TSUNEYUKI, Shinji [C class; 4800 (B), 0 (C)] (82)
— *Advancement of methods for predicting dielectric properties and structure exploration of materials*

1. Nuclear quantum effect on the elasticity of ice VII under pressure: A path-integral molecular dynamics study
J. Tsuchiya, M. Shiga, S. Tsuneyuki, and E.C. Thompson Phys. Rev.. Research ¥bf 6, 02330 (2024).
DOI:10.1103/PhysRevResearch.6.023302

2. Chemical bond based machine learning model for dipole moment: Application to dielectric properties of liquid methanol and ethanol
T. Amano, T. Yamazaki, and S. Tsuneyuki Phys. Rev. B ¥bf 110, 165159 (2024).
DOI:10.1103/PhysRevB.110.165159

3. Data-assimilated crystal growth simulation for multiple crystalline phases
Y. Kubo, R. Sato, Y. Zhao, T. Ishikawa, and S. Tsuneyuki J. Chem. Phys. ¥bf 161, 214113 (2024).
DOI:10.1063/5.0223390

4. Assessing the possible superconductivity in the doped perovskite hydride $KMgH_3$: Effects of lattice anharmonicity and spin fluctuations

S. Lu, R. Akashi, M. Kawamura, and S. Tsuneyuki accepted to Phys. Rev. B

5. Transferability of the chemical-bond-based machine learning model for dipole moment: The GHz to THz dielectric properties of liquid propylene glycol and polypropylene glycol
T. Amano, T. Yamazaki, N. Matsumura, Y. Yoshimoto, and S. Tsuneyuki accepted to Phys. Rev. B

6. Superconducting $LaPtH_6$ with triatomic hydrogen units
T. Ishikawa, Y. Tanaka, and S. Tsuneyuki submitted

TSURUTA, Kenji [B class; 550 (B), 100 (C)] (171)
— *Ab-initio and classical molecular-dynamics simulation on electron/phonon localization and transport in multilayer 2D materials*

UCHIDA, Takashi [B class; 200 (B), 60 (C)] (360)
— *Molecular spin dynamics study on the multiple-Q orders in Hubbard models*

UEMURA, Naoki [C class; 5400 (B), 650 (C)] (70)
— *First-principles study of mechanical properties on alloys*
1. First-Principles Study of Generalized Stacking Fault Energy in MgZnY Alloy with Long-Period Stacking-Ordered Structures
N. Uemura, S. Singhaneka, and R. Matsumoto Mater. Trans. **65**, 1080 (2024).
DOI:10.2320/matertrans.MT-M2024056

USUI, Hidetomo [B class; 400 (B), 90 (C)] (182)
— *First principles study on the thermoelectric properties of goniopolar compounds*

VENGAYIL, Krishnan [B class; 500 (B), 0 (C)] (334)
— *Criticality mediated interactions in supercooled liquids*
— *Yielding and aging of colloidal gels*

WAKABAYASHI, Daisuke [B class; 400 (B), 0 (C)] ()
— *Large-scale molecular-dynamics simulation of permanent densification in silica glass with ANN potentials*

WANG, Tianyi [C class; 1200 (B), 0 (C)] ()
— *Explore magnetic properties of transition metal carbide catalysts for nitrogen reduction reaction*

WANG, Yinqiao [C class; 800 (B), 200 (C)] ()
— *Mechanical and thermal properties of hyperuniform glasses*

WATANABE, Hiroshi [E class; 11000 (B), 1050 (C)] (255)
— *Analysis of the many-body effect of red blood cells in flow*
1. Fluctuation of a Bilayer Composed by Amphipathic Molecules
S. Kikuchi and H. Watanabe, J. Phys. Soc. Jpn. **93**, 114601 (2024).
DOI:10.7566/JPSJ.93.114601

2. Structural Changes and Percolation Transition in Networks after Aging Processes
R. Sekikawa and H. Watanabe, J. Phys. Soc. Jpn. **94**, 044004 (2025).
DOI:10.7566/JPSJ.94.044004

Data Repository
Simulation data of the aging process in a network

https://isspns-gitlab.issp.u-tokyo.ac.jp/kaityo256/aging_network_data

WATANABE, Hiroshi [B class; 400 (B), 70 (C)] (244)
— *Theoretical study of BCS-BEC crossover in strongly-correlated electron systems*

WATANABE, Satoshi [C class; 10400 (B), 900 (C)] (45)
— *Analyses on correlation between material properties and atomic structures in complex structures via ab-initio-based methods*
— *Analyses on local properties at complex structures via ab-initio-based methods*

1. The tendency of V segregation in Pd/V(110) and Pd/V(100) surfaces induced by H adsorption
   M. A. Palmero, K. Shimizu, H. Nakanishi, S. Watanabe, and A. A. B. Padama Phys. Scripta **99**, 065933 (2024).
   DOI:10.1088/1402-4896/ad3f88

2. Enhanced ionic conductivity through crystallization of glass-Li_3PS_4 by machine learning molecular dynamics simulations
   K. Shimizu, P. Bahuguna, S. Mori, A. Hayashi, and S. Watanabe J. Phys. Chem. C **128**, 10139-10145 (2024).
   DOI:10.1021/acs.jpcc.4c01076

3. Enthralling anodic protection by molybdate on high-entropy alloy based electrocatalyst for sustainable seawater oxidation
   S. Khatun, K. Shimizu, S. Pal, S. Nandi, S. Watanabe, and P. Roy Small **20**, 2402720 (2024).
   DOI:10.1002/smll.202402720

4. Two-Stage Feature Selection for Machine Learning-aided DFT-based Surface Reactivity Study on Single-Atom Alloys
   V. Z. Ordillo, K. Shimizu, D. B. Putungan, A. B. Santos-Putungan, S. Watanabe, R. L. de Leon, J. D. Ocon, K. E. S. Pilario, and A. A. B. Padama Model. Simul. Mater. Sci. Eng. **32**, 065003 (2024).
   DOI:10.1088/1361-651X/ad53ee

5. First-principles study of charge states effects of nitrogen vacancies on phonon properties in III-nitride semiconductors
   Y. Dou, K. Shimizu, H. Fujioka, and S. Watanabe Comput. Mater. Sci. **244**, 113264 (2024).
   DOI:10.1016/j.commatsci.2024.113264

6. Uncovering the Dynamics of Li–Au Alloying and Li Nucleation at the Au/LiPON Interface with In Situ Z Contrast and Surface Roughness Contrast Imaging via Scanning Electron Microscopy
   M. Motoyama, K. Shimizu, T. Kimura, T. Yamamoto, S. Watanabe, and Y. Iriyama JACS Au **4**, 4700-4714 (2024).
   DOI:10.1021/jacsau.4c00530

7. Investigating electronic properties of defective WS_2 thin films via neural network potential-aided first-principles study
   R. Otsuka, K. Shimizu, H. Wakabayashi and S. Watanabe Appl. Phys. Express **17**, 115501 (2024).
   DOI:10.35848/1882-0786/ad8b0c

8. Machine learning and density functional theory-based analysis of the surface reactivity of high entropy alloys: The case of H atom adsorption on CoCuFeMnNi
   A. A. B. Padama, M. A. Palmero, K. Shimizu, T. Chookajorn, and S. Watanabe Comput. Mater. Sci. **247**, 113480 (2025).
   DOI:10.1016/j.commatsci.2024.113480

9. Machine-learning potential for phonon transport in AlN with defects in multiple charge states
Y. Dou, K. Shimizu, J. Carrete, H. Fujioka, and S. Watanabe Phys. Rev. Mater. **9**, 034601 (2025).
DOI:10.1103/PhysRevMaterials.9.034601

10. Dimensionality-Induced Transition from Degenerate to Nondegenerate States in Nb-Doped WSe_2
K. Kanahashi, I. Tanaka, T. Nishimura, K. Aso, A. K. A. Lu, S. Morito, L. Chen, T. Kakeya, S. Watanabe, Y. Oshima, Y. Yamada-Takamura, K. Ueno, A. Azizi, and K. Nagashio ACS Nano **19**, 10244-10254 (2025).
DOI:10.1021/acsnano.4c17660

11. Construction of machine learning potentials toward the exploration of alloy cluster catalysts
K. Miyamoto, K. Shimizu, A. K. A. Lu, and S. Watanabe e-J. Surf. Sci. Nanotechnol., in press

12. Representing Born effective charges with equivariant graph convolutional neural networks
A. Kutana, K. Shimizu, S. Watanabe, and R, Asahi Sci. Rep., submitted.

13. Charge States of Ions around Σ5(310)/[001] Grain Boundary in Cubic-ZrO_2 Revealed by First-Principles Calculations
S. Arai, K. Shimizu, A. K. A. Lu, H. Masuda, H. Yoshida, and S. Watanabe e-J. Surf. Sci. Nanotechnol., submitted.

YAMADA, Atsuo [C class; 2600 (B), 400 (C)] (114)
— Exploration of novel rechargeable battery materials using first-principles and molecular dynamics calculations

1. Electrochemical Proton Intercalation Properties of Bronze-Type Vanadium Dioxide in Nonaqueous Protic Electrolyte
S. Park, S. Nishimura, A. Kitada, A. Yamada ACS Applied Energy Materials **7**, 4347 (2024).
DOI:10.1021/acsaem.4c00139

2. Sequential Structural Evolution Triggered by O — O Dimerization in Oxygen-Redox Reactions
X. Shi, K. Kawai, M. Okubo, A. Yamada, Advanced Energy Materials **15**, 2405714 (2025).
DOI:10.1002/aenm.202405714

YAMADA, Atsushi [C class; 1000 (B), 300 (C)] (234)
— A study of superconductivity and magnetism of strongly correrated electron systems using Hubbard model.

YAMADA, Masahiko [C class; 1400 (B), 350 (C)] (366)
— Large-scale calculation with a flux insertion for SU(N)-symmetric DMRG

YAMAGUCHI, Naoya [C class; 1600 (B), 450 (C)] (131)
— Development of Fast Calculation Codes of Berry Phases in First-principles Calculations and its Application to Energy Conversion Materials

1. First-Principles study on proton transfer in triazole molecules
K. Yakin, N. Yamaguchi, T. Nakajima, M. Mizuno, and F. Ishii Chem. Phys. Lett. **856**, 141582
DOI:10.1016/j.cplett.2024.141582

2. Effect of poly(acrylic acid) on proton transfer in triazole molecules: a first-principles study
K. Yakin, N. Yamaguchi, M. Mizuno, and F. Ishii Sci. Rep. Kanazawa Univ. **67**, 69

3. Dirac Electrons in Graphene Flakes
W. Amalia, N. Yamaguchi, S. Yunitasari, and F. Ishii J. Phys. Soc. Jpn. **93**, 104707

DOI:10.7566/jpsj.93.104707

YAMAJI, Youhei [E class; 6000 (B), 800 (C)] (217)
— *Massively parallel variational Monte Carlo method augmented by non-Markovian Monte Carlo and artificial neural networks*

1. Moiré superlattices of antimonene on a Bi(111) substrate with van Hove singularity and Rashba-type spin polarization
   T. Nakamura, Y. Chen, R. Nemoto, W. Qian, Y. Fukushima, K. Kawaguchi, R. Mori, T. Kondo, Y. Yamaji, S. Tsuda, K. Yaji, and T. Uchihashi Communications Materials **5**, 167 (2024).
   DOI:10.1038/s43246-024-00615-z

2. Self-Energy Spectroscopy and Artificial Neural Network
   Y. Yamaji J. Phys. Soc. Jpn. **94**, 031005 (2025).
   DOI:10.7566/JPSJ.94.031005

YAMAMOTO, Go [C class; 7600 (B), 800 (C)] (260)
— *Designing MWCNT Fiber Structures for High Mechanical Performance Composites*
— *Machine learning-assisted high-throughput MD simulation on structure-mechanical property relationships in carbon nanotube yarns*

YAMAMOTO, Tsuyoshi [D class; 450 (B), 0 (C)] (344)
— *Quantum heat flow in a dissipative qubit under continuous quantum measurement*

1. Energy exchange and fluctuations between a dissipative qubit and a monitor under continuous measurement and feedback
   T. Yamamoto, and Y. Tokura SciPost Phys. Core **8**, 016 (2025).
   DOI:10.21468/SciPostPhysCore.8.1.016

Data Repository
Numerical dataset for quantum trajectory simulations of a dissipative qubit under continuous measurement and feedback
https://zenodo.org/records/14252485
DOI:10.5281/zenodo.14252485

YAMASHITA, Tomoki [C class; 2400 (B), 350 (C)] (118)
— *Materials Development by Crystal Structure Prediction and First-principles Calculations*

1. Crystal structure prediction of $Li_{4x}Mg_{2(1-x)}P_2O_7$ by first-principles calculations
   T. Sato, T. Otani, S. Namamori, F. Utsuno, T. Honma, and T. Yamashita Jpn. J. Appl. Phys. **63**, 075503 (2024).
   DOI:10.35848/1347-4065/ad531d

YAMAUCHI, Kunihiko [C class; 3200 (B), 350 (C)] (109)
— *Understanding of spin-splitting phenomena in altermagnets*

1. Wide-range thermal conductivity modulation based on protonated nickelate perovskite oxides
   Hao-Bo Li, Zhiping Bian, Mitsuki Yoshimura, Kohei Shimoyama, Chengchao Zhong, Keiji Shimoda, Azusa N. Hattori, Kunihiko Yamauchi, Ikutaro Hamada, Hiromichi Ohta, and Hidekazu Tanaka, Applied Physic Letter **124**, 191901 (2024).
   DOI:10.1063/5.0201268

2. Observation of edge states derived from topological helix chains
   K. Nakayama, A. Tokuyama, K. Yamauchi, A. Moriya, T. Kato, K. Sugawara, S. Souma, M. Kitamura, K. Horiba, H. Kumigashira, T. Oguchi, T. Takahashi, K. Segawa, and T. Sato Nature

631, 54 (2024).
DOI:doi.org/10.1038/s41586-024-07484-z

3. Indication of exchange interaction induced spin splitting in unoccupied electronic states of the high-TC ferromagnet (Cr0.35Sb0.65)2Te3
C. W. Chuang, Y. Nakata, K. Hori, S. Gupta, F. M. F. de Groot, A. Fujimori, T. P. T. Nguyen, K. Yamauchi, I. Rajput, A. Lakhani, F.-H. Chang, H.-J. Lin, C.-T. Chen, F. Matsukura, S. Souma, T. Takahashi, T. Sato, and A. Chainani Phys. Rev. B 109, 195134 (2024).
DOI:10.1103/PhysRevB.109.195134

4. Isotope-dependent site occupation of hydrogen in epitaxial titanium hydride nanofilms
T. Ozawa, Y. Sugisawa, Y. Komatsu, R. Shimizu, T. Hitosugi, D. Sekiba, K. Yamauchi, I. Hamada, and K. Fukutani Nat. Commun. 15, 9558 (2024).
DOI:10.1038/s41467-024-53838-6

Data Repository
Isotope-dependent site occupation of hydrogen in epitaxial titanium hydride nanofilms
https://archive.materialscloud.org/record/2024.168
DOI:10.24435/materialscloud:je-ev

YANAGISAWA, Susumu [C class; 6800 (B), 0 (C)] ()
— *First-principles bandstructure calculation with the electron-phonon interaction of organic semiconductor crystals*
— *First-principles study on the electron-phonon coupling in organic semiconductors*

YANAGISAWA, Takashi [B class; 800 (B), 150 (C)] (235)
— *Optimized variational Monte Carlo study of high-temperature superconductivity of strongly correlated electrons*
— *Study of strongly correlated many-body problem based on the optimization quantum variational Monte Carlo method*

1. Strongly Correlated Electrons and High Temperature Superconductivity
T. Yanagisawa High-Temperature Materials 1, 10004 (2024).
DOI:10.35534/htm.2024.10004

2. Superconductivity and Inhomogeneous charge-ordered state in the two-dimensional Hubbard model
T. Yanagisawa preprint

YASUDA, Chitoshi [B,C class; 2600 (B), 70 (C)] (290, 291)
— *Effects of deficit on quantum spin systems*
— *Magnetism in the multiple-spin exchange model on a honeycomb lattice*

1. Classical Ground-State Phase Diagram of the Multiple-Spin Exchange Model on a Honeycomb Lattice
C. Yasuda and Y. Chibana submitted to J. Phys. Soc. Jpn.

YASUHARA, Sou [C class; 5200 (B), 0 (C)] (76, 77)
— *Exploration of Stable Structure in K2NdTa5O15 using First-Principles Phonon Calculations*
— *Investigation of atomic displacement mechanism during a polarization switching in LiGaO2*

YOKO, Akira [C class; 2600 (B), 350 (C)] (115)
— *Distortion of ultrasmall metal oxides and their electronic state*

1. Nonequilibrium Process for Doping Under Continuous-Flow Hydrothermal Synthesis of Cerium Oxide-Based Nanoparticles

Yoko, A., Han, C., Sakonaka, A., Seong, G., Tomai, T., Ohara, S., Adschiri, T. Precision Chemistry, (2025).
DOI:10.1021/prechem.5c00004

YOKOI, Tatsuya [C class; 2800 (B), 0 (C)] ()
— *Hierarchical machine-learning model for accurately predicting thermal and electronic properties of grain boundaries in compound semiconductors*

YOSHIMI, Kazuyoshi [C class; 2000 (B), 200 (C)] (232)
— *Ab-initio analysis of pressure-induced quantum phase transitions in molecular materials*

1. Combined x-ray diffraction, electrical resistivity, and ab initio study of $(TMTTF)_2PF_6$ under pressure
   Miho Itoi, Kazuyoshi Yoshimi, Hanming Ma, Takahiro Misawa, Takao Tsumuraya, Dilip Bhoi, Tokutaro Komatsu, Hatsumi Mori, Yoshiya Uwatoko, Hitoshi Seo Phys. Rev. Research **6**, 043308.
   DOI:10.1103/PhysRevResearch.6.043308

2. Pressure-induced topological changes in Fermi surface of two-dimensional molecular conductor
   T. Kobayashi, K. Yoshimi, H. Ma, S. Sekine, H. Taniguchi, N. Matsunaga, A. Kawamoto, Y. Uwatoko Phys. Rev. Materials **9**, L021801 (2025).
   DOI:10.1103/PhysRevMaterials.9.L021801

Data Repository
Dataset for Ab initio study of TMTTF2PF6 under pressure: implications to the unified phase diagram
https://isspns-gitlab.issp.u-tokyo.ac.jp/k-yoshimi/tmttfpf6-pdep
Dataset for Pressure-Induced Topological Changes in the Fermi Surface of the Two-Dimensional Molecular Conductor
https://isspns-gitlab.issp.u-tokyo.ac.jp/k-yoshimi/betap-ET2ICl2

YOSHIOKA, Hironori [C class; 1000 (B), 50 (C)] (154)
— *Calculation of electronic states for improving characteristics at the channel interface of power MOSFETs*

YUAN, Jiaxing [C class; 600 (B), 350 (C)] ()
— *Key roles of hydrodynamic interactions on coil-globule transition of polyelectrolytes*

YUHARA, Junji [B class; 400 (B), 90 (C)] (172)
— *Structural analysis of oxide quasicrystal thin films*

1. Schematic structural analysis of honeycomb structure ultrathin Ce-Ti-O films on Pt(111) using photoelectron holography and ab initio calculation
   X. Li, S. Yamada, Y. Yamada, M. Yoshida, Y. Hashimoto, T. Matsushita, W. Ma, E. Gaudry, and J. Yuhara J. Phys. Chem. C 128, 20238 (2024).
   DOI:10.1021/acs.jpcc.4c05269

ZHANG, Di [C class; 1400 (B), 0 (C)] (145)
— *Spin Promotion Effect in Magnetic Catalysis: Exploring High-Performance Metal-Nitrogen-Carbon Catalysts under External Magnetic Fields*

1. The potential of zero charge and solvation effects on single-atom MNC catalysts for oxygen electrocatalysis
   Di Zhang, Hao Li, Journal of Materials Chemistry A, 12, 23, 13742-13750 (2024).
   DOI:10.1039/D4TA02285H

2. Chromium Promotes Phase Transformation to Active Oxyhydroxide for Efficient Oxygen Evolu-

tion
Yong Wang, Sijia Liu, Yunpu Qin, Yongzhi Zhao, Luan Liu, Di Zhang, Jianfang Liu, Yadong Liu, Aimin Chu, Haoyang Wu, Baorui Jia, Xuanhui Qu, Hao Li, Mingli Qin, ACS Catalysis 14, 18, 13759-13767 (2024).
DOI:10.1021/acscatal.4c03974

3. Mapping degradation of ironnitrogencarbon heterogeneous molecular catalysts with electron-donating/withdrawing substituents
Fangzhou Liu, Di Zhang, Fangxin She, Zixun Yu, Leo Lai, Hao Li, Li Wei, Yuan Chen, ACS Catalysis, 14, 12, 9176-9187 (2024).
DOI:10.1021/acscatal.4c01752

4. Spin Manipulation of Heterogeneous Molecular Electrocatalysts by an Integrated Magnetic Field for Efficient Oxygen Redox Reactions
Zixun Yu, Di Zhang, Yangyang Wang, Fangzhou Liu, Fangxin She, Jiaxiang Chen, Yuefeng Zhang, Ruijie Wang, Zhiyuan Zeng, Li Song, Yuan Chen, Hao Li, Li Wei, Advanced Materials, 36, 45, 2408461 (2024).
DOI:10.1002/adma.202408461

5. Carbon-anchoring synthesis of Pt1Ni1@Pt/C core-shell catalysts for stable oxygen reduction reaction
Jialin Cui, Di Zhang, Zhongliang Liu, Congcong Li, Tingting Zhang, Shixin Yin, Yiting Song, Hao Li, Huihui Li, Chunzhong Li, Nature Communications, 15, 1, 9458 (2024).
DOI:10.1038/s41467-024-53808-y

6. Unraveling the Complexity of Divalent Hydride Electrolytes in Solid - State Batteries via a Data - Driven Framework with Large Language Model
Qian Wang, Fangling Yang, Yuhang Wang, Di Zhang, Ryuhei Sato, Linda Zhang, Eric Jianfeng Cheng, Yigang Yan, Yungui Chen, Kazuaki Kisu, Shin-ichi Orimo, Hao Li, Angewandte Chemie International Edition, e202506573 (2025).
DOI:10.1002/anie.202506573

7. Data - Driven Accelerated Discovery Coupled with Precise Synthesis of Single - Atom Catalysts for Robust and Efficient Water Purification
Keng-Qiang Zhong, Fu-Yun Yu, Di Zhang, Zheng-Hao Li, Dong-Hua Xie, Ting-Ting Li, Yun Zhang, Li Yuan, Hao Li, Zhen-Yu Wu, Guo-Ping Sheng, Angewandte Chemie International Edition, e202500004 (2025).
DOI:10.1002/anie.202500004

8. Why Do Weak-Binding MNC Single-Atom Catalysts Possess Anomalously High Oxygen Reduction Activity?
Di Zhang, Fangxin She, Jiaxiang Chen, Li Wei, Hao Li, Journal of the American Chemical Society, 147, 7, 60766086 (2025).
DOI:10.1021/jacs.4c16733

9. Divergent Activity Shifts of Tin - Based Catalysts for Electrochemical CO2 Reduction: pH - Dependent Behavior of Single - Atom Versus Polyatomic Structures
Yuhang Wang, Di Zhang, Bin Sun, Xue Jia, Linda Zhang, Hefeng Cheng, Jun Fan, Hao Li, Angewandte Chemie International Edition, 64, 8, e202418228 (2025).
DOI:10.1002/anie.202418228

10. Surface Charge Transfer Enhanced Cobalt - Phthalocyanine Crystals for Efficient CO2 - to - CO Electroreduction with Large Current Density Exceeding 1000 mA cm − 2
Tengyi Liu, Di Zhang, Yutaro Hirai, Koju Ito, Kosuke Ishibashi, Naoto Todoroki, Yasutaka Matsuo, Junya Yoshida, Shimpei Ono, Hao Li, Hiroshi Yabu, Advanced Science, 2501459 (2025).

DOI:10.1002/advs.202501459

ZHOU, Zizhen [D class; 10000 (B), 500 (C)] ()
— *Research on Improving Solid-State Battery Performance through Doped LiNbO3 Modification*

○ A class

Since this class is for trial use, research reports are not required.
When other classes are also used, their publications are shown in the list of B–E classes.
Then, the pages of their reports and publications are given in ( ).

AKUTSU, Hiroki [A class; 100 (B), 50 (C)] ()
— *Band structural calculations of organic conductors*

HAN, Jihae [A class; 100 (B), 50 (C)] ()
— *Reductive decomposition mechanism of fluorine-containing solvent at the electrode/electrolyte interface of lithium sulfur batteries by first-principles calculations*

KANEKO, Masashi [A class; 100 (B), 50 (C)] ()
— *Correlation between nuclear decay and electronic orbitals in actinide compounds using density functional theory calculations*

KAWAMURA, Taira [A class; 100 (B), 50 (C)] (333, 397)
— *Spatiotemporal dynamics of a superconducting order parameter in a nonequilibrium superconducting wire*

KIKUCHI, Shuta [A class; 100 (B), 50 (C)] ()
— *Analysis of the methods for improving the performance of Ising machines*

KINEFUCHI, Ikuya [A class; 100 (B), 50 (C)] ()
— *Preliminary study on gas separation mechanisms in facilitated transport membranes*

KITOH, Hirotaka [A class; 100 (B), 50 (C)] ()
— *Electronic Structure Calculations of Organic Solar Cell Materials*

1. Carrier Mobility and Luminescence Properties of a One-Step Synthesized π-Extended Diketopyrrolopyrrole Derivative
   T. Nishiyama, T. Yamaoka, K. Nakajima, S. Nakajima, Z. L. Goo, R. Akiyoshi, H. Kitoh-Nishioka, S. Tanaka, K. Sugimoto, D. Tanaka, and T. Okubo ACS Omega **10**, 11334 (2025).
   DOI:10.1021/acsomega.4c11150

KITOU, Shunsuke [A class; 100 (B), 50 (C)] ()
— *Analysis of short-range order in pyrochlore-type compounds using X-ray diffuse scattering data*

KOSHOJI, Ryotaro [A class; 100 (B), 50 (C)] (301, 397)
— *Mathematical Crystal Chemistry*

KUDO, Koji [A class; 100 (B), 50 (C)] ()
— *Topological phases in quantum Hall superconductor hybrids*

KUSANO, Akane [A class; 100 (B), 50 (C)] ()
— *Theoretical study on the structure and stability of new carbon allotropes*
— *Fundamental Materials Informatics Research on Binary Systems of Materials*

MIWA, Kazutoshi [A class; 100 (B), 50 (C)] ()
— *Theoretical prediction of thermal conductivity of hydrogen storage materials*

MURAMATSU, Mayu [A class; 100 (B), 50 (C)] ()
— *Development of a MD-FEM Coupling Analysis Method*

MURAOKA, Azusa [A class; 100 (B), 50 (C)] ()
— *Theoretical Study on Defect Structure of Sn/Ge Double Perovskite Solar Cells Using First-Principles Calculations*

ODA, Masato [A class; 100 (B), 50 (C)] (410)
— *Vibrational mode analysis of GaN crystals containing a large size of defects*

OSADA, Wataru [A class; 100 (B), 50 (C)] ()
— *The surface electronic state and adsorption property of the Be-Cu alloy*

SATO, Takeshi [A class; 100 (B), 50 (C)] (332, 418)
— *A molecular simulation study for dynamics of polyelectrolyte solutions*

SATO, Yusuke [A class; 100 (B), 50 (C)] ()
— *Development of the analysis programs for investigating the photoemission angular distribution*

SUMIYA, Yosuke [A class; 100 (B), 50 (C)] (422)
— *Elucidation of adhesion mechanism based on first principle calculations*

TADA, Yasuhiro [A class; 100 (B), 50 (C)] ()
— *Study of spin liquids under external fields*

TATSUMI, Toshinobu [A class; 100 (B), 50 (C)] ()
— *Theoretical study on molecular adsorption on metal catalyst surface*

UMEBAYASHI, Yasuhiro [A class; 100 (B), 50 (C)] ()
— *All-atom molecular dynamics simulation of the interaction between the cathode and the lithium metal anode and electrolytes for lithium sulfur batteries*

WANG, Jinxin [A class; 100 (B), 50 (C)] ()
— *Development of an MP-PIC-based solver for 3D circulating fluidized bed full-loop analyses*

YING, Chen [A class; 100 (B), 50 (C)] ()
— *Exploring new materials with noval properties using first-principles approaches combing machine learning*

YUHARA, Junji [A class; 100 (B), 50 (C)] (172, 432)
— *Structural analysis of oxide quasicrystal thin films*

□ SCCMS Projects

FUKUSHIMA, Tetsuya [2000 (B), 200 (C)] (371)
— *High-throughput calculations for magnetic materials with configurational and structural disorders*

1. Optimizing the composition of (Ce,La)(Co,Fe)5 for permanent magnet applications using density functional theory
   H. Okumura, T. Fukushima, T. Fukazawa, T. Miyake, H. Akai, and M. Ogura Journal of Physics: Condensed Matter **37**, 015802 (2024).
   DOI:10.1088/1361-648X/ad80f0

MATUBAYASI, Nobuyuki [2000 (B), 200 (C)] (373)
— *All-atom model calculations of the solubility of artificial polypeptides in solvents and factors important for their dissolution*

1. Solvent-Environment Dependence of the Excess Chemical Potential and Its Computation Scheme Formulated through Error Minimization
   Stefan Herv-Hansen, Kazuya Okita, Kento Kasahara, and Nobuyuki Matubayasi J. Chem. Theory Comput. **21**, 1064-1077 (2025).
   DOI:10.1021/acs.jctc.4c01000

2. Development of a force field for ATP how charge scaling controls self-association
   Tuan Minh Do, Nobuyuki Matubayasi, and Dominik Horinek Phys. Chem. Chem. Phys. **27**, 6325-6333 (2025).
   DOI:10.1039/d4cp04270k

MISAWA, Takahiro [4000 (B), 400 (C)] (368)
— *Estimation of Hamiltonians of quantum magnets using Bayes optimization*

SHIMAZAKI, Tomomi [4000 (B), 100 (C)] (370)
— *Theoretical study on proton behavior in fuel cell material based on first-principles method*Theoretical study on proton transfer in fuel cell material based on first-principles method with nuclear quantum effect

1. A theoretical study of the molecular passivation of p-/n-type defects on tin- and germanium-mixed perovskite surfaces using Lewis base/acid
   Emi Kino, Makito Takagi, Takumi Naito, Masanori Tachikawa, Koichi Yamashita, Tomomi Shimazaki Phys. Chem. Chem. Phys. **27**, 7429 (2025).
   DOI:10.1039/d4cp03817g

2. One-dimensional C60 arrays in noncovalent benzidine networks
   Takatsugu Wakahara, Chika Hirata, Dorra Mahdaoui, Kazuko Fujii, Yoshitaka Matsushita, Osamu Ito, Makito Takagi, Tomomi Shimazaki, Masanori Tachikawa, Shinjiro Yagyu, Yubin Liu, Yoshiyuki Nakajima, Takuro Nagai, Kazuhito Tsukagoshi Carbon **233**, 119838 (2025).
   DOI:10.1016/j.carbon.2024.119838

3. Theoretical study of short-range exchange interaction based on semiconductor dielectric function model toward time-dependent dielectric density functional theory
   Tomomi Shimazaki, Masanori Tachikawa J. Chem. Phys. **829**, 140744 (2024).
   DOI:10.1039/d4cp04656k

4. Theoretical and machine learning models for reaction-barrier predictions: acrylate and methacrylate radical reactions
   Makito Takagi, Tomomi Shimazaki, Osamu Kobayashi, Takayoshi Ishimoto, Masanori Tachikawa

Phys. Chem. Chem. Phys **27**, 1777 (2024).
DOI:10.1021/acs.jpcc.4c01525

5. Theoretical Study on Rate-Determining Reactions for Constructing Self-Assembling Molecular Cages Controlled by Distorted Ditopic Ligands
Yu Ichinose, Osamu Kobayashi, Tomomi Shimazaki, Shuichi Hiraoka, Masanori Tachikawa J. Phys. Chem. C **128**, 10643 (2024).
DOI:10.1021/acs.jpcc.4c01525

TADANO, Terumasa [2000 (B), 200 (C)] (375)
— *Development of functional Heusler alloys by first-principles calculations and data-driven approaches*

Data Repository
DXMag Heusler database
https://www.nims.go.jp/group/spintheory/database/

5 THESES

□ Doctor Theses

1. **AMAMIZU, Naoka**
   Theoretical Study on Relationship between Open-Shell Electronic State and Electron Conductivity of Single Molecules and Their Aggregates toward Applications to Molecular Devices
   Osaka University, 2025-03

2. **ARTUR, Akatov**
   Electronic structures and their instability analysis in magnetic shape memory alloys Fe_3X (X=Pd, Pt) by quasiparticle self-consistent GW approach
   Kanazawa University, 2025-03

3. **CHIDA, Takumi**
   Green ' s function approach for computing physical quantities in the framework of the transcorrelated method
   The University of Tokyo, 2025-03

4. **DE MELLO, Matheus**
   Impact of charge distribution on the stability of ferroelectric nematic liquid crystals
   Kyoto University, 2025-03

5. **DING, Mingda**
   Investigation on control of graphene interlayer interaction by nanospacer insertion
   Osaka University, 2025-03

6. **DOU, Ying**
   Theoretical analysis of phonon behavior in group-III nitride device structures
   The University of Tokyo, 2025-03

7. **ENRIQUEZ, John Isaac G.**
   Quantum Engineering Design of Diamond Surfaces: Surface Facet Dependence in Oxidation and Thermal Degradation and Effectiveness of Dangling Bond Saturation on Graphitization Suppression and Control
   Osaka University, 2024-07

8. **FURUTA, Tatsuhiro**
   Development and application of machine learning methods for time series data in materials science: Analysis of fluorescence time series data of quantum dots and fluorescently modified DNA using hidden Markov models
   Kyushu Institute of Technology, 2025-03

9. **GUO, Rulei**
   Investigation of thermal conductance of complex heterogeneous interfaces using optical pump probe method
   The University of Tokyo, 2025-03

10. **HARA, Keisuke**
    Dynamics between transition metal oxide/dichalcogenide and adsorbed molecules
    Chiba University, 2024-03

11. **HIRATA, Koichi**
    Branching Structure and Mechanical Properties of Colloidal Gel Networks
    Kyoto University, 2025-03

12. **IWASHITA, Wataru**
Theory of friction in macroscopic systems based on continuum analysis
Osaka University, 2025-03

13. **KAKIZAWA, Fumiya**
Numerical approaches to many-body problems in condensed matter physics
Saitama University, 2025-03

14. **KOSHOJI, Ryotaro**
Crystal structure prediction based on space-filling principles
The University of Tokyo, 2024-03

15. **LI, Junhuan**
Fundamental study on finite-size graphene-based materials with unique electronic structures toward catalyst-assisted microfabrication of semiconductor surfaces
Osaka University, 2024-09

16. **LI, Xu**
Growth and elucidation of the structure of X-Ti-O (X = Ba, Ce, Yb) ultra-thin films on Pt(111)
Nagoya University, 2025-03

17. **LIANG, Shaoji**
Fabrication of equiaxed HCP Multi-Principal Element Alloys and elucidation of their deformation mechanisms
The University of Tokyo, 2025-03

18. **LUSTINEC, Jakub**
Study on first-principles electronic structures of the magnetic shape memory Heusler alloys by quasiparticle self-consistent GW method
Kanazawa University, 2024-09

19. **LYU, Xinliang**
Three-Dimensional Real Space Renormalization Group using Tensor-Network Reformulation
The University of Tokyo, 2024-09

20. **MAJUMDER, Rinku**
Study on the nanotwin boundary migration in the modulated martensite phases of magnetic shape memory alloy from first-principles
Kanazawa University, 2024-09

21. **MATSUTANI, Kenta**
Investigation of intermediate-range order in GeO_2 glass through computational simulations
Yamagata University, 2025-03

22. **MUGITA, Daigo**
Structural relaxation and development of local structure analysis methods for dense hard disk (triangle) systems using non-reversible Monte Carlo
Nagoya Institute of Technology, 2025-03

23. **NAGAHASHI, Tomoya**
Theoretical Studies on Growth Processes and Electronic Properties of SiN Used for Charge Trapping Layer of NAND Flash Memories
Nagoya Universituy, 2025-03

24. **NEGAMI, Masahiro**
Durability improvement of thermal barrier coatings for industrial gas turbine
The University of Tokyo, 2024-09

25. **NOZAKI, Misa**
Theoretical studies on photoemission from organic materials
Chiba University, 2024-03

26. **SEO, Insung**
Magnetic properties of rare-earth magnet compounds studied from first principles
Tokyo Institute of Technology, 2024-09

27. **YOSHIDA, Akira**
Thermodynamic characterization of small-scale mixtures and nonequilibrium phase coexistence systems
Ibaraki University, 2024-03

28. **YOSHIMURA, Masataka**
Computational analysis of protein-ligand interactions
The University of Tokyo, 2025-03

□ Master Theses

1. **ABE, Eijyu**
   Magnetization process of a kagome antiferromagnet with $\{Y_3Cu_9(OH)_{19}Cl_8\}$-type distortion
   Tokyo University of Science, 2025-03

2. **ASANO, Rena**
   Development of an extension program for photoelectron spectroscopy analysis to periodic materials
   Chiba University, 2025-03

3. **ASHITAKA, Haruna**
   Anion species dependence of liquid Madelung potentials
   The University of Tokyo, 2025-03

4. **CHIBA, Isana**
   First-principles calculation of TiO_2 surface
   Iwate University, 2025-03

5. **ENDO, Ryusuke**
   First-principles study on electronic structure of FePd/2D material interface
   Kobe University, 2025-03

6. **FUJIMOTO, Itsuki**
   First-principles magnetic anisotropy calculation in the interface PtCoO/ZnO between ferromagnetic metal and ferroelectric semiconductor
   Kanazawa University, 2025-03

7. **FUNAKI, Nahoto**
   First-principles analysis for effect of NO annealing on mobility of SiC MOS interface
   Kobe University, 2025-03

8. **GU, Yuhan**
   Development of stretchable electret material for energy harvesting based on quantum chemistry
   The University of Tokyo, 2024-09

9. **HASHIMOTO, Kazuki**
   Magnetocrystalline anisotropy of permanent-magnet compounds
   Institute of Science Tokyo, 2025-03

10. **HASHIMOTO, Kota**
    A method for free-energy calculations with thermal expansion
    Institute of Science Tokyo, 2025-03

11. **HASHIMOTO, Masaru**
    Numerical Study on the Magnetization Process of the Distorted Diamond Spin Chain
    University of Hyogo, 2025-03

12. **HASHIMOTO, Taichi**
    First-principles study on electron-transport properties in arsenene fluoride nanoloads
    Hokkaido University, 2025-03

13. **HORIGANE, Koki**
    First-principles calculations of tunnel magnetoresistance effect in lattice-matched magnetic tunnel junction

Keio University, 2025-03

14. **IMAMURA, Ryo**
First-principles study of intrinsic hBN island nucleated during CVD initial growth on Cu(111)
Shimane University, 2025-03

15. **INOUE, Shinya**
Theoretical design of a fluorescence intensity-based ligand sensor protein
The University of Tokyo, 2025-03

16. **ITOKAZU, Shoichiro**
Microscopic theory for ferromagnetic transition in heavy fermion compound $CeRh_6Ge_4$
Okayama University, 2025-03

17. **IWAKI, Kota**
First-principles study on carrier mobility in XC_6 (X=Si,Ge,Sn,Pb) nanoribbons
Hokkaido University, 2025-03

18. **IWAMOTO, Yuya**
Theoretical design of a superlattice superconductor utilizing incipient band
Tottori University, 2025-03

19. **IWATA, Taiga**
Theoretical analysis of electrolyte decomposition process on lithium metal surface
The University of Tokyo, 2025-03

20. **JO, Hayate**
Free energies of β Ti-Al evaluated by first-principles cluster-expansion method
Institute of Science Tokyo, 2025-03

21. **KANEMASU, Ikumi**
Ab initio Molecular Dynamics Study of the Deformation Properties and Healing Mechanisms in Calcium Silicate Hydrate
Hiroshima Institute of Technology, 2025-03

22. **KASAI, Shoya**
Numerical Study of Superstructure Formation and Non-equilibrium Dynamics in Topological Spin Knots
The University of Tokyo, 2025-03

23. **KATO, Keita**
First-principles Calculations of Defect Formation Energy for $Cu_2Sn_{1-x}Ge_xS_3$
Nagaoka University of Technology, 2025-03

24. **KATO, Sae**
Theoretical design of protein folding pathways based on a statistical mechanical model
The University of Tokyo, 2025-03

25. **KIKYO, Haruya**
First-principles electron-transport property simulation of C_nN_m/graphene heterostacked structures under stress
Hokkaido University, 2025-03

26. **KITAGAWA, Aki**
Theoretical and Experimental Investigation of the Role of Surface Defect Sites in the Photocatal-

ysis
Chiba University, 2024-03

27. **KITAGAWA, Ryo**
Self-organized spatial inhomogeneity and final condensed states in self-propelled quasi-elastic hard disk systems
Nagoya Institute of Technology, 2025-03

28. **KITAYAMA, Rina**
Theoretical study on the stability of hydrogen impurity in cation-doped α-Al_2O_3
Hokkaido University, 2025-03

29. **KOISO, Hiroki**
Anharmonicity induced by thermal fluctuation and its impact on the thermal expansion of solids
Institute of Science Tokyo, 2025-03

30. **KOMATSU, Kenshin**
Theoretical design of nanographene realizing a 2-dimensional S=3/2 spin system derived from localized zero modes
University of Hyogo, 2025-03

31. **KOYAMADA, Hinata**
Development of a quantitative calculation method for electrode potential shifts
The University of Tokyo, 2025-03

32. **KURITA, Kaoru**
Theoretical design of a novel bilayer nickelate superconductor
Tottori University, 2025-03

33. **LIU, Yuxi**
High-performance Spectral Neighbor Analysis Potential for Al-Al_2O_3-H systems to investigate hydrogen embrittlement
The University of Tokyo, 2025-03

34. **MAKI, Raijyu**
First-Principles study of the formation mechanism of one-dimensional silver ribbons on the Ni(110) surface using the nudged elastic band method
Osaka Metropolitan University, 2025-03

35. **MATIN, Jubayer**
Study on methods to optimize the first-principles computation of phonons in materials with disordered configurations
Tokyo Institute of Technology, 2024-09

36. **MATSUMOTO, Ryo**
Multi-principal effect on phase transformation in TiHfNiPd shape memory alloys
The University of Tokyo, 2025-03

37. **MISU, Akari**
Theoretical study on electrical conduction properties of spiral graphene
Ochanomizu University, 2025-03

38. **MIYAKO, Yuki**
Exploration for stable surface structures and theoretical prediction of band positions for diamond and zinc-blende structures from first-principles lattice-dynamics calculations

Institute of Science Tokyo, 2025-03

39. **MIYAMOTO, Kentaro**
Construction of machine learning potentials toward exploreation of high-entropy alloy cluster catalysts
The University of Tokyo, 2025-03

40. **MIYAZAKI, Kouki**
First-principles electronic structure calculation and carrier density analysis of manganese thin film on sapphire substrate
Kanazawa University, 2025-03

41. **MURABAYASHI, Fumihiro**
Microwave response of edge states in the fractional quantum Hall droplet
The University of Tokyo, 2025-03

42. **NAGAI, Shun**
Prediction of the folding and binding mechanisms of an intrinsically disordered protein using an extended statistical mechanical model
The University of Tokyo, 2025-03

43. **NAKAJIMA, Kento**
Electronic structure calculations of novel p-type semiconductor materials with extended π-conjugated DPP derivatives
Kindai University, 2025-03

44. **NAKAMURA, Kou**
High-throughput molecular dynamics for advanced electrolyte discovery
The University of Tokyo, 2025-03

45. **NAKAMURA, Taisei**
Critical phenomena and network analysis in Vicsek model systems with non-reciprocal interactions
Nagoya Institute of Technology, 2025-03

46. **NAKAMURA, Tenga**
Electronic and optical properties of non-stoichiometric lithium niobates
University of Fukui, 2025-03

47. **NISHIDA, Amane**
confidential
Nara Institute of Science and Technology, 2025-03

48. **NODA, Hinata**
Theoretical study on edge states in MnBi2Te4 thin films
Ochanomizu University, 2025-03

49. **OYUMI, Tomoki**
Development and the Reaction Mechanism of CO2 Photoreduction to Fuels/Resources Using First Row Transition Metal Nanoparticles Supported on ZrO2
Chiba University, 2025-03

50. **SAITO, Ryota**
GNN prediction of cavity-induced hopping motion in deeply supercooled binary hard disk systems
Nagoya Institute of Technology, 2025-03

51. **SEKIKAWA, Ryuho**
Analyses of the aging process in scale-free networks
Keio University, 2025-03

52. **SHIMIZU, Haruki**
Tensor network simulations for non-orientable surfaces
The University of Tokyo, 2025-03

53. **SHIMOKAWA, Hikaru**
Analysis of the adsorption structure and electronic state of DPh-BTBT/Ag based on multiple scattering theory
Chiba University, 2025-03

54. **SUZUKI, Shunsuke**
Series expansion study of magnon spectra in triangular lattice antiferromagnets with interlayer coupling
Tokyo University of Science, 2025-03

55. **TAKAHASHI, Kosuke**
Phonon localization and electron transport control in two-dimensional layered materials
Okayama University, 2025-03

56. **TAMASHIRO, Yoshihito**
Study on Enhancement of Correlation Functions due to Bond Deficit in Antiferromagnets
University of the Ryukyus, 2025-03

57. **TAMURA, Tatsuya**
Analysis of ion transport in tantalum oxide using persistent homology
The University of Tokyo, 2025-03

58. **TANAKA, Iori**
Impact of local structures of silicon grain boundaries on their interfacial thermal resistance investigated using machine learning potential
Osaka University, 2025-03

59. **TANAKA, Junya**
Evaluation for thermal transition temperature of a quantum spin model by machine learning technique
University of Hyogo, 2025-03

60. **TANG, Ruona**
Ti-Al-O ternary phase diagram constructed using machine learning
Tokyo Institute of Technology, 2024-09

61. **TERAMOTO, Shotaro**
Theoretical study of spin-fluctuation and superconductivity in incipient band systems
Tottori University, 2025-03

62. **TOKUYOSHI, Taiki**
Diffusional characteristics and phase transition in dense hard triangle systems using Newtonian Event-Chain Monte Carlo
Nagoya Institute of Technology, 2025-03

63. **TOSAKI, Tomohiro**
Rheological Analysis of Polyelectrolyte Solutions Using Coarse-Grained Molecular Dynamics Sim-

ulations
Kyoto University, 2025-03

64. **WADASHIMA, Shusei**
Numerical study of spin liquid and glass behavior in quantum spin models with all-to-all p-spin interactions
The University of Tokyo, 2025-03

65. **WATARAI, Ryota**
First-principles study on magnetocrystalline anisotropy of Co_2FeSi and Co_3Mn
Institute of Science Tokyo, 2025-03

66. **YAMAI, Shin**
Crystal Structure Prediction of $Li_xCa_{1-x}Cl_{2-x}$ Using Evolutionary Algorithm and Cluster Expansion
Nagaoka University of Technology, 2025-03

67. **YAMAMOTO, Ayumu**
Rheological Analysis of Polymer Blends Using Coarse-Grained Molecular Dynamics Simulations
Kyoto University, 2025-03

68. **YAMAMOTO, Rikuto**
Modulation in electronic states of cleaved topological insulator Bi2Se3 by surface reconstruction
University of Hyogo, 2025-03

69. **YAMAMOTO, Tomiya**
Multi-Objective Generative Adversarial Network for Inorganic Chemical Compositions
Nara Institute of Science and Technology, 2025-03

70. **YAMANAKA, Masayoshi**
First-principles study of goniopolar thermoelectric material $Mg_3(Sb,Bi)_2$
Shimane University, 2025-03

71. **YONEYAMA, Haruki**
Theoretical analysis and derivation of effective model for the ladder type iron-based superconductors
Tottori University, 2025-03

72. **YOSHIDA, Yusaku**
First-principles calculations for the electronic structure of Ca2MnO4: Evaluation of the effect of oxygen octahedral rotation on low-energy properties
Kyushu Institute of Technology, 2025-03

73. **YUKI, Kanae**
First-Principles Molecular Dynamics Study of Ionic Diffusion Mechanism of RbAg4I5
University of the Ryukyus, 2025-03

74. **YUSE, Ryo**
Application of machine learning to incomplete information games about Geister
Keio University, 2025-03